

# **ADVANCES in ROBOTICS, MECHATRONICS and CIRCUITS**

**Proceedings of the 18th International Conference on Circuits  
(part of CSCC '14)**

**Proceedings of the 2014 International Conference on Mechatronics and  
Robotics, Structural Analysis (MEROSTA 2014)**

**Santorini Island, Greece  
July 17-21, 2014**



Cosponsored by the Italian Association of Robotics and Automation

# **ADVANCES in ROBOTICS, MECHATRONICS and CIRCUITS**

**Proceedings of the 18th International Conference on Circuits  
(part of CSCC '14)**

**Proceedings of the 2014 International Conference on Mechatronics and  
Robotics, Structural Analysis (MEROSTA 2014)**

**Santorini Island, Greece  
July 17-21, 2014**

**Copyright © 2014, by the editors**

All the copyright of the present book belongs to the editors. All rights reserved. No part of this publication may be reproduced, stored in a retrieval system, or transmitted in any form or by any means, electronic, mechanical, photocopying, recording, or otherwise, without the prior written permission of the editors.

All papers of the present volume were peer reviewed by no less than two independent reviewers. Acceptance was granted when both reviewers' recommendations were positive.

ISBN: 978-1-61804-242-2

# **ADVANCES in ROBOTICS, MECHATRONICS and CIRCUITS**

**Proceedings of the 18th International Conference on Circuits  
(part of CSCC '14)**

**Proceedings of the 2014 International Conference on Mechatronics and  
Robotics, Structural Analysis (MEROSTA 2014)**

**Santorini Island, Greece  
July 17-21, 2014**



## Organizing Committee

### Editors:

Prof. Nikos Mastorakis, Technical University of Sofia, Bulgaria and HNA, Greece  
Prof. Kleanthis Psarris, The City University of New York, USA  
Prof. George Vachtsevanos, Georgia Institute of Technology, Atlanta, Georgia, USA  
Prof. Philippe Dondon, École Nationale Supérieure d'Électronique, Talence, Cedex, France  
Prof. Valeri Mladenov, Technical University of Sofia, Bulgaria  
Prof. Aida Bulucea, University of Craiova, Craiova, Romania  
Prof. Imre Rudas, Obuda University, Budapest, Hungary  
Prof. Olga Martin. Politehnica University of Bucharest, Romania  
Prof. Bogdan Epureanu, University of Michigan, USA  
Prof. Cho W. Solomon To, University of Nebraska, USA  
Prof. Hyung Hee Cho, Yonsei University and The National Academy of Engineering of Korea, Korea

### Steering Committee:

Prof. Theodore B. Trafalis, University of Oklahoma, USA  
Prof. Charles A. Long, Professor Emeritus, University of Wisconsin, Stevens Point, Wisconsin, USA  
Prof. Maria Isabel García-Planas, Universitat Politècnica de Catalunya, Spain  
Prof. Reinhard Neck, Klagenfurt University, Klagenfurt, Austria  
Prof. Myriam Lazard, Institut Supérieur d'Ingenierie de la Conception, Saint Die, France  
Prof. Zoran Bojkovic, University of Belgrade, Serbia  
Prof. Claudio Talarico, Gonzaga University, Spokane, USA

### International Scientific Committee:

Prof. Lotfi Zadeh (IEEE Fellow, University of Berkeley, USA)  
Prof. Leon Chua (IEEE Fellow, University of Berkeley, USA)  
Prof. Michio Sugeno (RIKEN Brain Science Institute (RIKEN BSI), Japan)  
Prof. Dimitri Bertsekas (IEEE Fellow, MIT, USA)  
Prof. Demetri Terzopoulos (IEEE Fellow, ACM Fellow, UCLA, USA)  
Prof. Georgios B. Giannakis (IEEE Fellow, University of Minnesota, USA)  
Prof. George Vachtsevanos (Georgia Institute of Technology, USA)  
Prof. Abraham Bers (IEEE Fellow, MIT, USA)  
Prof. Brian Barsky (IEEE Fellow, University of Berkeley, USA)  
Prof. Aggelos Katsaggelos (IEEE Fellow, Northwestern University, USA)  
Prof. Josef Sifakis (Turing Award 2007, CNRS/Verimag, France)  
Prof. Hisashi Kobayashi (Princeton University, USA)  
Prof. Kinshuk (Fellow IEEE, Massey Univ. New Zeland),  
Prof. Leonid Kazovsky (Stanford University, USA)  
Prof. Narsingh Deo (IEEE Fellow, ACM Fellow, University of Central Florida, USA)  
Prof. Kamisetty Rao (Fellow IEEE, Univ. of Texas at Arlington, USA)  
Prof. Anastassios Venetsanopoulos (Fellow IEEE, University of Toronto, Canada)  
Prof. Steven Collicott (Purdue University, West Lafayette, IN, USA)  
Prof. Nikolaos Paragios (Ecole Centrale Paris, France)  
Prof. Nikolaos G. Bourbakis (IEEE Fellow, Wright State University, USA)  
Prof. Stamatios Kartalopoulos (IEEE Fellow, University of Oklahoma, USA)  
Prof. Irwin Sandberg (IEEE Fellow, University of Texas at Austin, USA),  
Prof. Michael Sebek (IEEE Fellow, Czech Technical University in Prague, Czech Republic)  
Prof. Hashem Akbari (University of California, Berkeley, USA)  
Prof. Yuriy S. Shmaliy, (IEEE Fellow, The University of Guanajuato, Mexico)  
Prof. Lei Xu (IEEE Fellow, Chinese University of Hong Kong, Hong Kong)  
Prof. Paul E. Dimotakis (California Institute of Technology Pasadena, USA)  
Prof. Martin Pelikan (UMSL, USA)  
Prof. Patrick Wang (MIT, USA)

Prof. Wasfy B Mikhael (IEEE Fellow, University of Central Florida Orlando, USA)  
Prof. Sunil Das (IEEE Fellow, University of Ottawa, Canada)  
Prof. Panos Pardalos (University of Florida, USA)  
Prof. Nikolaos D. Katopodes (University of Michigan, USA)  
Prof. Bimal K. Bose (Life Fellow of IEEE, University of Tennessee, Knoxville, USA)  
Prof. Janusz Kacprzyk (IEEE Fellow, Polish Academy of Sciences, Poland)  
Prof. Sidney Burrus (IEEE Fellow, Rice University, USA)  
Prof. Biswa N. Datta (IEEE Fellow, Northern Illinois University, USA)  
Prof. Mihai Putinar (University of California at Santa Barbara, USA)  
Prof. Wlodzislaw Duch (Nicolaus Copernicus University, Poland)  
Prof. Tadeusz Kaczorek (IEEE Fellow, Warsaw University of Tehcnology, Poland)  
Prof. Michael N. Katehakis (Rutgers, The State University of New Jersey, USA)  
Prof. Pan Agathoklis (Univ. of Victoria, Canada)  
Dr. Subhas C. Misra (Harvard University, USA)  
Prof. Martin van den Toorn (Delft University of Technology, The Netherlands)  
Prof. Malcolm J. Crocker (Distinguished University Prof., Auburn University, USA)  
Prof. Urszula Ledzewicz, Southern Illinois University , USA.  
Prof. Dimitri Kazakos, Dean, (Texas Southern University, USA)  
Prof. Ronald Yager (Iona College, USA)  
Prof. Athanassios Manikas (Imperial College, London, UK)  
Prof. Keith L. Clark (Imperial College, London, UK)  
Prof. Argyris Varonides (Univ. of Scranton, USA)  
Prof. S. Furfari (Direction Generale Energie et Transports, Brussels, EU)  
Prof. Constantin Udriste, University Politehnica of Bucharest , ROMANIA  
Dr. Michelle Luke (Univ. Berkeley, USA)  
Prof. Patrice Brault (Univ. Paris-sud, France)  
Prof. Jim Cunningham (Imperial College London, UK)  
Prof. Philippe Ben-Abdallah (Ecole Polytechnique de l'Universite de Nantes, France)  
Prof. Photios Anninos (Medical School of Thrace, Greece)  
Prof. Ichiro Hagiwara, (Tokyo Institute of Technology, Japan)  
Prof. Andris Buikis (Latvian Academy of Science. Latvia)  
Prof. Akshai Aggarwal (University of Windsor, Canada)  
Prof. George Vachtsevanos (Georgia Institute of Technology, USA)  
Prof. Ulrich Albrecht (Auburn University, USA)  
Prof. Imre J. Rudas (Obuda University, Hungary)  
Prof. Alexey L Sadovski (IEEE Fellow, Texas A&M University, USA)  
Prof. Amedeo Andreotti (University of Naples, Italy)  
Prof. Ryszard S. Choras (University of Technology and Life Sciences Bydgoszcz, Poland)  
Prof. Remi Leandre (Universite de Bourgogne, Dijon, France)  
Prof. Moustapha Diaby (University of Connecticut, USA)  
Prof. Brian McCartin (New York University, USA)  
Prof. Elias C. Aifantis (Aristotle Univ. of Thessaloniki, Greece)  
Prof. Anastasios Lyrantzis (Purdue University, USA)  
Prof. Charles Long (Prof. Emeritus University of Wisconsin, USA)  
Prof. Marvin Goldstein (NASA Glenn Research Center, USA)  
Prof. Costin Cepisca (University POLITEHNICA of Bucharest, Romania)  
Prof. Kleanthis Psarris (University of Texas at San Antonio, USA)  
Prof. Ron Goldman (Rice University, USA)  
Prof. Ioannis A. Kakadiaris (University of Houston, USA)  
Prof. Richard Tapia (Rice University, USA)  
Prof. F.-K. Benra (University of Duisburg-Essen, Germany)  
Prof. Milivoje M. Kostic (Northern Illinois University, USA)  
Prof. Helmut Jaberg (University of Technology Graz, Austria)  
Prof. Ardeshir Anjomani (The University of Texas at Arlington, USA)

Prof. Heinz Ulbrich (Technical University Munich, Germany)  
Prof. Reinhard Leithner (Technical University Braunschweig, Germany)  
Prof. Elbrous M. Jafarov (Istanbul Technical University, Turkey)  
Prof. M. Ehsani (Texas A&M University, USA)  
Prof. Sesh Commuri (University of Oklahoma, USA)  
Prof. Nicolas Galanis (Universite de Sherbrooke, Canada)  
Prof. S. H. Sohrab (Northwestern University, USA)  
Prof. Rui J. P. de Figueiredo (University of California, USA)  
Prof. Valeri Mladenov (Technical University of Sofia, Bulgaria)  
Prof. Hiroshi Sakaki (Meisei University, Tokyo, Japan)  
Prof. Zoran S. Bojkovic (Technical University of Belgrade, Serbia)  
Prof. K. D. Klaes, (Head of the EPS Support Science Team in the MET Division at EUMETSAT, France)  
Prof. Emira Maljevic (Technical University of Belgrade, Serbia)  
Prof. Kazuhiko Tsuda (University of Tsukuba, Tokyo, Japan)  
Prof. Milan Stork (University of West Bohemia , Czech Republic)  
Prof. C. G. Helmis (University of Athens, Greece)  
Prof. Lajos Barna (Budapest University of Technology and Economics, Hungary)  
Prof. Nobuoki Mano (Meisei University, Tokyo, Japan)  
Prof. Nobuo Nakajima (The University of Electro-Communications, Tokyo, Japan)  
Prof. Victor-Emil Neagoe (Polytechnic University of Bucharest, Romania)  
Prof. P. Vanderstraeten (Brussels Institute for Environmental Management, Belgium)  
Prof. Annaliese Bischoff (University of Massachusetts, Amherst, USA)  
Prof. Virgil Tiponut (Politehnica University of Timisoara, Romania)  
Prof. Andrei Kolyshkin (Riga Technical University, Latvia)  
Prof. Fumiaki Imado (Shinshu University, Japan)  
Prof. Sotirios G. Ziavras (New Jersey Institute of Technology, USA)  
Prof. Constantin Volosencu (Politehnica University of Timisoara, Romania)  
Prof. Marc A. Rosen (University of Ontario Institute of Technology, Canada)  
Prof. Thomas M. Gatton (National University, San Diego, USA)  
Prof. Leonardo Pagnotta (University of Calabria, Italy)  
Prof. Yan Wu (Georgia Southern University, USA)  
Prof. Daniel N. Riahi (University of Texas-Pan American, USA)  
Prof. Alexander Grebennikov (Autonomous University of Puebla, Mexico)  
Prof. Bennie F. L. Ward (Baylor University, TX, USA)  
Prof. Guennadi A. Kouzaev (Norwegian University of Science and Technology, Norway)  
Prof. Eugene Kindler (University of Ostrava, Czech Republic)  
Prof. Geoff Skinner (The University of Newcastle, Australia)  
Prof. Hamido Fujita (Iwate Prefectural University(IPU), Japan)  
Prof. Francesco Muzi (University of L'Aquila, Italy)  
Prof. Claudio Rossi (University of Siena, Italy)  
Prof. Sergey B. Leonov (Joint Institute for High Temperature Russian Academy of Science, Russia)  
Prof. Arpad A. Fay (University of Miskolc, Hungary)  
Prof. Lili He (San Jose State University, USA)  
Prof. M. Nasseh Tabrizi (East Carolina University, USA)  
Prof. Alaa Eldin Fahmy (University Of Calgary, Canada)  
Prof. Paul Dan Cristea (University "Politehnica" of Bucharest, Romania)  
Prof. Gh. Pascovici (University of Koeln, Germany)  
Prof. Pier Paolo Delsanto (Politecnico of Torino, Italy)  
Prof. Radu Munteanu (Rector of the Technical University of Cluj-Napoca, Romania)  
Prof. Ioan Dumitrache (Politehnica University of Bucharest, Romania)  
Prof. Miquel Salgot (University of Barcelona, Spain)  
Prof. Amaury A. Caballero (Florida International University, USA)  
Prof. Maria I. Garcia-Planas (Universitat Politecnica de Catalunya, Spain)  
Prof. Petar Popivanov (Bulgarian Academy of Sciences, Bulgaria)

Prof. Alexander Gegov (University of Portsmouth, UK)  
Prof. Lin Feng (Nanyang Technological University, Singapore)  
Prof. Colin Fyfe (University of the West of Scotland, UK)  
Prof. Zhaohui Luo (Univ of London, UK)  
Prof. Wolfgang Wenzel (Institute for Nanotechnology, Germany)  
Prof. Weilian Su (Naval Postgraduate School, USA)  
Prof. Phillip G. Bradford (The University of Alabama, USA)  
Prof. Ray Hefferlin (Southern Adventist University, TN, USA)  
Prof. Gabriella Bogner (University of Miskolc, Hungary)  
Prof. Hamid Abachi (Monash University, Australia)  
Prof. Karlheinz Spindler (Fachhochschule Wiesbaden, Germany)  
Prof. Josef Boercsoek (Universitat Kassel, Germany)  
Prof. Eyad H. Abed (University of Maryland, Maryland, USA)  
Prof. F. Castanie (TeSA, Toulouse, France)  
Prof. Robert K. L. Gay (Nanyang Technological University, Singapore)  
Prof. Andrzej Ordys (Kingston University, UK)  
Prof. Harris Catrakis (Univ of California Irvine, USA)  
Prof. T Bott (The University of Birmingham, UK)  
Prof. T.-W. Lee (Arizona State University, AZ, USA)  
Prof. Le Yi Wang (Wayne State University, Detroit, USA)  
Prof. Oleksander Markovskyy (National Technical University of Ukraine, Ukraine)  
Prof. Suresh P. Sethi (University of Texas at Dallas, USA)  
Prof. Hartmut Hillmer (University of Kassel, Germany)  
Prof. Bram Van Putten (Wageningen University, The Netherlands)  
Prof. Alexander Iomin (Technion - Israel Institute of Technology, Israel)  
Prof. Roberto San Jose (Technical University of Madrid, Spain)  
Prof. Minvydas Ragulskis (Kaunas University of Technology, Lithuania)  
Prof. Arun Kulkarni (The University of Texas at Tyler, USA)  
Prof. Joydeep Mitra (New Mexico State University, USA)  
Prof. Vincenzo Niola (University of Naples Federico II, Italy)  
Prof. Ion Chrysosoverghi (National Technical University of Athens, Greece)  
Prof. Dr. Aydin Akan (Istanbul University, Turkey)  
Prof. Sarka Necasova (Academy of Sciences, Prague, Czech Republic)  
Prof. C. D. Memos (National Technical University of Athens, Greece)  
Prof. S. Y. Chen, (Zhejiang University of Technology, China and University of Hamburg, Germany)  
Prof. Duc Nguyen (Old Dominion University, Norfolk, USA)  
Prof. Tuan Pham (James Cook University, Townsville, Australia)  
Prof. Jiri Klima (Technical Faculty of CZU in Prague, Czech Republic)  
Prof. Rossella Cancelliere (University of Torino, Italy)  
Prof. Dr-Eng. Christian Bouquegneau (Faculty Polytechnique de Mons, Belgium)  
Prof. Wladyslaw Mielczarski (Technical University of Lodz, Poland)  
Prof. Ibrahim Hassan (Concordia University, Montreal, Quebec, Canada)  
Prof. Stavros J. Baloyannis (Medical School, Aristotle University of Thessaloniki, Greece)  
Prof. James F. Frenzel (University of Idaho, USA)  
Prof. Vilem Srovnal, (Technical University of Ostrava, Czech Republic)  
Prof. J. M. Giron-Sierra (Universidad Complutense de Madrid, Spain)  
Prof. Walter Dosch (University of Luebeck, Germany)  
Prof. Rudolf Freund (Vienna University of Technology, Austria)  
Prof. Erich Schmidt (Vienna University of Technology, Austria)  
Prof. Alessandro Genco (University of Palermo, Italy)  
Prof. Martin Lopez Morales (Technical University of Monterey, Mexico)  
Prof. Ralph W. Oberste-Vorth (Marshall University, USA)  
Prof. Vladimir Damgov (Bulgarian Academy of Sciences, Bulgaria)  
Prof. P. Borne (Ecole Central de Lille, France)

## Additional Reviewers

Santoso Wibowo	CQ University, Australia
Lesley Farmer	California State University Long Beach, CA, USA
Xiang Bai	Huazhong University of Science and Technology, China
Jon Burley	Michigan State University, MI, USA
Genqi Xu	Tianjin University, China
Zhong-Jie Han	Tianjin University, China
Kazuhiko Natori	Toho University, Japan
João Bastos	Instituto Superior de Engenharia do Porto, Portugal
José Carlos Metrôlho	Instituto Politecnico de Castelo Branco, Portugal
Hessam Ghasemnejad	Kingston University London, UK
Matthias Buyle	Artesis Hogeschool Antwerpen, Belgium
Minhui Yan	Shanghai Maritime University, China
Takuya Yamano	Kanagawa University, Japan
Yamagishi Hiromitsu	Ehime University, Japan
Francesco Zirilli	Sapienza Universita di Roma, Italy
Sorinel Oprisan	College of Charleston, CA, USA
Ole Christian Boe	Norwegian Military Academy, Norway
Deolinda Rasteiro	Coimbra Institute of Engineering, Portugal
James Vance	The University of Virginia's College at Wise, VA, USA
Valeri Mladenov	Technical University of Sofia, Bulgaria
Angel F. Tenorio	Universidad Pablo de Olavide, Spain
Bazil Taha Ahmed	Universidad Autonoma de Madrid, Spain
Francesco Rotondo	Polytechnic of Bari University, Italy
Jose Flores	The University of South Dakota, SD, USA
Masaji Tanaka	Okayama University of Science, Japan
M. Javed Khan	Tuskegee University, AL, USA
Frederic Kuznik	National Institute of Applied Sciences, Lyon, France
Shinji Osada	Gifu University School of Medicine, Japan
Dmitrijs Serdjuks	Riga Technical University, Latvia
Philippe Dondon	Institut polytechnique de Bordeaux, France
Abelha Antonio	Universidade do Minho, Portugal
Konstantin Volkov	Kingston University London, UK
Manoj K. Jha	Morgan State University in Baltimore, USA
Eleazar Jimenez Serrano	Kyushu University, Japan
Imre Rudas	Obuda University, Budapest, Hungary
Andrey Dmitriev	Russian Academy of Sciences, Russia
Tetsuya Yoshida	Hokkaido University, Japan
Alejandro Fuentes-Penna	Universidad Autónoma del Estado de Hidalgo, Mexico
Stavros Ponis	National Technical University of Athens, Greece
Moran Wang	Tsinghua University, China
Kei Eguchi	Fukuoka Institute of Technology, Japan
Miguel Carriegos	Universidad de Leon, Spain
George Barreto	Pontificia Universidad Javeriana, Colombia
Tetsuya Shimamura	Saitama University, Japan



## Table of Contents

<b>Plenary Lecture 1: Floating Offshore Wind Turbines: The Technologies and the Economics</b> <i>Paul D. Sclavounos</i>	16
<b>Plenary Lecture 2: Detecting Critical Elements in Large Networks</b> <i>Panos M. Pardalos</i>	18
<b>Plenary Lecture 3: Overview of the Main Metaheuristics used for the Optimization of Complex Systems</b> <i>Pierre Borne</i>	20
<b>Plenary Lecture 4: Minimum Energy Control of Fractional Positive Electrical Circuits</b> <i>Tadeusz Kaczorek</i>	22
<b>Plenary Lecture 5: Unmanned Systems for Civilian Operations</b> <i>George Vachtsevanos</i>	24
<b>Plenary Lecture 6: Iterative Extended UFIR Filtering in Applications to Mobile Robot Indoor Localization</b> <i>Yuriy S. Shmaliy</i>	26
<b>Motion Control of an Exoskeleton Robot using Electromyogram Signals</b> <i>Mohammad Habibur Rahman, Cristobal Ochoa-Luna, Maarouf Saad, Philippe Archambault</i>	27
<b>Modeling of Movement of the Planning Robot</b> <i>Sergey F. Jatsun, Lyudmila Yu. Vorochayeva, Alexander V. Vorochayev</i>	34
<b>Design Optimization of a TIA for High Speed Data Applications using gm/ID Based Methodology</b> <i>Claudio Talarico, Gaurav Agrawal, Janet Wang-Roveda</i>	40
<b>Mathematical Model of the Quadrotor Type Unmanned Aerial Vehicle with Neurocontroller</b> <i>S. F. Jatsyn, V. E. Pavlovsky, O. V. Emelyanova, A. V. Savitsky</i>	46
<b>Robotic Assisted Trajectory Tracking for Human Arm Rehabilitation</b> <i>Cristóbal Ochoa-Luna, Mohammad Habibur Rahman, Maarouf Saad, Philippe S. Archambault</i>	51
<b>Pseudospectral Time-Domain (PSTD) Method to Predict Fast Transients in Transmission Lines</b> <i>Silvano Cruciani, Mauro Feliziani</i>	56
<b>Fuel-Efficient Motion Control of Tracked Robots Equipped with AC Electric Transmissions</b> <i>V. Kh. Pshikhopov, D. B. Pogosov</i>	60

<b>Emulators of Two-State Memcapacitor</b>	65
<i>Dalibor Biolek, Viera Biolkova, Zdenek Kolka</i>	
<b>Second-Order Sliding Mode Control Applied to an Inverted Pendulum</b>	71
<i>Sonia Mahjoub, Faical Mnif, Nabil Derbel</i>	
<b>A 21.5mW 3 Gbps CMOS OOK Receiver for the Next Generation Device to Device Communications</b>	78
<i>Ki-Jin Kim, Sanghoon Park, Suk-hui Lee, K. H. Ahn</i>	
<b>Modelling and Control of Water Tank Model</b>	82
<i>Jiri Vojtesek, Petr Dostal</i>	
<b>Real-Time Background/foreground Segmentation of RGBD Data</b>	88
<i>Abdenour Amamra, Tarek Mouats, Nabil Aouf</i>	
<b>Study of Control Forces and Torques Distribution Algorithms for Intelligent Control of Vehicle Actuators</b>	94
<i>V. Pshikhopov, M. Medvedev, V. Chufistov</i>	
<b>Design Considerations for Mobile Robotic Telepresence in Museums- A Report on the Pilot Users' Feedbacks</b>	98
<i>Anahita Bagherzadhalimi, Eleonora Di Maria</i>	
<b>Digital Smith Predictor for Control of Unstable and Integrating Time-delay Processes</b>	105
<i>V. Bobál, P. Chalupa, P. Dostál, M. Kubalčík</i>	
<b>RGBD Sensors Correction with Gaussian Process Regression</b>	111
<i>Abdenour Amamra, Nabil Aouf</i>	
<b>Network-on-Chip Application Mapping based on Domain Knowledge Genetic Algorithm</b>	115
<i>Yin Zhen Tei, N. Shaikh-Husin, Yuan Wen Hau, Eko Supriyanto, M. N. Marsono</i>	
<b>Cascade Adaptive Control of a Continuous Stirred Tank Reactor</b>	121
<i>P. Dostál, V. Bobál, J. Vojtěšek</i>	
<b>Concepts for an AC-Battery with Active Harmonics Compensation</b>	127
<i>K. H. Edelmoser, F. A. Himmelstoss</i>	
<b>Formal Verification of Safety Control System based on GHENESYS NET</b>	133
<i>Rodrigo Cesar Ferrarezi, Reinaldo Squillante Júnior, Jeferson A. L. Souza, Diolino J. Dos Santos Filho, José Reinaldo Silva, Paulo Eigi Miyagi, Lucas Antonio Moscato</i>	
<b>Cervix Position Recognition by Template Method using Linear Robot Ultrasound</b>	139
<i>Rino Ferdian Surakusumah, Christina Pahl, Muhammad Akmal Ayob, Eko Supriyanto</i>	

<b>Virtex-7 FPGA-based Reconfigurable Computer System RCS-7 for Digital Image Processing</b>	146
<i>Ilya I. Levin, Igor A. Kalyaev, Alexey I. Dordopulo, Liubov M. Slasten, Slava V. Gudkov</i>	
<b>Magnetically Dimmable Half Bridge Current Fed LED Driver</b>	150
<i>Selim Borekci, Nihal Cetin Acar</i>	
<b>Finding the Parameters of the Compensation Pulse with the Use of Iterative Nelder-Mead Method for Suppressing Residual Vibrations of Electronic Cam</b>	155
<i>Pavel Dostrašil</i>	
<b>Force Sensing of Teleoperated Robotized Cell Injection</b>	160
<i>Kostadin G. Kostadinov, Vladimir K. Kotev, Daniel M. Penchev</i>	
<b>Simulation of Robot Workcell Operation by Augmented Reality Technology Application</b>	164
<i>Jozef Novak-Marcincin, Miroslav Janak, Ludmila Novakova-Marcincinova</i>	
<b>Neural Network Position-Path Adaptive Regulator for Vehicles</b>	169
<i>V. Pshikhopov, M. Medvedev, D. Shanin</i>	
<b>Multiple Bands Antenna with Slots for Wireless Communication System</b>	173
<i>Evizal Abdulkadir, Eko Supriyanto, T. A. Rahman, S. K. A. Rahim, S. L. Rosa</i>	
<b>Hybrid FM Stereo Encoder using DDS for Carrier and pilot Signal Generation</b>	178
<i>Manolis G. Tampouratzis, George A. Adamidis</i>	
<b>Bias Driver of the Mach-Zehnder Intensity Electro-Optic Modulator, based on Harmonic Analysis</b>	184
<i>J. Svarny</i>	
<b>Synthesis and Analysis of a Memristor Frequency Converter for Radio-Receiver</b>	190
<i>Valeri Mladenov, Stoyan Kirilov</i>	
<b>Neural Network Method of Intellectual Planning of Mobile Robotic Object Movement in the Conditions of Uncertainty</b>	194
<i>V. Ph. Guzik, Yu. V. Chernukhin, A. O. Pyavchenko, M. Yu. Polenov, V. A. Pereverzev, R. V. Saprykin</i>	
<b>Automatic Rehabilitation Device based on Robot and Machine Vision</b>	201
<i>Miloslav Feriančik, Ondrej Líška</i>	
<b>High-Q Current-Mode CMOS Companding Bandpass Tunable Filter</b>	204
<i>A. Kircay</i>	
<b>Motorized Remote Control of Transesophageal Echocardiography (TEE) Probe Tip: Preliminary Testing</b>	209
<i>Dolwin C. C. Kho, Christina Pahl, Eko Supriyanto, Yin M. Myint, Ahmad A. M. Faudzi, Maheza I. M. Salim</i>	

<b>Manipulator Development for Telediagnosics</b> <i>Adam Kurnicki, Bartłomiej Stanczyk, Bartosz Kania</i>	214
<b>A 5-Tap Half-Rate DFE Receiver for Data-Edge Simultaneous Equalization</b> <i>Sung-Won Choi, Hyun-Wook Lim, Bai-Sun Kong</i>	219
<b>Principles of Structural Organization of the Intellectual Movement Planning System for Mobile Robotic Object</b> <i>V. Ph. Guzik, Yu. V. Chernukhin, A. O. Pyavchenko, V. A. Pereverzev, R. V. Saprykin</i>	223
<b>CMOS 60 GHz Power Amplifier Using Simple Open Drain and Source Architecture</b> <i>Ki-Jin Kim, Sanghoon Park, Suk-Hui Lee, K. H. Ahn</i>	228
<b>Cascade Wave-Based Control Applied to the Servomotor</b> <i>Ondřej Marek</i>	233
<b>Effect of Deposition Volume on PVC-based Mn(TPP)Cl Membrane for FET Sensitive to Histamine</b> <i>S. F. Mohammed Esa, Khuan Y. Lee, R. Jarmin</i>	238
<b>Linearity Error of Force Transducers Arising from Nonlinear Elasticity</b> <i>Jang H. Yi</i>	243
<b>Effect of Field Plate Length on Power Performance of GaN Based HEMTs</b> <i>Gokhan Kurt, Ahmet Toprak, Ozlem A. Sen, Ekmel Ozbay</i>	247
<b>An Efficient Hybrid Voltage/Current Mode Signaling Scheme for On-Chip Interconnects</b> <i>M. Kavicharan, N. S. Murthy, N. Bheema Rao</i>	251
<b>Effect of High Temperature on the Transconductance of AlGaIn/AlIn/GaN High Electron Mobility Transistors (HEMT)</b> <i>Rajab Yahyazadeh, Zahra Hashempour, Gasem Abdollahi, Belal Baghdarghi</i>	257
<b>Analog Non-Linear Function Synthesizer: HSPICE Design and Simulation</b> <i>Madina Hamiane</i>	264
<b>Wireless Remote Control of Transesophageal Echocardiography (TEE) Probe</b> <i>Dolwin C. C. Kho, Christina Pahl, Eko Supriyanto, Yin M. Myint, Ahmad A. M. Faudzi, Maheza I. M. Salim</i>	268
<b>A Novel Delay and Overshoot Estimation Model for VLSI Global Interconnects</b> <i>M. Kavicharan, N. S. Murthy, N. Bheema Rao</i>	272
<b>A Fuzzy Based Controller for Wind Energy Conversion System Using PWM CSI with Diode Rectifier and Buck Converter</b> <i>Shahram Javadi, Mehrnaz FardAmiri</i>	277

<b>Analysis of AM-to-PM Distortion Effect on ACPR Performances</b>	283
<i>Eun-Hee Kim, Hoyong Kang, Kwyro Lee</i>	
<b>Self-Localization in RFID-Tag Information Networks Using Extended UFIR Filtering</b>	286
<i>Juan Pomarico-Franquiz, Yuriy S. Shmaliy, Shunyi Zhao</i>	
<b>Strength Analysis of the Complex Planetary Gears</b>	293
<i>Sung Gil Han, Yoo-In Shin, Chan Heon Yoon, Chul Ki Song</i>	
<b>Haptics based Robotic Prosthetic Leg</b>	296
<i>Y. Kalyan Chakravarthy, R. Harish Kumar, B. Deepika, A. Srinath</i>	
<b>Turning Control for Quadruped Robots in Trotting on Irregular Terrain</b>	303
<i>Jeong Hoon Lee, Jong Hyeon Park</i>	
<b>An Enhancement Text Method for Image Acquired via Digital Cameras by PDE's Stable Model</b>	309
<i>Hassan El Bahi, Zouhir Mahani, Abdelkarim Zatni</i>	
<b>Prosthesis Design for Bilateral Hip Disarticulation Management</b>	314
<i>Mauricio Plaza Torres, William Aperador</i>	
<b>Authors Index</b>	318

## Plenary Lecture 1

### Floating Offshore Wind Turbines: The Technologies and the Economics



**Prof. Paul D. Sclavounos**

Professor of Mechanical Engineering and Naval Architecture  
Massachusetts Institute of Technology (MIT)  
77 Massachusetts Avenue  
Cambridge MA 02139-4307  
USA  
E-mail: pauls@mit.edu

**Abstract:** Wind is a vast, renewable and clean energy source that stands to be a key contributor to the world energy mix in the coming decades. The horizontal axis three-bladed wind turbine is a mature technology and onshore wind farms are cost competitive with coal fired power plants equipped with carbon sequestration technologies and in many parts of the world with natural gas fired power plants.

Offshore wind energy is the next frontier. Vast sea areas with higher and steadier wind speeds are available for the development of offshore wind farms that offer several advantages. Visual, noise and flicker impacts are mitigated when the wind turbines are sited at a distance from the coastline. A new generation of 6-10MW wind turbines with diameters exceeding 160m have been developed for the offshore environment. They can be fully assembled at a coastal facility and installed by a low cost float-out operation. Floater technologies are being developed for the support of multi-megawatt turbines in waters of moderate to large depth, drawing upon developments by the offshore oil & gas industry.

The state of development of the offshore wind energy sector will be discussed. The floating offshore wind turbine technology will be reviewed drawing upon research carried out at MIT since the turn of the 21st century. Floating wind turbine installations worldwide and planned future developments will be presented. The economics of floating offshore wind farms will be addressed along with the investment metrics that must be met for the development of large scale floating offshore wind power plants.

**Brief Biography of the Speaker:** Paul D. Sclavounos is Professor of Mechanical Engineering and Naval Architecture at the Massachusetts Institute of Technology. His research interests focus upon the marine hydrodynamics of ships, offshore platforms and floating wind turbines. The state-of-the-art computer programs SWAN and SML developed from his research have been widely adopted by the maritime, offshore oil & gas, and wind energy industries. His research

activities also include studies of the economics, valuation and risk management of assets in the crude oil, natural gas, shipping and wind energy sectors. He was the Georg Weinblum Memorial Lecturer in 2010-2011 and the Keynote Lecturer at the Offshore Mechanics and Arctic Engineering Conference in 2013. He is a member of the Board of the North American Committee of Det Norske Veritas since 1997, a member of the Advisory Committee of the US Navy Tempest program since 2006 and a member of the Advisory Board of the Norwegian Center for Offshore Wind Energy Technology since 2009. He has consulted widely for the US Government, shipping, offshore, yachting and energy industries.

<http://meche.mit.edu/people/?id=76>

## Keynote Lecture 2

### Detecting Critical Elements in Large Networks



**Professor Panos M. Pardalos**

Center for Applied Optimization (CAO)  
Department of Industrial and Systems Engineering,  
University of Florida, Gainesville, FL, USA.

and

Laboratory of Algorithms and Technologies for Networks Analysis (LATNA)  
National Research University, Higher School of Economics  
Moscow, Russia

E-mail: p.m.pardalos@gmail.com

**Abstract:** In network analysis, the problem of detecting subsets of elements important to the connectivity of a network (i.e., critical elements) has become a fundamental task over the last few years. Identifying the nodes, arcs, paths, clusters, cliques, etc., that are responsible for network cohesion can be crucial for studying many fundamental properties of a network. Depending on the context, finding these elements can help to analyze structural characteristics such as, attack tolerance, robustness, and vulnerability. Furthermore we can classify critical elements based on their centrality, prestige, reputation and can determine dominant clusters and partitions.

From the point of view of robustness and vulnerability analysis, evaluating how well a network will perform under certain disruptive events plays a vital role in the design and operation of such a network. To detect vulnerability issues, it is of particular importance to analyze how well connected a network will remain after a disruptive event takes place, destroying or impairing a set of its elements. The main goal is to identify the set of critical elements that must be protected or reinforced in order to mitigate the negative impact that the absence of such elements may produce in the network. Applications are typically found in homeland security, energy grid, evacuation planning, immunization strategies, financial networks, biological networks, and transportation.

From the member-classification perspective, identifying members with a high reputation and influential power within a social network could be of great importance when designing a marketing strategy. Positioning a product, spreading a rumor, or developing a campaign against drugs and alcohol abuse may have a great impact over society if the strategy is properly targeted among the most influential and recognized members of a community. The recent emergence of social networks such as Facebook, Twitter, LinkedIn, etc. provide countless applications for problems of critical-element detection.

In addition, determining dominant cliques or clusters over different industries and markets via critical clique detection may be crucial in the analysis of market share concentrations and debt

concentrations, spotting possible collusive actions or even helping to prevent future economic crises.

This presentation surveys some of the recent advances for solving these kinds of problems including heuristics, mathematical programming, dynamic programming, approximation algorithms, and simulation approaches. We also summarize some applications that can be found in the literature and present further motivation for the use of these methodologies for network analysis in a broader context.

**Brief Biography of the Speaker:** Panos M. Pardalos serves as Distinguished Professor of Industrial and Systems Engineering at the University of Florida. He is also an affiliated faculty member of the Computer and Information Science Department, the Hellenic Studies Center, and the Biomedical Engineering Program. He is also the Director of the Center for Applied Optimization. Dr. Pardalos is a world leading expert in global and combinatorial optimization. His recent research interests include network design problems, optimization in telecommunications, e-commerce, data mining, biomedical applications, and massive computing.

Full CV: [http://www.ise.ufl.edu/pardalos/files/2011/08/CV\\_Dec13.pdf](http://www.ise.ufl.edu/pardalos/files/2011/08/CV_Dec13.pdf)

Recent Achievements: <http://www.eng.ufl.edu/news/first-engineering-chair-appointed-under-ufs-preeminence-initiative-goes-to-big-data-expert/>

Profile in Scholar Google: [scholar.google.com/scholar?q=P+Pardalos&btnG=&hl=en&as\\_sdt=0,5](https://scholar.google.com/scholar?q=P+Pardalos&btnG=&hl=en&as_sdt=0,5)

## Plenary Lecture 3

### Overview of the Main Metaheuristics used for the Optimization of Complex Systems



**Professor Pierre Borne**

*Co-author: Mohamd Benrejeb*

Ecole Centrale de Lille

France

E-mail: pierre.borne@ec-lille.fr

**Abstract:** For complex systems such as in planning and scheduling optimization, the complexity which corresponds usually to hard combinational optimization prevents the implementation of exact solving methodologies which could not give the optimal solution in finite time. It is the reason why engineers prefer to use metaheuristics which are able to produce good solutions in a reasonable computation time. Two types of metaheuristics are presented here:

\* The local searches, such as: Tabu Search, Simulated Annealing, GRASP method, Hill Climbing, Tunnelling...

\* The global methods which look for a family of solutions such as: Genetic or Evolutionary Algorithms, Ant Colony Optimization, Particle Swarm Optimization, Bees algorithm, Firefly algorithm, Bat algorithm, Harmony search....

**Brief Biography of the Speaker:** Pierre BORNE received the Master degree of Physics in 1967 and the Master of Electrical Engineering, the Master of Mechanics and the Master of Applied Mathematics in 1968. The same year he obtained the Diploma of "Ingénieur IDN" (French "Grande Ecole"). He obtained the PhD in Automatic Control of the University of Lille in 1970 and the DSc in physics of the same University in 1976. Dr BORNE is author or co-author of about 200 Publications and book chapters and of about 300 communications in international conferences. He is author of 18 books in Automatic Control, co-author of an english-french, french-english « Systems and Control » dictionary and co-editor of the "Concise Encyclopedia of Modelling and Simulation" published with Pergamon Press. He is Editor of two book series in French and co-editor of a book series in English. He has been invited speaker for 40 plenary lectures or tutorials in International Conferences. He has been supervisor of 76 PhD Thesis and member of the committee for about 300 doctoral thesis . He has participated to the editorial board of 20 International Journals including the IEEE, SMC Transactions, and of the Concise Subject Encyclopedia . Dr BORNE has organized 15 international conferences and symposia, among them the 12th and the 17 th IMACS World Congresses in 1988 and 2005, the IEEE/SMC Conferences of 1993 (Le Touquet – France) and of 2002 (Hammamet - Tunisia) , the CESA IMACS/IEEE-SMC multiconferences of 1996 (Lille – France) , of 1998 (Hammamet – Tunisia) , of 2003 (Lille-France ) and of 2006 (Beijing, China) and the 12th IFAC LSS symposium (Lille France, 2010) He was chairman or co-chairman of the IPCs of 34 international conferences (IEEE, IMACS, IFAC) and member of the IPCs of more than 200 international conferences. He was the

editor of many volumes and CDROMs of proceedings of conferences. Dr BORNE has participated to the creation and development of two groups of research and two doctoral formations (in Casablanca, Morocco and in Tunis, Tunisia). twenty of his previous PhD students are now full Professors (in France, Morocco, Tunisia, and Poland). In the IEEE/SMC Society Dr BORNE has been AdCom member (1991-1993 ; 1996-1998), Vice President for membership (1992-1993) and Vice President for conferences and meetings (1994-1995, 1998-1999). He has been associate editor of the IEEE Transactions on Systems Man and Cybernetics (1992-2001). Founder of the SMC Technical committee « Mathematical Modelling » he has been president of this committee from 1993 to 1997 and has been president of the « System area » SMC committee from 1997 to 2000. He has been President of the SMC Society in 2000 and 2001, President of the SMC-nomination committee in 2002 and 2003 and President of the SMC-Awards and Fellows committee in 2004 and 2005. He is member of the Advisory Board of the "IEEE Systems Journal" . Dr. Borne received in 1994, 1998 and 2002 Outstanding Awards from the IEEE/SMC Society and has been nominated IEEE Fellow the first of January 1996. He received the Norbert Wiener Award from IEEE/SMC in 1998, the Third Millennium Medal of IEEE in 2000 and the IEEE/SMC Joseph G. Wohl Outstanding Career Award in 2003. He has been vice president of the "IEEE France Section" (2002-2010) and is president of this section since 2011. He has been appointed in 2007 representative of the Division 10 of IEEE for the Region 8 Chapter Coordination sub-committee (2007-2008) He has been member of the IEEE Fellows Committee (2008- 2010) Dr BORNE has been IMACS Vice President (1988-1994). He has been co-chairman of the IMACS Technical Committee on "Robotics and Control Systems" from 1988 to 2005 and in August 1997 he has been nominated Honorary Member of the IMACS Board of Directors. He is since 2008 vice-president of the IFAC technical committee on Large Scale Systems. Dr BORNE is Professor "de Classe Exceptionnelle" at the "Ecole Centrale de Lille" where he has been Head of Research from 1982 to 2005 and Head of the Automatic Control Department from 1982 to 2009. His activities concern automatic control and robust control including implementation of soft computing techniques and applications to large scale and manufacturing systems. He was the principal investigator of many contracts of research with industry and army (for more than three millions € ) Dr BORNE is "Commandeur dans l'Ordre des Palmes Académiques" since 2007. He obtained in 1994 the french " Kulman Prize". Since 1996, he is Fellow of the Russian Academy of Non-Linear Sciences and Permanent Guest Professor of the Tianjin University (China). In July 1997, he has been nominated at the "Tunisian National Order of Merit in Education" by the Republic of Tunisia. In June 1999 he has been nominated « Professor Honoris Causa » of the National Institute of Electronics and Mathematics of Moscow (Russia) and Doctor Honoris Causa of the same Institute in October 1999. In 2006 he has been nominated Doctor Honoris Causa of the University of Waterloo (Canada) and in 2007 Doctor Honoris Causa of the Polytechnic University of Bucharest (Romania). He is "Honorary Member of the Senate" of the AGORA University of Romania since May 2008 He has been Vice President of the SEE (French Society of Electrical and Electronics Engineers) from 2000 to 2006 in charge of the technical committees. He his the director of publication of the SEE electronic Journal e-STA and chair the publication committee of the REE Dr BORNE has been Member of the CNU (French National Council of Universities, in charge of nominations and promotions of French Professors and Associate Professors) 1976-1979, 1992-1999, 2004-2007 He has been Director of the French Group of Research (GDR) of the CNRS in Automatic Control from 2002 to 2005 and of a "plan pluriformations" from 2006 to 2009. Dr BORNE has been member of the Multidisciplinary Assessment Committee of the "Canada Foundation for Innovation" in 2004 and 2009. He has been referee for the nominations of 24 professors in USA and Singapore. He is listed in the « Who is Who in the World » since 1999.

## Plenary Lecture 4

### Minimum Energy Control of Fractional Positive Electrical Circuits



**Professor Tadeusz Kaczorek (Fellow IEEE)**

Warsaw University of Technology  
Poland

**Abstract:** The talk will consist of two parts. In the first part the minimum energy control of standard positive electrical circuits will be discussed and in the second part the similar problem for fractional positive electrical circuits. Necessary and sufficient conditions for the positivity and reachability of electrical circuits composed of resistors, coils and capacitors will be established. The minimum energy control problem for the standard and fractional positive electrical circuits will be formulated and solved. Procedures for computation of the optimal inputs and minimal values of the performance indices will be given and illustrated by examples of electrical circuits.

**Brief Biography of the Speaker:** Prof. Tadeusz Kaczorek graduated from the Faculty of Electrical Engineering Warsaw University of Technology in 1956, where in 1962 he defended his doctoral thesis. In 1964, he received a postdoctoral degree. In the years 1965-1970 he was head of the Department of Electronics and Automation, 1969-1970, and Dean of the Faculty of Electrical Engineering University of Warsaw. In the years 1970-1973 Vice-Rector of the Technical University of Warsaw in the years 1970-1981 the director of the Institute of Control and Industrial Electronics Warsaw University of Technology. He was also head of the Department of Control of the above Institute. In 1971 he received the title of Professor and Associate Professor of Warsaw University of Technology. In 1974 he received the title of professor of Warsaw University of Technology. In 1987-1988 he was chairman of the Committee for Automation and Robotics. Since 1986, corresponding member, and since 1998 member of the Polish Academy of Sciences. In 1988-1991 he was Head of the Scientific Academy in Rome. For many years a member of the Foundation for Polish Science. From June 1999 ordinary member of the Academy of Engineering. He is currently a professor at the Faculty of Electrical Engineering of Bialystok and Warsaw University of Technology. Since 1991 he is a member, and now chairman of the Central Commission for Academic Degrees and Titles (Vice-President in 2003-2006). In 2012 he was chairman of the Presidium of the Scientific Committee of the conference devoted to research crash of the Polish Tu-154 in Smolensk methods of science.

Scientific achievements

His research interests relate to automation, control theory and electrical engineering, including analysis and synthesis of circuits and systems with parameters determined and random polynomial methods for the synthesis of control systems and singular systems. Author of 20 books and monographs and over 700 articles and papers in major international journals such as

IEEE Transactions on Automatic Control, Multidimensional Systems and Signal Processing, International Journal of Control, Systems Science and Electrical Engineering Canadian Journal.

He organized and presided over 60 scientific sessions at international conferences, and was a member of about 30 scientific committees. He has lectured at over 20 universities in the United States, Japan, Canada and Europe as a visiting professor. He supervised more than 60 doctoral dissertations completed and reviewed many doctoral theses and dissertations. His dozens of alumni received the title of professor in Poland or abroad.

He is a member of editorial boards of journals such as International Journal of Multidimensional Systems and Signal Processing, Foundations of Computing and Decision Sciences, Archives of Control Sciences. From 1 April 1997, is the editor of the Bulletin of the Academy of Technical Sciences.

Honours, awards and honorary doctorates.

Honours

Tadeusz Kaczorek has been honored with the following awards:

\* Officer's Cross of the Order of Polonia Restituta Polish

\* Meritorious Polish

\* Medal of the National Education Commission

Honorary doctorates

He received honorary degrees from the following universities:

Silesian University of Technology (2014)

Rzeszow University of Technology (2012)

Poznan University of Technology (2011)

Opole University of Technology (2009)

Technical University of Lodz (3 December 2008)

Bialystok University of Technology (August 20, 2008)

Warsaw University of Technology (22 December 2004)

Szczecin University of Technology (November 8, 2004)

Lublin University of Technology (13 May 2004)

University of Zielona Gora (27 November 2002)

Honorary Member of the Hungarian Academy of Sciences and the Polish Society of Theoretical and Applied Electrical (1999). He received 12 awards of the Minister of National Education of all levels (including 2 team).

## Plenary Lecture 5

### Unmanned Systems for Civilian Operations



**Professor George Vachtsevanos**

Professor Emeritus

Georgia Institute of Technology

USA

E-mail: [george.vachtsevanos@ece.gatech.edu](mailto:george.vachtsevanos@ece.gatech.edu)

**Abstract:** In this plenary talk we will introduce fundamental concepts of unmanned systems (Unmanned Aerial Vehicles and Unmanned Ground Vehicles) and their emerging utility in civilian operations. We will discuss a framework for multiple UAVs tasked to perform forest fire detection and prevention operations. A ground station with appropriate equipment and personnel functions as the support and coordination center providing critical information to fire fighter as derived from the UAVs. The intent is to locate a swarm of vehicles over a designated area and report at the earliest the presence of such fire precursors as smoke, etc. the UAVs are equipped with appropriate sensors, computing and communications in order to execute these surveillance tasks accurately and robustly. Meteorological sensors monitor wind velocity, temperature and other relevant parameters. The UAV observations are augmented, when appropriate, with satellite data, observation towers and human information sources. Other application domains of both aerial and ground unmanned systems refer to rescue operations, damage surveillance and support for areas subjected to earthquakes and other natural disasters, border patrol, agricultural applications, traffic control, among others.

**Brief Biography of the Speaker:** Dr. George Vachtsevanos is currently serving as Professor Emeritus at the Georgia Institute of Technology. He served as Professor of Electrical and Computer Engineering at the Georgia Institute of Technology from 1984 until September, 2007. Dr Vachtsevanos directs at Georgia Tech the Intelligent Control Systems laboratory where faculty and students began research in diagnostics in 1985 with a series of projects in collaboration with Boeing Aerospace Company funded by NASA and aimed at the development of fuzzy logic based algorithms for fault diagnosis and control of major space station subsystems. His work in Unmanned Aerial Vehicles dates back to 1994 with major projects funded by the U.S. Army and DARPA. He has served as the Co-PI for DARPA's Software Enabled Control program over the past six years and directed the development and flight testing of novel fault-tolerant control algorithms for Unmanned Aerial Vehicles. He has represented Georgia Tech at DARPA's HURT program where multiple UAVs performed surveillance, reconnaissance and tracking missions in an urban environment. Under AFOSR sponsorship, the Impact/Georgia Team is developing a biologically-inspired micro aerial vehicle. His research work has been supported over the years by ONR, NSWC, the MURI Integrated Diagnostic program at Georgia Tech, the U.S. Army's Advanced Diagnostic program, General Dynamics,

General Motors Corporation, the Academic Consortium for Aging Aircraft program, the U.S. Air Force Space Command, Bell Helicopter, Fairchild Controls, among others. He has published over 300 technical papers and is the recipient of the 2002-2003 Georgia Tech School of ECE Distinguished Professor Award and the 2003-2004 Georgia Institute of Technology Outstanding Interdisciplinary Activities Award. He is the lead author of a book on Intelligent Fault Diagnosis and Prognosis for Engineering Systems published by Wiley in 2006.

## Plenary Lecture 6

### Iterative Extended UFIR Filtering in Applications to Mobile Robot Indoor Localization



**Professor Yuriy S. Shmaliy**  
Department of Electronics  
DICIS, Guanajuato University  
Salamanca, 36855, Mexico  
E-mail: shmaliy@ugto.mx

**Abstract:** A novel iterative extended unbiased FIR (EFIR) filtering algorithm is discussed to solve suboptimally the nonlinear estimation problem. Unlike the Kalman filter, the EFIR filtering algorithm completely ignores the noise statistics, but requires an optimal horizon of  $N$  points in order for the estimate to be suboptimal. The optimal horizon can be specialized via measurements with much smaller efforts and cost than for the noise statistics required by EKF. Overall, EFIR filtering is more successful in accuracy and more robust than EKF under the uncertain conditions. Extensive investigations of the approach are conducted in applications to localization of mobile robot via triangulation and in radio frequency identification tag grids. Better performance of the EFIR filter is demonstrated in a comparison with the EKF. It is also shown that divergence in EKF is not only due to large nonlinearities and large noise as stated by the Kalman filter theory, but also due to errors in the noise covariances ignored by EFIR filter.

**Brief Biography of the Speaker:** Dr. Yuriy S. Shmaliy is a full professor in Electrical Engineering of the Universidad de Guanajuato, Mexico, since 1999. He received the B.S., M.S., and Ph.D. degrees in 1974, 1976 and 1982, respectively, from the Kharkiv Aviation Institute, Ukraine. In 1992 he received the Dr.Sc. (technical) degree from the Soviet Union Government. In March 1985, he joined the Kharkiv Military University. He serves as full professor beginning in 1986 and has a Certificate of Professor from the Ukrainian Government in 1993. In 1993, he founded and, by 2001, had been a director of the Scientific Center “Sichron” (Kharkiv, Ukraine) working in the field of precise time and frequency. His books *Continuous-Time Signals* (2006) and *Continuous-Time Systems* (2007) were published by Springer, New York. His book *GPS-based Optimal FIR Filtering of Clock Models* (2009) was published by Nova Science Publ., New York. He also edited a book *Probability: Interpretation, Theory and Applications* (Nova Science Publ., New York, 2012) and contributed to several books with invited chapters. Dr. Shmaliy has authored more than 300 Journal and Conference papers and 80 patents. He is IEEE Fellow; was rewarded a title, Honorary Radio Engineer of the USSR, in 1991; and was listed in *Outstanding People of the 20th Century*, Cambridge, England in 1999. He is currently an Associate Editor for *Recent Patents on Space Technology*. He serves on the Editorial Boards of several International Journals and is a member of the Organizing and Program Committees of various Int. Symposia. His current interests include statistical signal processing, optimal estimation, and stochastic system theory.

# Motion Control of an Exoskeleton Robot using Electromyogram Signals

Mohammad Habibur Rahman, Cristobal Ochoa-Luna, Maarouf Saad, and Philippe Archambault

**Abstract**—We have developed a seven degrees of freedom exoskeleton robot (ETS-MARSE) for rehabilitation and assistance of upper limb movements in physically disabled individuals with impaired upper-limb function. Here we propose a new control strategy to maneuver the ETS-MARSE using skin surface electromyogram (EMG) signals, which are thought to reflect the user’s intention of motion. It is expected that the input of EMG signals to the robot controller will help maneuvering the robot in real time in assisting the subject’s arm motion. A nonlinear sliding mode control technique was used for this purpose, where EMG signals were used as input information to the controller. To evaluate the performance of the proposed control approach experiments were carried out with the healthy individuals. Experimental results indicate that with the proposed control strategy, ETS-MARSE can be effectively maneuvered with the EMG signals.

**Keywords**—Electromyogram signals, Exoskeleton Robot, Motion control, Sliding mode control.

## I. INTRODUCTION

TO rehabilitates individuals with impaired upper-limb function, extensive research has been carrying on in the field of assistive technology and rehabilitation robotics [1-4]. To contribute in this program we have developed an exoskeleton robot (ETS-MARSE) for rehabilitation and for assisting movements of the shoulder, elbow, forearm and wrist joints [4, 5]. Different control strategies were proposed and implemented in our previous research to maneuver the ETS-MARSE in providing passive rehabilitation therapy [6-8]. In the “passive movement” approach, it is assumed that a subject is completely unable to move his arm and therefore the robot’s task is to perform passive movement exercises (requiring no user effort) such as elbow flexion/extension, forearm pronation/supination etc. This type of therapy is mainly to increase joint range of motion. Following passive therapy, the next therapeutic mode which contributes to the restoration of

upper extremity function is known as active rehabilitation therapy. In this approach subjects actively participate in performing the exercises such as a reaching movement exercise, with the robot providing support against gravity and assisting with movement if needed [9]. As a first step to provide such active therapy, we developed a control strategy based on the subject’s surface EMG signals, which reflect the intention of movement. The primary objective of this research was to control an arm exoskeleton robot with the user’s surface EMG signals.

Using EMG signals to control exoskeleton robots or, robotic prostheses has gained a lot of attention since the last decade [10-14]. Indeed, different types of EMG based control approaches are found in the literature. Kiguchi et al. [10] proposed a fuzzy-neuro control method to control a mobile exoskeleton robot. Khokhar et al. [14] used pattern recognition method for the control of a wrist exoskeleton. Liu et al in [15] proposed an adaptive EMG based robot control system via use of adaptive neuro-fuzzy inference system to manipulate an industrial robot. Shenoy et al. [16] used a support vector machine (SVM) classifier technique to control a robotic arm. All these methods are computationally expensive and are not robust to deal with the nonlinearity of EMG signals. In this research we proposed a new EMG based control strategy using sliding mode control with exponential reaching law (*SMERL*) [17, 18] to drive the ETS-MARSE.

Although the input to the controller is the user’s skin surface EMG signals, this EMG signals are transformed into a position command. Therefore, the guiding principle of the ETS-MARSE is a position controller based on the EMG signals. Details of this control strategy are presented in section III, following a brief description of the ETS-MARSE (Section II). Experiments were carried out with healthy male subjects to control the ETS-MARSE with the EMG signals (Section IV). Finally, the paper ends with the conclusion in section V. It is anticipated that with the proposed control strategy, the ETS-MARSE can assist physically disabled individuals by providing them with arm motion.

## II. EXOSKELETON ROBOT, ETS-MARSE

The ETS-MARSE, as shown in Fig. 1, is a 7 degrees-of-freedom exoskeleton robot designed to be worn on the lateral side of upper extremity in order to provide naturalistic movements of the shoulder (i.e., vertical and horizontal flexion/extension, and internal/external rotation), elbow (i.e.,

M.H. Rahman is (Postdoctoral Fellow) with the School of Physical & Occupational Therapy, McGill University and (Research Assistant) Electrical Department, École de Technologie Supérieure, Montreal, Canada (email: mbrahim@ieec.org).

M. Saad is with the Electrical Engineering Dept., École de Technologie Supérieure, Montreal, Canada (email: maarouf.saad@etsmtl.ca).

C. Ochoa-Luna is (PhD candidate) with the Electrical Engineering Department, École de Technologie Supérieure, Montreal, Canada (email: cristobal.ochoa-luna.1@ens.etsmtl.ca).

P. S. Archambault is with the School of Physical & Occupational Therapy, McGill University, Canada (email: philippe.archambault@mcgill.ca).

flexion/extension), forearm (i.e., pronation/supination), and wrist joint (i.e., radial/ulnar deviation, and flexion/extension). Provision included in the design to adjust the link-lengths to accommodate a wide range of individuals. Brushless DC motors are used to actuate the ETS-MARSE. The individual joint's workspace of the ETS-MARSE is illustrated in Fig. 2.



Fig. 1 Exoskeleton Robot, ETS-MARSE

### III. EMG SIGNALS PROCESSING

The central nervous system sends motor command to each muscle via motor neurons. These signals activate the skeletal muscles (i.e., contractions and tensions), and thus produce necessary joint torques for posture control and voluntary movements. Surface EMG signals are used to measure those motor commands to be sent to the muscles.

These EMG signals are highly nonlinear in nature. For instance, to perform the same upper-limb movements, EMG

activity may vary from subject to subject. Even in the case where a same subject performs the same upper limb motion, EMG can vary depending on the subject's physiological condition such as fatigue, stress, placement of electrodes etc. These signals consist of a wide range of frequencies and it is often difficult to reduce noise by filtering. Therefore, raw EMG signals cannot be directly used to provide meaningful information to the controller. So, features have to be extracted from the noisy raw EMG signals. There are various features extraction methods. Some commonly used methods are: waveform length, mean absolute value, root mean square (RMS), average or full rectified value, zero crossing, slope sign changes, etc [19].

For this study RMS value is chosen to process raw EMG signals ( $\pm 5\text{mV}$ ). Note that, the RMS value is a measure of power of the signal and it is widely used in most applications.

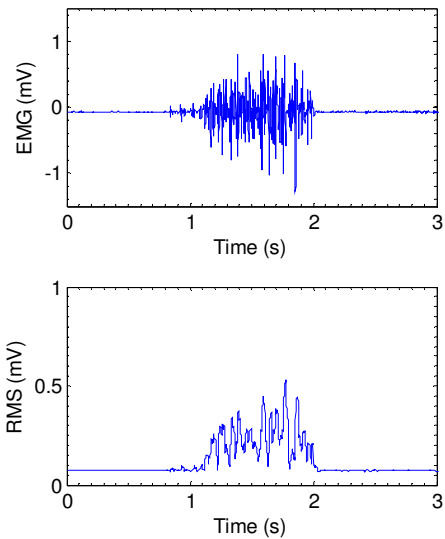


Fig. 3 Example of raw EMG signals and RMS value

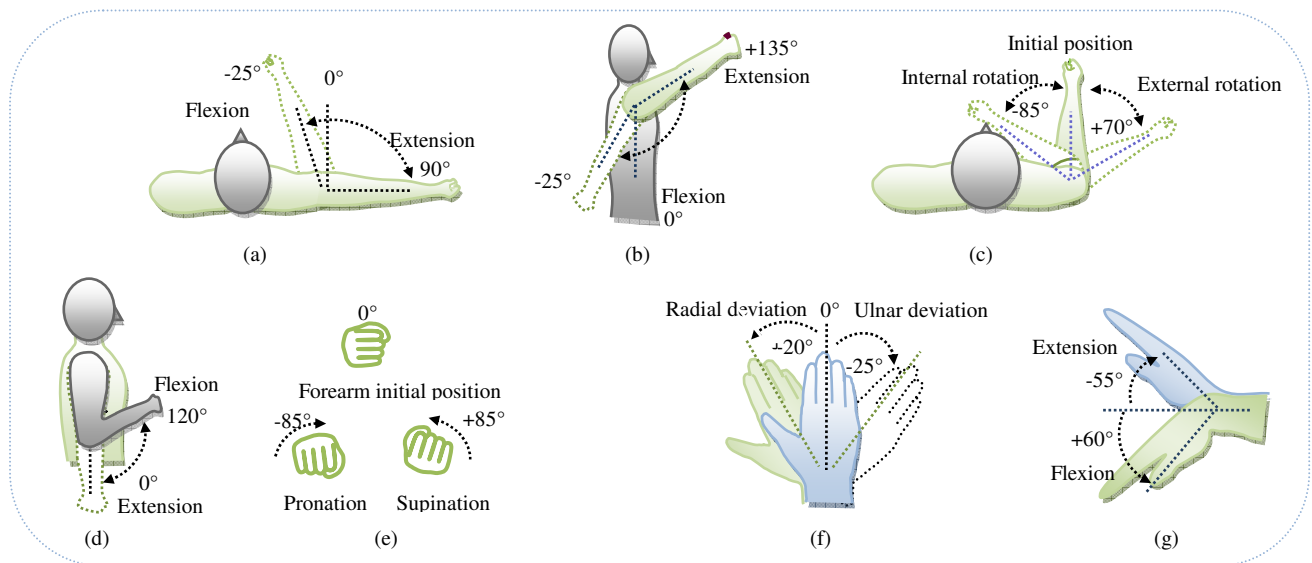


Fig. 2 Workspace of ETS-MARSE. (a) Joint-1: shoulder joint horizontal flexion-extension; (b) Joint-2: shoulder joint vertical flexion-extension; (c) Joint-3: shoulder joint internal-external rotation; (d) Joint-4: elbow flexion-extension; (e) Joint-5: forearm pronation-supination; (f) Joint-6: wrist joint radial-ulnar deviation; (g) Joint-7: wrist joint flexion-extension.

The equation of RMS value is written as:

$$RMS = \sqrt{\frac{1}{N} \sum_{i=1}^N v_i^2} \quad (1)$$

where  $v_i$  is the voltage value at the  $i^{\text{th}}$  sampling and  $N$  is the number of sample in a segment. The number of samples is set to be 50 and the sampling time is 0.5msec.

An example of the RMS value of raw EMG signals recorded from elbow muscles (biceps brachii) is depicted in Fig. 3.

#### IV. CONTROL SCHEME

##### A. Muscle Modeling

Joint movements are controlled by the actions of agonist and antagonist muscles (such as biceps brachii for elbow flexion, triceps brachii for elbow extension motion etc.). For single joint movements, multiple agonists and antagonists muscles may be involved (e.g., shoulder joint vertical flexion is controlled by the posterior part of deltoid, teres major, and latissimus dorsi muscles) [20]. Some muscles are responsible for multiple joint movements (e.g., posterior part of deltoid is responsible for external rotation, horizontal extension, and vertical extension motion of shoulder joint). In this study we have studied the upper-limb muscles to find single dominating muscle responsible for a specific joint movement. The study was experimentally validated by analyzing EMG activity of healthy individuals' muscles. Table 1 gives the antagonist and agonist muscles used to develop the proposed EMG based control approach.

##### B. Control Strategy

It is the skeletal muscles' forces which produce joint torques for the joint movements. A force/torque applied at the wrist joint of upper-limb (or at the end-effector of ETS-MARSE) can produce the same joint torques, and may results the same joint motions. For instance, as shown in Fig. 4a, a force applied along Z axis (i.e.,  $F_z$ ) or a torque applied around Y axis (i.e.,  $T_y$ ) can produce the same torque as produced by the elbow muscles force ( $F_m$ , Fig. 4b) at the elbow joint. Similarly

Table 1. Agonist and antagonist muscles of upper-limb (shoulder elbow and forearm [20])

Upper-limb motion	Agonist/Antagonist Muscles
Shoulder joint vertical flexion	Deltoid anterior part
Shoulder joint vertical extension	Teres major
Shoulder joint horizontal flexion	Pectoralis major calvicular part
Shoulder joint horizontal extension	Deltoid posterior part
Shoulder joint internal rotation	Latissimus Dorsi
Shoulder joint external rotation	Supraspinatus
Elbow flexion	Biceps brachii
Elbow extension	Triceps brachii
Forearm pronation	Pronator teres
Forearm supination	Supinator

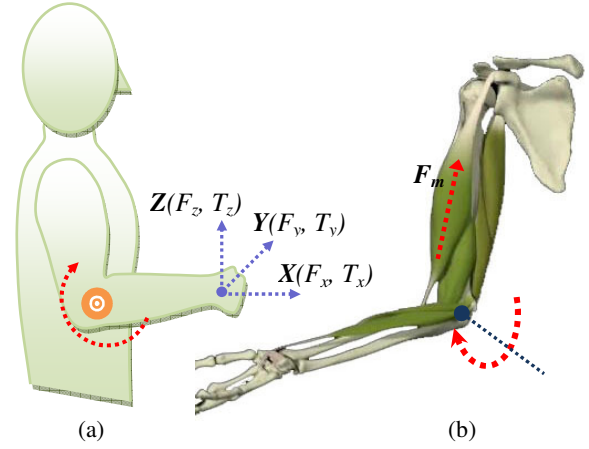


Fig. 4 Elbow joint flexion/extension mechanism. (a) Virtual force acting at the end-effector (wrist-joint), producing joint torques, (b) Elbow muscles producing equivalent elbow joint torques causing flexion/extension motion.

a torque applied around X axis ( $T_x$ ) will produce the same forearm motion as produced by the actions of pronator teres and supinator muscles. Therefore, in this case, the surface EMG signals, which are a measure of muscle activity, can be co-related to a virtual force/torque ( $F_v$ ) acting at the wrist joint of a subject. Let's assume that EMG signals recorded from the agonist and antagonist muscles ( $EMG_i$ ) for individual joint movements are proportional to the virtual force/torque vectors ( $F_v \in \mathbb{R}^{6 \times 1}$ ). The relation can be expressed as:

$$F_v = \Delta C_i \times EMG_i \quad (2)$$

where  $\Delta C_i$  = proportional constant for individual muscles.

Therefore, the virtual force/torque vector that represents the activity of agonist and antagonist muscles of elbow would be  $F_{v\_el} = [0 \ 0 \ F_z \ 0 \ T_y \ 0]^T$

where  $F_z = \Delta C_{f_z,i} \times EMG_i$ , and  $T_y = \Delta C_{T_y,i} \times EMG_i$ .

Similarly, for shoulder joint internal/external rotation due to the activity of agonist and antagonist muscles of shoulder, it would be  $F_{v\_sR} = [0 \ F_y \ 0 \ 0 \ 0 \ T_z]^T$ .

Consider a 6-axis virtual force/torque sensor (representing EMG activity of muscles) instrumented at the end-effector of the ETS-MARSE (Fig. 1). The simplified control architecture of the ETS-MARSE control system is depicted in Fig. 5. The principle of EMG based control approach (or active exercise) is that the subjects initiate the movement to complete a specified task.

As seen from the schematic (Fig. 5), control is carried out based on the skin surface EMG signals of subjects. The instantaneous EMG signals of muscles (i.e., subject's initiation of movement) and the previous joint angles of the ETS-MARSE are used to compute the desired position command (joint angles) of the robot to follow, which can be expressed as:

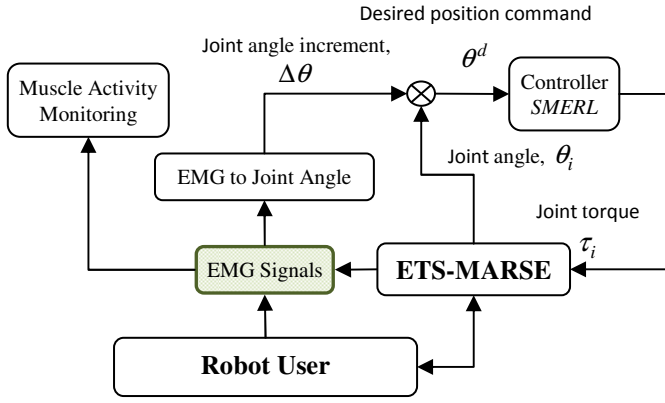


Fig. 5 Schematic diagram of EMG based control system

$$\theta^d = \theta_{old} + \Delta\theta(\tau_v(EMG_i)) \quad (3)$$

where  $\theta^d \in \mathbb{R}^{7 \times 1}$  is the desired joint angles vector,  $\theta_{old} \in \mathbb{R}^{7 \times 1}$  is the previous joint angles vector, and  $\Delta\theta \in \mathbb{R}^{7 \times 1}$  is the vector of infinitesimal changes of joints' angles corresponding to the instantaneous change of EMG signals, and  $\tau_v \in \mathbb{R}^{7 \times 1}$  is the virtual torques vector. Note that, the virtual force/torques  $F_v \in \mathbb{R}^{6 \times 1}$  as applied at the end-effector corresponding to the instantaneous change of EMG signals produce joints' torques ( $\tau_v \in \mathbb{R}^{7 \times 1}$ ) which can be expressed by the following relation.

$$\tau_v = J^T(\theta)F_v \quad (4)$$

where  $J(\theta) \in \mathbb{R}^{6 \times n}$  is the Jacobian matrix of ETS-MARSE ( $n=7$ ), and  $\theta \in \mathbb{R}^{7 \times 1}$  is the joint angle vector.

The change of joints' angle corresponding to the infinitesimal changes of  $F_v \in \mathbb{R}^{6 \times 1}$  is thus assumed to be proportional to the corresponding joints' torques  $\Delta\tau_v \in \mathbb{R}^{7 \times 1}$ , that is-

$$\Delta\tau_v = K_{pG}\Delta\theta \quad (5)$$

where  $K_{pG} \in \mathbb{R}^{7 \times 7}$  is the (diagonal) proportional gain matrix that transforms infinitesimal changes of joints' torques ( $\Delta\tau_v$ ) to the corresponding joint angles ( $\Delta\theta$ ). A detail of this transformation can be found in [21].

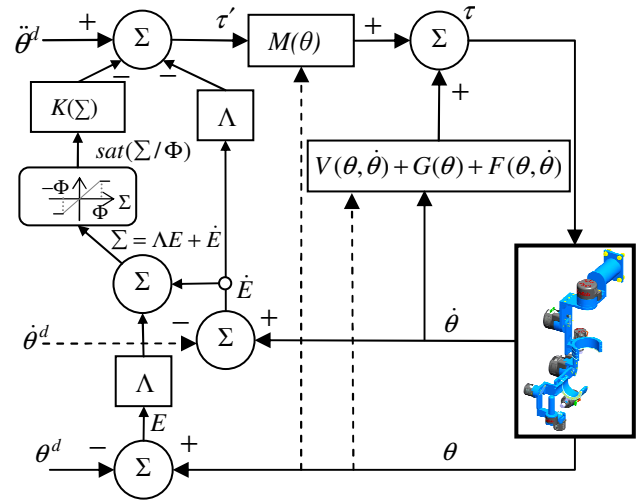
So, the sliding mode exponential reaching law (SMERL), as depicted in the schematic (Fig. 5), works mainly on the position regulation of the ETS-MARSE. In the next subsection, the theoretical structure of the sliding mode control technique with exponential reaching law (ERL) is presented for the dynamic trajectory tracking of the ETS-MARSE.

### C. Sliding mode control with ERL

The dynamic behaviour of the ETS-MARSE can be expressed by the well-known rigid body dynamic equation as:

$$M(\theta)\ddot{\theta} + V(\theta, \dot{\theta}) + G(\theta) + F(\theta, \dot{\theta}) = \tau \quad (6)$$

where  $M(\theta) \in \mathbb{R}^{7 \times 7}$  is the inertia matrix,  $V(\theta, \dot{\theta}) \in \mathbb{R}^{7 \times 1}$  is


 Fig. 6. Schematic diagram of sliding mode exponential reaching law in combination with *sat* function

the coriolis/centrifugal vector,  $G(\theta) \in \mathbb{R}^{7 \times 1}$  is the gravity vector, and  $F(\theta, \dot{\theta}) \in \mathbb{R}^{7 \times 1}$  is the friction vector. Note that the friction vector is modeled as a nonlinear coulomb friction, and can be expressed as:

$$\tau_{friction} = F(\theta, \dot{\theta}) = c \operatorname{sgn}(\dot{\theta}) \quad (7)$$

where  $c$  is the coulomb-friction constant. Equation (6) can be written as:

$$\ddot{\theta} = -M^{-1}(\theta)[V(\theta, \dot{\theta}) + G(\theta) + F(\theta, \dot{\theta})] + M^{-1}(\theta)\tau \quad (8)$$

$M^{-1}(\theta)$  always exists since  $M(\theta)$  is symmetrical and positive definite. The general layout of the sliding mode control technique is depicted in Fig. 6. The initial step in the sliding mode control is to choose the sliding (or switching) surface  $S$  in terms of the tracking error. Let the tracking error for each joint be defined as:

$$e_i = \theta_i - \theta_i^d \quad \dots \quad (i=1, \dots, m) \quad (9)$$

and the sliding surface as:

$$S_i = \lambda_i e_i + \dot{e}_i \quad \dots \quad (i=1, \dots, m) \quad (10)$$

where  $\theta_i^d$  is the desired trajectory for joint  $i$  and  $S_i$  is the sliding surface of each DoF.

Let  $\Sigma = [S_1 \ S_2 \ \dots \ S_m]^T$  be the sliding surface for the ETS-MARSE. Therefore, we have:

$$\Sigma = \begin{bmatrix} \lambda_1 e_1 + \dot{e}_1 \\ \vdots \\ \lambda_m e_m + \dot{e}_m \end{bmatrix} \quad (11)$$

Equation (11) is a first order differential equation, which implies that if the sliding surface is reached, the tracking error will converge to zero as long as the error vector stays on the surface.

Considering the following Lyapunov function candidate:

$$V = \frac{1}{2} \Sigma^T \Sigma \quad (12)$$

which is continuous and nonnegative, the derivative of  $V$  yields:

$$\dot{V} = \Sigma^T \dot{\Sigma} \quad (13)$$

By choosing  $\dot{\Sigma}$  as given in equation (14) relation (13) is ensured to be decreasing.

$$\dot{\Sigma} = -K \text{sign}(\Sigma), \forall t, K > 0 \Rightarrow \dot{V} < 0 \quad (14)$$

where

$$\text{sign}(\Sigma) = \begin{cases} 1 & \text{for } \Sigma > 0 \\ 0 & \text{for } \Sigma = 0 \\ -1 & \text{for } \Sigma < 0 \end{cases} \quad (15)$$

Expression (14) is known as the reaching law. It is to be noted that the discontinuous term  $K \text{sign}(\Sigma)$  in (14) often leads to a high control activity, known as chattering. One of the most known approaches found in the literature is to smoothen the discontinuous term in the control input with the continuous term  $K \text{sat}(\Sigma / \phi)$  [22].

where

$$\text{sat}(\Sigma / \phi) = \begin{cases} \Sigma / \phi & \text{for } |\Sigma / \phi| \leq 1 \\ 0 & \text{for } \Sigma / \phi = 0 \\ \text{sign}(\Sigma / \phi) & \text{for } |\Sigma / \phi| > 1 \end{cases} \quad (16)$$

Using equation (16), the reaching law therefore becomes:

$$\dot{\Sigma} = -K \text{sat}(\Sigma / \phi), \forall t, K > 0 \quad (17)$$

By performing this substitution, the convergence of the system stays within a boundary layer neighborhood (defined by  $\Phi$ ) of the switching surface. Therefore, with this approach, the chattering level is controlled in exchange of tracking performance. We have already demonstrated in our previous research [17] that the reaching law which combines ERL [18] with  $\text{sat}$  function [22] significantly reduce chattering and improve tracking. The ERL can be expressed as:

$$\dot{\Sigma} = -K(\Sigma) \text{sign}(\Sigma), \forall t, K > 0 \quad (18)$$

where

$$K(\Sigma) = \text{diag} \left( \frac{k_i}{N_i(S_i)} \right) \dots (i = 1, \dots, m), \text{ and} \quad (19)$$

$$N_i(S_i) = \delta_{0i} + (1 - \delta_{0i}) e^{-\alpha_i |S_i|^{P_i}} \quad (20)$$

where  $0 < \delta_{0i} \leq 1$ ;  $\alpha_i > 0$ , and,  $P_i > 0$ .

The values of  $\delta_{0i}$ ,  $\alpha_i$ , and  $P_i$  can be fixed as proposed in [18]. The new reaching law that combines the  $\text{sat}$  function and the concept of ERL can be written as follows:

$$\dot{\Sigma} = -K(\Sigma) \text{sat}(\Sigma / \phi), \forall t, K > 0 \quad (21)$$

Therefore and considering

$$\ddot{\theta}^d = [\ddot{\theta}_1^d \quad \ddot{\theta}_2^d \quad \dots \quad \ddot{\theta}_m^d]^T,$$

$$\dot{E} = [\dot{e}_1 \quad \dot{e}_2 \quad \dots \quad \dot{e}_m]^T, \text{ and } \Lambda = \text{diag}[\lambda_1 \quad \dots \quad \lambda_m]$$

$$\Sigma = \Lambda E + \dot{E} \Rightarrow \dot{\Sigma} = \Lambda \dot{E} + \ddot{E} \quad (22)$$

where,  $\ddot{E} = \ddot{\theta} - \ddot{\theta}^d$ . Thus, relation (22) can be written as:

$$\dot{\Sigma} = \Lambda \dot{E} + \ddot{\theta} - \ddot{\theta}^d \quad (23)$$

Substituting the value of  $\ddot{\theta}$  from equation (8) in equation (23) we obtain:

$$\begin{aligned} \dot{\Sigma} &= \Lambda \dot{E} - \ddot{\theta}^d + M^{-1}(\theta) \tau \\ &\quad - M^{-1}(\theta) [V(\theta, \dot{\theta}) + G(\theta) + F(\theta, \dot{\theta})] \end{aligned} \quad (24)$$

Replacing  $\dot{\Sigma}$  by its value given in equation (21):

$$\begin{aligned} -K(\Sigma) \text{sat}(\Sigma / \phi) &= \Lambda \dot{E} - \ddot{\theta}^d \\ -M^{-1}(\theta) [V(\theta, \dot{\theta}) + G(\theta) + F(\theta, \dot{\theta}) - \tau] \end{aligned} \quad (25)$$

The torque  $\tau$  can be isolated and thus yields:

$$\begin{aligned} \tau &= -M(\theta) (\Lambda \dot{E} - \ddot{\theta}^d + K(\Sigma) \text{sat}(\Sigma / \phi)) \\ &\quad + [V(\theta, \dot{\theta}) + G(\theta) + F(\theta, \dot{\theta})] \end{aligned} \quad (26)$$

where  $K$  and  $\Lambda$  are diagonal positive definite matrices. Therefore, the control law given in equation (26) ensures that the control system is stable. A detailed explanation of the stability analysis is given in [17].

## V. EXPERIMENTS AND RESULTS

Experimental setup of the developed ETS-MARSE system is depicted in Fig. 7. It consists of a CPU processor (NI PXI-8108) with a reconfigurable FPGA (field-programmable gate array), seven motor drivers, a custom designed main board,

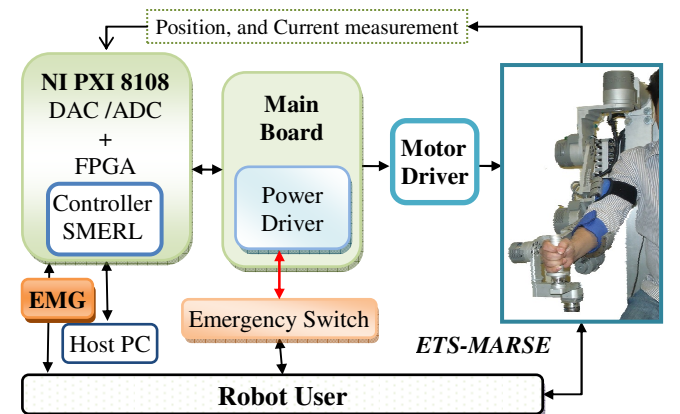


Fig. 7. Experimental setup.



Fig. 8 Electrode placement for elbow joint flexion/extension, forearm pronation supination and shoulder joint vertical flexion/extension motion

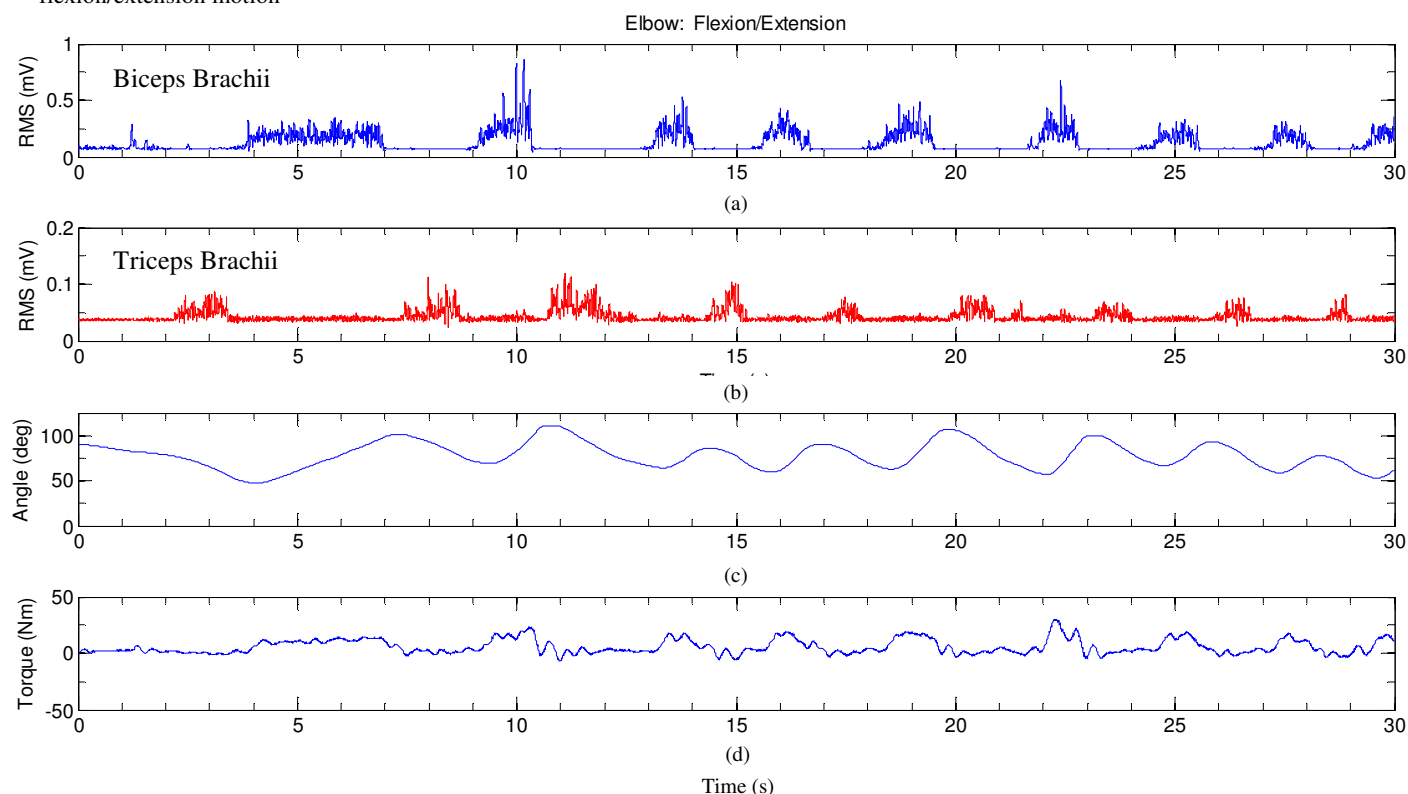


Fig. 9 Elbow joint flexion/extension motion

and a host PC. The main board as shown in Figure 7 acts as a motherboard, and is powered by an AC 120V (60Hz) power supply. The motherboard routes various analog and digital signals from/to the NI-PXI to/from the ETS-MARSE system. The control algorithm is executed in the NI-PXI.

The EMG electrodes (Delsys) placement on upper-limb muscles are depicted in Fig. 8. In this study, elbow muscles (e.g., biceps and triceps) of the subjects are monitored and used as input information to control of the ETS-MARSE. The experiment was conducted with subjects in a seated position with elbow joint angle at  $90^\circ$ . In experiments, the performance of the proposed EMG based control approach for motion control of the ETS-MARSE was evaluated. The experimental result for elbow joint flexion/extension movement is depicted in Fig. 9. The top most plots show the RMS values of EMG signals recorded from the biceps brachii muscle and that for

the triceps is shown in Fig. 9b. The elbow joint angles of ETS-MARSE corresponding to the biceps and triceps actions are shown in the Fig. 9c. It can be seen from the Fig. 9c, that when triceps is activating it produces extension motion of ETS-MARSE and when biceps is activating it produces flexion motion of ETS-MARSE. The trail was performed in different velocities for 30 sec. In all cases the developed EMG based control approach was able to maneuver the ETS-MARSE effectively and smoothly in providing flexion/extension motion of elbow joint using the EMG signals of muscles. Therefore, the control approach as proposed in this research can be effectively used in providing active rehabilitation exercises.

## VI. CONCLUSION

A new EMG based control strategy as proposed in this research was experimentally evaluated for the motion control of ETS-MARSE. A brief description of the ETS-MARSE was presented. A detail of the proposed control strategy was also presented. From the experimental results, it is evident that with the developed control approach the ETS-MARSE will be able to provide active assistance in arm movements. Future works will include developing a hybrid controller with the fusion of the force sensor based controller and the EMG based controller.

## ACKNOWLEDGMENT

The first author gratefully acknowledges the support provided for this research through a FRQNT-B3 (Fonds de

recherche du Québec – Nature et technologies) scholarship. The authors also acknowledge the support provided for this research by the INTER (le Groupe Ingénierie des technologies interactives en réadaptation ) research group.

## REFERENCE

- [1] K. Kiguchi, M. H. Rahman, and T. Yamaguchi, "Adaptation strategy for the 3DOF exoskeleton for upper-limb motion assist," in *2005 IEEE International Conference on Robotics and Automation, April 18, 2005 - April 22, 2005*, Barcelona, Spain, 2005, pp. 2296-2301.
- [2] K. Nagai, I. Nakanishi, H. Hanafusa, S. Kawamura, M. Makikawa, and N. Tejima, "Development of an 8 DOF robotic orthosis for assisting human upper limb motion," presented at the 1998 IEEE International Conference on Robotics and Automation, Leuven, Belgium, 1998.
- [3] T. Nef, M. Mihelj, and R. Riener, "ARMin: a robot for patient-cooperative arm therapy," *Medical & Biological Engineering & Computing*, vol. 45, pp. 887-900, Sep 2007.
- [4] M. H. Rahman, M. J. Rahman, O. L. Cristobal, M. Saad, J. P. Kenne, and P. S. Archambault, "Development of a Whole arm Wearable Robotic Exoskeleton for Rehabilitation and to Assist Upper Limb Movements," *Robotica*, DOI: <http://dx.doi.org/10.1017/S0263574714000034>, Published online: 28 January 2014, pp. 1-21, 2014.
- [5] M. H. Rahman, M. Saad, J. P. Kenne, and P. S. Archambault, "Modeling and Development of an Exoskeleton Robot for Rehabilitation of Wrist Movements," in *2010 IEEE/ASME International Conference on Advanced Intelligent Mechatronics (AIM 2010), 6-9 July 2010*, Montreal, Canada, 2010, pp. 25-30.
- [6] M. H. Rahman, P. S. Archambault, M. Saad, O. L. Cristobal, and S. B. Ferrer, "Robot Aided Passive Rehabilitation using Nonlinear Control Techniques," presented at the Asian Control Conference (ASCC 2013), Istanbul, Turkey, 2013.
- [7] M. H. Rahman, O. L. Cristobal, M. Saad, J. P. Kenne, and P. S. Archambault, "Cartesian Trajectory Tracking of an Upper Limb Exoskeleton Robot " in *IECON 2012*, Montreal, 2012.
- [8] M. H. Rahman, M. Saad, J. P. Kenne, and P.S. Archambault, "Robot assisted rehabilitation for elbow and forearm movements," *Int. J. Biomechanics and Biomedical Robotics*, vol. 1, pp. 206-218, 2011.
- [9] M. H. Rahman, M. J. Rahman, M. Saad, O. L. Cristobal, and P. S. Archambault, "Control of an Upper Extremity Exoskeleton Robot to Provide Active Assistive Therapy," *International Conference on Modelling, Identification & Control (ICMIC)* pp. 105-110, 31stAug.-2ndSept. 2013 2013.
- [10] K. Kiguchi, M. H. Rahman, and M. Sasaki, "Neuro-fuzzy based motion control of a robotic exoskeleton: considering end-effector force vectors," in *Proceedings. 2006 Conference on International Robotics and Automation*, Orlando, FL, USA, 2006, pp. 3146-8.
- [11] S. Komada, Y. Hashimoto, N. Okuyama, T. Hisada, and J. Hirai, "Development of a Biofeedback Therapeutic-Exercise-Supporting Manipulator," *IEEE Transactions on Industrial Electronics*, vol. 56, pp. 3914-3920, Oct 2009.
- [12] L. Lucas, M. DiCicco, and Y. Matsuoka, "An EMG-Controlled Hand Exoskeleton for Natural Pinching," *Journal of Robotics and Mechatronics*, vol. 16, pp. 482-488, 2004.
- [13] J. Rosen, M. Brand, M. B. Fuchs, and M. Arcan, "A myosignal-based powered exoskeleton system," *IEEE Transactions on Systems Man and Cybernetics Part a-Systems and Humans*, vol. 31, pp. 210-222, May 2001.
- [14] Z. O. Khokhar, Z. G. Xiao, and C. Menon, "Surface EMG pattern recognition for real-time control of a wrist exoskeleton," *Biomed Eng Online*, vol. 9, p. 41, 2010.
- [15] H. J. Liu and K. Y. Young, "An Adaptive Upper-Arm EMG-Based Robot Control System," *International Journal of Fuzzy Systems*, vol. 12, pp. 181-189, Sep 2010.
- [16] P. Shenoy, K. J. Miller, B. Crawford, and R. P. N. Rao, "Online electromyographic control of a robotic prosthesis," *Ieee Transactions on Biomedical Engineering*, vol. 55, pp. 1128-1135, Mar 2008.
- [17] M. H. Rahman, T. K. Ouimet, M. Saad, J. P. Kenne, and P. S. Archambault, "Control of an Exoskeleton Robot Arm with Sliding Mode Exponential Reaching Law," *International Journal of Control, Automation and Systems*, vol. 11, no.1, pp.92-104, 2013.
- [18] C. J. Fallaha, M. Saad, H. Y. Kanaan, and K. Al-Haddad, "Sliding-Mode Robot Control With Exponential Reaching Law," *IEEE Transactions on Industrial Electronics*, vol. 58, pp. 600-610, 2011.
- [19] K. Kiguchi, M. H. Rahman, M. Sasaki, and K. Teramoto, "Development of a 3DOF mobile exoskeleton robot for human upper-limb motion assist," *Robotics and Autonomous Systems*, vol. 56, pp. 678-691, Aug 31 2008.
- [20] H. Gray and C. D. Clemente, *Anatomy of the human body*, 30th American ed. Philadelphia: Lea & Febiger, 1985.
- [21] M. H. Rahman, T. K. Ouimet, M. Saad, J. P. Kenne, and P. S. Archambault, "Development of a 4DoFs Exoskeleton Robot for Passive Arm Movement Assistance," *Int. J. Mechatronics and Automation*, vol. 2, no.1, pp. 34-50, 2012.
- [22] H. Khalil, *Nonlinear systems*, 3rd ed. Upper Saddle River, N.J.: Prentice Hall, 2002.

# Modeling of movement of the planning robot

Sergey F. Jatsun, Lyudmila Yu. Vorochayeva and Alexander V. Vorochayev

**Abstract**— In this work we will look at a planning robot, whose controlled planning is provided by the wings and tail, develop a mathematical model which describes the apparatus' movement and pay special attention to the interaction of the wings and tail with the surrounding environment.

**Keywords**— planning robot, controlled flight, aerodynamic force, multilink system.

## I. INTRODUCTION

One of the developing area of robotics is to create devices moving with a jump from the surface, due to their high maneuverability over rough or uneven terrain and the possibility of their use in military and intelligence purposes, for the inspection of buildings and environmental monitoring after natural and man-made disasters. Extending the functionality of jumping devices, namely to increase the range and reduce vertical jump velocity component during the fall to protect against damage, wings used [1-6].

## II. MATHEMATICAL MODEL OF MOVEMENT OF THE ROBOT AT THE FLIGHT STAGE

In this work is a robot consisting of two modules: a jumping and a flying, whose scheme is shown on fig. 1. The jumping module comprises links 1 – 4, where link 1 – foot; links 2 and 3 form the leg; link 4 is the body; the flying module is formed by wings 5 and tail 6. In order to execute a jump it is necessary to position the links of the jumping module relative to each other and accelerate them. This is achieved by using 3 actuators. The leg's links can rotate relative to each other at the expense of the actuator 8 installed in it and the foot - relative to link 2 of the leg with the help of rotating actuator 7 attached to link 2, which allows the robot to position itself before its separation from the surfaces. Leg links 2 and 3 form a couple of progress, at the expense of which the acceleration of the apparatus required for the jump is achieved. This is realized by actuator 9. The flying module is used for planning after the

robot attains the highest point of the jump at the expense of the spread out wings and tail. In order to achieve a controlled flight the wings can rotate relative to the body with the help of actuator 10 and the tail attached to link 2 can change its angle of inclination relative to the body at the expense of actuator 8.

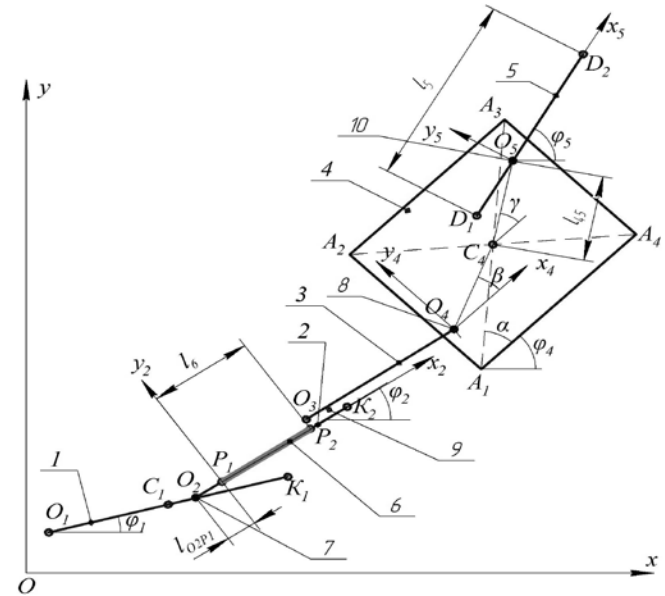


Fig. 1 Scheme of a planning robot.

We shall be looking at the apparatus' movement in the vertical plane  $Oxy$ , with each link except link 6 we will connect relative system of coordinates  $Ox_iy_i, i=1-5$ . In order to develop a mathematical model of the robot we'll introduce a series of assumptions. We'll assume that all the links of the device are absolutely rigid bodies; links 1 – 3, 5, 6 have lengths  $l_i, i=1-3, 5, 6$  and link 4 is a rectangle  $A_1A_2A_3A_4$  of dimensions  $2a \times 2b$ . At this stage we'll neglect the masses of links 5 and 6 since they are very small as compared to that of the other links. The centers of mass,  $m_i, i=1-4$  of the links are concentrated to their centers of symmetry, points  $C_i$ . The length of the leg is given by the distance  $l_{23}$  between the points  $O_2$  and  $O_4$ , while the position of the latter in the body is determined by distance  $l_4$  and angle  $\beta$ . The position of the point  $O_5$  of attachment of the wing in the body is given by distance  $l_{45}$  and angle  $\gamma$ . The tail, link 6, is attached to leg link 2 at a distance  $l_{O_2P_1}$  from point  $O_2$  and has length  $l_6$ , which is limited by points  $P_1$  и  $P_2$ .

The difference between the model in this article and that looked at in [7-11] is the presence of wings and a tail, therefore special attention is paid to the influence of the surrounding environment on the jump. During flight the device moves separately from the surface and the body's center of mass is displaced along axes  $Ox$  и  $Oy$ . Link 3 is rigidly connected to

Work is performed with RFFI, Project № 14-08-00581 «Studying of regularities of movement of the mobile multilink robots moving with a separation from a surface at the expense of energy saved up in elastic elements».

S. F. Jatsun is with the Southwest State University, Kursk, Russia (corresponding author to provide phone: 8-4712-523807; fax: 8-4712-523807; e-mail: teormeh@inbox.ru).

L. Yu. Vorochayeva is with the Southwest State University, Kursk, Russia (corresponding author to provide phone: 8-4712-523807; fax: 8-4712-523807; e-mail: mila180888@yandex.ru).

A. V. Vorochayev is with the Southwest State University, Kursk, Russia (corresponding author to provide phone: 8-4712-523807; fax: 8-4712-523807; e-mail: sasha-vorochaev@yandex.ru).

the device's body, while links 2 and 1, 2 and 3 are rigidly connected among themselves. Wing 5 and tail 6 are used for planning after attainment of the highest point of the jump in such a way that the rotation of the robot's body during flight doesn't occurred:  $\varphi_4=0$ . At this point we consider the case when during flight the wings are passive and their inclination angle relative to the body remains unchanged i.e.  $\varphi_5-\varphi_4=\text{const}$ . Flight control is achieved by changing the angle of rotation of the tail,  $\varphi_2$ . At the stage of flight the generalized coordinates are the projections of the position of the center of mass of the body along the axes of the absolute coordinate system,  $x_{C4}$  and  $y_{C4}$  and the tail's (leg's) angle of rotation -  $\varphi_2$  (fig. 2).

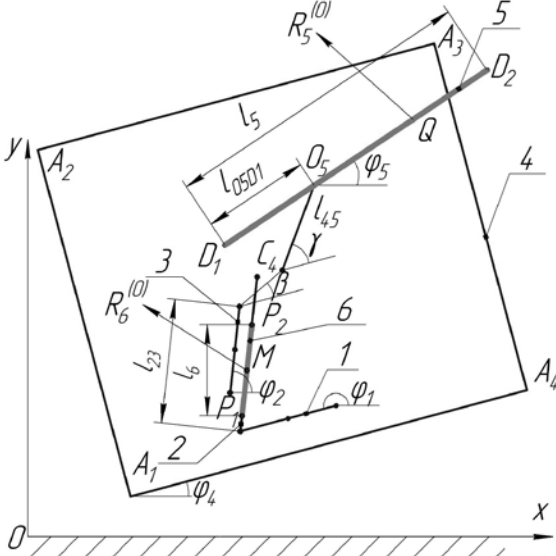


Fig. 2. Settlement scheme of the planning robot during flight.

The differential equations which describe the robot's dynamics during flight are as shown below:

$$\begin{aligned} & \ddot{x}_{C4}(m_1 + m_2 + m_3 + m_4) + \\ & + \ddot{\varphi}_2 \left[ m_1 \left( \frac{l_1}{2} \sin \varphi_1 + l_{23} \sin \varphi_2 \right) + \right. \\ & + m_2 \left( l_{23} - \frac{l_2}{2} \right) \sin \varphi_2 + m_3 \frac{l_3}{2} \sin \varphi_2 \left. \right] \\ & + \dot{\varphi}_2^2 \left[ m_1 \left( \frac{l_1}{2} \cos \varphi_1 + l_{23} \cos \varphi_2 \right) + \right. \\ & + m_2 \left( l_{23} - \frac{l_2}{2} \right) \cos \varphi_2 + m_3 \frac{l_3}{2} \cos \varphi_2 \left. \right] = -R_{5x}^{(0)} - R_{6x}^{(0)}, \quad (1) \end{aligned}$$

$$\begin{aligned} & \ddot{y}_{C4}(m_1 + m_2 + m_3 + m_4) - \\ & - \ddot{\varphi}_2 \left( m_1 \left( \frac{l_1}{2} \cos \varphi_1 + l_{23} \cos \varphi_2 \right) + \right. \\ & + m_2 \left( l_{23} - \frac{l_2}{2} \right) \cos \varphi_2 + m_3 \frac{l_3}{2} \cos \varphi_2 \left. \right) + \\ & + \dot{\varphi}_2^2 \left( m_1 \left( \frac{l_1}{2} \sin \varphi_1 + l_{23} \sin \varphi_2 \right) + \right. \\ & + m_2 \left( l_{23} - \frac{l_2}{2} \right) \sin \varphi_2 + m_3 \frac{l_3}{2} \sin \varphi_2 \left. \right) = \\ & = -(m_1 + m_2 + m_3 + m_4)g - R_{5y}^{(0)} - R_{6y}^{(0)} \quad (2) \end{aligned}$$

$$\begin{aligned} & \ddot{\varphi}_2 \left[ m_1 l_4 \left( \frac{l_1}{2} \cos(\varphi_1 - (\varphi_4 + \beta)) + \right. \right. \\ & \left. \left. + l_{23} \cos(\varphi_2 - (\varphi_4 + \beta)) \right) + \right. \\ & + m_2 \left( l_{23} - \frac{l_2}{2} \right) l_4 \cos(\varphi_2 - (\varphi_4 + \beta)) + \\ & \left. + m_3 \frac{l_3}{2} l_4 \cos(\varphi_2 - (\varphi_4 + \beta)) \right] + \\ & + \ddot{x}_{C4}(m_1 + m_2 + m_3) l_4 \sin(\varphi_4 + \beta) - \\ & - \ddot{y}_{C4}(m_1 + m_2 + m_3) l_4 \cos(\varphi_4 + \beta) - \\ & - \dot{\varphi}_2^2 \left[ m_1 l_4 \left( \frac{l_1}{2} \sin(\varphi_1 - (\varphi_4 + \beta)) + \right. \right. \\ & \left. \left. + l_{23} \sin(\varphi_2 - (\varphi_4 + \beta)) \right) + \right. \\ & + m_2 \left( l_{23} - \frac{l_2}{2} \right) l_4 \sin(\varphi_2 - (\varphi_4 + \beta)) + \\ & \left. + m_3 \frac{l_3}{2} l_4 \sin(\varphi_2 - (\varphi_4 + \beta)) \right] = \end{aligned}$$

$$= (m_1 + m_2 + m_3)g \frac{l_4}{2} \cos(\varphi_4 + \beta) + M_5 + M_6 \quad (5)$$

In the general case the aerodynamics forces  $R_5$  and  $R_6$  can be resolved into projections in the coordinate systems  $Ox_5y_5$ ,  $Oxy$  and  $O_2x_2y_2$  (fig. 3, fig. 4):

$$\bar{R}_5 = \bar{R}_{5x}^{(0)} + \bar{R}_{5y}^{(0)} = \bar{R}_{5x}^{(5)} + \bar{R}_{5y}^{(5)}, \quad (4)$$

$$\bar{R}_6 = \bar{R}_{6x}^{(0)} + \bar{R}_{6y}^{(0)} = \bar{R}_{6x}^{(2)} + \bar{R}_{6y}^{(2)}. \quad (5)$$

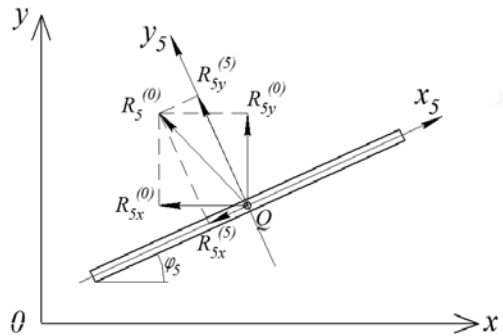


Fig. 3. The scheme of application of the aerodynamic force to the wing.

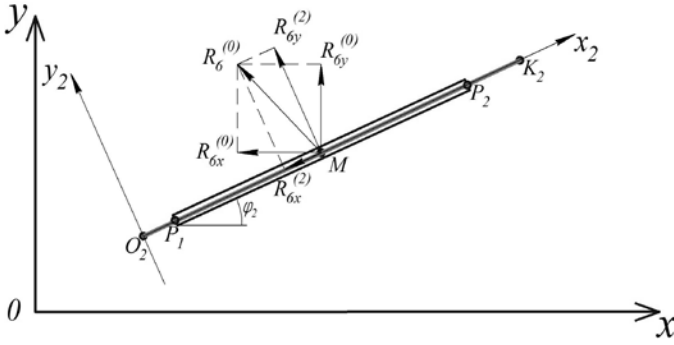


Fig. 4. The scheme of application of the aerodynamic force to the tail.

We'll assume that the wing and tail have zero width, then  $\bar{R}_5 = \bar{R}_{5y}^{(5)}$ ,  $\bar{R}_6 = \bar{R}_{6y}^{(2)}$ . We will look at point  $Q$  and point  $M$  as the points of application of the aerodynamic forces to the wing and to the tail respectively. The position of each of the points is determined as the center of mass which corresponds to the law of distribution of the aerodynamic force on the wing and tail respectively.

For the wing we get the following formula for the calculation of the aerodynamic force:

$$R_{5y}^{(5)} = \frac{C_R \rho S_5^{05x5}}{2} (\dot{y}_Q^{(5)})^2 = Al^2_{D1Q} + Bl_{D1Q} + C, \quad (6)$$

where distance  $l_{D1Q}$  equals:

$$l_{D1Q} = \frac{(3Al_5^2 + 4Bl_5 + 6C)l_5}{4Al_5^2 + 6Bl_5 + 12C}, \quad (7)$$

The coefficients  $A$ ,  $B$  и  $C$  are evaluated in the following way:

$$A = \frac{C_R \rho S_5^{05x5}}{2} \cdot \dot{\varphi}_5^2, \quad (8)$$

$$B = \frac{C_R \rho S_5^{05x5}}{2} \cdot (2\dot{y}_{C4} \dot{\varphi}_5 \cos \varphi_5 - 2\dot{x}_{C4} \dot{\varphi}_5 \sin \varphi_5) \quad (9)$$

$$C = \frac{C_R \rho S_5^{05x5}}{2} \cdot [x_{C4}^2 \sin^2 \varphi_5 - 2\dot{y}_{C4} \dot{x}_{C4} \sin \varphi_5 \cos \varphi_5 - 2\dot{x}_{C4} \dot{\varphi}_4 l_{45} \sin \varphi_5 \cos(\varphi_4 - \varphi_5 + \gamma) + \dot{y}_{C4}^2 \cos^2 \varphi_5 + 2\dot{x}_{C4} \dot{\varphi}_5 l_{05D1} \sin \varphi_5 + 2\dot{\varphi}_4 l_{45} \dot{y}_{C4} \cos(\varphi_4 - \varphi_5 + \gamma) \cos \varphi_5 - 2\dot{y}_{C4} \dot{\varphi}_5 l_{05D1} \cos \varphi_5 + \dot{\varphi}_4^2 l_{45}^2 \cos^2(\varphi_4 - \varphi_5 + \gamma) - 2\dot{\varphi}_4 l_{45} \dot{\varphi}_5 l_{05D1} \cos(\varphi_4 - \varphi_5 + \gamma) + \dot{\varphi}_5^2 l_{05D1}^2] \quad (10)$$

The projections of point  $Q$ 's velocity,  $\dot{y}_Q^{(5)}$  on axis  $O_5y_5$  are written in the following way:

$$\dot{y}_Q^{(5)} = -\dot{x}_{C4} \sin \varphi_5 + \dot{y}_{C4} \cos \varphi_5 + \dot{\varphi}_4 l_{45} \cos(\gamma + \varphi_4 - \varphi_5) - \dot{\varphi}_5 (l_{05D1} - l_{D1Q}) \quad (11)$$

The following equations are for the tail:

$$R_{6y}^{(2)} = \frac{C_R \rho S_6^{02x2}}{2} (\dot{y}_M^{(2)})^2 = Pl^2_{P1M} + Hl_{P1M} + N, \quad (12)$$

$$l_{P1M} = \frac{(3Pl_6^2 + 4Hl_6 + 6N)l_6}{4Pl_6^2 + 6Hl_6 + 12N}. \quad (13)$$

The coefficients  $P$ ,  $H$ ,  $N$  are equal to:

$$P = \frac{C_R \rho S_6^{02x2}}{2} \dot{\varphi}_2^2, \quad (14)$$

$$H = \frac{C_R \rho S_6^{02x2}}{2} (-2\dot{x}_{C4} \dot{\varphi}_2 \sin \varphi_2 + 2\dot{y}_{C4} \dot{\varphi}_2 \cos \varphi_2 - 2\dot{\varphi}_2 \dot{\varphi}_4 l_4 / 2 \cos(\varphi_2 - \varphi_4 - \beta) - 2\dot{\varphi}_2^2 (l_{23} - l_{O2P1})) \quad (15)$$

$$N = \frac{C_R \rho S_6^{02x2}}{2} [x_{C4}^2 \sin^2 \varphi_2 - 2\dot{x}_{C4} \dot{y}_{C4} \sin \varphi_2 \cos \varphi_2 + 2\dot{x}_{C4} \dot{\varphi}_4 l_4 / 2 \sin \varphi_2 \cos(\varphi_2 - \varphi_4 - \beta) + 2\dot{x}_{C4} \dot{\varphi}_2 (l_{23} - l_{O2P1}) \sin \varphi_2 + \dot{y}_{C4}^2 \cos^2 \varphi_2 - 2\dot{y}_{C4} \dot{\varphi}_4 l_4 / 2 \cos(\varphi_2 - \varphi_4 - \beta) \cos \varphi_2 - 2\dot{y}_{C4} \dot{\varphi}_2 (l_{23} - l_{O2P1}) \cos \varphi_2 + \dot{\varphi}_4^2 l_4^2 / 4 \cos^2(\varphi_2 - \varphi_4 - \beta) + 2\dot{\varphi}_2 \dot{\varphi}_4 l_4 / 2 (l_{23} - l_{O2P1}) \cos(\varphi_2 - \varphi_4 - \beta) + \dot{\varphi}_2^2 (l_{23} - l_{O2P1})^2] \quad (16)$$

The projections of point  $M$ 's velocity,  $\dot{y}_M^{(2)}$  on the axis  $O_2y_2$  is written in the following way:

$$\dot{y}_M^{(2)} = -\dot{x}_{C4} \sin \varphi_2 + \dot{y}_{C4} \cos \varphi_2 - \dot{\varphi}_4 l_4 / 2 \cos(\varphi_2 - (\varphi_4 + \beta)) - \dot{\varphi}_2 (l_{23} - l_{O2P1} - l_{P1M}) \quad (17)$$

The projections of the aerodynamic force on the absolute coordinate axes are calculated by the following formulas:

$$R_{5x} = \frac{C_R \rho S_5^{05x5}}{2} \cdot \dot{y}_Q^{(5)} \left| \dot{y}_Q^{(5)} \right| \cos \varphi_5, \quad (18)$$

$$R_{6x} = \frac{C_R \rho S_6^{02x2}}{2} \cdot \dot{y}_M^{(2)} \left| \dot{y}_M^{(2)} \right| \cos \varphi_2 \quad (19)$$

$$R_{5y} = \frac{C_R \rho S_5^{05x5}}{2} \cdot \dot{y}_Q^{(5)} \left| \dot{y}_Q^{(5)} \right| \sin \varphi_5, \quad (20)$$

$$R_{6y} = \frac{C_R \rho S_6^{02x2}}{2} \cdot \dot{y}_M^{(2)} \left| \dot{y}_M^{(2)} \right| \sin \varphi_2 \quad (21)$$

where  $\rho$  – the mass density of air,  $C_R$  – a dimensionless coefficient of aerodynamic force,  $S_5^{05x5}$  – the wing square along axis  $O_5x_5$ ,  $S_6^{02x2}$  – the square of the tail along axis  $O_2x_2$ .

Aerodynamic forces are determined from the following conditions:

$$R_{5x}^{(0)} = \begin{cases} R_{5x}^{(0)}, & \text{if } \dot{y}_{C4} < 0 \\ 0, & \text{if } \dot{y}_{C4} \geq 0 \end{cases}, \quad R_{5y}^{(0)} = \begin{cases} R_{5y}^{(0)}, & \text{if } \dot{y}_{C4} < 0 \\ 0, & \text{if } \dot{y}_{C4} \geq 0 \end{cases}. \quad (22)$$

$$R_{6x}^{(0)} = \begin{cases} R_{6x}^{(0)}, & \text{if } \dot{y}_{C4} < 0 \\ 0, & \text{if } \dot{y}_{C4} \geq 0 \end{cases}, \quad R_{6y}^{(0)} = \begin{cases} R_{6y}^{(0)}, & \text{if } \dot{y}_{C4} < 0 \\ 0, & \text{if } \dot{y}_{C4} \geq 0 \end{cases}. \quad (23)$$

The moments created by the aerodynamic forces are given below:

$$M_5 = R_{5x}^{(0)} (l_{45} \cos(\gamma + \varphi_4) - (l_{05D1} - l_{D1Q}) \cos \varphi_5) - R_{5y}^{(0)} (l_{45} \sin(\gamma + \varphi_4) - (l_{05D1} - l_{D1Q}) \sin \varphi_5). \quad (24)$$

$$M_6 = -R_{6x}^{(0)} (l_4 / 2 \sin(\varphi_4 + \beta) + (l_{23} - l_{O2P1} - l_{P1M}) \sin \varphi_2) + R_{6y}^{(0)} (l_4 / 2 \cos(\varphi_4 + \beta) + (l_{23} - l_{O2P1} - l_{P1M}) \cos \varphi_2) \quad (25)$$

### III. CONTROL SYSTEM OF A PLANNING ROBOT

The control of the jump is realized in stages 1 – 5, during which the links are positioned and accelerated in order to achieve separation from the surface. Stages 6 and 7 at which describe landing, are uncontrollable. The control system comprises comparator, logic and PID-regulators, control objects and feedback.

The controlling action, besides  $M_{43}^5$ , have the form of piecewise-continuous functions. In the comparator on whose input enter the signals of the actual magnitude of the controlled variables or values:  $\varphi_2$ ,  $\varphi_1$ ,  $\varphi_4$ ,  $\gamma_5$  and  $l_{23}$ , where  $\gamma_5$  – the angle of wing disclosure, occurs their comparison with the required values of certain parameters given in the control algorithm:  $\varphi_2^0$ ,  $\varphi_1^0$ ,  $\varphi_4^0$ ,  $\gamma_5^0$ ,  $l_{23}^*$ ,  $l_{23}^0$ . Errors calculated as the difference between actual and given values, with the exception of  $\Delta\varphi_4$ , enter on the logic regulator's input. In the latter controlling moments and a force are generated and these are relayed into the control object in correspondence to the following algorithm:

1) At the first stage

$$M_{43}^1 = \begin{cases} -M_{43}^{10}, & \text{если } \Delta\varphi_2 > 0, \\ 0, & \text{если } \Delta\varphi_2 \leq 0, \end{cases} \quad (26)$$

where  $\Delta\varphi_2 = (\varphi_2 - \varphi_2^0)$ ,

2) At the second stage

$$M_{21}^2 = \begin{cases} -M_{21}^{20}, & \text{если } \Delta\varphi_1 > 0, \\ 0, & \text{если } \Delta\varphi_1 \leq 0, \end{cases} \quad (27)$$

where  $\Delta\varphi_1 = (\varphi_1 - \varphi_1^0)$ ,

3) At the third stage

$$F_{32}^3 = \begin{cases} -F_{32}^{30}, & \text{если } \Delta l_{23}^3 < 0, \\ 0, & \text{если } \Delta l_{23}^3 \geq 0, \end{cases} \quad (28)$$

where  $\Delta l_{23}^3 = l_{23} - l_{23}^*$ ,

4) At the fourth stage

$$F_{32}^4 = \begin{cases} -F_{32}^{40}, & \text{если } \Delta l_{23}^4 < 0, \\ 0, & \text{если } \Delta l_{23}^4 \geq 0, \end{cases} \quad (29)$$

where  $\Delta l_{23}^4 = l_{23} - l_{23}^0$ , а  $F_{32}^{40} \gg F_{32}^{30}$ .

5) At the fifth stage

$$M_{45}^5 = \begin{cases} -M_{45}^{50}, & \text{если } \Delta\gamma_5 > 0, \\ 0, & \text{если } \Delta\gamma_5 \leq 0, \end{cases} \quad (30)$$

where  $\Delta\gamma_5 = \gamma_5 - \gamma_5^0$ .

The values of the moments and forces  $M_{43}^{10}$ ,  $M_{21}^{20}$ ,  $F_{32}^{30}$ ,  $F_{32}^{40}$ ,  $M_{45}^{50}$  is determined based on the requirements of the technical task during the design of the jumping robot.

The error  $\Delta\varphi_4$  enters on the PID-regulator and on its output

the controlling action in the form of the moment  $M_{43}^5$  is formulated, which provides the rotation of the tail and links 2 and 3 in such a way that  $\Delta\varphi_4 \rightarrow 0$ .

$$M_{43}^5 = K_p \cdot \Delta\varphi_4 + K_i \cdot \int \Delta\varphi_4 dt + K_d \cdot \frac{d(\Delta\varphi_4)}{dt}. \quad (31)$$

### IV. THE RESULTS OF NUMERICAL MODELING

The developed mathematical model allowed us to study the movement of a planning robot and reveal its peculiarities or special features. The modeling was carried out for a robot of mass  $m=0,1$  kg body's dimensions:  $a=0,1$  m,  $b=0,1$  m, wing length  $l_5=0,2$  m, tail length  $l_6=0,15$  m and wing square  $S_5=0,16$  m<sup>2</sup> and tail  $S_6=0,06$  m<sup>2</sup>. The mass density of air,  $\rho=1,2$  kgs<sup>2</sup>/m<sup>4</sup>; the aerodynamic force coefficient  $C_R=0,6$ .

On fig.5 are shown graphs of the trajectories of center of mass of the robot's body during a jump with an initial height,  $h=0,5$  m when the change of the relative angle between the wings and the body  $\varphi_{45}$ , lies in the range 0-15<sup>0</sup>, and also in the absence of wings. From the graphs it is clear that during planning the distance travelled by the device along axis  $Ox$  exceeds the same, but without planning by 40 % at  $\varphi_{45}=0^0$ , by 50 % at  $\varphi_{45}=5^0$ , by 63% at  $\varphi_{45}=10^0$ , by  $\varphi_{45}=15^0$  in 2,5 times. Based on that we can conclude that the effectiveness of planning increases as the relative angle between the wings and body increases.

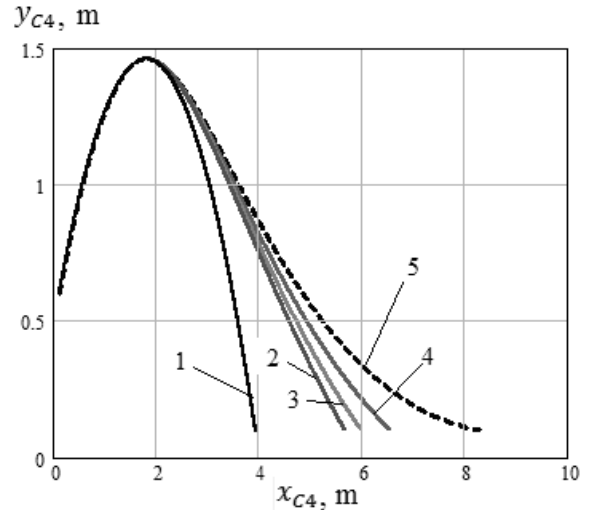


Fig.5 The trajectories of the movement of the body's center of mass:

1 – without wings; 2 -  $\varphi_{45}=0$ , 3 -  $\varphi_{45}=5^0$ , 4 -  $\varphi_{45}=10^0$ , 5 -  $\varphi_{45}=15^0$

The graphs of the relative angle of rotation of the tail are as shown in fig. 6. During movement without wings the angle of rotation of the tail remains unchanged for the rest of the flight and equal to the inclination angle of the legs after positioning  $\varphi_2^0$ . In all remaining cases an increase in the angle of rotation of the tail is observed and then its decrease along a curve similar to a half-wave sinusoid, and the value of angle  $\varphi_2$  attained towards the end of the flight is practically independent from the value of  $\varphi_{45}$  and always exceeds  $\varphi_2^0$ .

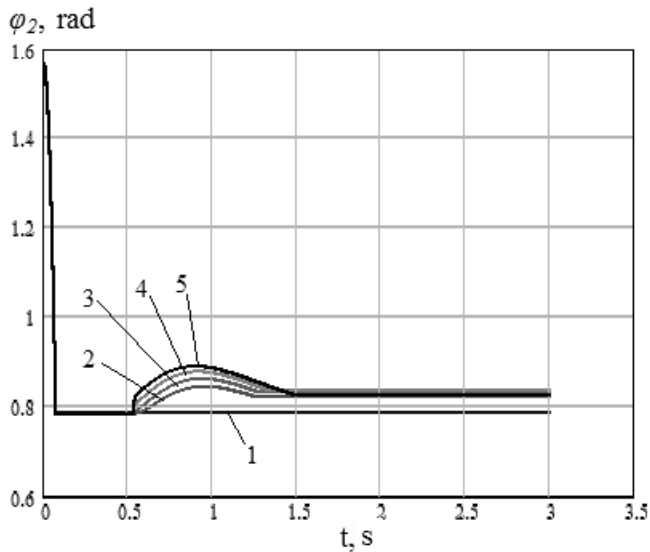


Fig. 6 Graphs of  $\varphi_2(t)$ : 1 – without wings; 2 -  $\varphi_{45}=0$ , 3 -  $\varphi_{45}=5^\circ$ , 4 -  $\varphi_{45}=10^\circ$ , 5 -  $\varphi_{45}=15^\circ$

From the graphs in fig. 7 it is clear that with an increase in wing area the range of flight increases, with an increment of  $S_5$  by 60% the flight range increases by 30%.

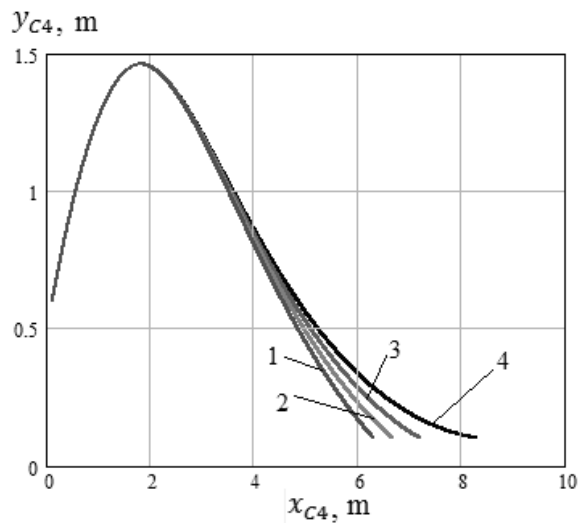


Fig. 7 The trajectories of the movement of the body's center of mass: 1 -  $S_5=0.05 \text{ m}^2$ , 2 -  $S_5=0.06 \text{ m}^2$ , 3 -  $S_5=0.07 \text{ m}^2$ , 4 -  $S_5=0.08 \text{ m}^2$

The graphs fig. 8 illustrate that with an increase in the inclination angle of link 2 of the accelerating module to the horizontal plane at which the jump takes place at constant accelerating force increases the height of the jump and the range of flight. This is explained by the fact that as angle  $\varphi_2^0$  increases, the vertical component of the velocity at the moment of separation of the device from the surface increases, which leads to the attainment of a greater height of the jump. This and a greater horizontal velocity component at the highest point in turn explains the more effective use of the jump.

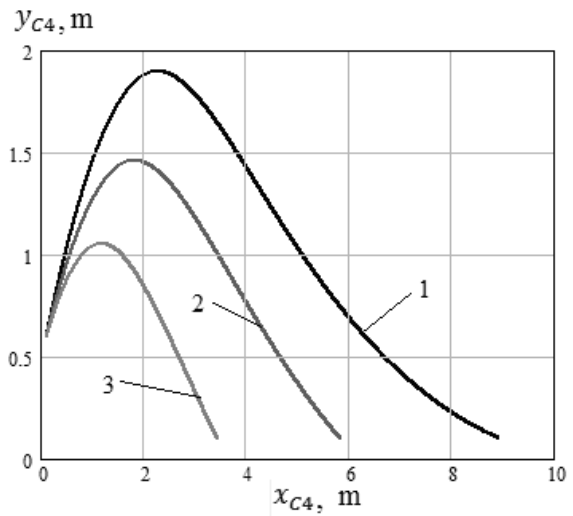


Fig. 8 The trajectories of the movement of the body's center of mass: 1 -  $\varphi_2^0=50^\circ$ , 2 -  $\varphi_2^0=45^\circ$ , 3 -  $\varphi_2^0=40^\circ$

The angle of rotation of the tail at this point changes as shown on fig. 9. When  $\varphi_2^0=50^\circ$  at first a sharp decrease in the value of  $\varphi_2$  is observed, then a smooth increase and decrease and the values before and after the flight are almost the same. When  $\varphi_2^0=40^\circ$  and  $\varphi_2^0=45^\circ$  at the beginning of the flight angle  $\varphi_2$  increases sharply and a jump by a large value occurs at less angles  $\varphi_2^0$ , after which the character of the change in the angle becomes similar to the one written down earlier. With an increase in the angle  $\varphi_2^0$  the value of the inclination angle of the tail after the flight increases.

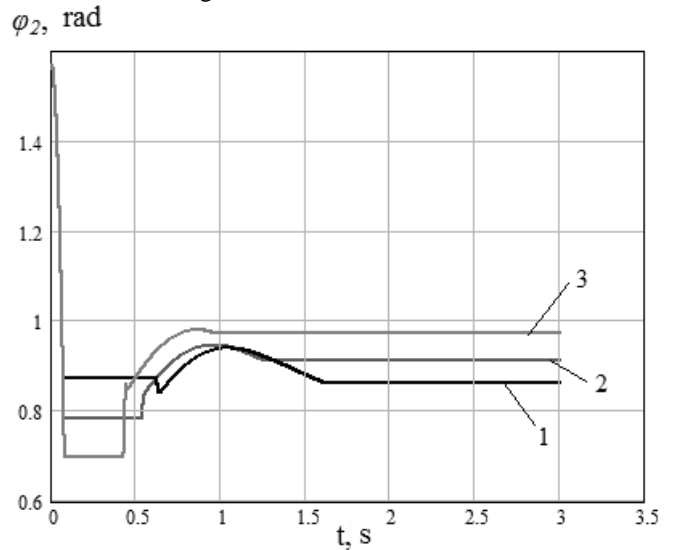


Fig. 9 Graphs of  $\varphi_2(t)$ : 1 -  $\varphi_2^0=50^\circ$ , 2 -  $\varphi_2^0=45^\circ$ , 3 -  $\varphi_2^0=40^\circ$

During a jump from different heights at the same angle of inclination to the horizontal plane with a constant accelerating force the robot in flight behaves in an analogous way: as the height  $h$  increases the range of flight also increases (fig. 10). Only in this case it is explained by the large value of the height, at which the wings and tail open.

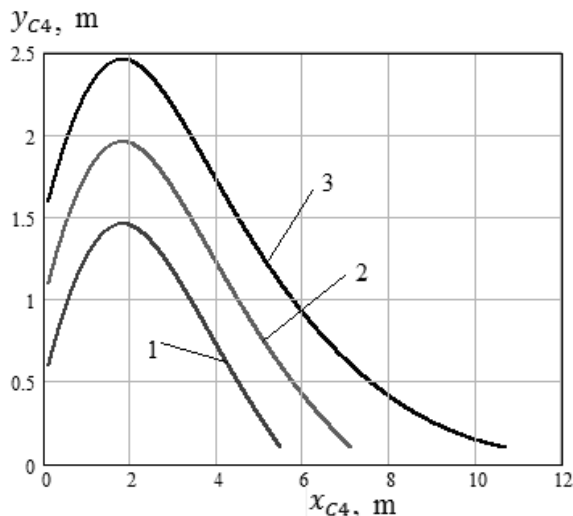


Fig. 10 The trajectories of the movement of the body's center of mass: 1 -  $h=0.5$  m, 2 -  $h=1$  m, 3 -  $h=1.5$  m

## V. CONCLUSION

In work the planning robot equipped with system of wings and a tail, revealing in the top point of a jump and providing operated planning of the device before interaction with a surface is considered. The mathematical model of movement of the device during a separation from a surface is developed, the special attention is paid to model of interaction of the robot with environment. Work of a control system as the device is described. The analysis of trajectories of movement of the robot received by numerical way allows to draw a conclusion that efficiency of use of planning systems increases at jumps from height, with increase of an inclination angle of wings to the body and the square of wings and a tail.

## REFERENCES

- [1] J. Burdick, P. "Fiorini Minimalist jumping robot for celestial exploration", *The International Journal of Robotics Research*, 2003, Vol. 22(7), p.653–674.
- [2] J. F. Roberts, J.-C. Zufferey, D. Floreano "Energy management for indoor hovering robots", *IEEE/RSJ International Conference on Intelligent Robots and Systems*, 2008, p. 1242–1247.
- [3] R. Armour, K. Paskins, A. Bowyer, J. F. V. Vincent, W. Megill "Jumping robots: a biomimetic solution to locomotion across rough terrain", *Bioinspiration and Biomimetics Journal*. 2007. No. 2. P. 65–82.
- [4] S. Hyon, T. Mita "Development of a biologically inspired hopping robot—Kenken", *IEEE International Conference on Robotics and Automation*. Stanford. 2002. P. 3984–3991.
- [5] S. A. Stoeter, P. E. Rybski, N. Papanikolopoulos "Autonomous stair-hopping with scout robots", *IEEE/RSJ international conference on intelligent robots and systems*. 2002. Vol. 1. p. 721–726.
- [6] P. Weiss "Hop. . . hop. . . hopbots!: designers of small, mobile robots take cues from grasshoppers and frogs", *Science News*. 2001. N. 159. 88 p.
- [7] С.Ф. Яцун, Л.Ю. Волкова "Моделирование движения многозвенного прыгающего робота и исследование его характеристик", *Известия РАН. Теория и системы управления*. 2013. - № 4. - С. 137–149.
- [8] С.Ф. Яцун, О.Г. Локтионова, Л.Ю. Волкова, А.В. Ворочаев "Этапы движения четырехзвенного робота, перемещающегося с отрывом от поверхности", *Научно-технические ведомости СПбГПУ*.

*Информатика. Телекоммуникации. Управление*. 2013. - №5. - С. 109-118.

- [9] С.Ф. Яцун, Л.Ю. Волкова, А.В. Ворочаев "Прыгающий робот для проведения поисковых работ", *Экстремальная робототехника - робототехника для работы в условиях опасной окружающей среды: труды 7-го международного симпозиума*. - Санкт-Петербург, 2013. - С. 152-159.
- [10] Л.Ю. Волкова, С.Ф. Яцун "Изучение влияния положения точки закрепления ноги прыгающего робота в корпусе на характер движения устройства", *Нелинейная динамика*. - 2013. - Т. 9. - № 2. - С. 327–342.
- [11] С.Ф. Яцун, Л.Ю. Волкова, А.В. Ворочаев "Исследование режимов разгона четырехзвенного прыгающего аппарата", *Известия Волгоградского государственного технического университета*. 2013. - № 24 (127). - С. 86-92.

## Sergey F. Jatsun

From 1975 to 1976 S.F. Jatsun worked as the junior researcher in Dnepropetrovsk mining institute, then enrolled in postgraduate study. He defended the master's dissertation in the Hungarian language at Mishkoltsky technical university (Hungary) in 1979, in 1982 the academic status of the associate professor is appropriated, in 1990 the doctoral dissertation (Riga, the Riga technical university) is prepared and defended. Since 1980 - the assistant, the senior teacher, the associate professor, and since 1989 - the head of the department "Theoretical mechanics and TMM" in the Kursk state technical university. In 1992 the academic status of professor is appropriated. Scientific interests of professor S.F. Jatsun are the directions "Vibration Machines and Technologies", "Dynamics and Durability of Machines", "Theory of Automatic Control", "Mechatronics", "Robotics". Sergey Fedorovich is the author and the coauthor of 12 monographs and more than 250 scientific works. He received about 120 copyright certificates and patents.

## Lyudmila Yu. Vorochayeva

Since 2010 the assistant to department of theoretical mechanics and mechatronics of Southwest state university, since 2011 the lecturer, since 2014 the senior lecturer. In 2014 the academic status of Candidate of Technical Sciences in "Dynamics, durability of machines, devices and the equipment" is awarded. Scientific interests are the directions "Modelling Mechatronics of Systems", "Multilink Systems", "Mechatronics", "Robotics". Vorochayeva L.Yu. are the author more than 40 scientific works, the coauthor of 2 monographs, the coauthor of 4 patents for useful model and 1 patent for the invention.

## Alexander V. Vorochayev

From 2008 to 2014 the student of Southwest state university in direction "Mechatronics and Robotics", in 2014 defended the master dissertation. Scientific interests are the directions "Modelling Mechatronics of Systems", "Programming and Algorithmization", "Mechatronics", "Robotics". Vorochayev A.V. is the author of 8 scientific works, the coauthor of 2 patents for useful model and 2 certificates on the state registration of programs.

# Design Optimization of a TIA for High Speed Data Applications using $g_m/I_D$ Based Methodology

Claudio Talarico, Gaurav Agrawal and Janet Wang-Roveda

**Abstract**—This paper presents the design optimization of a low power, low noise, broadband transimpedance amplifier (TIA) that finds application as a front-end stage in a fiber optic data receiver. The TIA achieves a gain of 65.5 dB $\Omega$ , a bandwidth of 2.44 GHz and an input referred current noise of 11.91 pA/Hz<sup>1/2</sup>. The design is implemented in a standard 0.18 $\mu$ m digital CMOS process and dissipates 18.32mW from a 1.8V supply.

**Keywords**— Broadband Amplifier, CMOS, Design Optimization, Fiber Optic Receiver, High Speed Data Communication, Transimpedance Amplifier.

## I. INTRODUCTION

A transimpedance amplifier is a critical block of any fiber optic data receiver: it affects significantly cost and performance in terms of speed, signal to noise ratio, and sensitivity. The design of a TIA requires the attentive optimization of a number of conflicting performance metrics including gain, bandwidth, noise, and power consumption [1]. Recent advances in nanoscale technologies made it economically viable to design CMOS TIA amplifiers that meet the stringent performances required by front-end optical transceivers applications. Unfortunately, the complexity of the models required to accurately describe the behavior of CMOS nanoscale transistors prevent the derivation of closed-form analytical expression that could be effectively used in the design optimization flow of even the most simple circuits [2]. This paper describes the development of a framework for the design optimization of nanometer analog and mixed-signal integrated circuits (IC) and applies it to the implementation of a high-speed, high-gain, low-noise and low-power TIA in a 0.18 $\mu$ m standard CMOS technology. The design optimization framework is implemented using MATLAB and is based on the  $g_m/I_D$  methodology [3],[4]. The ratio between transconductance  $g_m$  and bias current  $I_D$  is a figure of merit measuring a transistor ability to translate current (i.e. power) into transconductance (i.e. gain). The main advantage of using a  $g_m/I_D$ -based methodology is the capability to maintain a unified approach for all regions of operation of a MOS transistor. Having a systematic design approach from strong inversion to weak inversion makes the  $g_m/I_D$  methodology an ideal tool for the optimal sizing of transistors.

This is due to the possibility of taking full advantage of the moderate inversion region to optimize the speed-power trade off. Fig. 1 illustrates the relationship between a transistor's speed (i.e. the transistor's transient frequency  $f_T$ ) and its power efficiency (i.e.  $g_m/I_D$ ). The goal of the proposed framework is the development of a systematic design optimization approach to be used in absence of closed-form MOSFET equations.

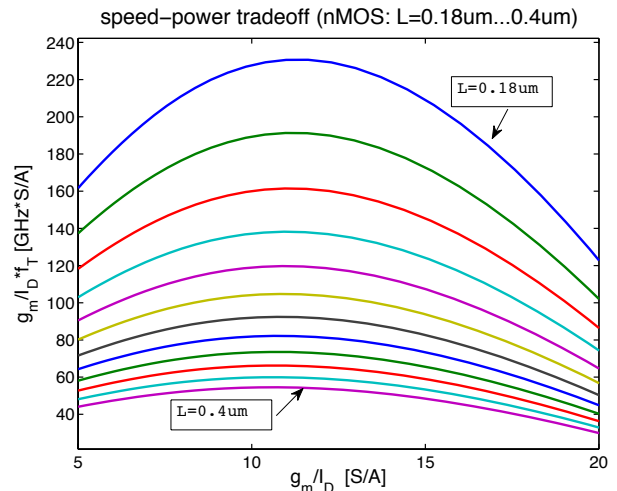


Fig. 1 Relationship between  $f_T * g_m/I_D$  and  $g_m/I_D$  for nMOS transistors with channel length  $L$  varying from 0.18 $\mu$ m to 0.4 $\mu$ m (0.18 $\mu$ m CMOS process)

The rest of the paper is organized as follows. Section II describes the TIA topology and the equations and approximations used to predict and optimize performances. Section III motivates and describes the optimization strategy used for the design of the TIA. Section IV discusses experimental results and compares them to theoretical expectations. Finally, Section V summarizes the results of our work and provides conclusions.

## II. TIA CIRCUIT DESCRIPTION

### A. TIA Topology

The main culprit in the design of a TIA is the capacitance of the photodiode interfacing the fiber optic and the receiver side of the communication system. The photodiode capacitance affects significantly both bandwidth and signal to noise ratio. Fig. 2 depicts the overall structure of a typical optical

communication (OC) system. The goal of an OC system is to transmit and receive large volumes of data across a long distance. A typical OC system consists of three components: a transmitter, a fiber, and a receiver [5]. The transmitter is composed of a mux that aggregates multiple data streams into a single stream, a driver, and an electro-optical transducer (i.e. a laser diode) that converts the electrical data into optical form. The fiber carries the light produced by the laser from the transmitting end to the receiving end. The receiver is composed by a photodetector (i.e. a photodiode) that senses the light coming from the fiber and converts it in electrical form (i.e. a current signal), a TIA, and a demux that decomposes the data back into multiple streams.

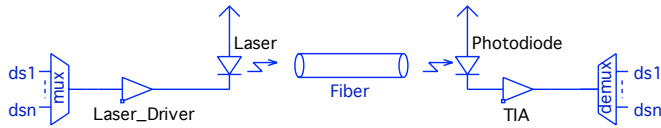


Fig. 2 Typical Optical Communication (OC) System

The main challenge in designing a TIA is to devise a circuit topology that makes it possible to relax the limitation caused by the photodiode capacitance present at the input node of the amplifier. Over the years, several circuit techniques have been proposed. The most commonly used techniques include capacitive peaking, inductive peaking, common gate input configuration and common drain configuration [6]-[8]. In this paper the TIA is implemented using a cascade of three stages. To minimize the effect of the large input capacitance due to the photodiode the input stage is a common gate with  $g_m$  boosted via pMOS current injection. The middle stage is a common source, and the output stage is a source follower. This topology provides low input impedance (thanks to the common gate), high gain (through the combination of the common gate and the common source stages), and the ability to drive a small resistive load (thanks to the low output impedance of the source follower). Despite the  $g_m$  boosting technique applied to the common gate stage, the level of  $g_m$  achievable with a  $0.18\mu\text{m}$  CMOS technology is not adequate to achieve the bandwidth required for optical communication applications. To overcome this challenge, the three basic stages of the TIA are surrounded by a global shunt-shunt resistive feedback. As predictable the feedback causes peaking in the amplifier's frequency response; for the proposed topology is possible to improve the closed loop stability of the TIA and eliminate peaking by using the feedback-zero compensation technique. The TIA is implemented in differential form. A differential TIA has two main advantages: 1) the signal to noise ratio (SNR) of the system is effectively doubled, and 2) the common source stage can be implemented as a differential pair, so the biasing is considerably simpler. Fig.3 illustrates the TIA's topology.

### B. TIA Circuit Analysis

The main bottleneck of the proposed topology is the poor frequency response of the common source. This is due to the

large time constant  $\tau_2$  at input of the common source stage. To reduce the effect of  $\tau_2$  the common source stage is cascoded. Cascoding provides two main advantages: 1) it reduces miller multiplication of the gate-to-drain capacitance and 2) it increases the intrinsic gain of the stage. These advantages are at the expense of a lower voltage swing. Fortunately, for the application at hand large signal swing is not a concern. Fig. 4 shows the complete circuit of the TIA. The photodiode is modeled by the input current signal  $i_{\text{input}}$  and the parasitic capacitances  $C_{pa}$  and  $C_{pb}$ . Fig. 5 shows the equivalent AC half circuit of the TIA. The AC half circuit includes the feedback loading and it is annotated with all capacitances affecting frequency response.

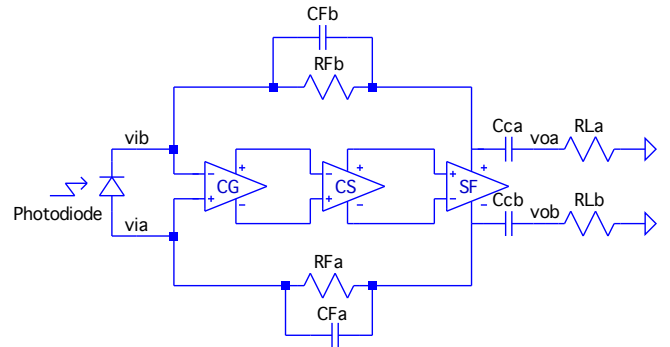


Fig. 3 TIA Topology

(CG = common gate, CS = common source, SF = source follower)

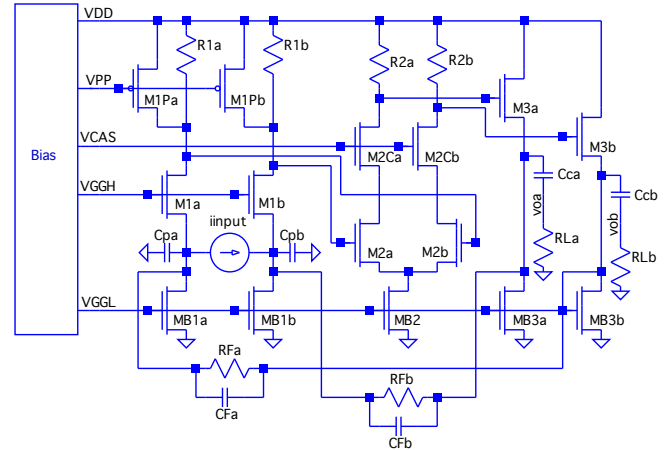


Fig. 4 TIA Schematic

The expressions used to analyze the performances of the TIA are derived from the AC half circuit. The transimpedance forward gain of the half circuit is:

$$a_0 = \frac{v_{out}}{i_{in}} \approx - \frac{g_{m1}^* R_F}{1 + g_{m1}^* R_F} R_1 \cdot g_{m2} R_2 \cdot \frac{g_{m3} R_{Lp}}{1 + g_{m3} R_{Lp}} \quad (1)$$

where  $g_{m1}^* = g_{m1} + g_{m1b}$  and  $R_{Lp} = R_L || R_F || (1/g_{m3b})$ . The shunt-shunt feedback factor is:

$$f_0 = - \frac{1}{R_F} \quad (2)$$

The loop gain is:

$$T_0 = a_0 f_0 \quad (3)$$

The overall closed loop transimpedance gain is:

$$A_0 = \frac{v_{out,diff}}{i_{input}} \approx \frac{2a_0}{1+T_0} \quad (4)$$

where  $i_{input} = i_{in}/2$  and  $v_{out,diff} = v_{oa} - v_{ob}$ . The time constant at the input of the common gate is:

$$\tau_{in} \approx C_{in} \left( R_F \parallel \frac{1}{g_{m1}^*} \right) \quad (5)$$

where  $C_{in} = C_P + C_F + C_{gs1} + C_{sb1} + C_{ddp1}$  and  $C_{ddp1} = C_{gd1} + C_{dbp1}$ . The time constant at the output of the common gate (that is the input of the common source) is:

$$\tau_2 \approx R_1 \cdot C_2 \quad (6)$$

where  $C_2 = C_{gd1} + C_{db1} + C_{gs2} + C_{gd2}(1 + g_{m2}/g_{m2C}^*)$ .

The time constant at the node between the common source transistor and the cascode transistor is:

$$\tau_{2C} \approx \frac{1}{g_{m2C}^*} C_{2C} \quad (7)$$

where  $C_{2C} = C_{db2} + C_{gs2C} + C_{sb2C}$ . The time constants at the output of the common source stage (that is the input of the source follower) are:

$$\tau_{3in} \approx R_2 \cdot C_{3in} \quad \text{and} \quad \tau_{3m} \approx C_{gs3} \frac{R_2 + R_{LP}}{g_{m3} R_{LP} + 1} \quad (8)$$

where  $C_{3in} = C_{db2C} + C_{gd2C} + C_{gd3}$ . The time constant at the output of the source follower is:

$$\tau_{3out} \approx R_{LP} \cdot (C_F + C_{sb3}) \quad (9)$$

The  $-3\text{dB}$  bandwidth of the TIA is estimated using the zero value time constant (ZVTC) method:

$$f_{-3dB} \approx \frac{1+T_0}{2\pi \sum_{for\ all\ i} \tau_i} \quad (10)$$

The input referred current noise power spectral density (PSD) is due to four primary sources: 1) the input referred current noise PSD due to  $R_F$ , 2) the input referred current noise PSD due to  $M_{B1}$ , 3) the input referred current noise PSD due to  $R_1$ , and 4) the input referred current noise PSD due to  $M_{1P}$ .

$$\frac{i_{noise}^2}{\Delta f} = \frac{1}{2} \left( \frac{4KT}{R_F} + 4KT\gamma_n g_{mB1} + \frac{4KTR_1}{A_{CG}^2} + 4KT\gamma_p g_{m1P} \frac{R_1^2}{A_{CG}^2} \right) \quad (11)$$

### III. OPTIMIZATION STRATEGY

For nanoscale devices the traditional analog design methodology based on modeling transistors' behavior through closed-form "square-law" equations is inaccurate and it results

in an excessively large number of iterations. The square-law design equations are based on physical parameters ( $\mu C_{ox}$ ,  $V_{th}$ ,  $V_{dsat}$ , etc.) that for short channel transistors are ill-defined, so achieving optimal performances by properly sizing the components of the circuit is extremely difficult.

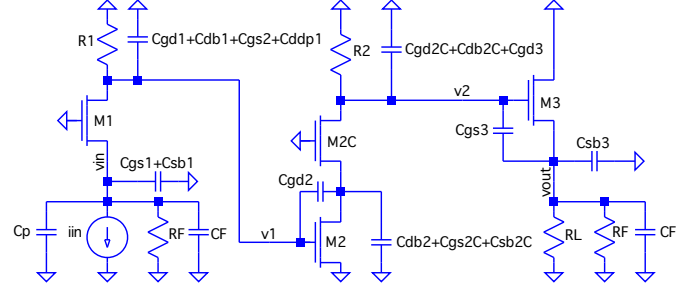


Fig. 5 TIA AC half circuit with feedback loading and relevant capacitances

In this paper rather than using the traditional "square law" methodology we propose to use a  $g_m/I_D$  based methodology. When designing with nanoscale transistors the  $g_m/I_D$  methodology has two main advantages. First, instead of relying on ill defined physical parameters (e.g.  $\mu C_{ox}$ ,  $V_{th}$ ,  $V_{dsat}$ , etc.) we can use design parameters (e.g.  $g_m$ ,  $f_T$ ,  $I_D$ , etc.) that are well defined at any scale and are easier to link with the specifications (e.g. power consumption, bandwidth, etc.). Second, devices can be modeled in the form of look up tables (or charts) rather than closed-form equations. In the case of nanoscale technologies look-up tables provides a more accurate and practical choice.

The key to optimally size transistors is to generate a set of look-up tables that are independent of the transistor gate width  $W$ . In this way the design can be carried out independently of transistors geometry. The optimization process is driven simply by the design specifications and a relevant set of figures of merit. In the proposed framework the figures of merit used are: 1) the transconductance efficiency  $g_m/I_D$ , 2) the transient frequency  $f_T$ , 3) the intrinsic gain  $g_{mro}$ , and 4) the current density  $I_D/W$ . The look-up tables are generated characterizing the given technology through HSPICE. From an analog design perspective, a large  $g_m/I_D$  allows to achieve low-power and high gain circuits, while a small  $g_m/I_D$  is suitable for high-speed applications. Table I summarizes the properties that characterize an analog design at different levels of transconductance efficiency. Fig. 6 illustrates the trade off between transconductance efficiency and transient frequency of a  $0.18\mu\text{m}$  nMOS technology at different levels of inversion  $V_{ov}$ . Fig. 7(a)-(c) plots the transient frequency, the intrinsic gain, and the current density of a  $0.18\mu\text{m}$  nMOS technology for different values of channel length  $L$ .

Given the TIA specifications ( $0.18\mu\text{m}$  CMOS technology, closed loop transimpedance gain of  $60\text{ dB}\Omega$ ,  $2\text{ pF}$  photodiode,  $250\Omega$  load, total current budget up to  $16\text{ mA}$ , and an input referred current noise PSD up to  $160 \times 10^{-24}\text{ A}^2/\text{Hz}$ ) the goal of the design is to maximize speed. The optimization flow

applied to the TIA design can be described as follows:

1. Set the loop gain  $T_0$  to an appropriate value ( $T_0 \geq 10$ ) and derive  $R_F$  based on the design objectives ( $A_0 \geq 60$  dB $\Omega$ ).
2. Set  $g_m/I_D$  for the transistor  $M_3$  (source follower) to allow max output signal swing (that is  $V_{IN3} = V_{DD}/2$ ) and compute the corresponding transient frequency  $f_T$ . Select and appropriate value of bias current based on  $C_{gg3}$  such that the time constants associated with the source follower are not dominant. Estimate the parasitic capacitances and compute the resulting gain  $A_{CD}$  of the source follower.

$$C_{gg3} = \frac{g_{m3}}{2\pi f_{T3}} \quad (12)$$

$$I_{D3} = \frac{g_{m3}}{g_{m3}/I_{D3}} \quad (13)$$

Fig. 8 summarizes the design exploration process described in this step.

3. Partition the amount of gain needed to meet specification between the common source and the common gate:

$$A_{CS}A_{CG} = \frac{a_O}{A_{CD}} \quad (14)$$

An excessive value of  $A_{CS}$  causes a strong miller effect at the intermediate node between the transistors  $M_2$  and  $M_{2C}$  and results in a non optimal value of the dominant time constant  $\tau_2$ . Similarly an excessive value of  $A_{CG}$  implies an excessive value of  $R_1$  and results in a suboptimal value of the dominant time constant  $\tau_2$ . Appropriate values of  $A_{CS}$  and  $A_{CG}$  are in the following ranges:

$$1 \leq A_{CS} \leq 10 \text{ and } \frac{a_o}{A_{CD}A_{CS\max}} \leq A_{CG} \leq \frac{a_o}{A_{CD}} \quad (15)$$

4. Set  $g_m/I_D$  of transistor  $M_1$  and the value of  $R_1$  as the primary design variables. The values of  $g_{m1}/I_{D1}$  and  $R_1$  set the value of  $A_{CG}$ . The value of  $A_{CG}$  set the value of  $A_{CS}$  and therefore the value of  $g_{m2}/I_{D2}$  and  $R_2$ .
5. Sweep  $g_{m1}/I_{D1}$  from weak inversion region ( $g_m/I_D=25$  S/A) to strong inversion region ( $g_m/I_D=5$  S/A) and  $R_1$  from  $A_{CG\min}$  to  $A_{CG\max}$ . Register the performance metrics of every feasible design in the explored space. Design feasibility and the current bias for the CG and CS are determined by the bias constrains.
6. Determine  $g_{m1}/I_{D1}$ ,  $I_{D1}$ ,  $R_1$ ,  $A_{CG}$ ,  $g_{m2}/I_{D2}$ ,  $I_{D2}$ ,  $R_2$ ,  $A_{CS}$ ,  $g_{m3}/I_{D3}$ ,  $I_{D3}$ , and  $A_{CD}$  for the TIA design that achieves the best bandwidthS2.
7. Finally, determine transistor widths from  $g_m/I_D$ , the calculated  $I_D$ , and the current density ( $I_D/W$ ) look-up tables.

TABLE I. TRANSISTOR'S PROPERTIES AT DIFFERENT LEVELS OF TRANSCONDUCTANCE EFFICIENCY

Transconductance Efficiency	
Low $g_m/I_D$	High $g_m/I_D$
Strong Inversion	Weak Inversion
Poor power efficiency	Good power efficiency
Low output voltage range	High output voltage range
High Transient Frequency	Low Transient Frequency
Small Transistor	Large Transistor

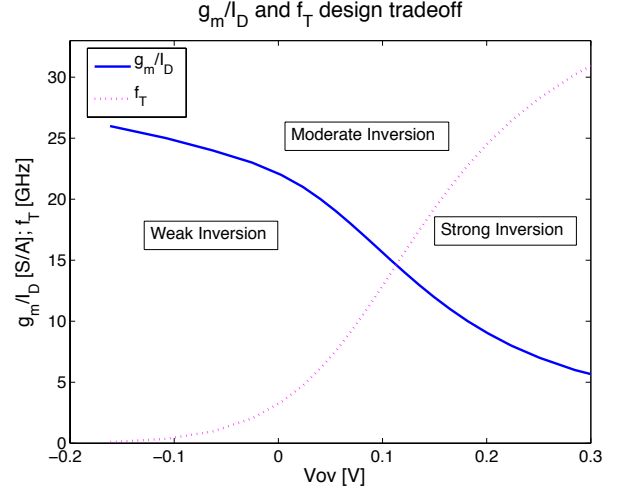


Fig. 6 Plot of  $g_m/I_D$  and  $f_T$  at different levels of inversion  $V_{ov}$  for an nMOS transistor with channel length  $L = 0.18\mu\text{m}$  ( $0.18\mu\text{m}$  CMOS process)

#### IV. EXPERIMENTAL RESULTS

The proposed optimization framework has been applied to the design of a high gain, high speed, low noise, low power TIA implemented in a standard  $0.18\mu\text{m}$  CMOS process. The experimental results match well (within 11.3%) the analytical results obtained through the MATLAB optimization scripts. Table II summarizes and compares the results. Table III summarizes the value of all devices employed in the design of the TIA. To optimize bandwidth all transistors in the signal path have minimum channel length of  $L=0.18\mu\text{m}$ . In contrast, all biasing transistors have channel length of  $L=0.36\mu\text{m}$ . As long as using longer channel length does not causes excessive parasitic capacitance, this choice has the advantage of reducing the loading caused by the bias transistors on the signal path transistors (higher channel length implies higher output resistance) and it lowers the sensitivity of the circuit to PVT variations. Fig. 9 shows the frequency response of the TIA with and without compensation. The value of the compensation capacitance  $C_F$  is calculated using MATLAB root locus plots. The closed loop zeros and poles location is determined through HSPICE pole/zero analysis. Fig. 10 shows the root locus of the amplifier without compensation. After compensation the peaking in the frequency response is completely eliminated and the phase margin is  $PM=45.19^\circ$ . Fig.11 shows the input referred current spectral density of the

system.

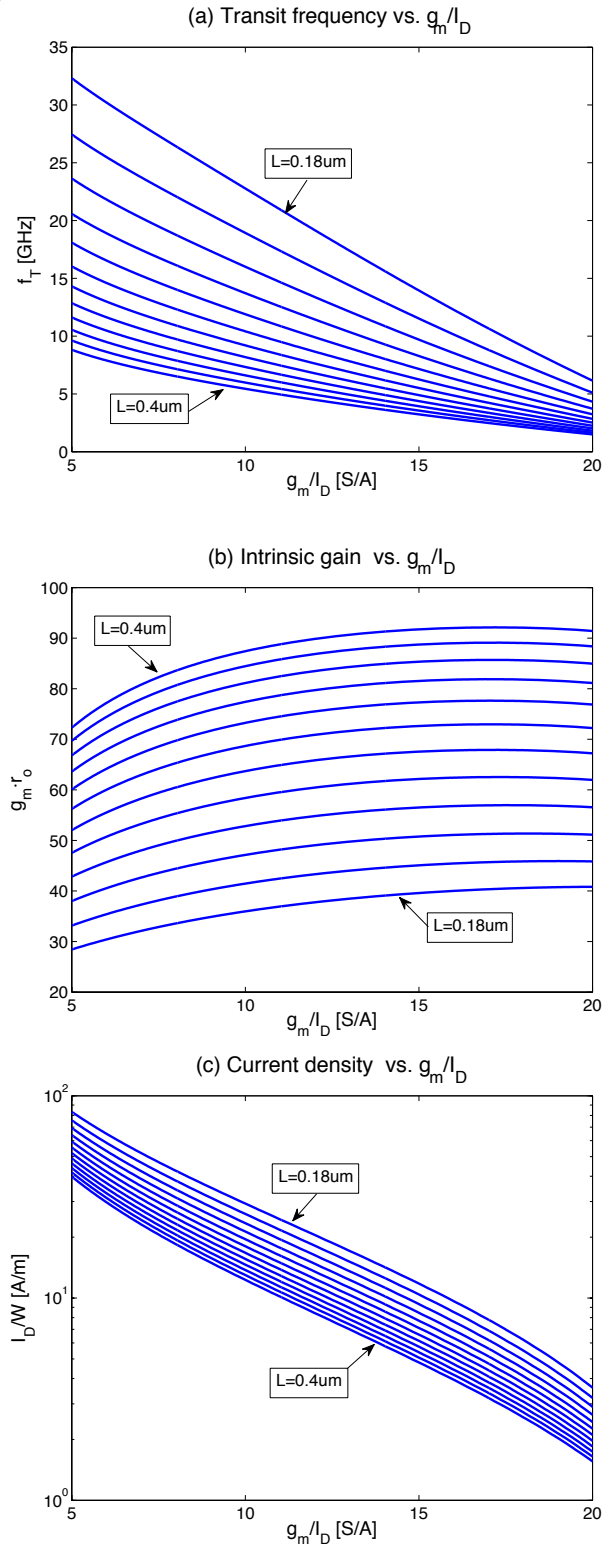


Fig. 7 (a)-(c) Plots of  $f_T$ ,  $g_m r_o$ , and  $I_D/W$  vs.  $g_m/I_D$  for nMOS transistors with channel length  $L$  varying from  $0.18\mu\text{m}$  to  $0.4\mu\text{m}$  ( $0.18\mu\text{m}$  CMOS process)

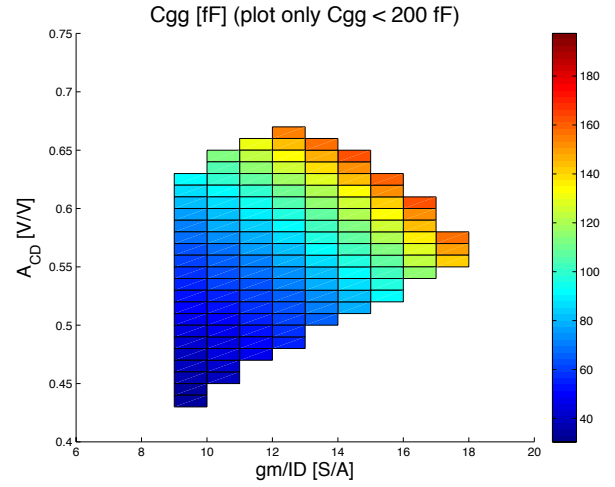


Fig. 8 Source follower design optimization:  $C_{gg}$  capacitance vs.  $g_m/I_D$  and gain  $A_{CD}$

TABLE II. COMPARISON BETWEEN ANALYTICAL RESULTS AND EXPERIMENTAL RESULTS

Performance Metric	Analysis	Simulation	% Relative Error
Gain [dBΩ]	65.37	65.50	-0.20
f3db [GHz]	2.49	2.44	2.01
Input ref. noise [pA/√Hz]	11.99	11.91	0.67
Power dissipated [mW]	20.34	18.32	11.03
Phase Margin [degrees]	47.48	45.19	5.07

TABLE III. TIA DEVICE SIZES

Device	TIA Device Sizing
CPa, CPb [pF]	2
RLa, RLb [Ω]	250
R1a, R1b [Ω]	2300
R2a, R2b [Ω]	590
RFa, RFb [Ω]	1000
CFa, CFb [fF]	110
M1a, M1b [μm]	L=0.18; W=160
M1Pa, M1Pb [μm]	L=0.36; W=50
MB1a, MB1b [μm]	L=0.36; W=150
M2a, M2b [μm]	L=0.18; W=80
M2Ca, M2Cb [μm]	L=0.18; W=50
MB2 [μm]	L=0.36; W=460
M3a, M3b [μm]	L=0.18; W=32
MB3a, MB3b [μm]	L=0.36; W=220

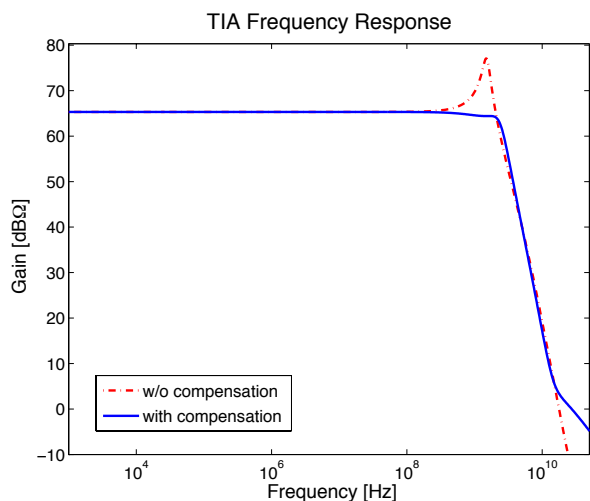


Fig. 9 TIA frequency response with and without compensation

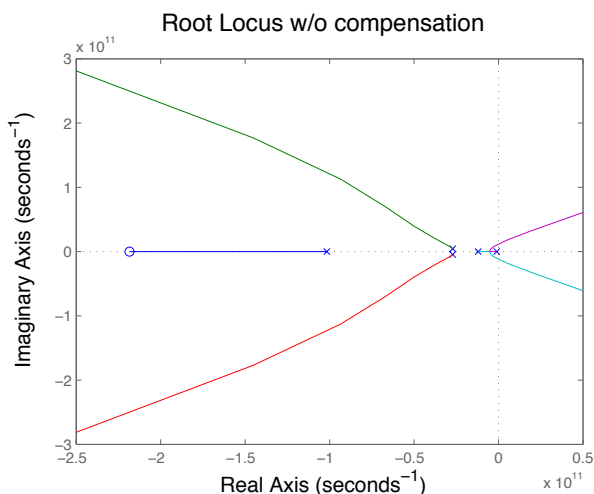


Fig. 10 Root Locus of TIA before compensation

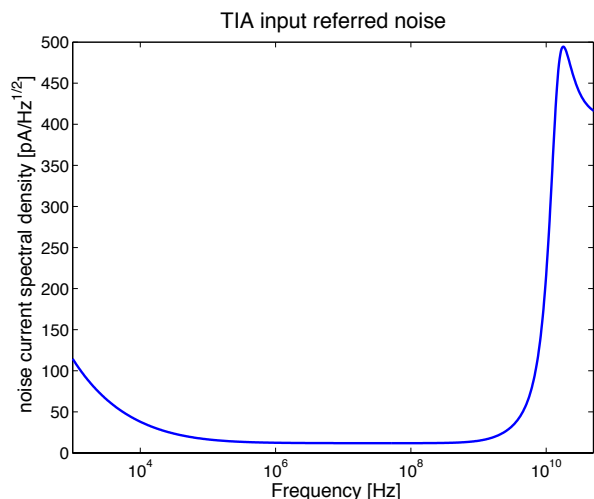


Fig. 11 TIA input referred current noise spectral density

V. CONCLUSION

This paper presents a framework for optimizing the design of nanometer analog and mixed analog-digital integrated

circuits. The viability and accuracy of the framework is validated by applying it to the design of a transimpedance front-end amplifier for a fiber optic receiver. The TIA consists of a cascade of a common gate, a common source and a source follower surrounded by a shunt-shunt feedback with phantom zero compensation. It achieves a transimpedance gain of 65.5 dBΩ, a bandwidth of 2.44 GHz, and an input referred current noise spectral density of 11.91 pA/√Hz. The amplifier is implemented in a standard 0.18μm digital CMOS process and it dissipates 18.32mW from a single 1.8 V supply.

REFERENCES

- [1] Sung Min Park and Hoi-Jun Yoo, "1.25-Gb/s Regulated Cascode CMOS Transimpedance Amplifier for Gigabit Ethernet Applications," IEEE Journal of Solid State Circuits, vol. 39, no. 1, pp. 112-121, Jan. 2004.
- [2] B. Murmann, *Analysis and Design of Elementary MOS Amplifier Stages*, NTS Press, 2013.
- [3] F. Silveira, D. Flandre, and P.G.A. Jesper, "A gm/ID based Methodology for the Design of CMOS Analog Circuits and its Application to the Synthesis of a Silicon-on-Insulator Micropower OTA," IEEE Journal of Solid State Circuits, vol. 31, no.9, pp. 1314-1319, Sept. 1996.
- [4] B. Murmann, *Analysis and Design of Elementary MOS Amplifier Stages*, NTS Press, 2013.
- [5] B. Razavi, *Design of Integrated Circuits for Optical Communications*, 2nd ed., Hoboken, New Jersey: Wiley, 2012, pp. 1-7.
- [6] H.M. Lavasani et al., "A 76 dBΩ 1.7 GHz 0.18μm CMOS Tunable TIA Using Broadband Current Pre-Amplifier for High Frequency Lateral MEMS Oscillators," IEEE Journal of Solid State Circuits, vol.44, no.1, pp. 224-235, january 2011.
- [7] Chih-Fan Liao and Shen-Iuan Liu, "10 Gb/s Transimpedance-AGC Amplifier and CDR Circuit for Broadband Data Receivers in 90 nm CMOS," IEEE Journal of Solid State Circuits, vol.43, no.3, pp. 642-655, March 2008.
- [8] J. Salvia, P. Lajevardi, M. Hekmat and B. Murmann, "A 56MΩ CMOS TIA for MEMS Applications," IEEE Custom Integrated Circuits Conference, pp. 199-202, 2009.

**Claudio Talarico** received B.S. and M.S. degrees in Electrical Engineering from University of Genova, Italy and a Ph.D. degree in Electrical Engineering from University of Hawaii. He is currently an Associate Professor of Electrical and Computer Engineering at Gonzaga University. Before joining Gonzaga University, he worked at Eastern Washington University, University of Arizona, and in industry, where he held both engineering and management positions at Siemens Semiconductors, IKOS Systems, and Marconi Communications. Dr. Talarico research interests include digital and mixed analog/digital integrated circuits and systems, computer-aided design methodologies, and design and analysis of embedded systems-on-chip.

**Gaurav Agrawal** received M.S. degree in Electrical and Computer Engineering from the University of Texas at Austin in 2007. He is currently employed at Google and has previously held hardware-engineering positions at Cisco Systems, NVIDIA and Texas Instruments. His research interests include parallel computing, electronic design automation, and design of high-speed digital integrated circuits.

**Janet M. Wang-Roveda** received a B.S. degree in computer science from The East China Institute in 1991, M.S., and Ph.D. degrees in electrical engineering and computer sciences from the University of California, Berkeley in 1998 and 2000, respectively. She is currently an associate professor in electrical and computer engineering department at the University of Arizona. Her primary research interests focus on robust VLSI circuit design, biomedical instrument design, Smart grid, VLSI circuit modeling and analysis, and low power multi-core system design. Dr. Roveda was a recipient of the NSF career award and the PEACASE award in 2005 and 2006, respectively. She received the best paper award in ISQED 2010 as well as best paper nominations in ASPDAC 2010, ICCAD 2007, and ISQED2005. She is the recipient of the 2008 R. Newton Graduate Research Project Award from DAC, and the 2007 USS University of Arizona Outstanding Achievement Award.

# Mathematical model of the quadrotor type unmanned aerial vehicle with neurocontroller

S.F.Jatsyn , V.E.Pavlovsky, O.V.Emelyanova, A.V.Savitsky

**Abstract** — In the work questions of mathematical modeling of motion of a quadcopter, taking into account mass-dimensional properties of four electric drives supplied with a reducers are considered. The calculation scheme is provided and the differential equations on the basis of the general theorems of dynamics which describe the interconnected electromagnetic and mechanical processes in electromechanical system of drives of propellers of a quadcopter are worked out. The offered nonlinear differential equations are solved together with the kinematic ratios, expressing projections of angular speed of a body to axes of the related system of coordinates through angular speeds of angles of roll, pitch and yaw. The neuronetwork method of synthesis of control is offered.

**Keywords** — UAV, quadcopter, mathematical model, neurocontroller

## I. INTRODUCTION

Quadcopter is an aerial vehicle with four main propellers which are mounting in opposite diagonal positions (Fig.1). It possesses a number of advantages in comparison with unmanned vehicles of plane type, such as: possibility of vertical take off and landing, maneuverability in flight, small take-off weight with an essential mass of payload, reliability and compactness, Thanks to simplicity of a design quadcopter are often used in special modeling, are convenient for inexpensive aero photo and video producing — the photo (TV) camera is taken out from an area of coverage of propellers.

For studying the main laws of movement of a quadcopter, features of a control system necessary for device stabilization in a standard position and movement of the center of mass on the given trajectory, it is necessary to elaborate the mathematical model describing spatial movement of the flying robot.

S.F.Jatsun, professor, Southwest State University, 94, 50 let Oktyabrya, Kursk, 305040, Russia (e-mail: teormeh@inbox.ru).

V.E.Pavlovsky, professor, Keldysh Institute of Applied Mathematics of RAS, Miusskaya sq., 4. Moscow, 125047, Russia (e-mail: vlpavl@mail.ru).

O.V.Emelyanova, Southwest State University, 94, 50 let Oktyabrya, Kursk, 305040, Russia (e-mail: oks-emelyanova@yandex.ru).

A.V.Savitsky, Lomonosov Moscow State University, mechanics-mathematics faculty, Leninskie Gory, 1, Moscow, 119991, Russia (e-mail: as@ttorr.ru)

## II. MATHEMATICAL MODEL OF A QUADROPTER

We will consider a quadcopter as the electromechanical system which body can be modeled as a solid body with 6 degrees of freedom [1], [2], [3], [4], [6], [9].

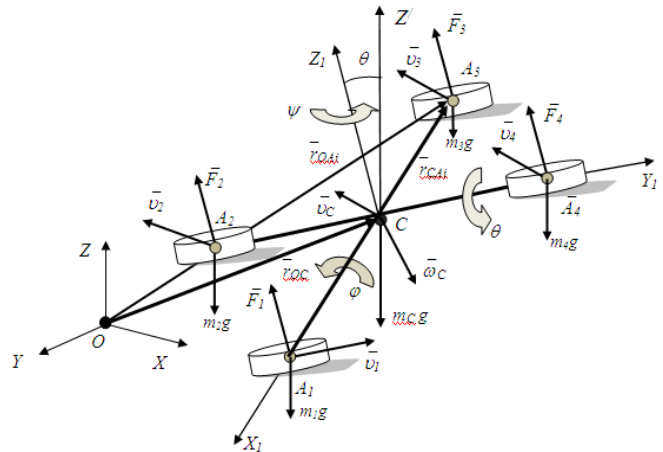


Fig. 1. Calculation scheme of a quadcopter

Let position of the center of mass of a quadcopter  $C$  coincide with the origin of relative system of coordinates of  $CX_1Y_1Z_1$ , and in absolute Cartesian system of coordinates is described by coordinates of  $X, Y, Z$  (fig. 1).

Orientation in space is set by Euler angles which are usually applied in the aircraft equipment at the description of movement of the device and are so-called roll, pitch and yaw. [5].

They correspond to the following sequence of turns:

1. Turn on an angle of  $\psi$  concerning vertical axis  $OZ$  ( $Rz, \psi$ ) — yaw.
2. Turn on an angle of  $\theta$  concerning main cross axis of inertia  $OY$  ( $Ry, \theta$ ) — pitch.
3. Turn on an angle  $\varphi$  concerning a longitudinal axis  $OX$  ( $Rx, \varphi$ ) axis — roll.

When quadcopter is on fly it is affected by aerodynamic forces of  $\bar{F}_1, \bar{F}_2, \bar{F}_3, \bar{F}_4$ , propellers attached to the centers of mass of rotors  $A_1, A_2, A_3, A_4$ , and forces of  $\bar{F}_i$  are parallel to the  $CZ_1$  axis. Gravity of the body  $m_Cg$  and rotors propellers of  $m_i g$  are enclosed in points  $C$  and  $A_i$  respectively (fig. 1) [3], [4].

Position of the center of mass of a quadcopter is determined by radius-vector  $r_{OC}=[X,Y,Z]^T$ .

We will agree further vectors in frames  $OXYZ$  and  $CX_1Y_1Z_1$  to designate by symbols  $(0)$  and  $(1)$  respectively. Then, for example, the projection of vectors of forces in  $(0)$  frame can be expressed through projections of forces in  $(1)$  frame by means of expression:

$$F_i^{(0)} = T_{10} \cdot F_i^{(1)}, \quad (1)$$

where  $T_{10}$  - a transition matrix from  $(1)$  to  $(0)$  system of coordinates.

The matrix  $T_{10}$  turns out by multiplication of three main matrixes of rotation and has the following appearance [6], [8], [9], [10]:

$$T_{10} = (\psi, \theta, \varphi) = R(z, \psi) \times R(y, \theta) \times R(x, \varphi) = \begin{bmatrix} \cos \psi \cos \theta & \cos \psi \sin \theta \sin \varphi - \cos \varphi \sin \psi & \sin \psi \sin \theta \sin \varphi + \cos \varphi \cos \psi \\ \sin \psi \cos \theta & \cos \psi \cos \theta \sin \varphi + \sin \psi \sin \theta & \cos \varphi \sin \psi \sin \theta - \cos \psi \\ -\sin \theta & \cos \theta \sin \varphi & \cos \varphi \cos \theta \end{bmatrix} \quad (2)$$

We will write down obvious equality:

$$r_{OA_i}^{(0)} = \bar{r}_{OC}^{(0)} + \bar{r}_{CA_i}^{(0)}, \quad (3)$$

where

$$\bar{r}_{CA_i}^{(0)} = T_{10} \cdot \bar{r}_{CA_i}^{(1)}. \quad (4)$$

Vectors  $\bar{r}_{CA_i}^{(1)}$  for points of  $A_i$  have an values:

$$\bar{r}_{CA1}^{(1)} = \begin{bmatrix} l \\ 0 \\ 0 \end{bmatrix}, \quad \bar{r}_{CA2}^{(1)} = \begin{bmatrix} 0 \\ -l \\ 0 \end{bmatrix}, \quad \bar{r}_{CA3}^{(1)} = \begin{bmatrix} -l \\ 0 \\ 0 \end{bmatrix}, \quad \bar{r}_{CA4}^{(1)} = \begin{bmatrix} 0 \\ l \\ 0 \end{bmatrix}, \quad (5)$$

where  $l$  - distance from the center of mass of a quadcopter  $C$  to the center of mass of rotors of  $A_i$ .

We will determine velocities of points of  $A_i$ , having differentiated equality (3) on time:

$$\bar{v}_{A_i}^{(0)} = \frac{d\bar{r}_{OA_i}^{(0)}}{dt} = \frac{d\bar{r}_{OC}^{(0)}}{dt} + \frac{d\bar{r}_{CA_i}^{(0)}}{dt} \quad (6)$$

The derivative on time from equality (4) gives:

$$\bar{v}_{A_i}^{(0)} = \bar{v}_N^{(0)} + \dot{T}_{10} \cdot \bar{r}_{CA_i}^{(1)} \quad (7)$$

where  $\bar{v}_N^{(0)} = \dot{X}\bar{i} + \dot{Y}\bar{j} + \dot{Z}\bar{k}$  - velocity of the center of mass of a quadcopter.

We will determine linear momentum for  $i$ -th mass by a formula:

$$\bar{q}_i = m_i \bar{v}_{A_i} = m_i (\bar{v}_C + \dot{T}_{10} \cdot \bar{r}_{CA_i}^{(1)}) \quad (8)$$

We will find change of linear momentum from expression:

$$\frac{d\bar{q}_i}{dt} = m_i \left( \frac{d\bar{v}_C}{dt} + \dot{T}_{10} \cdot \bar{r}_{CA_i}^{(1)} \right) = T_{10} \bar{F}_i^{(1)} \quad (9)$$

Vector of linear momentum of the considered system consisting of the body and 4 propellers, we will determine by a formula:

$$\bar{Q} = m_C \bar{v}_C + \sum_{i=1}^4 m_{A_i} \bar{v}_{A_i} \quad (10)$$

We will write down the theorem of change of linear momentum of mechanical system in a differential form:

$$\frac{d\bar{Q}}{dt} = m_C \frac{d\bar{v}_C}{dt} + \sum m_i \left( \frac{d\bar{v}_C}{dt} + \dot{T}_{10} \cdot \bar{r}_{CA_i}^{(1)} \right) = (m_C + \sum m_i) \frac{d\bar{v}_C}{dt} + \dot{T}_{10} \sum m_i \bar{r}_{CA_i}^{(1)} = T_{10} \sum \bar{F}_i^{(1)} \quad (11)$$

After the corresponding transformations we will receive system of the differential equations describing motion of the center of mass of considered system (quadcopter):

$$\begin{cases} m\ddot{X} = (\sin \psi \sin \varphi + \cos \psi \cos \varphi \sin \theta) \cdot \sum F_i^{(1)} \\ m\ddot{Y} = (\cos \varphi \sin \psi \sin \theta - \cos \psi \sin \varphi) \cdot \sum F_i^{(1)} \\ m\ddot{Z} = \cos \varphi \cos \theta \cdot \sum F_i^{(1)} - mg \end{cases} \quad (12)$$

where  $m = m_C + m_i$  - total mass of a quadcopter.

We will consider angular velocities of rotation of rotors of a quadcopter in local system of coordinates of  $CX_1Y_1Z_1$  (fig.2). For this purpose we will enter system of coordinates of  $A_i x_i y_i z_i$ , which coincides with the center of mass of  $m_i$  of rotors.

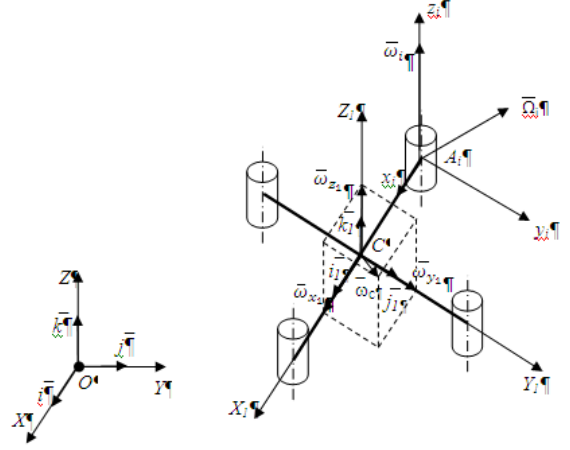


Fig. 2. Calculation scheme of definition of the kinetic momentum of a quadcopter

For  $i$ -th a rotor we will determine a vector of absolute angular velocity of rotation by a formula:

$$\bar{\Omega}_i = \bar{\omega}_i + \bar{\omega}_C, \quad i = 1 \dots 4; \quad (13)$$

$$\bar{\omega}_i = \bar{i}_i \omega_{ix} + \bar{j}_i \omega_{iy} + \bar{k}_i \omega_{iz};$$

$$\bar{\omega}_C = \bar{i}_1 \omega_{Cx1} + \bar{j}_1 \omega_{Cy1} + \bar{k}_1 \omega_{Cz1}, \quad (14)$$

where  $\bar{i}_i, \bar{j}_i, \bar{k}_i$  и  $\bar{i}_b, \bar{j}_b, \bar{k}_b$  - ort vectors of system of coordinates  $CX_1Y_1Z_1$  and  $A_i x_i y_i z_i$ ,  $\bar{\Omega}_i$  - absolute angular velocity of rotation  $i$ -th a rotor in system of coordinates  $CX_1Y_1Z_1$ ;  $\bar{\omega}_C, \bar{\omega}_i$  - vectors of angular velocities of rotation of the body and  $i$ -th rotor in system of coordinates of  $CX_1Y_1Z_1$  and  $A_i x_i y_i z_i$  we will consider as:

$$\bar{\omega}_C = \begin{bmatrix} \omega_{X1} \\ \omega_{Y1} \\ \omega_{Z1} \end{bmatrix}, \quad \bar{\omega}_i = \begin{bmatrix} 0 \\ 0 \\ \omega_i \end{bmatrix}, \quad \bar{\Omega}_i = \begin{bmatrix} \omega_{X1} \\ \omega_{Y1} \\ \omega_i + \omega_{Z1} \end{bmatrix} \quad (15)$$

$$\text{or} \quad \bar{\Omega}_i = \bar{i}_i \Omega_{ix} + \bar{j}_i \Omega_{iy} + \bar{k}_i \Omega_{iz} \quad (16)$$

We will define the moment in of linear momentum of a rotor in system of coordinates  $A_i x_i y_i z_i$

$$\bar{L}_{A_i} = I_{A_i} \bar{\Omega}_i, \quad (17)$$

where  $I_{A_i} = \begin{bmatrix} J_{A_i}^x & 0 & 0 \\ 0 & J_{A_i}^y & 0 \\ 0 & 0 & J_{A_i}^z \end{bmatrix}$  - tensor of inertia of a rotor.

Then the kinetic momentum is equal:

$$\bar{L}_{iA_i} = \begin{vmatrix} J_{A_i}^x & 0 & 0 \\ 0 & J_{A_i}^y & 0 \\ 0 & 0 & J_{A_i}^z \end{vmatrix} \begin{vmatrix} \omega_{X_1} \\ \omega_{Y_1} \\ \omega_i + \omega_{Z_1} \end{vmatrix} = \begin{vmatrix} J_{A_i}^x \omega_{X_1} \\ J_{A_i}^y \omega_{Y_1} \\ J_{A_i}^z (\omega_i + \omega_{Z_1}) \end{vmatrix} \quad (18)$$

We will define the kinetic momentum of system:

$$\bar{L} = \bar{L}_C + \sum \bar{L}_i, \quad (19)$$

where  $\bar{L}_C = I_C \bar{\omega}_C$  - the kinetic momentum of the body concerning the center of mass of a quadcopter;  $\bar{L}_i = I_i \bar{\omega}_i = (I_{A_i} + m_i l^2) \bar{\omega}_i$  - the kinetic momentum of  $i$ -th rotor concerning the center of mass of a quadcopter in system of coordinates  $CX_1Y_1Z_1$ .

Tensors of inertia  $I_C$  of the body and  $i$ -th rotor  $I_i$  taking into account that the main axes of inertia of mechanical system are the main central axes of inertia are equal:

$$I_C = \begin{vmatrix} J_C^{X_1} & 0 & 0 \\ 0 & J_C^{Y_1} & 0 \\ 0 & 0 & J_C^{Z_1} \end{vmatrix}, \quad I_i = \begin{vmatrix} J_{A_i}^x + m_i l^2 & 0 & 0 \\ 0 & J_{A_i}^y + m_i l^2 & 0 \\ 0 & 0 & J_{A_i}^z + m_i l^2 \end{vmatrix} \quad (20)$$

Then:

$$\bar{L}_C = \begin{vmatrix} J_C^{X_1} & 0 & 0 \\ 0 & J_C^{Y_1} & 0 \\ 0 & 0 & J_C^{Z_1} \end{vmatrix} \begin{vmatrix} \omega_{X_1} \\ \omega_{Y_1} \\ \omega_{Z_1} \end{vmatrix} = \begin{vmatrix} J_C^{X_1} \omega_{X_1} \\ J_C^{Y_1} \omega_{Y_1} \\ J_C^{Z_1} \omega_{Z_1} \end{vmatrix} \quad (21)$$

$$\bar{L}_i = \begin{vmatrix} J_{A_i}^x + m_i l^2 & 0 & 0 \\ 0 & J_{A_i}^y + m_i l^2 & 0 \\ 0 & 0 & J_{A_i}^z + m_i l^2 \end{vmatrix} \begin{vmatrix} \omega_{X_1} \\ \omega_{Y_1} \\ \omega_i + \omega_{Z_1} \end{vmatrix} = \begin{vmatrix} (J_{A_i}^x + m_i l^2) \omega_{X_1} \\ (J_{A_i}^y + m_i l^2) \omega_{Y_1} \\ (J_{A_i}^z + m_i l^2) (\omega_i + \omega_{Z_1}) \end{vmatrix} \quad (22)$$

Taking into account (21), (22) the expressions (19) will have an appearance:

$$L = \begin{vmatrix} (J_C^{X_1} + \sum J_{A_i}^x + \sum m_i l^2) \omega_{X_1} \\ (J_C^{Y_1} + \sum J_{A_i}^y + \sum m_i l^2) \omega_{Y_1} \\ (J_C^{Z_1} + \sum J_{A_i}^z + \sum m_i l^2) \omega_{Z_1} + (\sum J_{A_i}^z + \sum m_i l^2) \omega_i \end{vmatrix} = \begin{vmatrix} J^{X_1} \omega_{X_1} \\ J^{Y_1} \omega_{Y_1} \\ J^{Z_1} \omega_{Z_1} + \sum J_i^z \omega_i \end{vmatrix}, \quad (23)$$

where  $J^{X_1} = J_C^{X_1} + \sum J_{A_i}^x + \sum m_i l^2$ ,  $J^{Y_1} = J_C^{Y_1} + \sum J_{A_i}^y + \sum m_i l^2$ ,

$J^{Z_1} = J_C^{Z_1} + \sum J_{A_i}^z + \sum m_i l^2$ ,  $\sum J_i^z = \sum J_{A_i}^z + \sum m_i l^2$  - the given axial moments of inertia.

For receiving system of the differential equations describing rotation of considered system, we will apply the theorem of change of the kinetic momentum of mechanical system [6]:

$$\frac{d\bar{L}}{dt} = \frac{d\bar{L}}{dt} + (\bar{\omega}_C \times \bar{L}) = \sum \bar{M}_C^e \quad (24)$$

$$\frac{d\bar{L}}{dt} = \begin{vmatrix} J^{X_1} \dot{\omega}_{X_1} + \omega_{Y_1} \omega_{Z_1} (J^{Z_1} - J^{Y_1}) + \omega_{Y_1} \sum J_i^z \omega_i \\ J^{Y_1} \dot{\omega}_{Y_1} + \omega_{X_1} \omega_{Z_1} (J^{X_1} - J^{Z_1}) - \omega_{X_1} \sum J_i^z \omega_i \\ J^{Z_1} \dot{\omega}_{Z_1} + J_i^z \dot{\omega}_i + \omega_{X_1} \omega_{Y_1} (J^{Y_1} - J^{X_1}) \end{vmatrix} = \begin{vmatrix} M_{X_1}^e \\ M_{Y_1}^e \\ M_{Z_1}^e \end{vmatrix} \quad (25)$$

Then taking into account (12) and (25) full system of the differential equations describing motion of a quadcopter can be presented in a form:

$$\begin{cases} m\ddot{X} = (\sin \psi \sin \varphi + \cos \psi \cos \varphi \sin \theta) \cdot \sum F_i \\ m\ddot{Y} = (\cos \varphi \sin \psi \sin \theta - \cos \psi \sin) \cdot \sum F_i \\ m\ddot{Z} = \cos \varphi \cos \theta \cdot \sum F_i - mg \\ J^{X_1} \dot{\omega}_{X_1} + \omega_{Y_1} \omega_{Z_1} (J^{Z_1} - J^{Y_1}) + \omega_{Y_1} \sum J_i^z \omega_i = M_{X_1}^e \\ J^{Y_1} \dot{\omega}_{Y_1} + \omega_{X_1} \omega_{Z_1} (J^{X_1} - J^{Z_1}) - \omega_{X_1} \sum J_i^z \omega_i = M_{Y_1}^e \\ J^{Z_1} \dot{\omega}_{Z_1} + J_i^z \dot{\omega}_i + \omega_{X_1} \omega_{Y_1} (J^{Y_1} - J^{X_1}) = M_{Z_1}^e \end{cases} \quad (26)$$

The system of the equations (26) needs to be solved together with the kinematic ratios expressing formulas of projections of angular velocity of the device and angles of roll, pitch and yaw:

$$\begin{cases} \dot{\varphi} = \omega_{\bar{O}_1} - (\omega_{Z_1} \cos \varphi - \omega_{Y_1} \sin \varphi) \operatorname{ctg} \theta \\ \dot{\theta} = \omega_{Z_1} \sin \varphi + \omega_{Y_1} \cos \varphi \\ \dot{\psi} = \frac{1}{\cos \theta} (\omega_{Z_1} \cos \varphi - \omega_{Y_1} \sin \varphi) \end{cases} \quad (27)$$

Between the angular velocity of propellers and value of the operating voltage arriving on electric motors we will write down equation in a form [1], [2]:

$$\dot{\Omega}_i = \frac{-\tilde{n}_E \tilde{n}_M}{R} \eta N^2 \Omega_i - d \Omega_i^2 + \frac{\tilde{n}_M}{R} \eta N u_i(x, y, z, \varphi, \theta, \psi), \quad i = 1-4 \quad (29)$$

where  $K_M$  - the coefficient of proportionality called by a constant of the moment of the electric motor;  $N = \omega_i / \Omega_i$  - transfer relation of a reducer equal to velocity of the  $\omega_i$  electric motor to divide into velocity of the propeller  $\Omega_i$ ;  $\eta$  - effectiveness ratio which connects mechanical energy of an axis of the engine and the propeller;  $J_P, J_M$  - the moments of inertia of a rotor round an axis of the propeller and a motor axis respectively;  $c_E, c_{Mi}$  - the coefficients of proportionality called according to constant the electromotor force of the drive and the moment of the electric motor;  $d$  - aerodynamic constant;  $R$  - active resistance of a winding of a rotor.

As a result, the mathematical model of a quadcopter is presented by system of the equations (26)-(28). This model allows to build and investigate various six-DOF controlled motions of a quadcopter.

### III. NEUROCONTROLLER

In tasks for underactuated systems, some of which are considered in [7], control is based proceeding from properties of passivity of system with use of a energy method. In this section we will offer a neuronetwork method of synthesis of control. It, in particular, allows to overcome a problem of the specified deficiency.

On the basis of results of numerical modeling on basis of the model described above training set which covers space of possible movements is formed. Further in this space the network is trained, necessary weight coefficients are calculated and the network is used for synthesis of motion.

Two main options are considered. In the first linear sensors of coordinates and device angles (according to the navigation equipment), in the second - sensors of accelerations on six axes of the device were used. In this case the composite (hybrid) network represented in fig. 3 is realized. The first pairs of blocks 1-6 of the networks form a recurrent network of Jordan type for calculation of coordinates on accelerations

(actually, for double integration of accelerations), the finishing 7-th block, is a three-layer network for final calculation of control.

The carried-out modeling showed rather effective operability of this scheme.

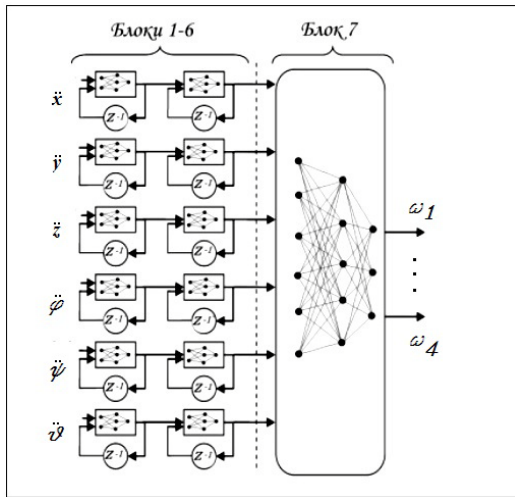


Fig. 3. Composite neuronet for synthesis of control on sensors of accelerations

#### IV. MODELLING OF PROCESS OF THE TAKE-OFF AND LANDING OF QUADROPTER

We will consider as an example the vertical take-off and landing of a quadcopter, with neurocontroller using, and angular velocities of all four propellers identical and are equal to  $\Omega$ .

We will break a trajectory into three stages: 1 – take-off, 2 – hovering quadcopter, 3 – descent and landing, also we will consider each of them.

1 stage.  $0 \leq z \leq H$ ,  $x=x_0$ ,  $y=y_0$ ,  $z=z(t)$ , where  $x_0, y_0$  – parameters of take-off,  $H$  – take-off height.

The detachment of a quadcopter from a surface, or, the beginning of flight, occurs if the condition is satisfied: normal reaction of the support surface  $R=0$  (Fig. 4).

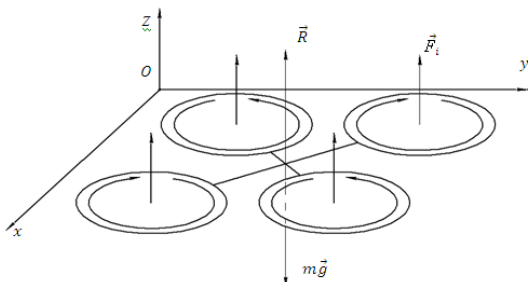


Fig.4. The detachment of a quadcopter from a surface:  $R$  – normal reaction of a surface,  $F_i$  – traction force of the propeller,  $mg$  – weight of quadcopter

Let take-off (flight) of a quadcopter from a surface occurs under the following law:

$$z = at^3 + bt^2 + ct + d, \quad (29)$$

and the law of change of velocity is:

$$\dot{z} = 3at^2 + 2bt + c \quad (30)$$

where  $a, b, c$  – constants, defined from boundary conditions:

$$\text{at } t = 0; \quad z = 0; \quad \dot{z} = 0, \quad (31)$$

$$\text{at } t = t_1; \quad z = H; \quad \dot{z} = 0, \quad (32)$$

Solving the equations (29) and (30) taking into account (31), (32) we define the equation describing vertical flight of a quadcopter on height of  $H$  during  $t_1$ :

$$z = z(t) = \frac{3H}{t_1^2}t^2 - \frac{2H}{t_1^3}t^3, \quad (33)$$

where  $t_1$  - time of take-off.

2 stage.  $z = H$ ,  $x=x_0$ ,  $y=y_0$ , time of hovering quadcopter -  $t_2$ .

3 stage.  $H \geq z \geq 0$ ,  $x=x_0$ ,  $y=y_0$ ,  $z=z(t)$ , where  $x_0, y_0$  - coordinates of landing point.

Descent from height  $H$  during time  $t_3$ , is carried out under the given law:

$$z = \frac{3H(t_3 - t)^2}{t_1^2} - \frac{2H(t_3 - t)^3}{t_1^3} \quad (34)$$

where  $t_1, t_3$  - take off and landing time of a quadcopter. Then  $T = \sum t_i$  – total time of flight.

The result of modeling of process of a take-off / landing is given on Fig.5.

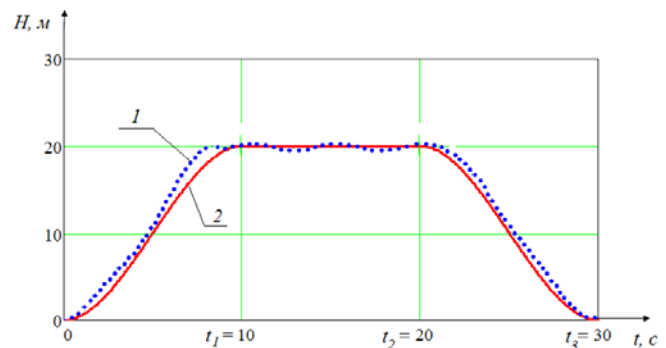


Fig.5. The graph of modes of take-off, hovering quadcopter, and landing of a quadcopter in time:

1- real, 2- theoretical;  $t_1$  – take-off time,  $t_1 - t_2$  - hovering quadcopter time,  $t_3 - t_2$  - hovering quadcopter and landing time for quadcopter

#### V. CONCLUSION AND FUTURE WORK

The calculation scheme and mathematical model of spatial movement of the quadcopter, considering the gyroscopic effects, rotating propellers, mass-dimensional properties of four electric drives supplied with a reducer, kinematic links, properties of electric motors, algorithms of elaboration of control data is offered. The method of synthesis of control on the basis of the neurocontroller is offered.

Further it is planned to create adaptive algorithm which consists in use of various techniques of stabilization on three angles of  $\psi, \theta, \phi$  for various modes and flight conditions. It is

assumed to solve a problem of optimum synthesis of criterion of speed when moving a quadrocopter from one point in another. It is assumed to choose areas of the rational parameters defining optimum operation of drives of a quadrocopter in various modes for the neurocontroller, which will allow to provide movement of a quadrocopter on the given trajectory.

## REFERENCES

- [1] Emelyanova O.V., Popov N.I., Jatsun S.F. Modeling of movement of the quadrorotatsionny flying robot Topical issues of science. Materials VIII of the International scientific and practical conference. Moscow.2013.c.6-8.
- [2] Emelyanova O.V., Popov N.I., Jatsun S.F. Modeling of movement of a quadrocopter in space//Aerospace technologies (AKT-2013). Works XIV of the All-Russian scientific and technical conference and school of young scientists, graduate students and students. Voronezh: Firm Elist, 2013. –C.131-138.
- [3] Popov N.I., Emelyanova O.V., Jatsun S.F., Savin A.I. Pesearch of ocsillations of quadrocopter under influence of external periodic disturbance // Basic researches. – 2014. – № 1 . – ctp. 28-32.
- [4] Popov N.I., Emelyanova O.V. Dynamic features of overhead high-voltage lines monitoring by means of quadrocopter // Modern problems of science and education – 2014. – № 2; URL: <http://www.science-education.ru/116-12773>.
- [5] Pavlovsky M.A., Akinfeev L. Yu., Boichuk O.F. Theoretical mechanics. Dynamics.: The higher school, 1990.-480 c.
- [6] Tommaso Bresciani. Modeling, identification and control of a quadrotor helicopter. Master's thesis, Department of Automatic control, Lund University, October 2008, p.170.
- [7] I. Fantoni, R. Lozano. Nonlinear management of mechanical systems with deficiency of operating influences. - Moscow-Izhevsk: "Kompyuternaya dinamika", 2013, 312 c.
- [8] J.C. Avila Vilchis, B. Brogliato, A. Dzule, R. Lozano, Nonlinear modelling and control of helicopters,. Automatica 39, 2003.
- [9] G. M. Hoffmann, H. Huang, S. L. Waslander, and C. J. Tomlin, Quadrotor helicopter flight dynamics and control: Theory and experiment, Proceedings of the AIAA Guidance, Navigation and Control Conference and Exhibit, Aug. 2007, 1-20.
- [10] Prouty R.W. Helicopter Performance, Stability, and Control. Krieger Publishing Company, 1995.

# Robotic assisted trajectory tracking for human arm rehabilitation

Cristóbal Ochoa-Luna<sup>1</sup>, Mohammad Habibur Rahman<sup>1,2</sup>, Maarouf Saad<sup>1</sup>, Philippe S. Archambault<sup>2,3</sup>

<sup>1</sup>Electrical Engineering Department, École de technologie supérieure (ETS)

<sup>2</sup>School of Physical & Occupational Therapy, McGill University

<sup>3</sup>Interdisciplinary Research in Rehabilitations (CRIR)

Montreal, Canada

cristobal.ochoa-luna.1@ens.etsmtl.ca, mhrahman@ieee.org, maarouf.saad@etsmtl.ca, philippe.archambault@mcgill.ca

**Abstract**— The following paper presents an assistive rehabilitation scheme for patients with upper limb impairments such as strokes. Based on the tracking of predefined trajectories either in Cartesian or joint space, the system allows an adjustable degree of variation with respect to the ideal trajectory. The amount of variations allowed is adjusted through the coefficients of an admittance function. It performs the transformation between the opposition forces, from the patient to the robot, and makes it divert, within certain limits, from the original trajectory.

**Keywords**—7DOF exoskeleton, admittance, assisted rehabilitation, upper limb rehabilitation.

## I. INTRODUCTION

Stroke is a sudden loss of blood flow to the brain. Most strokes occur by an occlusion (when a blood clot blocks a blood vessel in the brain, interrupting the supply of blood and oxygen to the brain cells in that area) or either a rupture of a major cerebral artery and the resulting bleeding. In both types of stroke, brain cells may die, causing the parts of the body they control to stop functioning [1, 2]. Strokes are a very important health issue in the world. According to the World Health Organization, 15 million people suffer from a stroke throughout the world every year. Out of all of these people, 5 million die directly because of it and another 5 million are left permanently disabled [3]. One of the most common consequences after a stroke is paralysis (the inability of a muscle or group of muscles to move voluntarily) which affects up to 90 percent of stroke survivors. Many stroke survivors experience one sided-paralysis. The most common kind (approximately 80 percent) is hemiparesis, which causes weakness or inability to move one side of the body. Spasticity affects roughly 40 percent of stroke survivors and is characterized by stiff or tight muscles that constraint movements [4]. The main treatment for these cases is rehabilitation: the process of helping an individual achieves the highest level of independence and quality of life possible. When rehabilitation is possible, it implies many hours of highly skilled and extensive physiotherapy procedures. However, the amount of people that can bring this support is not sufficient to carry out with all the patients. The recovery progression can be a lifelong process and while some people recover quickly, others can deal with it for a very long time, even for the rest of their lives. The use of robot assistance in rehabilitation is a very important point of interest.

For the purpose of providing rehabilitation assistance for the upper limb and daily assistance, the ETS - Motion Assistive Exoskeleton Robot for Superior Extremity (ETS-MARSE) is under development [5-7]. Currently it comprises a seven degree of freedom (DOF) exoskeleton, designed to cope with full motion capabilities of the arm's main movements, that are at the shoulder, elbow and wrist levels, combined or individually. So far the work has been developed to the point of passive rehabilitation, which means that the exoskeleton executes movements along predefined trajectories moving the subject's arm with its own movements to help improve the range of movement. This paper describes the first movement towards the next rehabilitation step: assistive rehabilitation, in which the robot takes information from the human-machine interaction, in this case through contact force feedback between the structure and the person's arm and uses it to actively modifying its rehabilitation task. In this step of the research, the robot also has the instruction to follow a predefined rehabilitation exercise; however, the system is measuring the force on the subject that opposes the predetermined movement and allows certain adjustable degrees of variation of the trajectory (or more or fewer degree of help from ETS-MARSE). This encourages the patients to actively participate in the exercise by attempting to follow the path, and motivates them to improve their accomplishments.

This paper is organized as follows. Section II, presents the scheme that will allow the robot to adjust the amount of assistance that will be provided to the patient. In Section III, the experimental setup of the system is described. Section IV summarizes the implementation and the results and finally, Section V presents the conclusions and the future work.

## II. TRAJECTORY DEFINITION

In robotics, a trajectory defines a movement of the robot in a multidimensional space. This trajectory has information regarding the position, velocity and acceleration for each degree of freedom in time [8]. To command the robot's movement, the user defines a desired trajectory that includes this information. It is generated usually by means of a trajectory planner.

### A. Trajectory planner

The base trajectory planner for ETS-MARSE is based on joint space specification. It is performed in real time on the

processor designed for that purpose of the system (PXI-8108), described in section III. Initial and final positions for each joint are specified as well as intermediate points, if desired. The transition between trajectory segments is always done with velocity of zero, because they generally indicate changes in the direction of the movement (i.e. to do a flexion and extension of the elbow means to move it from 90° to 170° and then back to 90°.) The trajectory is then calculated by the method of cubic polynomials [8].

In rehabilitation, it is often useful to specify a desired trajectory in the Cartesian space, that is, to specify movements with an immediate sense, as a straight line or for example following a geometrical shape as a triangle, rectangle, etc. For the ETS-MARSE robot, the trajectory can be specified either in the joint space or in Cartesian space (robot workspace); nevertheless, the trajectory tracking is always executed in joint space. Thus, it is necessary that given a position and orientation of the end effector in Cartesian space, find the joint positions of the robot that can accomplish this desired configuration. When the case arises, the method of the pseudo inverse of the Jacobian is used. It is known that the Jacobian matrix of a robot relates the joint velocities with linear and angular velocities of the Cartesian space.

$$\dot{\mathbf{X}} = \mathbf{J}(\mathbf{q})\dot{\mathbf{q}} \quad (1)$$

where  $\dot{\mathbf{X}} \in \mathbb{R}^6$  is the velocity vector of the end effector,  $\dot{\mathbf{q}} \in \mathbb{R}^n$  is the joint velocities vector and  $\mathbf{J}(\mathbf{q}) \in \mathbb{R}^{6 \times n}$  is the robot Jacobian matrix. However, for the case of a redundant robot like ETS-MARSE (7 DOF), the Jacobian matrix is rectangular. To obtain a solution for the inverse problem of (1), one possible solution is proposed [9]:

$$\dot{\mathbf{q}} = \mathbf{J}(\mathbf{q})^+ \dot{\mathbf{X}} \quad (2)$$

where  $\mathbf{J}(\mathbf{q})^+ = \mathbf{J}(\mathbf{q})^T (\mathbf{J}(\mathbf{q})\mathbf{J}(\mathbf{q})^T)^{-1}$  is the generalized pseudo-inverse. The method can be enriched by adding null space characteristics to the right side of the equation with the term  $(\mathbf{J}(\mathbf{q})^+ \mathbf{J}(\mathbf{q}) - \mathbf{I})\xi$ , where  $\xi \in \mathbb{R}^n$  is an arbitrary vector that can be used for tasks as obstacle avoidance.

### B. Admittance modified trajectory planner

For the assistive rehabilitation that is proposed in this paper, the idea is to modify the predefined trajectory in relation to the subjects' movement limitations. As it is described in Section III, the system measures the force exerted by the user at the level of the end effector of the robot. The first step is to transform this information in something more representative of how the subject's opposition force affects each DOF of the exoskeleton, i.e. joint torque.

Another property of the Jacobian matrix is that as a consequence of the virtual work principle, its transpose assigns Cartesian forces to joint torques. When the Jacobian matrix is expressed with respect to the base frame of the manipulator, the force-moment vector referenced to the same frame can be transformed as:

$$\boldsymbol{\tau} = \mathbf{0}_j^T \mathbf{F} \quad (3)$$

where  $\boldsymbol{\tau}$  is the  $7 \times 1$  vector of torque actuating in the articulations and  $\mathbf{F}$  is a force-moment Cartesian vector of  $6 \times 1$ . The zero leading super indexes specify that they are defined with respect to the base frame. This relation gives us the effect of the user's opposition force in terms of joint torques.

Impedance can be defined as a transfer function between the external force acting on the manipulator and its displacement [10]. Usually this kind of relation takes the form of a mechanical mass-spring-damper system. Knowing the result from (3) and applying the impedance definition in the form of an admittance relation, we have a direct form to modify the desired trajectory.

$$\mathbf{q}_a = \mathbf{q}_d + \boldsymbol{\tau} \left( \frac{1}{K - Cs} \right) \quad (4)$$

where  $\mathbf{q}_a$  is the new desired trajectory defined by the admittance,  $\mathbf{q}_d$  the original desired trajectory from the trajectory planner and the last right term of the equation in the parenthesis, the chosen admittance function.

## III. SYSTEM OVERVIEW

The current architecture of the system is depicted in Fig. 1. The exoskeleton robot arm is an open chain all revolute 7DOF wearable manipulator-like robot; it was designed for its joints to correspond to the principal degree of freedom of the human arm. Those are:

- 3DOF at shoulder level for horizontal flexion/extension, vertical flexion/extension and internal/external rotation,
- 1DOF for elbow flexion/extension,
- 1DOF for forearm pronation/supination, and
- 2DOF at the wrist level for radial/ulnar deviation and flexion/extension.

The exoskeleton structure has a force sensor mounted in the end effector (tip) of the robot, which is at the level of the handle where the patient's hand must be positioned. For

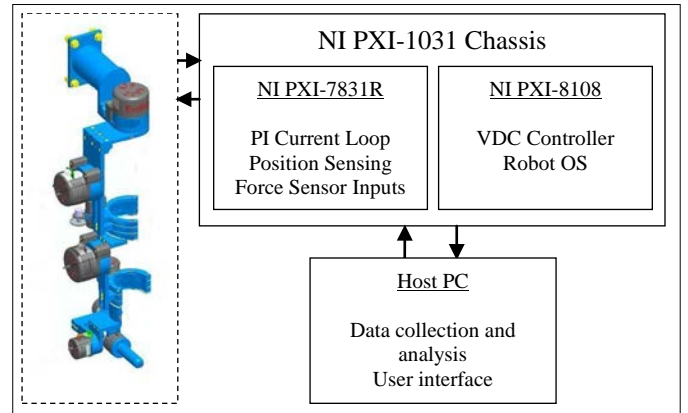


Fig. 1. ETS-MARSE system hardware overview.

illustrative purposes, a schematic of the ETS-MARSE as well as an image showing a person wearing it is presented in Fig. 2. The joints are driven by brushless DC motors, one for each articulation, incorporated with harmonic drives. An output driver that receives a voltage level as its reference control signal controls each motor. Also each motor has a Hall effect sensor, which are used for position feedback of the joints.

These drivers, among security, communication and general circuitry are mounted on a backplane card developed at the ETS. This backplane collects analogic and digital signals and connects through the proper interface cards to an NI PXI-7813R (Remote Input Output card) placed on an NI PXI-1031 chassis. The card has an integrated FPGA in which executes the low level control: A PI controller for the current loop of the motors, the position feedback via the Hall effect sensors monitoring and the collection of the force sensor inputs. Also in the chassis is mounted a PXI-8108 controller. Its embedded dual core processor (Intel® Core™ 2 Duo) executes the high level control: the robot's operating system which is responsible for running the MARSE through its different operation states, and the trajectory tracking controller. In this case we are using the nonlinear control technique known as Virtual Decomposition Control (VDC), a very effective newly control

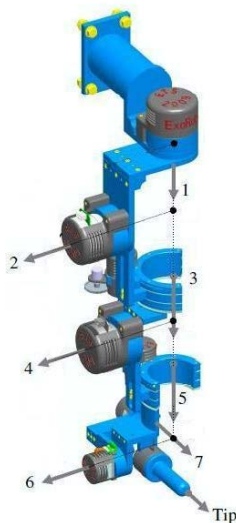


Fig. 2. ETS-MARSE and subject wearing ETS-MARSE.

technique [11]. The details about the implementation of the VDC are out of the scope of this paper.

Finally a PC is connected to the PXI via a local Ethernet network that collects from the PXI the data resulted from the robot execution. This data is used to analyze the performance in trajectory tracking and other useful data for development purposes. Also this computer works as the user interface from which the desired trajectory is selected, including the selection of Cartesian or articular space trajectory. The primitive commands to the robot are sent also from this PC, these are: system on, motors on, reset, initialize, start and abort (also the system have an emergency stop button, since it is a human-machine interface, security is a major concern issue.) The software limits of the joint movements in position and velocity can be setup from this interface. Finally the interface has the option of manual operation of the motors and it can provide feedback of motor position in real time in a user reasonable update rate (very much slower that the position refresh rate used in the controller).

#### IV. EXPERIMENTAL RESULTS AND SIMULATIONS

As was mentioned in Section III, the experimental setup was performed with the VDC technique that works at an update rate of 1 ms. The experiment described below was executed with a 31 years old healthy male subject with a mass of 83 Kg and 182 cm height. The experiment performed was an elbow extension-flexion movement. It can be seen in Fig. 3. The elbow initiates at a start position of  $90^\circ$ , then goes to  $5^\circ$ , then to  $115^\circ$  and ends at  $0^\circ$ .

If we analyze this movement in the Cartesian space, it can be seen as a portion ( $110^\circ$ ) of a semi-circle. Because the opposition force to this movement that the subject voluntarily (testing on a healthy subject) exerts toward the robot the trajectory deflects from the predefined one. Fig. 4 shows the effect of this action. It can be seen in red the original desired trajectory, and in blue the new trajectory that is affected by the user interaction. The black line shows the tracking of the controller that can be seen very close of the admittance modified trajectory. The controller performance is not part of the scope of this paper; nevertheless, it was developed to ensure reliable results of the experiments.

In order to test the effects of modifying the parameters of the admittance function, it is considered that two human force inputs to the system cannot be equal. For this reason, to be consistent in the comparison, the force sensor input captured from the experiment shown above, is fed into a simulation. The first result, shown in Fig. 5, preserves the admittance relation of the physical test. Thus it shows the same deflection, but with almost perfect tracking. Then, the admittance function is modified to force the robot to give more assistance to the subject. It can be seen in Fig. 6 that the trajectory will not allow so much drifting from the intended rehabilitation trajectory as in the previous case. Finally we relax the admittance function to provide low assistance, and the results of this trajectory will be a very erratic movement far away from the intended rehabilitation exercise as can be seen in Fig. 7.

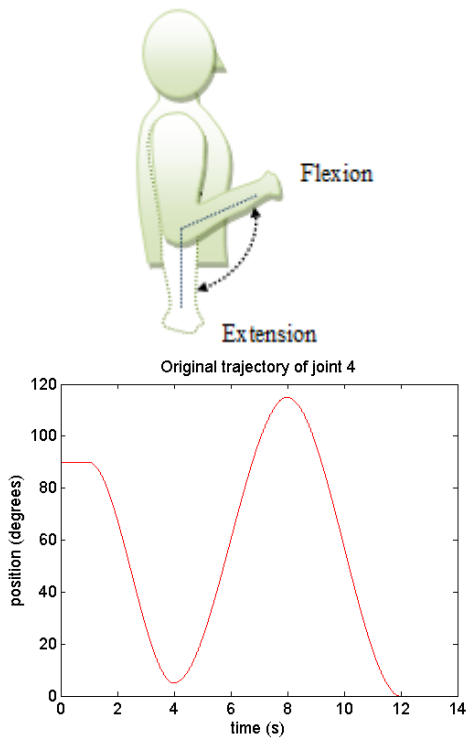


Fig. 3. Test performed: Elbow extension/flexion.

To finish the analysis from the Cartesian point of view, from the results of the experimented performed with the robot (Fig. 4), the trajectories for each Cartesian axis with the force and torque measured with the force sensor are shown in Fig. 8. In the plots of the left, which corresponds to the trajectories in the Cartesian axes, the solid line represents the original trajectory of the movement without any modification; the dotted line represents the trajectory modified by the admittance function that was followed by the human-robot system. It can be seen how the forces and torque, in the center and right columns respectively, affect the desired trajectory.

V. CONCLUSIONS AND FUTURE WORK

As can be seen from the experimental results, the present work can actively help a patient to accomplish a specified trajectory (a rehabilitation exercise). According to the evolution and the needs of the patients, the robot can vary the assistance provided. It is important to say that the robot will not force beyond capabilities of rehabilitation to the patient to

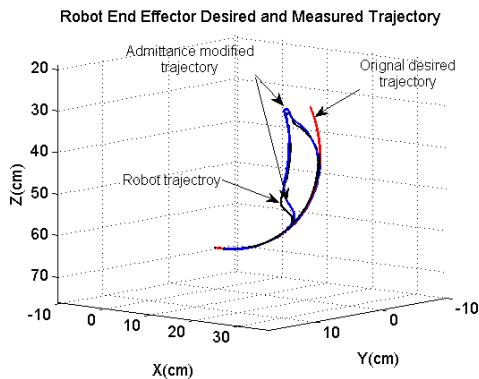


Fig. 4. Elbow flexion-extension results in Cartesian space.

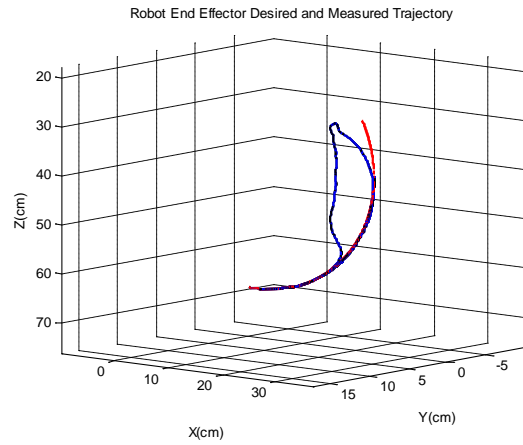


Fig. 5. Simulation of real results

fulfill a trajectory, a qualified therapist must adjust the limits according to the requirements. The amount of variation of the trajectory can be quantified as an excellent measurement of progression of the patient. As the next step for active assisted movement, the system will be provided with a virtual environment. It will provide the patients with visual help in the tracking of the movement objectives and will incorporate a variety of exercises in a game-based experience and incorporate powerful tools to track the evolution through the sessions. The next step in this research in force based

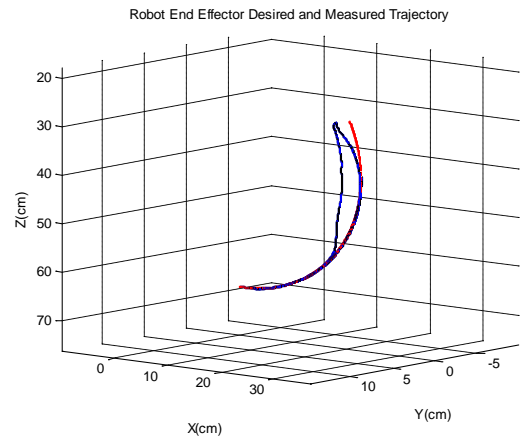


Fig. 6. Simulation with high degree of help.

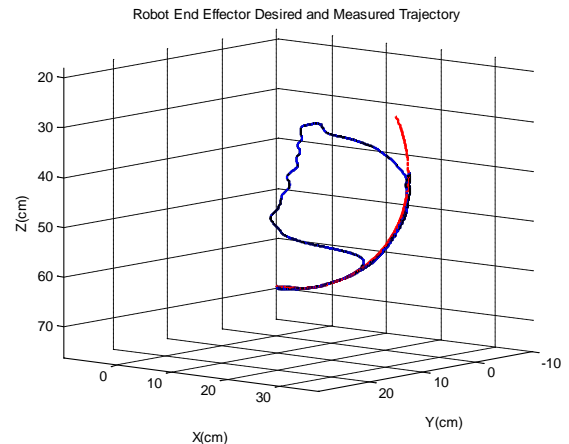


Fig. 7. Simulation with low degree of help.

rehabilitation is to move to active rehabilitation, which means that the patient will have control of his own movements without predefined trajectories, and the robot will help to accomplish that user desired movement.

REFERENCES

[1] N. M. Bornstein, *Stroke: Practical Guide for Clinicians*: Karger, 2009.  
 [2] Health\_Canada. (2006). *It's Your Health - Stroke*. Available: <http://www.hc-sc.gc.ca/hl-vs/iyh-vsv/diseases-maladies/stroke-vasculaire-eng.php>  
 [3] J. Mackay, Mensah, George A., *The Atlas of Heart Disease and Stroke*, 2004.  
 [4] N. S. Association@. (March 15th). *National Stroke Association@*. Available: [www.stroke.org](http://www.stroke.org)  
 [5] M. H. Rahman, T. K. Ouimet, M. Saad, J. P. Kenne, and P. S. Archambault, "Dynamic Modeling and Evaluation of a Robotic

Exoskeleton for Upper-Limb Rehabilitation," *International Journal of Information Acquisition*, vol. 8, pp. 83-102, 2011.  
 [6] M. H. Rahman, T. K. Ouimet, M. Saad, J. P. Kenne, and P. S. Archambault, "Development of a 4DoFs Exoskeleton Robot for Passive Arm Movement Assistance," *Int. J. Mechatronics and Automation*, vol. 2, pp. 34-50, 2012.  
 [7] M. H. Rahman, T. K. Ouimet, M. Saad, J. P. Kenne, and P. S. Archambault, "Development and Control of a Robotic Exoskeleton for Shoulder, Elbow and Forearm Movement Assistance," *Applied Bionics and Biomechanics*, vol. 9, pp. 275-292, 2012.  
 [8] J. J. Craig, *Introduction to robotics : mechanics and control*, 3rd ed. Upper Saddle River, N.J.: Pearson/Prentice Hall, 2005.  
 [9] H. Asada and J.-J. E. Slotine, *Robot analysis and control*. New York: J. Wiley, 1986.  
 [10] D. M. Gorinevsky, A. M. Formalsky, and A. Y. Schneider, *Force control of robotics systems*. Boca Raton, Flor.: CRC Press, 1997.  
 [11] W. H. Zhu, *Virtual Decomposition Control: Toward Hyper Degrees of Freedom Robots*: Springer, 2010.

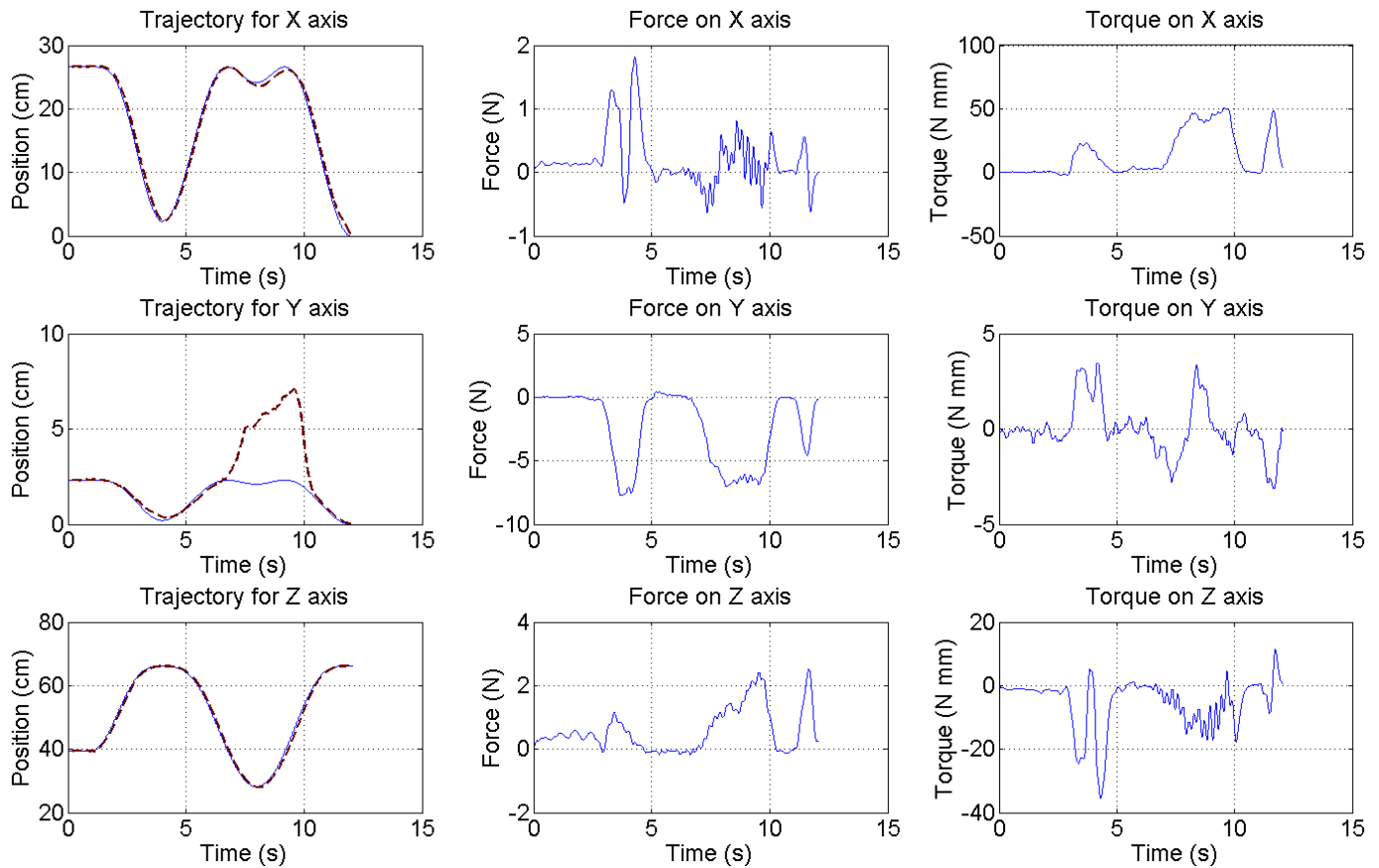


Fig. 8. Cartesian overview of the trajectory and forces and torques of the system.

# Pseudospectral Time-Domain (PSTD) method to predict fast transients in transmission lines

Silvano Cruciani and Mauro Feliziani

**Abstract**—The Pseudo spectral Time Domain (PSTD) method is proposed to analyze transient voltage and current wave propagation in transmission line (TL). The PSTD method uses the Fourier Transform to solve the spatial derivatives in the telegraphers' equations, while the time derivatives are approximated by central finite differences. The application of the PSTD method to TL equations requires adequate models to eliminate the wraparound effect produced by the FFT periodicity. In this work a lossy TL is proposed to model terminal conditions at the TL ends. Illustrative examples are given to compare the proposed PSTD method with the traditional Finite Difference Time Domain (FDTD) and analytical methods.

**Keywords**— Pseudospectral Time-Domain (PSTD) method, fast transients, telegraphers' equations, transmission lines.

## I. INTRODUCTION

TRANSMISSION line (TL) theory is widely applied to model wave propagation in one-dimensional domains as wires, cables, dielectric slabs, striplines, optical fibers, waveguides, carbon nano tubes and graphene structures used to transmit power or signals in electrical and electronics engineering. In many applications it is important to obtain the direct, time-domain solution of the TL equations and the knowledge of the electrical quantities along the TL axis. It generally occurs for nonlinear problem or to evaluate the radiated emission. To this aim the finite-difference time-domain (FDTD) method is widely applied for the analysis of transient wave propagation. By the FDTD method, the spatial and time derivatives of the telegraphers' equations are approximated by central finite differences, and the voltages and currents are located at different positions in a staggered grid. The FDTD method exhibits a second order accuracy in both space and time. Therefore, it achieves good accuracy only when the TL domain is finely discretized. Usually the spatial discretization must be of about 10-20 cells per wavelength at the highest frequency under consideration. In the PSTD method [1], the spatial derivatives are solved numerically by the Fast Fourier Transform (FFT) while the time derivatives are solved using a central finite differences scheme staggered in time by  $\Delta t/2$  using the leapfrog integration as in the FDTD method,  $\Delta t$  representing the time discretization.

S. Cruciani is with the Department of Industrial and Information Engineering and Economics, University of L'Aquila, L'Aquila, Italy (phone: +39-0862-434421; e-mail: silvano.cruciani@gmail.com).

M. Feliziani is with the Department of Industrial and Information Engineering and Economics, University of L'Aquila, L'Aquila, Italy (phone: +39-320-9231050; e-mail: mauro.feliziani@univaq.it).

With regard to the spatial discretization used in the PSTD method, the field components are in a collocated grid and not in a staggered one as in the traditional FDTD method since the spatial derivatives are approximated using the Fourier Transform and not by a finite difference. In this work, the PSTD method is applied to solve telegraphers' equations.

The FFT produces a spatial periodicity and the late-time solutions are corrupted by waves propagating from other periods. This phenomenon is known as the wraparound effect. In a TL the wraparound effect produces the following effect: the voltage and current waves transmitted at a TL termination do not disappear, but they will emerge again at the other end of the TL. This undesired effect can be removed by terminating the TL with an absorber realized as a distributed load.

Simple TL configurations are analyzed by the proposed PSTD method and the obtained results are discussed.

## II. TL EQUATIONS SOLUTION BY PSTD METHOD

A uniform lossy TL of length  $\ell$  and terminated on impedances  $Z_0$  and  $Z_\ell$  is considered as shown in Fig. 1. The telegraphers' equations in time domain are given by [4]-[7]

$$-\frac{\partial V(x,t)}{\partial x} = R'I(x,t) + L'\frac{\partial I(x,t)}{\partial t} \quad (1a)$$

$$-\frac{\partial I(x,t)}{\partial x} = G'V(x,t) + C'\frac{\partial V(x,t)}{\partial t} \quad (1b)$$

where  $x$  is the line axis,  $t$  is the time instant,  $V$  is the transient voltage,  $I$  is the transient current,  $R'$  the per unit length (p.u.l.) series resistance,  $L'$  the p.u.l. series inductance,  $G'$  the p.u.l. shunt conductance and  $C'$  the p.u.l. shunt capacitance.

The numerical solution of (1) is often obtained by the FDTD method using the Yee algorithm. By this approach, both spatial and time axes are discretized in spatial and time intervals,  $\Delta x$  and  $\Delta t$  respectively, and the spatial and time derivatives in (1) are approximated by central finite differences. Furthermore, (1a) and (1b) are solved at different time instants (staggered in time).

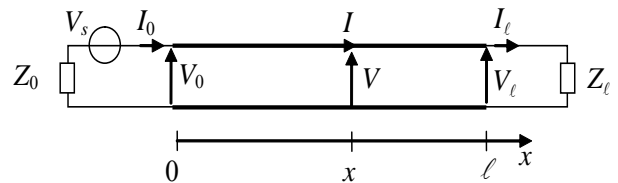


Figure 1. TL configuration.

In the PSTD method, the time derivatives in (1) are approximated by finite differences as in the FDTD method, but the spatial derivatives are solved by the Fourier Transform as explained in the following. The Fourier Transform of a function  $g(x)$  (solution of the wave equation) is defined as:

$$G(k_x) = F[g(x)] = \int_{-\infty}^{\infty} g(x) e^{-jk_x x} dx \quad (2)$$

where  $G$  represents the transformed function in the  $k$ -domain,  $F$  the Fourier Transform operator in  $x$ -direction and  $k_x$  is the variable representing the numerical wave vector along the  $x$ -axis [1]-[3].

The spatial derivative of  $g(x)$  is given in the Fourier domain by

$$\frac{\partial g(x,t)}{\partial x} = F^{-1}[-jk_x F[g(x,t)]] \quad (3)$$

where  $F^{-1}$  denotes the inverse Fourier Transform operator in the  $x$  direction.

By applying (3) to (1), it yields:

$$-F^{-1}[-jk_x F[V(x,t)]] = R' I(x,t) + L' \frac{\partial I(x,t)}{\partial t} \quad (4a)$$

$$-F^{-1}[-jk_x F[I(x,t)]] = G' V(x,t) + C' \frac{\partial V(x,t)}{\partial t} \quad (4b)$$

### III. SPATIAL AND TIME DISCRETIZATIONS OF PSTD MODEL

A great advantage of the PSTD over the FDTD is that the spectral domain method can be viewed as a finite difference method with infinite order of accuracy because the Fourier Transform resolves exactly the original spatial derivatives in the  $k$ -space. It means that the PSTD method is not affected by any numerical dispersion [1]. For this reason the PSTD will allow a much coarser discretization of the computational domain than that required by the FDTD method. Indeed, while the FDTD method requires a spatial discretization of a minimum of 10-20 cells per wavelength to achieve good accuracy, the PSTD method requires only 2 cells per wavelength as demanded by the Nyquist sampling theorem [1]. Then, the size of a cell in the PSTD method must be

$$\Delta x \leq \frac{\lambda_{\min}}{2} \quad (5)$$

where  $\lambda_{\min}$  is the minimum wavelength corresponding to the maximum frequency  $f_{\max}$  of the problem under consideration.

The Fourier transforms in (4) can be numerically carried out by the FFT in some fixed spatial points  $x_i$  separated each other by the spatial interval  $\Delta x$  [1]. Differently from the Yee algorithm, the PSTD method does not need the use of the staggered grid in space because the spatial derivatives are calculated via the Fourier Transform. So the voltage  $V$  and the

current  $I$  are calculated in the same points  $x_i$ . The time discretization in the PSTD method is not strictly related to the spatial discretization. This aspect is the most relevant difference from the FDTD method, where the time and spatial intervals are linked together by the leap-frog scheme and Courant stability condition.

In the PSTD method different time integration schemes have been used [1]-[3]. In this work, we use a simple second-order accurate-in-time scheme approximating the time derivatives by central differences. The time axis is uniformly discretized in equal time steps  $\Delta t$ . The voltage  $V$  and the current  $I$  are separated by  $\Delta t/2$  following the classic leapfrog integration scheme. It means that (4a) and (4b) are solved respectively at  $t=n\Delta t$  and  $t=(n+1/2)\Delta t$ , and (4) can be rewritten as:

$$-F^{-1}[-jk_x F[V_i^n]] = R' \frac{I_i^{n+1/2} + I_i^{n-1/2}}{2} + L' \frac{I_i^{n+1/2} - I_i^{n-1/2}}{\Delta t} \quad (6a)$$

$$-F^{-1}[-jk_x F[I_i^{n+1/2}]] = G' \frac{V_i^{n+1} + V_i^n}{2} + C' \frac{V_i^{n+1} - V_i^n}{\Delta t} \quad (6b)$$

assuming the following notation for the voltage and the current in the discrete spatial points  $x_i$ :  $V_i^n = V(i\Delta x, n\Delta t)$  and  $I_i^{n+1/2} = I(i\Delta x, (n+1/2)\Delta t)$ .

The updating equations are then obtained by (6) as:

$$I_i^{n+1/2} = \frac{\left(-\frac{R'}{2} + \frac{L'}{\Delta t}\right) I_i^{n-1/2} - F^{-1}[-jk_x F[V_i^n]]}{\frac{R'}{2} + \frac{L'}{\Delta t}} \quad (7a)$$

$$V_i^{n+1} = \frac{\left(-\frac{G'}{2} + \frac{C'}{\Delta t}\right) V_i^n - F^{-1}[-jk_x F[I_i^{n+1/2}]]}{\frac{G'}{2} + \frac{C'}{\Delta t}} \quad (7b)$$

For stability reasons, the time step  $\Delta t$  must satisfy the following condition [1]:

$$\Delta t \leq \frac{2}{\pi} \frac{\Delta x}{v} \quad (8)$$

where  $v$  is the maximum speed of propagation inside the transmission line.

It is interesting to compare the computational cost of the PSTD method with that of the FDTD method. The classical FDTD discretization of a 1D domain requires at least  $\Delta x_{FDTD} = \lambda_{\min}/10$  and  $\Delta t_{FDTD} = \Delta x_{FDTD}/v = \lambda_{\min}/10v$ , while

the PSTD requirements are:  $\Delta x_{PSTD} = \lambda_{\min} / 2$  and  $\Delta t_{PSTD} = 2\Delta x_{PSTD} / (\pi v) = \lambda_{\min} / (\pi v)$ . It is simple to evaluate  $\Delta x_{PSTD} / \Delta x_{FDTD} = 5$  and  $\Delta t_{PSTD} / \Delta t_{FDTD} = 10 / \pi$ . We will obtain  $N_{PSTD}$  spatial samples in the PSTD and  $N_{FDTD}$  in the FDTD scheme, and the spatial ratio is  $r_x = N_{PSTD} / N_{FDTD} = 5$ . The time discretization ratio is  $r_t = 2r_x / \pi$ . At each time step the computational complexity of the PSTD is  $O(N_{PSTD} \log_2(N_{PSTD}))$  and that of the FDTD is  $O(N_{FDTD})$ .

#### IV. PSTD METHOD APPLICATION TO TRANSMISSION LINE

The main disadvantage of the PSTD method consists in the wraparound effect. Because of the FFT use, a periodicity over  $x$  axis is assumed and the solution in the latter time is corrupted by wave coming from other spatial periods (wraparound effect) [1]. This effect can be mitigated by absorbing the outgoing wave at the end of the domain, i.e. TL termination ends. By this absorption, the wraparound effect is practically removed since the wave at the end of the TL after absorption is quite negligible. In the past, several authors have used Berenger's perfectly matched layers (PML) [8] to absorb the wraparound effect. This method can be successfully adopted in TL applications, but it is valid only for matched conditions of TLs, which are not always verified in practical TL applications. So it is necessary to introduce adequate models to simulate different TL terminal conditions, e.g., from short circuit conditions to open end conditions.

In this work lossy TLs located at both terminations of the line are proposed to eliminate the transmitted waves avoiding that they appear again at the other TL end. The lossy TLs must have the following two characteristics:

- 1) reflect the incident waves as demanded by the terminal load conditions;
- 2) absorb quite totally the transmitted waves.

These requirements can be obtained for a large class of load conditions by a lossy TL with an input impedance equal to that of the terminal load in order to satisfy 1) and with high attenuation in order to satisfy 2).

The lossy TLs can be modelled by a series cascade of lumped circuit cells as shown in Fig. 2. The number of the cells depends on the wave shape of the transmitted voltage and current waves. The lumped circuit parameters of the equivalent absorbers ( $R_{abs}$ ,  $L_{abs}$ ,  $G_{abs}$ ,  $C_{abs}$ ) are derived by the circuit theory depending on the number of the cells and on the required input impedance.

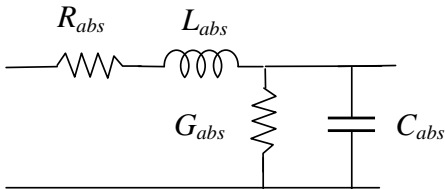


Figure 2. Lumped circuit cell.

The procedure to apply the proposed method is described as follows. First, the considered TL of length  $\ell$  is discretized uniformly in uniform sections of length  $\Delta x$  giving rise to  $N_x$  points  $x_i$  where the voltage  $V$  and the current  $I$  are calculated, i.e.  $x_i = i\Delta x$  being  $i=1, \dots, N_x$ . Then, a number of absorbing cells are introduced to eliminate the transmitted waves at both ends of the TL, i.e. ahead of point  $x_1$  and behind of point  $x_{N_x}$ , as shown schematically in Fig.3.

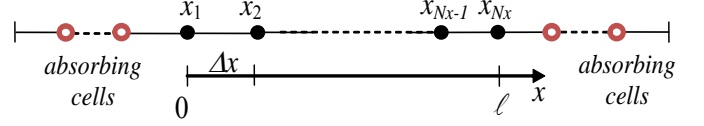


Figure 3. Spatial discretization of the TL and introduction of lumped circuit cells at both TL ends.

#### V. APPLICATIONS

An aerial wire conductor above a perfectly conductive ground is examined as test case. The configuration of the considered TL is: wire radius  $r_0=0.25$  mm, length  $\ell=20$  m and height  $h=0.1$  m. The TL parameters are: p.u.l. inductance  $L'=1.33$   $\mu\text{H}/\text{m}$ , p.u.l. capacitance  $C'=8.36$  pF/m. For lossless TL (i.e.,  $R'=G'=0$ ) the characteristic impedance is  $Z_c=398.9$   $\Omega$  and the line velocity  $v$  coincides with the free space velocity. The TL is matched at both ends and excited at the left end by a Gaussian pulse. The line matching is performed by PML cells located at both the extremities of the domain under study. In the first application the TL is considered to be lossless and the spatial domain is coarsely discretized assuming  $\Delta x=0.3$  m and  $\Delta t=318$  ps. The transient voltage wave at  $x=15$  m is shown in Fig.4, where the results are compared with the exact solution obtained by the analytical solution in frequency domain via the Fourier transform and with the FDTD solution. It is evident that the FDTD method is less accurate than the PSTD method for the considered configuration. Then, a finer spatial discretization is used assuming  $\Delta x=0.05$  m and  $\Delta t=53$  ps, and the obtained results are shown in Fig. 5. In this case the accuracy of the PSTD and FDTD methods is similar.

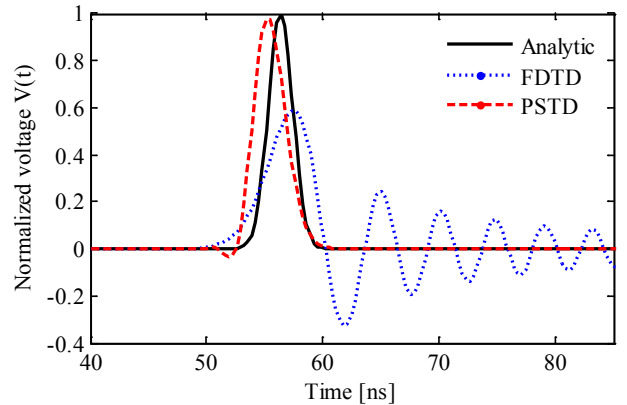


Figure 4. Transient voltage at  $x=15$  m assuming  $\Delta x=0.3$  m and  $\Delta t=318$  ps for a lossless TL matched at both ends ( $Z_0 = Z_l = Z_c$ ).

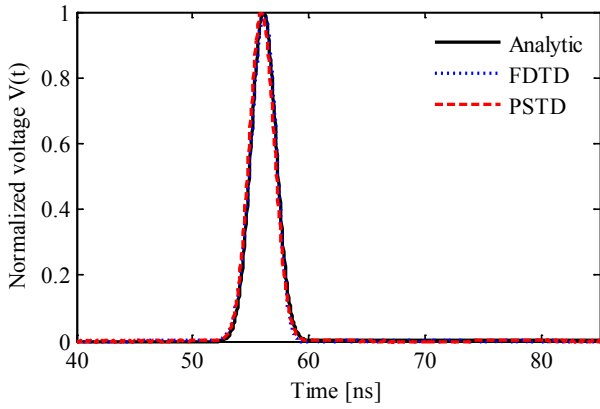


Figure 4. Transient voltage at  $x=15$  m assuming  $\Delta x=0.05$  m and  $\Delta t=53$  ps for a lossless TL matched at both ends ( $Z_0 = Z_l = Z_c$ ).

The same TL configuration is analyzed assuming a short-circuit condition at the right end. The voltage wave at  $x=15$  m is depicted in Fig. 6 where you can see the reflection produced by the short-circuit terminal condition.

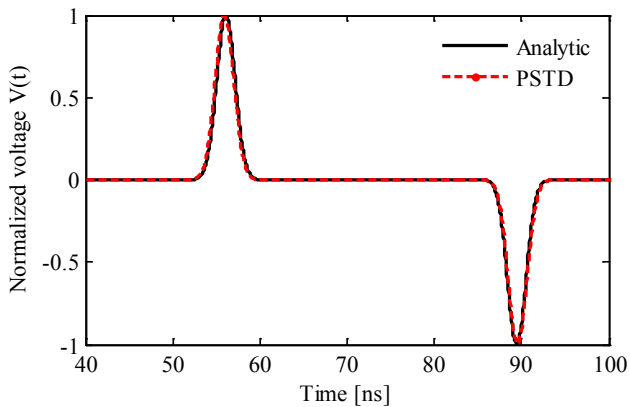


Figure 6. Transient voltage at  $x=15$  m assuming  $\Delta x=0.05$  m and  $\Delta t=53$  ps for a terminated lossless TL ( $Z_0 = Z_c$ ,  $Z_l = 0$ ).

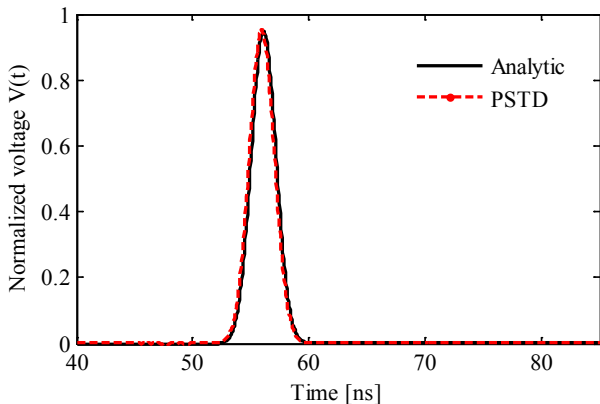


Figure 7. Transient voltage at  $x=15$  m assuming  $\Delta x=0.05$  m and  $\Delta t=53$  ps for a lossy TL matched at both ends ( $Z_0 = Z_l = Z_c$ ).

Finally the losses are introduced in the TL assuming a constant p.u.l. resistance  $R'=2.82 \Omega/\text{m}$  and  $G'=0$ . The transient voltage wave at  $x=15$  m for matched TL at both ends is shown in Fig.7, and for matched condition at the left end and short-circuited at the right end is shown in Fig. 8.

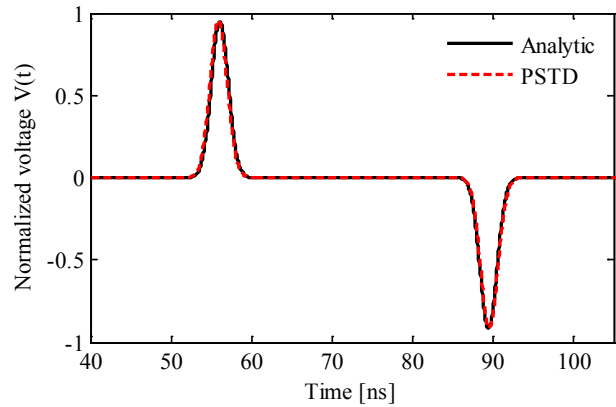


Figure 8. Transient voltage at  $x=15$  m assuming  $\Delta x=0.05$  m and  $\Delta t=53$  ps for a terminated lossy TL ( $Z_0 = Z_c$ ,  $Z_l = 0$ ).

## VI. CONCLUSIONS

A pseudospectral time-domain (PSTD) algorithm has been proposed to analyze the wave propagation of transient voltage and current in a transmission line. This method allows great saving in terms of memory occupation with respect to the FDTD method. Its accuracy is very high and the numerical dispersion is very low. The time computational cost is comparable with that of the FDTD method.

Lossy TLs have been introduced at the terminations of the line to simulate boundary conditions produced by the terminal loads and to absorb the transmitted waves in order to eliminate the wraparound effect. In future research, terminations with nonlinear loads will be considered in the PSTD method.

## REFERENCES

- [1] Q. H. Liu, "The PSTD algorithm: A time-domain method requiring only two cells per wavelength," *Microwave Optical Techn. Lett.*, vol. 15, no. 3, pp. 158-165, 20 June 1997.
- [2] Q. H. Liu, "Large-scale simulations of electromagnetic and acoustic measurements using the pseudospectral time-domain (PSTD) algorithm," *IEEE Trans. Geosc. Remote Sensing*, vol.37, no.2, pp. 917-926, Mar. 1999.
- [3] T. Lee and S. C. Hagness, "Pseudospectral time-domain methods for modeling optical wave propagation in second-order nonlinear materials," *J. Opt. Soc. Am. B*, vol. 21, no. 2, Feb. 2004.
- [4] K. Kunz and R. Luebbers, *The Finite Difference Time Domain Method for Electromagnetics*, Boca Raton, FL: CRC Press, 1993.
- [5] C. R. Paul, *Analysis of multiconductor transmission lines*, 2nd ed., John Wiley & Sons, New Jersey, 2008.
- [6] C. R. Paul, "Incorporation of terminal constraints in the FDTD analysis of transmission lines," *IEEE Trans. Electromag. Compat.*, vol.36, no.2, pp. 85-91, May 1994.
- [7] B. Kordi, J. LoVetri, and G. E. Bridges, "Finite-difference analysis of dispersive transmission lines within a circuit simulator," *IEEE Trans. Power Delivery*, vol.21, no.1, pp. 234- 242, Jan. 2006.
- [8] J. P. Berenger, *Perfectly Matched Layer (PML) for Computational Electromagnetics*, Morgan and Claypool Publishers, 2007.

# Fuel-efficient Motion Control of Tracked Robots Equipped with AC Electric Transmissions

V. Kh. Pshikhopov, D. B. Pogosov

**Abstract**—This paper is about synthesis of nonlinear control algorithms of tracked robots, based on the position-trajectory control method. This paper introduces method for motion with constant power of internal combustion engine, that well for a fuel efficient. The paper contains a nonlinear mathematical model of the robot's chassis, an electrical transmission, based on AC units and a diesel engine. The introduced solutions able to be used in any mobile object, which, in general, have a requirement about level of consumed power.

**Keywords**—Electric transmission, motion control, power control, tracked robot.

## I. INTRODUCTION

TRACKED robots (TR) are advanced systems for transportation, rescue or other tasks, their development objectives are mainly to increase motion speed, accuracy and optimization of power consumption.

Usually the unit power ratio of tracked vehicles is lower than of wheeled vehicles, so the energy optimization problem is important. Extent of energy efficiency in systems equipped with an internal combustion engine (ICE) is fuel consumption rate.

Constant speed of robot motion is requires changing of torques on the driven sprockets, causing changes ICE power in time. From ICE theory [1] known that a high dynamics of ICE causes higher fuel consumption, than low ICE dynamics with constant speed of its crankshaft and constant torque.

This leads a task of the organization of a robot movement with a constant output power of ICE. Control system in this mode should adapt controls to road conditions by changing the chassis speed, to work on the robot trajectory with high accuracy and ICE power maintained at a constant level.

To reach described advantages, we assume the robot contains an electric transmission, which enables to precision motion on smooth trajectory with, generally, different speeds on driven sprockets. There should be noted, that on classical (like hydraulic displacement) transmissions such motion modes

requires using of brakes. That is not only difficult to accurate control, also a negative effect on the energy efficiency.

This paper introduces a nonlinear control system of tracked robots (TR) motion, based on the position-trajectory control method [2]-[3]. Novelty is possibility of movement at mainly constant power, which an engine produced, or with limited of maximum engine power. The electric transmission (ET) we assume based on induction motor drives (ID) and synchronous motors drives (SD).

## II. MATHEMATICAL MODEL OF CONTROL OBJECT

### A. Chassis Model of Tracked Robot

We will consider TR with two traction motors and two frequency converters with generators and a diesel engine. The traction generators are connected to ICE through a primary gear. Each traction motor is connected to same side driven sprocket through a secondary gear.

Mathematical model of TR introduced by the following system of vector-matrix equations [2], [4]-[7]:

$$\dot{Y} = [P \quad \varphi]^T = R(\varphi)LX, \quad (1)$$

$$L_2^{-1}M\dot{X} = Q - L_2^{-1}F_R, \quad F_R = F_s f' + L_1^{-1}F_O + F_N, \quad (2)$$

$$R(\cdot) = \begin{bmatrix} \cos(\cdot) & \sin(\cdot) \\ -\sin(\cdot) & \cos(\cdot) \end{bmatrix}, \quad (3)$$

$$F_s = \text{diag}((G/2)\cos\alpha\cos\beta),$$

$$F_O = [G\sin\alpha + R_{TR} + F_a \quad M_r]^T,$$

$$M_r = (\mu Gl \cos\alpha \cos\beta (1 - (l\xi/2)^2))/4,$$

$$\dim Y = 3 \times 1, \quad \dim R = 3 \times 3, \quad \dim L = 3 \times 2,$$

$$\dim P = \dim X = 2 \times 1,$$

where  $Y$  – is vector of the chassis position  $P$  and orientation (yaw)  $\varphi$ ;  $R(\cdot)$  – is a rotation matrix;  $L, L_1, L_2$  – are matrixes of coordinates transformation;  $X$  – is vector of the driven sprockets speeds;  $Q$  – is vector of the driven sprockets torques;  $F_R$  – is vector of a motion resistance;  $f'$  – is vector of ground coefficients;  $M$  – is matrix of mass and inertia parameters with secondary gears ratio and efficiency;  $\alpha$  and  $\beta$  – are pitch and roll, accordingly;  $G$  – is weight;  $l$  – is length of a track;  $R_{TR}$  – is a trailer resistance;  $F_a$  – is the air resistance;  $M_r$  – is a turn resistance;  $\mu$  – is coefficient of the turn resistance;  $\xi$  – is turn poles shifting;  $F_N$  – is vector of im-

This work was supported by Grant of the President of Russia NSh-3437-2014-10.

Prof. V. Kh. Pshikhopov, is with the Southern Federal University, Rostov-on-Don, 347928, Russia (phone: +7-863-371694; fax: +7-863-371694; e-mail: toe@tgn.sfedu.ru).

D. B. Pogosov, is with the Southern Federal University, Rostov-on-Don, 347928, Russia (phone: +7-863-371694; fax: +7-863-371694; e-mail: deonisy2004@yandex.ru).

measurable disturbances.

### B. Electric Transmission Model

Advanced ET is based on AC units. In this paper we consider an induction motor (short-circuited rotor) and synchronous motor (constant rotor field, like DC inductor or permanent magnet).

High quality control of AC motors is possible by the vector control methods [8]-[10]. According to the method, first of all, voltage vector is calculated in the two-dimensional coordinate system  $dq$ , attached to the rotor field. Second, the voltage vector changes through a coordinate transformation (rotation on the field angle) to voltage vector of two-dimensional coordinate system fixed to the stator. Third and last coordinate transformation is conversation the vector to three-dimensional natural phase system.

Hereafter the vector in phase coordinates goes to input of an inverter, which produce real control actions. Construction of the inverter is widely described in [8], [9] so in this paper we will not describe it.

ID rotor have a large electromagnetic time constant and interlinkage may be changed slowly, so we assume that the rotor interlinkage is a constant and determined by a rated torque. This approach allows the synthesis system with possibility to rapid torque change in time to achieve TR control system characteristics of high accuracy and speed. During TR movement, the rotor interlinkage value may be changed with a time constant greater than the rotor time constant.

We introduce the model of ID with the following equations in vector-matrix form (one equation for each motor) [8]-[11]:

$$U_A = L_\Sigma \dot{I}_A + R_A I_A + \omega D I_A + \omega D_1 + L_m D_2, \quad (4)$$

$$D = \begin{bmatrix} L_\Sigma & 0 \\ 0 & 0 \end{bmatrix}, D_1 = \begin{bmatrix} 0 & L_\Sigma \Phi_R^{-1} L_m - L_R^{-1} L_m \Phi_R \end{bmatrix}^T,$$

$$R_A = \begin{bmatrix} 0 & 0 \\ 0 & r_A \end{bmatrix}, D_2 = [r_A / \Phi_R \quad 0]^T,$$

$$Q_A = L_m K_m I_A, K_m = \begin{bmatrix} 0 & \frac{3Z_p \Phi_R}{2L_R} \end{bmatrix}, \quad (5)$$

$$\dim U_A = \dim I_A = \dim D_2 = 2 \times 1, \dim K_m = 1 \times 2$$

$$\dim R_A = \dim D = 2 \times 2,$$

where  $U_A$  – is a vector of ID stator voltage;  $L_\Sigma$  – is an equivalent dissipation inductance, depend on  $L_m$ ;  $L_m$  – is a main inductance (is a nonlinear function of  $q$  part stator current, if constant rotor flux);  $L_R$  – is the rotor inductance;  $r_A$  – is total resistance of stator winding;  $\Phi_R$  – is rotor interlinkage;  $I_A$  – is a vector of ID stator current;  $\omega$  – is the flux angular velocity;  $Z_p$  – is quantity of pair of poles;  $Q_A$  – is the torque on ID shaft.

The current is measured and the angle of the rotor flux is calculated according to the method of direct field oriented control [8].

We introduce the model of SD with the following expressions in vector-matrix form [8]-[11]:

$$U_S = L_S \dot{I}_S + r_S I_S + \omega_R L_S D_3 I_S + \omega_R D_4, \quad (6)$$

$$D_3 = \begin{bmatrix} 0 & -1 \\ 1 & 0 \end{bmatrix}, D_4 = [0 \quad \Phi_R]^T,$$

$$Q_S = K_{m1} I_S + I_S^T K_{m2} I_S, K_{m1} = [0 \quad 1.5Z_p \Phi_R], \quad (7)$$

$$K_{m2} = \begin{bmatrix} 0 & 0 \\ 1.5Z_p L_\Delta & 0 \end{bmatrix},$$

$$\dim U_S = \dim I_S = \dim D_4 = 2 \times 1, \dim K_{m1} = 1 \times 2,$$

$$\dim K_{m2} = \dim D_3 = 2 \times 2,$$

where  $U_S$  – is a vector of SD stator voltage;  $L_S$  – is a diagonal matrix of stator inductance on axes  $d$  and  $q$ ;  $r_S$  – is a diagonal matrix of total resistance of stator winding;  $\Phi_R$  – is the rotor constant flux;  $I_S$  – is a vector of SD stator current;  $\omega_R$  – is the rotor angular speed;  $L_\Delta$  – difference between  $d$  and  $q$  stator inductance (is zero for implicit-pole motors);  $Q_S$  – is the torque on SD shaft.

The current is measured.

As was written earlier, to get the phase voltage of AC motors, we execute the coordinate transformation of (6) or (4) by (3):

$$U_{3A} = P_S R^{-1}(\gamma_\omega) U_A, \quad (8)$$

$$U_{3S} = P_S R^{-1}(\gamma_R) U_S, \quad (9)$$

$$P_S = \begin{bmatrix} 1 & -1/2 & -1/2 \\ 0 & \sqrt{3}/2 & -\sqrt{3}/2 \end{bmatrix}^T,$$

$$\dim K_{m2} = \dim D_3 = 2 \times 2,$$

where  $U_{3A}$  – is a vector of ID phase voltages,  $U_{3S}$  – is a vector of SD phase voltages,  $\gamma_\omega$  – is an angle of ID rotor flux,  $\gamma_R$  – is an angle of SD rotor, other values were described earlier.

Due to the fact, that the theory of alternators control well-developed for constant power systems [11], [12], [13] for simplicity reasons, we represent the model of the pair alternator-inverter (two sides) as an inertial part:

$$U_G = K_G X_G \Phi_G - \tilde{I} r_G, \quad (10)$$

$$Q_G = J_G \dot{X}_G = K_{pG} K_{mg} \tilde{I} \Phi_G, \quad (11)$$

$$\tilde{I} = \text{diag} I,$$

$$\dim U_G = \dim \Phi_G = \dim r_G = 2 \times 1 = \dim Q_G,$$

$$\dim K_G = \dim X_G = \dim K_{mg} = 2 \times 2,$$

where  $U_G$  – is a vector of alternators voltages;  $r_G$  – is total

resistance of windings;  $K_G, K_{PG}, K_{mg}$  – are diagonal matrixes of constants;  $\Phi_G$  – is a vector of alternators fluxes;  $Q_G$  – is vector of loads on alternators shafts;  $X_G$  – is a vector of shafts speeds;  $J_G$  – is scalar inertia of the shaft,  $K_{PG}$  – the primary gear ratio.

Follows equation shown ICE crankshaft speed  $\omega_e$  and alternators shafts speeds:

$$[1 \ 1]^T \omega_e = K_{PG}^{-1} X_G.$$

### C. Diesel Engine Model

This paper we assume the diesel combustion engine. The engine characterization [14] is shown on Fig.1.

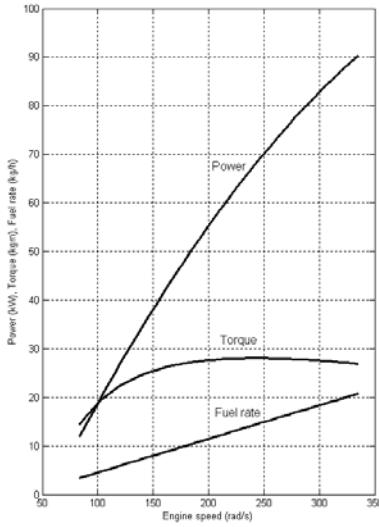


Fig. 1 the diesel engine characteristics: power (kW), torque (kg·m) and fuel rate (kg/h), all depending on engine speed (rad/s)

The curves are shown only for engine speed limited by 330 rad/s, because between 330 rad/s and 420 rad/s the engine torque is drop and power is not raised, so this mode is not useful for constant power motion. At the engine speed more than 420 rad/s the torque is much drop and this mode should be limited in any diesel combustion engine.

The torque model is becomes as follows [1]:

$$J_e \dot{\omega}_e = M_{ind} - M_{fr} - M_{pump}, \quad (12)$$

where  $J_e$  – is the engine inertia,  $M_{ind}$  – is the indicated engine torque,  $M_{fr}$  – is the friction engine torque,  $M_{pump}$  – is the pump torque.

Engine torque components can be represented as follows [15]-[16]:

$$M_{ind} = \frac{k_F U_F Q_{LHV} R_{gas} T_{im} (e_0 + e_1 \omega_e + e_2 \omega_e^2)}{\eta_V V_d P_{im}}, \quad (13)$$

$$\eta_V = e_3 + e_4 \omega_e + e_5 \omega_e^2, \quad (14)$$

$$M_{fr} = \frac{1000 V_d (e_6 + e_7 \omega_e + e_8 \omega_e^2)}{2 \pi n_R}, \quad (15)$$

$$M_{pump} = e_9 P_{im} + e_{10}, \quad (16)$$

where  $U_F$  – is a fuel rate;  $Q_{LHV}$  – is the fuel lower heating value;  $R_{gas}$  – is the gas constant,  $P_{im}$ ;  $T_{im}$  – are pressure and temperature in intake manifold, respectively;  $V_d$  – is the engine volume;  $\eta_V$  – is volumetric efficiency;  $n_R$  – is number of revolutions for each power stroke, per cycle;  $k_F, e_0 - e_{10}$  – are constants. We assume measurable of intake manifold pressure and temperature.

### III. SYNTHESIS OF CONTROL SYSTEM

We define the control system task for the synthesis as movement on a trajectory at a desired constant power of traction motor drives (both).

We set a trajectory of TR by following vector equation [2], as function  $N_1$  of external coordinates (1) in implicit form [17]:

$$\Psi_T = [N_1(P) \ 0]^T, \dim \Psi_T = 2 \times 1. \quad (17)$$

We set power consumption at desired level  $w_j$  at steady state, by the following vector equation, as a function of internal coordinates and their derivatives (2):

$$\tilde{W} = [0 \ -|X|^T M \dot{X} + |X|^T F_R - w_j]^T, \dim \tilde{W} = 2 \times 1. \quad (18)$$

We assume control vector, which contain motors voltages (8) or (9), generators flux (10) and fuel rate (13):

$$\tilde{U} = [U_F \ \Phi_G \ U_3]^T, \dim \tilde{U} = 6 \times 1. \quad (19)$$

We define the desired character of TR motion as a closed-loop system by follows system of vector-matrix equations:

$$\Psi = \Psi_T + A \dot{\Psi}_T, \quad (20)$$

$$\tilde{\Psi} = \Psi + T \tilde{W} + T \dot{\Psi}, \quad (21)$$

$$\tilde{\tilde{\Psi}} = \tilde{\Psi} + C \dot{\tilde{\Psi}}, \quad (22)$$

where  $A$ ,  $T$  and  $C$  – are diagonal matrixes of constant coefficients, which define the desired character of the system action and transient.

According to the position-trajectory control method [3], we differentiate equations (9) three times, (1) twice and (2), (5) or (7) once. Then we solve them together with (20)-(22), then with (10), (11) and at last with (12)-(16). So, we obtain the following control algorithm of TR:

$$U_F = K_{ICE}(M_{fr} + M_{pump} + K_E K_{mg} \tilde{I} \Phi_G), \quad (23)$$

$$K_{ICE} = \frac{\eta_V V_d P_{im}}{k_F Q_{LHV} R_{gas} T_{im} (e_0 + e_1 \omega_e + e_2 \omega_e^2)},$$

$$K_E = J_e J_G^{-1} K_{PG} [1 \quad 1], \quad (24)$$

$$\Phi_G = K_G K_{PG}^{-1} \omega_e (U_D + \tilde{I} r_G), \quad (25)$$

$$U_S = L_S (K_{m1} + K_{m2} I_S^T)^{-1} (M \ddot{X} + \dot{F}_R) + K_S, \quad (26)$$

$$K_S = r_S I_S + \omega_R L_S D_3 I_S + \omega_R D_4,$$

$$U_A = L_\Sigma (K_m J_L \tilde{I} + K_m L_m)^{-1} (M \ddot{X} + \dot{F}_R) + K_A,$$

$$K_A = R_A I_A + \omega D I_A + \omega D_1 + L_m D_2,$$

$$\ddot{X} = K_0^{-1} (K_1 \dot{Y} + K_2 \ddot{Y} + K_3 \ddot{X} + \Psi_T + T \tilde{W} + K_4),$$

$$K_0 = -CTAJ - CTJ_W,$$

$$K_1 = (A + T + C)J + (TA + CT + CA)\dot{J} + CTA\ddot{J},$$

$$K_2 = (TA + CT + CA)J + CTA\dot{J},$$

$$K_3 = 2CTAJ\dot{R}L,$$

$$K_4 = CTAJ\ddot{R}LX + CTK_W,$$

$$J = \frac{\partial \Psi_T}{\partial Y^T}, \quad \tilde{I} = \text{diag} I, \quad J_W = [0_{(n-1) \times 2} \quad -|X|^T M]^T,$$

$$K_W = [0_{n-1} \quad -|\dot{X}|^T M \dot{X} + |\dot{X}|^T F_R + |X|^T \dot{F}_R]^T,$$

$$\dim K_0 = \dim K_2 = \dim K_3 = \dim J_W = 2 \times 2,$$

$$\dim K_1 = \dim K_4 = \dim K_W = \dim \Gamma = 2 \times 1, \quad \dim J = 2 \times 3.$$

Equations (23), (24) and (26) define the components of the vector control (19) for system with ID and  $I = I_A$ . Equations (23)-(25) define the components of the vector control (19) for system with SD and  $I = I_S$ .

#### IV. SIMULATION

Simulation of the introduced control algorithms (24)-(25) was accomplished in the software package MATLAB.

Chassis TR is presented by (1)-(2) and has the following parameters: weight 12 tons, length 5.5 m, width 3.8 m, inertia is  $1150 \text{ kg}\cdot\text{m}^2$ , radius of the driven wheel is 0.2 m, secondary gear ratio is 1:2. Traction motors are represented by (6)-(7) and have the following parameters: maximum voltage is 400 V, maximum power is 90 kW,  $L_S = \text{diag}(0.05)$ ,  $\Phi_R = 23$ ,  $L_\Lambda = 0$ ,  $r_S = \text{diag}(0.1)$ ,  $Z_p = 1$ .

The first test is constant power running on a circle. The task of TR motion (17) is the circle of radius 100 m centered at the origin and the expression (18), corresponding to the stabilization of constant power at level 70 kW. Adjustment matrices (20)-(22) are unitary matrixes. The initial position of the robot is  $Y = [90 \quad 0 \quad \pi/4]^T$  and the robot does not move. Simulation time is 287.4 s. Without loss of generality, we represent the motion resistance vector by constants, equal to 4725. After 70 s from the start of simulation, the vector of resistance will increase to 13300 during 20 s. After 170 s from the start of simulation, the vector resistance reduced to 4725 during 20 s. This simple test allows facilitating analysis of the reaction of

the system to changing the motion resistance and corresponds to the rise on hill and downhill.

The control system (24)-(25), should provide a stable movement on the trajectory with a root-mean-square error less than 0.3, at steady state.

The result of simulated trajectory is presented on Fig.2.

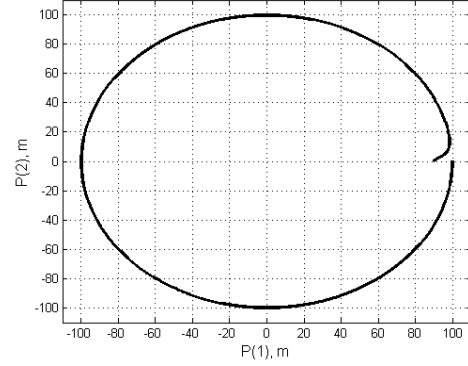


Fig. 2 the trajectory of TR motion, the first test

The result of simulated speed and rising resistance of motion are presented on Fig.3.

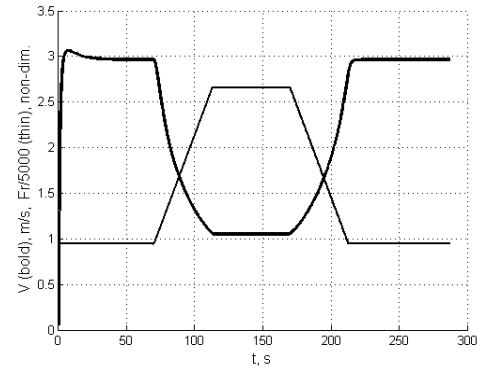


Fig. 3 the speed and motion resistance, the first test (constant power)

The voltage and current of traction motors, before coordinates transform (9), are presented on Fig.4.

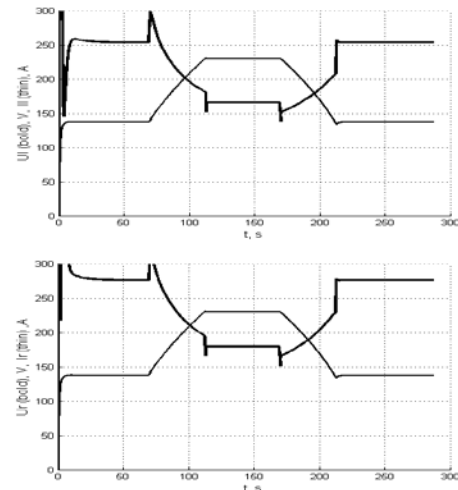


Fig. 4 the traction motors voltage and current, the first test (constant power)

The root-mean-square error is 0.12 at steady state, which correspond to the requirements. The fuel consumption for this test is 1.1779 kg.

The second test is constant speed running on a circle. The task of TR motion is same, the TR parameters and traction motors parameters are same like the first test. The motion resistance is same too. Constant speed level is 2.2 m/s. This test need to compare fuel consumption of the introduced this paper algorithm and constant speed algorithm from [2]-[3]. Simulation time is 287.4 s.

The result of simulated trajectory is same as in Fig.2, simulated speed and rising resistance of motion are presented on Fig.5.

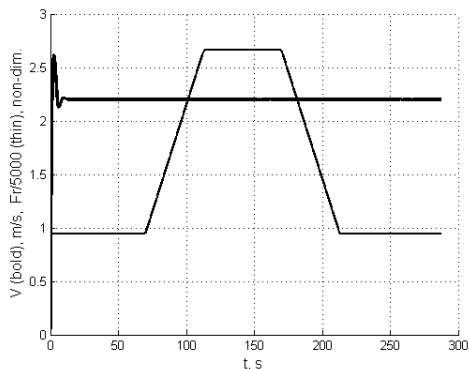


Fig. 5 the speed and motion resistance, the second test (constant speed)

The voltage and current of traction motors, before coordinates transform (9), are presented on Fig.6.

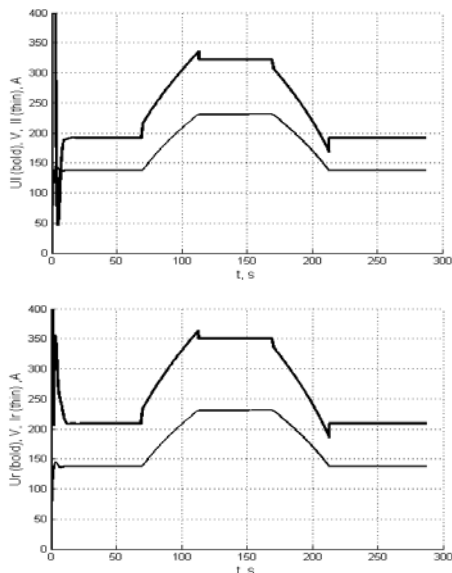


Fig. 6 the traction motors voltage and current, the second test (constant speed)

The fuel consumption for this test is 1.4259 kg. So, the fuel consumption during the constant power test is 82.6% of the fuel consumption during the constant speed test. Such significant difference is consequence of significant change of the motion resistance (more than three times), which leads to rapid engine acceleration. This is the reason of the high fuel con-

sumption rate in this case. It should be noted that the effectiveness of the introduced algorithm depends on changing the motion resistance during movement. If the changes are minor (in a case of roads), a constant speed might be more preferable for the tasks the organization of transportation or movement in a stream of other objects, moving evenly. However, the proposed algorithms able to significantly reduce fuel consumption for off-road vehicles, such as TR.

## V. CONCLUSION

Introduced in this paper solutions extend the position-trajectory control method for a class of systems, which movement realize with a constant power.

The paper introduces solutions to synthesis of nonlinear control algorithms for mobile robots equipped electric transmission with AC units. The solutions allow to improving the functionality of mobile robots, minimizing fuel consumption without deterioration the quality characteristics, such as accuracy and speed.

## REFERENCES

- [1] J. B. Heywood, "Internal Combustion Engine Fundamentals," McGraw-Hill, 1988, 930 p.
- [2] V. Kh. Pshikhopov, "Position-trajectory Control of Moving Objects," TTI SFU, 2009, 183 p.
- [3] V. Kh. Pshikhopov, M. Yu. Medvedev, R. V. Fedorenko, M. Yu. Sirotenko, V. A. Kostyukov, B. V. Gurenko, "Control of Aeronautic Complexes: Theory and Design Technology," Fizmatlit, 2010, 394 p.
- [4] A. T. Le, "Modelling and Control of Tracked Vehicles. Sydney," University of Sydney, 1999, 208 p.
- [5] J. Y. Wong, "Theory of Ground Vehicles," Wiley, 2008, 592 p.
- [6] D. B. Pogosov, "Synthesis and Analysis of Mathematical model of Highly-maneuverable Tracked Robots," *Journal KBNC RAN I*, pp. 301–306, 2011.
- [7] L. V. Sergeev, "Tank Theory," Academy publishing, 1973, 493 p.
- [8] A. B. Vinogradov, "Vector Control of AC Motors," Ivanovo, 2008, 297 p.
- [9] V. V. Pankratov, "Vector Control of Induction Motors," Novosibirsk, 1999, 66 p.
- [10] A. A. Usoltzev, "Frequency Control of Induction Motors," ITMO, 2006, 94 p.
- [11] A. I. Voldek, "Electric Machines," Energiya, 1978, 832 p.
- [12] V. I. Klyuchev, "Theory of Electric Drive," Energoatomizdat, 1998, 697 p.
- [13] M. G. Chilikin, A. S. Sandler, "General Course of Electric Drive," Energoatomizdat, 1981, 576 p.
- [14] D. Pogosov, "Position-Trajectory Control of Advanced Tracked Robots with Diesel-Electric Powertrain," *Robot Intelligence Technology and Applications 2*, vol. 274, pp. 393–403, Dec. 2013.
- [15] M. Jankovic, I. Kolmanovsky, "Constructive Lyapunov Control Design for Turbocharged Diesel Engines," *IEEE-transactions on Control Systems Technology*, vol. 8, no. 2, pp. 288–299.
- [16] D. Yanakiev, I. Kanellakopoulos, "Engine and Transmission Modeling for Heavy-Duty Vehicles," PATH, 1995, 64 p.
- [17] D. Pogosov, "Transformation of High-order Spline-functions to implicit form," *SWorld conference proceedings 3*, vol. 4, pp. 84–87, Jun. 2012.

# Emulators of Two-State Memcapacitor

Dalibor Biolek, Viera Biolkova, and Zdenek Kolka

**Abstract**—This study describes possible ways of implementing the emulators of two-state memcapacitor, which exhibits unambiguous constitutive relation of “flux-integral of charge” type. Instead of classical mutator approach, the technique of switched capacitors is used, representing an effective method of emulating the floating two-terminal devices.

**Keywords**—memcapacitor, switched capacitor, constitutive relation, charge, flux.

## I. INTRODUCTION

CAPACITOR, resistor, and inductor belong to the group of ideal circuit elements. From a more general point of view, they form only a subset of fundamental circuit elements from Chua’s periodical table [1]. Currently, the intense researching of other elements from the table is conducted, particularly those which can be potentially utilized as nonvolatile memories for computer industry. The most widely known is memristor [2], but also memcapacitor and meminductor [3], [4] come into notice. Since these devices are not still available for experimenting, a lot of their SPICE models were developed [5]–[15]. Recently, a growing number of papers deal with a construction of hardware emulators of these devices [16]–[27]. However, most of them suffer from two kinds of drawbacks: 1) They mimic the behavior based on an analogy with the so-called TiO<sub>2</sub> memristor. It is in contradiction with the needs of emulating the device with arbitrary type of the constitutive relation [16]–[20]. 2) The emulated device does not preserve all fundamental fingerprints of ideal mem-elements, which can be important for experimenting with the emulator [17], [18], [21].

A possible method of the synthesis of two-state memcapacitor emulator is described below. This emulator preserves all the fingerprints of memcapacitor with two possible states of its memcapacitance. The hitherto published designs of memcapacitor emulators start from the mutator approach, which transforms non-linear resistor into memristor and then memristor into memcapacitor [18], [21], [26], [27]. Such emulator of two-state memcapacitor would consist of

This work was supported in part by COST project Nr. LD14013, and by the Project for the development of K217 Department, UD Brno, Czech Republic. The research described was performed in laboratories supported by the SIX project.

D. Biolek is with the Department of Microelectronics/Electrical Engineering, Brno University of Technology/University of Defence, Czech Republic (phone: +420 973442487; e-mail: dalibor.biolek@unob.cz).

Viera Biolkova and Zdenek Kolka are with the Department of Radio Electronics, Brno University of Technology, Czech Republic (e-mails: {biolkova kolka}@fec.vutbr.cz).

nonlinear resistor with piece-wise current-voltage characteristics and two mutators. This can represent rather complicated circuit implementation. On the other hand, the emulators proposed in this study start from a direct synthesis of the memcapacitor, the so-called binary capacitor (BC) being its basic component. The BC is a capacitor whose capacitance takes two possible states, depending on internal state variable of the memcapacitor. For voltage-controlled memcapacitor, this variable is a flux – integral of terminal voltage. It will be shown that the BC can be implemented by the well-known switched-capacitor technique, which provides a proper definition of initial conditions at time instants of changing the memcapacitor states. The analysis reveals that it is an important condition of a proper operation of the emulator, which then will show all the known memcapacitor fingerprints. A demonstration of computer simulation of the designed emulator is given in the final part of the paper.

## II. EMULATOR CONCEPTION

The object of the emulation is the memcapacitor with the constitutive relation  $TIQ(\varphi)$  according to Fig. 1 (a), where  $TIQ$  is time-domain integral of memcapacitor charge  $q$  and  $\varphi$  is flux, i.e. time-domain integral of the terminal voltage  $v$  [28]:

$$TIQ = \int_{-\infty}^t q(\xi) d\xi, \quad \varphi = \int_{-\infty}^t v(\xi) d\xi. \quad (1)$$

The memcapacitance  $C_M$  is defined as a derivative of  $TIQ$  with respect to  $\varphi$ . According to Fig. 1 (a), it takes the values of either  $C_L$  or  $C_H$  depending whether the flux  $\varphi$  occurs inside or outside the interval  $(-\Phi, +\Phi)$ , where  $\Phi$  is a threshold value. Consistent with a definition, the memcapacitor from Fig. 1 (a) is a capacitor whose capacitance is controlled by a state variable, here by the flux  $\varphi$ . Its basic equation is therefore [28]

$$q = C_M(\varphi)v. \quad (2)$$

The fundamental block diagram of the emulator of such type of the memcapacitor is in Fig. 1 (b). The memcapacitor voltage is integrated into the flux  $\varphi$ . The memcapacitance  $C_M$  is then derived from the flux, and  $C_M$  together with  $v$  define the charge according to Eq. (2). A capacitor with two possible capacitances  $C_L$  and  $C_H$ , denoted thereafter as binary capacitor (BC), serves as the voltage-to-charge converter.

Figure 1 (c) shows more detailed implementation of floating memcapacitor. The terminal voltage is processed by differential-input integrator. The sign of its output voltage is removed by the absolute-value circuit (ABS), and the result is compared with the threshold level  $\Phi$ . The comparator output controls the state of binary capacitor.

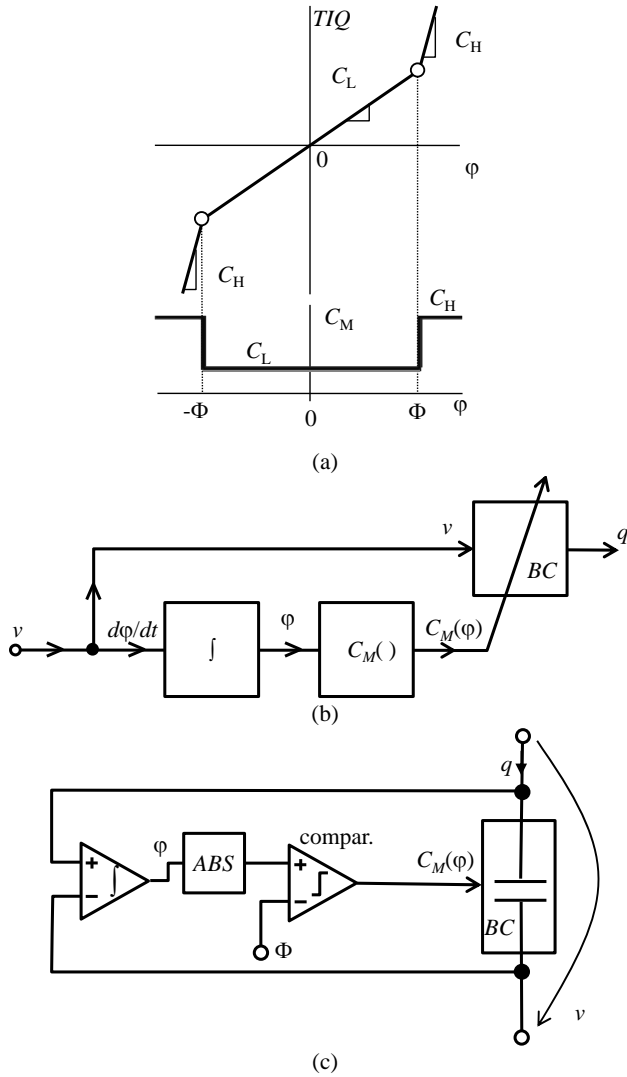


Fig. 1 (a) Constitutive relation  $TIQ(\varphi)$  of memcapacitor, (b) fundamental diagram for controlling the binary capacitor (BC), (c) emulator schematics employing integrator, absolute value circuit (ABS), comparator, and binary capacitor.

It follows from the above that the binary capacitor must behave as non-stationary linear capacitor whose capacitance can be toggled between two various states. The BC synthesis should be done such that the circuit in Fig. 1 (c) would preserve all the known fingerprints of ideal memcapacitor.

### III. REQUIRED BEHAVIOR OF BINARY CAPACITOR

Figure 1 (a) shows discontinuities of the capacitance of BC at thresholds  $-\Phi$  and  $+\Phi$ . The Coulomb-voltage characteristic of BC thus consists of two linear charge-to-voltage dependences according to Fig. 2 (a) whose slopes define capacitances dependent on the state of controlling variable.

The binary capacitor is defined by the constitutive relation between electric charge and voltage

$$q(t) = C_M(t)v(t). \quad (3)$$

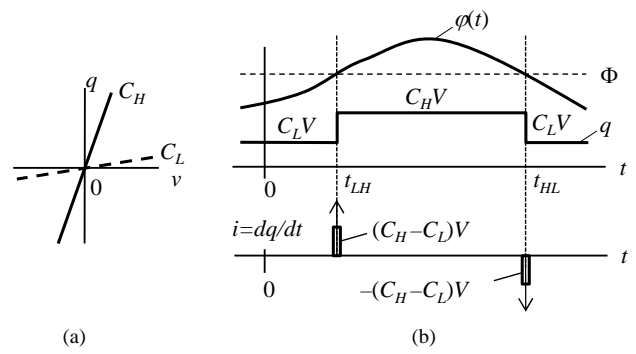


Fig. 2 (a) Coulomb-voltage characteristic of binary capacitor, (b) example of waveforms of flux  $\varphi$ , charge  $q$  and current  $i$  for constant voltage  $V$ .

The current through the binary capacitor will be as follows:

$$i(t) = \frac{dq(t)}{dt} = \frac{dC_M(t)}{dt}v(t) + C_M(t)\frac{dv(t)}{dt}. \quad (4)$$

For the BC in one of its limiting states  $C_L$  or  $C_H$ , its current is given only by the second right-side term of Eq. (4). If the controlling variable crosses the threshold level  $\Phi$  or  $-\Phi$  at time instant  $t_x$ , the Dirac impulse with the strength  $\pm(C_H - C_L)v(t_x)$  appears at this moment in the current waveform. The sign plus/minus holds for the capacitance increase/decrease. These current impulses of the ideal BC appear also for constant voltage  $v(t) = V \neq 0$  applied across the device. It is a consequence of the discontinuity of the charge. This case is illustrated in Fig. 2 (b).

In the following, the synthesis of the BC using the technique of switched capacitors with fixed capacitances will be described. We show that a simple toggling of two fixed capacitors  $C_L$  and  $C_H$  to the capacitive port does not solve the problem without a proper setting the initial conditions at time instants of abrupt changes of the BC state.

### IV. SYNTHESIS OF BINARY CAPACITOR

Consider the preliminary version of the BC in Fig. 3 (a). Two capacitors with fixed capacitances  $C_L$  and  $C_H$  are toggled depending on the controlling variable.

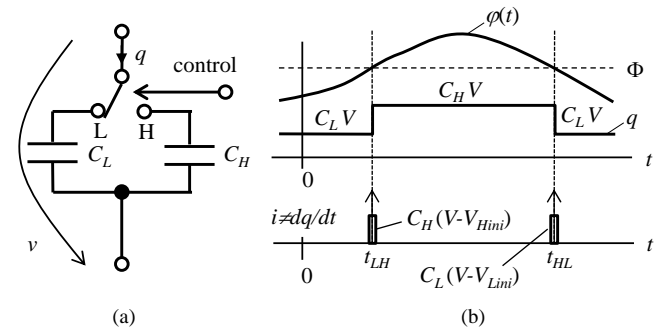


Fig. 3 (a) Incorrect implementation of binary capacitor (without handling initial conditions), (b) flux, charge and current waveforms.

Consider that the toggle-switch changes its state from L to

H (see Fig. 3 a) at time instant  $t_{LH}$  and back to the state L at time instant  $t_{HL}$ . Suppose that the voltage source  $v(t)$  excites the BC terminals and that the capacitor  $C_H$  is charged to the voltage  $V_{Hini}$  just before changing the switch state at time  $t_{LH}$ . Then due to the abrupt change from L to H state, the capacitor  $C_H$  is suddenly connected to the voltage source, and the BC outlets will conduct the pulse current in the form of Dirac impulse with the strength of  $C_H(v(t_{LH})-V_{Hini})$ . However, according to Fig. 2 (b), its correct value is  $(C_H-C_L)v(t_{LH})$ . Similarly, the H to L state change will cause the current Dirac impulse with the strength of  $C_L(v(t_{HL})-V_{Lini})$ , where  $V_{Lini}$  is the  $C_L$  voltage just before the state change. Note that the correct value is  $-(C_H-C_L)v(t_{HL})$ . In the simple example in Fig. 3 (b) when the voltage is constant,  $V_{Hini} = V_{Lini} = V$  and Dirac impulses from Fig. 2 (b) do not appear at all.

It is thus obvious that the circuit in Fig. 3 (a) should be completed by auxiliary circuitry for automatic presetting the initial voltages  $V_{Lini}$  and  $V_{Hini}$  of capacitors  $C_L$  and  $C_H$  at time instants just before the states of the binary capacitor are modified. The following equations read:

$$C_H(v(t_{LH})-V_{Hini})=(C_H-C_L)v(t_{LH}), \quad (5)$$

$$C_L(v(t_{HL})-V_{Lini})=-(C_H-C_L)v(t_{HL}). \quad (6)$$

From Eqs. (5) and (6), the initial voltages are as follows:

$$V_{Hini}=\frac{C_L}{C_H}v(t_{LH}), \quad (7)$$

$$V_{Lini}=\frac{C_H}{C_L}v(t_{HL}). \quad (8)$$

One of several examples of providing the above initial conditions is given in Fig. 4. In the L state, the capacitor  $C_H$  is charged via the amplifier  $A_H$  to the port voltage  $v$  multiplied by the amplifier gain  $C_L/C_H$ . In this way, the initial condition (7) is provided at time instant of the toggling into the H state. Similarly, the capacitor  $C_L$  is charged in the H state via amplifier  $A_L$  with the gain  $C_H/C_L$ , thus providing the initial condition (8) when toggling into the L state.

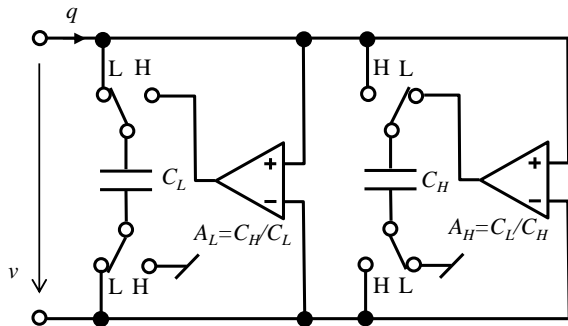


Fig. 4 An example of implementing the binary capacitor.

The advantage of this implementation consists in easy emulation of floating two-terminal device. As a drawback, it is

necessary to use two amplifiers with high spread of gains. It results in low dynamic range of the processed signals.

Other circuit implementation of the binary capacitor is shown in Fig. 5. If the switches are in H state, only the capacitor  $C_a$  is connected to the input port. For the state L, the capacitive port is formed by capacitors  $C_a$  and  $C_b$  in series, thus

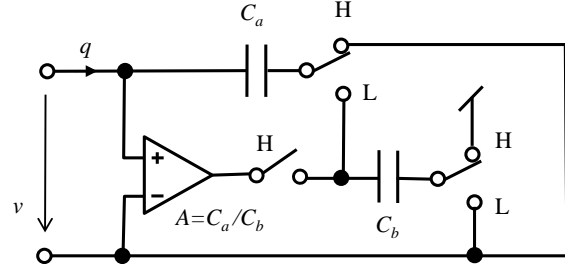


Fig. 5 Economical implementation of binary capacitor.

$$C_H=C_a, C_L=\frac{C_a C_b}{C_a+C_b}. \quad (9)$$

Consider again the constant voltage  $V$  at the input port according to Fig. 2 (b). During the state L, the capacitors  $C_a$  and  $C_b$  are connected in series, both being charged from the input port to the charge  $C_L V$ . After switching to state H, this way charged capacitor  $C_a$  is connected to the input port. The charge abruptly withdrawn from the port is thus  $C_a V - C_L V = (C_H - C_L)V$ . It is in agreement with the strength of the Dirac impulse of current in Fig. 2 (b) for time instant of the transition from L to H state.

During the state H, the capacitors  $C_a$  and  $C_b$  are charged to voltages  $V$  and  $AV$ , respectively, where  $A$  is the gain of amplifier in Fig. 5. After switching from H to L state, the series connection of this way charged capacitors appears at the input port. The charge  $C_L(V - V - AV) = -AC_L V$  is therefore withdrawn abruptly from this port. As obvious from Fig. 2 (b), this charge must be  $-(C_H - C_L)V$  for a proper operation of binary capacitor. It leads to the following gain formula:

$$A=\frac{C_H}{C_L}-1=\frac{C_a}{C_b}. \quad (10)$$

There are three advantages of the circuit in Fig. 5 in comparison with the implementation from Fig. 4: Simpler construction (it employs only one amplifier and less number of switches), lower capacitance ratio ( $C_a:C_b=1$  for  $C_H:C_L=2$ ), and lower amplifier gain and thus higher dynamic range (for example,  $C_H:C_L=2$ ,  $A=1$ , which leads to a simple voltage buffer).

Other versions of BC implementations can be found, utilizing the above approach, with the aim of searching for simple implementations, simultaneously providing a reasonable dynamic range for a specified ratio  $C_H:C_L$ .

## V. COMPUTER SIMULATIONS

In order to verify the correctness of the principle of the proposed circuits, behavioral models of binary capacitors from

Figs. 3, 4, and 5 have been developed. Then they have been used for PSpice modeling of the memcapacitor from Fig. 1 (c). The corresponding PSpice codes are listed in the Appendix. The memcapacitor was designed with the parameters  $C_L=100\text{pF}$ ,  $C_H=200\text{pF}$ , and  $\Phi=100\mu\text{Vs}$ . The memcapacitor behavior depends on its initial state, i.e. on the initial position of the operating point in  $C_M(\varphi)$  characteristic from Fig. 1 (a). This phenomenon is analyzed below.

Since the memcapacitor consists of blocks with discontinuous behavior (comparing, absolute value, switching), it represents, in conjunction with the presence of ideal capacitors, potential convergence problems in SPICE-family programs. To overcome this issue, smoothing technique from [29] has been used (see function *if2smooth* defined in the circuit file in Appendix). For modeling internal switches of binary capacitors, classical SPICE models with smooth dependences of switch resistances on control voltages are used [30].

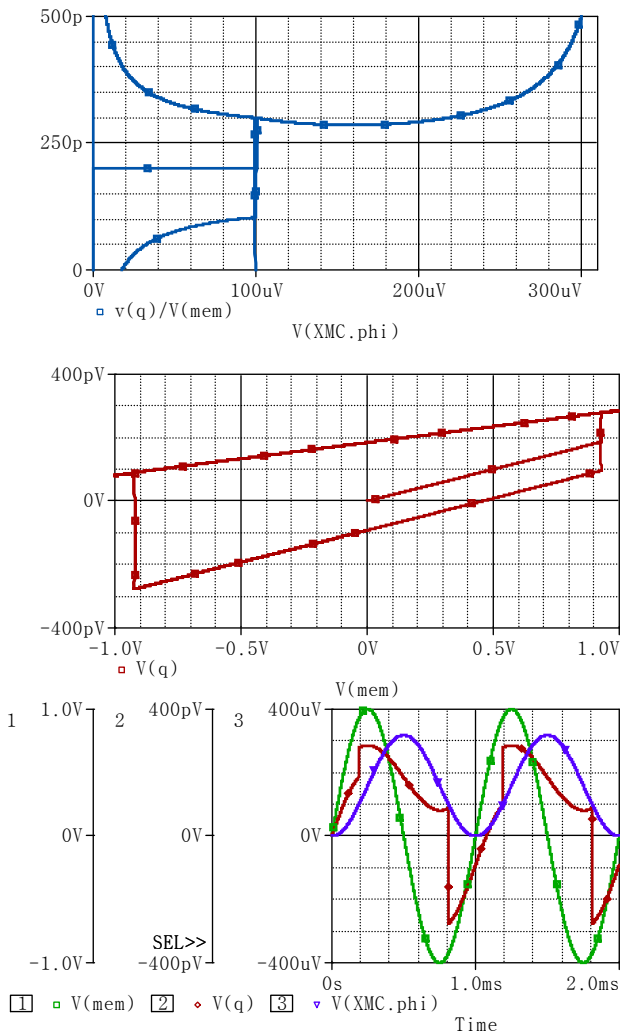


Fig. 6 Simulation of “memcapacitor“ employing BC from Fig. 3 (a),  $\varphi(0)=0$ . Bottom figure: waveforms of voltage  $V(\text{mem})$ , charge  $V(q)$  and flux  $V(\text{XMC}.\text{phi})$ . Middle figure: pseudo-pinched voltage-charge hysteresis loop. Upper figure: Ambiguous “memcapacitance“ versus flux relationship.

In all the cases, the memcapacitor is driven by ideal voltage source with sinusoidal 1 V/1 kHz waveform and  $10\ \Omega$  serial resistance. The following guidelines can be used for examining if the simulation results are consistent with the behavior of the emulated memcapacitor: 1) The voltage and charge waveforms must cross zero levels at identical time instants, 2) Coulomb-voltage characteristic must exhibit a typical pinched hysteresis loop, 3) The two-state  $C_M(\varphi)$  (see Fig. 1 a) must be unambiguous and independent of the way of the circuit excitation.

Figure 6 shows the simulation results for the case of improper implementation of BC from Fig. 3 (a). Note that all the above memcapacitor fingerprints are violated.

The memcapacitor behavior becomes correct after replacing the BC implementation by circuits from Fig. 4 or 5. Figure 7 demonstrates the simulation results, utilizing the binary capacitor from Fig. 5, considering initial flux to be zero.

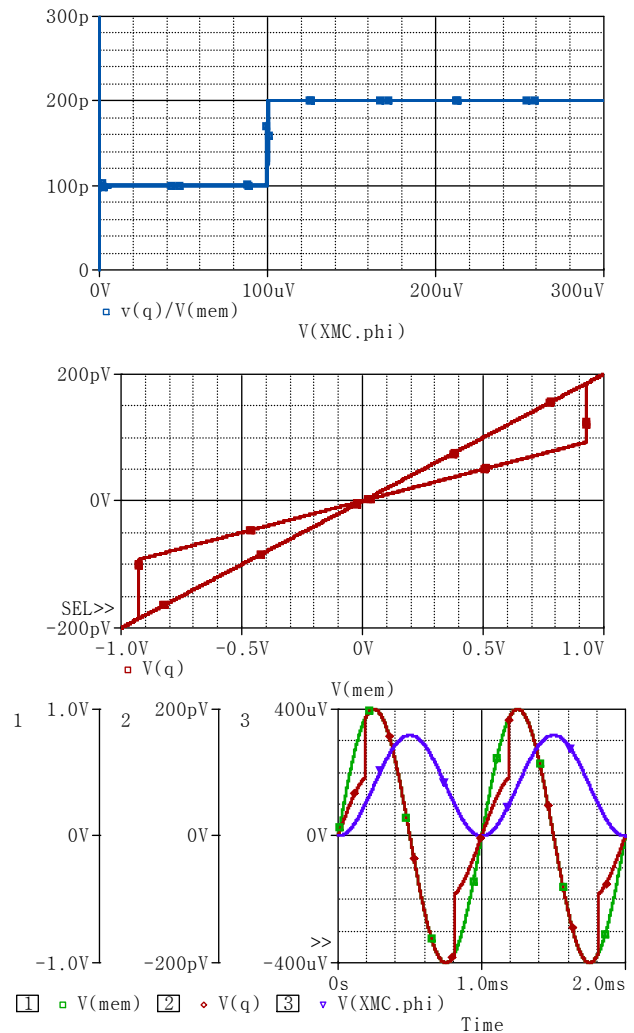


Fig. 7 Simulation of memcapacitor employing BC from Fig. 5,  $\varphi(0)=0$ . Bottom figure: waveforms of voltage  $V(\text{mem})$ , charge  $V(q)$  and flux  $V(\text{XMC}.\text{phi})$ . Middle figure: pinched voltage-charge hysteresis loop. Upper figure: Unambiguous memcapacitance versus flux relationship.

It follows from the bottom figure 7 that the flux of the emulated device, thus time-domain integral of the voltage, is nonnegative for each time. That is why the operating point on the  $C_M(\varphi)$  characteristic moves only along the parts for positive flux (see upper part of Fig. 7). This fact is reflected into a typical charge-volt pinched hysteresis loop, which is composed of two linear segments passing through the origin. Their slopes are determined by capacitances  $C_H$  a  $C_L$ . The operating point switches between these arms if the flux crosses the thresholds  $+\Phi$  and  $-\Phi$ .

Figure 8 illustrates the same simulation conditions with the exception of the initial flux, which is  $-200\mu\text{Vs}$ . Now the operating point swings along another parts of the  $C_M(\varphi)$  characteristic as shown in the upper part of Fig. 8. Note that the pinched hysteresis loop changes accordingly to another typical shape.

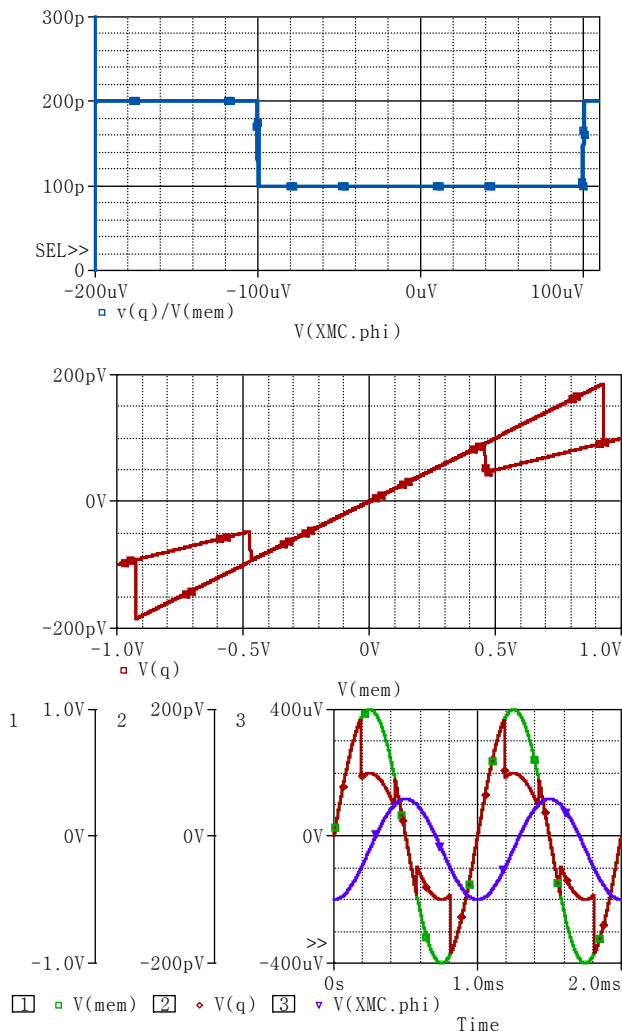


Fig. 8 Simulation of memcapacitor employing BC from Fig. 5,  $\varphi(0) = -200\mu\text{Vs}$ . Bottom figure: waveforms of voltage  $V(\text{mem})$ , charge  $V(q)$  and flux  $V(\text{XMC}.\text{phi})$ . Middle figure pinched voltage-charge hysteresis loop. Upper figure: Unambiguous memcapacitance versus flux relationship.

Note that the anomaly at terminal points of the  $C_M(\varphi)$  characteristic from upper part of Fig. 8 (PSpice evaluated the memcapacitance outside the realistic values) is caused by numerical errors: the memcapacitance is computed as the charge to voltage ratio, and the voltage waveform crosses zero at given points.

## VI. CONCLUSIONS

The memcapacitor with two-state memcapacitance for binary memories is basically a capacitor with two possible values of its capacitance. These values are commutated, depending on the instantaneous value of the integral of the terminal voltage of memcapacitor. It is shown in this study that the memcapacitive port can be emulated via fixed capacitors and electronic switches, but that the switching must be executed under some exact conditions. Their violation results in the violation of fundamental fingerprints of the emulated memcapacitor. Two possible circuit implementations are proposed, and SPICE simulations prove the correctness of their principle.

## APPENDIX

### Circuit file for memcapacitor testing in PSpice

#### Memcapacitor testing

```
*
.param f=1k
.func if2smooth(x,thres,a)
+      {-1+2*(1/(1+exp(-(x/thres+1)/a))-1/(1+exp(-(x/thres-1)/a)))}
Ein in 0 value={sin(2*pi*f*time)}
Eq q 0 value={sdt(-i(Ein))}
Rs in mem 10
XMC mem 0 MC
.tran 0 2000u 0 20n
.probe
.lib memcap.lib
.end
```

#### Library file memcap.lib

```
*model of memcapacitor from Fig. 1 (c)*
.subckt MC plus minus params:
+ CL=100p CH=200p thres=100u phi0=0
Gint 0 phi value={v(plus,minus)}
Cint phi 0 1 IC={phi0}
Raux phi 0 1T
Econtrol control 0 value={if2smooth(v(phi),thres,10m)}
*model of Binary capacitor BC0 is used below;
* for other models, replace "BC0" by "BC1" or "BC2"
XBC plus minus control BC0
+ params: CL={CL} CH={CH} Ron=100 Roff=100meg
.ends MC
```

```
*model of "Binary Capacitor" from Fig. 3 (a)*
.subckt BC0 plus minus control params:
```

```
+ CL=1n CH=5n Ron=10 Roff=100meg
CL L minus {CL}
CH H minus {CH}
S1 plus L 0 control switch
S2 plus H control 0 switch
.model switch VSWITCH
+ Ron={Ron} Roff={Roff} Von=0.5 Voff=-0.5
.ends BC0
```

\*model of Binary Capacitor from Fig. 4\*

```
.subckt BC1 plus minus control params:
+ CL=1n CH=5n Ron=10 Roff=100meg
CL L1 L2 {CL}
CH H1 H2 {CH}
E1 O1 minus value={CH/CL*V(plus,minus)}
E2 O2 minus value={CL/CH*V(plus,minus)}
S1 plus L1 control 0 switch
S2 minus L2 control 0 switch
S3 O1 L1 0 control switch
S4 0 L2 0 control switch
S5 O2 H1 control 0 switch
S6 0 H2 control 0 switch
S7 plus H1 0 control switch
S8 minus H2 0 control switch
.model switch VSWITCH
+ Ron={Ron} Roff={Roff} Von=0.5 Voff=-0.5
.ends BC1
```

\*model of Binary Capacitor from Fig. 5\*

```
.subckt BC2 plus minus control
+ params: CL=1n CH=5n Ron=10 Roff=100meg
.param Ca={CH} Cb={1/(1/CL-1/CH)}
Ca plus a1 {Ca}
Cb b1 b2 {Cb}
E1 O1 minus value={Ca/Cb*V(plus,minus)}
S1 minus a1 0 control switch
S2 a1 b1 control 0 switch
S3 O1 b1 0 control switch
S4 b2 0 0 control switch
S5 minus b2 control 0 switch
.model switch VSWITCH
+ Ron={Ron} Roff={Roff} Von=0.5 Voff=-0.5
.ends BC2
```

#### REFERENCES

- [1] L. O. Chua, "Nonlinear circuit foundations for nanodevices, Part I: The four-element torus," *Proc IEEE*, vol. 91, no. 11, pp. 1830–1859, 2003.
- [2] L. O. Chua, "Memristor – the missing circuit element," *IEEE Trans Circuit Theory*, vol. 18, no. 5, pp. 507–519, 1971.
- [3] L. O. Chua, Invited talk on *Memristor and Memristive Systems Symposium*, UC Berkeley, Berkeley, CA, Nov. 21, 2008.
- [4] M. Di Ventra, Y. V. Pershin, and L. O. Chua, "Circuit elements with memory: memristors, memcapacitors, and meminductors," *Proc IEEE*, vol. 97, no. 10, pp. 1717–1724, 2009.
- [5] S. Benderli, and T. A. Wey, "On SPICE macromodeling of TiO2 memristors," *Electron. Lett.*, vol. 45, no. 7, pp. 377–379, 2009.
- [6] A. Rák, and G. Cserey, "Macromodeling of the memristor in SPICE," *IEEE Trans. Comput. Aided Des. Integr. Circuits Syst.*, vol. 29, no. 4, pp. 632–636, 2010.
- [7] K. Eshraghian et al., "Memristive device fundamentals and modeling: applications to circuits and systems simulation," *Proc IEEE*, vol. 100, no. 6, pp. 1991–2007, 2012.
- [8] D. Biolek, and Z. Biolek, "Fourth Fundamental Circuit Element: SPICE Modeling and Simulation," in *Memristors and Memristive Systems*, Springer Science+Business Media New York, 2014, pp. 105–162.
- [9] Z. Biolek, D. Biolek, and V. Biolková, "Spice model of memristor with nonlinear dopant drift," *Radioengineering*, vol. 18, no. 2, pp. 210–214, 2009.
- [10] F. Corinto, and A. Ascoli, "A boundary condition-based approach to the modeling of memristor nano-structures," *IEEE Trans. Circuits Syst. Regul. Pap.*, vol. 59, no. 11, pp. 2713–2726, 2012.
- [11] S. Shin, K. Kim, and S.M. Kang, "Compact models for memristors based on charge-flux constitutive relationships," *IEEE Trans. Comput. Aided Des. Integr. Circuits Syst.*, vol. 29, no. 4, pp. 590–598, 2010.
- [12] T. Prodromakis, B.P. Peh, C. Papavassiliou, and C. Toumazou, "A versatile memristor model with non-linear dopant kinetics," *IEEE Trans. Electron Devices*, vol. 58, no. 99, pp. 1–7, 2011.
- [13] S. Kvatinsky, E.G. Friedman, A. Kolodny, and U.C. Weiser, "TEAM: Threshold adaptive memristor model," *IEEE Trans. Circuits Syst. Regul. Pap.*, vol. 60, no. 1, pp. 211–221, 2012.
- [14] R. Kozma, R.E. Pino, and G.E. Paziienza (eds.), *Advances in Neuromorphic Memristor Science and Applications*, Springer, New York, 2012.
- [15] K. Eshraghian, O. Kavehei, K.R. Cho, J.M. Chappell, A. Iqbal, S.F. Al-Sarawi, and D. Abbot, "Memristive device fundamentals and modeling: applications to circuits and systems simulation," *Proc. IEEE*, vol. 100, no. 6, pp. 1991–2007, 2012.
- [16] J. Valsa, D. Biolek, and Z. Biolek, "An analogue model of the memristor," *Int J Numer Modell Electron Networks Devices Fields*, vol. 24, no. 4, pp. 400–408, 2011.
- [17] X. Y. Wang et al., "Implementation of an analogue model of a memristor based on a light-dependent resistor," *Chin Phys B*, vol. 21, no. 10, 108501-1-8, 2012.
- [18] X. Y. Wang et al., "Design of a memcapacitor emulator based on a memristor," *Physics letters A*, vol. 376, pp. 394–399, 2012.
- [19] B. Muthuswamy, "Implementing memristor based chaotic circuits," *Int J Bifurcation Chaos*, vol. 20, no. 5, pp. 1335–1350, 2010.
- [20] H. Kim et al., "Memristor emulator for memristor circuit applications," *IEEE Trans Circuits Syst Regul Pap.*, vol. 59, no. 10, pp. 2422–2431, 2012.
- [21] Y. V. Pershin and M. Di Ventra, "Emulation of floating memcapacitors and meminductors using current conveyors," *Electron Lett*, vol. 47, no. 4, pp. 243–244, 2011.
- [22] D. Biolek et al., "Mutators for transforming nonlinear resistor into memristor," In *20th European Conf. on Circuit Theory and Design (ECCTD)*, Linköping, Sweden, pp. 488–491, 2011.
- [23] V. Biolkova, D. Biolek, and Z. Kolka, "Unified approach to synthesis of mutators employing operational transimpedance amplifiers for memristor emulation," In *Proc. of the 11th Int. Conference on Instrumentation, Measurement, Circuits and Systems (IMCAS'12)*, Rovaniemi, Finland, pp. 110–115, 2012.
- [24] Z. Kolka, D. Biolek, and V. Biolkova, "Hybrid modeling and emulation of mem-systems," *Int J Numer Modell Electron Networks Devices Fields*, vol. 25, no. 3, pp. 216–225, 2012.
- [25] D. Biolek, "Memristor emulators," in *Memristive networks*. Springer book, New York, 2014, pp. 487–504.
- [26] D. Biolek, V. Biolkova, "Mutator for transforming memristor into memcapacitor," *Electronics Letters*, vol. 46, no. 21, pp. 1428–1429, 2010.
- [27] D. Biolek, V. Biolkova, and Z. Kolka, "Mutators simulating memcapacitors and meminductors," In *Proc of the 11th biennial IEEE Asia Pacific Conference on Circuits and Systems (APCCAS 2010)*, Kuala Lumpur, Malaysia, pp. 800–803, 2010.
- [28] D. Biolek, Z. Biolek, V. Biolkova, "SPICE modelling of memcapacitor," *Electronics Letters*, vol. 46, no. 7, pp. 520–522, 2010.
- [29] D. Biolek, M. Di Ventra, and Y. V. Pershin, "Reliable SPICE Simulations of Memristors, Memcapacitors and Meminductors," *Radioengineering*, vol. 22, no. 4, pp. 945–968, 2013.
- [30] PSpice A/D Reference Guide. Product Version 16.5. Cadence Design Systems, Inc., June 2011.

# Second-order sliding mode control applied to an inverted pendulum

Sonia Mahjoub, Faïçal Mnif, and Nabil Derbel

*Abstract*—In this paper first and second order sliding mode controllers for underactuated manipulators are proposed. Sliding mode control SMC is considered as an effective tool in different studies for control systems. However, the associated chattering phenomenon degrades the system performances. To overcome this phenomenon and to track a desired trajectory a twisting and a super-twisting algorithms are presented. The stability analysis is done using a Lyapunov function for the proposed controllers. Further, 3 different controllers are compared. As an illustration, the example of an inverted pendulum is considered. Simulation results are given to demonstrate the effectiveness of the proposed approaches.

*Keywords*—Underactuated manipulator, sliding mode control, twisting algorithm, super-twisting algorithm, inverted pendulum.

## I. INTRODUCTION

UNDERACTUATED Mechanical Systems UMS are increasingly present in the robotic field. They have less actuators than degrees of freedom. In these systems, we find manipulators, vehicles and humanoids with several passive joints. Underactuations arise by deliberating in the design for the purpose of reducing the weight of the manipulator or might be caused by actuator failures. The difficulty in controlling underactuated mechanisms is due to the fact that techniques, developed for fully actuated systems, cannot be directly used. These systems are not feedback linearizable, yet they exhibit nonholonomic constraints and nonminimum phase characteristics [1]. Moreover, it has been shown that it is difficult to stabilize this class of systems by classical continuous controllers. This yields to the fact that the class of underactuated mechanical systems present challenging control problems. One of the common methods used to control underactuated systems is the sliding mode control SMC based on Lyapunov design. The SMC has been always considered as an efficient approach in control systems, due to its high accuracy and robustness with respect to various internal and external disturbances. The SMC approach consists in two steps. The first one is to choose a manifold in the state space that forces the state trajectories to remain along it. The second one is to design a discontinuous state-feedback capable of forcing the system to reach the state on the manifold in finite time. However, the drawback of the SMC is the presence of the chattering effect, caused by the switching frequency of the control [2]. The high frequency components of the control propagate on the system, to excite the unmodeled

fast dynamics and therefore to cause undesired oscillations. In fact, this can degrade the system performances or may even lead to instability. In the literature, three main approaches has been presented, that help to reduce the chattering effects. The class of methods consists in the use of the saturation control instead of the discontinuous one. It ensures the convergence to a boundary layer of the sliding manifold. Moreover, in [3] and [4], a switching function, inside the boundary layer of the sliding manifold, has been approximated by a linear feedback gain. However, the accuracy and the robustness of the sliding mode are partially lost.

The second class of methods consist in the use of a system observer-based approach [5]. It can reduce the problem of robust control to the problem of exact robust estimation. This phenomenon can lead to the deterioration of the robustness with respect to the plant uncertainties or disturbances.

Using the high order sliding mode controllers given by Levant [6], [7] as a way to reduce the chattering phenomenon and to keep the main advantages of the original approach of the SMC is another way to eliminate chattering. The high order sliding mode consists in the sliding variable system derivations. It maintains the robustness of the system. Specially, the second order sliding mode control is relatively simple to implement and it gives good robustness to external disturbances. The second-order sliding-mode SSMC approach can reduce the number of differentiator stages in the controller. However, the stability proofs are based usually on a geometrical or homogeneity methods since the Lyapunov function is a difficult task to define [8]. The stability and the convergence using SSMC is a challenge and several trials were made to deal with those difficulties. Recently, in [9] authors construct a Lyapunov function. It provides a finite time convergence, a robustness and an estimate of the convergence time for super twisting algorithm. In [10], a multivariable super twisting structure is proposed, which analyses the stability using the ideas of Lyapunov function given in [9].

Inverted pendulum system is a typical benchmark of nonlinear underactuated mechanical systems [11]. For this system, the control input is the force  $u$  that moves the cart horizontally and the output is the angular position of the pendulum  $\theta$ . Therefore, the inverted pendulum has been a popular candidate to illustrate different control methods. However, despite its simple mechanical structure, this prototype is not easy to control and it requires sufficiently sophisticated control designs. Indeed it is proven that the system is not feedback linearizable and has no corresponding constant relative degree [12]. Moreover, Zhao and Spong [13] have shown that several geometric properties of the system are lost when the pendulum

S. Mahjoub and N. Derbel : Advanced Control and Energy Management Laboratory(CEM-Lab),University of Sfax, Sfax Engineering School, BP W, 3038 Sfax, Tunisia Fax: +216-74-275595 e-mail: mahjoubsonia@yahoo.fr

F. Mnif is with the Department of Electrical and Computer Engineering Sultan Qaboos University, Muscat, Oman.

moves through horizontal positions. The principal control task considered for the cart pendulum is to swing up the pendulum from the stable equilibrium point to the unstable equilibrium point, and stabilizing the cart in a desired position. In general, the main difficulty is to swing up the pendulum from the downward vertical position and to keep the cart stable. Numerous control techniques have been evolved to stabilize the inverted pendulum such as Proportional-Integral-Derivative (PID) controllers where the control gains are adjustable and updated online with a stable adaptation mechanism [14].

In this paper, the objective is to develop a robust position tracking controller based on the first and the second order sliding mode approach applied to an inverted pendulum. Stability of the closed loop system is carried out using a candidate Lyapunov function for the proposed controllers. The paper is organized as follows. Section 2 describes the model of the inverted pendulum and the first sliding mode controller. Section 3 deals with the sliding mode controllers and the design of second order sliding mode controllers. Section 4 discusses the simulation results of the proposed controllers.

## II. DYNAMIC MODEL AND CONTROL APPROACH FOR AN INVERTED PENDULUM

### A. Dynamic model

The dynamical behavior of inverted pendulum can be described by the following differential equations [13]:

$$\begin{aligned} (m + M)\ddot{y} + ml(\ddot{\theta} \cos \theta - \dot{\theta}^2 \sin \theta) &= \tau \\ \ddot{y} \cos \theta + l\ddot{\theta} + g \sin \theta &= 0 \end{aligned} \quad (1)$$

where  $l$  is the length of the pendulum,  $m$  is the pendulum mass,  $M$  is the cart mass,  $\tau$  is the horizontal force action,  $\theta$  is the angular deviation,  $y$  is the position of the cart which is moving horizontally.

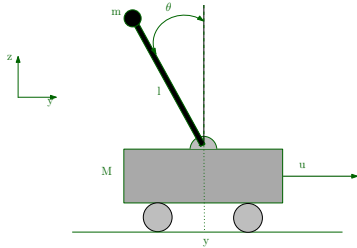


Fig. 1. Inverted pendulum

Letting  $x_1 = y$ ,  $x_2 = \dot{y}$ ,  $x_3 = \theta$ ,  $x_4 = \dot{\theta}$ , and according to the canonical form of a class of underactuated systems, we can transform equations (1) into the following state space representation:

$$\begin{aligned} \dot{x}_1 &= x_2 \\ \dot{x}_2 &= f_1 + b_1 \tau \\ \dot{x}_3 &= x_4 \\ \dot{x}_4 &= f_2 + b_2 \tau \end{aligned} \quad (2)$$

$x = [x_1, x_2, x_3, x_4]^T$  is the state variable vector,  $\tau$  is the control input.  $f_1, f_2, b_1$  and  $b_2$  are nominal nonlinear functions, described as:

$$\begin{aligned} f_1 &= \frac{mlx_4^2 \sin x_3 - mg \sin x_3 \cos x_3}{M + m \sin^2 x_3} \\ f_2 &= \frac{(m + M)g \sin x_3 - mlx_4^2 \cos x_3}{l(M + m \sin^2 x_3)} \\ b_1 &= \frac{1}{M + m \sin^2 x_3}; \quad b_2 = \frac{-\cos x_3}{l(M + m \sin^2 x_3)} \end{aligned} \quad (3)$$

Letting

$$\tau = M + m \sin^2 x_3 u - (mlx_4^2 \sin x_3 - mg \sin x_3 \cos x_3) \quad (4)$$

equation (3) becomes:

$$\dot{X} = \begin{bmatrix} \dot{x}_1 \\ \dot{x}_2 \\ \dot{x}_3 \\ \dot{x}_4 \end{bmatrix} = \begin{bmatrix} x_2 \\ 0 \\ x_4 \\ \frac{g \sin x_3}{l} \end{bmatrix} + \begin{bmatrix} 0 \\ 1 \\ 0 \\ \frac{-\cos x_3}{l} \end{bmatrix} u$$

$$\dot{X} = f(x) + g(x)u \quad (5)$$

$$\begin{bmatrix} \dot{x}_1 \\ \dot{x}_2 \\ \dot{x}_3 \\ \dot{x}_4 \end{bmatrix} = \begin{bmatrix} 0 & 1 & 0 & 0 \\ 0 & 0 & 0 & 0 \\ 0 & 0 & 0 & 1 \\ 0 & 0 & \frac{g \sin x_3}{lx_3} & 0 \end{bmatrix} \begin{bmatrix} x_1 \\ x_2 \\ x_3 \\ x_4 \end{bmatrix} + \begin{bmatrix} 0 \\ 1 \\ 0 \\ \frac{-\cos x_3}{l} \end{bmatrix} u \quad (6)$$

[15], [16] proposed a method that can approximate the original system with an input-output linearizable control system in new coordinates. This stabilization method of nonlinear system using sliding mode control, is based on coordinate transformation by the mapping  $T : x \mapsto \xi$  defined by:

$$\xi_i = L_f^{i-1} h(x), \quad i \in 1, 2, 3, 4 \quad (7)$$

with  $\xi = (\xi_1 \ \xi_2 \ \xi_3 \ \xi_4)^T$ .  $T$  is defined as a local diffeomorphism with  $T(0) = 0$ .

The dynamical system in the new coordinates can be approximated by the system model:

$$\begin{aligned} \dot{\xi}_1 &= \xi_2 \\ \dot{\xi}_2 &= \xi_3 \\ \dot{\xi}_3 &= \xi_4 \\ \dot{\xi}_4 &= L_f^4 h(T^{-1}(\xi)) + L_g L_f^3 h(T^{-1}(\xi)) u \end{aligned} \quad (8)$$

$L_f h(x)$  is the Lie derivative of  $h(x)$  along the vector  $f(x)$ . Consider the output system function of (5) defined by [16]:

$$z = h(x) = x_1 + l \ln \left( \frac{1 + \sin x_3}{\cos x_3} \right) \quad (9)$$

with  $\xi = T(x)$  and  $T_1(x) = h(x) = \xi_1$ . Define the transformation  $T : x \mapsto \xi$  by:

$$T(x) = \begin{bmatrix} h(x) \\ L_f h(x) \\ L_f^2 h(x) \\ L_f^3 h(x) \end{bmatrix} = \begin{bmatrix} \xi_1 = T_1(x) \\ \xi_2 = T_2(x) \\ \xi_3 = T_3(x) \\ \xi_4 = T_4(x) \end{bmatrix} = \xi \quad (10)$$

then

$$T(x) = \begin{bmatrix} x_1 + l \ln \left( \frac{1 + \sin x_3}{\cos x_3} \right) \\ x_2 + \frac{lx_4}{\cos x_3} \\ \tan x_3 \left( g + \left( \frac{lx_4}{\cos x_3} \right) \right) \\ \left( \frac{2}{\cos^3 x_3} - \frac{1}{\cos x_3} \right) lx_4^3 + \left( \frac{3g}{\cos^2 x_3} - 2g \right) x_4 \end{bmatrix} \quad (11)$$

$T(x)$  defines a diffeomorphism locally at  $x = 0$ . Differentiating  $\xi$  we obtain:

$$\begin{aligned} \dot{\xi}_1 &= z^{(1)} = x_2 + \ln \left( \frac{lx_4}{\cos x_3} \right) \\ \dot{\xi}_2 &= z^{(2)} = \tan x_3 \left( g + \frac{lx_4}{\cos x_3} \right) \\ \dot{\xi}_3 &= z^{(3)} = \left( \frac{2}{\cos^3 x_3} - \frac{1}{\cos x_3} \right) lx_4^3 \\ &\quad + \left( \frac{3g}{\cos^2 x_3} - 2g \right) x_4 - 2x_4 \tan x_3 u \\ \dot{\xi}_4 &= z^{(4)} = f_e(x) + g_e(x)u \end{aligned} \quad (12)$$

where

$$\begin{aligned} f_e(x) &= \left( \frac{6 \sin x_3}{\cos^4 x_3} - \frac{\sin x_3}{\cos^2 x_3} \right) l^4 x_4 + \frac{6g \sin x_3}{\cos^3 x_3} x_4^2 \\ &\quad + \left( \frac{2g \sin x_3}{\cos^3 x_3} - \frac{g \sin x_3}{\cos x_3} \right) 3x_4^2 \\ &\quad + \left( \frac{3g}{\cos^2 x_3} - 2g \right) \frac{g \sin x_3}{l} \\ g_e(x) &= \frac{-6x_4^2}{\cos^2 x_3} + 3x_4^2 - \frac{3g}{l \cos x_3} + \frac{2g \cos x_3}{l} \end{aligned} \quad (13)$$

by neglecting  $2x_4 \tan(x_3)$  [16], we obtain a feedback linearizable nonlinear system in the state  $\xi$ , with:

$$\begin{aligned} \dot{\xi}_1 &= \xi_2 \\ \dot{\xi}_2 &= \xi_3 \\ \dot{\xi}_3 &= \xi_4 \\ \dot{\xi}_4 &= f_e(\xi) + g_e(\xi)u \\ z &= \xi_1 \end{aligned} \quad (14)$$

### B. First order sliding mode controller

Define the surface  $s = \{\xi \in R^4 \mid s(\xi) = 0\}$ , for  $\lambda > 0$ .

$$s(\xi) = \left( \frac{d}{dt} + \lambda \right)^3 (z - z_d) \quad (15)$$

We choose  $z_d = [2 \ 0 \ 0 \ 0]^T$ . The time derivative of  $s$  along the system trajectory  $\xi$  is equal to:

$$\begin{aligned} \dot{s}(\xi) &= \xi^{(4)} + 3\lambda\xi^{(3)} + 3\lambda^2\xi^{(2)} + \lambda^3\xi^{(1)} \\ &= f_e(\xi) + g_e(\xi)u + 3\lambda z^{(3)} + 3\lambda^2 z^{(2)} + \lambda^3 z^{(1)} \end{aligned} \quad (16)$$

The sliding mode control is expressed by :

$$u = u_{eq} + u_{sw} \quad (17)$$

where  $u_{sw}$  is the switching control and  $u_{eq}$  is the equivalent control yielded from  $\dot{s}(\xi) = 0$ :

$$\begin{aligned} u_{eq} &= -\frac{f_e(z) + 3\lambda z^{(3)} + 3\lambda^2 z^{(2)} + \lambda^3 z}{g_e(\xi)} \\ u_{sw} &= \eta \text{sign}(s) + ks \end{aligned} \quad (18)$$

where  $\eta$  and  $K$  are positive constants.

It is notable that for small deviations, we have :  $g_e(\xi) < -3 - \frac{g}{l} < 0$ . Choosing the Lyapunov candidate as:

$$V = \frac{1}{2} s^2 \quad (19)$$

Differentiating  $V$  along the trajectories of (14) yields to

$$\dot{V} = s\dot{s} = -\eta|s| - ks^2 \leq 0 \quad (20)$$

Then the system is stable and the convergence of the sliding mode is guaranteed.

### III. SECOND ORDER SLIDING MODE CONTROLLER

The drawback of the first order sliding mode control is the chattering phenomenon. As a solution to resolve this problem, a higher order sliding mode HOS is proposed. In fact, HOS appears as an effective application to counteract the chattering phenomenon and the switching control signals, with higher relative degrees in finite time [8], [18].

The HOS has been introduced by Emel'yanov et al. [6], with the goal to get a finite time on the sliding set of order  $r$  defined by:  $s = \dot{s} = \ddot{s} = \ddot{\ddot{s}} = \dots = s^{(r-1)} = 0$ .

$s$  defines the sliding variable with the  $r$ th order sliding and with its  $(r - 1)$  first time derivatives depending only on the state  $x$ . The first order sliding mode tries to keep  $s = 0$ . In the case of second order sliding mode control SSMC, which only needs its measurement or evaluation of  $s$ , the following relation should be verified:

$$s(x) = \dot{s}(x) = 0 \quad (21)$$

In the following, twisting algorithm and the super-twisting algorithm with a prescribed convergence law are used.

### A. Twisting controller

1) *Controller Approach*: Consider the sliding surface

$$s_1 = \left( \frac{d}{dt} + \lambda_1 \right)^2 \xi \quad (22)$$

Differentiating twice (22) gives:

$$\begin{aligned} \ddot{s}_1 &= f_e(\xi) + g_e(\xi)u + 2\lambda_1 z^{(3)} + \lambda_1^2 z^{(2)} \\ \dot{s}_1 &= \Psi(\xi) + \varphi u \end{aligned} \quad (23)$$

where  $\Psi(\xi) = f_e(\xi) + 2\lambda_1 z^{(3)} + \lambda_1^2 z^{(2)}$ ,  $\varphi(\xi) = g_e(\xi)$ . we assume that function  $\Psi$  and  $\varphi$  are bounded as:

$$|\Psi| \leq \Psi_d \quad 0 < \varphi_m \leq \varphi \leq \varphi_M, \quad (24)$$

$\Psi_d, \varphi_m, \varphi_M$  and  $\varphi_d$  are positive scalars. Then, we have

$$\left| \frac{\Psi}{\varphi} \right| < \frac{\Psi_d}{\varphi_M} \quad (25)$$

By annulling  $\ddot{s}_1 = 0$  the equivalent control can be expressed as:  $u_{eq} = -\Psi/\varphi$ .

2) *Stability study*: The dynamic control law using the twisting algorithm is given by [8]:

$$u_{sw} = \frac{K}{g_e(\xi)} (s_1 + \beta \text{sign}(\dot{s}_1)) \quad (26)$$

with  $\beta > 0$ ,  $0 < K \leq K_M$  and  $K_M > \frac{1}{1-\beta} \frac{\Psi_d}{\varphi_M}$ . The total control is defined by:

$$u = u_{eq} + u_{sw} \quad (27)$$

The Lyapunov function can be chosen as:

$$V_1 = \frac{1}{2} \lambda_2 s_1^2 + \frac{1}{2} \dot{s}_1^2 \quad (28)$$

Differentiating (28) yields:

$$\begin{aligned} \dot{V}_1 &= \lambda_2 s_1 \dot{s}_1 + \dot{s}_1 \ddot{s}_1 \\ &= \lambda_2 s_1 \dot{s}_1 + \dot{s}_1 (\Psi(\xi) + g_e(\xi)u) \\ &= \dot{s}_1 [\lambda_2 s_1 - K s_1 - K \beta \text{sign}(\dot{s}_1)] \\ &= \dot{s}_1 \text{sign}(\dot{s}_1) [\lambda_2 s_1 \text{sign}(\dot{s}_1) - K s_1 \text{sign}(\dot{s}_1) - K \beta] \\ &= |s_1| [(\lambda_2 |s_1| - K |s_1|) \text{sign}(\dot{s}_1) - K \beta] \\ &\leq |\dot{s}_1| [(\lambda_2 - K) |s_1| - K \beta] \leq 0 \end{aligned} \quad (29)$$

Therefore the system is stable if  $\lambda_2 - K < 0$ .

### B. Super twisting controller

SSMC controllers require the knowledge of values of the derivatives except for the super twisting algorithm (STW). The STW is a continuous SM algorithm ensuring main properties of the first order sliding mode control for systems with Lipschitz continuous matched uncertainties or disturbances with bounded gradients [8]. It has been developed to control

systems with a relative degree equal to one in order to avoid chattering.

Trajectories on the 2 sliding plane are characterized by twisting around the origin, but the continuous control law  $u(t)$  is constituted by two terms. The first one is defined by the discontinuous time derivative and the second one is a continuous function of the available sliding variable [2].

1) *Controller approach*: The derivative of the sliding surface is given as

$$\dot{s} = f_e(\xi) + g_e(\xi)u + 3\lambda z^{(3)} + 3\lambda^2 z^{(2)} + \lambda^3 z^{(1)} \quad (30)$$

which can be expressed as:

$$\dot{s} = \Psi_1(\xi) + \varphi(\xi)u \quad (31)$$

where  $\Psi_1(\xi) = f_e(\xi) + 3\lambda z^{(3)} + 3\lambda^2 z^{(2)} + \lambda^3 z^{(1)}$ . The total controller can be expressed by [8]:

$$u = \frac{u_1 - \Psi_1(\xi)}{\varphi(\xi)} \quad (32)$$

where the super twisting controller

$$u_1 = -k_1 \text{sign}(s) |s|^{1/2} - k_2 s + \sigma \quad (33)$$

Variations of the term  $\sigma$  are described by:

$$\dot{\sigma} = -k_3 \text{sign}(s) - k_4 s \quad (34)$$

where  $k_1, \dots, k_4$  are positive scalars.

The substitution of (32) and (33) into (31) gives:

$$\dot{s} = -k_1 \text{sign}(s) |s|^{1/2} - k_2 s + \sigma \quad (35)$$

2) *Stability study*: For the stability proof, the Lyapunov function candidate given in [10] is used:

$$V_2(s, z) = 2k_3 |s| + k_4 s^2 + \frac{k_5}{2} \sigma^2 + \gamma^2 \quad (36)$$

where  $k_5$  a positive scalar and

$$\gamma = k_1 \text{sign}(s) |s|^{1/2} + k_2 s - \sigma. \quad (37)$$

We have introduced the positive scalar  $k_5$  for a more flexibility of the stability conditions and for more generality of the expression of  $V_2$ . The substitution of (37) into (36) gives:

$$\begin{aligned} V_2(s, \sigma) &= 2k_3 |s| + k_4 s^2 + \frac{k_5}{2} \sigma^2 + \left( k_1 \frac{s}{\sqrt{|s|}} + k_2 s - \sigma \right)^2 \\ &= \frac{1}{2|s|} (4k_3 |s|^2 + 2k_4 s^2 |s| + k_5 \sigma^2 |s| + 2k_1^2 s^2 \\ &\quad + 4k_1 k_2 s^2 \sqrt{|s|} - 4k_1 \sigma \sqrt{|s|} + 2k_2^2 s^2 |s| \\ &\quad - 4k_2 s |s| \sigma + 2\sigma^2 |s|) \end{aligned} \quad (38)$$

Define the subspace

$$\kappa = \{((s, \sigma)) \in \mathbb{R}^2 / s = 0\} \quad (39)$$

Differentiating with respect to time (38) gives:

and

$$\begin{aligned}
 \dot{V}_2(s, \sigma) &= \frac{V_2 ds}{ds dt} + \frac{V_2 d\sigma}{d\sigma dt} \\
 &= \frac{V_2 \dot{s}}{ds} + \frac{V_2 \dot{\sigma}}{d\sigma} \\
 &= \frac{-\dot{s}}{|s|^{\frac{5}{2}}} \left\{ -2k_3 |s|^{\frac{5}{2}} \text{sign}(s) - 2k_4 |s|^{\frac{5}{2}} \right. \\
 &\quad - 2k_1^2 |s|^{\frac{3}{2}} - 4k_1 k_2 |s|^2 + k_1 k_2 s^2 |s| \text{sign}(s) \\
 &\quad + 2k_1 \sigma |s|^2 - k_1 \sigma |s|^2 s - 2k_2^2 |s|^{\frac{5}{2}} \\
 &\quad \left. + 2k_2 |s|^{\frac{5}{2}} + k_1^2 s^2 \text{sign}(s) \sqrt{|s|} \right\} \\
 &\quad - \frac{\dot{\sigma}}{|s|} \left( -k_5 \sigma |s| + 2k_1 s \sqrt{|s|} + 2k_2 s |s| - 2\sigma |s| \right)
 \end{aligned} \tag{40}$$

$$\begin{aligned}
 \Upsilon_{11} &= 4k_1^2 k_2 \\
 \Upsilon_{22} &= 2k_2^3 \\
 \Upsilon_{13} &= -k_1 k_2 \frac{s}{|s|} \\
 \Upsilon_{23} &= \frac{1}{2} k_4 k_5 - 2k_2^2 \\
 \Upsilon_{32} &= \Upsilon_{23} \\
 \Upsilon_{33} &= 2k_2
 \end{aligned} \tag{45}$$

The closed loop is stable if matrices  $\Psi$  and  $\Upsilon$  are positive definite.

Matrix  $\Psi$  is positive definite if:

substituting (35) and (34) into (40) yields:

$$\begin{cases} \Psi_{11} > 0 \\ \Psi_{22} > 0 \\ \det(\Psi) > 0 \end{cases} \tag{46}$$

$$\begin{aligned}
 \dot{V}_2(s, \sigma) &= \frac{-6k_1^2 k_2 s^2}{|s|} + \frac{4k_1^2 \sigma s}{|s|} + \frac{k_1^3 s^4}{|s|^{\frac{7}{2}}} - \frac{6k_1 k_2^2 s^2}{\sqrt{|s|}} \\
 &\quad + 4k_2^2 s \sigma - \frac{2k_1^3 s^2}{|s|^{\frac{3}{2}}} - \frac{2k_1 \sigma^2}{\sqrt{|s|}} - 2k_2^3 s^2 \\
 &\quad - 2k_2 \sigma^2 + \frac{2k_1^2 k_2 s^4}{|s|^3} - \frac{2k_1^2 s^3 \sigma}{|s|^3} + \frac{8k_1 k_2 s \sigma}{\sqrt{|s|}} \\
 &\quad - \frac{k_3 k_5 s \sigma}{|s|} - k_5 k_4 s \sigma - \frac{2k_1 k_2 s^3 \sigma}{|s|^{\frac{5}{2}}} \\
 &\quad + \frac{k_1 k_2^2 s^4}{|s|^{\frac{5}{2}}} + \frac{k_1 s^2 \sigma^2}{|s|^{\frac{5}{2}}}
 \end{aligned} \tag{41}$$

These conditions are fulfilled if:

$$-16k_1^4 - 5k_3^2 k_5^2 + 20k_1^2 k_3 k_5 > 0 \tag{47}$$

that is to say if:

$$-\left(4k_1^2 - \frac{5}{2} k_3 k_5\right)^2 + \frac{5}{4} k_3^2 k_5^2 > 0 \tag{48}$$

it is obvious that matrix  $\Psi$  is positive definite if

Define  $X = (|s|^{1/2} \ s \ \sigma)^T$ . Then, it is easy to show that:

$$4k_1^2 = \frac{5}{2} k_3 k_5 \tag{49}$$

The matrix  $\Upsilon$  is positive definite if:

$$\dot{V}_2(s, \sigma) \leq -\frac{1}{|s|^{1/2}} X^T \Psi X - X^T \Upsilon X \tag{42}$$

where

$$\begin{cases} \Upsilon_{11} > 0 \\ \Upsilon_{22} > 0 \\ \det(\Upsilon) > 0 \end{cases} \tag{50}$$

$$\Psi = \begin{bmatrix} \Psi_{11} & 0 & \Psi_{13} \\ 0 & \Psi_{22} & \Psi_{23} \\ \Psi_{31} & \Psi_{23} & \Psi_{33} \end{bmatrix}, \quad \Upsilon = \begin{bmatrix} \Upsilon_{11} & 0 & \Upsilon_{13} \\ 0 & \Upsilon_{22} & \Upsilon_{23} \\ \Upsilon_{31} & \Upsilon_{23} & \Upsilon_{33} \end{bmatrix} \tag{43}$$

These conditions are carry out if:

$$-k_4^2 k_5^2 + 8k_2^2 k_4 k_5 - 2k_2^4 > 0 \tag{51}$$

with

namely if:

$$\begin{aligned}
 \Psi_{11} &= k_1^3 \\
 \Psi_{22} &= 5k_1 k_2^2 \\
 \Psi_{13} &= \frac{s}{|s|} \left( \frac{k_1 k_5}{2} - k_1^2 \right) \\
 \Psi_{23} &= -2k_1 k_2 \\
 \Psi_{31} &= \Psi_{13} \\
 \Psi_{32} &= \Psi_{23} \\
 \Psi_{33} &= k_1
 \end{aligned} \tag{44}$$

$$-2(k_2^2 - 2k_4 k_5)^2 + 7k_4^2 k_5^2 > 0 \tag{52}$$

then that matrix  $\Psi$  is positive definite if we choose

$$k_2^2 = 2k_4 k_5 \tag{53}$$

So the matrices  $\Psi$  and  $\Upsilon$  are positive definite and consciously  $\dot{V}_2(s, \sigma) \leq 0$ . Thus, we can conclude that the system is stable.

IV. SIMULATION RESULTS

Parameters of the inverted pendulum system are set as:  $M = 20$  kg,  $m_0 = 1.8$  kg,  $l = 0.3$  m,  $g = 9.8$ . Initial conditions of the cart pendulum are  $(y_0, \dot{y}_0) = (0, 0)$ ,  $(\theta_0, \dot{\theta}_0) = (0.1, 0)$  and the desired position are set as  $y_d = 2$ ,  $\theta_d = 0$  and  $\dot{y}_d = \dot{\theta}_d = 0$ . Simulations are done using:  $\lambda = 1$  and  $k = 20$  for the SMC,  $k_1 = 40$  and  $k_2 = 90$  for the twisting controller.

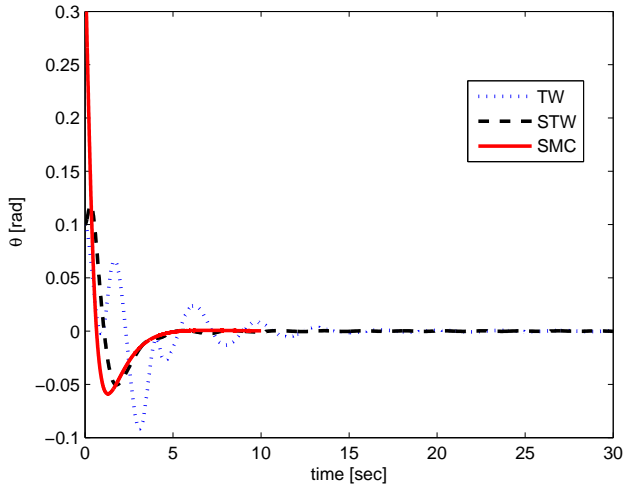


Fig. 2. Evolution of the position of  $\theta$  for the uncertain system

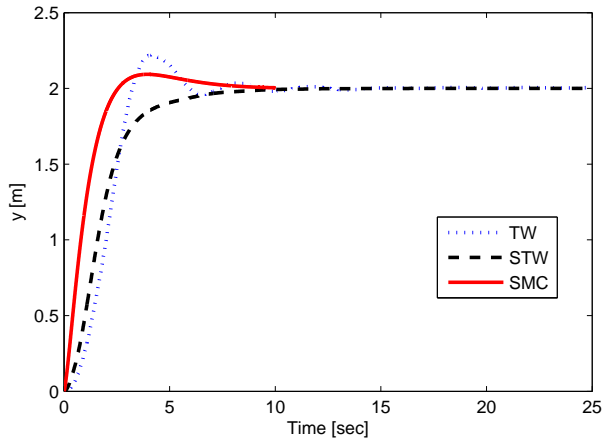


Fig. 3. Evolution of the position of  $y$  for the uncertain system

In Figs. 2 and 3, simulation results for the three controllers have been done. The convergence of state variables have been established for all controllers. Furthermore, state variables for STW controller converge faster than those of TW and SMC. In this simulation, 20% of mass uncertainties, have been considered for the pendulum and cart. We can notice the robust behavior of the controllers with respect to parametric

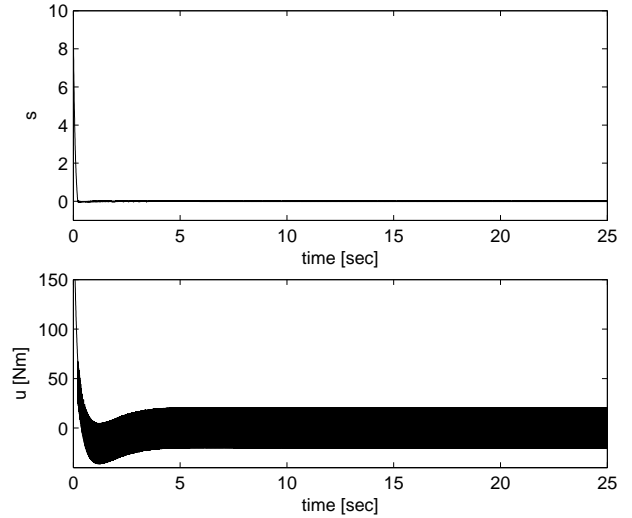


Fig. 4. Evolution of sliding surface and Control by SMC

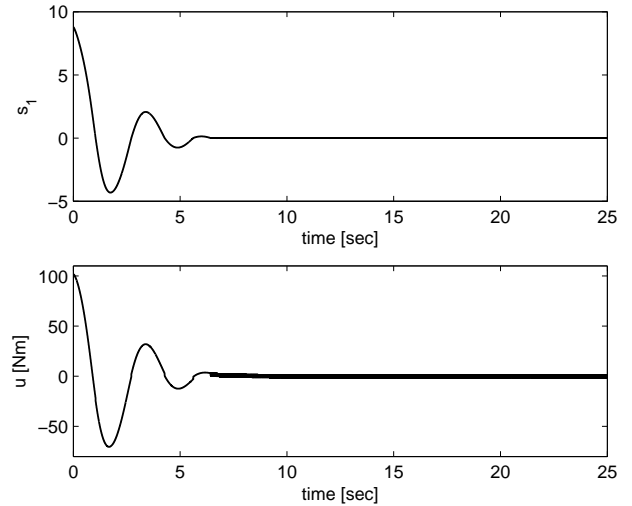


Fig. 5. Evolution of the sliding surface and the control using TW

uncertainties Figs. 4, 5 and 6 show that the proposed SSMC is able to compensate effectively the chattering phenomenon better than the first order sliding mode. Moreover, with the super-twisting controller the chattering is eliminated.

V. CONCLUSION

In this paper, a second order sliding mode controller SSMC has been designed for underactuated manipulators. This controller keeps main advantages of the original sliding mode approach, and removes the chattering caused by the sliding mode approach. Simulation results of the twisting and the super-twisting controllers show that the proposed controller give better performances compared to the first order sliding mode controller. It has been shown that the new sliding surface for the twisting controller reduces the chattering phenomenon. Moreover, the second-order sliding-mode controller is an effective tool for the control of uncertain nonlinear systems since

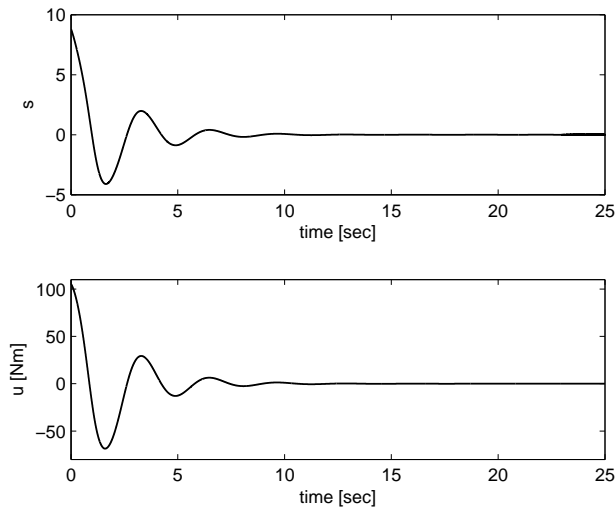


Fig. 6. Evolution of the sliding surface and the control using STW

it overcomes main drawbacks of the classical sliding-mode control approach

#### REFERENCES

- [1] A.Isidori. Nonlinear Control Systems, Springer Verlag, 1995.
- [2] W.PERRUQUETTI and J.P. BARBOT . Sliding Mode Control in Engineering. CRC Press, 2002.
- [3] J. A. BURTON and A. S. I. ZINOBER. Continuous approximation of variable structure control, *Int. J. Syst. Sci.*, vol. 17, no. 6, pp. 875–885, 1986.
- [4] H.Lee, V. I. Utkin. Chattering suppression methods in sliding mode control systems. *Annual Reviews in Control.* vol.31, pp.179–188, 2007.
- [5] K.C. VELUVOLU, Y.C. SOH and W. CAO. Robust observer with sliding mode estimation for nonlinear uncertain systems, *IET Control Theory Appl*, vol. 1, no.5, pp. 1533–1540, 2007.
- [6] S. V.Emel'yanov,S. V. Korovin, and Levantovsky, L. V. Higher-order sliding modes in control systems, *Differential Equations*, vol. 29, no. 11, pp. 1627–1647, 1993.
- [7] A. Levant. Higher-order sliding modes, differentiation and outputfeedback control, *International Journal of Control*, vol. 76, no. 9, pp. 924–941, 2003.
- [8] A.Levant.Chattering analysis, *Proceedings of the European Control Conference*, 2007.
- [9] J.A.Moreno, M.Osorio. Strict Lyapunov Functions for the Super Twisting Algorithm, *Automatic Control, IEEE Transactions*, vol. 57, no. 4, pp. 1035–1040, 2012.
- [10] I. Nagesha, C. Edwards. A multivariable super-twisting sliding mode approach, *IEEE Transaction on automatique control*, Vol. 50, no. 3, pp. 984988, 2014.
- [11] I. Fantoni , R. Lozano. Non-linear Control for Underactuated Mechanical Systems, Springer, London, pp. 21–42, 2002.
- [12] B. Jakubczyk and W. Respondek. On the linearization of control systems, *Bult. Acad. Polon. Sei. Math .*, vol. 28, pp. 517–522, 1980.
- [13] Jun Zhao, M. W. Spong . Hybrid control for global stabilization of the cart pendulum system, *Automatica* , vol. 37, no. 12, pp. 1941–1951, 2001.
- [14] W. D.Chang, R.Hwang, J. G. CHsieh. A self-tuning PID control for a class of nonlinear systems based on the lyapunov approach, *Journal of Process Control*, vol. 12, pp. 233–242, 2002.
- [15] D. Voytsekhovskiy, d R. Hirschorn, Stabilization of single-input nonlinear systems using higher-order term compensating sliding mode control. *Int. J. Robust Nonlinear Control* vol. 18, pp. 468–480, 2008.
- [16] C. Aguilar, R. Hirschorn. Stabilization of an Inverted Pendulum. Report on Summer NSERC Research Project. Queens University at Kingston, Department of Mathematics and Statistics, summer, 2002.
- [17] A. Levant , M. Taleb, and F. Plesta . Twisting-controller gain adaptation, *50th IEEE Conference on Decision and Control and European Control Conference (CDC-ECC)* Orlando, FL, USA, 2011.
- [18] G. Bartolini, A. Levant, E. Usai, A. Pisano. 2-Sliding Mode with Adaptation, *Proceedings of the 7th Mediterranean Conference on Control and Automation (MED99)* Haifa, June 28–30, 1999.
- [19] Y.Orlov. Advances in variable structure and sliding mode control, Extended invariance principle and other analysis tools for variable structure systems, *In C. Edwards, E. F. Colet, and L. Fridman (Eds.)*. Berlin, Heidelberg, New York: Springer, pp. 3-22, 2006.
- [20] I. Boiko, L. Fridman, M. I. Castellanos. Analysis of second order sliding mode algorithms in the frequency domain. *IEEE Transactions on Automatic Control*, vol. 49, no. 6, pp. 946-950, 2004.
- [21] S. Mahjoub, F. Mnif, N. Derbel. A Sliding mode control applied to whirling pendulum , *International Conference on Signals Circuits and Systems (SCS'08)* Hammamet, Tunisia, Nov.2008.

# A 21.5mW 3 Gbps CMOS OOK Receiver for the Next Generation Device to Device Communications

Ki-Jin Kim, Sanghoon Park, Suk-hui LEE, and K.H. Ahn

**Abstract**—Recently, the high speed device to device(D2D) wireless communication technology has been studied for short distant mobile data transfer application. This paper presents 60 GHz OOK(On-Off Keying) non-coherent receiver which is a strong candidate for high speed D2D communication technology. The OOK receiver architecture is used because of its simple structure and low power characteristic. The receiver consists of three-stage low noise amplifier(LNA), fully differential envelop detector, and limiting amplifier(LA). The measured receiver shows 54 dB peak gain at -55 dBm input power level. The sensitivity of the receiver is measured -50 dBm under 3 Gbps data rate. The proposed receiver is fabricated with 65 nm CMOS process and its measured power consumption is only 21.5 mW. As a result, the proposed receiver achieves energy efficiency of 7.12 pJ/bit.

**Keywords**—Device to Device communications, 60 GHz low noise amplifier, On-off keying receiver, 60 GHz receiver, millimeter wave communications

## I. INTRODUCTION

RECENTLY demand for short-range high speed data communications such as a fast file transfer by “Device-to-device communication” which requires user friendly interface is increasing so it attracted great deal of interest from both academia and industries over the past few years. High speed(>Gbps), high energy efficiency (<100pJ/bit) and low cost(CMOS process) are the prerequisite condition. Non-coherent UWB heterodyne transceiver showed 15Mbps with 2680pJ/bit[1] and homodyne transceiver showed 1Mbps with 373pJ/bit[2]. A six port transceiver showed low power and high data rate but the input sensitivity limits applications[3]. At V band (50 ~ 75 GHz), the large bandwidth allocated at around 60 GHz offers great opportunities for high data rate communication. The QPSK(Quadrature Phase Shift Keying) modulation requires PLL(Phase Locked Loop) to demodulate

the received data. This de-modulation scheme increases system complexity and also power consumption which is not suitable for low power short range communications. The OOK(On-Off Keying) modulation naturally presents a phase noise immunity and requires neither PLL nor ADC(Analog to Digital Converter) so it can be used for device-to-device communication solution. Previous study showed 6 Gbps data communication with the OOK modulation[4].

In this paper, 60 GHz band OOK receiver composed of LNA, demodulator and LA(Limiting Amplifier) is implemented. We propose miller capacitor compensated LNA to boost gain and reduce noise figure. In addition, the incorporation of the high sensitivity non-coherent 60 GHz OOK demodulator, right after LNA, increases receiver sensitivity comparing to previous studies [5], [6]. The LA amplifies demodulated signals in full scale as a 1-bit data slicer which is power efficient and easy to implement. Differential configuration is adopted throughout the receiver design to provide common mode noise rejection.

The paper is organized in the following manner. The LNA structure is first discussed in Section II. This is then followed by the structure of demodulator and LA in Section III. The Section IV will show and discuss the receiver measurement results. Finally conclusions are drawn in Section V.

## II. TRANSFORMER FEEDBACK MILLER CAPACITOR COMPENSATED LNA

Fig. 1 shows the schematic of the proposed three-stage LNA. The single ended configuration is chosen to minimize noise figure and DC power consumption. The CS(Common Source) structure is adopted instead of cascode structure because a CS structure offers more available gain than the cascode structure in millimeter wave frequency. It is reported that there is optimum current density for CS LNA to have minimum noise figure and reasonable available gain which is around 0.15 mA/ $\mu\text{m}$ [7]. So this paper also uses 0.15 mA/ $\mu\text{m}$  bias condition. On chip micro strip transmission lines are used to design both the input and output matching network as well as source degeneration inductor which makes the input matching easy.

In the CS structure miller capacitor  $C_{gd}$  degrades the amplifier’s gain and reverse isolation especially when the amplifier is operating at the millimeter wave frequency as shown in equation (1).

This research was funded by the MSIP (Ministry of Science, ICT & Future Planning), Korea in the ICT R&D Program 2014.

Ki-Jin Kim is with the Convergence Communication Components Research Center of Korea Electronics and Technology Institute, Korea (corresponding author to provide phone: 82-31-789-7226; fax: 82-31-789-7259; e-mail: sergeant@keti.re.kr).

Sanghoon park, Suk-hui Lee and K. H. Ahn are with the Convergence Communication Components Research Center of Korea Electronics and Technology Institute, Korea (corresponding author to provide phone: 82-31-789-7225; fax: 82-31-789-7259; e-mail: khajoh@keti.re.kr).

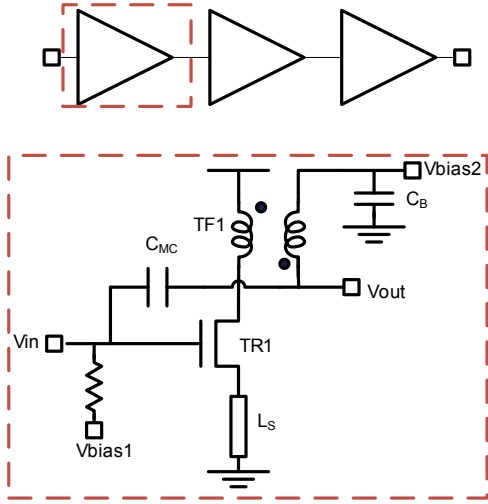


Fig1. Proposed three-stage LNA structure

$$G_m \approx \frac{g_m}{1 + j\omega(C_{gs} + C_{miller})R_g} \quad (1)$$

To boost gain by compensating  $C_{gd}$  is achieved by using differential topology[8]. In the differential structure, opposite phase output signal is feed backed into the gate of the amplifier with  $C_{MC}$  capacitor. Therefore the miller capacitor is neutralized simply. However differential structure requires double the DC power, and increases noise figure which is not favorable in this paper's application.

We propose the transformer feedback miller compensation capacitor as shown in Fig 1. The input signal is amplified by the  $G_m$  of the transistor TR1 and the effective load of the transformer TF1. The output signal is feedback through TF1 and  $C_{MC}$  capacitor which has the same feedback effect just like the differential amplifier. Because of the loss in TF1, larger capacitor value of  $C_{MC}$  is required but it will not cause any problems. The only matter to concern is low self-resonance frequency in TF1 configuration so, smaller size transformer rather than optimum size is used to enhance self-resonance frequency. The below equation illustrates the effect of the proposed capacitor compensation. The coefficient  $\alpha$  comes from loss of the transformer.

$$\begin{aligned} C_{eq} &= C_{gs} + C_{gd} + A_v(C_{gd} - \alpha C_{MC}) \\ &\cong C_{gs} + C_{gd} \end{aligned} \quad (2)$$

Like the equation (2), miller capacitor ( $A_v C_{gd}$ ) is compensated by inserting capacitor  $C_{MC}$ . Therefore the gain of the amplifier will be boosted especially when the operating frequency is millimeter frequency as explained in equation(1).

The S-parameter simulation results are shown in fig 2. We designed two LNA for the purpose of comparison. One is the LNA without transformer feedback (w/o FB), and the other is the LNA with the FB(w/ FB). As the operating frequency goes up, the effect of the gain boosting appears clearly. At 65 GHz,

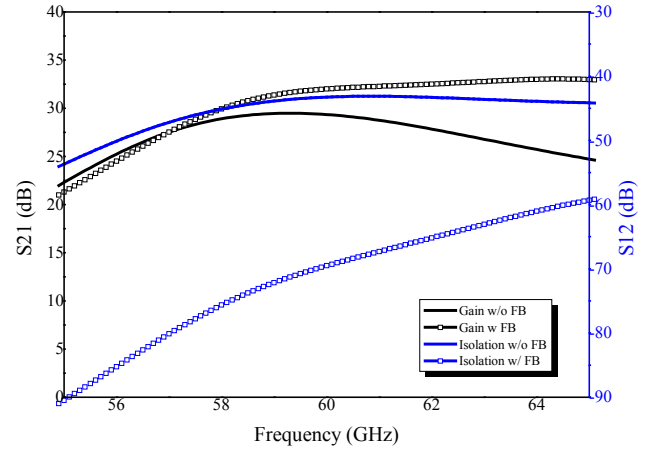


Fig2. Simulated gain(S21) and isolation(S12) characteristics of the LNA with/without transformer feedback

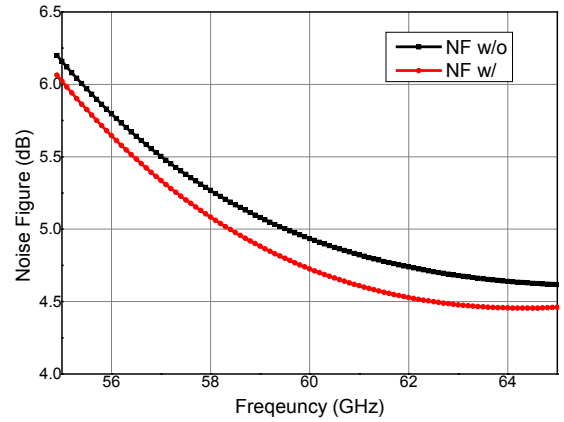


Fig3. Simulated noise figure characteristic of the LNA with/without transformer feedback

the gain boosting is 8 dB which is comparable to one stage CS amplifier in millimeter wave so we can achieve more than 30 dB gain which is essential parameter for high sensitivity OOK receiver. The isolation characteristic (S12) is enhanced by at least 15 dB over the entire frequency (57 ~ 65 GHz), which means that the miller capacitors are almost compensated. Thus the stability of the LNA is reinforced automatically.

The NF(Noise Figure) of the transformer feedback LNA is approved by 0.2 dB throughout operating frequency as shown in fig 3. The reason for this noise enhancement is cause by the noise feedback mechanism. Unlike the differential miller compensation scheme, the proposed feedback circuit uses its own CS transistor as a feedback source, thus the channel noise of the transistor is reduced proportional to  $\alpha C_{MC}$ . The LNA consumes about 12 mA with 1V supply. As a result, the proposed LNA is a good candidate for this 60 GHz application.

### III. OOK DEMODULATOR AND LIMITING AMPLIFIER

#### A. OOK Demodulator

The OOK demodulator is the key block in OOK receiver system because this block is main noise contributor of the total noise figure especially when the input power is low. Thus it's



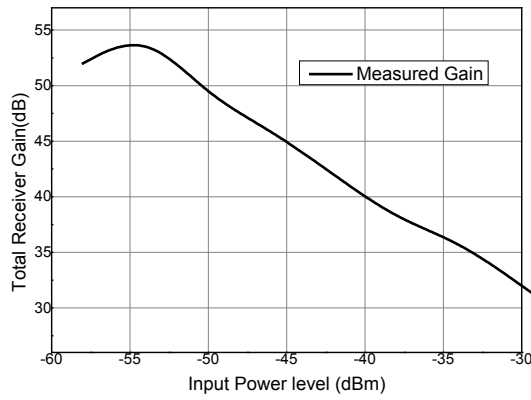


Fig6. Proposed limiting amplifier circuit

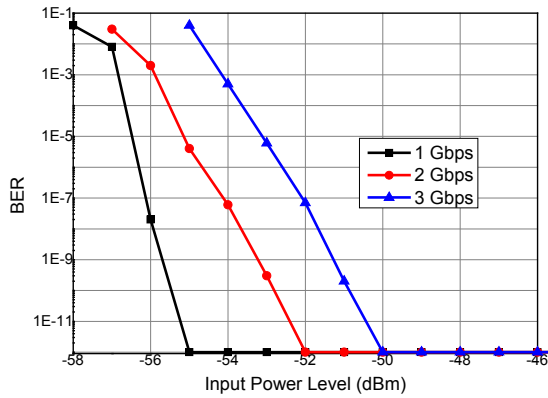


Fig7. Proposed limiting amplifier circuit

CMOS technology. On chip micro-strip lines and transformers are modeled by HFSS 3D simulator. The short stub micro-strip line is designed as an input matching circuit to provide matching and ESD protector simultaneously. From the 1V supply voltage the receiver consumes only 21.5 mW including bias circuits.

For the test purpose, OOK transmitter module was designed by using Hittite millimeter wave solutions. The conversion gain of the receiver was measured at 60 GHz frequency as shown in fig 6. The peak gain is 54 dB when the input power is -55 dBm and after that gain is decreased because LA becomes saturated.

To measure BER performance, A 27-1 PRBS stream with a data rate from 1 Gbps to 3 Gbps were fed to the receiver and the BER was measured. It is found that the minimum required input power of error-free 3 Gbps data rate is -50 dBm. Table I compares proposed work to previous studies.

Table I. Performance Comparison

ref	Technology	Data rate	Power Consumption	Sensitivity
2	CMOS 90nm	3 Gbps	103 mW	-16 dBm
5	CMOS 90nm	3.5 Gbps	108 mW	-40 dBm
10	SiGe 0.25µm	4 Gbps	27.5 mW	-22 dBm
11	CMOS 90nm	1.2 Gbps	51 mW	-47 dBm
12	CMOS 90nm	3 Gbps	36 mW	-44

				dBm
This Work	CMOS 65 nm	3 Gbps	21.5mW	-50 dBm

V. CONCLUSIONS

To realize a low power, short range device-to-device communication solution at 60 GHz frequency, the OOK receiver with LNA, OOK de-modulator, and LA is illustrated and simulated. To demonstrate the demodulator, the proposed circuit is fabricated using TSMC 65nm technology and gain and sensitivity of the receiver is measured. The measured sensitivity shows outstanding low sensitivity with only 21.5 mW power consumption which is 7.12 pJ/bit of energy efficiency. As a result, the proposed receiver will be one of the candidates for device-to-device communication solution.

REFERENCES

- [1] H. Ishizaki, et al. "FDM-based Wireless Source Synchronous 15-mbps TRx with PLL-less Receiver and 1-mm On-Chip Integrated Antenna for 1.25 cm Touch and Proceed Communication," *Symp. VLSI Circuits*, pp.73-74, June 2010.
- [2] J. Lee, et al. "A Low-Power Fully Integrated 60GHz Transceiver System with OOK Modulation and On-Board Antenna Assembly," *ISSCC Dig. Tech.* pp. 316-317, Feb. 2009.
- [3] Benjamin Laemmle, et al. "A Fully Integrated 120-GHz Six-Port Receiver Front-End in a 130-nm SiGe BiCMOS Technology," *SiRF 2013*, pp 129-131, Jan. 2013
- [4] Amin Hamidian, Andrea Malignaggi, Ran Shu, Ali M. Kamal, and Georg Boeck, "Multi-Gigabit 60 GHz OOK Front-End in 90 nm CMOS," *SiRF 2013*, pp 96-98, Jan. 2013
- [5] E. Juntunen, M.C.-H Leung, F. Barsal, A. Rachamadugu, D.A. Yeh, B.G. Perumana, P. Sen, D. Dawn, S. Sarkar, S. Pintel, and J. Laskar, "A 60-GHz 38-pJ/bit 3.5-Gb/s 90-nm CMOS OOK digital radio," *Microwave Theory and Technique*, vol.58, no.2, pp 348-355, Feb. 2010
- [6] C. W. Byeon, J.J. Lee, K.C. Eun, and C.S. Park "A 60 GHz 5Gb/s gain-boosting OOK demodulator in 0,13µm CMOS," *IEEE Microwave and Wireless Components Letters*, vol.21, no.2, pp 101-103, Jan. 2011
- [7] T. Yao, M. Q. Gordon, K. K. W. Tang, K. H. K. Yau, M.-T, Yang, P. Schvan, and S. P. Voinigescu "Algorithmic design of CMOS LNA and PAs for 60-GHz radio," *IEEE J. Solide State Circuits*, vol. 42, no.5, pp 1044-1057, May. 2007
- [8] E. Cohen, et al "Robust 60 GHz 90 nm and 40nm CMOS Wideband neutralized Amplifiers with 23 dB gain 4.6 dB NF and 24 % PAE," *IEEE SiRF 2012*, pp 207-210, Jan. 2012
- [9] P.-C Huang, Y.-H. Chen, and C.-K. Wang, "A 2-V CMOS 455-kHz FM/FSK demodulator using feed-forward offset cancellation limiting amplifier," *IEEE JSSC*, vol 36, no.1, pp 135-138, Jan. 2001
- [10] U. Yodprasit, C. Carta and F. Ellinger, "11.5-Gbps 2.4-pJ/bit 60-GHz OOK Demodulator Integrated in a SiGe BiCMOS Technology," *European Microwave Integrated Circuits Conference*, pp 1-4, Oct. 2013
- [11] K. Kang, F. Lin, D. D. Pham, J. Brinkhoff, C.H. Heng, Y. X. Guo, and X. Yuan, "A 60-GHz OOK Receiver With an On-chip Antenna in 90 nm CMOS," *IEEE JSSC*, vol 45, no. 9, pp 1720-1731, Sept. 2010
- [12] C. W. Byeon, C. H. Yoon, and C. S. Park, "A 67-mW 10.7 Gb/s 60-GHz CMOS Transceiver for Short-Range Wireless Communications," *IEEE Trans. Microwave Theory and Techniques*, vol 61. No. 9, pp 3391-3401, Sept. 2013

# Modelling and Control of Water Tank Model

Jiri Vojtesek and Petr Dostal

**Abstract**—The paper is focused on the description of the procedure from the modelling and simulation to the adaptive control of model of the water tank as a part of the Process Control Teaching system PCT40. First, the mathematical model of the water tank is derived with the use of material balance inside and the resulting nonlinear ordinary differential equation is solved numerically with the use of the mathematical software Matlab. Results from the steady-state and dynamic analyses are then used for the choice of the optimal working point and the choice of the External Linear Model for the control. The adaptive approach here uses polynomial approach, recursive identification and pole-placement method with spectral factorization. Resulted controller has one tuning parameter – position of the root inside the closed loop and the choice of this root affects mainly the speed of the control and the overshoots.

**Keywords**—Water Tank, Adaptive Control, Mathematical Model, Pole-placement Method, Recursive Identification.

## I. INTRODUCTION

THE modelling and simulation is of the first step before the choice of the optimal working point and control strategy. These days, when computation power and speed of personal or industrial computers are very high and the price is low the role of the simulation grows.

The system could be described either mathematically or practically [1], [2]. The mathematical description for example uses material, heat etc. balances [3] depending on the type of the system, whether it is chemical reactor (Russell and Denn 1972), heat exchanger or electric motor. On the other hand, real model is usually small representation of the originally nonlinear system and we expect that results of experiments on this model are also valid or comparable to those on the real system. The big advantage of the mathematical modelling is in its safety – experiments on some real systems could be sometime hazardous. Nevertheless, experiments on the real or abstract model are usually much cheaper than those on the original system which is sometimes big and components are expensive.

This goal of this contribution is to describe how the simulation could help us with the designing of the controller for real model of the water. This real model is represented here by the Armfield's Process Control Teaching System

J. Vojtesek is with the Department of Process Control, Tomas Bata University in Zlin, nam. TGM 5555, 76001 Zlin, Czech Republic (corresponding author to provide phone: +420576035199; fax: +420576032716; e-mail: vojtesek@fai.utb.cz).

P. Dostal is with the Department of Process Control, Tomas Bata University in Zlin, nam. TGM 5555, 76001 Zlin, Czech Republic (e-mail: dostalp@fai.utb.cz).

PCT40 [4] which has several process control models and one of them is the water tank.

The mathematical model of this water tank system is mathematically described by the first order nonlinear Ordinary Differential Equation (ODE) [1]. This mathematical model is then subtracted to static and dynamic analyses.

The static analysis means solving of this ODE in the steady-state, i.e. the derivatives with the respect to time are equal to zero [3]. The nonlinear ODE is then reduced to the nonlinear algebraic equation which can be solved for example with the use of simple iteration methods [5]. The result of the static analysis could be optimal operating point or the range where the input variable could vary from the practical point of view.

On the other hand, the dynamic analysis observes the behavior of the system after the step change of the input quality, in this case the change of the feed volumetric flow rate inside the water tank. The dynamic analysis means mathematically the use one of numerical methods for solving of the ODE. The main groups of numerical methods are one-step methods for example Euler's method, Runge-Kutta's method, or multi-step methods Predictor-Corrector etc. [6]. The advantage of these methods is that they are easily programmable even more they are build-in functions in the mathematical software like Matlab [7], Mathematica etc. [8].

The adaptive control [9] approach here is based on the choice of the External Linear Model (ELM) of the originally nonlinear system [10], parameters of which are estimated recursively and the control design employs polynomial approach with pole-placement method and spectral factorization. These methods satisfies basic control requirements such as stability, disturbance attenuation and reference signal tracking.

The ELM here uses so called delta-models [11] which are special types of discrete-time models parameters of which are related to the sampling period which means that these parameters approaches to the continuous ones if the sampling period is adequately small.

The on-line identification was realized by the Recursive Least-Squares (RLS) Method which is simple, easily programmable method and if we combine this method with some kind of forgetting, for example exponential or directional, it provides satisfactory results.

All methods are verified by simulations in the mathematical software Matlab, version 7.0.1.

## II. MODEL OF THE WATER TANK

The equipment under the consideration is the real model of the water tank which is one part of the Multifunctional process control teaching system PCT40 from Armfield [4] – see Fig. 1. The PCT40 includes also other models of processes such as Continuous Stirred Tank Reactor (CSTR) or heat exchanger.

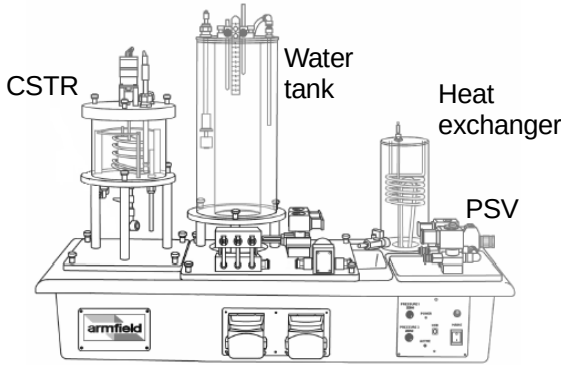


Fig. 1 Multifunctional process control teaching system PCT40

This system combines both modelling techniques – it is small representation of the water tank with the volume of 4-liter original of which is usually much bigger with huge volume. The mathematical model of this system could be also easily derived. The schematic representation of the water tank can be found in Fig. 2.

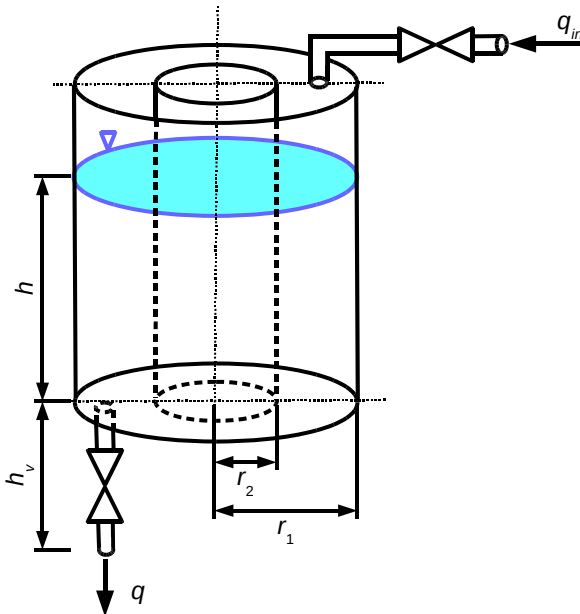


Fig. 2 Schematic representation of the water tank

The model consists of plastic transparent cylinder with inner radius  $r_1 = 0.087 \text{ m}$ . There is another plastic transparent cylinder inside due to quicker dynamic response of the system lower usage of feeding water. The outer radius of this smaller cylinder is  $r_2 = 0.057 \text{ m}$  and the maximal water level in the tank is  $h_{max} = 0.3 \text{ m}$ .

In the Fig. 2,  $q$  denotes the volumetric flow rate,  $h$  is used for the water level and  $r$  are radiuses of inner and outer cylinders. The input variable is the volumetric flow rate of the feeding water  $q_{in}$  and state variables are water level  $h$  in the tank and output volumetric flow rate of the water which comes from the tank,  $q$ .

The mathematical model comes from the material balance inside the tank which is in the word form [3]:

$$\boxed{\text{Flow rate into the system}} = \boxed{\text{Flow rate out of the system}} + \boxed{\text{Rate of accumulation}}$$

and mathematically:

$$q_{in} = q + \frac{dV}{dt} \quad (1)$$

where  $V$  is a volume of the water inside the tank and  $t$  is used for the time.

The volume of the tank is generally

$$V = F \cdot h \quad (2)$$

for  $F$  as a area of the base due to cylindrical shape of the tank. It means, that balance (1) could be rewritten to the form

$$q_{in} = q + F \cdot \frac{dh}{dt} \quad (3)$$

where  $F$  is in this case

$$F = \pi \cdot r_1^2 - \pi \cdot r_2^2 = 1.36 \cdot 10^{-2} \text{ m}^2 \quad (4)$$

It is also known, that volumetric flow rate through the water valve is nonlinear function of the water level, i.e.

$$q = k \cdot \sqrt{h} \quad (5)$$

where  $k$  is a valve constant which is specific for each valve and depend on the geometry and type of the valve.

If we put equation (5) inside (3) the resulting mathematical model is:

$$\frac{dh}{dt} = \frac{q_{in} - k \cdot \sqrt{h}}{F} \quad (6)$$

There should be introduced one simplification – the height of the discharging valve,  $h_v$  in Fig. 2, is neglected.

The unknown constant  $k$  could be computed for example from the steady state (variables with superscript  $(\cdot)^s$ ), where  $q_{in}^s = q^s$  and equation (5) is

$$q^s = k \cdot \sqrt{h^s} \Rightarrow k = \frac{q^s}{\sqrt{h^s}} \quad (7)$$

The water tank is fed via Proportioning Solenoid Valve (PSV) which could be operated in the range 0 – 100%. This range is from the practical point of view limited to the range  $0 - 2.5 \cdot 10^{-5} \text{ m}^3 \cdot \text{s}^{-1}$ .

The equation (7) have still one unknown – the constant of the outlet valve,  $k$ . This constant could be computed from the reference measurement where we know the input volumetric flow rate,  $q_{in}$ , and after some time also the steady-state value of the water level,  $h^s$ . For example, we made the measurement for the step change from 0 to 60% of the volumetric flow rate and the results are shown in Fig. 3 – solid line.

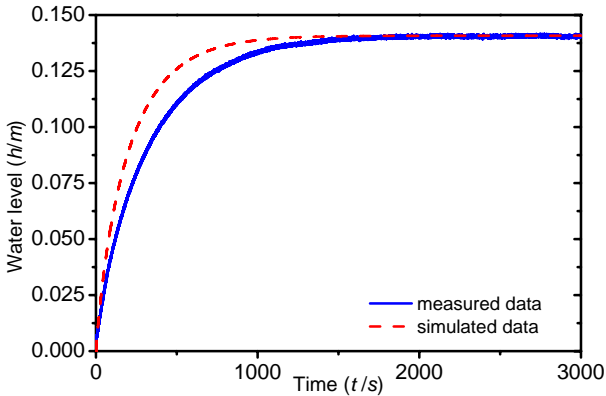


Fig. 3 Measured and simulated data for  $q_{in} = 1.5 \cdot 10^{-5} \text{ m}^3 \cdot \text{s}^{-1}$  – computation without the valve

The volumetric flow rate is in this case  $q_{in} = 1.5 \cdot 10^{-5} \text{ m}^3 \cdot \text{s}^{-1}$  and the final (steady-state) value of the water level  $h$  is  $h^s = 0.141 \text{ m}$ . It means, that the valve constant  $k$  is

$$k = \frac{q_{in}}{\sqrt{h^s}} = \frac{1.5 \cdot 10^{-5}}{\sqrt{0.141}} = 4.01 \cdot 10^{-5} \quad (8)$$

The simulation is very often connected to the verification part because it is good to know if the derived mathematical model is accurate enough.

The result of the first simulation analysis for the same input volumetric flow rate  $q_{in} = 1.5 \cdot 10^{-5} \text{ m}^3 \cdot \text{s}^{-1}$  is shown in Fig. 3 – the dashed line. It is clear, that although simulated and measured outputs reaches the same final value, the dynamics is much different – the mathematical model has quicker output response. This statement means that the mathematical model (6) is not accurate and we must neglect some simplifications. In this case we did not take into the account the height of the valve,  $h_v = 0.076 \text{ m}$ , which has also impact to the mathematical model of the system.

If we count with this height, new constant of the valve for the same step change as in previous case is

$$k = \frac{q_{in}}{\sqrt{h^s}} = \frac{1.5 \cdot 10^{-5}}{\sqrt{(0.141 + 0.076)}} = 3.22 \cdot 10^{-5} \quad (9)$$

The comparison of the measured and simulated data for this new constant of the valve is shown in Fig. 4.

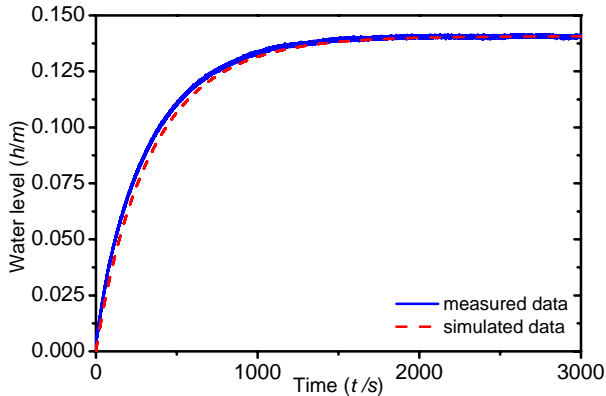


Fig. 4 Measured and simulated data for  $q_{in} = 1.5 \cdot 10^{-5} \text{ m}^3 \cdot \text{s}^{-1}$  – computation with the valve

#### A. Steady-state Analysis.

The steady-state analysis means that we solve the mathematical model with the condition  $d(\cdot)/dt = 0$ , i.e. ODE (6) is transferred to the nonlinear algebraic equation:

$$h^s(q_{in}) = \left( \frac{q_{in}}{k} \right)^2 \quad (10)$$

where the optional variable is the input volumetric flow rate,  $q_{in}$ . There were done simulation analysis for the range  $q_{in} = \langle 0; 2.5 \cdot 10^{-5} \rangle \text{ m}^3 \cdot \text{s}^{-1}$  and results are shown in the Fig. 5.

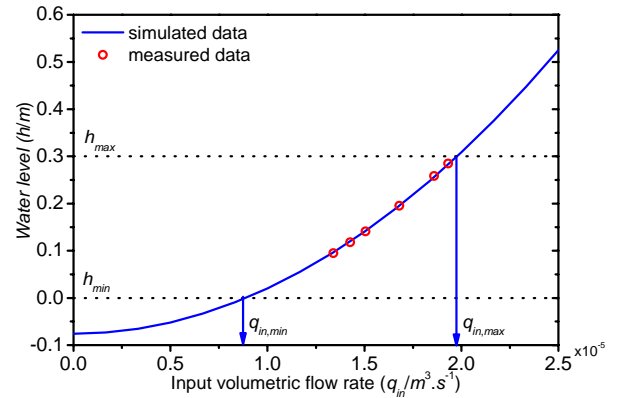


Fig. 5 The steady-state analysis of the mathematical model

This analysis shows nonlinear behavior of the system and also we can choose the volumetric flow rate in the range  $q_{in} = \langle 8.86 \cdot 10^{-6}; 1.98 \cdot 10^{-5} \rangle \text{ m}^3 \cdot \text{s}^{-1}$  because lower value of  $q_{in}$  means that we did not get enough water in the tank and vice versa – the flow rate bigger than  $q_{in} = 1.98 \cdot 10^{-5} \text{ m}^3 \cdot \text{s}^{-1}$  results in bigger water level than its maximal value  $h_{max}$ . Dots in the Fig. 5 display results of measured steady-state values.

#### B. Dynamic Analysis.

The dynamic analysis solves the ODE with the use of some numerical methods. In this case, the Runge-Kutta's standard method was used because it is easily programmable and even more it is build-in function in used mathematical software Matlab. The working point was characterized by the input volumetric flow rate  $q_{in}^s = 1.5 \cdot 10^{-5} \text{ m}^3 \cdot \text{s}^{-1}$  which is in the middle of the operating interval defined after the static analysis in the Fig. 5.

The input variable,  $u(t)$ , is the change of the initial  $q_{in}^s$  in % and the output variable is the water level in the tank. The input and the output variables are then generally:

$$u(t) = \frac{q_{in}(t) - q_{in}^s}{q_{in}^s} \cdot 100 [\%]; \quad y(t) = h(t) [m] \quad (11)$$

The simulation time was 3000 s, six step changes of the input variable  $u(t)$  were done and results are shown in Fig. 6.

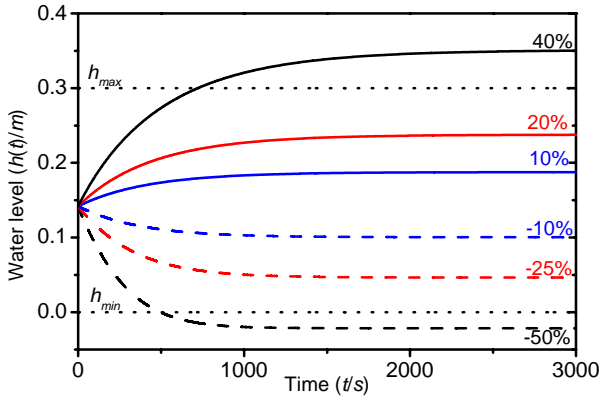


Fig. 6 The dynamic analysis for various step changes of the input volumetric flow rate  $q_{in}$

Output responses show that this output has asymmetric responses – the final value is different in sign and also in order for positive and negative step changes. Even more, for it is inappropriate to choose the input step change of the volumetric flow rate lower than approximately -40% and bigger than +30% because the resulted water level is lower or higher than physical properties of the water tank.

### III. ADAPTIVE CONTROL

The adaptive control was used for control of this system. There are several adaptive approaches which can be used. The method here uses External Linear Model (ELM) as a linear description of the originally nonlinear system. Parameters of and the structure of the controller are derived from this ELM and its parameters are identified recursively during the control. Parameters of the controller are recomputed in each time period too which means that this controller adopts its parameters according to the actual state and behavior of the controlled system.

In this case, all output responses in Fig. 6 could be expressed by the first or the second order transfer functions (TF), for example in the continuous-time

$$G_1(s) = \frac{b(s)}{a(s)} = \frac{b_0}{s + a_0} \quad (12)$$

$$G_2(s) = \frac{b(s)}{a(s)} = \frac{b_1s + b_0}{s^2 + a_1s + a_0}$$

#### A. Control System Synthesis

The controller is constructed with the use of polynomial synthesis and the control structure with 1DOF is shown in Fig. 7.

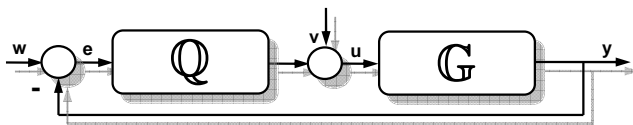


Fig. 7 1DOF control configuration

The block  $G$  denotes transfer function (12) of controlled

plant,  $w$  is the reference signal (wanted value),  $v$  is disturbance,  $e$  is used for control error,  $u$  is control variable and  $y$  is a controlled output. The transfer function of the feedforward part  $Q(s)$  of the controller is designed with the use of polynomial synthesis:

$$\tilde{Q}(s) = \frac{q(s)}{s \cdot \tilde{p}(s)} \quad (13)$$

where degrees of polynomials  $\tilde{p}(s)$  and  $q(s)$  are computed from:

$$\deg q(s) = \deg a(s) + \deg f(s) - 1 \quad (14)$$

$$\deg \tilde{p}(s) \geq \deg a(s) - 1$$

and parameters of these polynomials are computed by the Method of uncertain coefficients which compares coefficients of individual  $s$ -powers from the Diophantine equation, e.g. [12]:

$$a(s) \cdot s \cdot \tilde{p}(s) + b(s) \cdot q(s) = d(s) \quad (15)$$

and the polynomial  $d(s)$  on the right side of (15) is an optional stable polynomial. It is obvious, that the degree of this polynomial is:

$$\deg d(s) = \deg a(s) + \deg \tilde{p}(s) + 1 \quad (16)$$

Roots of this polynomial are called poles of the closed-loop and their position affects quality of the control.

This polynomial could be designed for example with the use of Pole-placement method. A choice of roots needs some a priori information about the system's behavior. It is good to connect poles with the parameters of the system via spectral factorization. The polynomial  $d(s)$  can be then rewritten to the form

$$d(s) = n(s) \cdot (s + \alpha_i)^{\deg d - \deg n} \quad (17)$$

where  $\alpha_i > 0$  is an optional coefficient reflecting closed-loop poles and stable polynomial  $n(s)$  is obtained from the spectral factorization of the polynomial  $a(s)$

$$n^*(s) \cdot n(s) = a^*(s) \cdot a(s) \quad (18)$$

The Diophantine equation (15), as it is, is valid for step changes of the reference and disturbance signals which means that  $\deg f(s) = 1$  in (14). The feedback controller  $Q(s)$  ensures stability, load disturbance attenuation and asymptotic tracking of the reference signal.

#### B. External Linear Model (ELM)

The ELM here comes from the dynamic analysis as it is written above. The TF in (12) belongs to the class of continuous-time (CT) models. The identification of such processes is not very easy.

One way, how we can overcome this problem is the use of so called  $\delta$ -model. This model belongs to the class of discrete models but its parameters are close to the continuous ones for very small sampling period as it is proved in [13].

The  $\delta$ -model introduces a new complex variable  $\gamma$ , for example

$$\gamma = \frac{z-1}{T_s} \quad (19)$$

If we choose for simplification first order TF  $G_1$  in (12), the differential equation will be

$$y_\delta(k) = b_0^\delta u_\delta(k-1) - a_0^\delta y_\delta(k-1) \quad (20)$$

where  $b_0^\delta$  and  $a_0^\delta$  are delta parameters different from the parameters  $b_0$  and  $a_0$  in (12) and the individual parts in Equation (20) can be written as

$$y_\delta(k) = \frac{y(k) - y(k-1)}{T_v}; \quad u_\delta(k-1) = u(k-1) \quad (21)$$

$$y_\delta(k-1) = y(k-1);$$

The regression vector  $\varphi_\delta$  is then

$$\varphi_\delta(k-1) = [-y_\delta(k-1), u_\delta(k-1)]^T \quad (22)$$

and the vector of parameters  $\theta_\delta$  is generally

$$\theta_\delta(k) = [a_1^\delta, a_0^\delta, b_1^\delta, b_0^\delta]^T \quad (23)$$

which is computed from the differential equation

$$y_\delta(k) = \theta_\delta^T(k) \cdot \varphi_\delta(k-1) + e(k) \quad (24)$$

where  $e(k)$  is a general random immeasurable component.

As it is written in the previous part, control system synthesis is done in continuous time, but recursive identification uses discrete time steps. The resulted, so called “hybrid”, controller works in the continuous time but parameters of the polynomials  $a(s)$  and  $b(s)$  are identified recursively in the sampling period  $T_v$ . This assumption results in the condition, that the parameters of the  $\delta$ -model are close the continuous ones for the small sampling period.

#### IV. SIMULATION RESULTS

Simulation analyses do the control exercises on the mathematical model of the water tank (6) where the reference signal (wanted value) is the level of the water in the tank,  $h$ , which is controlled by the change of the input volumetric flow rate  $q_{in}$ .

The sampling period was  $T_v = 1$  s, the simulation time was 5000 s and 5 different step changes of the reference signal was done during this time. The controller could be tuned with the choice of the parameter  $\alpha_i$ . The affect of this parameter are shown in following figures.

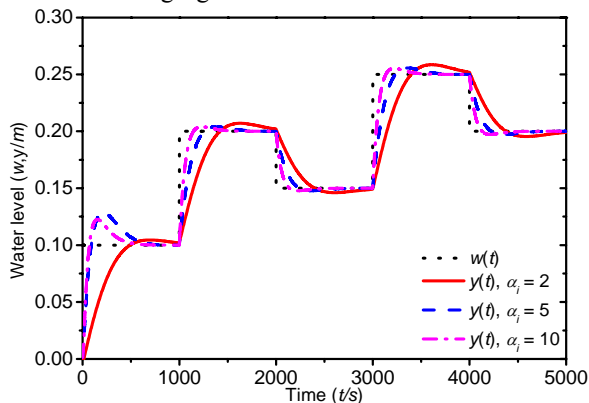


Fig. 8 The course of the reference signal,  $w(t)$ , and the output variable,  $y(t)$ , for different values of  $\alpha_i$

The Fig. 8 clearly shows the effect of the tuning parameter

$\alpha_i$  – increasing value of this parameter results in quicker output response with the overshoots. The output response for the lowest value, i.e.  $\alpha_i = 2$ , produces more smoother course of the output variable without the overshoot at the very beginning in the first step change.

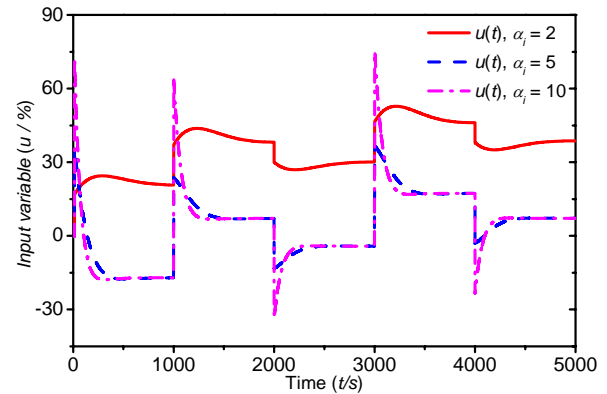


Fig. 9 The course of the input variable,  $u(t)$ , for different values of  $\alpha_i$

The course of the input variable on the other side is very similar for  $\alpha_i = 5$  and 10. The third course for  $\alpha_i = 2$  is different and smoother on the contrary.

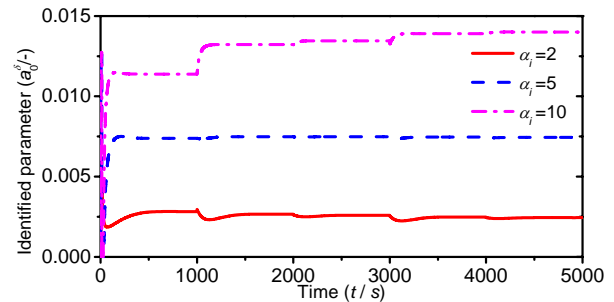


Fig. 10 The course of the identified parameter  $a_0^\delta$  for different values of  $\alpha_i$

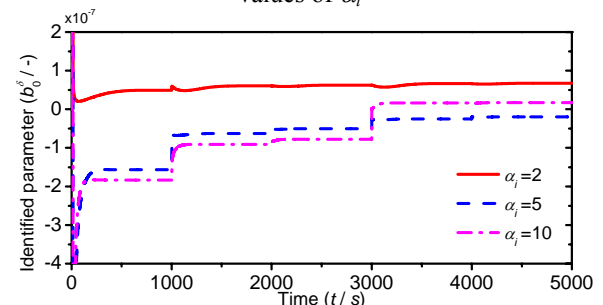


Fig. 11 The course of the identified parameter  $b_0^\delta$  for different values of  $\alpha_i$

Last graphs in Fig. 10 and Fig. 11 shows values of the estimated parameters  $a_0^\delta$  and  $b_0^\delta$ . It is clear, that used recursive identification has not problem with the on-line identification except the very beginning of the control, which is caused by the uncertainty of the system which needs some time for estimation of the real parameters of the system. This is typical feature of this type of adaptive control.

## V. CONCLUSION

The goal of this contribution is to show one way how to design the controller for the real system. At first, the mathematical model with one ordinary differential equation is derived. This model was then verified by the simulations of the steady-state and dynamics and the results are compared with the measurements on the real system. This comparison shows disproportion between simulated and measured data which is caused by the inaccuracy of the model which does not take into the account the height of the outlet valve. If we include this height into the computation, the results are much more accurate. The control approach here is based on the choice of the external linear model of the originally nonlinear system, parameters of which are identified recursively. The simple controller with one degree-of-freedom is designed with the use of polynomial approach with pole-placement method and spectral factorization. The resulted controller is stable and satisfies basic control requirements. Moreover, it can be tuned by the choice of the parameter  $\alpha_i$  – increasing value of this parameter results in quicker output response but possible overshoots. Introduced hybrid adaptive controller produces good control results although the system has nonlinear behavior. The future work is connected with the verification of the proposed control strategy on the real model of the water tank.

## REFERENCES

- [1] Luyben, W. L. 1989. *Process Modelling, Simulation and Control for Chemical Engineers*. McGraw-Hill, New York 1989. ISBN 0-07-039-1599
- [2] Maria A. 1997. Introduction to modeling and simulation. In: *Proceedings of the 1997 Winter Simulation Conference*. 7-13.
- [3] Ingham, J.; I. J. Dunn; E. Heinzle; J. E. Prenosil. 2000 *Chemical Engineering Dynamics. An Introduction to Modeling and Computer Simulation*. Second. Completely Revised Edition. VCH Verlagsgesellschaft. Weinheim, 2000. ISBN 3-527-29776-6.
- [4] Armfield: Instruction manual PCT40, Issue 4, February 2005
- [5] Saad, Y. 2003. *Iterative Methods for Sparse Linear Systems*. Society for Industrial & Applied. ISBN 08-987-153-42
- [6] Johnston, R. L. 1982. *Numerical Methods*. John Wiley & Sons. ISBN 04-718-666-44
- [7] Mathews, J. H.; K. K. Fink. 2004. *Numerical Methods Using Matlab*. Prentice-Hall. ISBN 01-306-524-82.
- [8] Kaw, K.; C. Nguyen; L. Snyder. 2014. *Holistic Numerical Methods*. Available online <<http://mathforcollege.com/nm/>>
- [9] Astrom, K.J., Wittenmark, B. 1989: *Adaptive Control*. Addison Wesley. Reading, MA, 1989, ISBN 0-201-09720-6.
- [10] Bobal, V.; J. Böhm; J. Fessler; J. Machacek. 2005 *Digital Self-tuning Controllers: Algorithms, Implementation and Applications*. Advanced Textbooks in Control and Signal Processing. Springer-Verlag London Limited. 2005, ISBN 1-85233-980-2.
- [11] Middleton, H., Goodwin, G. C. 2004: *Digital Control and Estimation - A Unified Approach*. Prentice Hall. Englewood Cliffs, 2004, ISBN 0-13-211798-3.
- [12] Kucera, V 1993. Diophantine equations in control – A survey. *Automatica*. 29, 1993, p. 1361-1375.
- [13] Stericker, D. L., Sinha, N. K. 1993: Identification of continuous-time systems from samples of input-output data using the  $\delta$ -operator". *Control-Theory and Advanced Technology*. vol. 9, 1993, 113-125.

# Real-time background/foreground segmentation of RGBD data

Abdenour amamra, Tarek mouats and Nabil aouf

**Abstract** - This paper presents a novel approach for background/foreground segmentation of RGBD data with the Gaussian Mixture Models (GMM). We first start by the background subtraction from the colour and depth images separately. The foregrounds resulting from both streams are then fused for a more accurate detection. Our segmentation solution is implemented on the GPU. Thus, it works at the full frame rate of the sensor (30fps). Test results show its robustness against illumination change, shadows and reflections.

**Keywords** - Background subtraction; Gaussian Mixture Models; RGBD sensors; real-time tracking; image data fusion.

## I. INTRODUCTION

NOWADAYS, real-time object tracking has become one of the largest studied subjects in robotics and computer vision domains. To track moving objects with a camera, we first need to detect them in the image. This detection requires a tool able to extract foreground pixels using a background model. Hence arises the need to decide whether a new frame contains foreground regions or not. In addition, where the detected objects are located if there are any.

Several problems should be tackled by a good background removal algorithm. Such algorithm should be robust against non-stationary backgrounds like waving trees, sudden illumination changes and camouflage. Most of the current algorithms in the literature are able to decently cope with all the issues listed above. However, robustness and processing time constraints are critical requirements for a real-time tracking solution. To this end, we propose a new approach based on a well-established foreground/background segmentation algorithm (GMM) that uses two modalities (colour and depth images) to extract foreground regions. Furthermore, we benefit from the growing power of the GPUs to handle the relatively large amount of data in real-time.

## II. RELATED WORK

Many works from the literature addressed the possibility to jointly use the depth and colour images for foreground/background segmentation. Cristani et al. [2] proposed an overview on background subtraction solutions for mono as well as stereo cameras. Abramoff et al. [3] used a stereo pair of cameras for an automatic segmentation algorithm. Gordon et al. [1] added the disparity information to the GMM for background modelling. In their approach, the authors found that the combination of stereo and colour data helps to overcome the classic problems of colour segmentation. However, stereo images themselves result from a pair of RGB

images. Thus, they hold weaknesses toward illumination change and shadow. Friedman and Russell first proposed the GMM approach for background removal [3]. Few years later, innovations were introduced to the basic model by Stauffer and Grimson [4]. Their paper is often considered as the reference of the GMM for background/foreground segmentation. Lee et al. [2] later proposed a GPU implementation of Stauffer and Grimson's algorithm.

To the best of the author's knowledge, this work is the first time when GMM background subtraction algorithm is implemented on the GPU for joint colour and depth background removal. Our approach is innovative in three points: the data is streamed by a cheap depth camera. This data is both the colour image and the range map. Hence, two different modalities independent from each other. It also leverages the GPU to reduce the computational load.

## III. GAUSSIAN MIXTURE MODELS FOR RGBD DATA

### A. Background modelling

The GMM is a parametric probability density function represented as a weighted sum of Gaussian densities [5]. Foreground detection generally follows the steps listed below:

- Modelling the values of a particular pixel as  $\mathbf{M}$  ( $3 \leq \mathbf{M} \leq 5$ ) mixture of Gaussians  $\mathcal{G}\{\boldsymbol{\mu}_i, \boldsymbol{\sigma}_i, \mathbf{w}_i\}; 1 \leq i \leq \mathbf{M}$  Fig 1(a). Where each distribution is characterised by a mean  $\boldsymbol{\mu}_i$  and a variance  $\boldsymbol{\sigma}_i^2$  as well as a weighting factor  $\mathbf{w}_i$  to define the importance of each Gaussian. The  $\mathbf{w}_i$  are positive and add up to 1.
- Determining the Gaussian that corresponds to the background model based on the mean and the variance of each of the  $\mathbf{M}$  distributions.
- The foreground is then defined by the pixels that do not fit the background.
- Updating the Gaussians with the newly detected foreground pixels.
- The pixel values that do not match one of the  $\mathbf{M}$  background Gaussians are grouped to form a foreground blob.

For every new frame  $\mathbf{f}$ , the GMM algorithm computes the distance between the pixel  $\mathbf{f}(\mathbf{u}, \mathbf{v})$  and each of the means  $\boldsymbol{\mu}_i(\mathbf{u}, \mathbf{v})$  characterising the  $\mathbf{M}$  Gaussians Fig 1(b). We test the new pixel against the highly weighted distribution and vice

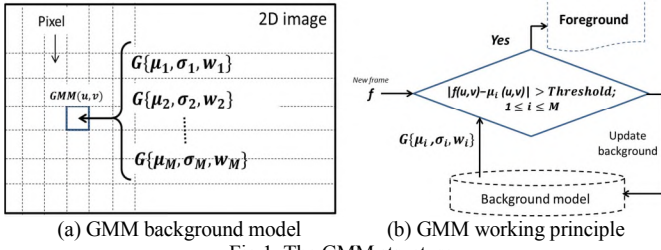


Fig 1. The GMM structure

versa. If the new pixel does not match any of the recorded distributions then it is a foreground element. The background model is then updated.

### B. GMM on RGBD data

Light intensity images are naturally sensitive to the illumination change and the shadow. On the other hand, the depth data is proven to be robust against the lighting of the scene. The concept of fusing the depth and the RGB images for background removal can be approached in two different ways: The first is the **augmentation** of the three colour channels with a fourth component for depth. The experimental test results showed that the resulting image still suffers from the classic artefacts of RGB based GMM. The contribution of the depth data in this segmentation model is weakened by the three other intensity bytes. Hence, the resulting image is almost the same as the one without considering depth information Fig 2.

On the other hand, in our work we have completely **separated** the two modalities during the background removal phase. In other word, we apply the GMM on the RGB image and the depth map independently. The resulting binary foreground images are combined to produce the final result Fig 3.

### C. RGBD Background fusion

Before mixing the results of the two independent segmentations, we transform the depth foreground image to the colour space. This mapping is required because the two modalities do not share the same reference frame. Afterwards, we adapt the algorithm in List 1 to fuse the two binary foreground images:

```

2D binary image f'_{i\_RGB}, f'_{i\_D}, I'_{Forg} // foreground
2D integer array cpt;
For every pixel (u,v)
  If (f'_{i\_RGB}(u,v) == f'_{i\_D}(u,v))
    I'_{Forg}(u,v) ← f'_{i\_D}(u,v)
    cpt(u,v) ← 0
  Else //different
    If (cpt(u,v) == +3)
      I'_{Forg}(u,v) ← f'_{i\_rgb}(u,v)
      cpt(u,v) ← 0
    Else if (cpt(u,v) == -3)
      I'_{Forg}(u,v) ← f'_{i\_d}(u,v)
      cpt(u,v) ← 0
    Else If (I'_{Forg}(u,v) == f'_{i\_rgb}(u,v))
      cpt(u,v) ← cpt(u,v)+1;
    Else If (I'_{Forg}(u,v) == f'_{i\_d}(u,v))
      cpt(u,v) ← cpt(u,v)-1;
  end
end
    
```

List 1. RGBD foreground fusion algorithm

When the two responses are different, then a decision should be taken regarding the fused outputs. To this end, we apply


 (a) RGB (b) RGB+D  
 Fig 2. RGBD segmentation (the depth as a fourth component)

 (a) RGB (b) RGB+D (c) RGB&D  
 Fig 3. RGBD segmentation (the depth as a separate component)

this rule: The pixel keeps the same state (as it was before the confusion occurs), as long as no three successive frames sharing the same state are streamed List 1. This assumption is motivated by the fact that we noticed that permanent incoherence between the colour and the depth GMMs is considered as a noise disturbing the current state of the pixel.

## IV. GPU ACCELERATION OF THE GMM

Naturally, image data can be processed in parallel on the GPU by associating a thread to each pixel. In our case, we only use VGA resolution (640×480) colour and depth data. When we naively adapt such approach (thread to each pixel), the maximum achievable frame rate on the GPU was **18fps**. Consequently, other optimisation strategies should be taken into account to fully exploit all the available hardware capability. Basically, the design of heterogeneous algorithms aims a higher occupancy of the processors and a full usage of the bandwidth when exchanging data within the GPU and between the central memory (RAM) and the global memory of the GPU (GMGPU). To this end, we focus on: **running asynchronous transfers** of the following frame ( $f_{i+1}$ ) from the RAM to the GMGPU, and the already available result from GMGPU to the RAM ( $f_{i-1}$ ). Simultaneously, the current frame ( $f_i$ ) is processed on the device Fig 4(a). We perform the exchange of data on the bus when the GPU processes the current frame.

**Memory coalescing** is another optimisation that significantly helps to increase the probability of threads in the same warp to feed from neighbouring memory placements. Appropriately organising the data in the device memory allows such contiguous access to automatically happen. Fig 4(b) illustrates what happens when a thread calls a given cell in the global memory. The GPU automatically loads the content of the adjacent cells because the internal design of the device assumes that it is highly probable that the neighbouring data will be sooner requested as well [6]. The programmer should consider this fact by transforming the array of structures data to a structure of arrays. We therefore apply some changes on our

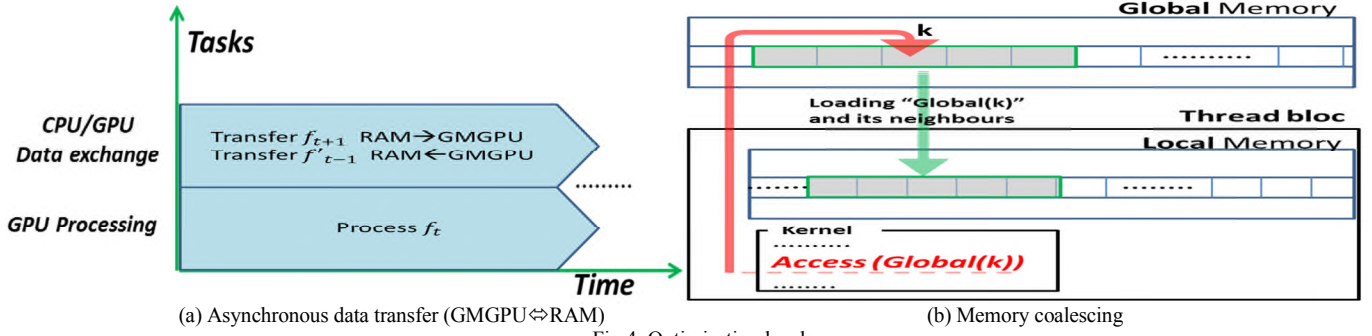


Fig 4. Optimisation levels

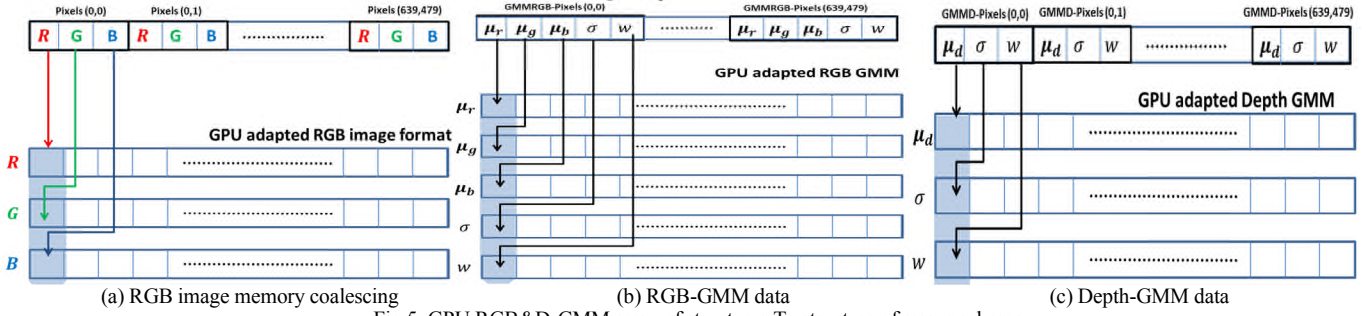


Fig 5. GPU RGB&amp;D-GMM array of structures To structure of arrays scheme

RGB image. In other words, the RGB data is transformed to three arrays each corresponding to the one of the channels (Red, Green and Blue) Fig 5(a). On the other hand, the depth map does not need to be reorganised as it naturally holds one component, which is the actual depth reading. We apply the same change on all the parameters of the GMM by splitting them on contiguous arrays Fig 5(b), (c). The kernel is shown in List 2.

```

CPU Data  $f_{i\_RGB}, F_{i\_D}, R, T, f_{i\_D}, I_{Forg}$ ;
GPU Data  $f'_{i\_RGB}, f'_{i\_D}, I'_{Forg}$ ;

// read a pair of images from the sensor
LoadNewPairOfFrames ( $f_{i\_RGB}, F_{i\_D}$ )
// map the depth data to fit the RGB image
AlignDepthOnRGB( $f_{i\_RGB}, F_{i\_D}, R, T$ )
// filter the depth map  $F_{i\_D}$ 
FilterDepth( $F_{i\_D}, f_{i\_D}$ )
// upload the newly received frames to the GPU
CopyAsyn_RAM->GPU( $f_{i\_RGB}, f_{i\_D}, f'_{i\_RGB}, f'_{i\_D}$ )
// download resulting foreground image from the GPU
CopyAsyn_GPU->RAM( $I_{Forg}, I'_{Forg}$ )
// launch background removal Kernel
LaunchKernelGMM<<...>>( $f'_{i\_RGB}, f'_{i\_D}, I'_{Forg}$ )
    
```

List 2. Background removal algorithm

## V. KINECT DEPTH FILLING

Before being segmented, the raw depth map output by the sensor can be corrected with a hole filling approach. The latter is necessary to exploit as much as possible the augmentation of our segmentation algorithm with depth data. We used Kinect as an RGBD sensor which is well-known that the generated depth map contains holes. It is also well-known that the Kinect's generated depth map might contain holes (i.e. gaps). This is

mainly due to the sensors involved in the process. In particular, this problem arises when the imaged scene contains transparent and specular surfaces. Several approaches have been investigated to deal with this failure. One particular path of interest is the multispectral stereo matching. Indeed, successful stereo matching leads to disparity maps from where one can infer depth maps. The latter can then be fused with the Kinect's own depth map. However, it is to be noted that visible imagery and near infrared (NIR) imagery differ greatly. Indeed, knowing the value of a pixel in an RGB image does not give any indication on its value in its NIR counterpart. In [7] authors started by investigating how the RGB channels can be combined in order to mimic the image response of the NIR sensor. They then generalized their framework in [8] by proposing a learning strategy for combining the RGB channels. Other alternatives to depth gap filling were also investigated and mainly focus on filtering techniques such as bilateral filtering and its varieties [9]. In this work, we focus on the problem addressed in [7], [8] and give a more general solution. Our interest is therefore computing a second depth map to be fused with the Kinect's. We took inspiration from our previous work on multispectral stereo matching [10]. Instead of learning to combine RGB channels to resemble NIR imagery, we represent both images using moment images. As it is shown in Fig 6, the images are alike using this representation.

According to [11], the geometric moment of the image pixel  $I(x, y)$  with respect to a window neighborhood of size  $(2N + 1)$  is given by:

$$m_{pq}(I(x, y)) = \sum_{i=-N}^N \sum_{j=-N}^N i^p j^q I(x - i, y - j) \quad (1)$$

where  $p$  and  $q$  represent the orders of the moment in the corresponding axis. As suggested in [10], the alternative image representation by means of image moment provides invariance

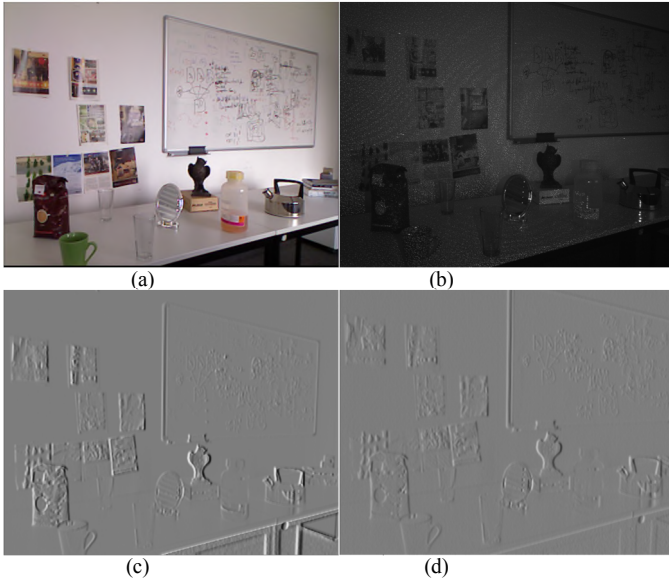


Fig 6. Illustration of the original images (a) (b) with their moment images (c) (d).

to illumination changes. This representation is obtained by combining different image moments of the original image  $I(x, y)$  to compute the moment image  $J(x, y)$  as follows:

$$J(x, y) = \frac{m_{01}(I(x, y))}{m_{20}(I(x, y))} \quad (2)$$

The parameters  $p$  and  $q$  used in this specific representation of moment image were chosen to improve interest point matching by mapping the original (non-similar) images into more similar images. Different parameters would yield different results that are not suitable for our aim.

In order to obtain dense disparity maps, we implemented a dense multimodal matching based on a modified version of OpenCV semi-global block matching. Alternatively, the approach presented in [10] can be used in a dense fashion. This is achieved by relaxing the threshold on the number of detected features in both modalities. The downside of this methodology is the added burden with regard to computation times.

## VI. EXPERIMENTAL RESULTS

### A. Hole filling

The proposed approach was tested against a dataset obtained generated in [7] using the Microsoft Kinect. The dataset contains a set of images obtained with covered IR projector and another set under normal operational conditions. Different neighborhood window sizes  $N$  were tested to compute the moment images. The value of  $N$  that yielded the best results was  $N = 5$ . An efficient approach was used to compute the moment images using adequate filters.

As shown on Fig 7, our methodology allows the recovery of Kinect's missing depth values. The approach was tested on images with the IR projector working normally (i.e. not covered). From Fig 7 (e), we can notice that the Kinect's disparity on textureless regions such as the wall and the table is remarkable. However, it fails on problematic surfaces (black areas in Fig 7 (e)). This is where our approach improves on the

original disparity map as shown in Fig 7 (d). The fusion scheme we used is a basic union operation of the original and the computed disparity maps as shown in Fig 7 (g).

### B. RGBD-GMM

To validate our finding, we conducted two experiments on an ordinary scene with two major illumination changes and a gently moving background, and a challenging scene where the illumination keeps changing during the whole capture. The evaluation parameter  $F_1$  [12] is computed based on the false and the true positives and negatives ( $TP, FP, TN, FN$ ). the *recall* is the true positive rate:

$$R = TP / (TP + FN) \quad (3)$$

And the *precision* which is the ratio between the number of correctly detected pixels and the total number of pixels marked as foreground.

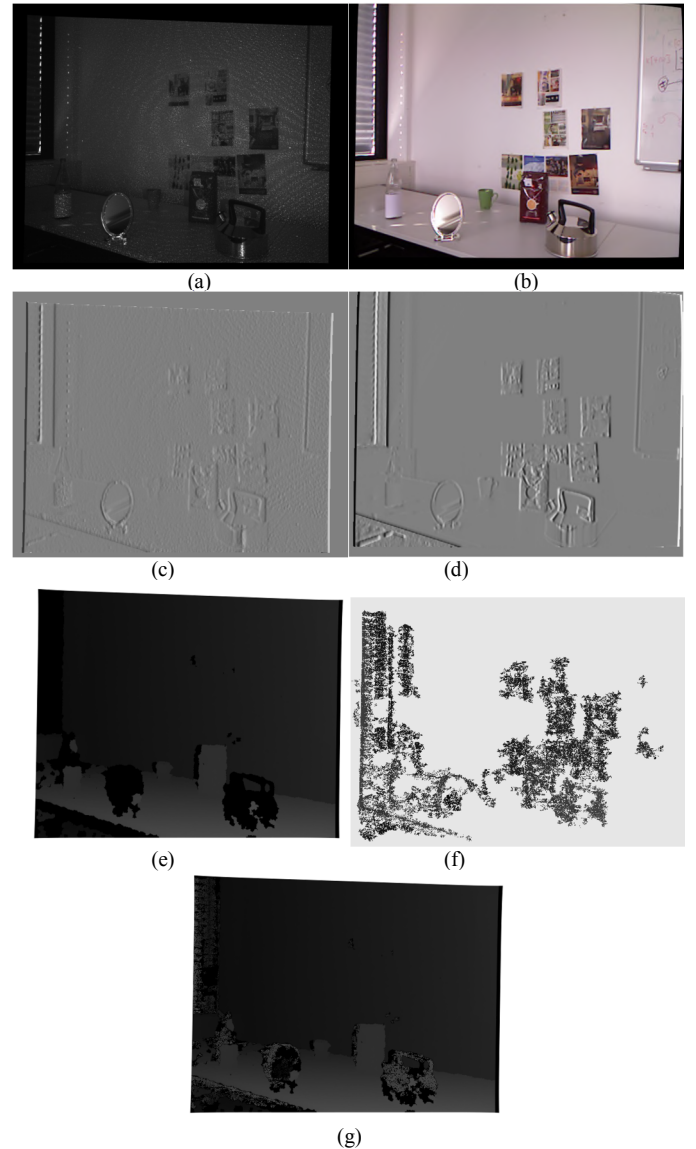


Fig 7. Illustration of obtained results with our approach: (a) (b) original NIR and RGB images respectively (c) (d) their corresponding moment images (e) Kinect's disparity map (black correspond to gaps) (f) computed disparity map from the moment images (g) fused disparity maps.

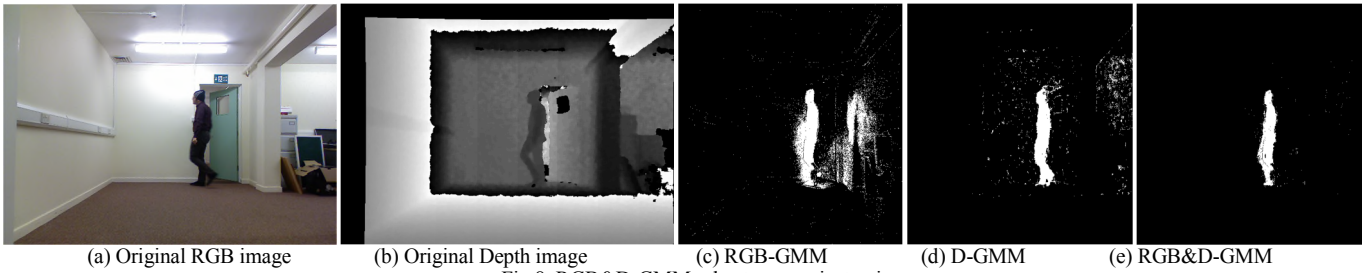


Fig 8. RGB&amp;D-GMM robustness against noise

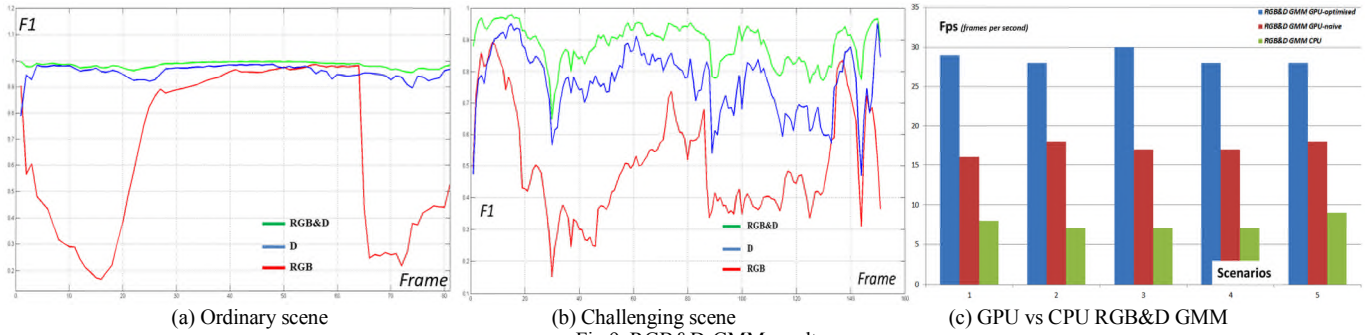


Fig 9. RGB&amp;D-GMM results

$$P = TP / (TP + FP) \quad (4)$$

Accuracy metric  $F_1$  combines the *precision* and *recall* to effectively evaluate the accuracy of segmentation

$$F_1 = 2 \frac{PR}{P+R} \quad (5)$$

$F_1$  is a good tool to evaluate the robustness. The higher the value of this metric becomes, the better the performance will be.

The graphs in Fig 9(a), (b) illustrate the behaviour of  $F_1$  in two different experiments where we plot  $F_1$  for all three responses (**RGB**, **Depth**, and the fusion of the two **RGB&D**). In Fig 9(a)  $F_1$  characterising the colour image undergoes two major drops which correspond to important perturbations mainly due to sudden illumination change (Red). Whereas, the depth map suffers less from problems of illuminations (Blue) its  $F_1$  mostly remains above 0.90.  $F_1$  for the fused outputs (Green) is above 0.97 which clearly shows the robustness of our segmentation algorithm. On the other hand, in Fig 9(b) all three methods suffer from perturbations along the whole capture. RGB image remains the most affected though. The depth map is also affected because the background was very dynamic but the latter kept the effectiveness.  $F_1$  mostly remains above 0.80 for the fused outputs although the highly challenging situation.

### C. Processing time metrics

The implementation of our algorithm in the GPU allowed us to fully benefit from the available frame rate of Kinect sensor (30fps). The latter remains just below 30fps for different five experimental scenarios. The effectiveness of the GPU can be clearly seen (blue and red bars in Fig 9(c), against the green bars). More importantly, the improvements after considering the memory coalescing and the data exchange optimisations increased the final frame rate of the segmentation algorithm to achieve almost 30fps.

## VII. CONCLUSION AND FUTURE WORKS

We presented an innovative approach to couple RGB and Depth images for real-time background removal. Based on native GMM (implemented on the CPU), we designed a parallel algorithm which benefits from asynchronous data exchange between the host (CPU) and the device (GPU). In addition, we organised our data structures in the GPU to permit a higher memory coalescing. We also proposed an approach to fill the holes in the native depth map of the depth camera. Finally, we validated our findings on some real test scenarios run in different conditions. The results were very promising, although we only applied background subtraction. This work opens a new perspective on using RGBD data to tackle the classic problems of RGB imagery. Our next step is to jointly using multiple RGBD sensors to detect moving robots in an indoor scene based on the background subtraction we already achieved.

## REFERENCES

- [1] G. Gordon, T. Darrell, M. Harville, and J. Woodfill, "Background estimation and removal based on range and color," in *Proceedings. 1999 IEEE Computer Society Conference on Computer Vision and Pattern Recognition (Cat. No PR00149)*, 1999, pp. 459–464.
- [2] S. Lee and C. Jeong, "Real-time Object Segmentation based on GPU," in *2006 International Conference on Computational Intelligence and Security*, 2006, pp. 739–742.
- [3] F. E. Alsaqre and Y. Baozong, "Moving object segmentation from video sequences: an edge approach," in *Proceedings EC-VIP-MC 2003. 4th EURASIP Conference focused on Video/Image Processing and Multimedia Communications (IEEE Cat. No.03EX667)*, 1997, vol. 1, pp. 193–199.
- [4] C. Stauffer and W. Grimson, "Adaptive background mixture models for real-time tracking," in *Proceedings. 1999 IEEE Computer Society Conference on Computer Vision and Pattern Recognition (Cat. No PR00149)*, 1999, pp. 246–252.
- [5] D. Reynolds, "Gaussian mixture models," *Encyclopedia of Biometrics*, 2009.

- [6] E. Kilgariff and R. Fernando, "The GeForce 6 series GPU architecture," *ACM SIGGRAPH 2005 Courses*, 2005.
- [7] W. Chiu, U. Blanke, and M. Fritz, "Improving the kinect by cross-modal stereo," *British Machine Vision Conf. BMVA*, pp. 1–10, 2011.
- [8] W.-C. Chiu, U. Blanke, and M. Fritz, "I spy with my little eye: Learning optimal filters for cross-modal stereo under projected patterns," in *2011 IEEE International Conference on Computer Vision Workshops (ICCV Workshops)*, 2011, pp. 1209–1214.
- [9] M. Camplani and L. Salgado, "Efficient spatio-temporal hole filling strategy for Kinect depth maps," in *Three-Dimensional Image Processing (3DIP) and Applications II*, 2012.
- [10] T. Mouats and N. Aouf, "Cross-Spectral Stereo Matching Based on Local Self-Similarities and Image Moments," *IEEE International Conference on Systems, Man, and Cybernetics*, pp. 4048–4053, Oct. 2013.
- [11] R. Mukundan and K. R. Ramakrishnan, *Moment Functions in Image Analysis — Theory and Applications*. World Scientific Publishing Co. Pte. Ltd., 1998.
- [12] E. J. Fernandez-Sanchez, J. Diaz, and E. Ros, "Background subtraction based on color and depth using active sensors.," *Sensors (Basel, Switzerland)*, vol. 13, no. 7, pp. 8895–915, Jan. 2013.

# Study of control forces and torques distribution algorithms for intelligent control of vehicle actuators

V. Pshikhopov, M. Medvedev, and V. Chufistov

**Abstract**—In this paper control forces and torques automatic distribution algorithms for a vehicle actuators are considered. Base control algorithm is designed by position and path control method for vehicles [1] – [3]. This control algorithm is based on kinematics and dynamics equations of vehicle. Distribution of control forces and torques between actuators is solved by applying of the pseudoinverse matrix. Another approach is mathematical programming problem solution. These two approaches does not separate control channel as it is in conventional control systems [4]. The considered methods are applied in the control system of unmanned airship. Modeling results and estimation of algorithms accuracy and performance are presented.

**Keywords**—Actuators, control, multilinked systems, vehicles.

## I. INTRODUCTION

MODERN control systems of vehicles are based on movement separation and control of actuator as single input – single output system [5], [6]. In other word separate component of vehicle motion is controlled by separate actuator. For example, an aircraft pitch is controlled by an elevator [7]. This approach limits the abilities of vehicle control systems and modern control design methods. In this paper control system consists of two levels. The high level is designed by position and path control design method for vehicle. The result of the system high level operation is control forces and torques. These forces and torques are inputs of the low level of the control system. But the output of the system low level is actuator’s thrusts and angles. Such approach is valid if performance of actuators is high. This approach is used in different vehicles control systems [3], [8] – [10]. In this case control system of actuator is local SISO system. Therefore the required thrusts and angles of engines are calculated as solution of the algebraic equations system. For instance, in [11] – [13] the algebraic equations system with

This work was supported by Russian Scientific Foundation (project 14-19-01533) in Southern Federal University, Rostov-on-Don, Russian Federation.

V. Pshikhopov is with the Southern Federal University, Rostov-on-Don, Russia (e-mail: pshichop@rambler.ru).

M. Medvedev is with the Southern Federal University, Rostov-on-Don, Russia (+7(8634)37-16-94; fax: +7(8634)68-18-94; e-mail: medvmihal@gmail.com).

V.Chufistov is with the Southern Federal University, Rostov-on-Don, Russia (e-mail: pshichop@rambler.ru).

rectangular matrix is solved by minimization of the required thrusts. In [12] – [13] the number of the algebraic system solutions is 96. Therefore the optimal solution is finding by exhaustive search in real time. In common case it is necessary to apply high performance algorithms.

## II. TASK STATEMENT

Let us consider a vehicle in a n-dimensional space. Control forces and torques are included in  $n \times 1$  vector  $F_u$ . The number of a vehicle actuators is  $m$ . Every actuator has three components  $[P_{ix} P_{iy} P_{iz}]^T$ ,  $i = \overline{1, m}$ . Coordinates of actuator is given by the vector  $[x_i y_i z_i]^T$ ,  $i = \overline{1, m}$ , in associated coordinate system. In this case components of actuator’s forces and components of the control vector satisfy the next matrix equation:

$$F_u = UP \tag{1}$$

where  $P = [P_{1x} P_{1y} P_{1z} P_{2x} P_{2y} P_{2z} \dots P_{mx} P_{my} P_{mz}]^T$ ;

$$U = \begin{pmatrix} 1 & 0 & 0 & 1 & 0 & 0 & \dots & 1 & 0 & 0 \\ 0 & 1 & 0 & 0 & 1 & 0 & \dots & 0 & 1 & 0 \\ 0 & 0 & 1 & 0 & 0 & 1 & \dots & 0 & 0 & 1 \\ 0 & z_1 & -y_1 & 0 & z_2 & -y_2 & \dots & 0 & z_m & -y_m \\ z_1 & 0 & -x_1 & z_2 & 0 & -x_2 & \dots & z_m & 0 & -x_m \\ -y_1 & x_1 & 0 & -y_2 & x_2 & 0 & \dots & -y_m & x_m & 0 \end{pmatrix} \tag{2}$$

It is necessary to find vector  $P$  as the most accurate solution of system (1).

## III. PROBLEM SOLUTION ON BASE OF PSEUDOINVERSE MATRIX

If  $U$  (2) is rectangular matrix, then system (1) has infinite set of solutions [14]. But the single solution determined by linear superposition of the rows and columns of conjugate matrix  $U^*$ . This solution is called pseudoinverse matrix  $U^+$  [14]. It is known that the pseudoinverse matrix  $U^+$  determines the best solution of system (1) in term of criterion of a minimum of least squares.

Thus vector  $P$  is:

$$P = U^+ F_u \tag{3}$$

Thrusts and rotation angles of actuators are:

$$p_i = \sqrt{P_{ix}^2 + P_{iy}^2 + P_{iz}^2} \quad (4)$$

$$\alpha_i = \arctan \frac{P_{iy}}{P_{ix}} \quad (5)$$

$$\beta_i = \arctan \frac{P_{iz}}{P_{ix}} \quad (6)$$

where  $p_i$  is the thrust of  $i$ -th actuator;  $\alpha_i$  is the rotation angle of  $i$ -th actuator in the vertical plane of associated coordinate system;  $\beta_i$  is the rotation angle of  $i$ -th actuator in the horizontal plane of associated coordinate system. Consider example of vehicle control system based on position and path method and algorithms (1) – (6). Consider control system of the prototype of stratospheric airship, similar to Lockheed-Martin P-791. It is shown in Fig. 1.

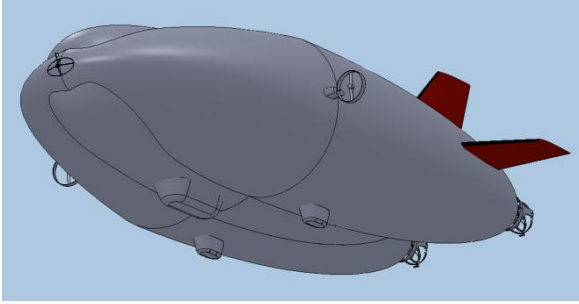


Fig. 1 Hybrid airship

Main parameters of the airship: length 38 m, width 17 m, height 10 m, envelope volume 4 100 m<sup>3</sup>, weight (with empty ballonets) 3 300 kg, one ballonnet volume 900 m<sup>3</sup>. Coordinates of gravity center in reference to volume center (0 m, -1.5 m, 0 m). Main propulsion engines generate thrust of 5 000 N each. Engines are rotated in vertical plane in range from -180° up to +180°. Coordinates of main engines gravity centers are (0 m, 0 m, ±9 m). Tail steering motors generates up to 500 N each. They rotate in range from -90° up to +90° both in horizontal and vertical planes. They are located in tail part of airship and have coordinates (-20 m; 0 m; ±3.5 m).

Thus vector  $P$  for the given airship is:

$$P = [P_{1x} P_{1y} P_{2x} P_{2y} P_{3x} P_{3y} P_{3z} P_{4x} P_{4y} P_{4z}]^T \quad (7)$$

The power of steering motors is poor to control lateral motion of the airship. Therefore position and path control system calculates 5×1 vector of the control forces and torques:

$$F_u = [F_{ux} F_{uy} N_{ux} N_{uy} N_{uz}]^T \quad (8)$$

Algorithms of calculation of vector (5) are presented in [2], [3], [15], [16].

In this case matrix (2) is:

$$U = \begin{bmatrix} 1 & 0 & 1 & 0 & 1 & 0 & 0 & 1 & 0 & 0 \\ 0 & 1 & 0 & 1 & 0 & 1 & 0 & 0 & 1 & 0 \\ 0 & z_1 & 0 & z_2 & 0 & z_3 & -y_3 & 0 & z_4 & -y_4 \\ z_1 & 0 & z_2 & 0 & z_3 & 0 & -x_3 & z_4 & 0 & -x_4 \\ -y_1 & x_1 & -y_2 & x_2 & -y_3 & x_3 & 0 & -y_4 & x_4 & 0 \end{bmatrix} \quad (9)$$

Coordinates of the airship propellers are:  $x_1=0$ ;  $x_2=0$ ;  $x_3=-$

21.63;  $x_4=-21.63$ ;  $y_1=0$ ;  $y_2=0$ ;  $y_3=0$ ;  $y_4=0$ ;  $z_1=-10.7$ ;  $z_2=10.7$ ;  $z_3=-4.1$ ;  $z_4=4.1$ .

Modeling results of the airship closed-loop system are presented in fig. 2 – 4. Linear coordinated of the airship are presented in fig. 2. The airship motors thrusts and rotation angles are presented in fig. 3 and fig. 4.

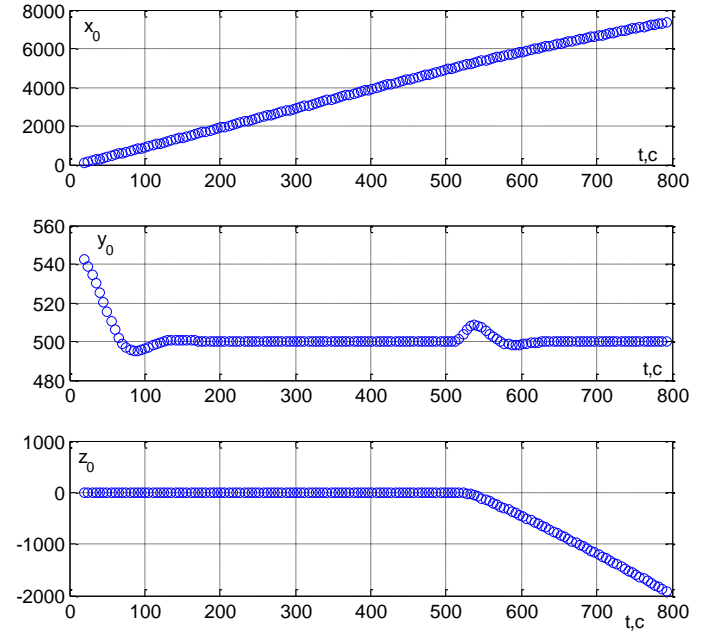


Fig. 2 The airship linear coordinates

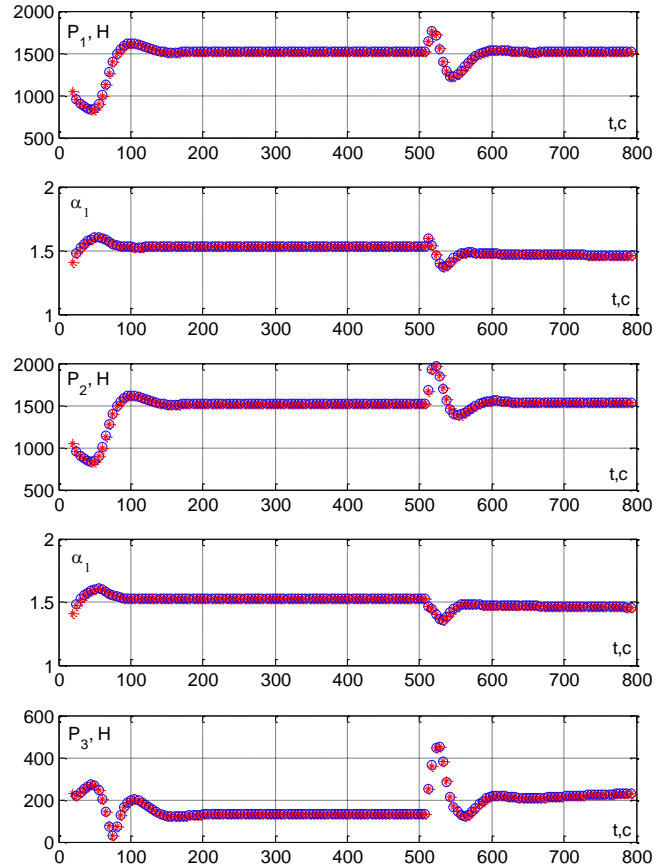


Fig. 3 The airship main motors thrusts and rotation angles

Notations in fig. 2 are:  $x_0$  and  $z_0$  are the airship coordinates in horizontal plane;  $y_0$  is altitude of the airship.

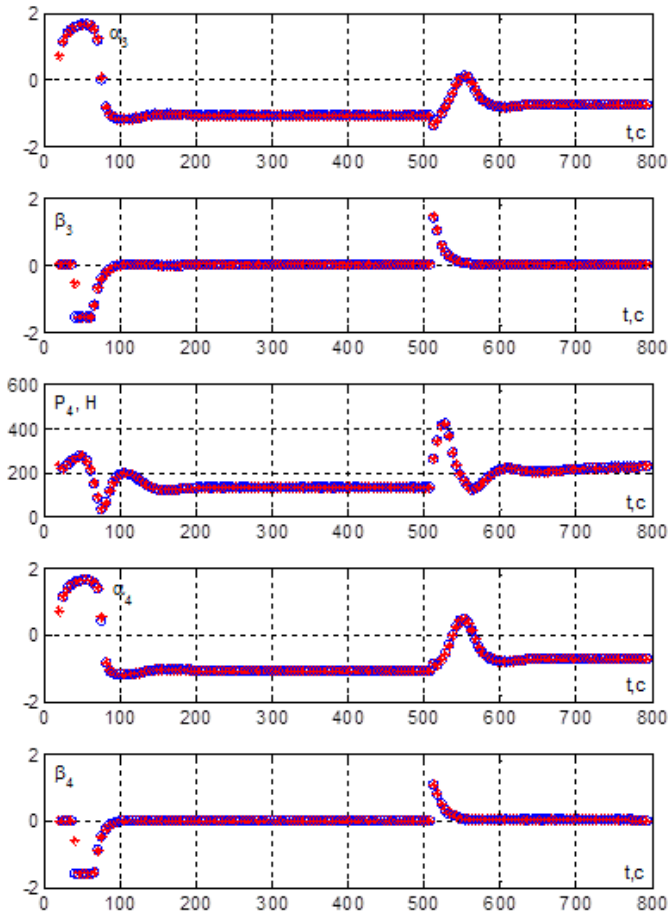


Fig. 4 The airship steering motors thrusts and rotation angles

On the first stage the airship is moving from point (0; 550; 0) to point (5000; 500; 0). After the airship is moving to point (7000; 500; 6000). The airship ground speed is 10 m/s. Wind speed is 5 m/s.

The main advantage of this method is automatic distribution of the control forced and torques between actuators. Searching operations and iterations are not used. Disadvantage of the method is miss of the motors thrusts and rotation angles limitations. But the limitations can be accounted after performing (1) – (6).

It is necessary to note that algorithms (1) – (6) allow synchronize vehicle actuators in the steady-state modes. In conventional vehicles control systems the synchronization of actuators is performing by designers for every movement mode. From fig. 3 and fig. 4 it is clear that thrusts and rotation angles of the left and right motors are equal to same values. In the transients thrusts and rotation angles of the left and right motors are different.

#### IV. PROBLEM SOLUTION ON BASE OF THE METHOD OF MATHEMATICAL PROGRAMMING

The problem described in section II can be formulated as the problem of mathematical programming:

$$P^* = \min_p (\text{norm}(F_u - UP)) \quad (10)$$

$$P_{1x}^2 + P_{1y}^2 < P_1^{\max}; P_{2x}^2 + P_{2y}^2 < P_2^{\max}; \quad (11)$$

$$P_{3x}^2 + P_{3y}^2 + P_{3z}^2 < P_3^{\max}; P_{4x}^2 + P_{4y}^2 + P_{4z}^2 < P_4^{\max}$$

where  $P_1^{\max}, P_2^{\max}, P_3^{\max}, P_4^{\max}$  are maximal values of the airship thrusts.

The problem (10), (11) is solved by Matlab function *fmincon*. This function is based on the trust-region-reflective algorithm [17]. Modeling results of the closed-loop control system of the airship are presented in fig. 5 and fig. 6.

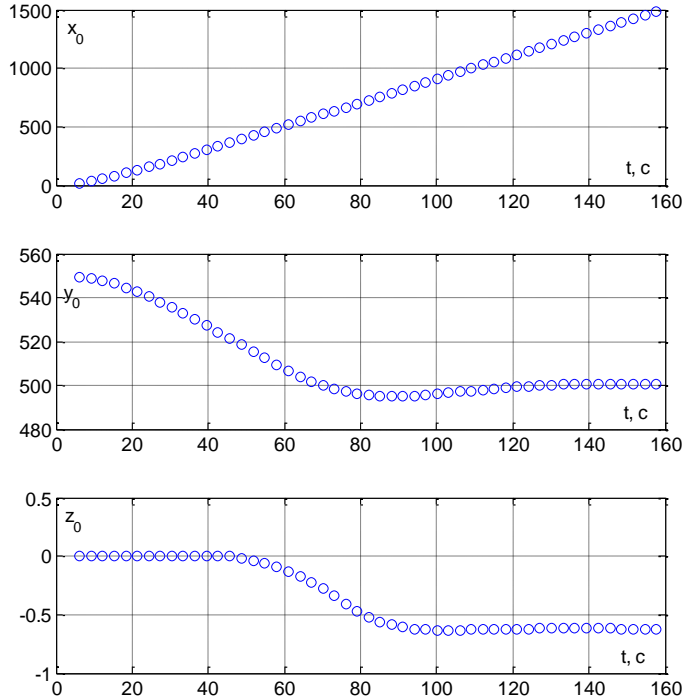


Fig. 5 The airship linear coordinates with problem (10), (11)

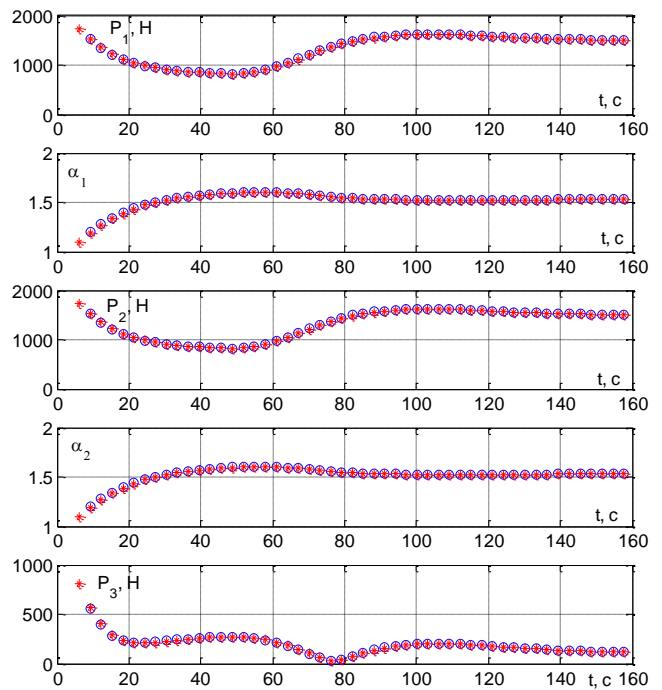


Fig. 6 The airship main motors thrusts and rotation angles with problem (10), (11)

The method of nonlinear mathematical programming allows to account nonlinear convex limitations in the searching area of (1). But the method of nonlinear mathematical programming requires high performance of the computer and depends from initial point of solution.

V. CONCLUSION

In this paper two methods of the control forces and torques distribution between vehicle actuators are studied. The problem is solution of the linear algebraic equations system with rectangular matrix. The first method is solution based on the pseudoinverse matrix. The second method is minimization of the solution error norm by the method of mathematical programming. These two methods are applied in the airship control system. The first method ensures for the given control system accuracy about  $10^{-14}$  N. Time of the problem solution is about 1 nanoseconds. The second method ensures accuracy about  $10^{-3}$  N and time of the problem solution about 1,5 microseconds. The studied methods are characterized by the absence of decomposition procedure "control channel - controlled variable". The problem is solved, if the time constants of actuators are much less than the time constants of a vehicle. If the inertia of the actuators is comparable with the inertia of a vehicle, the system (1) becomes the differential one. In this case it is possible to apply control algorithms described in [15], [16]. Described methods are able to compensate failure of actuators. Consider failure of the airship tail motors. In this case matrix (2) is

$$U = \begin{bmatrix} 1 & 0 & 1 & 0 \\ 0 & 1 & 0 & 1 \\ 0 & z_1 & 0 & z_2 \\ z_1 & 0 & z_2 & 0 \\ -y_1 & x_1 & -y_2 & x_2 \end{bmatrix} \quad (12)$$

Simulation results of the airship flight with only main propulsion motors in fig. 7. Wind speed is 5 m/s. Coordinates of the main propulsion engines are:  $x_1=5$  m;  $x_2=5$  m;  $y_1=-2$  m;  $y_2=-2$  m;  $z_1=-10.7$  m;  $z_2=10.7$  m. From fig. 7,8 it is clear that error of control system is about 70 m. In addition in steady state mode we can see oscillations of the airship altitude.

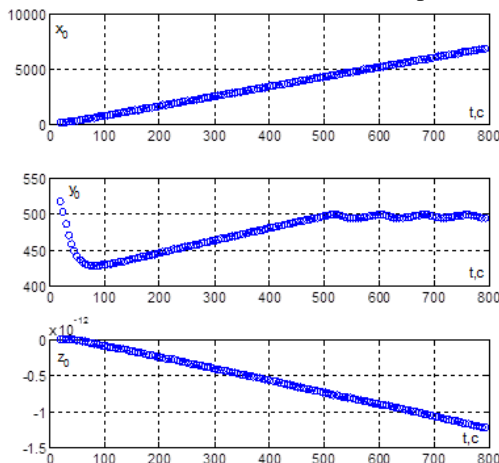


Fig. 7 The airship linear coordinates with motors failure

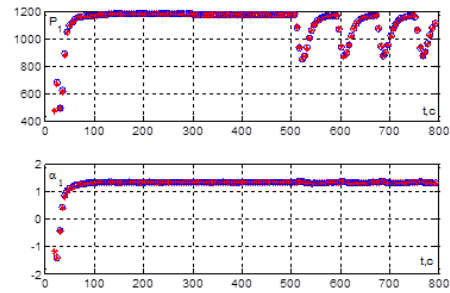


Fig. 8 The airship motors thrusts and rotation angles with failure

REFERENCES

- [1] V.Kh. Pshikhopov, A.S. Ali, "Hybrid motion control of a mobile robot in dynamic environments", *In proc. of 2011 IEEE International Conference on Mechatronics, ICM 2011*, pp. 540-545.
- [2] V.Kh. Pshikhopov, M.Y. Medvedev, M.Y. Sirotenko and V.A. Kostjukov "Control System Design for Robotic Airship". *In Proc. of the 9-th IFAC Symposium on Robot Control*. Pp. 123-128. 2009. Gifu, Japan.
- [3] V. Pshikhopov, M. Medvedev, V. Kostjukov, R. Fedorenko, B. Gurenko, V. Krukhmalev, "Airship autopilot design", *SAE Technical Papers*. October 18-21, 2011. doi: 10.4271/2011-01-2736.
- [4] A. Elfes, S. Siqueira Bueno, M. Bergerman and J.G. Ramos A. "Semi-autonomous robotic airship for environmental monitoring missions", *In Proc. of IEEE International Conference on Robotics and Automation*. 1998. Volume 4. Pp:3449 - 3455.
- [5] P.D. Krutjko, "Control of longitudinal motion of aircrafts. Design of algorithms by inverse problems of dynamics method", *RAS Transactions. Theory and control systems*. 1997. N 6. Pp. 62-79.
- [6] P.D. Krutjko, "Control of lateral motion of aircrafts. Design of algorithms by inverse problems of dynamics method", *RAS Transactions. Theory and control systems*. 2000. N 4. Pp. 143-164.
- [7] G.S. Bjushgens, R.V. Studnev, "Dynamics of aircraft. Three-dimensional motion", *Moscow: Mashinostroenie*, 1983.
- [8] V.Kh. Pshikhopov, V.A. Krukhmalev, M.Yu. Medvedev, R.V. Fedorenko, S.A. Kopylov, A.Yu. Budko, V.M. Chufistov, "Adaptive control system design for robotic aircrafts", *Proceedings - 2013 IEEE Latin American Robotics Symposium, LARS 2013* PP. 67 - 70. doi: 10.1109/LARS.2013.59.
- [9] V. Pshikhopov, N. Sergeev, M. Medvedev, A. Kulchenko, "The design of helicopter autopilot", *SAE Technical Papers* 5, 2012, doi: 10.4271/2012-01-2098.
- [10] V.K. Pshikhopov, M.Y. Medvedev, B.V. Gurenko, "Homing and docking autopilot design for autonomous underwater vehicle", *Applied Mechanics and Materials*, N 490-491, 2014, PP. 700 - 707. doi: 10.4028/www.scientific.net/AMM.490-491.700.
- [11] V.Kh. Pshikhopov, M.Yu. Medvedev, A.R. Gaiduk, B.V. Gurenko, "Control system design for autonomous underwater vehicle", *Proceedings - 2013 IEEE Latin American Robotics Symposium, LARS 2013*, PP. 77 - 82. doi: 10.1109/LARS.2013.61.
- [12] V. Pshikhopov, M. Medvedev, R. Neydorf, A. Gaiduk, V. Voloshin, "Impact of the feeder aerodynamics characteristics on the power of control actions in steady and transient regimes", *SAE Technical Papers* 5, 2012.
- [13] V. Pshikhopov, V. Krukhmalev, M. Medvedev, R. Neydorf, "Estimation of energy potential for control of feeder of novel cruiser/feeder MAAT system", *SAE Technical Papers* 5, 2012.
- [14] F. Gantmakher, "The theory of matrix", *Moscow, FIZMATLIT*, 2004. ISBN 5-9221-0524-8.
- [15] V.Kh. Pshikhopov, M.Yu. Medvedev, "Block design of robust control systems by direct Lyapunov method", *2011 IFAC Proceedings Volumes (IFAC-PapersOnline)*, 18 (PART 1) P3. 10875 - 10880.
- [16] V.Kh. Pshikhopov, M.Yu. Medvedev, "Robust control of nonlinear dynamic systems", *2010 IEEE ANDESCON Conference Proceedings*. doi: 10.1109/ANDESCON.2010.5633481.
- [17] T.F. Coleman and Y. Li, "An Interior, Trust Region Approach for Nonlinear Minimization Subject to Bounds," *SIAM Journal on Optimization*, Vol. 6, pp. 418-445, 1996.

# Design considerations for mobile robotic telepresence in museums- A report on the pilot users' feedbacks

Anahita Bagherzadhalimi, Eleonora Di Maria

**Abstract**—The current paper is a user-centered study that intends to evaluate the usability of MRP (mobile robotic telepresence) systems inside museums from pilot users' perspective by obtaining feedbacks from users who deploy a MRP system to visit a museum. The main aim of this study is to provide some guidelines which might contribute greatly to design and development of future telepresence robots that support individuals' access to museums and cultural heritage over the internet by providing the interaction requirements in these contexts. In order to conduct the study, a set of tasks are listed that pilot users had to perform through a MRP system to visit a museum from a remote location. Eventually, problems and difficulties with application of MRP systems in museums are reported and some solutions which most of them were proposed by the users are discussed. All of the methods used in this paper have been previously used in other domains.

**Keywords**— Human-Robot Interaction, Mobile Robotic Telepresence, Museum, Robot, Usability Test

## I. INTRODUCTION

MRP systems and their applications in different areas have recently attracted the attention of many researchers. Studies conducted in these areas contributed greatly to the advanced progression and development by providing novelties to the system from a variety of aspects. Different types of MRP systems in different shapes have been designed and developed to operate in populated environments such as in office buildings, hospitals, elderly homes, museums and schools. Telepresence robots in these environments perform a variety of services such as educating, entertaining or assisting people. Accordingly, plenty of studies have been done to investigate the application of MRP systems in these environments. In the sector of museum and populated exhibitions, projects such as TOURBOT [9] and WebFAIR [10] have been conducted with the aim of developing technologies that provide and support safe, reliable and effective operation of mobile robots in populated exhibitions. The current paper is a user-centered study that intends to evaluate the usability of MRP

systems inside museums and art galleries by obtaining feedbacks from pilot users who deploy a MRP system to visit a museum. The main objective of this study is to provide some guidelines which might contribute to some extend to the design and development of future telepresence robots that better fit environments such as museums and exhibitions.

Many user-centered studies have been done to test the usability of MRP systems in different environments especially in hospitals and elderly homes; however, to the best of our knowledge, no study has been conducted to obtain pilot users' feedback regarding usability of MRP systems to visit a museum. We believe that the set of technologies required to pursue a particular application varies depending on the type of tasks implied by the application and the environment in which the robot is supposed to operate. Consequently, studding the usability of robot based on the environment's context and situation is important and critical. In addition to design guidelines, we try to investigate the pilot users' willingness to adopt the robotic solution, its advantages, disadvantages and suggestions for improvements.

## II. RELATED WORKS

When evaluating a new technology, one of the effective methods is extensive end-user evaluation which is a process that employs people who are representative of the target audience to assess the degree to which a product can support specific usability criteria.

Usability testing is applied as a valuable research method that aims to answer some questions such as whether the state of the art technology or the new product is easy to use or become skilled at? Does it perform the required tasks? Does the task performance is done in the manner that is expected? In order to conduct this type of study, evaluators need to hire typical users of the technology and assigne tasks for them to perform. The process in this approach requires the users to do the tasks while the evaluator observe their performance and make notes about their observations. During the evaluation process, issues and difficulties in application of the product or technology show up with this method and any fails to complete the tasks are discovered. However, a decision on a way to solve the issues and difficulties is an additional challenge. According to [7] , with every

\*Resrach supported by Telecomitalia.

Anahita Bagherzad halimi is with the joint PhD program from University of Verona, University of Padova, and University of Ca foscari Venez. Padova, Italy (corresponding author phone: 00393473041481; e-mail: anahita.bagherzadhalimi@univr.com).

Eleonora Di maria is with University of Padova, Padova, Italy (e-mail: eleonora.dimaria@unipd.it).

emergence of new technologies in telecare, researchers perform some usability tests in order to evaluate the attitudes and level of acceptance in both elderly and caregivers. Depending on the nature of the test and the level of necessary formality, researchers may choose a variety of test plans and formats, however, majority of the usability test plans have the sections of evaluation purpose, research questions, participant characteristics, method, data to be collected, measurement tools, list and type of tasks, evaluation environment, report of analysis and presentation. Examples of research works that evaluate end users' attitudes toward MRP systems implemented in a variety of environments are not few. Study by [4] is a usability research work that reports on the application of mental workload analysis to evaluate a remote user interface in social robotic telepresence area. Kiselev and his colleague's argue was about the importance of user interfaces for a high qualified interaction. They also suggested a set of tools for assessment of the user interface. [2] evaluated a robotic telepresence platform that was used by elderly. The authors' argue was about the initial application of long term assessment applied in usability testing. [6] performed another usability test with robotic telepresence systems. They explored the extent to which the new robotic technology is able to help aged people to live independent. They discussed some technical approaches for their study and then reported the results from their usability tests. [3] discussed about the requirements and design considerations for a fully immersive robotic telepresence system that was applied in FP7 EU telepresence project. They evaluated the system and reported on the problems. Cohen and his colleagues proposed a set of tasks to be done by users that the system was expected to support. Eventually they suggested some potential design tradeoffs. [5] conducted their usability test on MRP systems in workplace for a duration of 2-18 months. Results obtained from their interviews, observations, and surveys from participants illustrated how the MRP system allowed the remote employees interact and work with local colleagues in the destination almost as if they were together and physically presented in the remote environment. They argued that despite of prior studies regarding telepresence robots that focused on functionalities such as navigation, obstacle avoidance, audio, visualization and interface aspects, it is important to validate acceptance of the technological system by potential users concerning more personal and practical aspects of the technology.

### III. DOUBLE TELEPRESENCE ROBOT DESIGN AND SET UP

The robot used for this paper is the commercially available Double telepresence robot. Double telepresence robot is a remotely controlled robot consisting of a base with an adjustable close to human height (can control to adjust the height between 47" and 60" tall, about 120cm to 150cm). The robot's weight is about 15 lbs (7kg), including the weight of the iPad. At each side of cylindrical base, there are two wheels and robot can turn into different directions. The

robot does not have any camera, display, speaker and microphone, however, on the top of the body, there is an iPad cradle which is used to hold the iPad or any other iOS device such as iPhones, iPod touches that can be connected to another device which is supposed to provide drive commands, control the movements and pass on the video and audio from the remote location, such as a computer on which a Chrome browser and Double extension is installed. There is a small mirror in the back that reflects the rear-facing camera which enables the pilot to look down at the robot's base that helps to avoid obstacles.

### IV. METHOD

Application of MRP systems by users with different level of technological ICT-knowledge might cause different problems in use of the technology and obtaining a satisfying interaction for the users. Consequently, it is necessary to achieve clear understanding about the way people perceive MRP systems and make a "high-quality" interaction through the device. It is our aim to assess the MRP system in different forms of interaction. A variety of techniques has been used in this paper to evaluate the MRP interface usability. The "usability testing" is a technique that is used to evaluate a technological system or a product by obtaining feedbacks from people to evaluate how much the product or technological system meet the necessary usability criteria [1]. In order to obtain a clear understanding of the usability of MRP systems inside a museum, we used a Double telepresence robot inside the lab. We simulated a museum of painting works inside the lab (Twente university) to conduct some usability experiments. We tried to make the environment as similar as possible to a real painting museum to identify the possible potential problems that might take place to visit a museum from a remote location through a MRP system and to evaluate different interactions with the system itself and the local users. This test is only valuable as an initial experimental research work; however, the test should be repeated in a real museum in natural setting as the interaction might be different in a real setting.

User evaluation sessions are proposed with potential users of the system to study the system's corresponding aspects. During each interaction session, experimenter observes the user's actions carefully by concentrating on the difficulties and problems that take place to perform the tasks. Moreover, the questionnaire is delivered to the participants to ask their opinion about the system components, usability and ease of use. Finally, some interviews are conducted to discover more problems and obtain more understandings regarding how the participants perceive the interaction through the MRP system and what is their recommendation for the improvement of the systems that can maintain an standard interaction as much as possible similar to interaction between humans.

### V. USER-CENTERED EVALUATION AND PARTICIPANTS

Experiments conducted in this paper are exploratory investigations involved individual adults interacting with a

Double telepresence robot. The trial area was chosen and designed in order to simulate a close to real experience of using the robot inside a real museum setting. A large part of the lab environment and some parts of the hallway have been prepared for this purpose and decorated like a painting museums. The whole set up took almost one week. The participant sample set consisted of 12 adult volunteers took part in the usability experiment (Figure 1 shows some snapshots from a video taken from one of the participants). 9 were male and another 3 were female with the mean age of 27.8, however, the youngest participant was 19 years old. They were students, faculty staff (e.g. lecturers, professors) and researchers all recruited from the university. One of the advantages of usability method is that a few number of users are able to discover the most serious usability disadvantages at the very beginning of the test.

We purposely selected 50% of the participants from people who had previous experience with driving MRP system working in a robotics or technology-relevant sections such as computer science and human media interaction department, and 50% from people who never had prior experience with a telepresence robot at all that came from a non-technology related section, such as psychology and business. All of the participants expressed that they had previous experience in using computer and videoconferencing systems such as skype. We chose experienced and non-experienced participants purposely to hypothesize that:

*The perception of the system usability is different between the users who had previous experience with MRP system and those who have not any experience.*

## VI. EXPERIMENT PROCEDURE

In this study, we evaluate the interaction between pilot and the user interface (HCI). Before the experiment starts, all the participants received some training about the procedures and the tasks they had to do. Pilot users learned how to connect to the robot and drive it through different part of the scenarios. The tasks for pilot users included (1) Navigation in the environment; (2) Having a conversation with a local user; (3) Visiting the paintings in the museum and (4) Parking back the robot in the allocated point. Another person was assigned to play the role of the local user who was supposed to accompany the robot (pilot user) during the trial in the environment and talk and interact with

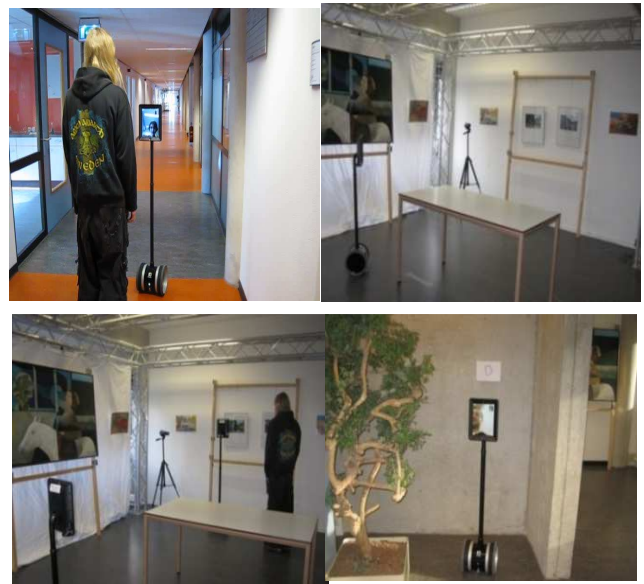


Fig. 1. Snapshots from different scenarios of the experiment

the pilot user through the MRP system. The hall path was marked by arrows on the wall to guide the user drivers to find their way to the simulated museum where the paintings were located. some key points in each part of the path were assigned: The MRP parking place (A), the point where the driver is supposed to meet the local user and start the conversation (B), The lab environment in which museum was simulated (C), and finally the second parking point which was in another place (D) but still very close to the lab door. The experimenter that trained the pilot users in the first step asked each of them to start the robot application by logging into the server and connecting to the Double telepresence robot that was parked in the (A) point. Once connected, the pilot user started to move the robot from point (A) through the hallway toward the point (B), where he had to meet the local visitor and start the conversation about a topic they were both interested (some topics for conversation have been proposed before they start) (S1). They continue the conversation while they were moving on toward point (C) (S2). Then they started to visit the paintings. They were asked to discuss about what they see in each painting for a few seconds (the purpose was to keep the simultaneous interaction between the pilot and the partner) (S3). After visiting the paintings, the pilot had to drive the robot to the (D) point and park the robot there (S4).

## VII. ANALYSIS AND FINDINGS

### A. Measurements, observations and user reports:

In this part, the survey measurements and results obtained from the observations, and interviews conducted with the participants are briefly discussed. The numerical data was analyzed first for each group separately and then results compared between experienced and inexperienced users. Independent sample t tests were run between the experienced and inexperienced participants in order to see whether there were significant differences in how the



Double telepresence robot was perceived and accepted. A qualitative report of the interview has been conducted and the most relevant feedbacks are discussed in terms of positive and negative aspects of the MRP system. Cronbach's Alphas were calculated on the set of items intended to measure each variable to evaluate the reliability of the indices. All indices were reliable.

B. Usability of the system

The participants were asked to state their opinions regarding the perceived usability of the Double telepresence robot. They had to give their answer on a 5 point likert scale from 1= strongly disagree to 5= strongly agree. 33.3% of the participants agreed on this question, and 25% disagree and the rest of the participants had a neutral opinion; Moreover, some environment- related difficulties as well as some robot specific problems have been identified which would be more discussed in details in the following parts. The mean value for the overall perceived usefulness was M=3.08 with the standard deviation of SD= 0.79296.

Independent sample t tests showed that there was a significant difference regarding perceived usability between the inexperienced group and the experienced group (TS= t10= 3.796, p=0.004<0.05). Comparing the means between the two groups illustrated that the experienced group perceived the system as being more usable. The reason might be because experienced users are able to get better use of the robot.

TABLE1  
Mean differences

Based on the information I have received, I think the system is usable for visiting a museum?			
Groups	N	M	SD
Experienced	6	3.66	.51640
Inexperienced	6	2.50	.54772

*Users' comments about perceived usability:* The participants were asked to comment in free text on why they did or did not think the Double telepresence robot was usable for the assigned tasks. Although most of the comments about the usability were not actually directly relevant to the usability, however the comments could illustrate the participants' concerns about the probable collisions in the remote environment. Some examples: **Comment 1:** "I didn't feel comfortable to drive the robot. I could not see my back properly. Even when I shifted the camera to see my back, I still could not make a safe drive. I think I cannot use it in more populated places because I afraid to make accidents with people". **Comment2:** "It was a problem when I stopped the robot, it still moves forward a little bit, so I guess I should stop the robot a few seconds sooner, before the actual place I want to be." Some of the participant mentioned that the experience was not very real to them. **Comment 3:** "I guess this cannot replace a real museum visit tour. I couldn't feel myself inside a museum."

C. Perceived ease of use

Application of MRP systems should be easy to use for both remote and local users. The participants were asked to rank the ease of use of the system in every scenario starting from learning how to connect to the robot to how to park the robot back in the last scenario. All the participants declared that the system was in general easy to learn and easy to use, except they had difficulties in some parts such as entering the room and driving backwards as they found these tasks a bit challenging. They had to give their answer on a 5 point likert scale from 1= strongly disagree to 5= strongly agree. Overall ease of use was calculated by another statement (I think the overall application of the MRP system was easy to use). The mean value for the overall ease of use was 3.16 with the standard deviation of 1.0298.

There was a significant difference regarding perceived overall system ease of use between the inexperienced group and the experienced group based on the results obtained from independent sample t test TS= t10= 5.000, p=0.001<0.05. Comparing the means between the two groups illustrated that the experienced group perceived the system as being more easy to use.

TABLE2  
Mean differences

I think the overall application of the MRP system was easy to use			
Groups	N	M	SD
Experienced	6	4.00	.51640
Inexperienced	6	2.500	.63246

Evaluation of each single item for users' perceived ease of use showed significant differences regarding perceived system ease of use between both groups except for some items including leaving the docking station TS= t10= .620, p=0.549>0.05, find the person you met TS= t10= 1.000, p=0.341>0.05, stopping the robot TS= t10= 51.342, p=0.209>0.05, hanging up the call TS= t10= 1.118, p=0.290>0.05, hearing the person you met TS= t10= 1.195, p=0.260>0.05 and seeing the person you met TS= t10= .368, p=0.721>0.05.

*Comments about Perceived ease of use:* The participants were also asked to comment in free text about the difficulties that they had when performing the tasks through the MRP system. Most of the difficulties, especially for novice participants came from keeping the appropriate distance to the people or objects and driving backward. Another most frequent comment was regarding the simultaneous conversation and navigation, particularly for novice participants. The reason might be due to the amount of workload in performing both tasks at the same time; however this was less problematic for the experienced group. **Comment 1:** "It was difficult for me to roll the robot backward. It was worse when I wanted to park back because I needed to shift the camera 2 or 3 times." **Comment 2:** "I wanted to focus on driving. When I was talking to another person, I sometimes got distracted. I didn't want to make any accident."

D. Satisfaction, enjoyment, likelihood to use MRP system in future

In Human-Computer interaction research, usability is usually evaluated by some of the variables including effectiveness, efficiency, and satisfaction. The level of satisfaction of the user from interaction with the system was measured by asking participants the question of “How much of a sense of satisfaction or accomplishment did you feel after you finished the tasks using the system [1 = not at all satisfying to 5 = Very much satisfying]?” Moreover, the level of enjoyment was measured by asking participants the question of “How enjoying was your interaction with the system [1=not at all enjoying 5=very much enjoying]?” Eventually, the likelihood that the participants would use an MRP system to visit a museum in future was assessed by asking the question of “Would you like to use the robot in the future to visit a museum or exhibition? [1=not at, 2=likely, 3= very likely]?” This dependent variable assesses the behavioral intentions in users.

Comparing the mean value between the two groups illustrated that experienced users ( $M= 4$ ,  $SD= 0.63246$ ) obtained more satisfaction from interaction with the user interface  $TS= t_{10}= 4.000$ ,  $p=0.003<0.05$  in compare to inexperienced users ( $M=2.66$ ,  $SD= 0.51640$ ). Comparing the mean value between the groups for the level of enjoyment from application of MRP illustrated the same results  $TS= t_{10}= 3.354$ ,  $p=0.007<0.05$  ( $M=4.66$ ,  $SD=0.51640$  for experience users and  $M=3.44$ ,  $SD=0.51640$  for inexperienced users). Moreover, experienced users were expected to report a higher probability to apply a MRP system to visit a museum and this was not the case  $TS= t_{10}= 1.861$ ,  $p=0.0092>0.05$  ( $M=1.83$ ,  $SD=0.40825$  for experience users and  $M=1.33$ ,  $SD=0.51640$  for inexperienced users).

#### E. Technical evaluations

Many prior studies have assessed the technical features connected to the telepresence robots and the user interfaces. Some usability tests has been conducted by researchers in a variety of environments and user interface in MRP systems have been assessed in terms of effectiveness, security of application, navigation strategies, and mental workload. In this study, some particular technical aspects have been tested to evaluate if these technical aspects contribute to usability and to what extent is this contribution.

#### F. Visual communication aspects

Visual aspect was also evaluated by a subjective measure. In a part of the questionnaire, participants were asked to rank the following statement “ I think the live video was clear enough to use the MRP system to visit artworks in a real museum” to find out whether or not they think that the visual aspect of the system can generally support a clear visualization inside the environment. They had to give their answer on a 5 point likert scale from 1= strongly disagree to 5= strongly agree. The analysis of the results showed that 66.7% of the participants disagree with this statement and the rest of the participants answered strongly disagree or neutral. The mean value was  $M= 2.16$

with the standard deviation of  $SD= 0.57735$ . Therefore, the overall visualization system of the MRP was not perceived as being qualified enough to support a clear visit of artworks inside a real museum. Interview has been conducted to discover the reasons for this result. Based on the feedbacks from participants, pilot users evaluated the visualization clear enough to allow for general navigation in the environment but not entirely acceptable to perform precise visual tasks, such as reading a text or identifying the state of some specific objects or visit the precise details of paintings or other artworks. The following comments are example of these types of problem.

**Comment1:** “I tried to see more details of the paintings, but I couldn’t see some parts because there was a reflection of the ceiling light on some of the paintings. I tried to get closer; I could see better but the problem was still there.”

**Comment2:** “I think the video was clear enough to see people and environment. I had problems with watching the paintings. I changed my position, moved forward and backward to see them better.”

Most of the comments had the same perceptions. If, telepresence robots are supposed to be used inside museums, they should be accepted by people and these problems should be solved first by the designers. One solution would be to improve the quality of the camera and to provide a zoom feature. Many of these problems have been already solved in some types of MRP systems.

#### G. Audio

Participants were also asked to rank the statement of “I can see myself using MRP for communicating in more noisy and populated environments?” related to the audio aspect of the system. They had to give their answer on a 5 point likert scale from 1= strongly disagree to 5= strongly agree. According to the analysis result, 75% of the participants agreed with the statement. The rest of the participants (25%) were neutral. The mean value was  $M=3.75$  and the standard deviation was  $SD=0.45227$ .

Feedbacks from participants illustrated that the overall audio quality was acceptable; however in more noisy areas either in the local environment or in the remote location, hearing was difficult for both remote and the local users. So, they had to increase the volume and decrease it again in less noisy places.

**Comment:** “I could hear him clearly when he was talking, but sometimes I turned the volume up to hear him better.”

#### H. Navigation

It might not be very much challenging to visit a place that one have already been by a MRP; however, it is much more complicated to navigate through an environment you have never been before. Therefore, the participants were also asked to rank the following statement:

“I can see myself using the MRP for communicating as a possibility to visit a place I have never been before?”

Results showed that around 66.7% of the participants agreed with the statement and the rest of the participants reported a neutral answer. The mean value was  $M= 3.66$  and the standard deviation was  $SD=0.49237$ .

One of the situations in which most pilot users usually face difficulty is navigation. They have to find their path while they should avoid collisions with objects and local visitors in the environment. Some difficulties also happened in places where the robot had to move through narrow spaces, for instance, when they had to turn and pass through a door to enter a room. Despite all these issues, the navigation in the environment was rated as generally satisfactory. Although most of the participants agreed that they are able to navigate in a place they have not been before, feedbacks from participants again shows their concern about moving backwards.

**Comments:** *"I needed to shift the camera several times to fix my position... otherwise I couldn't see if a person was coming to pass from my back..."* Prior studies suggested that collision avoidance might solve this problem to some extent. This could ease the navigation.

#### VIII. ADVANTAGES AND DISADVANTAGES OF USING A MRP SYSTEM TO VISIT A MUSEUM

Participants were also asked to think of some advantages and disadvantages of using a MRP to visit a museum. They described some advantages for application of the robot. Majority of the comments mentioned that cost reduction especially for traveling is one of the core advantages. Some comments are as follow: *"...It is wonderful that I can visit places that I might not be able to travel because it is expensive for me to travel there..."* Another participant declared that: *"...I think this works very well for people who are sick and cannot walk a long distance to go and visit museums and exhibitions"*, one of them said *"I think it is fun to sit and visit a museum from comfort of your home..."*

In addition to advantages, participants also mentioned some disadvantages for the system use. The primary concern was about the human health due to lack of body movement in this way. *"... I afraid the new technologies make people more lazy..."* One participant declared that *"... I still cannot think of myself using a telepresence robot to visit a museum as I afraid to hurt somebody or break something.... When I drive the robot it is hard for me to judge the distances from an object..."*, another person said that *"... I think it is fun but somehow boring... because the robot moves so slowly and I should concentrate to avoid any accident and this makes me a bit nervous"*.

#### IX. PROPOSE OF APPLICATION AREA

In this part of the usability test, participants had to answer the following question by voting for some proposed application of a MRP system for a museum. Moreover, they were asked to give suggestions for more application

possibilities. Which of the following applications do you think for telepresence robots? (1) a virtual visit of the museum without the need to go there (2) a preview of the museum before planning a visit(3) the possibility to visit places in the museum where the public is not allowed. The analysis of the results showed that 50% of the participants voted for the application of the system for a virtual visit of the museum without the need to go there, 33.3% voted for application of the system for a preview of the museum before planning a visit and the rest of the participants 16.7% chose the application of a MRP system for the possibility to visit places in the museums where the public is not allowed. One of the participants proposed that the system can be used for less physically advantaged people.

#### X. ACCEPTANCE

Application of MRP systems in every different areas and environments depends highly on the users' acceptance of the system. In order to enhance the acceptance among users, physical components of the system should be able to support the requirements of the application. From a pilot users' perspective, the system should allow the user to be immersed in the remote location with the least amount of cognitive disturbance and operational workload. The system should enable the users to concentrate more on the communication and the tasks rather than operating the system. Telepresence robot meant to be used inside a museum should be designed to assort a wide variety of users from kids to aged people even people with disabilities. Another important issue is the matter of safety that is important for both the pilot user and the bystanders in the remote location. Application of the system should be safe inside the environment; particularly when the connectivity is distracted and the user loose the system control. Combination of physical components including audio and visualization should support the users sense of "being there in the remote location". Visual devices of the MRP system inside museum should provide qualified visualization including clear video and zoom in/out camera to capture the details in the artworks. In addition to the system's physical factors, environmental factors also play important roles in the users' acceptance of the MRP system. Environment in which the robot is supposed to be used should support the application of the system and facilitate the use of the system. Minimum amount of obstacles in the remote environment can reduce the number of collisions and improve safety. Automatic doors can help the driver to navigate through the environment without difficulties. Minimizing the number of stairs and use of escalators can allow the pilot user to drive the robot freely between floors. Moreover, characteristics of the users are very important factors to accept the technology of telepresence robots. As it was also illustrated in the study results, the two groups of experienced and inexperienced users showed to have different perceptions regarding the application of the MRP. Experienced users perceived the system as being more usable in compare to the other group. They also reported a higher perception of system overall ease of use. These are mostly due to the difference in their

skills. People with a variety of skills and characteristics have different perceptions about the system and therefore their level of acceptance is also different. Attention to these differences can reduce the risk of future market failures.

## XI. DISCUSSION OF FINDINGS FROM THE MRP USABILITY TEST

The aim of this study was to predict the acceptability of MRP systems for visiting a museum. The results obtained from surveys, interviews, and observations illustrated that the robotic telepresence system can be applied for a variety of tasks and social activities in a museum, however there are still plenty of issues to be solved. Generally, experienced users perceived the system as to be more usable in compare to novice users who were experiencing the interaction through a MRP system for the first time; therefore, such participants are most probable to be future customers of remote application of a robotic telepresence inside a museum. Experiencing more interaction with the system may partially influence the attitude of the users and the level of acceptance by them. However, if this is true and prior experience plays a critical role in acceptance of the MRP, it should be noticed that not all the people have prior experience of interaction with a telepresence robot; in fact this applies to a majority of people.

## XII. CONCLUSION

The motivation behind our experiment in this study was to locate objective metrics based on them to develop and improve the MRP systems proper to be used in museums. User evaluation studies mostly cover issues such as users' attitude, acceptance, quality of interaction, societal and ethical topics and technical evaluations. The results of these evaluations in an application area with its specific challenges outline a set of design implications for developers of future MRP systems. This research work applied a mixed method approach to evaluate the usability of telepresence robot systems for museums; however it has been conducted inside the university lab. Therefore, this study as an initial research work provides guidelines for future user tests in real museums with natural settings with a variety of participants from young children to adult and aged people even physically less advantaged people as they might also be potential customers of telepresence robots. Although based on users' experience and capabilities, performing some tasks might be to some extent challenging, some of these difficulties come from the technical limitations of the systems. Regardless of the technical difficulties, users could conceive the advantages in application of telepresence robots inside museums and view the positive aspects of it. Some other versions of MRP systems developed to overcome the technological challenges and difficulties experienced in another studies in a variety of application areas by the researchers. Therefore, concerning this matter, the results obtained from this study induce the requirement for a larger series of trials, for a longer period of time to test a variety of

MRP systems with different features in addition to studies regarding cost analysis.

## XIII. LIMITATIONS AND FUTURE WORK

Although participants of this exploratory trial were all employed from academic people, the results might be to some extent different if we repeat the experiment with participants with a wide variety of backgrounds. For example, if we include aged people into the sample set, we may get a variety of feedbacks and results different from what we've obtained in this study as aged people are normally more reluctant to new technologies. In addition to this matter, studies inside the lab includes some limitations as they do not duplicate a real natural environment, moreover, the situation and type of interactions in an innate setting is very different. Therefore, the current findings in our study offer scope for future research works in a real museum and in more natural settings in order to obtain more valuable results.

## ACKNOWLEDGMENT

Special thanks to Prof. Vanessa Evers from Twente University who supported my study by providing us with the necessary equipments for our experiment.

## REFERENCES

- [1] Barnum C (2002). Usability Testing and Research. New York: Pearson Education.
- [2] Cesta, A., et al. (2012). Addressing the Long-term Evaluation of a Telepresence Robot for the Elderly. ICAART (1).
- [3] Cohen, B., et al. (2011). Requirements and design considerations for a fully immersive robotic telepresence system. Proceedings of HRI 2011 Workshop on Social Robotic Telepresence.
- [4] Kiselev, A., et al. (2014). The effect of field of view on social interaction in mobile robotic telepresence systems. Proceedings of the 2014 ACM/IEEE international conference on Human-robot interaction, ACM.
- [5] Lee, M. K. and L. Takayama (2011). Now, I have a body: Uses and social norms for mobile remote presence in the workplace. Proceedings of the SIGCHI Conference on Human Factors in Computing Systems, ACM.
- [6] Lowet, D., et al. (2012). Robotic Telepresence for 24/07 remote Assistance to Elderly at Home. Proceedings of social robotic telepresence workshop on IEEE international symposium on robot and human interactive communication. Paris, France.
- [7] Rubin, J. and D. Chisnell (2008). "Handbook of Usability Testing: Howto Plan, Design, and Conduct Effective Test."
- [8] <http://www.ics.forth.gr/tourbot/>.
- [9] <http://www.ics.forth.gr/webfair/>.

# Digital Smith Predictor for Control of Unstable and Integrating Time-delay Processes

V. Bobál, P. Chalupa, P. Dostál, and M. Kubalčík

**Abstract**—Time-delays (dead time) are found in many processes in industrial practice. Time-delays are mainly caused by the time required to transport mass, energy or information, but they can also be caused by processing time or accumulation. This paper deals with a design of algorithms for digital control of the unstable and integrating time-delay processes using one suitable modification of the Smith Predictor (SP). This digital modification of the Smith Predictor is based on Linear Quadratic (LQ) method. A minimization of the quadratic criterion is realized using spectral factorization. The designed algorithms have universal usage; they are suitable for control of stable, non-minimum phase, unstable and integrative time-delay processes. The main contribution of this paper is design and simulation verification of this Smith Predictor for control of the unstable and integrative processes, because classical continuous Smith Predictors are not suitable for control of such processes. Of course, some continuous-time modifications have been designed for control of like these processes. The designed algorithms for control of individual processes influenced by external disturbance were verified. The program system MATLAB/SIMULINK was used for simulation of designed algorithms.

**Keywords**—Digital control, Integrating process, LQ control, Polynomial approach, Simulation of control loops, Smith predictor, Time-delay, Unstable process.

## I. INTRODUCTION

**T**IME-delay appear in many processes in industry and other fields, including economical and biological systems They are caused by some of the following phenomena [1]:

- the time needed to transport mass, energy or information,
- the accumulation of time lags in a great numbers of low order systems connected in series,
- the required processing time for sensors, such as analyzers; controllers that need some time to implement a complicated control algorithms or process.

Time- delay is very often encountered in various technical systems, such as electric, pneumatic and hydraulic networks, chemical processes, long transmission lines, robotics, etc. The existence of pure time lag, regardless if it is present in the

control or/and the state, may cause undesirable system transient response, or even instability. Consequently, the problem of controllability, observability, robustness, optimization, adaptive control, pole placement and particularly stability and robust stabilization for this class of systems, has been one of the main interests for many scientists and researchers during the last five decades.

A part of time-delay systems can be unstable or have integrating properties. Typical examples of such processes are e.g. pumps, liquid storing tanks, distillation columns or some types of chemical reactors.

Most authors are designing continuous-time algorithms for control of such processes. Integrating and unstable processes with a time-delay often cannot be controlled by usual controllers designed without consideration of the dead-time. There are various ways to control such systems. Several tuning rules for PI or PID controllers in the classical feedback closed-loop continuous-time structure have been presented in literature for these systems, see e.g. [2] – [7]. But when processes include long time-delay, the performances of these classical controllers become worsen [8]. In these cases, the use of a time-delay compensator in the structure of the closed-loop control system can be available [9].

The first time-delay compensation algorithm was proposed by Smith [10] in 1957. This time-delay compensator (TDC) known as the Smith predictor (SP) contained a dynamic model of the time-delay process and it can be considered as the first model predictive algorithm. Control results of a good quality can be achieved by modified Smith predictor methods, see e.g. in [11] – [17]. The control scheme 2DOF (Two Degrees Of Freedom) is used in [18] - [20]. The design of controllers using polynomial approach [21], [22] can be found in [23] and the control system structure with two feedback controllers is proposed in [24]. The idea of the IMC (Internal Model Control) is employed in [25].

The problems of continuous-time control of integrating or unstable time-delay systems including the robustness, disturbance rejection and the extension of suitable compensators have been analyzed in other articles, see e.g. [26] - [34].

Historically first modifications of time-delay algorithms were proposed for continuous-time (analog) controllers. In industrial practice the implementation of the time-delay compensators on analog technique was difficult. Therefore the

Manuscript received March 14, 2014. V. Bobál, P. Chalupa, P. Dostál and M. Kubalčík are with the Department of Process Control, Faculty of Applied Informatics, Tomas Bata University in Zlin, Nad Stranemi 4511, 760 05 Zlin, Czech Republic (e-mails: [bobal@fai.utb.cz](mailto:bobal@fai.utb.cz), [chalupa@fai.utb.cz](mailto:chalupa@fai.utb.cz), [dostalp@fai.utb.cz](mailto:dostalp@fai.utb.cz), [kubalcik@fai.utb.cz](mailto:kubalcik@fai.utb.cz)).

Smith Predictors and its modified versions can be implemented since 1980s together with the use of microprocessors in the industrial controllers. In spite of the fact that all these algorithms are implemented in digital platforms, most of the literature analyzes, as mentioned above, only the continuous-time version.

The first digital time-delay compensators are presented e.g. in [35] – [38]. Some Self-tuning Controller (STC) modifications of the digital Smith Predictors (STCSP) are designed in [39] – [41]. Two versions of the STCSP were implemented into MATLAB/SIMULINK Toolbox [42], [43]. The scope of paper [44] is a design and an analysis of 2DOF discrete time-delay compensators for stable and integrating processes, the simple robust discrete time-delay compensator for unstable processes is proposed in [45].

It is well known that classical analog Smith Predictor is not suitable for control of unstable and integrating time-delay processes. The designed digital LQ Smith Predictor eliminates this drawback.

The paper is organized in the following way. The general problem of a control of the time-delay systems is described in Section 1. The principle of the continuous-time Smith Predictor is introduced in Section 2 and digital version in Section 3. Three modifications of digital controllers that are used for self-tuning versions SPs are proposed in Section 4. Section 5 contains brief description of the recursive identification procedure. Simulation configuration is presented in Section 6. Results of simulation experiments are summed in Section 7.

## II. PROCESS MODELS

Consider a continuous-time dynamical linear SISO (single input  $u(t)$  – single output  $y(t)$ ) system with time-delay  $L$ .

$$G_L(s) = G(s)e^{-Ls} \quad (1)$$

where  $G(s)$  is an unstable or an integrating time-delay free part of the process and the transfer function of a pure transportation lag is  $e^{-Ls}$ , where  $s$  is complex variable. A more complete description of the process must include external disturbances, which are normally represented in the linear model as an additive signal at process output.

This paper presents digital control of the unstable second order systems with time-delay which can be described by the following continuous-time transfer function:

1) System with one unstable pole:

$$G_1(s) = \frac{K}{(T_1s+1)(T_2s-1)}e^{-Ls} \quad (2)$$

2) System with two unstable poles:

$$G_2(s) = \frac{K}{(T_1s-1)(T_2s-1)}e^{-Ls} \quad (3)$$

3) Oscillatory unstable system:

$$G_3(s) = \frac{K}{T^2s^2 + 2\zeta Ts - 1}e^{-Ls}; \quad 0 < \zeta < 1 \quad (4)$$

4) Non-minimum phase unstable system with one unstable pole:

$$G_4(s) = \frac{K(T_3s-1)}{(T_1s+1)(T_2s-1)}e^{-Ls} \quad (5)$$

5) Non-minimum phase unstable system with two unstable poles:

$$G_5(s) = \frac{K(T_3s-1)}{(T_1s-1)(T_2s-1)}e^{-Ls} \quad (6)$$

6) Oscillatory non-minimum phase unstable system:

$$G_6(s) = \frac{K(T_3s-1)}{T^2s^2 + 2\zeta Ts - 1}e^{-Ls} \quad (7)$$

where  $K$  is static gain,  $T$ ,  $T_1$ ,  $T_2$ ,  $T_3$  are time constants and  $\zeta$  is damping factor.

The following integration systems were chosen for verification of the proposed digital SP algorithm:

7) Integrating system with one stable pole:

$$G_7(s) = \frac{K}{s(T_1s+1)}e^{-Ls} \quad (8)$$

8) Integrating system with one unstable pole:

$$G_8(s) = \frac{K}{s(T_1s-1)}e^{-Ls} \quad (9)$$

9) Double integrating system:

$$G_9(s) = \frac{K}{s^2}e^{-Ls} \quad (10)$$

## III. DIGITAL SMITH PREDICTOR

The discrete versions of the SP and its modifications are more suitable for time-delay compensation in industrial practice. The block diagram of a digital SP (see [39], [40]) is shown in Fig. 1. The function of the digital version is similar to the classical analog version.

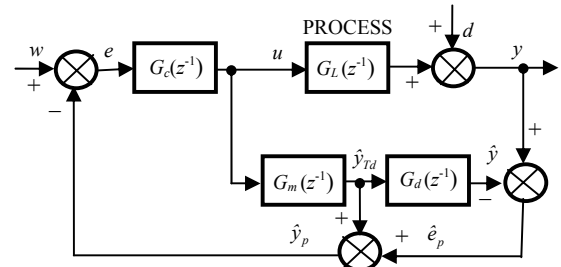


Fig. 1 Block diagram of a digital Smith Predictor

Number of higher order industrial processes can be approximated by a reduced order model with a pure time-delay. In this paper the following second-order linear model with a time-delay is considered

$$G_L(z^{-1}) = \frac{B(z^{-1})}{A(z^{-1})} z^{-d} = \frac{b_1 z^{-1} + b_2 z^{-2}}{1 + a_1 z^{-1} + a_2 z^{-2}} z^{-d} \quad (11)$$

The term  $z^{-d}$  represents the pure discrete time-delay. The time-delay is equal to  $dT_0$  where  $T_0$  is the sampling period.

The block  $G_m(z^{-1})$  represents process dynamics without the time-delay and is used to compute an open-loop prediction. The numerator in transfer function (11) is replaced by its static gain  $B(1)$ , i.e. for  $z = 1$ . This is to avoid problem of controlling a model with a  $B(z^{-1})$ , which has non-minimum phase zeros caused by a high sampling period or fractional delay. Since  $B(z^{-1})$  is not controllable as in the case of a time-delay, it is moved out of the prediction model  $G_m(z^{-1})$  and is treated together with the time-delay block, as shown in Fig. 1. The difference between the output of the process  $y$  and the model including time-delay  $\hat{y}$  is the predicted error  $\hat{e}_p$  as shown in Fig. 1, whereas  $e$  and  $v$  are the error and the measured disturbance,  $w$  is the reference signal. The primary (main) controller  $G_c(z^{-1})$  can be designed by different approaches (for example digital PID control or methods based on polynomial approach). The outward feedback-loop through the block in Fig. 1 is used to compensate load disturbances and modelling errors.

For the second order model (11) first compensator has the form

$$G_m(z^{-1}) = \frac{(b_1 + b_2)z^{-1}}{1 + a_1 z^{-1} + a_2 z^{-2}} = \frac{b_r z^{-1}}{1 + a_1 z^{-1} + a_2 z^{-2}}; \quad b_r = b_1 + b_2 \quad (12)$$

and second compensator is given by the transfer function

$$G_d(z^{-1}) = \frac{b_1 z^{-1} + b_2 z^{-2}}{b_r z^{-1}} z^{-d} \quad (13)$$

#### A. Design of Primary Polynomial 2DOF Controller

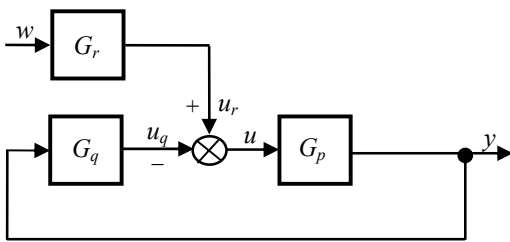


Fig. 2 Block diagram of a closed loop 2DOF control system

Polynomial control theory is based on the apparatus and methods of a linear algebra (see e.g. [21], [22], [46], [47]). The design of the controller algorithm is based on the general block scheme of a closed-loop with two degrees of freedom (2DOF) according to Fig. 2.

The controlled process is given by the transfer function in the form

$$G_p(z^{-1}) = \frac{Y_p(z)}{U(z)} = \frac{B(z^{-1})}{A(z^{-1})} \quad (14)$$

where  $A$  and  $B$  are the second order polynomials. The controller contains the feedback part  $G_q$  and the feedforward part  $G_r$ . Then the digital controllers can be expressed in the form of a discrete transfer functions

$$G_r(z^{-1}) = \frac{R(z^{-1})}{P(z^{-1})} = \frac{r_0}{(1 + p_1 z^{-1})(1 - z^{-1})} \quad (15)$$

$$G_q(z^{-1}) = \frac{Q(z^{-1})}{P(z^{-1})} = \frac{q_0 + q_1 z^{-1} + q_2 z^{-2}}{(1 + p_1 z^{-1})(1 - z^{-1})} \quad (16)$$

According to the scheme presented in Fig. 2 and equations (11) and (14) – (16), it is possible to derive the characteristic polynomial

$$A(z^{-1})P(z^{-1}) + B_r(z^{-1})Q(z^{-1}) = D_4(z^{-1}) \quad (17)$$

where  $B_r(z^{-1}) = b_r z^{-1}$  and

$$D_4(z^{-1}) = 1 + d_1 z^{-1} + d_2 z^{-2} + d_3 z^{-3} + d_4 z^{-4} \quad (18)$$

is the fourth degree characteristic polynomial.

The procedure leading to determination of polynomials  $Q$ ,  $R$  and  $P$  in (15) and (16) can be briefly described as follows (see [48]). A feedback part of the controller is given by a solution of the polynomial Diophantine equation (17). A feedback controller to control a second-order system with time-delay will be derived from equation (17). A system of linear equations can be obtained using the uncertain coefficients method

$$\begin{bmatrix} b_r & 0 & 0 & 1 \\ 0 & b_r & 0 & a_1 - 1 \\ 0 & 0 & b_r & a_2 - a_1 \\ 0 & 0 & 0 & -a_2 \end{bmatrix} \begin{bmatrix} q_0 \\ q_1 \\ q_2 \\ p_1 \end{bmatrix} = \begin{bmatrix} d_1 + 1 - a_1 \\ d_2 + a_1 - a_2 \\ d_3 + a_2 \\ d_4 \end{bmatrix} \quad (19)$$

An asymptotic tracking is provided by a feedforward part of the controller given by a solution of the polynomial Diophantine equation

$$S(z^{-1})D_w(z^{-1}) + B_r(z^{-1})R(z^{-1}) = D_4(z^{-1}) \quad (20)$$

For a step-changing reference signal value, polynomial  $D_w(z^{-1}) = 1 - z^{-1}$  and  $S$  is an auxiliary polynomial which does not enter into controller design.

For a step-changing reference signal value it is possible to solve Equation (23) by substituting  $z = 1$

$$R = r_0 = \frac{D(1)}{B(1)} = \frac{1 + d_1 + d_2 + d_3 + d_4}{b_r} \quad (21)$$

The 2DOF controller output is given by

$$u(k) = r_0 w(k) - q_0 y(k) - q_1 y(k-1) - q_2 y(k-2) + (1 - p_1)u(k-1) + p_1 u(k-2) \quad (22)$$

#### B. Minimization of LQ Criterion

The linear quadratic control methods try to minimize the quadratic criterion by penalization the controller output

$$J = \sum_{k=0}^{\infty} \left\{ [w(k) - y(k)]^2 + q_u [u(k)]^2 \right\} \quad (23)$$

where  $q_u$  is the so-called penalization constant, which gives the rate of the controller output on the value of the criterion (where the constant at the first element of the criterion is considered equal to one). In this paper, criterion minimization will be realized through the spectral factorization for an input-output description of the system.

For the coefficients of the second order characteristic polynomial

$$D_2(z^{-1}) = 1 + d_1 z^{-1} + d_2 z^{-2} \quad (24)$$

of the closed loop the following expressions were derived [48]

$$d_1 = \frac{m_1}{\delta + m_2}; \quad d_2 = \frac{m_2}{\delta} \quad (25)$$

The parameters  $m_1$ ,  $m_2$  and  $\delta$  are computed as follows:

$$\delta = \frac{\gamma + \sqrt{\lambda^2 - 4m_2^2}}{2}; \quad \gamma = \frac{m_0}{2} - m_2 + \sqrt{\left(\frac{m_0}{2} + m_2\right)^2 - m_1^2} \quad (26)$$

$$m_0 = q_u (1 + a_1^2 + a_2^2) + b_r^2; \quad m_1 = q_u (a_1 + a_1 a_2); \quad m_2 = q_u a_2$$

#### IV. PRIMARY LQ CONTROLLER OF DIGITAL SP

From the previous paragraph, it is obvious that using analytical spectral factorization, only two parameters  $d_1$  and  $d_2$  of the second degree polynomial  $D_2(z^{-1})$  can be computed. This approach is applicable only for control of processes without time-delay (out of Smith Predictor). The primary controller in the digital Smith Predictor structure requires usage of the fourth degree polynomial  $D_4(z^{-1})$  (18) in equations (17) and (20). The polynomial  $D_2(z^{-1})$  has two different real poles  $\alpha$ ,  $\beta$  or one complex conjugated pole  $z_{1,2} = \alpha \pm j\beta$  (in the case of oscillatory systems). These poles must be included into polynomial  $D_4(z^{-1})$  (18). A suitable pole assignment was designed for both types of the processes:

##### 1<sup>st</sup> possibility:

Polynomial (18) has two different real poles  $\alpha$ ,  $\beta$  (computed from (24)) and user-defined real poles  $\gamma$ ,  $\delta$ . Then it is possible to write polynomial (18) as a product root of factor

$$D_4(z) = (z - \alpha)(z - \beta)(z - \gamma)(z - \delta) \quad (27)$$

and its individual parameters can be expressed as

$$\begin{aligned} d_1 &= -(\alpha + \beta + \gamma + \delta) \\ d_2 &= \alpha\beta + \gamma\delta + (\alpha + \beta)(\gamma + \delta) \\ d_3 &= -[(\alpha + \beta)\gamma\delta + (\gamma + \delta)\alpha\beta] \\ d_4 &= \alpha\beta\gamma\delta \end{aligned} \quad (28)$$

##### 2<sup>nd</sup> possibility:

Polynomial (18) has the complex conjugate pole  $z_{1,2} = \alpha \pm j\beta$  (computed from (24)) and user-defined real poles  $\gamma$ ,  $\delta$ . Then polynomial (18) has the form

$$D_4(z) = (z - \alpha - j\beta)(z - \alpha + j\beta)(z - \gamma)(z - \delta) \quad (29)$$

and its individual parameters can be expressed as

$$\begin{aligned} d_1 &= -(2\alpha + \gamma + \delta) \\ d_2 &= 2\alpha(\gamma + \delta) + \alpha^2 + \beta^2 + \gamma\delta \\ d_3 &= -[2\alpha\gamma\delta + (\alpha^2 + \beta^2)(\gamma + \delta)] \\ d_4 &= (\alpha^2 + \beta^2)\gamma\delta \end{aligned} \quad (30)$$

The control algorithm based on the LQ control method contains the following steps:

- The parameters of the polynomial  $D_2(z^{-1})$  are computed according to equations (25) and (26).
- If the polynomial (24) has the real poles  $\alpha$ ,  $\beta$ , its parameters are computed according to equations (28), otherwise, they are computed according to equations (30).
- The controller parameters are computed using matrix equation (19) and equation (21).
- The controller output is given by equation (22).
- Penalization of the controller output is performed by setting  $q_u \geq 0$ .

With increased penalization constant, the amplitude of the controller output decreases and thereby, the flow of the process output is smoothed and any possible oscillations or instability are damped.

#### V. SIMULATION VERIFICATION AND RESULTS

Simulation is useful tool for the synthesis of control systems, allowing us not only to create mathematical models of a process but also to design virtual controllers in a computer. The mathematical models provided are sufficiently close to a real object that simulation can be used to verify the dynamic characteristics of control loops when the structure or parameters of the controller change. The models of the processes may also be excited by various random noise generators which can simulate the stochastic characteristics of the processes noise signals with similar properties to disturbance signals measured in the machinery. A simulation verification of the designed predictive algorithm was performed in MATLAB/SIMULINK environment. It is possible to influence the output of the process with the non-measurable disturbance  $d$ . The designed digital Smith Predictor has universal usage for control of a large group of processes with time-delay.

Because the range of this paper is limited, only the following models with an exacting dynamic behavior were used for simulation experiments:

System with two unstable poles – (3)

$$G_2(s) = \frac{2}{(5s-1)(2s-1)} e^{-8s} \quad (31)$$

Oscillatory unstable non-minimum phase system – (7)

$$G_6(s) = \frac{2(4s-1)}{4s^2+2s-1} e^{-8s} \quad (32)$$

Integrating system with one unstable pole – (9)

$$G_8(s) = \frac{2}{s(5s-1)} e^{-8s} \quad (33)$$

Let us now discretize (31), (32) and (33) using a sampling period  $T_0 = 2$  s. The discrete forms of these transfer functions are (see (11))

$$G_2(z^{-1}) = \frac{0.6516z^{-1} + 1.0386z^{-2}}{1 - 4.2101z^{-1} + 4.0552z^{-2}} z^{-4} \quad (34)$$

$$G_6(z^{-1}) = \frac{2.1695z^{-1} + -3.5409z^{-2}}{1 - 2.06539z^{-1} + 0.3679z^{-2}} z^{-4} \quad (35)$$

$$G_8(z^{-1}) = \frac{0.9782z^{-1} + 1.0491z^{-2}}{1 - 2.4918z^{-1} + 1.4918z^{-2}} z^{-4} \quad (36)$$

The processes which are described by the above mentioned transfer functions were used in the Simulink control scheme for the verification of the dynamical behavior of the individual closed control loops. In time 500 – 800 s an exponential external disturbance

$$d(t) = 0.5(1 - e^{-0.1t}) \quad (37)$$

acted on the system output. The computed poles  $\alpha, \beta$  and user-defined real poles  $\gamma, \delta$  are introduced for individual simulation experiments including characteristic polynomial (18). For all experiments, the penalization factor was chosen  $q_u = 1$ .

#### A. Simulation Control of Model $G_2(z^{-1})$

The poles:  $\alpha, \beta = 0.3912 \pm 0.1488i$ ;  $\gamma = 0.1$ ;  $\delta = 0.5$

The characteristic polynomial:

$$D_4(z) = z^4 - 1.3824z^3 + 0.6947z^2 - 0.1442z + 0.0088$$

The courses of the control variables are shown in Fig. 3, the quality of control is very good.

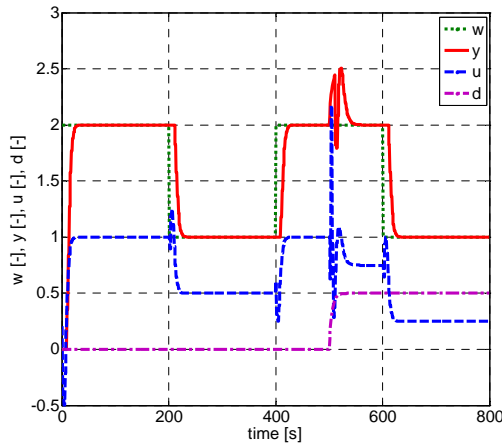


Fig. 3 Control of model  $G_2(z^{-1})$

#### B. Simulation Control of Model $G_6(z^{-1})$

The poles:  $\alpha, \beta = 0.2188 \pm 0.11137i$ ;  $\gamma = 0.1$ ;  $\delta = 0.75$

The characteristic polynomial:

$$D_4(z) = z^4 - 1.2875z^3 + 0.5077z^2 - 0.0845z + 0.0046$$

The courses of the control variables are shown in Fig. 4, the quality of control is very good.

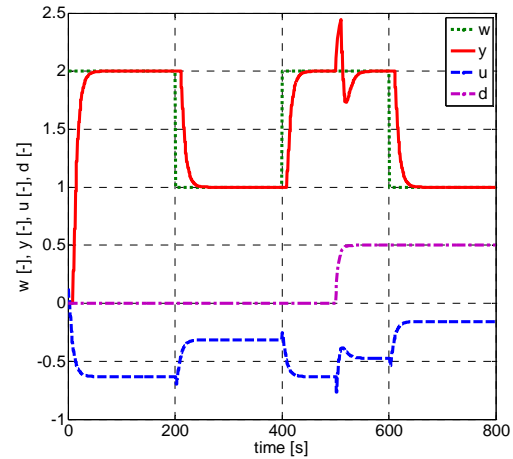


Fig. 4 Control of model  $G_6(z^{-1})$

#### C. Simulation Control of Model $G_8(z^{-1})$

The poles:  $\alpha, \beta = 0.2652 \pm 0.2752i$ ;  $\gamma = 0.1$ ;  $\delta = 0.5$

The characteristic polynomial:

$$D_4(z) = z^4 - 1.1305z^3 + 0.5144z^2 - 0.1142z + 0.0073$$

The courses of the control variables are shown in Fig. 5, the quality of control is very good.

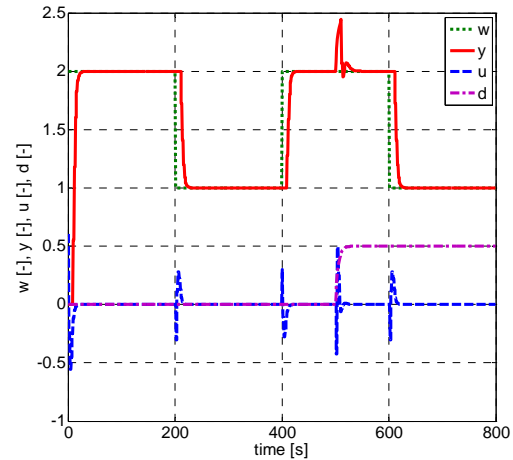


Fig. 5 Control of model  $G_8(z^{-1})$

## VI. CONCLUSION

The paper presents a new unified approach for design of the digital LQ Smith Predictor for control unstable and integrating systems with time-delay. The primary controller is based on minimization of the linear quadratic criterion. Minimization of the criterion is realized through spectral factorization. This controller was derived purposely by analytical way (without utilization of numerical methods) to obtain algorithms with easy implementability in industrial practice. Three models (two unstable and one integrating with unstable pole) were used for simulation verification. Main contribution of designed method is the universal applicability of this Smith

Predictor for digital control of large spectrum processes (stable, unstable, non-minimum phase, integrating) with time-delay.

## VII. REFERENCES

- [1] J. E. Normey-Rico and E. F. Camacho. Control of Dead-time Processes. London: Springer-Verlag, 2007.
- [2] M. De Paor, „A modified Smith predictor and controller for unstable processes with time delay. Int. J. Control, vol. 58, pp. 1025-1036, 1985.
- [3] B. D. Tyreus and W. L. Luyben, „Tuning PI controllers for integrator/dead time processes,“ *Ind. Eng. Chem. Res.*, vol. 31, pp. 2625-2628, 1992.
- [4] L. Wang and W. R. Cluett, „Tuning PID controllers for integrating processes,“ *IEE Proc. Control Theory Appl.*, vol. 144, no. 4, pp. 385-392, 1997.
- [5] J. H. Park, S. W. Sung and I. Lee, „An enhanced PID control strategy for unstable processes,“ *Automatica*, vol. 34, no. 4, pp. 751-756, 1998.
- [6] Y. Lee, J. Lee and S. Park, “PID controller tuning for integrating and unstable processes with time-delay,“ *Chemical Engineering Science*, vol. 55, pp. 3481-3493, 2000.
- [7] G. J. Silva, A. Datta, and S.P. Bhattacharyya, *PID Controllers for Time-Delay Systems*. Boston-Berlin-Basel: Birkhäuser, 2005.
- [8] K. J. Åström and T. Hägglund, *PID Controllers: Theory, Design and Tuning*. North Carolina: Instrument Society of America, 1995.
- [9] T. Hägglund, “An industrial dead-time compensating PI controller,“ *Automatica*, vol. 4, no. 6, pp. 749-756, 1996.
- [10] O. J. Smith, “Closed control of loops,“ *Chem. Eng. Progress*, vol. 53, pp. 217-219, 1957.
- [11] K. J. Åström, C. C. Hang and B. C. Lim. “A new Smith predictor for controlling a process with an integrator and long dead time,“ *IEEE Trans. Automat. Control*, vol. 39, no. 2, pp. 343-345, 1994.
- [12] W. D. Zhang and Y. X. Sun, “Modified Smith predictor for controlling integrator/time delay processes,“ *Ind. Eng. Chem. Res.*, vol. 35, pp. 2796-2772, 1996.
- [13] M. R. Matausek and A. D. Micić, “A modified Smith predictor for controlling a process with an integrator and long dead-time,“ *IEEE Trans. Automat. Control*, vol. 41, no. 8, pp. 1199-1203, 1996.
- [14] M. R. Matausek and A. D. Micić, “On the modified Smith predictor for controlling a process with an integrator and long dead-time,“ *IEEE Trans. Automat. Control*, vol. 44, no. 8, pp. 1603-1606, 1999.
- [15] H. J. Kwak, S. W. Sung and I. B. Lee, “Modified Smith predictor with a new structure for unstable processes,“ *Ind. Eng. Chem. Res.*, vol. 38, pp. 405-411, 1999.
- [16] S. Majhi and D. P. Atherton, “Obtaining controller parameters for a new Smith predictor using autotuning,“ *Automatica*, vol. 36, no. 11, pp. 1951-1658, 2000.
- [17] W. D. Zhang, D. Gu, W. Wang and X. Wu, “Quantitative performance design of a modified Smith predictor for unstable processes with time delay, *Ind. Eng. Chem. Res.*,“ vol. 43, pp. 56-62, 2004.
- [18] Q. -C. Zhong and J. Normey-Rico, “Control of integral processes with dead-time. Part 1: disturbance observer-based 2 dof control scheme,“ *Control Theory Appl.*, *IEEE Proc.*, vol. 149, no. 4, pp. 285-290, 2002.
- [19] T. Liu, W. Zhang, and D. Gu, “Analytical design of two-degree-of-freedom control scheme for open-loop unstable process with time delay,“ *Journal of Process Control*, vol. 15, pp. 559-572, 2005.
- [20] S. Rao and M. Chidambaram, “Enhanced two-degrees-of-freedom control strategy for second-order unstable processes with time delay,“ *Ind. Eng. Chem. Res.* vol. 45, pp. 3604-3614, 2006.
- [21] M. Vidyasagar, *Control System Synthesis: A Factorization Approach*. Cambridge M.A.: MIT Press, 1985.
- [22] V. Kučera, “Diophantine equations in control – a survey,“ *Automatica*, vol. 29, pp. 1361-1375, 1993.
- [23] P. Dostál, V. Bobál, and M. Sysel, „Design of controllers for integrating and unstable time delay systems using polynomial method,“ in *Proceedings of 2002 American Control Conference*, Anchorage, Alaska, USA, 2002, pp. 2773-2778.
- [24] P. Dostál, F. Gazdoš and V. Bobál, „Design of controllers for time delay systems Part II: Integrating and unstable systems,“ *Journal of Electrical Engineering*, vol. 59, no 1, pp. 3-8, 2008.
- [25] W. Tan, H. J. Marquez and T. Chan, “Imc-based design of unstable processes with time delays,“ *Journal of Process Control*, vol. 13, no. 8, pp. 203-213, 2003.
- [26] W. D. Zhang and X. M. Xu, „Quantitative performance design for integrating processes with time delay,“ *Automatica*, vol. 35, no. 4, pp. 719-723, 1999.
- [27] J. E. Normey-Rico and E. F. Camacho, “Robust tuning of dead-time compensators for process with an integrator and long dead-time,“ *IEEE Trans. Automat. Control*, vol. 44, no. 8, pp. 1597-1603, 1999.
- [28] C. S. Jung, H. J. Song and J. C. Hyun, “Direct synthesis tuning method of unstable first-order plus time delay systems,“ *Journal of Process Control*, vol. 9, no. 3, pp. 265-269, 1999.
- [29] J. E. Normey-Rico and E. F. Camacho, “A unified approach to design dead-time compensators for stable and integrative processes with dead-time,“ *IEEE Trans. Automat. Control*, vol. 47, no. 2, pp. 299-305, 2002.
- [30] Q. -C. Zhong and L. Mirkin, “Control of integral processes with dead-time. Part 2: Quantitative analysis,“ *IEE Control Theory Appl.*, vol. 149, no. 4, pp. 291-296, 2002.
- [31] I. -L. Chien, S. C. Peng, and J. H. Liu, “Simple control method for integrating processes with long deadtime,“ *Journal of Process Control*, vol. 12, no. 1, pp. 365, 2003.
- [32] Q. -C. Zhong, “Control of integral processes with dead-time. Part 3: deadbeat disturbance response,“ *IEEE Trans. Automat. Control*, vol. 48, no. 1, pp. 153-305, 2003.
- [33] P. García, P. Albertos and T. Hägglund. “Control of unstable non-minimum-phase delayed systems,“ *Journal of Process Control*, vol. 16, pp. 1099-1111, 2006.
- [34] M. Shamsuzzuha and M. Lee. “Enhanced disturbance rejection for open-loop unstable process with time delay,“ *ISA Transactions*, vol. 48, pp. 237-244, 2009.
- [35] E. F. Vogel and T. F. Edgar, “A new dead time compensator for digital control,“ in *Proc. ISA Annual Conference*, Houston, 1980, pp. 29-46.
- [36] Z. J. Palmor and Y. Halevi, “Robustness properties of sampled-data systems with dead time compensators,“ *Automatica*, vol. 26, pp. 637-640, 1990.
- [37] S. M. Guo, W. Wang and L. S. Shieh, “Discretisation of two degree-of-freedom controller and system with state, and output delays,“ *IEE Proceedings. Control Theory and Applications*, vol. 147, no. 1, pp. 87-96, 2000.
- [38] J. E. Normey-Rico and E. F. Camacho, “Dead-time compensators: A unified approach,“ in *Proc. of IFAC Workshop on Linear Time-Delay Systems (LDTS'98)*, Grenoble, 1998, pp. 141-146.
- [39] C. C. Hang, K. W. Lim and B. W. Chong, “A dual-rate adaptive digital Smith predictor,“ *Automatica*, vol. 20, pp. 1-16, 1989.
- [40] C. C. Hang, H. L. Tong and K. H. Weng. *Adaptive Control*, North Carolina: Instrument Society of America, 1993.
- [41] V. Bobál, P. Chalupa, P. Dostál and M. Kubalčík, “Design and simulation verification of self-tuning Smith predictor,“ *International Journal of Mathematics and Computers in Simulation*, vol. 5, no. 4, pp. 342-351, 2011.
- [42] V. Bobál, P. Chalupa, J. Novák, J. and P. Dostál, “MATLAB Toolbox for CAD of self-tuning of time-delay processes,“ in *Proc. of the International Workshop on Applied Modelling and Simulation*, Roma, pp. 44 – 49, 2012.
- [43] V. Bobál, P. Chalupa, and J. Novák, “Toolbox for CAD and Verification of Digital Adaptive Control Time-Delay Systems,“ Available from [http://nod32.fai.utb.cz/promotion/Software\\_OBD/Time\\_Delay\\_Tool.zip](http://nod32.fai.utb.cz/promotion/Software_OBD/Time_Delay_Tool.zip)
- [44] B. C. Torricco, and J. E. Normey-Rico, “2DOF discrete dead-time compensators for stable and integrative processes with dead-time,“ *Journal of Process Control*, vol. 15, pp. 341-352, 2005.
- [45] J. Normey-Rico and E. Camacho, „Simple robust dead-time compensator for first-order plus dead-time unstable processes,“ *Ind. Eng. Chem. Res.* vol. 47, no. 14, pp. 4784-4789, 2008.
- [46] V. Kučera, *Discrete Linear Control: the Polynomial Equation Approach*. Chichester: John Wiley, 1979.
- [47] V. Kučera, *Analysis and Design of Discrete Linear Control Systems*. London: Prentice Hall, 1991.
- [48] V. Bobál, J. Böhm, J. Fessl, and J. Macháček, *Digital Self-tuning Controllers: Algorithms, Implementation and Applications*. London: Springer-Verlag, 2005.

# RGBD sensors correction with Gaussian process regression

Abdenour amamra, Nabil aouf

**Abstract** - In this work, we present a novel method to accurately calibrate active depth sensors such as the Microsoft Kinect. Our approach is based on the Gaussian Process Regression (GPR). It is applied after the standard calibration and it is particularly useful for the aging depth cameras. The latter, were proven to suffer from inaccuracies that cannot be fixed with the standard pinhole camera calibration procedure. Experimental results show the weaknesses of this naïve calibration and the corrective of effect our algorithm. We further justify the possibility to extend the same approach to any other type of cameras with similar characteristics.

**Keywords** — RGBD; Gaussian process regression; camera calibration; Kinect; depth map.

## I. INTRODUCTION

NOWADAYS, RGBD cameras such as the Microsoft Kinect become increasingly popular in many computer vision, image processing and robotics applications [1]. Although the widespread success these sensors achieved, their accuracy issues were narrowly addressed. Prior studies from the literature focused on ordinary monocular camera calibration (the colour and the infrared cameras separately), and the stereo calibration, where both the RGB and the IR cameras are jointly characterised [2]. During our experimentation with the Kinect, we noticed a significant drop in the accuracy of the range measurements within the worn sensors. This phenomenon happens even after performing a correct standard calibration. Up to our knowledge, this fact about the active depth sensors was not covered previously in any research work. Such drawback negatively affects the performance of all the subsequent stages relying on the raw outputs of the camera.

The working principle of our correction module is motivated by some finding the authors in [3] discovered. In addition, a learning approach based on the Gaussian process is applied to correct the drift depth readings. The Gaussian process has been chosen because it provides a probabilistic framework to directly work with priors on a space of functions. It also provides a more accurate prediction and correction of the outputs. On the other hand, a major limiting factor for the acceptance of the GPR in practice is the computational effort associated to large training datasets. However, the training phase in our specific case is applied offline just like the normal calibration, which is required only once for the sensor. More importantly, our algorithm needs a maximum of 130 elements to work properly. This correction

applies on  $z$  coordinate (depth). The remaining  $x$  and  $y$  components are computed based on the corrected  $z$  and the ordinary camera parameters.

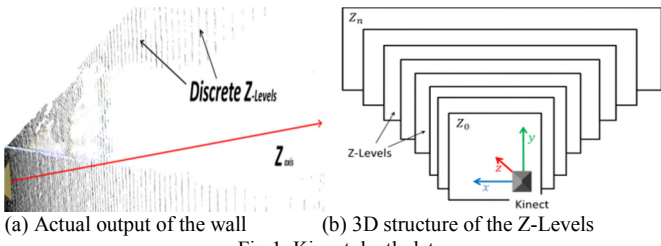
## II. RELATED WORK

Few works from the literature discussed the issue of accuracy when using a depth camera as a measuring tool. Zhu et al. [4] combined a Time Of Flight camera (ToF) with a stereo pair to correct the distribution of depth data. Chiu et al. [5] combined the depth images captured from a range sensor and the disparity map issued by the IR-RGB pair to improve the accuracy of the 3D data. Xul et al. [6] used the same technique to increase the accuracy of the depth image covering the scene. Henry et al. [7] combined visual features from RGB camera and the shape-based alignment from a range sensor to build a reliable 3D geometry. Moreover, Matyunin et al. [8] used a temporal filtering of the RGBD images to cope with occlusions and to improve the temporal stability of the 3D data. In all of the above cited works, the authors either compensate one sensor's accuracy with others. Or they filter the raw data streamed by the sensor itself. Nevertheless, our solution corrects the active depth sensors that cannot be dealt with the standard calibration. It uses a more accurate sensor's data. It also uses a set of characteristic properties of depth cameras and a learning algorithm (GRP) to readjust the measurements.

## III. KINECT DEPTH MAP STRUCTURE

Kinect sensor is an RGBD camera which has the ability to capture the depth map of the scene and its colour image simultaneously. The camera works at a frame rate of 30Hz for an image resolution of  $640 \times 480$  pixels. It also computes the depth map of the scene with a triangulation process [3].

To study the structure of the depth map, the authors in [3] pointed the sensor parallel to a large flat wall. This experiment allows them to capture a cloud of points from the whole operating range of the camera (0.8m to 4.0m) Fig 1(a). The 3D distribution of the different depth levels is illustrated in Fig 1(b). The point data within the capture lie in independent parallel planes that the authors in [3] called **Z-Levels**. Each of these planes ( $Z_0 \dots Z_n$ ) has its own depth value  $Z_k$ , and contains a set of points  $P_i(x_i, y_i, Z_k)$ . These points share the same  $Z_k$ . The number of Z-Levels determines the precision of the depth computation. In other word, the denser the Z-Levels become, the higher the precision will be. The discrete levels



result from the quantisation of the real distance separating the sensor from the scene. In addition, they are limited in number ( $n + 1 \approx 730$  different depth values), and they are the same for all the Kinects running the same driver. The gap between two successive Z-Levels ( $Z_{k+1} - Z_k$ ) increases proportionally to the square distance separating the scene from the sensor [2].

#### IV. PROBLEM STATEMENT

In all the following sections, the Kinects have undergone a good standard monocular calibration ( $f_x, f_y; c_x, c_y$ ) for both the RGB and the Depth cameras. In addition, a stereo calibration is performed to issue the pose ( $\mathbf{R}, \mathbf{T}$ ) of each camera (IR and RGB) relative to the other. Let  $K_h$  be a **healthy** Kinect. This camera's accuracy is the same as the native resolution of the sensor within its operating range ( $\pm 1.5 \text{ mm}$  at  $80 \text{ cm}$  and  $\pm 5.0 \text{ cm}$  at  $4.0 \text{ m}$ ). On the other hand,  $K_f$  is a faulty Kinect, for which the accuracy ( $\pm 1.8 \text{ mm}$  at  $80 \text{ cm}$  and  $\pm 10.0 \text{ cm}$  at  $3.90 \text{ m}$ ) cannot be recovered with the ordinary calibration procedure. Hence, the problem becomes; given the trustworthy depth readings of  $K_h$ , How could one correct the wrong disparity image issued by  $K_f$ ?

The phenomenon of drop in accuracy is well explained in Fig 2.  $K_h$  sensor covers all the operating range of the camera (0.8m to 4.0m) at a good accuracy Fig 2(a). The error in depth estimation is shown with the green intervals in Fig 2(a). On the other hand,  $K_f$  camera range is smaller (0.8m to 3.9m). Moreover, the uncertainty in the depth estimation is larger compared to  $K_h$  (red intervals in (Fig 2(b)).

Throughout the experiments (object tracking and 3D registration applications), we noticed that the drop of accuracy appears only within the aging sensors. Up to the authors' knowledge, the state of the art calibration and studies on Kinect camera have not yet addressed neither this issue nor a solution to fix it. Before raising this work, we attempted many times to correct the shift of the normal depth values with optical calibrations procedures. However, the erroneous range

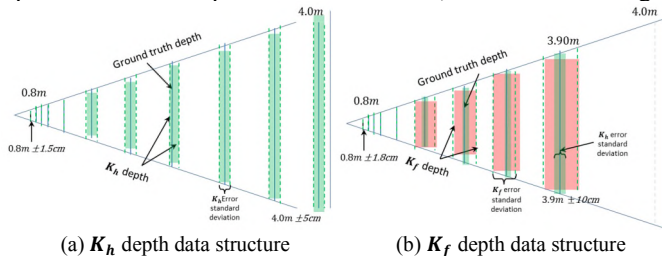


Fig 2. Accuracy difference between  $K_h$  and  $K_f$

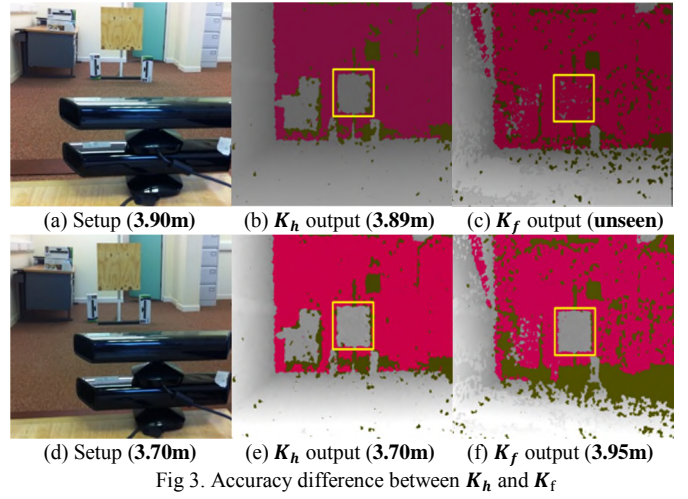


Fig 3. Accuracy difference between  $K_h$  and  $K_f$

readings persist. In the technical specs of the sensor, we found that the computation of the disparity map is based on a triangulation algorithm applied on the pair IR projector/camera. The projector is an output device. Thus incapable to capture any kind of calibration patterns. The factory stereo parameters of the IR projector/camera setup are embedded in the sensor and inaccessible from the outside.

To illustrate this problem in a real scenario, we fix a flat wooden panel parallel to the planes of two Kinects at a distance of **3.90m** Fig 3(a). The upper camera ( $K_h$ ) is working properly, but the other one ( $K_f$ ) is drifts. In this experiment, we read the range separating the panel from both sensors. The disappearance of the panel from the image means that it was not detected within the native operating range of the sensor (0.8m to 4.0m). At **3.90m** the depth map captured by the healthiest camera shows that the panel is located at **3.89m** Fig 3(b). However, the faulty camera is unable to see the object at all Fig 3(c). Afterwards, we move the panel forward to **3.70m** so both Kinects can capture it Fig 3(d).  $K_h$  indicates that the object is at **3.70m** Fig 3(e). Whereas  $K_f$  locates it at **3.95m** Fig 3 (f).

To fix this problem within the IR setup, we use a learning algorithm that leverages the precise outputs of the healthy camera to eliminate the shift that occurs in the depth data of the drifts sensor.

#### V. GPR ON KINECT DEPTH DATA

The Gaussian Process Regression is a generic supervised learning method primarily designed to solve regression problems. The GPR has the advantages of being **predictive**; it interpolates all the available training data. It is **probabilistic**; one can compute empirical confidence intervals that may be used to refit the prediction in some regions of interest. It is **versatile**; different linear regression models can be specified [9].

Given a set of  $N$  training pairs of points  $\{(z_i, \tilde{z}_i)\}$ , where  $z_i$  denotes the erroneous depth measurements and  $\tilde{z}_i$  refers to the correct correspondents. The purpose of the GPR is to learn a function  $f(z_i)$ . The latter should be able to attribute to every query depth element  $z_*$  in the captured depth image, a unique

accurate correspondent  $f(\mathbf{z}_*)$ . This correspondent better represents the actual range seen from the query pixel. The process is modelled by the function:  $\tilde{\mathbf{z}}_i = f(\mathbf{z}_i) + \boldsymbol{\varepsilon}_i$ . Where  $\boldsymbol{\varepsilon}_i$  is a Gaussian white noise of variance  $\sigma_n^2$ . As a result, the observed targets can also be described with a Gaussian distribution  $\tilde{\mathbf{z}} \sim \mathcal{N}(\mathbf{0}, \mathbf{K}(\mathbf{Z}, \mathbf{Z}) + \sigma_n^2 \mathbf{I})$  where  $\mathbf{Z} = \{\mathbf{z}_i\}$  and  $\mathbf{K}(\mathbf{Z}, \mathbf{Z})$  is the covariance matrix computed using a known covariance function. Gaussian kernels are the frequently used covariance functions [4]. They are defined by:

$$k(x_p, x_q) = \sigma_s^2 e^{-\frac{1}{2}(x_p - x_q)^T W (x_p - x_q)} \quad (1)$$

Where  $\sigma_s^2$  denotes the signal variance and  $\mathbf{W}$  represents the widths of the kernel. The joint distribution of the observed  $\tilde{\mathbf{z}}$  and predicted values ( $f(\mathbf{z}_*)$ ) for a query point  $\mathbf{z}_*$  is given by:

$$\begin{bmatrix} \tilde{\mathbf{z}} \\ f(\mathbf{z}_*) \end{bmatrix} \sim \mathcal{N}\left(\mathbf{0}, \begin{bmatrix} \mathbf{K}(\mathbf{Z}, \mathbf{Z}) + \sigma_n^2 \mathbf{I} & k(\mathbf{Z}, \mathbf{z}_*) \\ k(\mathbf{z}_*, \mathbf{Z}) & k(\mathbf{z}_*, \mathbf{z}_*) \end{bmatrix}\right) \quad (2)$$

The fact of conditioning the joint distribution yields the predicted mean value  $f(\mathbf{z}_*)$  along with its variance  $\mathbf{V}(\mathbf{z}_*)$ :

$$f(\mathbf{z}_*) = \mathbf{k}_*^T (\mathbf{K} + \sigma_n^2 \mathbf{I})^{-1} \tilde{\mathbf{z}} = \mathbf{k}_*^T \boldsymbol{\alpha} \quad (3)$$

$$\mathbf{V}(\mathbf{z}_*) = k(\mathbf{z}_*, \mathbf{z}_*) - \mathbf{k}_*^T (\mathbf{K} + \sigma_n^2 \mathbf{I})^{-1} \mathbf{k}_* \quad (4)$$

With  $\mathbf{k}_* = \mathbf{k}(\mathbf{Z}, \mathbf{z}_*)$ ,  $\mathbf{K} = \mathbf{K}(\mathbf{Z}, \mathbf{Z})$  and  $\boldsymbol{\alpha}$  denotes the prediction vector. The hyper-parameters of a Gaussian process with Gaussian kernel are given by  $\boldsymbol{\theta} = [\sigma_n^2, \sigma_s^2, \mathbf{W}]$ . The latter are the only open parameters. Their optimal values for a particular dataset can be automatically estimated by maximizing the *log* marginal likelihood using standard optimisation methods [4].

The purpose of using the GPR in our work is to learn a function  $f(\mathbf{z}_*)$  from the training data  $\{\mathbf{z}_i, \tilde{\mathbf{z}}_i\}$ . This function will serve to correct all the query points  $\mathbf{P}_*(\mathbf{x}_*, \mathbf{y}_*, \mathbf{z}_*)$  issued by the faulty sensor. The correction applies only on the depth variable  $\mathbf{z}_*$ . Thereafter, the computation of the remaining two others coordinates ( $\hat{\mathbf{x}}_*$ ,  $\hat{\mathbf{y}}_*$ ) requires the corrected depth  $\hat{\mathbf{z}}_*$ , and the beforehand computed calibration parameters ( $f_{x\_ir}, f_{y\_ir}; c_{x\_ir}, c_{y\_ir}$ ) of the IR camera as shown below:

$$\begin{cases} \hat{\mathbf{x}}_* = (\hat{\mathbf{z}}_* / f_{x\_ir})(u_* - c_{x\_ir}) \\ \hat{\mathbf{y}}_* = (\hat{\mathbf{z}}_* / f_{y\_ir})(v_* - c_{y\_ir}) \end{cases} \quad (5)$$

$(u_*, v_*)$  are the 2D image coordinates of the target pixel where the depth value  $\mathbf{z}_*$  was captured.

## VI. DEPTH MAP CORRECTION APPROACH

To correct the drifty sensor  $\mathbf{K}_f$ , we propose the pipeline in Fig 4. The latter starts with a **training** stage Fig 4(a) followed by a **correction** stage (test) Fig 4(b). The pairs of points  $\{(P_i, \tilde{P}_i)\}$  are necessary to extract the training data  $\{(z_i, \tilde{z}_i)\}$ . These points are selected from a variety of features covering the whole operating range of the camera. At this level, both cameras ( $\mathbf{K}_f$ ,  $\mathbf{K}_h$ ) are supposed to be accurately calibrated (mono calibration IR, RGB separately, and stereo calibration IR/RGB jointly). More importantly, in this experiment the ground truth camera  $\mathbf{K}_h$  was verified

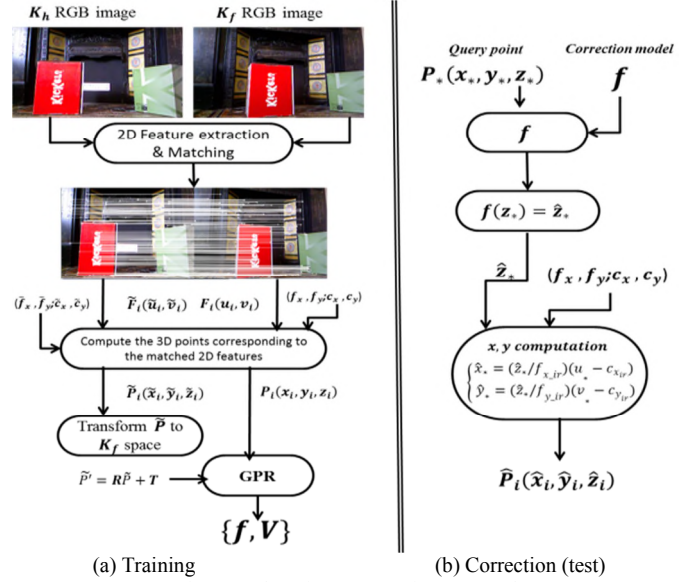


Fig 4. Faulty Kinect correction approach

against an accurate range measurement device<sup>1</sup>. We choose the RGB pair of images ( $\mathbf{K}_f$  RGB,  $\mathbf{K}_h$  RGB) as a basis to extract corresponding features because they are more reliable. In addition, one can visually select different points from all the existing depth levels, which is not possible to do with the depth map. This image is noisier and less discriminative. Hence, not suitable to extract good features.

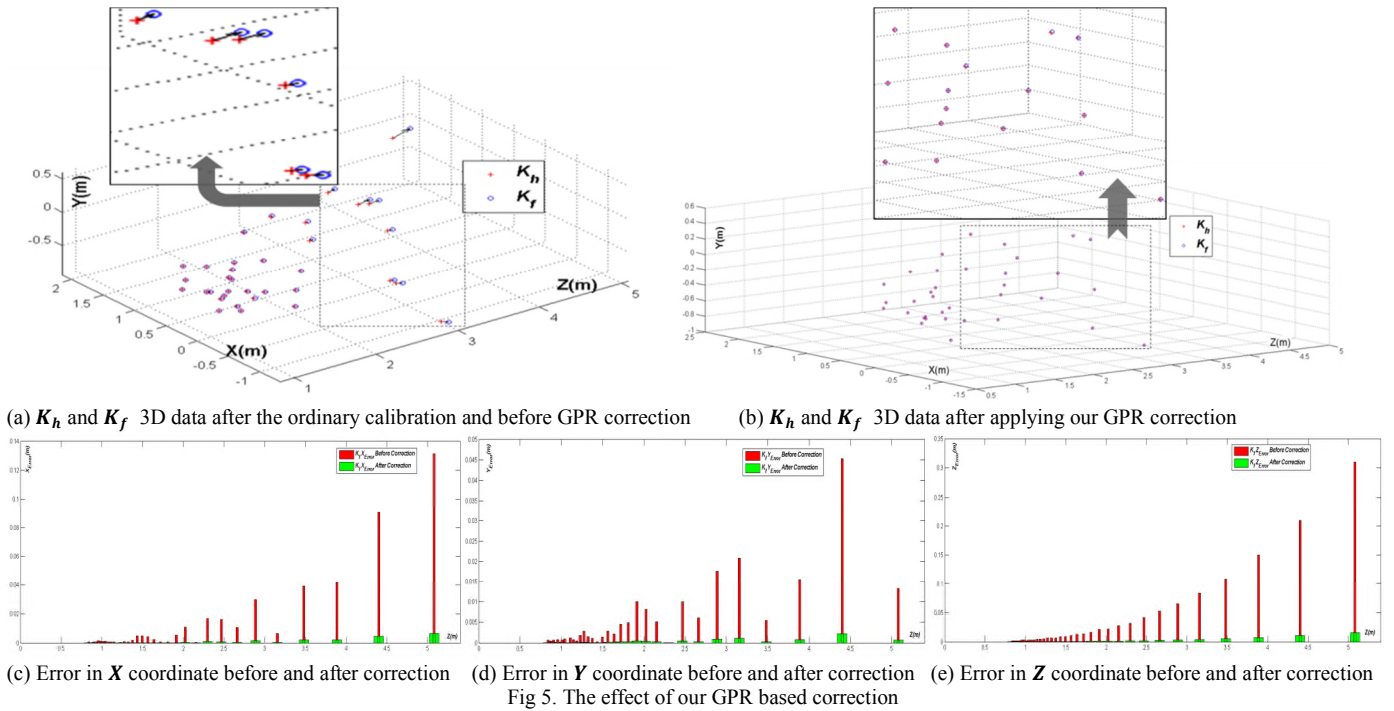
The training stage begins with the matching of the extracted 2D features Fig 4(a). The 3D points ( $P_i(x_i, y_i, z_i)$ ,  $\tilde{P}_i(\tilde{x}_i, \tilde{y}_i, \tilde{z}_i)$ ) are then computed based on the  $(u_i, v_i)$  positions of their respective 2D counterparts ( $F_i(u_i, v_i)$ ,  $\tilde{F}_i(\tilde{u}_i, \tilde{v}_i)$ ) Fig 4(b) and the calibration parameters of each camera. After computing the 3D points, we proceed through the actual GPR, which produces the correction model  $f$ . This new entity will be associated to the faulty sensor as a new calibration parameter.

The correction phase uses the outputs of the training algorithm ( $f$ ) to readjust the wrongly captured depth readings Fig 4(b). The whole depth map  $\{z_*\}$  undergoes the correction in the same way the ordinary calibration parameters are applied. Subsequently, the corrected depth data  $\hat{\mathbf{z}}_*$  is used to process the remaining two coordinates  $\{x_*, y_*\}$ . As a result, we get a more accurate 3D point cloud  $\hat{P}_i(\hat{x}_i, \hat{y}_i, \hat{z}_i)$ .

## VII. RESULTS AND DISCUSSIONS

To validate our findings about GPR-based RGBD sensors correction, we conducted a series of experiments where a set of 3D points were extracted from both the healthy camera ( $\mathbf{K}_h$ ) and the drifty one ( $\mathbf{K}_f$ ). After applying the ordinary camera calibration, we plot the 3D points in the same graph Fig 5(a). From the graph, we can clearly see the shift caused to the range data of the faulty sensor (black arrows between the red crosses and the blue circles). The length of these arrows represents the magnitude of the error. The latter is the distance between the correct points and their erroneous correspondent.

<sup>1</sup> Bosch Laser Range Finder DLE40



This distance is proportional to the range separating the sensor and the points.

After applying the correction, the error was significantly reduced. The wrongly captured depth values were corrected with the GPR. The improvements in the accuracy can be seen in Fig 5 (b). The graphs in Fig 5 (c), (d), (e) illustrate the error in points position before (red) and after the correction (green). The error in  $z$  is increasing with increasing depth. However, the error in both  $x$  and  $y$  does not depend only on the depth, but also on the position of the pixel according the centre of the image. Table 1 further shows a comparison between the RMSE before and after the correction.

TABLE 1. RMSE ERROR BEFORE AND AFTER THE GPR CORRECTION

	$X(m)$	$Y(m)$	$Z(m)$	Overall (m)
Before correction	0.0295	0.0102	0.0743	0.0809
After correction	0.0015	0.0051	0.0037	0.0065

## VIII. CONCLUSIONS

We presented a novel phenomenon that appears within the depth map of RGBD sensors. We demonstrated the weakness of the classical mono and stereo calibration methods to solve the lack of accuracy within the worn sensors. In addition, we presented an innovative approach based on our findings and the Gaussian Process Regression to overcome the lack of precision. As future work, we will investigate the effectiveness of the same method on other RGBD sensors like Asus Xtion. Moreover, we will study the applicability of the same approach to jointly correct a setup of multiple depth cameras. This allows the sensors with less accuracy to compensate with the more reliable ones.

## REFERENCES

- [1] J. Smisek, M. Jancosek, and T. Pajdla, "3D with Kinect," in *2011 IEEE International Conference on Computer Vision Workshops (ICCV Workshops)*, 2011, pp. 1154–1160.
- [2] K. Khoshelham and S. O. Elberink, "Accuracy and resolution of Kinect depth data for indoor mapping applications.," *Sensors (Basel, Switzerland)*, vol. 12, no. 2, pp. 1437–54, Jan. 2012.
- [3] A. Amamra and N. Aouf, "Robust and Sparse RGBD Data Registration of Scene Views," in *2013 17th International Conference on Information Visualisation*, 2013, pp. 488–493.
- [4] J. Davis, "Fusion of time-of-flight depth and stereo for high accuracy depth maps," in *2008 IEEE Conference on Computer Vision and Pattern Recognition*, 2008, pp. 1–8.
- [5] W. Chiu, U. Blanke, and M. Fritz, "Improving the Kinect by Cross-Modal Stereo.," *BMVC*, 2011.
- [6] K. Xu, L. Qin, and L. Yang, "RGB-D fusion toward accurate 3D mapping," in *2011 IEEE International Conference on Robotics and Biomimetics*, 2011, pp. 2618–2622.
- [7] P. Henry, M. Krainin, E. Herbst, X. Ren, and D. Fox, "RGB-D mapping: Using Kinect-style depth cameras for dense 3D modeling of indoor environments," *The International Journal of Robotics Research*, vol. 31, no. 5, pp. 647–663, Feb. 2012.
- [8] S. Matyunin, D. Vatolin, Y. Berdnikov, and M. Smirnov, "Temporal filtering for depth maps generated by Kinect depth camera," in *2011 3DTV Conference: The True Vision - Capture, Transmission and Display of 3D Video (3DTV-CON)*, 2011, pp. 1–4.
- [9] S. Seo, M. Wallat, T. Graepel, and K. Obermayer, "Gaussian process regression: Active data selection and test point rejection," *Mustererkennung 2000*, 2000.

# Network-on-Chip Application Mapping based on Domain Knowledge Genetic Algorithm

Yin Zhen Tei\*, N. Shaikh-Husin\*, Yuan Wen Hau<sup>†</sup>, Eko Supriyanto<sup>†</sup>, M. N. Marsono\*

\*Department of Electronic and Computer Engineering, Faculty of Electrical Engineering

<sup>†</sup>IJN-UTM Cardiovascular Engineering Center, Faculty of Biosciences and Medical Engineering  
Universiti Teknologi Malaysia

81310 Skudai, Johor, Malaysia

Email: yztei2@live.utm.my, nasirsh@fke.utm.my, {hauyuanwen, eko}@biomedical.utm.my, nadzir@fke.utm.my

**Abstract**—This paper addresses application mapping technique targeted for large-scale Network-on-chip (NoC). The increasing number of intellectual property (IP) cores in multi-processor System-on-Chips (MPSoCs) makes NoC application mapping more challenging to find optimum core-to-topology mapping. The factorial increase in possible mappings space requires a mapping algorithm to efficiently look for potential mapping space. This paper proposes an application mapping technique that incorporates domain knowledge into genetic algorithm (GA) to minimize the energy consumption of NoC communication. The GA is initialized with knowledge on network partition whereas the genetic crossover operator is guided with communication demands. The effects of domain knowledge GA on initial population and genetic operator are analysed in terms of the solution quality and convergence speed. Through simulation results on the MCSL real application traffic traces, the knowledge-based genetic operator gives 28% energy saving compared to application mapping using conventional GA. By combining both domain knowledge technique into GA, the solution quality can further save energy by 5% and convergence speed by 86% compared to knowledge-based crossover GA. Our experiment suggests that domain knowledge in GA initialization and crossover operation obtain low energy application mapping effectively for large-scale NoC-based MPSoC.

**Index Terms**—Application mapping, domain knowledge, genetic algorithm, Network-on-Chip, network partitioning

## I. INTRODUCTION

Network-on-chip (NoC) has emerged as a promising on-chip communication architecture providing modularity and scalability for MPSoCs. Application mapping determines the placement of IP cores to the routers on the Network-on-Chip (NoC) tiles such that the performance or cost metrics of interest are optimized [1]. It is an NP-hard problem that exhaustive algorithm cannot be applied. Therefore, an effective mapping algorithm to reduce the large search space and to obtain optimum mapping is required. Optimization search with refinement such as simulated annealing (SA) [2] and genetic algorithm (GA) [3] have been used in application mapping in NoC. GA could provide near optimum solution with limited known information [4] but it relies on the initial population, genetic operators and selection mechanism. Domain-knowledge has been used in crossover and mutation to improve GA mapping and convergence [3] by checking each gene's communicating distances among cores. These

will cause computation time to increase drastically for highly communicating applications and large-scale NoCs.

Large-scale MPSoCs are mostly combinations of few subsystems. One IP core may only communicate with several cores in such a large system. Network partitioning (NP) decomposes a large system into several smaller subsystems in which highly communicating cores are grouped in the same partition. Based on this knowledge, NP may be done prior to the application mapping to narrow down the search space and to reduce the core mapping complexity. A good initial mapping can be loosely defined as one that increases the probability to reach near optimum mapping [5]. It is important to investigate the effect of domain knowledge GA for NoC application mapping in terms of final solution quality and convergence speed especially for large-scale NoCs.

This paper proposes an application mapping technique that incorporates domain knowledge into genetic algorithm (NP-DKGA) to minimize the energy consumption of NoC communication. The initial GA population is initialized with network partitioning knowledge whereas the genetic operator crossover is guided with the knowledge on cores communication demands. NP-DKGA application mapping technique operates in two phases: a  $k$ -way partitioning of application graph into assigned partitions as initial population; and using knowledge-based genetic algorithm (DKGA) to search for near optimum mapping. The authors have tested the effectiveness of NP-DKGA on several real benchmarks applications [6]. Based on our simulation results, our proposed VOPD core mapping obtained the best mapping identical to reference [7]. For large applications, our technique show an overall improvement in the final mapping quality and in term of convergence. All results are compared with the mapping using conventional genetic algorithm (CGA).

## II. RELATED WORK

Many application mapping techniques have been proposed for optimizing different costs and performance metrics. The first mapping algorithm based on a modified bit energy model [8] was proposed by Hu and Marculescu using branch and bound technique such that energy consumption can be minimized with bandwidth reservation [9]. Reference [5] compares few application mapping algorithms using the bit energy

model which is targeted for low energy systems. Simulated annealing (SA) [2] and genetic algorithm (GA) [3] were also proposed as application mapping techniques to optimize energy consumption using bit energy model.

Multi-objective evolutionary algorithm with random-based initial population mapping and crossover with hot spotremap was proposed to optimize execution time and power consumption [10]. The author claimed that more effective genetic operators have a great impact on the final mapping [10]. In reference [11], GA is initialized with a random initial mapping and the crossover is based on swapping communicating cores with neighbouring cores. There are few crossover techniques such as remap hotspot [10], [12] and cycle crossover [13]. All of these crossover techniques do not include useful NoC mapping knowledge. The convergence is slow especially for large-scale NoC. In the domain-knowledge evolutionary algorithm [3], mapping similarity crossover (MS) has been proposed that maintains the common characteristic between parents and the rest using greedy mapping. Mapping similarity is able to handle symmetric problem in mesh topology but the technique increases the computation time as the NoC size increases.

As the NoC size increases, the complexity of communication ranking placement can hardly obtain good mappings. Large SoC system can be divided into several clusters (partitions). Cluster-based application mapping techniques have been proposed in [14], [15]. The author in [14] proposed a cluster-based relaxation for integer linear programming formulation for application mapping in order to reach the optimum result within tolerable time limits. Authors in [13] proposed a partition-based application mapping with near-convex core placement for large NoC. However, these three techniques map cores without improving cross partition movement. Although they show shorter runtime, the final mapping quality is affected [13]. A mapping algorithm based on Kernighan-Lin (K-L) partitioning, called LMAP, has been proposed to explore search space via flipping the partitions and cores in a hierarchical fashion [16].

References [15] proposed a cluster-based initial mapping for simulated annealing (CSA) to speed up the convergence to near-optimal solutions. These work shows the runtime advantage without compromising the quality of solution compared to the pure SA approach. Given an random initial mapping, optimized simulated annealing (OSA) [2] improves SA by clustering communicating cores implicitly during swapping process. OSA shows better mapping quality compared to CSA. However, author in [3] has shown that evolutionary algorithm perform better than OSA. Particle Swarm Optimization (PSO) has been proposed with deterministic initial mapping to explore the search space [17]. The domain knowledge applied on initial mapping using greedy-based approach where IP cores are placed on the NoC topology based on the descending ranking of total communication cost defined in APCG. This initial mapping technique can hardly obtain good mapping as the NoC size increases.

### III. DOMAIN-KNOWLEDGE GENETIC ALGORITHM APPLICATION MAPPING

This paper proposes an application mapping technique that incorporates domain knowledge into genetic algorithm (NP-DKGA) to minimize the energy consumption of NoC communication. The initial population of GA is initialized with network partitioning (NP) knowledge whereas the genetic operator crossover is guided with communication demands knowledge as shown in Fig. 1. The proposed two-phase application mapping is targeted for low power large-scale NoC. The first phase is shown in dashed-box in Fig. 1. All cores are mapped onto the assigned partitions on the mesh-based topology as the knowledge-based initial population. The second phase involves the optimization of energy consumption using domain-knowledge crossover genetic algorithm (DKGA) to search for optimum mapping. Some definitions used in this paper are listed next.

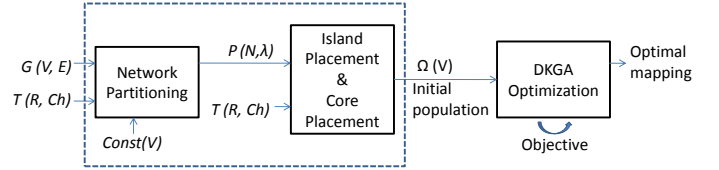


Fig. 1: Overview of the proposed technique, NP-DKGA.

#### A. Problem Formulation

**Definition 1:** An application characteristic graph (APCG),  $G = G(V, E)$  is a directed graph, where each vertex  $v_i \in V$  represents an IP core and each directed edge  $e_{(i,j)} \in E$  characterizes the total communication volume in bits from vertex  $v_i$  to vertex  $v_j$ . Application tasks are assumed to be assigned to all vertices,  $v_i$  and scheduled to each IP core.

**Definition 2:** NoC mesh-based network,  $T(R, Ch)$  is a labelled graph, where each  $r_i \in R$  denotes a router and each  $ch_i \in Ch$  denotes a channel. All routers can have a maximum of 5 ports with 4 ports connected to neighbouring routers via channels and one connection to the processing core.  $T$  is placed on a grid in the XY plane with unit distances between adjacent routers.  $x(r_i)$  and  $y(r_i)$  denote the  $x$  and  $y$  coordinates for a router  $r_i \in R$ .

**Definition 3:** Given an input APCG, network partitioning decomposes APCG into smaller subsystems according to size the mesh-based topology. APCG will be partitioned or divided into  $m$  partitions,  $P_1, P_2, \dots, P_m$ . Network partitioning is to find  $P(N, \lambda)$  where  $N$  is number of cores in each partition and  $\lambda$  is inter-partition traffic. The objective of network partitioning is to reduce inter-partition traffic (min-cut partitioning),  $\lambda$  subject to constraints,  $Const(V)$  to obtain a balanced number of cores for all partitions.

**Definition 4:** The placement for the partitioned APCG involves partition placement and core placement. Assume a partitioned graph  $P(N, \lambda)$  and topology  $T(R, Ch)$ . Partition placement,  $\omega : P \rightarrow T$  assigns certain regions on the mesh-based topology,  $T$  to a particular partition,  $P_i$ . For core

placement,  $\omega : V \rightarrow R$  where each core  $v_i$  in each partition is associated with the router  $r_i$  in the assigned topology region.

### B. Network partitioning as knowledge-based GA initial mapping

Network partitioning (NP) decomposes a large NoC system into a few smaller partitions. In this proposed NoC application mapping, NP is implemented in two stages: mesh topology partitioning and application partitioning. In the first stage, mesh topology is assigned into a few smaller regions where each region represents one partition. The partitioning level will depend to the size of the topology. For the cases where mesh topology cannot be bipartitioned, such as  $3 \times 3$  and  $5 \times 5$ ,  $k$ -way partitioning can be implemented. Mesh topology is partitioned into  $k$  partitions with the same number of tiles for each partition.

In the second stage, the multilevel-KL (Kernighan-Lin) algorithm decomposes IP cores in APCG into halves and refines the partitions at each subsequent level. This algorithm is chosen due to its high-quality partitions and is scalable for large network [18]. The application is partitioned according to number of tiles available in each mesh partition. Each partition must have at least four available tiles. If the partition size is too small, the role of NP to group the highly communicating cores will be insignificant. The objective of NP is to achieve min-cut with the lowest inter-partition traffic. There is a single constraint to core balance each partition. Fig. 2 shows an example of 2-level partitioning on  $4 \times 4$  mesh-topology and the VOPD application [19]. The dashed lines show the first-level partitioning while dashed-dot lines show the second-level partitioning for the VOPD application.

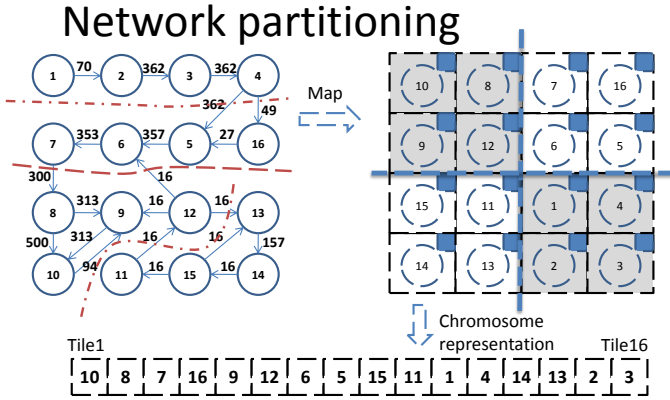


Fig. 2: VOPD application and  $4 \times 4$  mesh-based topology partitioning. Partition and core mapping of VOPD application onto NP knowledge-based initial population and the associated integer chromosomes.

The outcome of the two-stage NP is used to generate an initial population for GA in the second phase. Thus, instead of detail hierarchical mapping for all partitions and cores, core placement are done randomly within the assigned region of mesh topology. The min-cut partitioning technique groups heavily communicating IP cores closer to each other to reduce communication energy consumption. It results in a

better initial mapping compared to random-based mapping and increases the probability for GA to converge and to reach near optimum solution.

### C. Knowledge-based genetic algorithm

Instead of utilizing conventional genetic algorithm (CGA), we propose a domain-knowledge genetic algorithm that applies NP as initial population and heuristic crossover (NP-DKGA). The detail of each GA components are presented next.

1) *Problem Representation:* Permutation chromosome is used to represent the application mapping problem. It consists of a series of genes with each gene corresponds to a tile in the mesh topology. Each gene is assigned an integer which represents an IP core in APCG that is attached to the corresponding router in each tile. Fig. 2 shows examples of integer chromosome for a  $4 \times 4$  mesh topology. A gene associated to a router is assigned null value if no IP core is assigned to the router. A valid permutation chromosome cannot have two genes with the same integer because it would represent a core connected to two routers.

2) *Population:* The population is the main element of a genetic algorithm. Research has shown that the initial population may have effect on the best fitness function value and these effects may last for several generations [4]. For a large NoC, the possible mapping space is extremely large which could slow down the convergence. Hence, a good initial population may result in faster convergence. On the other hand, the population size influence is also another parameter to decide the coverage of mapping space. A population that is too large takes time to evolve whereas a population that is too small will lead to a local minima. Population size is proportional to the application size.

In this paper, the NP initial mapping that groups communicating cores within the same partition provides a potential low energy mapping. This enables GA to explore the reduced search space for low energy mapping with faster convergence instead of random exploration of the huge search space. Fig. 2 show NP initial population for  $4 \times 4$  VOPD application after random island and core mapping.

3) *Fitness Function:* Fitness function represents the desired optimization goal. For NoC application mapping, the fitness function is closely related to the distance between the source and destination cores. According to literature, energy optimization is the primary goal for NoC. This paper targets energy minimization where bit energy model is utilized. Ye at al. [8] proposed a model to calculate power consumption in a switch fabric that accounts for each data bit goes through the network router. Then, Hu and Marculescu [9] modified the bit energy model such that it is suited to mesh-based network. Based on these previous works, this paper applies the bit energy model to optimize,  $E_{bit}^{vs,vD}$ , the required energy for a bit of data from source core to destination core.

$$E_{bit}^{vs,vD} = n_{hops} E_{Lbit} + (n_{hops} + 1) E_{Rbit} \quad (1)$$

where  $n_{hops}$  is the number of hops for a path from the source core to the destination core (i.e., one hop is the distance

between two adjacent routers) with XY deterministic routing.  $E_{L_{bit}}$  is the energy consumption for a link between adjacent router and  $E_{R_{bit}}$  is the energy consumption for the router. The  $E_{R_{bit}}$  and  $E_{L_{bit}}$  are set to 0.43pJ and 5.445pJ respectively according to [8]. The overall energy consumption  $E^A$  is the summation of all energy bit consumed by all bit transmissions.

$$E_A = \sum_{\text{all } S,D} (E_{bit}^{v_S,v_D} \times e_{S,D}) \quad (2)$$

where  $e_{S,D}$  is the total communication traffic in bit from the source core to the destination core.

4) *Crossover*: Crossover is used to produce offspring, and fitter chromosomes are searched to form a new population. In this paper, knowledge-based is proposed as described in Algorithm 1. Crossover point are randomly set according to the nature randomization behaviour of GA. Two children chromosome are generated from two selected parents. After the crossover between parents, if the same integer is assigned to two genes, the latter gene in the resulting chromosome is labelled as *InvalidGene*. Cores that are not assigned to any gene are labelled as *UnmappedCores*. In CGA, all *InvalidGenes* are randomly remapped with *UnmappedCores*. However, in the proposed DKGA, we applied a heuristic crossover technique. The *UnmappedCores* will determine its communication with the adjacent router of *InvalidGene*. The *UnmappedCores* will be remapped to *InvalidGene* which has the highest communication with *NeighborCore*. This crossover algorithm is done iteratively until the generated children chromosomes reach the population size. This implicit clustering approach aids GA to explore the mapping space efficiently for low power mapping.

---

**Algorithm 1** Knowledge-based Crossover Algorithm
 

---

*Population* is the population size  
*TotalParent* is total parent chromosomes  
*B* is the length of chromosome  
**for**  $i = \text{TotalParent} + 1$  to *Population* **do**  
 Select parent chromosome using roulette wheel,  $P1$  and  $P2$ .  
 Select random crossover point,  $C \in B$ .  
 $\text{Child}(i) \leftarrow$  Crossover between  $P1$  and  $P2$ .  
 Check *InvalidGene*.  
 Check *UnmappedCores*.  
 $\text{NeighborCore} = \text{GetAdjacentCore}(\text{InvalidGene})$   
 $\text{CommunicatingCore} = \text{GetCommCore}(\text{NeighborCore}, \text{UnmappedCores})$   
 $\text{InvalidGene} \leftarrow \max(\text{CommunicatingCore})$   
**end for**

---

5) *Mutation*: Mutation is the operation that uses only one parent and creates one child by applying some kind of randomized change to the chromosome [20]. Probability of mutation is the probability for each gene in every chromosome to undergo mutation [21]. Since NoC application mapping consists of a large size chromosome, checking the probability for each gene is time consuming. Thus, population-based probability mutation is applied which refers to probability of one chromosome to undergo mutation in a population. For the selected chromosome, only two genes are randomly selected and mutated. Otherwise, the gene remains in the chromosome.

#### IV. SIMULATION METHODOLOGY AND RESULT DISCUSSION

This section discusses the benchmarks, parameter setting and simulation results for NP-DKGA. A realistic traffic benchmark suite MCSL [6] that supports several NoC architectures is used to generate real traffic traces in this experiment. Six real applications were included in MCSL: FFT, FPPPP, SPARSE, ROBOT, RSenc and RSdec. A  $12 \times 12$  mesh-based architecture is chosen for assessing the scalability of the proposed algorithm and additionally, we also implement VOPD (video object plane decoder) [19] for  $4 \times 4$  mesh-based network. This application mapping is evaluated on mesh-based NoC and XY deterministic routing. All tasks in each applications are scheduled and mapped into the IP cores available on meshed network. For all the benchmarks, network partitioning is implemented using *Chaco* [18] tool before the application mapping stage. *Chaco* performs bisection partitioning by grouping highly communicating cores in the same partition and at the same time, performs the min-cut operation.

This paper studies the effectiveness knowledge-based crossover and effectiveness network partitioning as initial mapping for GA optimization in term of the solution quality and convergence. Several parameters in GA are fixed with probability for crossover of 0.8, population-based mutation rate of 0.3, and population size of 100 for  $12 \times 12$  network size and 50 for the  $4 \times 4$  network. This work does not analyse the optimal parameters for DKGA but rather to assess the effectiveness of the knowledge-based in initial population and genetic operator. The termination of GA is set to 1000 generations for MCSL applications and 300 generations for VOPD application. In order to obtain highly accurate results for GA with random-based optimization method, statistical analysis based on different energy level; the highest, the lowest and the average energy consumption for each application benchmarks.

TABLE I: Connectivity degree for all benchmarks.

Benchmark	Range of connectivity degree
RSenc	0-14
ROBOT	0-15
FFT	60-116
RSdec	0-43
SPARSE	0-9
FPPPP	0-80
VOPD	1-4

TABLE I shows the connectivity degree for all benchmarks used in the experiments. The connectivity degree is defined as the total incoming and outgoing communication for each core in the benchmark. The FFT has a high connectivity degree between 60 and 116. On the other hand, other benchmarks contain IP cores that are not communicating to other cores. The relationship between the connectivity degree with the GA convergence will be analysed next.

We analysed the convergence speed of GA with knowledge-based crossover and NP initial mapping for all benchmarks

compared to CGA. The convergence of GA is calculated by Equation (3). GA is determined to have converged only if the convergence is less than 1% last for 100 generations.

$$Convergence = \frac{E_A[i - 100] - E_A[i]}{E_A[i - 100]} \leq 1\% \quad (3)$$

TABLE II: The convergence speed improvement for R-DKGA and NP-DKGA compared to conventional GA (CGA).

Benchmarks	Convergence speed improvement (%)	
	R-CCA NP-DKGA	R-DKGA NP-DKGA
RSenc	65%	62%
ROBOT	56%	65%
FFT	14%	67%
RSdec	5%	86%
SPARSE	33%	44%
FPPPP	38%	47%
VOPD	69%	55%

TABLE II shows the percentage of convergence speed improvement using knowledge-based crossover and NP knowledge-based initial mapping with the speed convergence defined in (3). The knowledge-based crossover (R-DKGA) shows improvements in all benchmark applications. FFT is the largest communicating application among all benchmarks. For highly communicating applications: FFT, FPPPP and RSdec, knowledge domain on initial mapping helps DKGA converges faster. These applications show that advanced NP initial mapping helps highly communicating applications to converge faster and assists the GA in obtaining high quality mapping. The improvement in term of quality mapping solution will be discussed in detail next.

TABLE III shows the percentage of energy minimization after several simulation runs for the domain knowledge crossover GA (R-DKGA) and the domain knowledge in initial mapping (NP-DKGA) compared to conventional GA (CGA). It is easily observed that all applications improve significantly with domain knowledge applied GA compared to CGA. With the knowledge-based crossover, energy saved up to 28% for the highest communicating application (FFT). Besides, with the NP knowledge-based initial mapping, all applications show NoC communication energy saving up to 29%. TABLE III shows that the NP initial population assists GA to obtains better mapping quality. The NP-DKGA gives better energy saving compared to R-DKGA. Furthermore, the VOPD application optimized using R-DKGA and NP-DKGA achieved the global minimum identical to reference [7].

Fig. 3 shows the energy consumption for 10 simulations in comparison to R-CGA, R-DKGA, and NP-DKGA with CGA used as the reference. The error-bar shows the lowest, highest and average energy consumption of all 10 simulation runs for R-CGA, R-DKGA, and NP-DKGA. The result shows that knowledge-based crossover and initial mapping have significantly improved the quality of the final mapping. In term of convergence and quality mapping, NP knowledge-based initial mapping and knowledge-based crossover need to

TABLE III: Percentage of energy minimization of the best case with and without domain knowledge in crossover and domain knowledge in initial mapping.

Benchmarks	Energy improvement (%)	
	R-CCA R-DKGA	R-CCA NP-DKGA
RSenc	2%	2%
ROBOT	14%	16%
FFT	28%	29%
RSdec	10%	10%
SPARSE	25%	27%
FPPPP	10%	15%
VOPD	1%	1%

be added into GA in order to obtain better mapping quality and faster convergence speed. The knowledge-based crossover gives better final mapping regardless if the NP initial mapping is applied. The results show that NP could further facilitate DKGA to improve the application mapping quality and speed up the convergence when targeted for low power large-scale NoC.

## V. CONCLUSION

This paper presented the NP-DKGA technique that uses network partitioning knowledge as initial mapping and knowledge-based crossover in GA in order to optimize NoC application mapping. This algorithm is targeted for large-scale low energy NoC. We performed analysis on the effectiveness of domain knowledge applied in initial population and genetic operator of GA based on several real benchmarks. The NP knowledge-based initial mapping shows significant energy saving compared to random initial mapping. Moreover, the convergence speed can be improved up to 86%. The effectiveness of the knowledge-based crossover gives significant effect in energy reduction compared to the NP initial mapping GA. For less communicating application, knowledge-based crossover GA (DKGA) could converged well. However, for highly communicating application, our experiment shows that the knowledge-based initial mapping in DKGA can improve both the application mapping quality and speed up the convergence. NoC is meant for heavy communication and large scale MPSoC. Hence, domain knowledge GA in initial population and crossover operation are needed in order to obtain low energy large-scale NoC-based MPSoC.

In a future work, we plan to consider for multi-objective environment. Thermal balanced in an issue to reduce faults in NoC and increase reliability of NoC. For energy and thermal balanced, network partitioning need to be done with balanced load and min-cut. This work can be extended into more accurate evaluation using cycle accurate NoC simulator.

## REFERENCES

- [1] R. Marculescu, U. Ogras, L.-S. Peh, N. Jerger, and Y. Hoskote, "Outstanding research problems in NoC design: System, microarchitecture, and circuit perspectives," *IEEE Transactions on Computer-Aided Design of Integrated Circuits and System*, vol. 28, no. 1, pp. 3–21, January 2009.

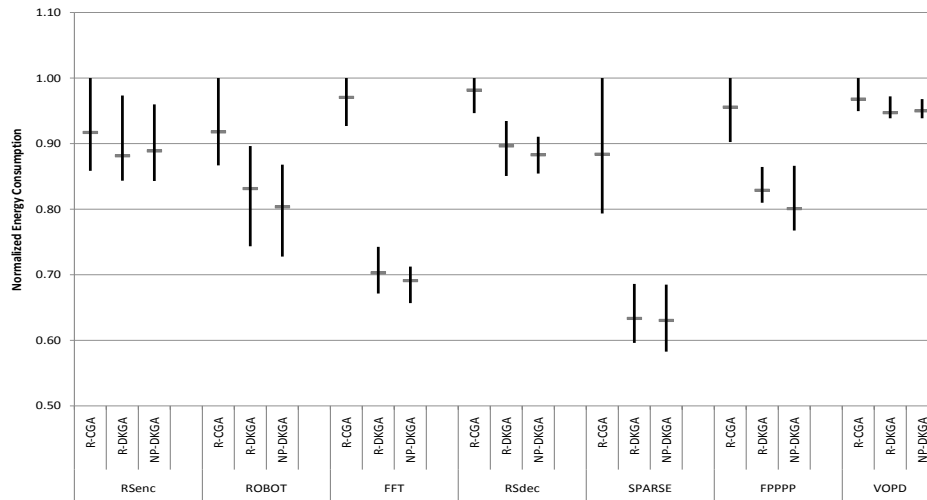


Fig. 3: Normalized energy consumption for all benchmarks. Y-errorbar shows minimum, average and maximum energy consumption.

- [2] C. Radu and L. Vintan, "Domain-knowledge optimized simulated annealing for network-on-chip application mapping," in *Advances in Intelligent Control Systems and Computer Science*, ser. Advances in Intelligent Systems and Computing, L. Dumitrache, Ed. Springer Berlin Heidelberg, 2013, vol. 187, pp. 473–487.
- [3] C. Radu, M. S. Mahub, and L. Vintan, "Developing domain-knowledge evolutionary algorithms for network-on-chip application mapping," *Microprocessors and Microsystems*, vol. 37, no. 1, pp. 65 – 78, 2013.
- [4] H. Maaranen, K. Miettinen, and A. Penttinen, "On initial populations of a genetic algorithm for continuous optimization problems," *J. of Global Optimization*, vol. 37, no. 3, pp. 405–436, Mar. 2007.
- [5] C. Marcon, E. Moreno, N. Calazans, and F. Moraes, "Comparison of network-on-chip mapping algorithms targeting low energy consumption," *IET Computers Digital Techniques*, vol. 2, no. 6, pp. 471–482, November 2008.
- [6] W. Liu, J. Xu, X. Wu, Y. Ye, X. Wang, W. Zhang, M. Nikdast, and Z. Wang, "A noc traffic suite based on real applications," in *VLSI (ISVLSI), 2011 IEEE Computer Society Annual Symposium on*, 2011, pp. 66–71.
- [7] P. K. Sahu and S. Chattopadhyay, "A survey on application mapping strategies for network-on-chip design," *Journal of Systems Architecture*, vol. 59, no. 1, pp. 60 – 76, 2013.
- [8] T. Ye, L. Benini, and G. De Micheli, "Analysis of power consumption on switch fabrics in network routers," in *Design Automation Conference, 2002. Proceedings. 39th*, 2002, pp. 524–529.
- [9] J. Hu and R. Marculescu, "Energy-aware mapping for tile-based noc architectures under performance constraints," in *Design Automation Conference, 2003. Proceedings of the ASP-DAC 2003. Asia and South Pacific*, 2003, pp. 233–239.
- [10] G. Ascia, V. Catania, and M. Palesi, "Multi-objective mapping for mesh-based noc architectures," in *Proceedings of the 2nd IEEE/ACM/IFIP International conference on Hardware/software codesign and system synthesis (CODES+ISSS '04)*, 2004, pp. 182–187.
- [11] A. A. Morgan, H. Elmiligi, M. W. El-Kharashi, and F. Gebali, "Multi-objective optimization of noc standard architectures using genetic algorithms," in *Proceedings of the The 10th IEEE International Symposium on Signal Processing and Information Technology*, ser. ISSPIT '10. Washington, DC, USA: IEEE Computer Society, 2010, pp. 85–90.
- [12] A.A.Morgan, "Networks-on-chip: Modeling, system-level abstraction, and application-specific architecture customization," Ph.D. dissertation, University of Victoria, 2011.
- [13] W. Jang and D. Pan, "A3map: Architecture-aware analytic mapping for networks-on-chip," in *Design Automation Conference (ASP-DAC), 2010 15th Asia and South Pacific*, 2010, pp. 523–528.
- [14] S. Tosun, "Cluster-based application mapping method for network-on-chip," *Advances in Engineering Software*, vol. 42, no. 10, pp. 868–874, October 2011.
- [15] Z. Lu, L. Xia, and A. Jantsch, "Cluster-based simulated annealing for mapping cores onto 2d mesh networks on chip," in *Proceeding of the 11th IEEE Workshop on Design and Diagnostics of Electronic Circuits and Systems (DDECS 2008)*, April 2008, pp. 1–6.
- [16] P. Sahu, N. Shah, K. Manna, and S. Chattopadhyay, "A new application mapping algorithm for mesh based network-on-chip design," in *India Conference (INDICON), 2010 Annual IEEE*, 2010, pp. 1–4.
- [17] P. Sahu, T. Shah, K. Manna, and S. Chattopadhyay, "Application mapping onto mesh-based network-on-chip using discrete particle swarm optimization," *Very Large Scale Integration (VLSI) Systems, IEEE Transactions on*, vol. 22, no. 2, pp. 300–312, Feb 2014.
- [18] B. Hendrickson and R. Leland, "The Chaco user's guide version 2.0," 1995.
- [19] E. B. Van Der Tol and E. G. T. Jaspers, "Mapping of MPEG-4 decoding on a flexible architecture platform," in *Media Processors 2002*, 2002, pp. 1–13.
- [20] A. E. Eiben and J. E. Smith, *Introduction to Evolutionary Computing*. SpringerVerlag, 2003.
- [21] E. Vonk and R. Johnson, *Automatic generation of neural network architecture using evolutionary computation*, ser. Advances in Fuzzy Systems-Applications and Theory. Singapore: World Scientific, 1997.

# Cascade adaptive control of a continuous stirred tank reactor

P. Dostál, V. Bobál, and J. Vojtěšek

**Abstract**— The paper deals with cascade adaptive control of a continuous stirred tank reactor with an exothermic reaction. The control is performed in primary and secondary control-loops where the primary controlled output of the reactor is the concentration of the reaction product, and, the secondary output is the reactant temperature. A common control input is the coolant flow rate. The controller in the primary control-loop is a nonlinear P-controller, and, the controller in the secondary control-loop is an adaptive controller. The proposed method is verified by control simulations.

**Keywords**— Adaptive control, cascade control, continuous stirred tank reactor, control simulation.

## I. INTRODUCTION

CONTINUOUS stirred tank reactors (CSTRs) are equipments widely used in chemical industry, biotechnologies, polymer manufacturing, and many others. From the system theory point of view, CSTRs belong to a class of nonlinear systems with mathematical models described by sets of nonlinear differential equations as it can be seen e.g. in [1] and [2].

It is well known that the control of chemical reactors often represents very complex problem. The control problems are due to the process nonlinearity and high sensitivity of the state and output variables to input changes. One way to obtain an effective control is to use some methods of adaptive or nonlinear control. Such methods were described e.g. in [3], [4] or [5].

Another alternative is the use of a cascade control, see, e.g. [6] – [8] with combination with the adaptive control.

In this paper, the CSTR control strategy is based on the fact that concentrations of components of reactions taking place in the reactor depend on the reactant temperature. Then, in the cascade control-loop, the concentration of a main product of the reaction is considered as the primary controlled variable, and, the reactant temperature as the secondary controlled variable. The coolant flow rate represents a common control input.

The primary control variable is measured in discrete time intervals. The primary controller determining the set point for the secondary (inner) control-loop is derived as a discrete

nonlinear proportional controller using the steady state characteristics of the reactor. Since the controlled process is nonlinear, a continuous-time adaptive controller is used as the secondary controller. The procedure for the adaptive control design in the inner control-loop is based on approximation of the nonlinear model of the CSTR by an continuous-time external linear model (CT ELM) with recursively estimated parameters. In the process of parameter estimation, an external delta model with the same structure as the CT model is used. The basics of delta models have been described e.g. in [9] – [12].

The resulting adaptive CT controller in the 2DOF control system structure is derived using the polynomial approach and the pole placement method, see, e.g. [13] – [16].

The cascade control is verified by simulations on the nonlinear model of the CSTR.

## II. NONLINEAR MODEL OF THE CSTR

Consider a CSTR with the first order consecutive exothermic reaction according to the scheme  $A \xrightarrow{k_1} B \xrightarrow{k_2} C$  and with a perfectly mixed cooling jacket. Using the usual simplifications, the model of the CSTR is described by four nonlinear differential equations

$$\frac{dc_A}{dt} = -\left(\frac{q_r}{V_r} + k_1\right)c_A + \frac{q_r}{V_r}c_{Af} \quad (1)$$

$$\frac{dc_B}{dt} = -\left(\frac{q_r}{V_r} + k_2\right)c_B + k_1c_A + \frac{q_r}{V_r}c_{Bf} \quad (2)$$

$$\frac{dT_r}{dt} = \frac{h_r}{(\rho c_p)_r} + \frac{q_r}{V_r}(T_{rf} - T_r) + \frac{A_h U}{V_r(\rho c_p)_r}(T_c - T_r) \quad (3)$$

$$\frac{dT_c}{dt} = \frac{q_c}{V_c}(T_{cf} - T_c) + \frac{A_h U}{V_c(\rho c_p)_c}(T_r - T_c) \quad (4)$$

with initial conditions  $c_A(0) = c_A^s$ ,  $c_B(0) = c_B^s$ ,  $T_r(0) = T_r^s$  and  $T_c(0) = T_c^s$ . Here,  $t$  stands for the time,  $c$  for concentrations,  $T$  for temperatures,  $V$  for volumes,  $\rho$  for densities,  $c_p$  for specific heat capacities,  $q$  for volumetric flow rates,  $A_h$  is the heat exchange surface area and  $U$  is the heat transfer coefficient. Subscripts denoted  $r$  describe the reactant mixture,  $w$  the metal walls of tubes,  $c$  the coolant,  $f$  the inlet

values and the superscript  $s$  steady-state values.

The reaction rates and the reaction heat are expressed as

$$k_j = k_{0j} \exp\left(\frac{-E_j}{RT_r}\right), \quad j = 1, 2 \quad (5)$$

$$h_r = h_1 k_1 c_A + h_2 k_2 c_B \quad (6)$$

where  $k_0$  are pre-exponential factors,  $E$  are activation energies and  $h$  are reaction enthalpies. The values of all parameters, feed values and steady-state values are given in Table 1.

TABLE I  
PARAMETERS, INLET VALUES AND INITIAL CONDITIONS

$V_r = 1.2 \text{ m}^3$	$c_{pr} = 4.05 \text{ kJ kg}^{-1} \text{K}^{-1}$
$V_c = 0.64 \text{ m}^3$	$c_{pc} = 4.18 \text{ kJ kg}^{-1} \text{K}^{-1}$
$\rho_r = 985 \text{ kg m}^{-3}$	$A_h = 5.5 \text{ m}^2$
$\rho_c = 998 \text{ kg m}^{-3}$	$U = 43.5 \text{ kJ m}^{-2} \text{min}^{-1} \text{K}^{-1}$
$k_{10} = 5.616 \cdot 10^{16} \text{ min}^{-1}$	$E_1/R = 13477 \text{ K}$
$k_{20} = 1.128 \cdot 10^{18} \text{ min}^{-1}$	$E_2/R = 15290 \text{ K}$
$h_1 = 4.8 \cdot 10^4 \text{ kJ kmol}^{-1}$	$h_2 = 2.2 \cdot 10^4 \text{ kJ kmol}^{-1}$
$c_{Af}^s = 2.85 \text{ kmol m}^{-3}$	$c_{Bf}^s = 0 \text{ kmol m}^{-3}$
$T_{rf}^s = 323 \text{ K}$	$T_{cf}^s = 293 \text{ K}$
$q_r^s = 0.08 \text{ m}^3 \text{min}^{-1}$	

The desired reaction product is a concentration of the component  $B$ .

### III. THE CONTROL OBJECTIVE

A basic scheme of the cascade control is in Fig. 1.

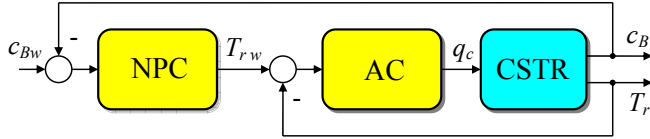


Fig. 1 Cascade control scheme.

Here, NPC stands for the nonlinear proportional controller, AC for the adaptive controller and CSTR for the reactor.

The control objective is to achieve a concentration of the component  $B$  as the primary controlled output near to its maximum. A dependence of the concentration of  $B$  on the reactant temperature is in Fig. 2.

There, an operating area consists of two parts. In the first subarea, the concentration  $B$  increases with increasing reactant temperature, in the second subarea it again decreases. The endpoints of the intervals defining both subareas are given as  $c_B^{\min} = 0.9$ ,  $c_B^U = 1.675$ . It can be seen that the maximum value of the  $c_B$  can be slightly higher than  $c_B^U$ . However, with respect to some following procedures, the maximum desired value of  $c_B$  will be limited just by  $c_B^U$ .

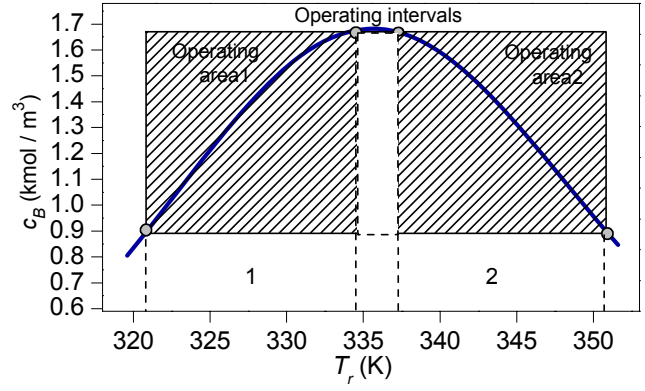


Fig. 2 Steady-state dependence of the product  $B$  concentration on the reactant temperature.

### IV. THE NPC DESIGN

The procedure in the design of the NPC appears from inverted steady-state characteristics and its subsequent polynomial approximation.

The boundaries of operating intervals are determined as

$$0.9 \leq c_B \leq 1.6, \quad 320.9 \leq T_r \leq 331.6$$

$$1.6 < c_B \leq 1.675, \quad 331.6 < T_r \leq 334.8$$

in the first operating interval, and

$$1.675 \geq c_B > 1.6, \quad 336.8 \leq T_r < 339.5$$

$$1.6 \geq c_B \geq 0.9, \quad 339.5 \leq T_r \leq 350.8$$

in the second operating interval.

For purposes of approximation, the temperature is transformed as

$$\xi = \frac{T_r - T_r^L}{T_r^U - T_r^L}, \quad \xi \in \langle 0, 1 \rangle \quad (7)$$

where the approximation interval is chosen a little larger than the operating interval so that  $T_r^L = 319.6$  and  $T_r^U = 356.0$ .

Then, the polynomials approximating inverse characteristics and corresponding to above intervals then take forms

$$\xi = -0.6479 + 1.3829 c_B - 0.9588 c_B^2 + 0.2963 c_B^3 \quad (8)$$

$$\xi = 21.9485 - 27.4096 c_B + 8.686 c_B^2 \quad (9)$$

in the first operating interval, and,

$$\xi = -22.5685 + 29.2384 c_B - 9.243 c_B^2 \quad (10)$$

$$\xi = 1.6587 - 1.6398 c_B + 1.139 c_B^2 - 0.3405 c_B^3 \quad (11)$$

in the second operating interval.

Inverse characteristics together with approximations are in Figs. 3 and 4.

Now, a difference of the desired value of the reactant temperature in the output of the NPC can be computed for each  $c_B$  as

$$\Delta T_{rw} = K_w (T_r^U - T_r^L) \left( \frac{d\xi}{dc_B} \right)_{c_B} \Delta c_{Bw} \quad (12)$$

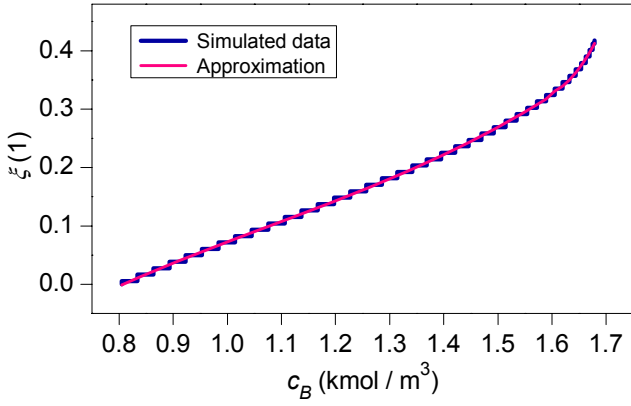


Fig.3 Inverse steady-state characteristics in the interval 1.

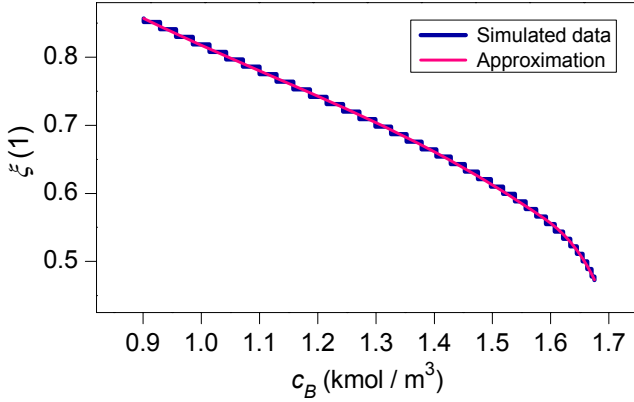


Fig.4 Inverse steady-state characteristics in the interval 2.

where  $K_w$  is a selectable gain coefficient.

Formulas for computing of derivatives corresponding to (8) – (11) are

$$\frac{d\xi}{dc_B} = 1.3829 - 1.9176c_B + 0.8888c_B^2 \quad (13)$$

$$\frac{d\xi}{dc_B} = -27.4096 + 17.3714c_B \quad (14)$$

in the first operating interval, and,

$$\frac{d\xi}{dc_B} = 29.2384 - 18.4859c_B \quad (15)$$

$$\frac{d\xi}{dc_B} = -1.6398 + 2.2781c_B - 1.0216c_B^2 \quad (16)$$

in the second operating interval.

## V. ADAPTIVE CONTROL SYSTEM DESIGN

The nonlinearity of the reactor is evident from the shape of the steady-state characteristics shown in Fig. 5.

### A. External Linear Model of the CSTR

For the control purposes, the controlled output and the control input are defined as

$$y(t) = \Delta T_r(t) = T_r(t) - T_r^s, \quad u(t) = q_c(t) - q_c^s \quad (17)$$

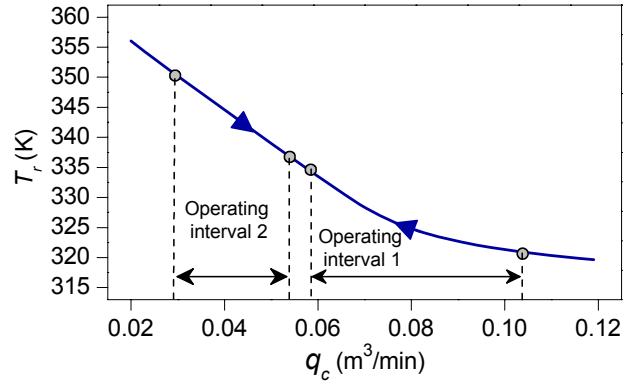


Fig. 5 Steady-state characteristics of the CSTR.

The CT ELM is proposed in the time domain on the basis of simulated step responses shown in Fig. 6 in the form of the second order differential equation

$$\ddot{y}(t) + a_1 \dot{y}(t) + a_0 y(t) = b_0 u(t) \quad (18)$$

and, in the complex domain as the transfer function

$$G(s) = \frac{b_0}{s^2 + a_1 s + a_0} \quad (19)$$

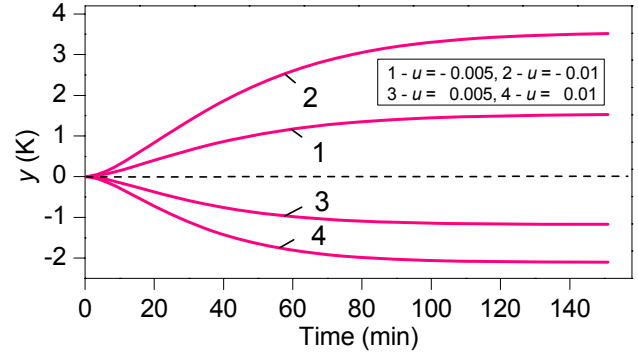


Fig. 6 Controlled output step responses.

### B. External Delta Model

Establishing the  $\delta$  operator

$$\delta = \frac{d-1}{T_0} \quad (20)$$

where  $d$  is the forward shift operator and  $T_0$  is the sampling period, the delta ELM corresponding to (18) takes the form

$$\delta^2 y(t') + a'_1 \delta y(t') + a'_0 y(t') = b'_0 u(t') \quad (21)$$

where  $t'$  is the discrete time.

When the sampling period is shortened, the delta operator approaches the derivative operator, and, the estimated parameters  $a', b'$  reach the parameters  $a, b$  of the CT model.

### C. Delta Model Parameter Estimation

Substituting  $t' = k - 2$ , equation (21) can be rewritten to the form

$$\delta^2 y(k-2) + a'_1 \delta y(k-2) + a'_0 y(k-2) = b'_0 u(k-2). \quad (22)$$

Then, establishing the regression vector

$$\Phi_{\delta}^T(k-1) = (-\delta y(k-2) \quad -y(k-2) \quad u(k-2)) \quad (23)$$

where

$$\delta y(k-2) = \frac{y(k-1) - y(k-2)}{T_0} \quad (24)$$

the vector of delta model parameters

$$\Theta_{\delta}^T(k) = (a'_1 \quad a'_0 \quad b'_0) \quad (25)$$

is recursively estimated by the least squares method with exponential and directional forgetting from the ARX model, e.g. [19].

$$\delta^2 y(k-2) = \Theta_{\delta}^T(k) \Phi_{\delta}(k-1) + \varepsilon(k) \quad (26)$$

where

$$\delta^2 y(k-2) = \frac{y(k) - 2y(k-1) + y(k-2)}{T_0^2} \quad (27)$$

#### D. Controller Design

For the adaptive control purposes, the 2DOF controller is used. It is known that this type of the controller often provides smoother control actions than a standard feedback controller. The 2DOF controller consists of the feedback part  $Q$  and the feedforward part  $R$  as shown in Fig. 7.

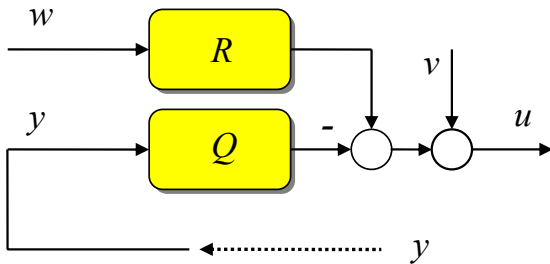


Fig. 7 The 2DOF controller.

In the scheme,  $w$  is the reference signal  $w = T_{rw} - T_r^s$ ,  $y$  is the controlled output and  $u$  the control input to the CSTR. The reference  $w$  and the disturbance  $v$  are taken into account as sequences of step functions with transforms

$$W_k(s) = \frac{w_{k0}}{s}, \quad V_k(s) = \frac{v_{k0}}{s} \quad (28)$$

The transfer functions of both controller parts are in forms

$$R(s) = \frac{r(s)}{p(s)}, \quad Q(s) = \frac{q(s)}{p(s)} \quad (29)$$

where  $q$ ,  $r$  and  $p$  are coprime polynomials in  $s$  fulfilling the condition of properness  $\deg r \leq \deg p$  and  $\deg q \leq \deg p$ . For a step disturbance with the transform (28), the polynomial  $p$  takes the form  $p(s) = s \tilde{p}(s)$ .

The controller design described in this section follows from the polynomial approach. It is known that an admissible

controller ensuring stability and internal properness of the control system, asymptotic tracking of the reference and disturbance attenuation results from a solution of the couple of polynomial equations

$$a(s)s\tilde{p}(s) + b(s)q(s) = d(s) \quad (30)$$

$$t(s)s + b(s)r(s) = d(s) \quad (31)$$

with a stable polynomial  $d$  on their right sides. The polynomial  $t(s)$  is an auxiliary polynomial which does not enter into the controller design but it is necessary for calculation of (31).

For the transfer function (19) with  $\deg a = 2$ , the controller transfer functions take forms

$$Q(s) = \frac{q(s)}{s\tilde{p}(s)} = \frac{q_2 s^2 + q_1 s + q_0}{s(s+p_0)} \quad (32)$$

$$R(s) = \frac{r(s)}{s\tilde{p}(s)} = \frac{r_0}{s(s+p_0)}$$

Moreover, the equality  $r_0 = q_0$  can easily be obtained.

The controller parameters then follow from solutions of polynomial equations (30) and (31) and depend upon coefficients of the polynomial  $d$ .

In this paper, the polynomial  $d$  with roots determining the closed-loop poles is chosen as

$$d(s) = n(s)(s + \alpha)^2 \quad (33)$$

where  $n$  is a stable polynomial obtained by spectral factorization

$$a^*(s)a(s) = n^*(s)n(s) \quad (34)$$

and  $\alpha$  is the selectable parameter that can usually be chosen by way of simulation experiments. Note that a choice of  $d$  in the form (33) provides the control of a good quality for aperiodic controlled processes. The polynomial  $n$  has the form

$$n(s) = s^2 + n_1 s + n_0 \quad (35)$$

with coefficients

$$n_0 = \sqrt{a_0^2}, \quad n_1 = \sqrt{a_1^2 + 2n_0 - 2a_0} \quad (36)$$

The controller parameters can be obtained from solution of the matrix equation

$$\begin{pmatrix} 1 & 0 & 0 & 0 \\ a_1 & b_0 & 0 & 0 \\ a_0 & 0 & b_0 & 0 \\ 0 & 0 & 0 & b_0 \end{pmatrix} \cdot \begin{pmatrix} p_0 \\ q_2 \\ q_1 \\ q_0 \end{pmatrix} = \begin{pmatrix} d_3 - a_1 \\ d_2 - a_0 \\ d_1 \\ d_0 \end{pmatrix} \quad (37)$$

where

$$\begin{aligned} d_3 &= n_1 + 2\alpha, \quad d_2 = 2\alpha n_1 + n_0 + \alpha^2 \\ d_1 &= 2\alpha n_0 + \alpha^2 n_1, \quad d_0 = \alpha^2 n_0 \end{aligned} \quad (38)$$

Evidently, the controller parameters can be adjusted by the selectable parameter  $\alpha$ .

## VI. SIMULATION RESULTS

Consider the measurement of the concentration  $c_B$  in

periods  $t_B$  (min). The aim of simulations is to show an effect of this period and an effect of the parameter  $K_w$  on some control responses.

The simulations started at the starting point  $c_B^s = 1.2$ ,  $T_r^s = 324.8$  and  $q_c^s = 0.08$  in the first operating area, and, at  $c_B^s = 0.9$ ,  $T_r^s = 350.8$  and  $q_c^s = 0.029$  in the second operating area. For the start (the adaptation phase), the P controller with a small gain was used in all simulations.

For the  $\delta$ -model parameter recursive identification, the sampling period  $T_0 = 1$  min has been chosen. The value of the selectable parameter  $\alpha$  is stated under each figure.

An effect of the parameter  $K_w$  on the control responses in the first operating area is evident from Figs. 8 – 10.

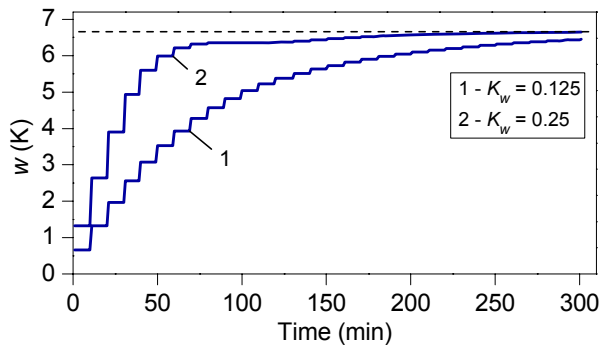


Fig. 8 Reference signal courses ( $t_B = 10$ ,  $\alpha = 0.2$ ).

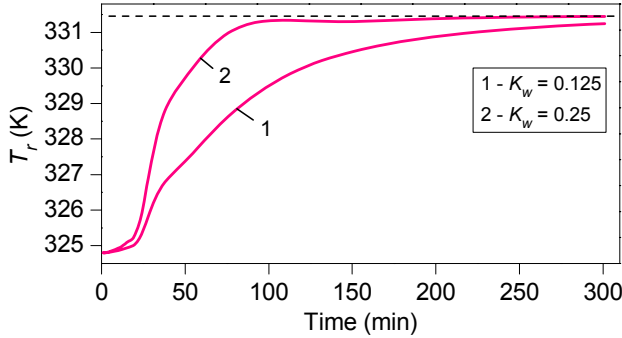


Fig. 9 Reactant temperature responses ( $t_B = 10$ ,  $\alpha = 0.2$ ).

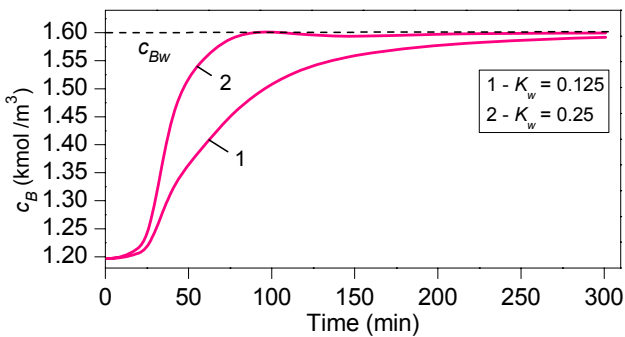


Fig. 10 Concentration  $c_B$  responses ( $t_B = 10$ ,  $\alpha = 0.2$ ).

An increasing  $K_w$  accelerates all signals in the control loop. However, its value is not unrestricted and its convenient value should be found experimentally.

An effect of the period  $t_B$  in the same operating interval can be seen in Figs. 11 – 13. Although shortening  $t_B$  leads to faster control responses, its length is determined by possibilities of measurement.

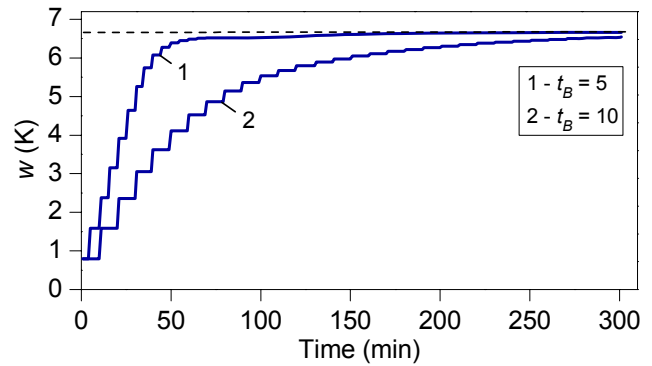


Fig. 11 Reference signal courses ( $K_w = 0.15$ ,  $\alpha = 0.2$ ).

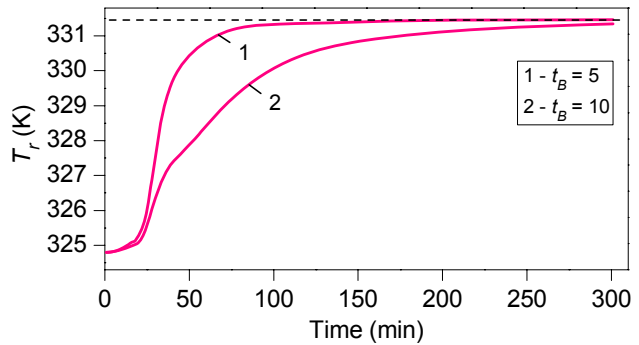


Fig. 12 Reactant temperature responses ( $K_w = 0.15$ ,  $\alpha = 0.2$ ).

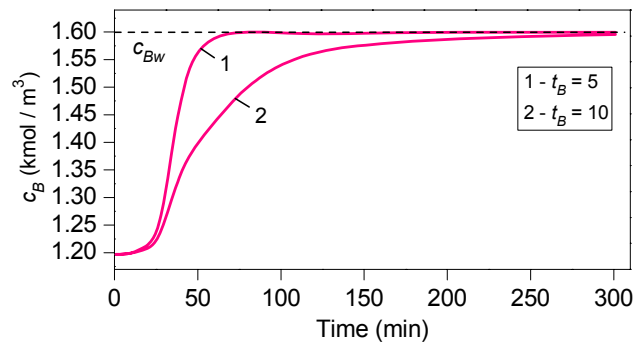


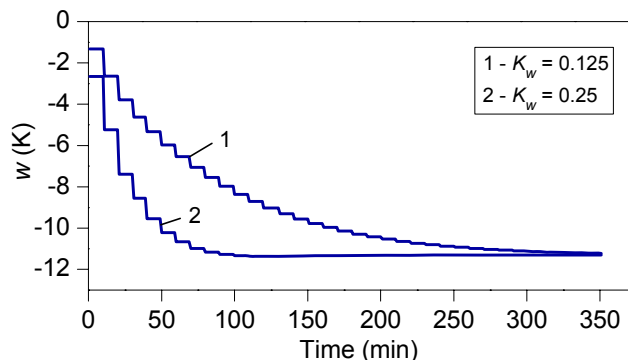
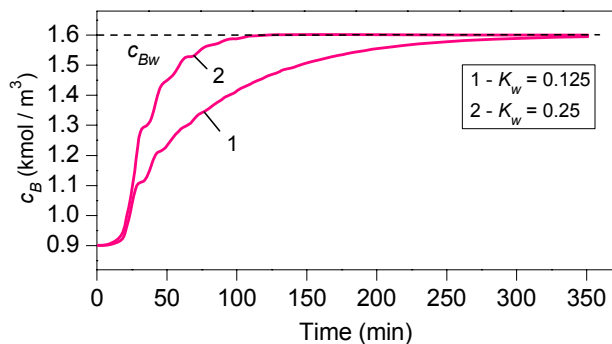
Fig. 13 Concentration  $c_B$  responses ( $K_w = 0.15$ ,  $\alpha = 0.2$ ).

The reference signal courses and the concentration  $c_B$  responses simulated in the second operating area are shown in Figs. 14 and 15. Here, the same conclusions are valid as for results shown in Figs. 8 and 10 in the first operating area.

The adaptive controller parameters depend upon a selection of the parameter  $\alpha$ . An effect of this parameter on the control quality has been in detail presented in other publications, see, e.g. [17] and [18].

## VII. CONCLUSIONS

The subject of the article is the cascade control design of a

Fig. 14 Reference signal courses ( $t_B = 10$ ,  $\alpha = 0.4$ ).Fig. 15 Concentration  $c_B$  responses ( $t_B = 10$ ,  $\alpha = 0.4$ ).

continuous stirred tank reactor. A necessary condition for the use of the presented method is measurement of a main product of the reaction taking place in the reactor. The control is performed in the external and inner closed-loop where the concentration of a main product is the primary and the reactant temperature the secondary controlled variable. A common control input is the coolant flow rate.

The controller in the external control-loop is a discrete nonlinear P-controller derived on the basis of steady-state characteristics of the reactor. The controller in the inner control-loop is a 2DOF adaptive continuous-time controller. In its derivation, the recursive parameter estimation, the polynomial approach and the pole placement method are applied.

The control is tested by simulations on the nonlinear model of the CSTR.

#### REFERENCES

- [1] R. Smith, *Chemical process design and integration*. Chichester: John Wiley and Sons, 2005.
- [2] J.-P. Corriou, *Process control. Theory and applications*. London: Springer – Verlag, 2004.
- [3] Chen I, Chyi-Tsong, Chuang I, Yao-Chen, and Hwang, Chyi, "A simple nonlinear control strategy for chemical processes," in *Proc. 6th Asian Control Conference*, Bali, Indonesia, 2006, pp. 64-70.
- [4] P. Dostál, J. Vojtěšek, and V. Bobál, "Simulation of adaptive control of a continuous stirred tank reactor," in *Proc. 23rd European Conference on Modelling and Simulation ECMS 2009*, Madrid, Spain, 2009, pp. 625-630.
- [5] A. Astolfi, D. Karagiannis, and R. Ortega, *Nonlinear and adaptive control with applications*. London: Springer-Verlag, 2008.
- [6] D.E. Seborg, T.F. Edgar, and D.A. Mellichamp, *Process dynamics and control*. Chichester: John Wiley and Sons, 1989.
- [7] J.F. Smuts, *Process control for practitioners*. New York: OptiControls, 2011.
- [8] M. Morari, and E. Zafiriou, *Robust process control*. New York: Prentice Hall, 1989.
- [9] G.P. Rao, and H. Unbehauen, "Identification of continuous-time systems," *IEE Proc.-Control Theory Appl.*, vol. 153, pp. 185-220, 2006.
- [10] D.L. Stericker, and N.K. Sinha, "Identification of continuous-time systems from samples of input-output data using the delta-operator," *Control-Theory and Advanced Technology*, vol. 9, pp. 113-125, 1993.
- [11] H. Garnier, and L. Wang (eds.), *Identification of continuous-time models from sampled data*, London: Springer-Verlag, 2008.
- [12] P. Dostál, V. Bobál, and F. Gazdoš, "Adaptive control of nonlinear processes: Continuous-time versus delta model parameter estimation," in *Proc. 8th IFAC Workshop on Adaptation and Learning in Control and Signal Processing ALCOSP 04*, Yokohama, Japan, 2004, pp. 273-278.
- [13] M.J. Grimble, *Robust industrial control. Optimal design approach for polynomial systems*. London: Prentice Hall, 1994.
- [14] V. Kučera, "Diophantine equations in control – A survey," *Automatica*, vol. 29, 1993, pp. 1361-1375.
- [15] W.L. Brogan, *Modern control theory*. New Jersey, Prentice Hall, 1991.
- [16] G.F. Franklin, J.D. Powell, and A. Emami-Naeini, *Feedback control of dynamic systems*. New Jersey: Pearson Prentice Hall, 2006.
- [17] P. Dostál, F. Gazdoš, V. Bobál, and J. Vojtěšek, "Adaptive control of a continuous stirred tank reactor by two feedback controllers," in *Proc. 9th IFAC Workshop Adaptation and Learning in Control and Signal Processing ALCOSP'2007*, Saint Petersburg, Russia, 2007, P5-1 – P5-6.
- [18] P. Dostál, J. Vojtěšek, and V. Bobál, "Simulation of adaptive temperature control in a tubular chemical reactor," *International Review on Modelling and Simulations*, vol. 5, 2012, pp. 1049-1058.
- [19] V. Bobál, J. Böhm, J. Fessler, and J. Macháček, *Digital self-tuning controllers*, Berlin: Springer Verlag, Berlin, 2005.

# Concepts for an AC-Battery with Active Harmonics Compensation

K. H. Edelmoser  
Institute of Electrical Drives and Machines  
Technical University Vienna  
Gusshausstr. 27-29, A-1040 Wien  
AUSTRIA  
kedel@pop.tuwien.ac.at

F. A. Himmelstoss,  
Technikum Wien  
University of Applied Science  
Hochstaedtplatz 5, A-1200 Wien  
AUSTRIA  
himmelstoss@technikum-wien.at

*Abstract:* - Solar inverters feeding a local grid have to fulfil some basic conditions. They must have a low output impedance to permit a stiff voltage, they should have low harmonic distortion, and they should have some storage device to buffer energy when no or low energy from the solar generator is available and to follow transients of the load. The UPS-function can be realized by an AC-battery and the harmonics can be reduced by a power factor device. These two devices (functionalities) can be connected in one device. Two concepts are explained and the small signal gain is described.

*Key-Words:* AC-Battery, Active Harmonics Compensation, Solar Generator

## 1-Introduction

To realize an effective and efficient solar system to feed an island or a microgrid some basic conditions have to be fulfilled:

- The output impedance has to be low to realize a stiff supply.
- There must be some storage equipment to follow quick load changes.
- There should be a constant energy flux out of the solar generator.
- The voltage should have low harmonic distortion, or when feeding into the mains

the current should have low harmonic distortion.

- There should be an intelligent power management (e.g. to store energy when there is low load)

In this paper we treat the first four points and show possible concepts. Fig. 1 shows the basic system. The block *solar inverter* represents the complete DC to AC transformation and the output impedance of this system. The block *UPS/AC-Batt* represents the storage device and the harmonics compensator and is especially treated in this paper.

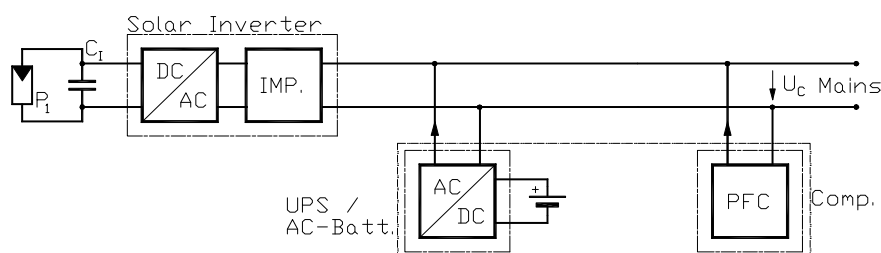


Fig.1. Solar inverter with active ripple compensation of the power-line interface and UPS function

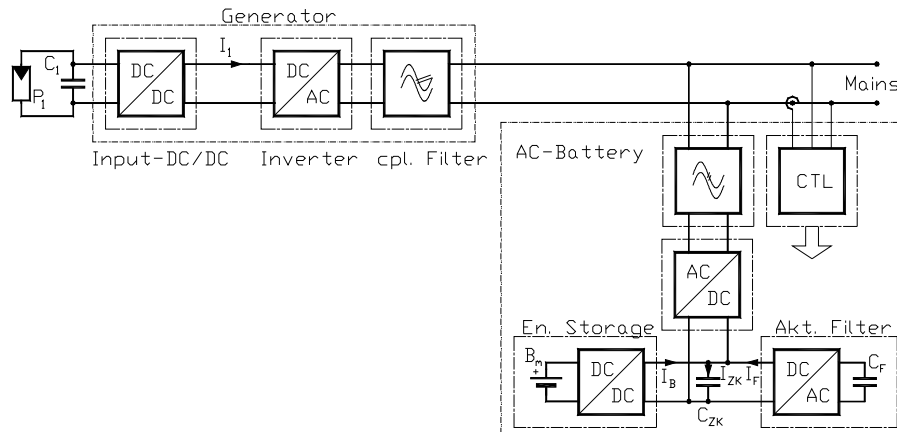


Fig. 2. Innovative solar inverter system with battery backup and active mains current ripple compensation

In the concept shown in Fig. 1 the uninterruptible power supply function represented by the AC battery (a combination between a bidirectional AC/DC converter and a battery) and the harmonics compensator (symbolized by the block PFC) are independent. Fig. 2 shows now a combination of the battery back-up and the harmonics compensator in the block *AC-Battery*.

## 2-System Analysis

There are two storage mediums: the battery ( $B_m$ ) for backup and for following large load transients and the capacitor ( $C_F$ ) for compensating the high frequency ripple. Both storage mediums are connected with a DC voltage link with the capacitor ( $C_{ZK}$ ). This DC voltage link is connected by an AC/DC converter to the mains. Therefore, this converter has also to compensate the harmonics and must be very fast. Avoiding this can be done in two ways. The high frequency converter and the low frequency storage converter can be connected in series or in parallel between the mains wires (or the output of the solar generator).

### 2.1-Parallel Concept:

Fig. 3 shows the parallel concept. There is an (relative low frequent) inverter for energy storage and for helping the system at large transients and a high frequency inverter compensating the high frequency ripple.

The solar generator consists of several DC/AC converters with their own maximum power point trackers feeding the mains. The storage section uses the *HF-Filter* block to compensate the harmonics. The block *Ref GEN* generates the actual value of the

current or the voltage. This signal is fed to a high-pass filter  $F_2$  to generate the high frequency component only.

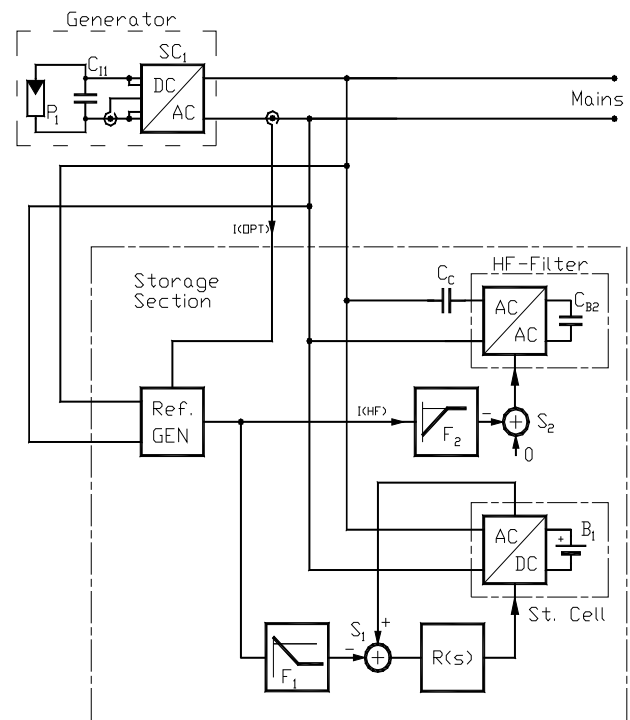


Fig. 3. Full parallel compensation: The storage cell and the filter stage use different inverter stages and are operated fully in parallel using different power inverters

The nominal-actual value comparison is symbolized by  $S_2$ . The controller is included in the converter of the *HF-Filter*. As shown, the high frequency component should be zero. The storage cell with the battery is controlled only by the low frequency component of the actual value.



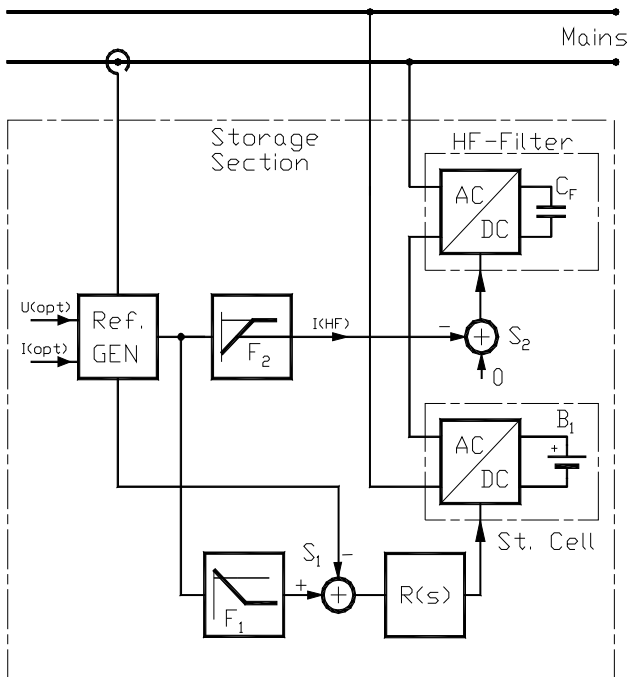


Fig. 5. Battery buffered solar inverter system with active harmonics compensation built up as serial compensator

Fig. 6 shows the equivalent circuit of the series-connected system. The inverters are depicted as voltage sources.  $Z_M$  is the output impedance of the solar generator.  $Z_L$  represents the mains impedance.  $Z_1$  is the output impedance of the compensator

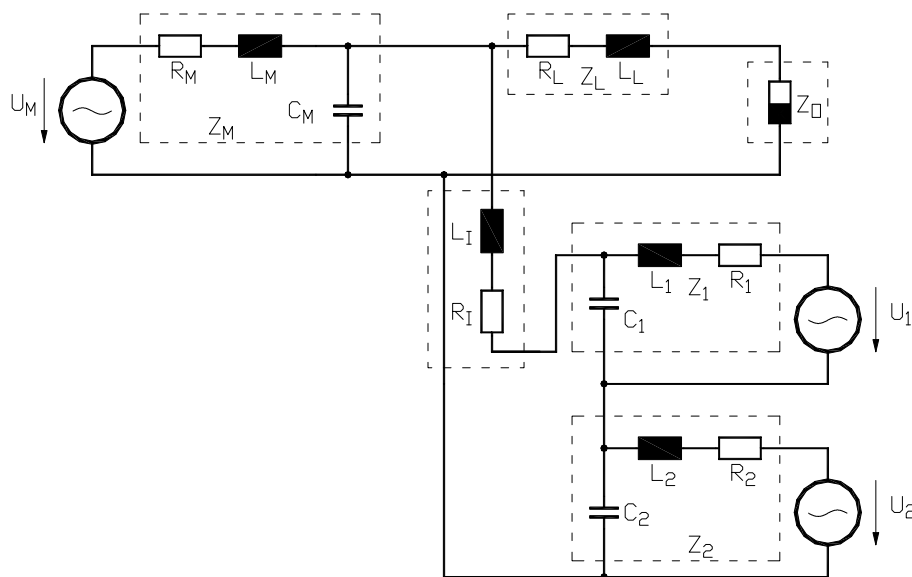


Fig. 6. Equivalent circuit of the battery buffered solar inverter system with active harmonics compensation in series connection

$$Z_1 = \frac{(R_1 + j\omega L_1)}{1 + j\omega R_1 C_1 - \omega^2 L_1 C_1},$$

and  $Z_2$  is the output impedance of the storage inverter

$$Z_2 = \frac{(R_2 + j\omega L_2)}{1 + j\omega R_2 C_2 - \omega^2 L_2 C_2}.$$

The impedance, which is connected in parallel between the mains and the output filter of the solar generator, is

$$Z_B = \frac{(R_1 + j\omega L_1)}{1 + j\omega R_1 C_1 - \omega^2 L_1 C_1} + \frac{(R_2 + j\omega L_2)}{1 + j\omega R_2 C_2 - \omega^2 L_2 C_2}.$$

### 3-Simulation results

The output impedance of the system is of main importance concerning the stiffness on the voltage and of the dynamics concerning transients.

Figs. 7 and 8 show the output voltage (the voltage across the load) in dependence of the voltage across the main converter (G-P), the output voltage in dependence on the low frequency converter (G-C<sub>2</sub>), and the output voltage in dependence on the high frequency converter (G-C<sub>1</sub>) for the parallel or the series connection.

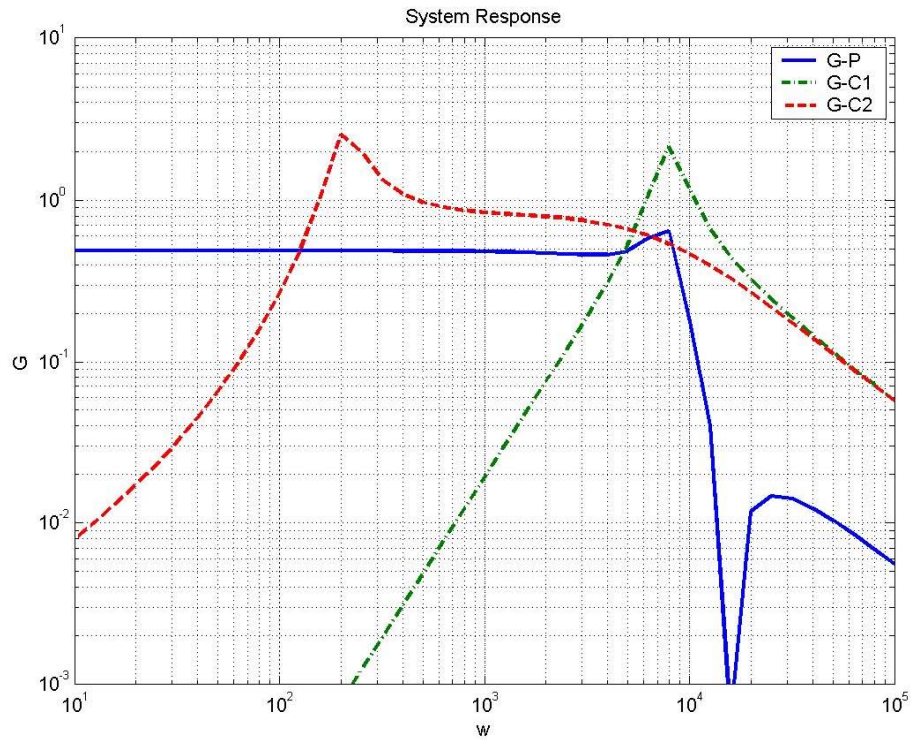


Fig. 7. Battery converter with active harmonics compensation: G-P: Output of the AC-inverter’s power path, G-C<sub>1</sub>: influence of a conventional active harmonics filter operating in parallel, G-C<sub>2</sub>: improved filter stage with reduced output impedance, both operating in parallel compensation mode

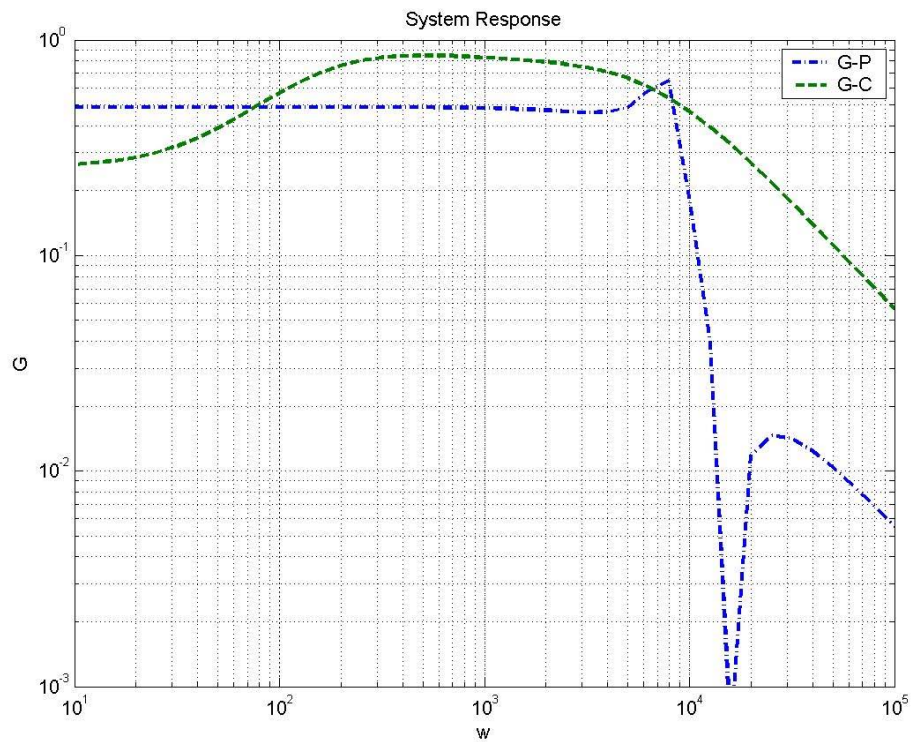


Fig. 8. Battery converter with compensator improvements: G-P: Output of the AC-inverter’s power path, G-C: optimized compensator with common power path using serial compensation

## 4-Conclusion

The approach discussed in this paper uses a combined structure of an active filter and a back-up battery system to realize a very stable and rugged isolated grid with a rather low mains impedance. Intelligent control of the battery system can also be used to minimize the input current ripple of the cells when a cooperation with the solar inverter is established. This can help to realize string-optimized maximum power point tracking and optimal power quality of the supplying grid. The topology presented in this paper shows an improvement of the mains impedance and flicker behavior as well as an enhanced EMC. Consequently, it is well suited for solar power inverter applications. The topology presented in this paper is a simple and effective solution for small to medium power grid coupled applications and is well suited for wind-, solar- and renewable energy as well as for aerospace applications. The current ripple generated by the mains inverter can be kept under control and held below the limits. The proposed topology can be used as an alternative to multi-stage converters with a constant DC-link voltage and an active switching DC-to-AC inverter.

## Literature

- [1] Wai, R; Lin, C.: Active Low-Frequency Ripple Control for Clean-Energy Power Conditioning Mechanism, pp.: 1-10, Proceedings of the IEEE Transactions on Industrial Electronics 1-2010, Vol.: PP , Issue: 99.
- [2] Veerachary, M.; Senjyu, T.; Uezato, K.: Maximum power point tracking control of IDB converter supplied PV system, pp: 494 – 502, Proceedings of the IEE Electric Power Applications 2001, Vol.: 148 , Issue: 6.
- [3] Duran, E.; Galan, J.; Sidrach-de-Cardona, M.; Segura, F.: An application of interleaved DC-DC converters to obtain I-V characteristic curves of photovoltaic modules, pp.: 2284 – 2289, Proceedings of the 34th IEEE Annual Conference of Industrial Electronics, IECON 2008.
- [4] Hung, J.-C.; Wu, T.-F.; Tsai, J.-Z.; Tsai, C.-T.; Chen, Y.-M.: An active-clamp push-pull converter for battery sourcing applications, pp.1186-1192, Proceedings of the Twentieth Annual IEEE Applied Power Electronics Conference and Exposition, APEC 2005. Volume 2, March 6-10, 2005.
- [5] Edelmoser, K.H.; Himmelstoss, F.A.: Battery Buffered Multi Filter Stage Solar Inverter, pp. 106 – 112, Proceedings of the 15th WSEAS International Conference on Circuits, Systems, Communications and Computers CSCC '11, Latest Trends on Circuits, July 14.-16. 2011, Corfu Island, Greece, ISBN: 978-1-61804-017-6.
- [6] Edelmoser, K.H., Himmelstoss, F. A.: Dual Filter Stage for EMI-Optimized Solar Inverter Array, Proceedings of the international Power Conversion Conference PCIM '11, May 17 - 19, 2011, Nuremberg / Germany, CD-ROM.

# Formal verification of safety control system based on GHENESYS NET

Rodrigo Cesar Ferrarezi, Reinaldo Squillante Júnior, Jeferson A. L. Souza, Diolino J. Dos Santos Filho, José Reinaldo Silva, Paulo Eigi Miyagi, Lucas Antonio Moscato

**Abstract**—Due to the high complexity of the actual Productive Systems, the current industrial standards, and the possible negative impacts on the human being, on the environment and on equipment in case of faults, the development of control solutions that are both secure and stable – as some systems have to operate nonstop – is much demanded. In this context, the development of safety control systems which simultaneously present high reliability and availability is required. The concepts of SIS, according to experts, may be one solution to these problems. Due the complexity of these systems, project mistakes are expected during their development and thus, validation and verification processes became an imperative – as well as a normative requirement – before the actual deployment of the control software on site. One of the most outstanding system verification techniques is the Model Checking, which performs an exhaustive search on the state space of an event driven system and checks some specific properties written in temporal logic. The GHENeSys environment will be used as computational tool, as it provides a complete solution for modelling and verifying systems based on the GHENeSys network. The proposed methodology will then be applied to the development of a SIS control system to be implemented on a flexible manufacture system, which simulates assembly and handling of parts.

**Keywords**—GHENeSys nets, Model Checking, Safety Instrumented System, Verification.

## I. INTRODUCTION

The growing demand on cost and quality of products and services, the highly competitive market with several players, the increasing hardware storage capacity, processing power and networks speeds, and above all, the concern with the environment, the foundation of all current suitability policies caused an implementation of more complex control systems in the most diverse areas, from the production of consumer products to services [1].

The increasing implementation of processes automation, mandatory for costs reductions and quality improvements, key factors to the survival of a company in a highly competitive market, induced an ever increasing complexity of the control systems required for these systems [2] [3]

The authors would like to thank the Brazilian governmental agencies CNPq, FAPESP, and CAPES for their financial support to this work.

All authors are with Polytechnic School – Department of Mechatronics Engineering and Mechanical Systems - University of São Paulo - São Paulo, Brazil (phone: +55 11 3091-5337 ; e-mail: [rferrarezi@usp.br](mailto:rferrarezi@usp.br), [reinaldo.squillante@usp.br](mailto:reinaldo.squillante@usp.br), [jeferson.souza@usp.br](mailto:jeferson.souza@usp.br), [diolinos@usp.br](mailto:diolinos@usp.br), [reinaldo@usp.br](mailto:reinaldo@usp.br), [pemiyagi@usp.br](mailto:pemiyagi@usp.br), [lamoscat@usp.br](mailto:lamoscat@usp.br)).

Being the control software increasingly complex, and the quality requirements more and more severe, there is a demand for more detailed and concise specification as well as a better control of the development process. It is also required a deeper understanding of the system to be controlled, including details regarding all relevant sub-systems and furthermore, how several system interacts and communicates with each other and with the environment, as the behavior of an interconnected system depends not only of its internal variables, but also of external events originated from the surrounds of the system [4] [5].

Additionally, any industrial system, as modern and innovative as it can be, still may pose serious risks to equipment, to operators and to the environment, in the event of a fault failing to be diagnosed and treated correctly [6]. Although many studies have been presented for diagnosis and treatment of faults, accidents still occur. The main problem is that there is no zero risk in process industries since: (i) physical devices do not have zero risk of fault, (ii) human operators do not have zero risk of error and (iii) there is no computational system that can predict all the reachable states by the system [7].

According to experts, the concepts of safety instrumented systems (SIS), is one solution to these types of issues. They strongly recommend the implementation of layers of risk reduction based on control systems organized hierarchically in order to manage risks by either preventing or mitigating faults, bringing the process to a safe state. In this sense, some safety standards such as IEC 61508 [8], IEC 61511 [9] among others, guide different activities related with a SIS Safety Life Cycle (SLC), such as design, installation, operation, maintenance, tests and others [10][11].

On this context, the processes of understanding, specifying, modelling and validating these systems became a highly complex task, resulting in great hardships on their development. Due all this, project mistakes are associated with the development of these systems and thus, validation and verification processes became an imperative before the actual deployment of the control software on the actual plant [3] [4]. Besides the obvious necessity of verifying and validating critical systems, these activities are required by the safety standard IEC 61511 [9] as part of the safety program development cycle, also known as “V-model.

Model Checking is a verification technique for finite state concurrent systems, and thanks to this restriction, the

verification processes can be performed semi-automatically, being human interaction only needed for the analysis of the results. The basic procedure performs an exhaustive search of the space state of an event driven system, verifying properties specified from propositions described using some temporal logic. Given enough time and computational power, the procedure will always finish with a positive or negative result, in case of a negative result; a counterexample is given by the system, helping the designer to find the source of error [12].

In this work we propose the first steps towards the development of a framework for the modelling and formal verification of SIS control programs based on the IEC 61511 standard. On the framework, we expect to propose methods, techniques and systematics to comply with all phases of the “V model” according to the IEC 51511 standard. With the complete framework we expect to aid the control engineers to develop SIS control programs in a structured and well defined way as well as fulfilling the requirements of the IEC 51511 standard.

The GHENeSys environment will be used as computational tool modelling and verification processes, the environment is a proposal of the DesignLab from USP and was originally designed as unified approach to cover several types of Petri Nets as well as its extensions, support for timed nets was implemented later on.

This paper is organized as follows: Section 2 presents the main concepts of Model Checking, GHENeSys nets and TCTL. Section 3 presents the SIS Control System Modelling proposal. Section 4, presents the application example. Section 5 presents the conclusion. References are presented thereafter.

## II. MAIN CONCEPTS

### A. Model checking

The Model Checking technique is composed by the following main tasks [12]:

- Modelling: First the system is converted to a formalism accepted by the chosen verification tool.
- Specification: Before the verification process, it is necessary to list the required system properties. These specifications must also be supplied in some kind of formalism. Usually temporal logic is used to specify the system behavior.
- Verification – Usually the verification process is performed automatically by the tool, except by the results analysis – in case of errors being found. In this case, the tool will supply counterexamples for the verified property, helping the designer finding the source of error on the system.

Concurrent systems can frequently interact with their environments and usually are operating non-stop, therefore, these systems cannot be properly modelled by their input output behavior. The first feature of these systems that must be taken into account is the state. A state can be defined as an instantaneous description of the system, containing the value of every system variable in a single instant. Also it is important to understand how the states change as result of

some action of the system. This change can be described as the state of the system before and after the some action, this pair of states determines a transition of the system [12].

In order to represent the behavior of concurrent systems several types of used graphs might be used, among them we have Kripke structures [12], automata [13], Petri Nets [14] and its extensions, as the GHENeSys nets [15].

There are many different types of concurrent systems (synchronous and asynchronous systems, sequential systems, parallel process, etc.) and due to this diversity, it is necessary to adopt unifying formalism in which these systems can be represented regardless of its type. For such representations will be used first order logic formulas, which are able to represent a great variety of systems [12].

In order to write specifications to describe the properties of a concurrent system it is necessary to define a set of atomic propositions  $AP$ . Such propositions have the form  $v = d$  where  $v \in V$  and  $d \in D$ , an atomic proposition  $v = d$  is said to be true in a state  $s$  if  $s(v) = d$  [12].

Temporal logic was proved to be very useful for specifying concurrent systems due to its capacity to describe the ordering of events without introducing time explicitly, and thanks to this feature, it was possible to develop completely automated verification algorithms.

### B. Timed Computation Tree Logic (TCTL)

TCTL [16] was proposed as an extension of the CTL (Computation Tree Logic) proposed in [12], for the interpretation of temporal formulas over computational trees for systems modelled by temporized graphs. TCTL can be defined semantically related to a structure  $\mathcal{M} = (\mathcal{S}, \mu, f)$ , where  $\mathcal{S}$  is the set of states,  $\mu : \mathcal{S} \rightarrow 2^{AP}$  the labelling function which labels each state with the set of atomic prepositions that hold on this state and  $f$  the mapping that assigns for each  $s \in \mathcal{S}$  a set of  $s$ -paths through  $\mathcal{S}$  that obey the closure properties [16].

The formula  $\phi$  of TCTL can be inductively defined as [16]:

$$\phi ::= p \mid \text{false} \mid \neg \phi \mid \phi_1 \rightarrow \phi_2 \mid \phi_1 \wedge \phi_2 \mid \exists [\phi_1 U_{\sim c} \phi_2] \mid \forall [\phi_1 U_{\sim c} \phi_2], \text{ where } p \in AP \text{ and } c \in \mathbb{N}.$$

TCTL formulas are composed of path quantifiers and temporal operators. There are two path quantifiers:

- $\forall$  (for all computation paths)
- $\exists$  (for some computation path)

Quantifiers are used to specify if from some state, if all paths or just some paths must have some propriety. Temporal operators are used to describe the properties of a path belonging to some computational tree and were defined by adding timing limitations to the classical CTL operators [16]:

- $\diamond_{\sim c} \phi = \text{true } U_{\sim c} \phi$  ( $\phi$  must hold eventually in some state of the computational path for  $\sim c$  time units);
- $\square_{\sim c} \phi$  ( $\phi$  must hold in all states of the computational path for  $\sim c$  time units);
- $\phi_1 U_{\sim c} \phi_2$  ( $\phi_2$  must hold in some state and  $\phi_1$  must hold in all previous states of the computational path for  $\sim c$  time units).

Where  $\sim$  may represent any of the following binary operators  $<, \leq, =, >, \geq$ . It is important to note that TCTL, as opposed to CTL, does not defines the temporal operator that requires that some property must hold on the next state, because as the time is considered dense, by definition, there is not only one next state [16].

Given a TCTL structure  $\mathcal{M} = (\mathcal{S}, \mu, f)$  and a state  $s \in \mathcal{S}$ , a TCTL formula  $\phi$  holds  $(\mathcal{M}, s) \models \phi$  if [16]:

- $s \models p$  if  $p \in \mu(s)$
- $s \not\models \text{false}$ ;
- $s \models (\phi_1 \rightarrow \phi_2)$  if  $s \not\models \phi_1$  or  $s \models \phi_2$ ;
- $s \models \exists(\phi_1 U_{\sim c} \phi_2)$  if for some  $\rho \in f(s)$ , for some  $t \sim c$ ,  $\rho(t) \models \phi_2$ , and for all  $0 \leq t' < t$ ,  $\rho(t') \models \phi_1$ .
- $s \models \forall(\phi_1 U_{\sim c} \phi_2)$  if for each  $\rho \in f(s)$ , for some  $t \sim c$ ,  $\rho(t) \models \phi_2$ , and for all  $0 \leq t' < t$ ,  $\rho(t') \models \phi_1$ .

### C. GHENeSys environment

A SIS control system can be seen as an event driven system and presents functional characteristics as asynchronism, possibility of reset, parallelism, concurrence, etc., thus this class of system can be classified as a discrete event system (DES), and thus be modelled through Petri Nets [14] [17] and its extensions.

The GHENeSys environment was developed as an extended Petri net with object orientation and abstraction mechanisms defined through hierarchy concepts, which are included as well as synthesis mechanisms that are implemented through a structured approach supported by the encapsulation introduced by the use of objects [15].

The GHENeSys environment is being developed with the goal of representing, in a unified way, classical Petri Nets, its extensions defined on the ISO/IEC 15909 standard, as well as High Level Petri Nets. The GHENeSys environment is composed of the following basic modules. The GHENeSys nets, the Editor tool, the simulation module and the verification tool [18].

The GHENeSys environment implements also several concepts to aid the modeling process, such as: Pseudoboxes that allow the modelling of the exchange of information between different parts of the system; Hierarchy that allows the encapsulation of subnets without losing any properties by using macro elements; The representation of non-deterministic time durations, where a set of time intervals can be defined for each transition.

The GHENeSys net is the tuple  $G = (L, A, F, K, \Pi, C_0, \tau)$ , where:

- $L = B \cup P$  is the set of places, which can be boxes or pseudoboxes;
- $A$  are the activities, or active elements;
- $F \subseteq (L \times A \rightarrow \mathbb{N}) \cup (A \times L \rightarrow \mathbb{N})$  is the flux relation;
- $K : L \rightarrow \mathbb{N}^+$  is the capacity function;
- $\Pi : (B \cup A) \rightarrow \{0,1\}$  is the function that identify the macro elements or the hierarchy;
- $C_0 = \{(l, \sigma_j) | l \in L, \sigma_j \in \mathbb{R}^+ | l| < K(l)\}$  is the set of initial marks;
- $\tau : (B \cup A) \rightarrow \{\mathbb{Q}^+, \mathbb{Q}^+ \cup \{\infty\}\}$  is the function that maps

the dense time intervals for each element.

The set of markings is the pair  $(l, \sigma_j)$  with  $l \in L$ , defining which place each token can be found and  $\sigma_j$  defining for how long this token will remain in place. The time measurement is globally synced and updated after each transition.

The GHENeSys verification tool performs the formal verification of real time concurrent systems modelled as GHENeSys net through Model Checking [12] techniques. The space state is constructed using the enumerative approach based on the state class [19] concept. The tool has options to build SCG, SSCG and CSCG state graph types. Checked properties are specified through TCTL [20].

The GHENeSys environment will be used in this work due to several reasons: (i) Due characteristics of the SIS, the amount of checked properties can be very large, so it might be desirable that the space state is generated through the enumerative approach instead of being generated “on the fly” several times. As the space state generation is done in exponential space and time, and the verification of a property is performed in polynomial time, if the space state is already constructed. (ii) The use of the dense time approach, as several SIS properties are time dependent. (iii) PNML [21] is implemented as the default transfer format, thanks to that, the interchange of information between the GHENeSys tools is possible, as well as with external tools that support the standardized format. (iv) The environment allows that all modelling and verification tanks to be performed without the need of external modules or tools. (v) The space state generation and the specification of the tested properties are done on the same tool.

### D. Requirements for safety control programs

According to [9] and [22], safety control programs must be developed according to the development cycle proposed by the IEC 61511 standard as shown on Fig. 1 and using modularity concepts.

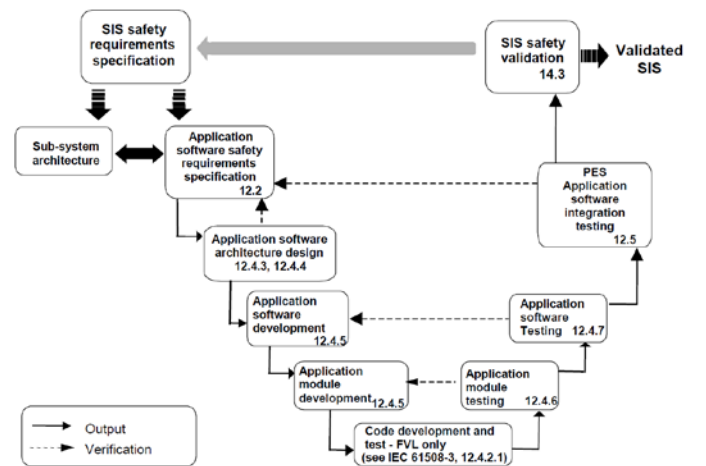


Fig. 1. Safety program development cycle or "V-model"

The development cycle is the combination of several phases ranging from the requirements analysis to the formal verification of the entire control program. The development phases, located on the left, also include steps related with the

description of the operation of each SIS module, the choice of methods and tools to aid the development, the development of the control program and its modules integration and the control code development. The verification phases, located on the right, include the formal verification of the modules and their integration and the final tests of the control program and hardware integration.

### III. SIS CONTROL PROGRAM MODELING

The initial step towards the proposed framework has already been done on the previous section. There, the GHENeSys environment was chosen as the modelling and verification tool, as well as the choice was justified as required by the standard as part of the second phase of the development cycle.

Through the concepts of modularity, we can break the SIS control program in two parts. The prevention module is responsible to detect dangerous events represented as critical faults and deploy the suitable treatment to degenerate the system leading it to a safe state. The mitigation module is responsible to detect the effects of a fault not being treated correctly – or even not being detected by the prevention module – and deploy the suitable treatment to degenerate the system and to extinguish the effects before they disseminate to other parts of the plant. The definition of the main control program modules and thus the high level control program architecture are the second part of the second phase of the development cycle.

The development of the framework will be performed according to the Model Based Design (MbD) approach [3]. Although this approach is not referred in the IEC 61511 standard, as according to the standard, all control programs are directly developed in an implementation language. The standard requires that a final validation shall be carried out by the end of the development cycle, and modeling is one of the recommended tools for validation. Thus by adopting the MbD, the framework will be not only complying with the standard but also improving the modularity of the SIS control programs.

The third and fourth phases of the development cycle are related with de control program development. On these phases must be chosen methodologies for the development of the prevention and mitigation modules. These methodologies must be based on formal models and must have been proposed according the requirements of the IEC 61508 and IEC 61511 standards.

The prevention module development methodology must first be able to define which faults the SIS will treat. This definition can be made through HAZOP reports, cause-effect matrix or other applicable technique. With knowledge of the faults, formal methods to discover the causal relations leading to each fault, that is, how – by which sensors – each fault can be detected must be presented. The methodology then must be able to propose actions to deal with each fault, through the actuation of some component – such as control valves – and/or the shutdown of an endangered component.

Now a mitigation module development methodology must

be chosen. The same methodology as used on prevention can be adopted; as well as other methodology can be adopted, as long as the same criteria – as described on the previous paragraph – are used.

As opposite as the prevention activity, the mitigation activity does not need to define the treated faults through documents or reports. The mitigation activity shall treat the prevention activity faults, that is, the system will mitigate the consequences of the prevention system not being able to lead the plant or process to a safe state.

The sixth and seventh phases of the development cycle are related with the formal verification of the models. Due to the Model Based approach, the verifications are performed on the control program models and not on the control code. All properties specified no natural language shall be translated to TCTL according to the patterns proposed in [23].

### IV. APPLICATION EXAMPLE

Now we will present a simple application example of the development of a prevention SIS control program according with the IEC 61511 phases already covered by the presented framework. We will begin the application example by choosing the methodology to develop the prevention SIS module, then the methodology will be applied and the resulting control program model will be verified.

The systematic proposed in [24] was chosen. Briefly, the faults that will be treated by the prevention SIS are extracted from the HAZOP report. The detection models are generated from cause-effect matrixes, where those matrixes are converted on Bayesian Networks, which are finally converted on Petri Nets. The treatment models, that is, the actuators related with each treated fault are generated from the HAZOP report.

The systematic was then applied to a flexible manufacturing system prototype. This prototype is composed by three manufacture cells: feeder, inspection and assembly. The cells are connected by a conveyor belt transportation system. On this example, the prevention SIS control system was developed for the assembly cell. This cell is composed of a three axis manipulator robot [24].

Case	X_Axis_Fail	S9.1	S9.2	X_Encoder_Fail	B9.2
1	1	0	0	0	1
2	1	0	0	1	0
3	1	0	0	1	1
4	1	0	1	0	0
5	1	0	1	0	1
6	1	0	1	1	0
7	1	0	1	1	1
8	1	1	0	0	0
9	1	1	0	0	1
10	1	1	0	1	0
11	1	1	0	1	1
12	1	1	1	0	0
13	1	1	1	0	1
14	1	1	1	1	0
15	1	1	1	1	1

Where:  
 X\_Axis\_Fail: X axis movement fail  
 S9.1: External limit sensor 1 fail  
 S9.2: External limit sensor 2 fail  
 X\_Encoder\_Fail: Encoder fail  
 B9.2: Initial position sensor fail

Fig. 2. Cause-effect Matrix "X Axis Movement Fault"

The first step of the systematic was the construction of the cause-effect matrix together with the definition of which fault will be treated by the SIS. On Fig. 2 is displayed the cause-effect matrix for 15 cases of “X axis movement fault” on the manipulator robot. For each case the combination of the four sensors that can detect this type of fault is presented.

On the next step, the data Fig. 2 was inputted into the proper algorithms for construction of the Bayesian Network. The resulting Bayesian Network for the diagnostic model was then converted on the GHENeSys net presented on Fig. 4. The grayed places displayed on the models are pseudo-boxes. These boxes carry the marking information of their master elements. The master element can be identified by the name of each pseudo-box.

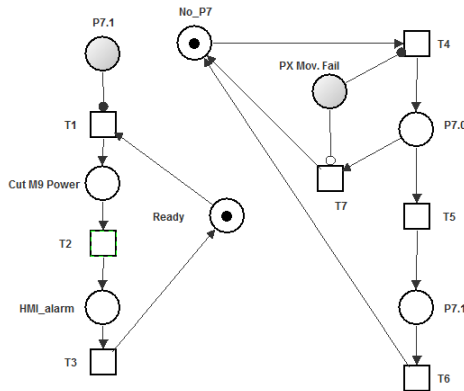
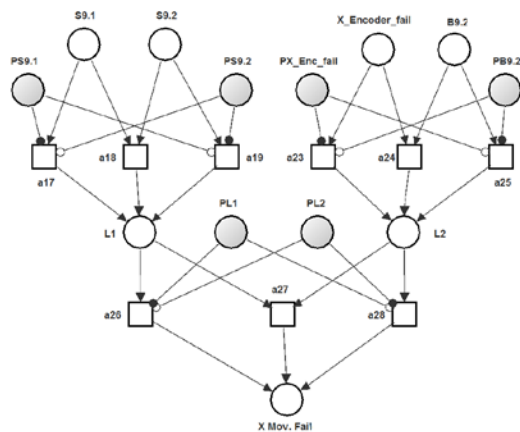


Fig. 3. GHENeSys net coordination model (left) and treatment model (right)

On the final step, the Safety Instrumented Function (SIF) for the manipulator robot “X” axis is determined based on the risk analysis HAZOP, and then the SIF treatment and coordination models were constructed as displayed Fig. 3. The function of each transition and place used on the treatment and coordination models is explained on Fig. 5.



Place	Transition	Description
S9.1	-	"X" axis limit sensor 1
S9.2	-	"X" axis limit sensor 2
X_Encoder	-	"X" axis encoder fail signal
B9.2	-	"X" axis position sensor
A1	-	Intermediate Place 1
A2	-	Intermediate Place 1
X_Axis_f	-	"X" axis movement fail diagnostic
-	T1	Logical (S9.1 OR S9.2) transition
-	T2	Logical (X_Encoder_Fail OR B9.2) transition
-	T3	Logical (A1 OR A2) transition

Fig. 4. Diagnostic model for “X axis movement fault”

A spurious events filter was implemented on the coordination model. This filter prevents the activation of the treatment model during a preset time, thus avoiding the degeneration of the plant and the costs associated with restating the plant in case of spurious readings from some sensor.

SIF-01 treatment model.

Place	Transition	Description
P7.1	-	Failure cause found: X axis movement error
P2	-	Action: Cut M9 motor power
P3	-	HMI Alarm: X axis movement error
P4	-	Error acknowledgment signal
Ready	-	Sistem ready for fail treatment
-	T1	T1 fired if (X_Axis_Fail AND Ready)
-	T2	After the power for M9 is cut, T2 is fired
-	T3	T3 fired if (HMI alarm AND fail is acknowledged)

SIF-01 coordination model

Place	Transition	Description
P7	-	X axis fail diagnosticted through the BPN
No_P7	-	No X axis fail detected
P7.0	-	Enable the call the SIF-01 treatment model
P7.1	-	Calls the SIF-01 treatment model after Δt
-	T1	T1 fired if (X_Axis_Fail & No_P7 == 1)
-	T2	T2 fired if (P7.0 == 1) & (P7 == 0)
-	T3	T3 fired if (P7.0 == 1) & Δt >= preset

Fig. 5. Models elements descriptions

Currently there is no template or standard to determine a set of the system properties to be tested, thus, these properties usually are chosen by the control engineers based on previous knowledge and expertise [3].

Table I. Checked Properties

1	<p>If any of the sensors B9.2, S9.1, S9.2 or X_Encoder_Fail are triggered for longer than the pre-set time the treatment model is called.</p> $\forall \square_{\geq 10} ((B9.2 \vee S9.1 \vee S9.2 \vee X\_Encoder\_Fail) \rightarrow \forall \diamond_{\geq 0} (X \text{ Mov. Fail}))$
2	<p>The motor remain turned off until no sensor is detecting the fault anymore</p> $\neg \exists ((B9.2 \vee S9.1 \vee S9.2 \vee X\_Encoder\_Fail) U_{\geq 10} ((\text{Cut M9 Power}) \wedge (B9.2 \vee S9.1 \vee S9.2 \vee X\_Encoder\_Fail)))$
3	<p>Motors are not turned off until a fault is detected by the sensors</p> $\neg \forall (\neg (B9.2 \vee S9.1 \vee S9.2 \vee X\_Encoder\_Fail) U_{\geq 0} (\text{Cut M9 Power}))$

Thus, we propose do extract the basic properties from the SIFs descriptions, through that we have the main properties that the system was designed to fulfil. Besides the properties the system must fulfil, as we are working with safety systems, it is also imperative to check if the system reaches undesirable – or unsafe – states. So we have the following natural language properties and their respective translated TCTL propositions on Table I.

The verification tool displays the results in a colored square

besides the formula: (i) green if the formula holds, or (ii), red if the formula does not hold. On Fig. 6 all tested formulas are presented with their verification results on a extract of the verification tool output window. All formulas were verified with satisfactory results.



Fig. 6. TCTL Propositions and verification results

## V. CONCLUSIONS

In this work, the first steps towards a framework for modeling and verifying SIS control programs were presented, the framework is based on the safety software development cycle from the IEC 61511 standard associated with the model based design approach. As demanded by the IEC 61511 standard, tools and methodologies to comply with some phases of development cycle were chosen, the initial high level control architecture was proposed, guidelines to choose the methodologies for developing the prevention and mitigation activities were also proposed. Also guidelines for TCTL propositions mapping from natural language properties – which we consider one of the most difficult tasks when using model checking techniques – were chosen.

SIS control program, as the one developed on this work, are critical to the systems they protect, as they responsible for the identification and treatment of critical faults. These faults, if not treated might lead to severe accidents and the loss of human lives. Frameworks as the one introduced on the present work, became crucial in order to enable these systems to be correctly interpreted and developed allowing the SIS to present a lesser probability of faults.

The next steps on the development of the framework might include more detailed modules architecture and functionalities, as well as systematics for the refinement of the high level modules; Methodologies for automatic isomorphic transformation of the models in IEC 61131-3 code; Methodologies for the integration of the prevention and mitigation modules, as well as modules for the treatment of several faults; And finally, systematics to verify the integrated SIS models and the study the relation between its modules.

## REFERENCES

- [1] M. Bani Younis and G. Frey, "Formalization of Existing PLC Programs: A survey," Kaiserslautern, 2003.
- [2] Leonardo Rodrigues Sampaio, *Validação Visual de Programas Ladder Baseada em Modelos*. Campina Grande: Universidade Federal de Campina Grande, 2011.
- [3] Mauro Mazzolini, Alessandro Brusaferrri, and Emanuele Carpanzano, "An Integrated Framework for Model-based Design and Verification of discrete Automation Solutions," in *Proceedings 2011 9th IEEE International Conference on Industrial Informatics*, Milan, 2011, pp. 545-550.
- [4] Michel Diaz, *Petri Nets - Fundamental Models, Verification and Applications*. London: John Wiley & Sons, 2009.
- [5] Peter Hoffmann, Reimar Schumann, Talal M.A Maksoud, and Giuliano C. Premier, "Virtual Commissioning of Manufacturing Systems," in *24th European Conference on Modelling and Simulation*, Kuala Lumpur, Malaysia, 2010, pp. 175-181.
- [6] M. Sallak, C. Simon, and J.-F. Aubry, "A Fuzzy Probabilistic Approach for Determining Safety Integrity Level," *IEEE Transactions on Fuzzy Systems*, vol. 16, no. 1, pp. 239-248, 2008.
- [7] Reinaldo Squillante Jr., Diolino J. Santos Filho, Jeferson A. L. de Souza, Paulo E. Miyagi, and Fabricio Junqueira, "Safety in Supervisory Control for Critical Systems," in *Technological Innovation for the Internet of Things*, Costa de Caparica, 2012, pp. 261-270.
- [8] IEC, "IEC 61508 - Functional safety of electrical/electronic/programmable electronic safety-related systems," International Electrotechnical Commission, Geneva, Switzerland, 2010.
- [9] IEC, "IEC 61511 - Safety instrumented systems for the process industry sector," International Electrotechnical Commission, Geneva, 2003.
- [10] Mary Ann Lundteigen and Marvin Rausand, "Architectural constraints in IEC 61508: Do they have the intended effect?," *Reliability Engineering & System Safety*, vol. 94, no. 2, pp. 520-525, 2009.
- [11] Laihua Fang and Lijun Wei and Ji Liu Zongzhi Wu, "Design and Development of Safety Instrumented System," in *Proceedings of the IEEE International Conference on Automation and Logistics*, Qingdao, 2008, pp. 2685 - 2690.
- [12] Edmund M. Clarke, Orna Grumberg, and Doron A. Peled, *Model Checking*, 1st ed. Cambridge: MIT Press, 1999.
- [13] Rajeev Alur and David L. Dill, "A theory of timed automata," *Theoretical Computer Science*, vol. 126, no. 2, pp. 183-235, 1994.
- [14] T. Murata, "Petri nets: Properties, analysis and applications," *Proceedings of IEEE*, vol. 77, no. 4, pp. 541-580, 1989.
- [15] Pedro M. Gonzalez del Foyo and José Reinaldo Silva, "Towards a unified view of Petri nets and object oriented modeling," in *In 17th International Congress in Mechanical Engineering*, São Paulo, 2003, pp. 518-524.
- [16] Rajeev Alur, Costas Courcoubetis, and David Dill, "Model-Checking in Dense Real-time," *Information and Computation*, vol. 104, no. 1, pp. 2-34, 1993.
- [17] Richard Zurawski and MengChu Zhou, "Petri nets and industrial applications: a tutorial," *IEEE Transactions on Industrial Electronics*, vol. 41, no. 6, pp. 567-583, 1994.
- [18] Pedro M. G. del Foyo, A. S. P. José Miralles, and José Reinaldo Silva, "UM VERIFICADOR FORMAL EFICIENTE PARA SISTEMAS DE TEMPO REAL," in *X SBAI - Simpósio Brasileiro de Automação Inteligente*, vol. X, São João del-Rei, 2011, pp. 1220-1225.
- [19] Bernard Berthomieu and Miguel Menasche, "An Enumerative Approach For Analyzing Time Petri Nets," in *Proceedings IFIP*, Paris, 1983, pp. 41-46.
- [20] Rajeev Alur, Costas A. Courcoubetis, and David L. Dill, "Model-checking for real-time systems," in *Proceedings of the Fifth Annual IEEE Symposium on Logic in Computer Science*, Philadelphia, 1990, pp. 414-425.
- [21] ISO/IEC, "Software and Systems Engineering - High-level Petri Nets, Part 2: Transfer Format, International Standard WD ISO/IEC 15909. Wd version 0.9.0," 2005.
- [22] Alois Mayr, Reinhold Plösch, and Matthias Saft, "Towards an Operational Safety Standard for Software - Modelling IEC 61508 Part 3," in *18th IEEE International Conference and Workshops on Engineering of Computer-Based Systems*, Las Vegas, 2011, pp. 97-104.
- [23] Matthew B. Dwyer, George S. Avrunin, and James C. Corbett, "Property Specification Patterns for Finite-state Verification," in *Proceedings of 2nd Workshop on Formal Methods in Software Practice*, Clearwater Beach, 1998, pp. 7-15.
- [24] Reinaldo Squillante Júnior, Diolino Jose Santos Filho, Fabricio Junqueira, and Paulo Eigi Miyagi, "Development of Control Systems for Safety Instrumented Systems," *IEEE (Revista IEEE America Latina) Latin America Transactions*, vol. 9, no. 4, pp. 451-457, 2011.

# Cervix Position Recognition by Template Method using Linear Robot Ultrasound

Rino Ferdian Surakusumah, Christina Pahl, Muhammad Akmal Ayob, Eko Supriyanto

**Abstract**--Cervical cancer is the second-most common cause of death among women worldwide. Ultrasound is the non-invasive, fastest and cheapest method for imaging cervical cancer. In order to improve comfort, reduce operator dependency and increase image resolution, a new method for autonomous ultrasound cervix scanning has been developed. The platform consists of a mechanical frame, which is attached to a patient bed, able to hold the ultrasound probe with five degrees of freedom (DOF) including orthogonal coordinates in X, Y, Z direction, as well as rotation R and angle A. The developed automatic cervix identification algorithm is able to detect cervix with accuracy of 98 %. Test results show that the system can be used to capture images in bigger areas, where a large field of view is required and simultaneously record the position of the probe. Consequently, this system will enable the future of autonomous ultrasound cervix scanning and comfortable early cervix cancer detection.

**Keywords**--Ultrasound, Cervix Recognition, Medical Robot

## I. INTRODUCTION

Referring to the most recent cancer statistics provided on the World Health Organisation (WHO) database, maintained by the International Agency of Research on Cancer (IARC), cervical cancer represents the second most common cancer in women worldwide. The international incidence rates of cervical cancer show that almost 80 % of cervix cancer cases occur in low-income countries [1]. Therefore, in developing countries like Malaysia, cervical cancer has become a serious problem and is currently part of discussions in health politics.

In 70 % of the cervical cancer cases, a HPV infection is regarded as its cause [2]. Fig.1 refers to the development of cervical cancer and was adapted from [3]. It shows that a HPV infection of a normal cervix can develop precancerous lesions, which can lead to cervical cancer, in the case, the infection remains persistent. Otherwise, the lesion regresses and the infected cervix is cleared when the infection is only transient. Actually, cervical cancer is the overgrowth of abnormal cells in the cervix. WHO, defines cancer a term used for the malignant, autonomous and uncontrolled growth of cells and tissues [1]. Those cells are forming tumors, which come with the risk to invade other parts of the body. The competition of the cells for nutrients and oxygen leads to the elimination of healthy cells [1]. It is the second leading cause of cancer deaths among women worldwide [4]. According to WHO projections, 99% of the cervical cancer cases are linked to genital infection with HPV. However, cervical cancer is reported with about 500 000 new cases and 260 000 deaths each year [1]. Almost 80% of cases occur in low-income countries, where cervical cancer occurs more often in women compared to developed countries.

Ultrasound represents a technique with the lowest risk factors and costs. Although, ultrasonography is highly operator dependent and provides a low contrast resolution, it is used to evaluate the size and extent of cervical tumors [5]. Among the above mentioned imaging techniques, ultrasound is preferred to be used in the examination of the cervix. Ultrasonography is an affordable imaging technique compared to MRI, PET and CT, widely available, noninvasive, non-ionizing and painless [6]. The diagnostic capability of ultrasonography is based on piezoelectric transducers generating sound waves. These waves are transmitted into the body and partially reflected by boundaries, where the density changes. The reflected acoustic echoes are then received by the transducer probe and generated into electrical signals, which are then processed by the ultrasound machine in order to display the scanned area as an image [7].

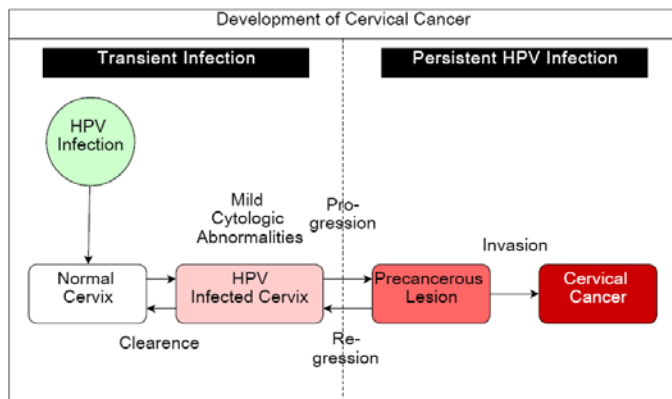


Fig.1 Development of Cervical Cancer

This work was supported by Cardio Centre Flagship Project, Universiti Teknologi Malaysia, Skudai UTM, Malaysia.

F. S. Rino and Pahl C. are with Faculty of Bioscience and Medical Engineering, Universiti Teknologi Malaysia (e-mail: rinoferdian@gmail.com).

Supriyanto, E and M.A. Ayob are with the IJN-UTM Cardiovascular Engineering Centre, Universiti Teknologi Malaysia, Skudai UTM, Malaysia (Corresponding author : +6075558551, e-mail: eko@biomedical.utm.my).

Table 1. Comparison of Cervix Abnormality Screening and Imaging Methods

Modality	Invasive	Cost	Time	Sensitivity
Biopsy	Yes	Medium	Long	High
Cervicography	Yes	Medium	Short	High
Colposcopy	Yes	Medium	Medium	High
CT	No	High	Medium	Medium
MRI	No	Very High	Medium	Medium
Pap Test	Yes	Low	Long	High
Ultrasound	No	Low	Short	Low

Ultrasonography can provide information about a shortened cervix leading potentially to preterm birth, neoplasms, several stages of cervical carcinoma according to the classification of International Federation of Gynecology and Obstetrics (FIGO) and other anatomical abnormalities. Ultrasonography for cervix examination purposes is either performed using transvaginal, transrectal or transabdominal transducer probes. Due to the discomfort caused by the usage of the first two mentioned probes, transabdominal ultrasound cervix examination represents the preferred method to detect abnormalities like cancer.

However, the use of ultrasound in cervix examinations encompasses some limitations. A major drawback of ultrasonography is high operator dependency [8]. Since ultrasonic image acquisition is complex, diagnostic accuracy in ultrasound is directly related to skills, training and experience of the operator [9]. Those skills encompass the correct localization of the cervix and measurement according to knowledge. Moreover, experience is highly required in analyzing and interpreting the anatomical appearance of cervical structures. One and the same ultrasound image of the cervix may be interpreted by each operator differently. This may result in variations of measurements and thus varying diagnoses. In avoidance of this, an operator independent platform needs to be provided.

One approach towards this represents the usage of a robot performing the abdominal cervix scan. Its high accuracy in moving the transducer probe, stability in keeping a desired position and coordination [10] allow highly comparable data. Automatic detection of the cervix may be another approach towards operator independence. Using such an algorithm in combination with an automatic machine may allow moving the transducer probe on the predefined abdominal surface until the cervix is detected. Since cervical structures are less clear on conventional 2D ultrasound images and require good experience in being detected, two applications will be shown in order to improve the resolution and subsequently facilitate image processing.

II. DESIGN AND IMPLEMENTATION

Concerning the limited capabilities of ultrasound in cervix imaging as mentioned above, it is important to develop alternative approaches to remove the current disadvantages in cervix ultrasound imaging. Autonomous systems, such as robots can help in minimizing operator dependency, to increase reproducibility and thus to increase comparability of image data for further diagnosis. Moreover, these autonomous cervix detection approaches allows a novel method in cervix imaging. Therefore, this study focuses on the development of a robot-based ultrasound transducer probe control system. This platform for automatic ultrasound scanning shall be cost-effective, stable and provide a high movement resolution. An algorithm is developed and allows operator independent detection of the cervix in ultrasound images.

The developed system is subsequently tested using three phantoms and 10 subjects. However, it should be noted that this research aims not at providing a ready to use device for

clinical purposes since required safety modalities are out of focus.

Ultrasonography is often the first choice for cervix imaging purposes because of its benefits being comfortable, safe, low-cost, portable and real-time capable. However, the role of ultrasonography in detecting cervical abnormalities is limited due to the given operator dependency, low-contrast resolution, noise impact and limited field of view. These restrictions prevent ultrasonography from taking a prominent role in abnormality detection of the human cervix.

Since the classification of cervical abnormalities, such as shortened cervix and cervical cancer, is limited due to the above mentioned factors, alternative imaging procedures are often required. In avoidance of cost-intensive (MRI or PET) and ionizing radiation-based (CT) imaging techniques, the here pursued approach aims at counteracting the given disadvantages. Hence, this study improves the existing ultrasound-based imaging methods by providing a robotbased scanning system. Precise transducer probe movements allow accurate image capturing and best possible prerequisites for subsequent processing of acquired data. The detection of ultrasound images containing cervical structures allows a higher degree of operator independence.

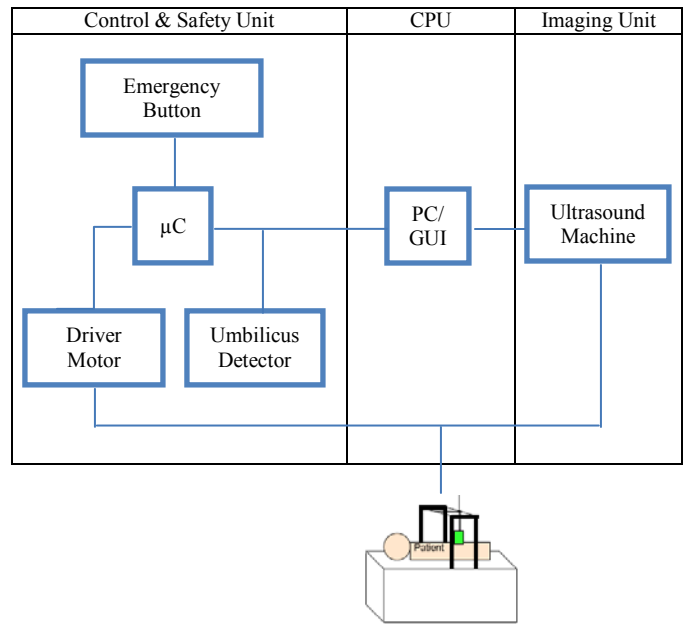


Fig.2 Function Structure of Proposed Scanning System

A. System Function

The system can be divided into mechanical and electrical parts. The scanning system can be divided into three discipline related parts: mechanics, electronics and computing. The mechanical part includes the frame of the scanning system, which is connected to the patient bed, supports the probe holder and restricts this unit in its maximum movement range. Furthermore the gear used to transmission the movement to the linear motion system and four motors, for the generation of motion proportional to the signal of the drivers. The electrical part consists of the drivers, which are providing the motors

electric current according to the data they receive from the controller. The last part involves computing. The processor of the PC should be at least 2.66 GHz for the processing of the video grabber device, the Operating System (OS) should be at least Windows 2000 or any other OS like OS X 10.3 or Linux 2.6x. The hard disc should be able to store at least 5 GB, which represents 100 videos captured for a distance of 10 cm with a motion resolution of 10<sup>4</sup>m. The RAM should have a capacity of at least 256 MB.

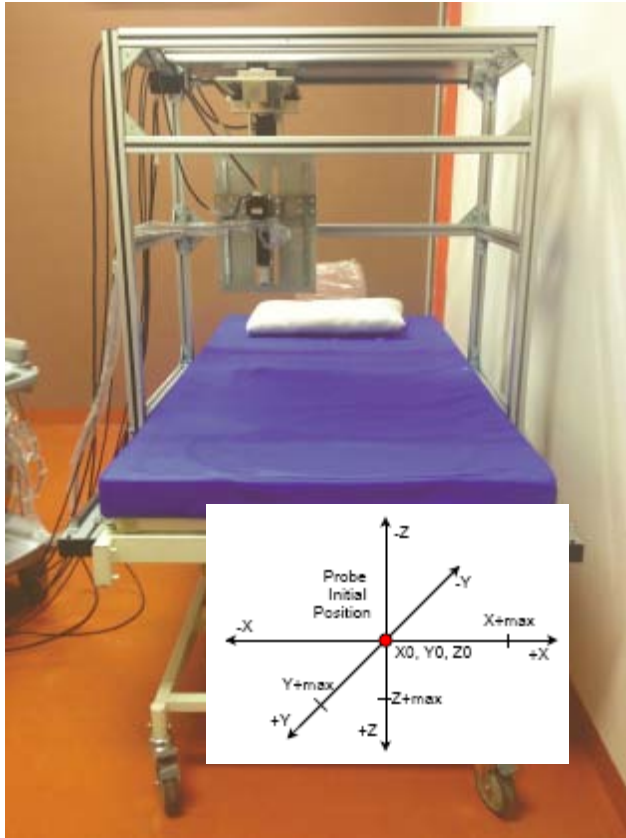


Fig 3. Mechanical Construction of Ultrasound Probe Holder and orientation

The function structure 3.1 includes the main parts of the autonomous scanning system. The system can be divided into three units, which enclose pulse control, central processing and imaging. This is because the system aims at using only those parts, which are needed to process autonomous scans and these parts can be classified by the means of their function. The controlling unit controls the movement of the probe holder. It obtains information about location, pressure and angle of the transducer probe. The processing unit performs algorithms for cervix detection and 3D reconstruction. The imaging unit obtains images of the cervix. Moreover, the patient is a part of the system. Since the cervix is the point of interest, the patient is female. Here, the computer plays a superior role. It acts as an interface between imaging and controlling. As the main processor, the computer receives data from the imaging unit, processes these data according the algorithms explained below and sends the results to the controlling unit. Imaging consists here of three subunits. The scan is performed using an ultrasound probe on

the surface of the lower abdomen. While scanning, the cervix shall be differentiated from and adjacent organs, so that a detection can be done. The ultrasound machine performs the calculations and provides power supply for the probe. Furthermore, the ultrasound machine controls the changes of the transducer pulse in terms of amplitude, frequency and duration. In this setup the display, which is used for displaying processed data is not needed. The same is with the printer and the keyboard, which is used for taking measurement manually and recording patient details. These are parts of the machine but are not utilized here. A frame grabber physically interfaces the ultrasound machine with the computer. It accepts and processes raw video data and provides it to the computer. Here, the data will be further processed by the means of an image processing algorithm. The aim of this algorithm is to detect the cervix in the ultrasound image and by that influence the scan procedure of the robot. Furthermore, the computer processes personal data about the patient like height, weight and circumference for a personalized scanning procedure.

### B. Cervix Recognition Algorithm

To ensure the true positive detection of the cervix during autonomous ultrasound examination an algorithm for its detection is required. The procedure developed for this purpose is based on the comparison of the the histograms of a predefined template and a comparison image. First, a threshold needs to be defined in order to allocate the compared image to the image class related to cervical structures if the threshold is not exceeded. Otherwise it will be defined as an image not containing cervical structures. After both images are loaded into MATLAB, the true-color image gets inverted to gray-scale by eliminating the hue and saturation information while retaining the luminance. This step simplifies subsequent processing since each pixel carries only intensity information. After this, the image is rectangular cropped in order to eliminate unnecessary information stored in the images, which are taken from the imaging system after the processing chain.

After cropping, the gray-scale image gets converted into binary image using a threshold of 0.4. In order to calculate the normalized histogram of the image at this stage, a conversion into double-precision intensity image is required. After the normalized histograms of each image are calculated, their values are used to obtain the difference of the images by subtracting their squared error. In the case the output is equal zero, it means there is no difference between the template image and the compared image. The higher the difference value is, the more difference exists in their histograms.

Since this approach is based on the distribution of intensities, the requirement for a successful recognition of cervix images lies in the choice of an appropriate template image, which represents the same orientation of the images captured for comparison purposes. This method is not meant to find the exact location of the cervix but to identify those ultrasound images, which have a higher probability of a captured cervix.

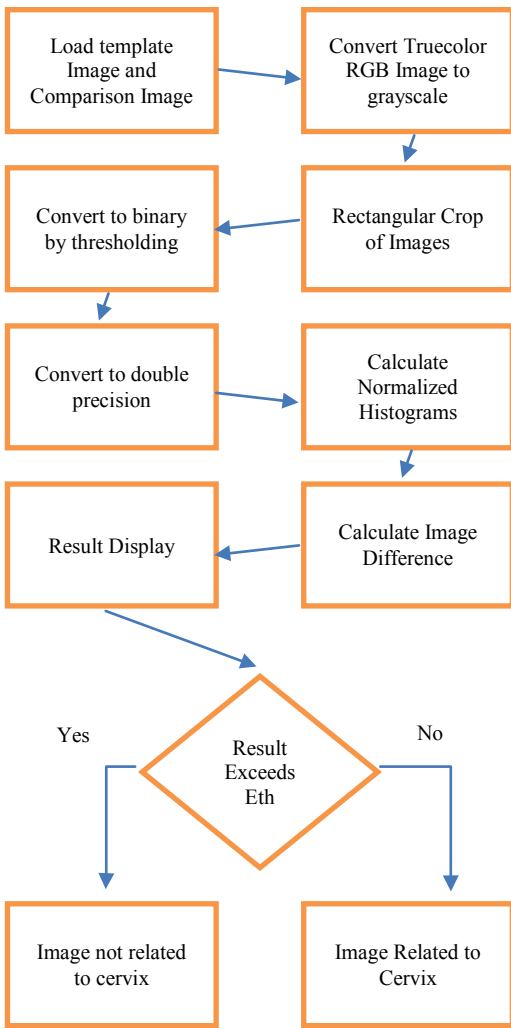


Fig. 4 Block Diagram of Cervix Recognition Algorithm

### III. RESULT AND ANALYSIS

#### A. Subject Specifications

Before subsequent system parameters can be defined, the scanning area, belonging to the uterine cervix, requires an analysis. This information defines the minimum of action field and thus theoretical limits the probe movement. Therefore, ten subjects have been scanned for determining the scanning area. Here, table 4.1 gives an overview about measured individual characteristics. The table lists down each subject (S) with a number. Age (A), circumference (C), height (H) as well as the distances between head and umbilicus (HU), umbilicus and pubic bone (UV) and umbilicus feet are measured respectively. The circumference refers to the abdomen on the height of the umbilicus. Furthermore, individual sensitivity against pressure on the lower abdomen was measured manually using a load cell based measurement device. The sensitivity is divided into four classes: soft pressure (SP), medium pressure (MP), hard pressure (HP) and painful pressure (PP)

Table 2. Characteristics of Scanned Subjects

Char	S1	S2	S3	S4	S5	S6	S7	S8	S9	S10
A[years]	36	29	28	26	24	23	23	22	21	21
C[cm]	79	76	74	71	69	63	87	73	73	75
H[cm]	154	148	152	164	152	169	158	147	158	164
W[kg]	59	49	61	57	52	58	54	50	58	65
SP[N]	5	8	15	7	7	9	4	5	6	7
MP[N]	27	11	24	14	12	15	11	8	9	11
HP[N]	40	15	29	21	18	24	18	11	14	18
PP[N]	50	18	35	27	25	29	22	18	19	25
HU[cm]	61	61	62	65	63	71	65	62	62	67
UV[cm]	18	20	19	26	23	26	19	21	21	23
UF[cm]	93	87	90	95	91	98	93	86	96	97

The device used for these means displays a first impression about the individual pressure sensitivity. The Sundoo SN-100 force gauge with a resolution of 0.5 N was used here. Among the subjects three different races can be found. The races enclosing Malay, Chinese, and Indians show strong differences in physique. Thus, the subsequent test results in chapter cover a wide range of differences, which results in better average values of these tests.

#### B. Cervix Recognition Testing

Ultrasound cervix recognition is used to detect images containing the cervix for autonomous scanning purposes. Since the purpose of this method is to differentiate images with a high probability of containing cervical structures from others, the detection rate does not reflect the visibility of the cervix. However, these images are performed using sagittal view (see 2.7). Figure 4.2 displays the chosen template image. Neighboring structures like bladder, uterus and vagina are marked in this image. The bladder represents a dominant organ in this view when filled. The uterus is located below the bladder and the cervix connects the body of the uterus with the vagina.

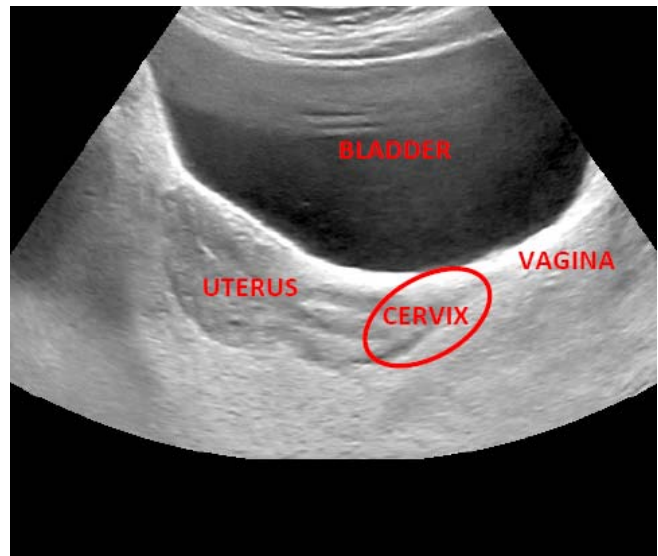
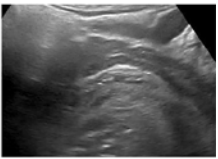
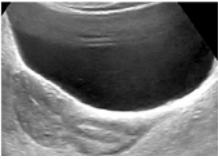
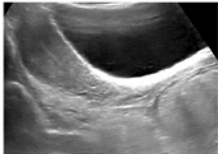
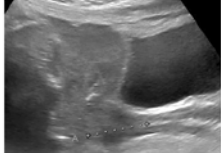
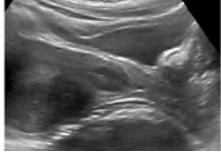
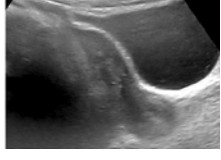
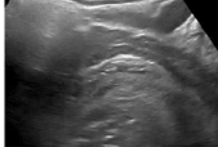


Fig. 5 Ultrasound Template Image for Automatic Cervix Detection

In order to differentiate cervix ultrasound images from others, the algorithm 3.3.1 was developed. In table 4.2 ultrasound images taken from ten subjects introduced in ?? were processed with reference to 4.2. Processing the data in MATLAB requires approximately 1.2 seconds. It can be seen, that the difference rates for cervical structures range from 0.0010 to 0.0050. The smaller the values are, the higher is the similarity between the compared images. The calculation of the rate is based on squared histogram differences between the images. In the case of subject 3, to whom the template image can be assigned to, the value is zero. This is because there is no difference between the histogram of the template image and the image compared with. Furthermore, ultrasound image data from different tissues and organs have been acquired manually and processed in table 4.3. The data encloses different body parts. The highest difference rate exists between the ear and the cervix template, whereas intestines show the highest similarity. This is due to the fact, that intestines and cervix are part of the abdomen and provide similar histograms respectively.

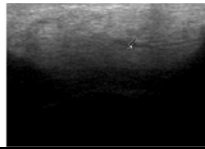
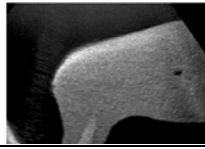
Table 3. Quality measurement of image with different filters; MSE = Mean square error; PSNR= power signal to noise ratio

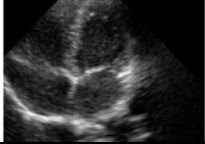
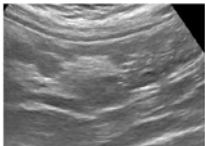
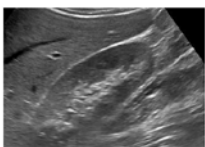
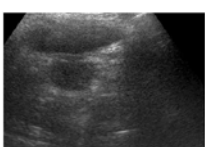
Subject	Diff. Rate	X	Y	Z	Image
S1	0.0033	0.1	15.1	2.4	
S2	0.0031	1.4	13.5	3.7	
S3	0.0000	0.8	11.6	2.8	
S4	0.0029	-0.2	13.6	3.0	
S5	0.0010	0.4	15.1	2.3	

S6	0.0019	1.2	11.5	3.4	
S7	0.0041	0.2	13.25	4.8	
S8	0.0051	2.2	13.6	1.8	
S9	0.0021	-0.9	14.7	3.3	
S10	0.0031	1.5	11.2	2.9	

However, from table 4.3 it can be obtained that the differences between the cervix template ultrasound image and ultrasound image data showing non-cervical structures, is higher compared to the difference rates in table 4.2. This is due to the histograms of those images being more different compared to those of cervix ultrasound images. The images here were obtained from male and female subjects. This supports the difference of images, which are used to be compared. The highest difference, which could be obtained for the ear canal is not shown in 4.3 due to demonstration purposes.

Table 4. Processing Results for Non-Cervical Structures

Structure	Diff. Rate	Image
Ear	0.1869	
Fetus	0.0357	

Heart	0.0294	
Intestines	0.0064	
Kidney	0.0078	
Prostate	0.0087	

The fact, that both data series, the cervix ultrasound images and the images containing non-cervical structures, differ clearly from each other, can be used to insert a line dividing the data (see figure 4.3). Doing so, leads to one data class with a higher similarity according to the template image being separated from the other class showing lower similarity rates. In this case, the dividing line has a value of 0.0057. This value may change for different data classes and template images used. This approach of automatic cervix ultrasound image detection can be used for future analysis of 3D ultrasound image data consisting of 2D image slices.

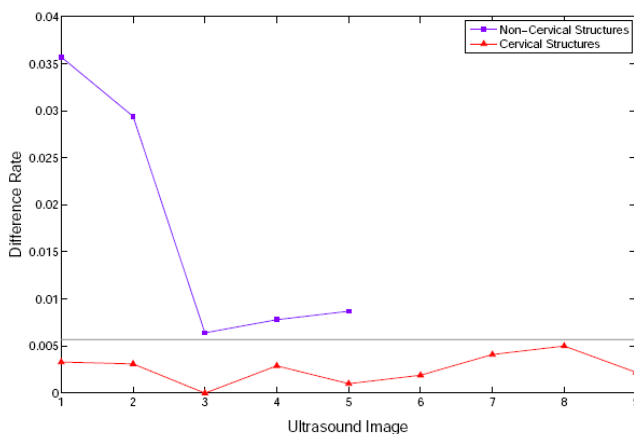


Fig 6. Differentiation of Data after Cervix Recognition

#### IV. CONCLUSION

A novel method to enable autonomous ultrasound cervix scanning has been successfully developed. The method combines a mechanical platform, electronics and a software for probe motion control purposes, manage safety buttons, identify

the umbilicus position, and localize the scanning start and endpoints.

Test results show that the system is able to capture the ultrasound images of phantoms and subjects with a scanning resolution of 10<sup>1</sup>. The captured ultrasound images and positions are planned to be used for the reconstruction of 2D panorama images in order to have a larger field of view as well 3D images with excellent resolution. In order to have 2D panoramic view with excellent resolution, it is recommended to use merging algorithms in combination with image registration and finite element modelling. The captured 2D ultrasound images including position information can be used for 3D reconstruction using VTK software. This, however may need a high performance computer for image processing and analysis. In order to obtain volumetric information of the cervix, 3D reconstruction algorithms have been applied. In order to obtain volumes of a with better resolution, it is suggested to use VR instead of MPR, for further post processing like 3D segmentation of the cervix. With this system, it is possible to perform autonomous ultrasound cervix scanning with high comfort, resolution and safety. This will enable future operator independent computed tomography (CT) ultrasound scanning, not only for cervix scanning but also for other internal organ imaging.

#### ACKNOWLEDGMENT

The authors would like to express our thanks to Universiti Teknologi Malaysia and the Biotechnology Research Alliance for supporting and funding this study. Our appreciation also goes to the Advanced Diagnostics and E-Health Research Group members for their ideas and comments on this paper.

#### REFERENCES

- [1] W.H.O. Comprehensive cervical cancer control: a guide to essential practice. WHO. 2006.
- [2] Munoz, N., Bosch, F., Castellsagué, X., Díaz, M., de Sanjose, S., Hammouda, D., Shah, K. and Meijer, C. Against which human papillomavirus types shall we vaccinate and screen? The international perspective. *International Journal of Cancer*, 2004. 111(2): 278–285.
- [3] Wright Jr, T., Schiffman, M. et al. Adding a test for human papillomavirus DNA to cervical-cancer screening. *The New England journal of medicine*, 2003. 348(6): 489.
- [4] Parkin, D., Bray, F., Ferlay, J. and Pisani, P. Global cancer statistics, 2002. *CA: a cancer journal for clinicians*, 2005. 55(2): 74–108.
- [5] Pandey, K., Pradhan, A., Agarwal, A., Bhagoliwal, A. and Agarwal, N. Fluorescence Spectroscopy: A New Approach in Cervical Cancer. *The Journal of Obstetrics and Gynecology of India*, 2012: 1–5.
- [6] Henderson, J., Saraiya, M., Martinez, G., Harper, C. and Sawaya, G. Changes to cervical cancer prevention guidelines: Effects on screening among US women ages 15–29. *Preventive Medicine*, 2012.
- [7] Charboneau, J. and Levine, D. Diagnostic ultrasound. *JAMA*, 2012. 307(7).
- [8] Rouyer, J., Lasaygues, P. and Mensah, S. Novel Ultrasound Tomography for Anatomical Inspection. *Acoustical Imaging*, 2012: 3–10.
- [9] Wong, A. and Scharcanski, J. Monte Carlo despeckling of transrectal ultrasound images of the prostate. *Digital Signal Processing*, 2012.
- [10] Rockland, R., Kimmel, H., Carpinelli, J., Hirsch, L. and Burr-Alexander, L. Medical Robotics in K-12 Education. *Robots in K-12 Education*, 2012: 120.

- [11] Alcázar, J., Aubá, M. and Olartecoechea, B. Three-dimensional ultrasound in gynecological clinical practice. Reports in Medical Imaging, 2012. 5: 1–13.129

# Virtex-7 FPGA-based Reconfigurable Computer System RCS-7 for digital image processing

Ilya I. Levin, Igor A. Kalyaev, Alexey I. Dordopulo, Liubov M. Slasten, Slava V. Gudkov

**Abstract**— The problem of locating image features by template matching belongs to the area of digital image processing and is typical example of use of multiprocessor computer systems. The paper covers design principles, technical parameters and design features of a reconfigurable computer system RCS-7, specially created for such type of tasks and based on Xilinx Virtex-7 FPGAs. The distinctive features of RCS-7 are its high real performance, low power consumption during execution of application tasks and practically linear growth of the performance when hardware resource is growing. In the paper we describe the RCS-7 software suit for solving tasks of digital image processing. We also give current results, which show effectiveness of the suggested approach and the real performance during execution of the task of digital image processing.

**Keywords**— reconfigurable architecture, programmable soft-architecture, FPGA, reconfigurable computer system, high performance, parallel processing, pipeline processing, computer-aided circuit design, high-level programming language for reconfigurable systems, architecture description language.

## I. INTRODUCTION

RECONFIGURABLE computer systems (RCS) are widely used for solving of computationally laborious tasks of various domains of science and technology. In comparison with cluster multiprocessor computer systems RCSs have several significant advantages such as high real and specific performances during execution of tasks, high energy effectiveness, etc. Different Russian and foreign vendors produce both stand-alone accelerators with one or two FPGAs and computational complexes. Such vendors as Nallatech [2] and Pico Computing [3] produce a number of accelerators and carrier boards with few (less than 4) FPGAs, which are used

for design of servers and heterogeneous cluster systems by HP and IBM. The companies Convey [4] and Maxeler Technologies [5] design hybrid supercomputers on the base of their own heterogeneous cluster nodes that can contain 1-4 FPGA chips and several general-purpose processors. The company SRC [6] uses a similar solution which produces nodes, also called MAP processors for 1U, 2U and 4U racks (MAPstation). The MAPstation 1U contains one MAP processor. The MAPstation 2U contains up to three MAP processors. The MAPstation 4U can contain up to 10 various modules such as a MAP processor, a module with a general-purpose microprocessor, or a memory module.

In contrast to the abovementioned companies, the scientific team of SRI MCS SFU design supercomputers which contain printed circuit boards, united into a single computational resource. Each printed circuit board contains a set of FPGA chips [1]. The principal computing element of such RCSs is hardware resource of FPGAs, united into a single computational field by high-speed data transfer channels.

The methods of design and creation of such systems have been successfully developed in SRI MCS SFU (Taganrog, Russia). Owing to the concept of RCS design [7] we could create quite a number of quantity produced high-performance systems of various architectures and configurations based on Xilinx FPGAs of Virtex-4, Virtex-5 and Virtex-6 families. These RCS are successfully used in various organizations and enterprises of the Russian Federation for solving of computationally laborious tasks from various problem domains. One of our up-to-date systems is the reconfigurable computer system RCS-7 designed on the base of Xilinx Virtex-7 FPGAs.

## II. RCS-7 BASED ON XILINX VIRTEX-7 FPGAS

The reconfigurable computer system RCS-7 on the base of Virtex-7 FPGAs contains a computational field of 576 Virtex-7 XC7V585T-FFG1761 FPGAs (58 million equivalent gates each), united within a 47U computational rack with the peak performance 1015 fixed-point operations per second.

The principal structural component of the RCS-7 is a computational module 24V7-750 (Pleiad), which can be placed into a standard 19" computational rack, and which consists of:

- 4 printed circuit boards of the computational module 6V7-180 (see Fig. 1);
- a control module CM-7;

This work was supported in part by the Russian Ministry of Education under Grant MK-1262.2014.9

A. Scientific Research Institute of Multiprocessor Computer Systems at Southern Federal University, Taganrog, Russia (phone: 8634-31-9092; fax: 8634-360-376; e-mail: levin@mvs.tsure.ru).

B. Scientific Research Institute of Multiprocessor Computer Systems at Southern Federal University, Taganrog, Russia (phone: 8634-36-0357; fax: 8634-360-376; e-mail: [kaliaev@mvs.tsure.ru](mailto:kaliaev@mvs.tsure.ru)).

C. Southern Scientific Centre of Russian Academy of Sciences, Rostov-on-Don, Russia (e-mail: scorpio@mvs.tsure.ru)

D. Southern Scientific Centre of Russian Academy of Sciences, Rostov-on-Don, Russia (e-mail: [lmstasten@yandex.ru](mailto:lmstasten@yandex.ru)).

E. Scientific Research Institute of Multiprocessor Computer Systems at Southern Federal University, Taganrog, Russia (phone: 8634-31-5491; e-mail: [Slava\\_Gudkov@mail.ru](mailto:Slava_Gudkov@mail.ru)).

- a power supply subsystem;
- a cooling subsystem, etc.

Fig. 2 shows the computational module 24V7-750.

The board of the computational module 6V7-180 contains:

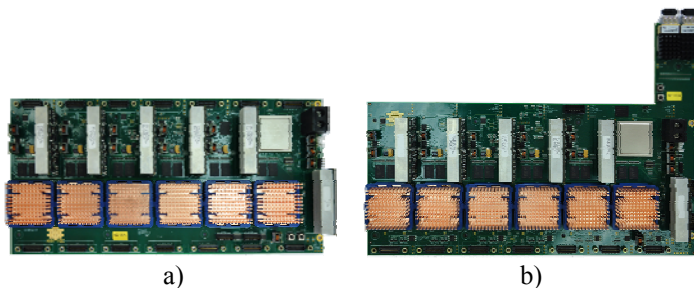


Fig. 1. The board of the computational module 6V7-180 (a – the board №0-2 of the module 24V7-750, b – the board №3 of the module 24V7-750 with an optical connector for connection with other computational modules 24V7-750)

- a computational field, which consists of 6 Xilinx Virtex-7 XC7V585T-1FFG1761 FPGAs, connected sequentially by 144 LVDS differential lanes running at frequency of 800 MHz;



Fig. 2. The computational module 24V7-750 (a - open, b - closed)

- a controller of the board of the computational module, based on Xilinx XC6V130T-1FFG1156C FPGAs;
- 12 LVDS channels running at frequency of 800 MHz, 25 differential pairs each (SS4 connectors), applied for connection with other computational modules;
- blocks of general and reserve FPGA programming through the interfaces JTAG-1 and JTAG-2;
- a synchronization subsystem (generators ECS-2033-250-BN and clock buffers IDT5T9316NLI);
- a distributed memory which consists of 12 DRAM chips (MT47H128M16HR-25E, 128 M\*16 and with the read/write frequency up to 400 MHz). Each FPGA of the computational field and of the controller of the computational module's board are connected to two DDR2 memory chips. The RAM size of the computational module's board is 3 Gbyte;
- 2 LVDS channels (20 differential pairs each) for connection with a personal computer and external devices;
- a subsystem of FPGA loading;
- a power supply subsystem, which includes DC-DC voltage converters, which provide the supply voltages: +1 V for FPGA cores; +2.5 V for the clock generator; +1.8 V for DDR2 memory chips, +3.3 V for FPGA buffer stages.



Fig. 3. . RCS-7

The performance of the one board 6V7-180 is 645.9 GFlops for 32-digit floating point data, and the performance of the computational module 24V7-750 is 2.58 TFlops for 32-digit floating point data. The performance of the RCS-7 (see Fig. 3), when it contains 24-36 computational modules 24V7-750 is 62-93 TFlops for 32-digit floating point data and 19.4-29.4 TFlops for 64-digit floating point data.

The application area of the RCS-7 and computer complexes designed on its base is digital signal processing and multichannel digital filtration.

### III. RCS-7 SOFTWARE

The majority of existing commercial CAD-systems such as Xilinx ISE, Altium Designer, etc. provide work with only one FPGA chip within one project. Therefore, if it is necessary to design a configuration for several interconnected FPGA chips, the circuit engineer has to distribute all components of the computing structure, which corresponds to the algorithm of the solving task, between different projects, which will correspond to certain FPGA chips of the multichip RCS. Besides, he has to take into account the RCS topology and connections between FPGA chips. A large number of features of RCS architecture, topology and components, which are to be taken into account by the circuit engineer, significantly complicates design of RCS configurations, required for the task which is solved on the multichip RCS, and practically rules out porting of the complete solution to some other RCS which has a different architecture or configuration. The RCS programming consists of two stages. At the first stage, the circuit engineer creates the computing structure for the task. At the second stage, the application programmer develops the parallel program, which determines data flows in the designed computing structure. That is why the time period, usually needed for creation of the RCS task solution, is rather long (4-

9 months).

To program RCSs, designed and implemented in Scientific Research Institute of multiprocessor computer systems at Southern Federal University (Taganrog, Russia), we use a software suit, developed by our team of scientists [1, 7, 9, 11]. The software suit is based on structural-procedural methods of organization of computations and determines both the structure of the computer system within the field of FPGA logical cells, and organization of parallel processes and data flows. Principles of RCS programming [7-10] are based on the principles of structural procedural organization of computations and are the same for all generations of RCSs designed in SRI MCS SFU. So, applications for the RCS-7 are developed with the help of the high-level programming language COLAMO [1, 11]. After translation of the program the configuration of the computer systems is created automatically, and it consists of bitstream files of all FPGAs (the structural component of the parallel application). The other part of translation result is the parallel program, which controls data flows and organization of computations in the RCS. The distinctive features of the software suit based on the programming language COLAMO in comparison with the development tools MitrionC [12] and CatapultC [13], are automatic mapping, synchronization and generation of configuration for multichip RCSs, 60-90% of used hardware resource of each FPGA chip and high frequencies (250 – 350 MHz).

The basic components of the software tools of application development with the help of the high-level programming language COLAMO:

- translator of the programming language COLAMO, which translates the source COLAMO-program into the information graph of the parallel application;
- synthesizer of multichip circuit solutions FireConstructor, which maps the information graph, generated by the translator of the programming language COLAMO, on the RCS architecture, places the mapped solution into the FPGA chips and automatically synchronizes all fragments of the information graph in different FPGA chips;
- library of IP-cores, which correspond to the COLAMO instructions and are all-in-one structurally implemented circuit solutions for various problem domains, and interfaces, applied for data processing speed matching and for connection into the single computing structure.

The unique feature of the RCS-7 software suit is support of special-purpose soft-architectures, which are applied for creation and programming of macroobjects. A macroobject is a set of computational nodes which perform a certain set of operations, and which are united by some communication system. For each class of tasks, solved in RCS, we can select a certain set of optimal computing structures (macroobjects), which provide the most effective solution of the tasks of the given class. It is possible to change the number of functional nodes and parameters of any functional node (such as the operand capacity, the number of data channels, the instruction

set, etc.) of any macroobject, but their functions cannot be changed. So, from the viewpoint of the RCS programmer the macroobject is a “pattern” which can be redefined by the RCS programmer during design of some engineering solution, and then it can be replicated in FPGAs of computational modules in the required quantity and be connected with similar or any other macroobjects into computing structures, which optimally correspond to the structure of the solving task.

On the base of macroobjects we can create various RCS soft-architectures. An RCS soft-architecture is a computing structure, designed by the circuit engineer. It consists of macroobjects and allows modification of connections between its components only by program re-adjustment and without re-programming of the FPGA chips of the computational field (no re-loading of FPGA bitstream files). So, we can create any computing structures, which are required for task solving.

Owing to soft-architectures, fundamental programming principles and high-level RCS programming language it is possible to adapt very easily all software RCS development tools to any new RCS architectures and topologies of computational modules with no cardinal modifications of the source code of any component of the software suit and to reduce the time of task solution.

#### IV. SOFT-ARCHITECTURE PROGRAMMING FOR PROBLEM DOMAINS

For creation of soft-architectures we have developed a language SADL (Soft-Architecture Development Language) [14]. The SADL-description of the soft-architecture is translated into a virtual architecture of the computer system. Then the synthesizer FireConstructor maps the information graph of the task on the virtual architecture.

Creation of any soft-architecture requires the following actions:

- creation of a SADL-description of the soft-architecture;
- translation of the soft-architecture description into an intermediate description with the help of the synthesizer FireConstructor;
- mapping of all soft-architecture components on the hardware platform with the help of the synthesizer of scalable parallel-pipeline procedures SteamConstructor.

The SADL-translator converts the program into an intermediate form, which is placed by the synthesizer FireConstructor on the RCS hardware platform. The result of placement is a modified file of the intermediate form and bitstream files of all FPGA chips, occupied during placement of the soft-architecture on the RCS hardware platform. After successful placement of the soft-architecture on the RCS hardware platform, it can be used for solving of various tasks of the certain problem domain.

Development of any parallel application on the base of the RCS soft-architecture requires the following actions:

- to develop a parallel application in the high-level language COLAMO;
- to translate the parallel application and to generate structural and procedural components;

- to map the structural component of the parallel application on the soft-architecture using the synthesizer SteamConstructor;
- to translate the procedural component of the parallel application into assembler instructions of soft-architecture components;
- to generate executable file of the parallel application (with instructions for the soft-architecture components) for loading into the RCS;
- to load FPGA bitstream files, which were generated during placement of the soft-architecture components on the RCS hardware platform, into the RCS;
- to load the executable file of the parallel application;
- to load input data of the task into the RCS soft-architecture;
- to run the application and to save calculation results.

Figure 4 shows interaction of application development software tools.

Owing to the created software tools, development and modification of soft-architectures requires no highly qualified circuit engineer for modification of the computing structure. The time, which is usually needed for design or modification of the soft-architecture is significantly reduced, and the effectiveness of the generated multichip architectural solutions is comparable with solutions, implemented manually by circuit engineers. According to the basic principles of the language COLAMO parallel applications can be easily modified and adapted to the available computational resource. Owing to automatic mapping of information graphs on the RCS hardware resource, the application programmers can consider the RCS as a virtual FPGA with a huge number of logic cells, but not as a set of FPGA chips. Using the developed software suit, the RCS programmer can develop and debug RCS parallel applications, paying no attention to the features of the RCS architecture.

#### V. SOLVING OF THE PROBLEM OF LOCATING IMAGE FEATURES WITH THE HELP OF SOFT-ARCHITECTURES

As an example of the task for implementation on the RCS-7, using soft-architectures, we have selected the task of locating image features. The solution of this task is based on the method of template matching. The template is moving along the image from left to right and from top to bottom and it is being compared with all features of the image. As an evaluation criterion we use cross correlation between the initial image and the template. The position of the correlation maximum corresponds to the position of the located feature. As the views of the target feature may be considerably different, it is necessary to define not only its position, but also to measure similarity between the target feature and each template, and only then the final decision can be made. The input image is partitioned into sections which are processed one by one with overlapping. If it is necessary, zero bits will be included into the last section to make its length proper.

During implementation of the task of locating image features on the RCS-7 on the base of the method of template matching, we used the following basic parameters:

- the size of the input image is 512×512 (or 544×544, if we take into account additional zeroes);
- the size of the used templates is 32×32;
- the size of the selected section is 64 (32 zeroes are added to the last section);
- the number of sections within the image is 256;
- the size of overlapping between sections is 32.

The task was implemented on the RCS-7, which contained 24 24V7-750 computational modules. The real performance which was reached during execution of the task was 41.8 TFlops or 67.4% from the peak performance.

#### VI. CONCLUSION

Owing to the design solutions of the RCS-7 based on Xilinx Virtex-7 FPGA, we can obtain a high-performance computational resource within one 47U computational rack. Besides, the specific performance of the RCS-7 is comparable with the performance of the best cluster computer systems in the world. Therefore, it is possible to consider RCSs based on Xilinx Virtex-7 FPGAs as a basis for new generation high-performance computer complexes, which provide highly effective computations and practically linear growth of performance for expanding computational resource.

#### REFERENCES

- [1] A.V. Kalyaev, I.I. Levin, Modular-scalable multiprocessor systems with structural procedural organization of calculations. Moscow, Janus-K, 2003. 380 pp.
- [2] <http://www.nallatech.com>
- [3] <http://www.nallatech.com>
- [4] <http://picocomputing.com>
- [5] <http://www.conveycomputer.com>
- [6] <http://www.maxeler.com>
- [7] <http://www.srccomp.com>
- [8] I.A. Kalyaev, I.I. Levin, E.A. Semernikov, V.I. Shmoilov, Reconfigurable multipipeline computing structures. Rostov-on-Don, SSC RAS Publishing, 2009. 344 pp.
- [9] I.A. Kalyaev, I.I. Levin, Family of high real performance reconfigurable computer systems. *Papers of international scientific conference "Parallel computing technologies"*. Nizhny Novgorod, 2009, 186-196 pp.
- [10] A.I. Dordopulo, I.A. Kalyaev, I.I. Levin, E.A. Semernikov, High-performance reconfigurable computer systems of a new generation. *Papers of International supercomputer conference and youth scientific school "Scientific service in the Internet: exaflop future"*, Moscow, MSU Publishing, 2011, 42-49 pp.
- [11] I.A. Kalyaev, I.I. Levin, E.A. Semernikov, A.I. Dordopulo, Reconfigurable computer systems on the base of Virtex-6 FPGAs // *Paper of International scientific conference "Parallel computer technologies 2011"*, Chelyabinsk, 2011, 203-210 pp.
- [12] I.A. Kalyaev, I.I. Levin, E.A. Semernikov, V.I. Shmoilov, (2012). Reconfigurable multipipeline computing structures. Nova Science Publishers, New York.
- [13] <http://www.mitronics.com>
- [14] <http://calypto.com/en/products/catapult/overview>
- [15] E.A. Semernikov, V.B. Kovalenko Organization of multilevel programming of reconfigurable computer systems *Herald of computer and information technologies*, Moscow, Mashinostroyeniye, 2011, № 9, 3-10 pp.

# Magnetically Dimmable Half Bridge Current Fed LED Driver

Selim Borekci and Nihal Cetin Acar

**Abstract**—In this paper, a new LED (Light Emitting Diode) driver and dimming techniques are introduced. Half bridge current fed resonant LED driver is designed and implemented. Rather than using traditional dimming techniques, dimming is accomplished magnetically. The proposed driver is implemented on 33 LEDs. LEDs are dimmed from 33 W to 20 W.

**Keywords**—dimming, LED driver, resonant converter, variable inductor

## I. INTRODUCTION

T5 and T8 fluorescent lamps have been used widely for indoor and outdoor lightening. Recently LEDs are also becoming very popular, because of their high efficacy (light output per watt), long life, no start up and striations problems and very low maintenance requirements [1]-[2].

Some of the grid connected AC applications result in harmonics because of conduction angle. To overcome this problem and provide isolation between the grid system and LEDs, high frequency resonant converters with transformers are implemented.

Voltage fed high frequency converters such as LLC type resonant topologies are commonly utilized. For low current ripple and better starting transients, current fed circuits give better performance.

Most of the high frequency LED drivers have two stages shown in (Fig. 1). In the first stage, 50/60 Hz AC power converted to DC with an IC which provides low THD and better power factor. In the second stage, DC power is converted to high frequency AC. In this stage, LEDs are connected to the circuit with rectifier having an electrolytic capacitor.

In LEDs data sheets, it can be seen that led luminance is proportional to its forward led current. LED current is associated with LED illumination linearly. For energy saving

S. Borekci was working in lighting industry for several years in MS, USA. He is now with the Department of Electrical and Electronics Engineering at Akdeniz University, Antalya, TURKEY (e-mail: sborekci@akdeniz.edu.tr).

Nihal C. Acar is working as a research and teaching assistant at Electrical and Electronics Engineering Dept at Akdeniz University, Antalya, Turkey (e-mail: nihalcetinacar@gmail.com).

and luminous flux adjustment in a space, LED brightness dimming becomes important. In addition to new generation IC solutions for dimming, voltage control and pulse width modulation (PWM) techniques are used to adjust led luminous flux [3]-[4].

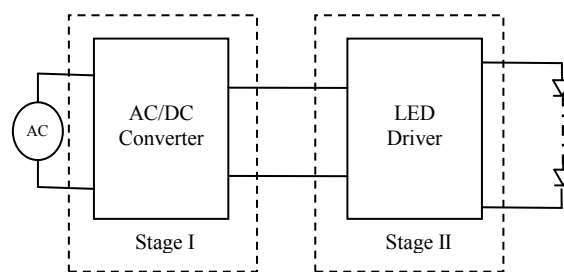


Fig. 1 Two Stage LED Driver.

Varying the LED voltage results in changes in the LED current. The relation between them is not linear. Because of that, controlling the LED current requires complex circuit structure [5]-[7].

In PWM techniques, LEDs are turned on and off in a period and control scheme adjusts the duty ratio of LEDs [8]-[9]. In high frequency applications, that reduces LED life span [10]-[11]. PWM technique may also cause electromagnetic interference (EMI) noise problems.

In this paper, a new dimmable LED driver is introduced. A half bridge current fed topology is used to drive LEDs and also galvanic isolation is provided. A new LED dimming technique is accomplished by using variable inductor. The proposed technique is designed and implemented on 1 Watt 33 power LEDs.

## II. LED AND LUMINANCE

V-I characteristic of power LEDs is defined by an exponential function. Nonlinearity characteristics of LEDs make their driver circuits complicated. Current and voltage relationship is given by equation (1) and (Fig. 2) shows a typical V-I curve of a LED.

$$I = I_s(e^{(V_D + q)/(n \cdot k \cdot T)} - 1) \quad (1)$$

- where I diode forward current
- I<sub>s</sub> reverse bias saturation current
- V<sub>D</sub> diode forward voltage
- n diode ideality factor
- V<sub>T</sub> thermal voltage
- k Boltzman's constant
- T temperature
- q charge on an electron

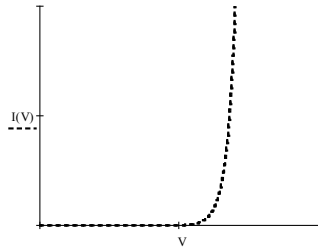


Fig. 2 V & I Characteristic of a LED.

As seen in (Fig. 3), there are two operating states; on and off. Figure (a) and (b) show the equivalent circuit of LED for on and off states respectively. Capacitive and resistive effects of LEDs during on and off are illustrated in (Fig. 3) as C<sub>on</sub>, C<sub>off</sub>, R<sub>on</sub> and R<sub>off</sub> respectively. In the figure, V<sub>on</sub> represents the forward bias voltage of a LED.

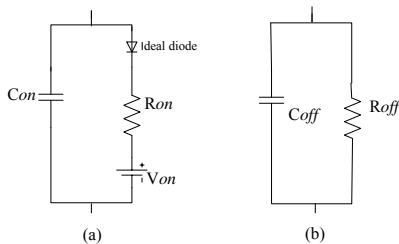


Fig. 3 Electrical Model of a LED.

It is important that LED forward current determines the brightness of a LED. Figure 4 shows a typical relation between the forward current and relative luminous of a LED. LED luminous flux increases linearly with its current, while the voltage is almost constant. Therefore, the efficacy of LEDs can be assumed to be constant.

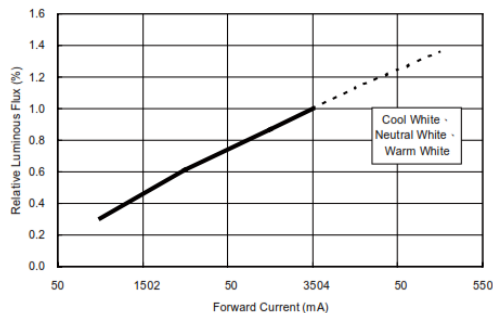


Fig. 4 Lamp Current versus LED Relative Luminous Flux.

There are several topologies for LED drivers as mentioned. Commonly used ones have two stages as shown in (Fig.1). In the first stage, AC grid is converted to DC. ICs are utilized for better power factor correction, THD and DC voltage regulation. The function of the first stage is a DC power supply.

In the second stage, a LED driver is designed such that LED current results in desired led brightness. Dimming feature can also be added in this stage.

### III. PROPOSED SOLUTION

The second stage is the focus of this research. A current fed half bridge converter shown in (Fig. 5) is implemented. In the circuit, two electrolytic capacitors C<sub>dc</sub> are used to divide the DC voltage and two choke inductors L<sub>dc</sub> takes place to regulate the current. A snubber capacitor C is used across power switches. There are two MOSFETs which are driven by IR2153. Magnetization impedance of the transformer L<sub>p</sub> and resonant capacitor C<sub>r</sub> determines the resonant frequency of the converter. The secondary voltage of the transformer is rectified by diodes. For the better output regulation, an electrolytic capacitor C<sub>o</sub> is placed in parallel with the LEDs.

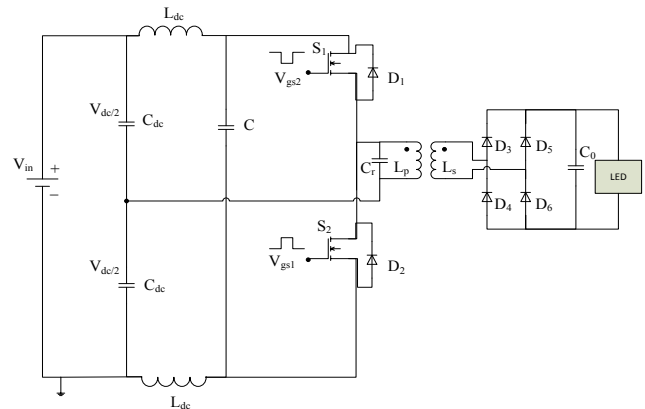


Fig. 5 Proposed LED Driver.

DC voltage, V<sub>in</sub>, is applied to the half bridge current fed resonant converter. Primary and secondary voltages of the transformer are in sinusoidal shape. The peak value of the primer voltage for the first harmonic is calculated as

$$V_{ppk} = \frac{\pi \cdot V_{in}}{4} \quad (2)$$

Number of LEDs m and forward voltage of selected LEDs V<sub>led</sub> are determined at the beginning of the design. Therefore, the peak value of the secondary voltage can be obtained from equation (3).

$$V_{spk} = m \cdot V_{led} \quad (3)$$

When the primary and secondary voltages are known, the turn ratio of the transformer can be calculated as

$$n = \frac{V_{ppk}}{V_{spk}} \quad (4)$$

For high frequency applications, ferrite cores can be used. The saturation of the ferrite core is around 0.3 T. Better material can have higher saturation level. Selected frequency of the circuit, effective cross section area of the core, and the secondary voltage of the transformer determine the number of secondary turns as in equation (5). Multiplying the turn ratio with the number of secondary turns gives the number of primary turns.

$$N_s = \frac{V_{spk}}{2 * \pi * f * A_c * B} \quad (5)$$

Selected magnetic core has its own effective permeability  $\mu_{eff}$ , cross section area  $A_{eff}$  and effective magnetic length  $L_{eff}$ . From the number of primary turns and core information, primer reactance can be calculated by equation (6).

$$L_p = \left( \frac{L_{eff}}{\mu_{eff} * A_{eff}} \right)^{-1} * N_p^2 \quad (6)$$

The relationship between primary and secondary currents of the transformer is given in equation (7).  $R_p$  and  $R_s$  represent copper losses for the primary and secondary respectively.  $k_{ps}$  is the coupling coefficient between primary and secondary windings.  $V_p$  and  $V_s$  are primary voltage and secondary voltages and  $I_p$  and  $I_s$  are primary and secondary currents respectively.  $\omega$  is the radian frequency of the circuit and  $R_{LED}$  is the equivalent resistance of LEDs.

$$(V) = (Z) * (I) \quad (7)$$

where,

$$(I) = \begin{pmatrix} I_p \\ I_s \end{pmatrix}, \quad (V) = \begin{pmatrix} V_p \\ 0 \end{pmatrix}$$

$$(Z) = \begin{pmatrix} i * \omega * \left( \frac{k_{ps}}{n} \right)^2 * L_s + R_p & i * \omega * \left( \frac{k_{ps}}{n} \right)^2 * L_s \\ i * \omega * \left( \frac{k_{ps}}{n} \right)^2 * L_s & i * \omega * L_s + R_s + R_{LED} \end{pmatrix}$$

To tune the resonant frequency, resonant capacitor  $C_r$  is selected from equation (6).

$$f_r = \frac{1}{\sqrt{(L_p * C_r) * 2 * \pi}} \quad (8)$$

For dimming purpose, a current controlled inductor shown in (Fig. 6) is used. When dc control current is increased, the value of the inductor decreases. Detailed analyses of magnetically control inductor design can be found in [12].

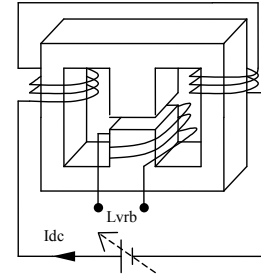


Fig. 6 Current Controlled Inductor.

To dim LEDs, the inductor is integrated with the circuit given in (Fig. 5). Figure 7 shows the magnetically dimmable half bridge current fed LED driver. The current controlled inductor acts as an additional impedance in the secondary of the transformer and functions as ballast.

#### IV. EXPERIMENTAL AND SIMULATION RESULTS

The proposed circuit shown in (Fig. 7) is implemented on 33 LEDs. Resonant frequency is tune to 22 800 Hz and Mosfets are driven by 23 500Hz by IR2153. The circuit has 400 Vdc input and 100 Vdc output. Table I shows the components used in the implementation.

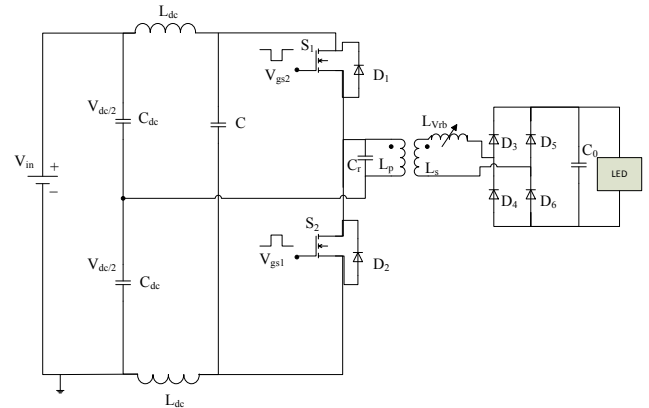


Fig. 7 Proposed LED Driver with dimming function.

Table 1 The List of components.

Item	Font
$L_{dc}$	5mH
$L_p$	730uH
$L_s$	65uH
$C_r$	68nF
33 x1W Power Led	350mA, 100 lumen
$C$	2nF
$C_o$	47uF
$C_{dc}$	100uF
Mosfets	SK2605
$L_{vrb}$	1470uH-175uH

D3,D4,D5,D6	MUR160
$V_{in}$	400V

To meet the desired LED current, the value of inductance of the variable inductor is tuned by the control current. Figure 8 shows the relations between the control current and inductance value. When the inductor value is high, LEDs' current becomes low and vice versa.

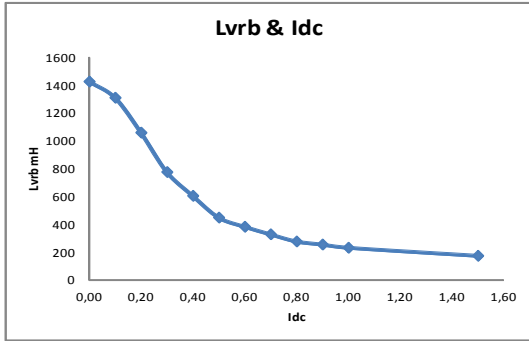


Fig. 8 Inductance Variation with Control Current.

With the proposed technique, lamp current is changed from 215 mA to 350 mA. The waveforms of 215mA and 350mA LED currents and their voltages are illustrated in (Figs 9 and 10) respectively.

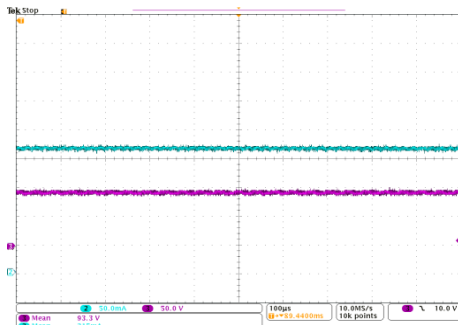


Fig. 9 LED Current and Voltage for Low Power.

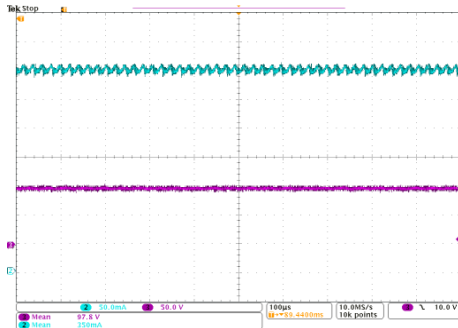


Fig. 10 LED Current and Voltage for Nominal Power.

The control current of the inductor is increased from 0 to 1.6 A. As a result of this, LEDs luminous flux is increased too. Led power versus dc control current is plotted in (Fig. 11).

It can be seen that in the proposed approach, the switching frequency is kept constant and LEDs are not subjected to be on and off in a dimming period.

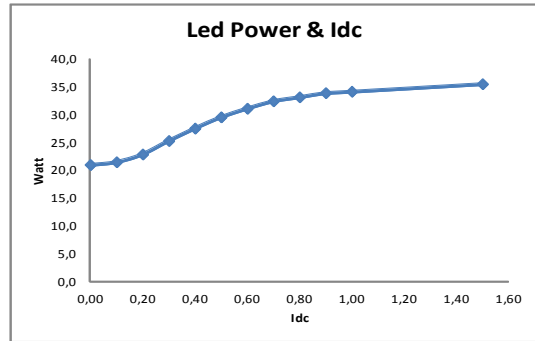


Fig. 11 LEDs Power versus Control Current.

Zero voltage switching is also accomplished with the proposed technique. While the body diode is in forward bias, MOSFET becomes on. As an example, 350 mA led current, drain current and drain source voltage of upper MOSFET are shown in (Fig. 12).

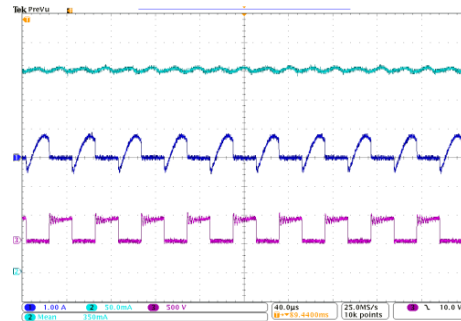


Fig. 12 LED current, Drain Current and Drain Source Voltage of MOSFET.

## V. CONCLUSION

A unique dimmable current fed half bridge led driver is proposed in this study. Dimming is accomplished magnetically to meet desired led luminous flux. The proposed circuit is implemented on 33x1W LEDs. LEDs are driven within 20 W to 33 W. That range may be increased by integrating pulse density modulation technique with the current controlled inductor.

## REFERENCES

- [1] J. Zhang, L. Xu, X. Wu, and Z. Qian, "A precise passive current balancing method for multi-output LED drivers," *IEEE Trans. Power Electron.*, vol. 26, no. 8, pp. 2149–2159, Aug. 2011.
- [2] D. Rand, B. Lehman, and A. Shteynberg, "Issues, models and solutions for TRIAC modulated phase dimming of LED lamps," in *Proc. IEEE Power Electron. Spec. Conf.*, 2007, pp. 1398–1404.
- [3] O. Tetevnoks, I. Galkin and A. Avotins, "Illumination Detection for LED Dimming Process Efficiency Evaluation", *Elektronika ir Elektrotechnika (Electronics and Electrical Engineering)*, vol. 19, no. 1, pp 44-47, 2013.
- [4] I. Galkin, O. Teteryonok and I. Milashevski, "Weight and Size Estimation of Energy Efficient LED Ballast", *Elektronika ir Elektrotechnika (Electronics and Electrical Engineering)*, vol. 120, no. 4, pp. 55-60, 2012.
- [5] Qingcong Hu; Zane, R., "LED Driver Circuit with Series-Input-Connected Converter Cells Operating in Continuous Conduction Mode," *IEEE Transactions on Power Electronics*, vol. 25, no. 3, pp. 574-582, March, 2010.
- [6] Ray-Lee Lin, Yi-Chun Chang, and Chia-Chun Lee, "Optimal Design of LED Array for Single-Loop CCM Buck-Boost LED Driver," *IEEE Transactions on Power Electronics*, vol. 49, no. 2, pp. 761-768, March, 2013.
- [7] Y. Hu and M. M. Jovanovic, "LED Driver With Self-Adaptive Drive Voltage," *IEEE Transactions on Power Electronics*, vol. 23, no. 6, pp. 3116-3124, Nov., 2008.
- [8] Y. Chen, Y. Nan, and Q. Kong, "A Loss-Adaptive Self-Oscillating Buck Converter for LED Driving," *IEEE Trans. Power Electron.*, vol. 27, no. 10, pp. 4321-4328, Oct. 2012
- [9] C.S.Moo, Y.J. Chen, and W.C. Yang, "An Efficient Driver for Dimmable LED Lighting," *IEEE Trans. Power Electron.*, vol. 27, no. 11, pp. 4613-4618, Nov. 2012.
- [10] M. S. Lin, and c.L. Chen, "An LED Driver With Pulse Current Driving Technique," *IEEE Transactions on Power Electronics*, vol. 27, no. 11, pp. 4594-4601, Nov., 2012.
- [11] W. K. Lun, K. H. Loo, S. C. Tan, Y. M. Lai, and C. K. Tse, "Bilevel current driving technique for LEDs," *IEEE Trans. Power Electron.*, vol. 24, no. 12, pp. 2920-2932, Dec. 2009.
- [12] Medini G, Michael G, Sam B.Y., "Inductor-Controlled Current Sourcing Resonant Inverter and Its Application As A High Pressure Discharge Lamp Driver." *Applied Power Electronics Conference and Exposition*, Vol. 1, pp: 434-440, Feb. 1994

**Selim Borekci** was received the M.Sc and Ph.D. degrees in electrical engineering from New Mexico State University, Las Cruces, New Mexico, USA, in 1997 and 2003, respectively.

He was worked as a designed engineer at Howard Ind. Laurel, MS, USA from 2001 to 2004. He worked with Electrical and Electronic Engineering Department of Pamukkale for 6 years. Since 2010, He has been working in Electrical and Electronics Eng. Dept. at Akdeniz Universities, Turkey. Now, he is an Associate Professor at Akdeniz University. His research interest includes the applications of power electronics such as power filters, reactive power control techniques, power supplies, multi-level inverters, electronic ballasts, resonant circuits, and induction heating systems.

**Nihal C. Acar** was received the M.Sc and Ph.D. degrees in electrical engineering from Akdeniz University, Antalya, Turkey. Her research interests are application of power electronics such as LED driver design and induction heating systems.

# Finding the parameters of the compensation pulse with the use of iterative Nelder-Mead method for suppressing residual vibrations of electronic cam

Pavel Dostrašil

**Abstract**—The paper deals with compensation residual spurious vibrations in the rest regions of displacement diagrams of electronic cam mechanisms. Specifically, it is a method of compensation of residual oscillations by superposing the displacement diagram with a harmonic pulse. The method has been previously validated by manually adjusting the pulse parameters. The article describes the automation of the process using the iterative method Nealder-Mead. A dual-mass system was used for testing which cause significant problems in the standard control system of electronic cam. The method was proven on the numerical model and real stand.

**Keywords**—Electronic Cam, Nealder-Mead, Residual Vibration, Displacement Diagram.

## I. INTRODUCTION

Electronic cams have been significantly enforced only in the last several years. Rotary motion rockers of classical cam replace a rotary movement of the servomotor shaft. An integral part of this system is of course the controller, which in its memory (in the form of data) stores a desired shape of displacement diagram (0<sup>th</sup>, 1<sup>st</sup> and 2<sup>nd</sup> derivative) and is able to convert it to the appropriate electrical signals to a servomotor. This concept is the base of so-called flexible automation, for which a quick and cheap change is crucial in physical function according to current requirements. It can be utilized, especially in small batch production, which increases the modularity of production machines.

Electronic cams have many unique properties thanks to electronic drive control actuators. This is combined with programming options of the PLC to control the position and the dynamics of motion functions. A very important feature of this servomotors control system in the mode of an electronic cam is a compensation of spurious residual vibration in the rest areas of displacement diagrams. Conventional cam mechanisms in this regard are very limited.

This work was supported by Czech Ministry of Industry and Trade under Project FR-TI1/594 (Investigation of sophisticated methods for the design and development of single-purpose machines, components and peripheries of processing machines).

Pavel Dostrašil is with the Department of Mechatronic, VÚTS Liberec, a.s., Liberec, Czech Republic (phone: +420 485 302 701, e-mail: pavel.dostrasil@vuts.cz).

Particular methods are most commonly divided into two groups. The first group are the so-called feedback methods using immediate knowledge of output (or state) variables of the system. These methods are usually more difficult to implement and require intensive interventions to standard PLC regulatory structures. In extreme cases are made entirely outside the PLC in special digital signal processors. The second group are the methods that act in the direct way of the control loop, so-called the feedforward control. Their practical implementation is quite difficult even in sophisticated PLC. Typical representatives are methods using inverse dynamics and methods using a signal shaper, or "Input shaping". Work [1] deals in detail with implementation and problems that are associated with it. Work [2] deal in detail with analysis and comparison of methods using the shaping of the input signal.

Besides the above mentioned methods, there are others that are not so easily classified. For example, the method of wave-based control [3] or the method of compensation residual vibration superposition of displacement diagram to the harmonic pulse. The second method was first mentioned in [4] and subsequently extended in [5] and [6]. The main condition for the proper function of the algorithm is to find the correct parameters of the compensation pulse. This can be achieved by a numerical calculation on the exact model of the controlled system or through manual adjustment on the real system. It is very difficult to obtain an exact model of a real system in practice. Supervision of a qualified operator can be expensive. The logical consequence was to automate this process. The following paragraphs deal with the selection, implementation and testing of the iterative algorithm for the automatic finding of suitable parameters of the compensation pulse.

## II. ELECTRONIC CAM

The electronic cam mechanism can be viewed in terms of kinematics, similarly to a conventional cam mechanism. The rotary motion of the rocker is replaced by a rotary movement of the servomotor shaft. This paper focuses on electronic cam systems produced by the Japanese company Yaskawa. It is a servomotor SGMGV 30D (2.9 kW), servopack SGDA-A3-AE.

The low voltage section includes a controller MP2300 with a communication module LIO-02, providing processing data from the external encoder.

The electronic cam is used on an experimental physical model, which is equipped with a gearbox with reduced backlash Spinea TS 170-33-P24, flexible shaft (stiffness 859.7 N·m/rad, damping 0.235 N·m·s/rad), flywheel (moment of inertia 0,103 kg·m<sup>2</sup>) and an external encoder as shown in Fig. 1.

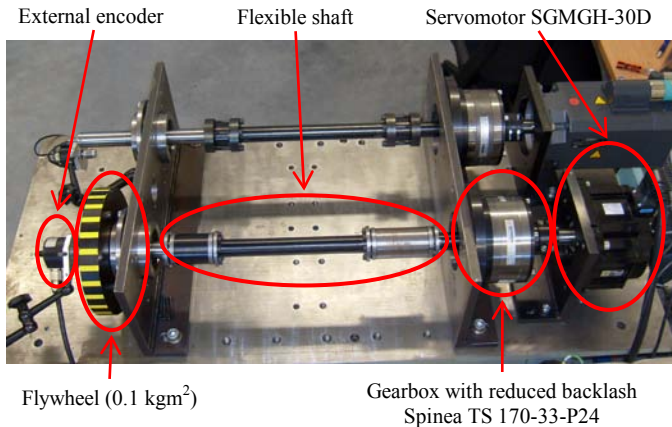


Fig. 1 – The physical model of electronic cam

Electronic cam Yaskawa, as well as the most similar drives from other manufacturers, uses cascading control circuit [7] Fig. 2. There are three hierarchically arranged feedback: current, speed and position. Proper function is provided by two PI controllers for current and speed loop and a P controller for position loop. To increase the position accuracy a controller is equipped with two feedforwards.

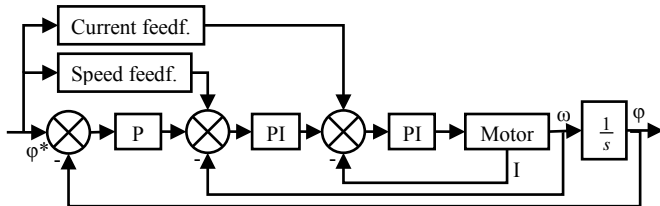


Fig. 2 – Cascade control structure, including speed feedforward and current feedforward

Although this controller design provides high robustness, a dual-mass system oscillating at a relatively low frequency, this is a significant problem. The physical model is designed similarly to a real system and the controller has only information about the position of the motor shaft from the internal encoder. External encoder on the load is used only for the purpose of measuring and evaluating the quality of regulation.

### III. COMPENSATION METHOD

Currently there are many different methods to suppress residual vibrations of electronic cams. Logically, it follows that all algorithms must work fundamentally the same. Either manipulated variable is adjusted that the controlled system does not oscillate, or it actively responds to oscillation and

adjust manipulated variable to suppress them. The paper deals with a compensation algorithm of residual oscillations by superposing the displacement diagram with harmonic pulse. The algorithm excels with the minimum requirements for the control circuit.

The principle of the algorithm is illustrated in Fig. 3. Displacement has a length of 180° and is based on a parabolic displacement diagram (shape was chosen for better understanding, leap in second derivative may cause problems in practice and therefore are normally used displacement diagrams based on higher order polynomials or other functions without discontinuities in the second derivative). In the point of virtual master rotation 120° is displacement diagram superposed with a harmonic pulse, which suppresses all oscillations incurred on the load. Thus ensuring almost complete suppression of the oscillation in rest of the displacement diagram as illustrated in Fig. 4. From another point of view, we can actually say that the compensation pulse itself at the end of the working displacement diagram excite oscillations of the same amplitude as the original displacement diagram, only the phase-shifted so that both oscillations cancel each other completely. The method focuses exclusively on the suppression of oscillations at the end of the displacement, the beginning of the rest part displacement diagram. This area is the most important in practice, because the technological process is usually carried out here.

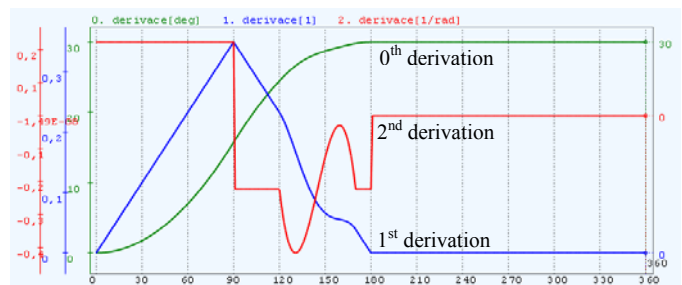


Fig. 3 - Example of creating modified displacement diagram

Although the amplitude of the compensation pulse is usually much smaller it needs to modify the original displacement diagram so as not to change the overall displacement. It results in a slight deformation of the shape of the displacement diagram. However, this slight deformation in the working part of the displacement diagram is irrelevant in practice.

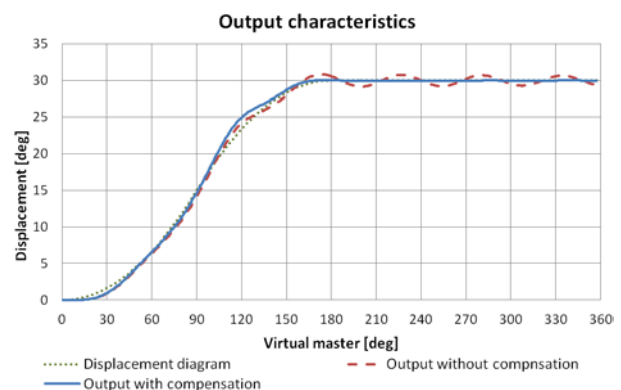


Fig. 4 - Output characteristics measured on a physical model

IV. AUTOMATIC SEARCH THE PARAMETERS OF THE COMPENSATION PULSE USING THE METHOD NEALDER-MEAD

The compensation pulse is essentially only a scaled unit displacement diagram placed in the correct position. This type of function is selected at first. In all the graphs in this article the 5<sup>th</sup> degree polynomial function is used. Other functions have been tested such as parabola or cycloidal function, but in general they achieve similar results. For a precise definition of the pulse it requires only three parameters: length, amplitude and position as illustrated in Fig. 5. The length and position are given in degrees relative to the rotation of the virtual master.

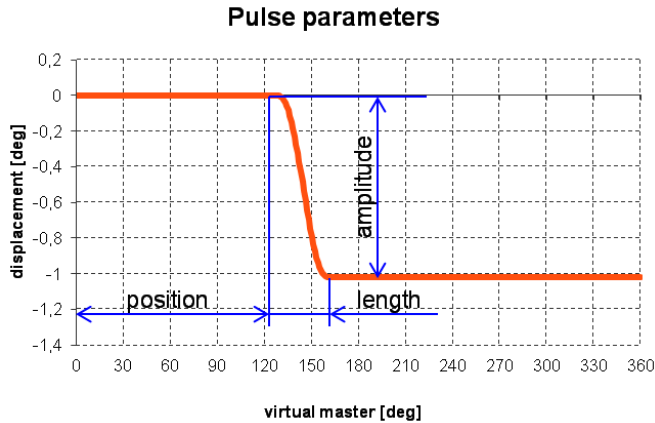


Fig. 5 – Pulse parameters

If we consider the connection of the flywheel through an elastic shaft, which can be replaced as elasticity and damping (where each real system contains the element with nonzero damping) we can assume that each pulse of any length excites an oscillation. Of course, there are limits. Too short pulse requires high acceleration that can exceed the possibilities of the servomotor. Too long pulses requires high amplitude, and it could cause excessive deformation of the original displacement diagram. A good starting point is the natural frequency of load, the rough estimate is usually not a problem to obtain by a simplified model or measurement.

It remains to determine the position and amplitude of the pulse. For their exact calculation it is necessary to know the precise model of the controlled system. The following Fig. 6 shows the size distribution of the residual oscillations depending on the position and size of the pulse at a constant length of 35°. It is obvious that there are more minimums, positive and negative polarity pulses. Their mutual distance is determined by the natural frequency of the controlled system. The graph also shows a slight shift of the minimums to horizontal axis with an increasing pulse position. This phenomenon is dependent on the size of damping of the flexible shaft so that is increasing with the damping. The earlier pulse is located, the larger amplitude has to be to generated desired size oscillation on the end of the working part of displacement.

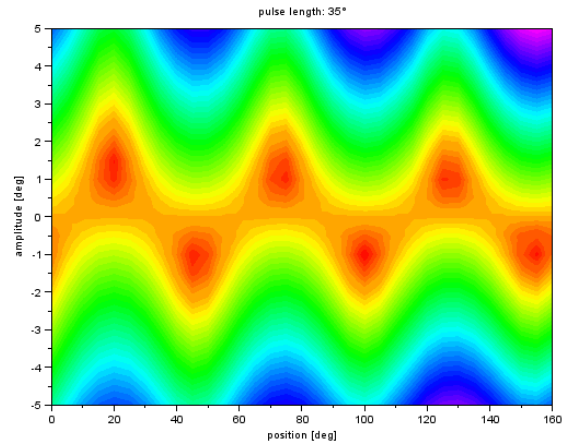


Fig. 6 – The influence of the pulse position and amplitude to the size of residual oscillations

Data in the previous figure was obtained from a numerical model of the system. But the model is usually not available in practice, so the algorithm uses a different approach. The algorithm created in the first step an estimate of the position and amplitude, which improves the subsequent steps based on the information about quality control. It is not a classical feedback that requires precise knowledge of the output position in real time. It can be an indirect measurement, with considerable delay. This process of adjustment is relatively easy for an experienced technician. However, the goal was to achieve a fully automated process, without human intervention. A data flow diagram of the algorithm cooperating with physical model is shown in Fig. 7.

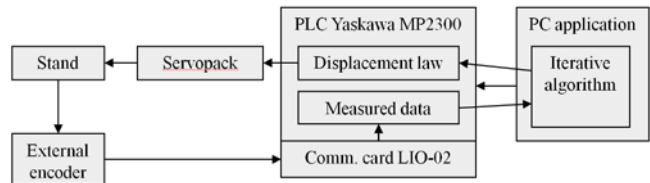


Fig. 7 – Data flow diagram of the test stand

First there was a tested bisection method and its modifications (particularly for one and then for the second axis). This way of finding a minimum was very sensitive to the initial conditions. Also, it was adversely affected by the measurement errors. In a practical use on a test stand, this iterative method became unusable, so it was decided to test the sophisticated iterative method Nealder-Mead [8].

This method is one of the comparative methods. It searches for the minimum of the cost function comparing their values in specific selected points in  $R^n$  and does not require knowledge of their derivation. The method is generally n-dimensional, but in this case it is used a two-dimensional variation. The first step is the selection of the initial simplex (points L, S and H), where H (high) represents the worst point and L (Low), the best point. The following steps of iterative algorithm are trying to replace the point with the highest value of cost function H with better. It uses several different transformations. In this

case, is used four basic transformations mentioned in Fig. 8. Detailed descriptions of the algorithm can be found in [8].

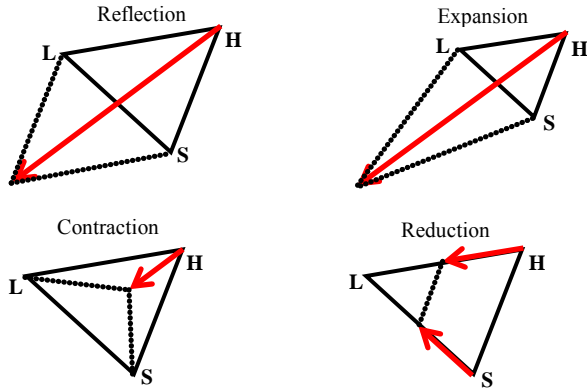


Fig. 8 – Transformation of simplex

V. THE MEASUREMENT OF THE ITERATION PROCESS

The next few graphs demonstrate the iteration process in the search for the compensating pulse. The original displacement diagram is based on a 5<sup>th</sup> order polynomial function this time. As you can see in the Fig. 9 displacement was 20° and length of the working part of the displacement diagram was 120°. Virtual master speed was set to 130 min<sup>-1</sup>.

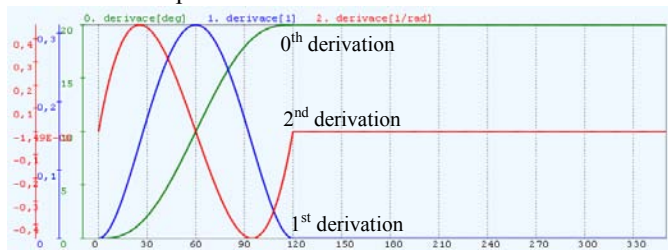


Fig. 9 – 1<sup>st</sup> measurement – original displacement diagram

Fig. 10 already demonstrate the displacement diagram at the end of the iteration process after the superposition with the compensation pulse. In this case the pulse is positive, it is located approximately in the middle of the working part of the displacement diagram. It causes only very small changes in the critical values of the acceleration that is important for the design of the drive.

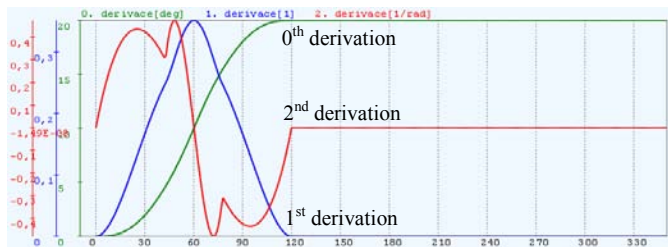


Fig. 10 – 1<sup>st</sup> measurement – modified displacement diagram

The following Fig. 11 shows several specific measurements of the rest part of displacement diagram during the iterative process compared with measurements without any compensation pulse.

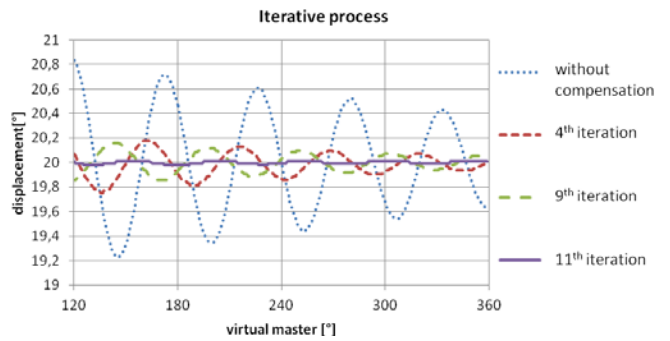


Fig. 11 – 1<sup>st</sup> measurement - selected curves of the iterative process in the rest part of displacement diagram

The second measurement is based on the same displacement diagram and the same speed of virtual master axis, but the initial simplex of the iterative process is located elsewhere. Fig. 12 shows that iterative process finished with a different result than in Fig. 10. In this case pulse is in negative and is located in the second half of the working part of the displacement diagram. This will lead to a more significant shift of the maximum negative acceleration values compared to the first measurement.

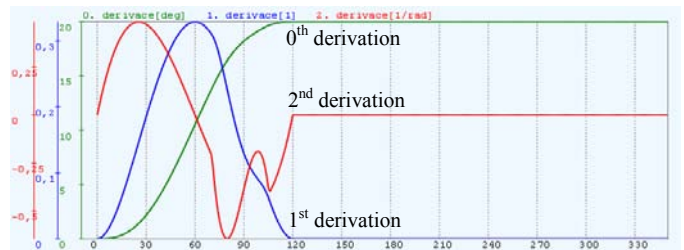


Fig. 12 – 2<sup>nd</sup> measurement – modified displacement diagram

Fig. 13 shows selected curves of the iterative process and compared them with the first measurement in Fig. 11, there is obviously a different behavior. For example 4<sup>th</sup> iteration brings only minimal improvement and 8<sup>th</sup> iteration causes a very good damping of vibrations. The convergence process of the first measurement was entirely different.

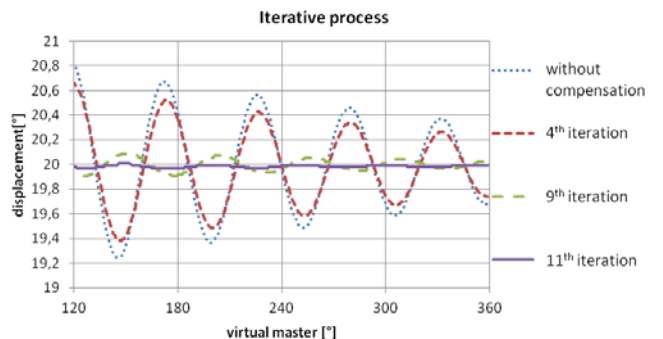


Fig. 13 – 2<sup>nd</sup> measurement - selected curves of the iterative process in the rest part of displacement diagram

The iterative process is based on the transformation of the initial simplex in the best possible shape. Simplex is formed by three points H, S and L, where H is the point with the highest error S with a mean error and L with the least error. The following two figures focus on comparing of iterative

processes in the first and second measurements. Fig. 14 and Fig. 15 compares the process of minimizing errors simplexes for all points.

A different speed is clearly seen of the convergence in different parts of the iterative process. It is important that in both cases demonstrated iterative process reach the state with very low oscillations after about 15 steps. Further iterations are not important, because of big measurement errors. Similar results were also observed in other measurements, but there is not enough space for their publication.

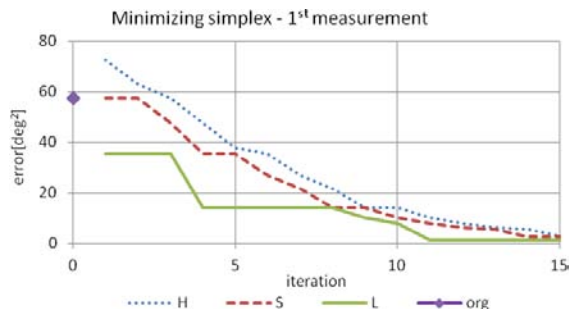


Fig. 14 – Minimizing simplex errors during iteration process for the 1<sup>st</sup> measurement

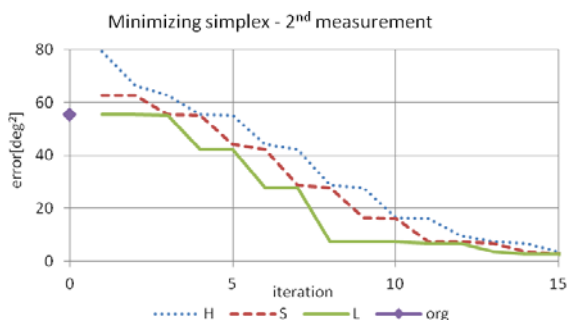


Fig. 15 – Minimizing simplex errors during iteration process for the 2<sup>nd</sup> measurement

During simplex minimizing, there are the adjusting of two parameters of the pulse (position and amplitude) and it is therefore possible draw the process into graph as shown in Fig. 16 (only the motion of point L is showing, because the points are replaced with each other and when plotting all points of the simplex image became confusing). Both initial simplexes have a same shape and size and differ only by shifting the position of the pulse.

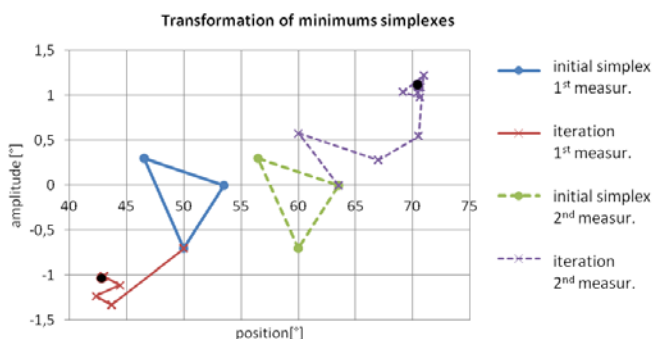


Fig. 16 – Transformation of minimums simplexes for 1<sup>st</sup> and 2<sup>nd</sup> measurements

## VI. CONCLUSION

The method of compensation of residual oscillations by superposing the displacement diagram with harmonic pulse does not try to replace existing methods, it only fills the empty space between the other methods. Extending its implementation for automatic adjustment further improves its position, thus reducing the requirements for qualification of operators and thus reduces costs.

Tens of testing adjustments have been carried out and most of them achieves similar results. Problems occur only with very poorly chosen initial simplexes. Iterative method Nealder-Mead is characterized by a relatively fast and reliable convergence to the minimum value unlike other simple methods. Its implementation is not too complicated, so it can be implemented as a subroutine directly into the PLC control program. This subroutine can be easily triggered by operators at any time or it can be triggered automatically when the quality of regulation is deteriorated.

Further extensions of this method could result in a modification length of the compensation pulse during an iteration process and expanding the criteria of minimizing the total acceleration of the servomotor.

## REFERENCES

- [1] LINDR, David. *Control of Servodrives in Dynamic-Intensive Application*. Liberec, 2011. 141 p. Dissertation. Technical University of Liberec, Faculty of Mechatronics, Informatics and Interdisciplinary Studies, The Institute of Mechatronics and Computer Engineering. Thesis supervisor Pavel Rydlo.
- [2] BENEŠ, Petr. *Input Shaping Control with Generalised Conditionst*. Praha, 2012. 105 p. Dissertation. Czech Technical University in Prague, Faculty of Mechanical Engineering, Department of Mechanics, Biomechanics and Mechatronics. Thesis supervisor Michael Valásek.
- [3] MAREK, Ondřej. *Servo Control Using Wave-Based Method*. In: *Advances in Mechanisms Design: Proceedings of TMM 2012*. Netherlands: Springer, 2012, pp. 531-536. Volume 8. ISBN 978-94-007-5124-8/ISSN 2211-0984. DOI: 10.1007/978-94-007-5125-5\_70. Available: [http://link.springer.com/content/pdf/10.1007%2F978-94-007-5125-5\\_70.pdf](http://link.springer.com/content/pdf/10.1007%2F978-94-007-5125-5_70.pdf)
- [4] JIRÁSKO, Petr. *Methodology of electronic cam applications in drives of working links of mechanisms of processing machines*. Liberec, 2010. 207 p. Dissertation. Technical University of Liberec, Faculty of Mechatronics and Interdisciplinary Studies.
- [5] VÁCLAVÍK, Miroslav, Pavel DOSTRAŠIL a Petr JIRÁSKO. A methodology to suppress the residual vibrations of excited compliant systems. In: *Proceedings of the 11th International Conference on Vibration Problems (ICOVP-2013)*. Lisbon, Portugal: APMTAC, 2013. ISBN 978-989-96264-4-7.
- [6] VÁCLAVÍK, Miroslav, Pavel DOSTRAŠIL a Petr JIRÁSKO. The Issues of Spurious Residual Oscillations in the Displacement Laws of Cam Systems. In: *New Advances in Mechanisms, Transmissions and Applications: Proceedings of the Second Conference MeTrApp 2013*. Springer Netherlands, 2013, pp. 99-106. ISBN 978-94-007-7485-8/ISSN 2211-0984. DOI: 10.1007/978-94-007-7485-8\_13. Available: [http://link.springer.com/chapter/10.1007%2F978-94-007-7485-8\\_13](http://link.springer.com/chapter/10.1007%2F978-94-007-7485-8_13)
- [7] SOUČEK, Pavel. *Servomechanismy ve výrobních strojích*. 1st ed. Praha: Vydavatelství ČVUT, 2004, 210 p. ISBN 80-010-2902-6.
- [8] ČERMÁK, Libor a Rudolf HLAVIČKA. *Numerické metody*. 2nd ed. Brno: Akademické nakladatelství CERM, 2008, 110 p. ISBN 978-80-214-3752-4.

# Force sensing of teleoperated robotized cell injection

Kostadin G. Kostadinov, Vladimir K. Kotev and Daniel M. Penchev

**Abstract**—This paper describes cell injection process and mechanical deformation over the cell contour. The main purpose is to be developed an algorithm that determines the value and direction of operator force interaction on the cell. This force information is calculated using the visual deformation of the cell contour. After evaluation of the force vector it is feed back to the operator through human-machine interface tool with force feedback unit. Several subtasks for this process are described and short presentations of the used environments are given in the paper.

**Keywords**—cell injection, force interaction, micro robot.

## I. INTRODUCTION

THE ability to inject various organic and inorganic substances at the cellular level allows scientists in biology and biochemistry to study the reactions and changes that occur. Work issues in the micro and nano world are largely related to the fact that the operator has no sense and complete control over the studied objects and thus realistic sense of environment should be simulated virtually.

The purpose of this article is to develop an approach for force sensing of human operator at tele operated robotic cell injection based on the method to determine the reaction forces of the object of study - the cell at external manipulation on it. By visually monitoring the deformation of the shape of the cell while its injection by a pipette and using a theoretical model for determining the elasticity of the cell membrane to determine the force with which the cell membrane react to the tool. Magnitude of this force and its direction are used to form a force feedback to the operator. Thus, the operator would receive a sense of force with which the investigated object has been affected. This will facilitate his ability to control the injection process .

Another objective of this work is to synthesize an approach and algorithm for separating the object from the generated image of the microscope and isolate any noise environment. Must be individual cells - the subject of research of the tools by which research is carried out.

This work was supported by the project AComIn - *Advanced Computing for Innovation*, Grant 316087, funded by the FP7 Capacity Program (Research Potential of Convergence Regions initials).

K. G. Kostadinov is with the Institute of Mechanics – BAS, Sofia, Bulgaria; Bulgaria (phone: +359-2-979-27-23; Sofia, Bulgaria e-mail: kostadinov@imbm.bas.bg).

Vl. K. Kotev was with the Institute of Mechanics – BAS, Sofia, Bulgaria. He is now with the Institute of Information and Communication Technologies (IICT) - BAS, Sofia, Bulgaria; e-mail: kotev@imbm.bas.bg).

D. M. Penchev is with the Institute of Mechanics – BAS, Sofia, Bulgaria; Bulgaria (e-mail: daniel.penchev@ gmail.com).

## II. MODEL OF THE INJECTION PROCESS OF A CELL

To achieve the objective the study of the cells and their chemical interaction with the injected therein organic or synthetic materials need to be carried out, and mechanical action on them. Such attachments are of micro and nano research object on the work staging is injected with a glass pipette, and the like . In this article we will discuss the process of injection. It is associated with disruption of the cell membrane and the positioning of the needle inside the cell . The piercing of the membrane of the cell is a mechanical process , and is coupled with the mechanical rupture of the wall . For this purpose you should take into account the forces acting on the cell at the time of breaking deformation that causes the pressure of the instrument .

Let us consider the setting for the study and manipulation of objects in the micro and nano world. In general, the scene consists of the object you are studying two instruments pipettes and devices interface between the operator and the nanoworld - microscope and manipulator functionality feedback forces . One dropper is used to position the cell in the field of operation while manipulating it. The other pipette is used for injection. These components determine the type of deformation at the time of injection . Also to be taken into account when determining the forces of interaction and intracellular forces.

Figure 1 is a schematic model of the forces of reaction during the injection process. Of course the composition of the cell is not uniform, as well as a surface coating is not uniform and Compression cannot be uniform. To examine non-uniform deformation of the cell surface, the cell is represented as a two-dimensional model in three-dimensional environment and is examined in deformation 2-D surface. [1] OZ is a symmetry axis of the cell. CL denotes a length of the entire 2-D surface of the cell.

Ca strain curve is described by the following formula:

$$\mathcal{F}_{ca} = 2\pi k_c \int_0^L \frac{1}{2} \left( \frac{d\varphi}{ds} + \frac{\sin \varphi}{r} + c_0 \right)^2 r ds + 2\pi k_G \int_0^L \frac{d\varphi}{ds} \sin \varphi ds$$

With note S the arc length of the surface of the cell at any point. T is the angle of deflection, i.e., at a point tangent to the contour of the deformed cell axis o OR. The objective is to determine the magnitude and direction of the force FI, which is to return such information to the operator. Magnitude of FI have to determine visually examine deformation of the surface of the object.

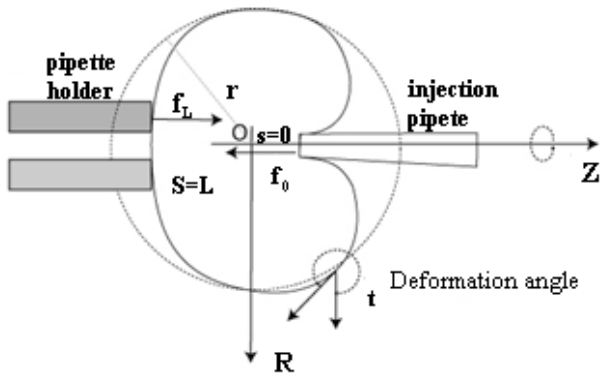


Fig. 1. Deflection of the cell membrane in injecting it with a glass pipette.

### III. ALGORITHM FOR VISUAL SEPARATION OF THE OBJECT FROM THE ENVIRONMENT

Before we can conduct research on the visual deformation of the surface of the object must be given useful information is not useful . For useful information not consider that which does not belong to the object's surface - ie Contour . These are any additional dust or others who are affected by fields of research. We also need to separate the two pipettes - research tools, because visual information from us is necessary for the evaluation of the deformation of the object.

To start with we will look at the process of isolating the instruments - dropper . This is an easy task, because their shape is well known and does not change. For detection and isolation of the instruments we use algorithm patterned line (pattern matching algorithm).

The first step of the algorithm (Fig. 2. ) Is to define a rectangle that most accurately describes the tools . We start with the eyedropper, which holds the object field of research because its position is determined. Having defined the template begin to move around the stage , as every step we determine the extent of differences between the template and the current station.

$$R(x,y) = \frac{\sum_{x',y'} [T(x',y') - I(x+x',y+y')]^2}{\sqrt{[\sum_{x',y'} T(x',y')^2 \cdot \sum_{x',y'} I(x+x',y+y')^2]}}$$

I, T and R are respectively studied part of the scene , the pattern and outcome . The minimum of this function determines the best match between the template and the study of the scene and it means that we have found the sought object - ie eyedropper holder . here:

$$\begin{aligned} 0 \leq x' \leq w - 1, \\ 0 \leq y' \leq h - 1, \end{aligned}$$

As the color sample holder is always one half of the test formulation, may be optimized by the process:

$$\begin{aligned} 0 \leq x \leq (w - 1)/2, \\ 0 \leq y \leq h - 1. \end{aligned}$$

W and h are respectively the width and height of the stage. When we find a matching rectangular pattern defined by the pipette, filling, surrounded by him of the scene in color. So remove the pipette from the scene.

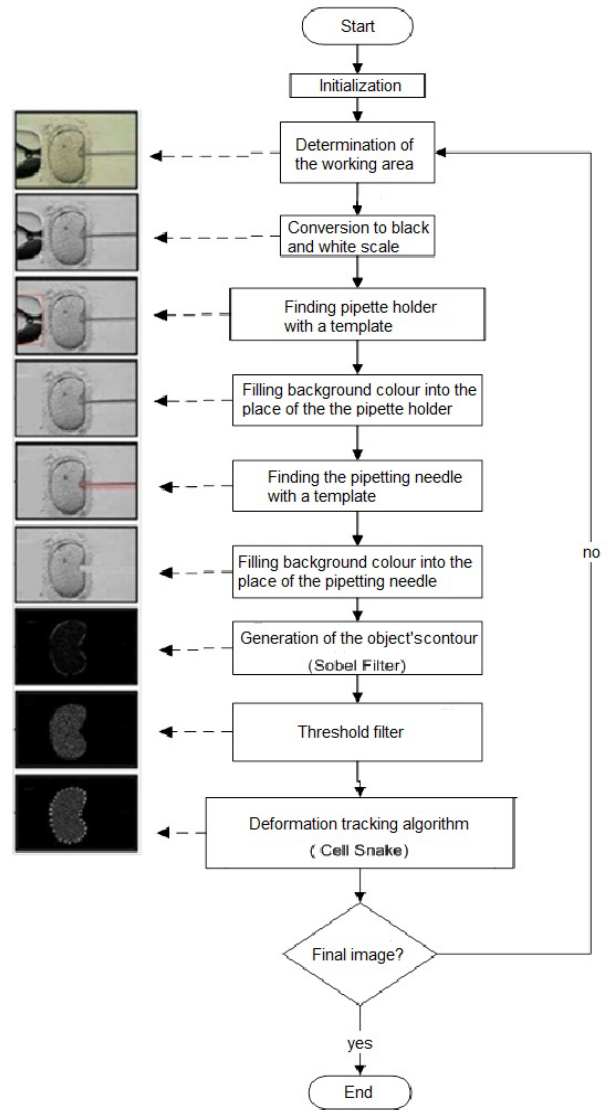


Fig . 2 Algorithm for visual separation of the object from the environment.

By the same algorithm and remove the image of the injection pipette lights . This difference is admissible set the width of the scene:

$$\begin{aligned} w_{holding-pipette} \leq x \leq w - 1, \\ 0 \leq y \leq h - 1. \end{aligned}$$

The next step is to separate the elements of the scene that are not the subject of study and pollutants play. Such are the dust particles from the environment or supporting cell micro and nano particles and noise of the picture microscope caused by compression of the image and the loss of quality associated with it . Use sobelova filtration (Sobel Filter) [2] . The method is characterized in that the contour is emphasized in the image of the objects are cleaned and those parts which are of too small a difference in the relative values of the function of the intensity of the image.

For administration of sobel filter used and a plurality of thresholds, the function describing the intensity of the image. For each point of the picture apply:

$$dst(x,y) = \begin{cases} \max - value & \text{if } src(x,y) > threshold \\ 0 & \text{if } src(x,y) \leq threshold \end{cases}$$

Where thresholds are predefined thresholds. Thus part of the image that have small relative differences will unify and merge with the background. Thus there is a clear outline of the study site. Deformation of this loop is the purpose of our research and study.

#### IV. ALGORITHM TO ACCOUNT FOR THE DEFORMATION OF THE CELL AFTER EXTERNAL INFLUENCE ON IT.

After we isolated the object of the study - the cell is to be applied the algorithm to track the deformation upon injection . There are many methods razllini video tracking deformations , but we use the so-called . Cell Snake algorithm. The idea of this algorithm is dynamically generated curve that describes the edges of the research object, while its influence on the walls , ie change the energy balance. Therefore, the task for the description of the deformation of the cell walls is reduced to the task of minimizing the energy of the surface of the object [2] .

The curve of the contour of the cell wall can be described by the following formula :

$$v(s,t) = (x(s,t), y(s,t)); s \in \Omega, t \in T$$

Where s and t are respectively the spatial and temporal parameters.

The full power of the cell surface during the pressure of the needle comprises the internal and external energies. The internal energy is in turn composed of the elastic energy and the strain energy . So we get the formula:

$$E_{total} = E_{elastic} + E_{deformation} + E_{external}$$

Elastic energy and deformation are internal energies of the contour of the object and do not depend on the generated image. To generate smoother distortion deformation must find the minimum of their functions :

$$E_{elastic} = \frac{1}{2} \int_{\Omega} \alpha(s) |v_s|^2 ds$$

$$E_{deformation} = \frac{1}{2} \int_{\Omega} \beta(s) |v_{ss}|^2 ds$$

Where  $v_s = \frac{dv_x}{ds}$  and  $v_{ss} = \frac{d^2v_x}{ds^2}$  .

Climate Energy and the cause of the deformation of the contour , the result of the action of external force . To describe how to realize this , we present the resulting deformed image as a result of the original image and described by the formula:

$$E_{external} = -Y|VI|^2$$

Where VI describe the original image. Thus, the image represented by the relative variations of intensity (gradient image) has the highest intensity values of the boundary contour of the object.

The discrete form of Cell Snake contour can be represented as a vector of n elements u [3]. These points of the contour can be described by the formula:

$$v_{(ih)} = (x_{(ih)}, y_{(ih)}), \text{ where } i=0..n \text{ and } h=1/n-1.$$

So discrete formulas for the energies can be represented in the form:

$$E_{elastic}(i) = \frac{1}{2} \alpha(i) \left| \frac{u_i - u_{i-1}}{h} \right|^2$$

$$E_{deformation}(i) = \frac{1}{2} \beta(i) \left| \frac{u_{i-1} - 2u_i + u_{i+1}}{h^2} \right|^2$$

$$E_{external}(i) = -\gamma |VI(u_i)|^2$$

In the formulas above  $u_i = (x_i, y_i)$  describes the position of the node i in the digitized contour.

#### V. PATTERNS AND CHARACTERISTICS OF TOOLS FOR THE MANIPULATION OF OBJECTS AND THEIR VISUAL REPRESENTATION

Many scientific and applied problems in micro and nano technology, [4], [5] using force sensors in the range  $\mu N / nN$ . Such sensors need to be integrated in the executive arm of the robot in the field in which you run the operations, [6]. The reaction forces of the cell membrane is in the range of 1-30  $\mu N$ . On Fig.3 is shown power sensor [7] developed to respond to the forces of less than 1  $\mu N$ , in order to provide a power management system processor nN resolution .

One of the important parameters of the MEMS sensor is developed to establish the maximum limit of sensitivity. It is the magnitude of the force to which the sensor is broken. Developed optical system [8] help to determine the breaking point of the sensor tip. With incremental load on top, which is attached to a static console , recognize its deformation . Find that point his strength is offset between 160  $\mu m$  and 164  $\mu m$  ( Fig. 4) . This means that from the point of view of safety the operating threshold of the sensor should be at an offset of about 140  $\mu m$ .

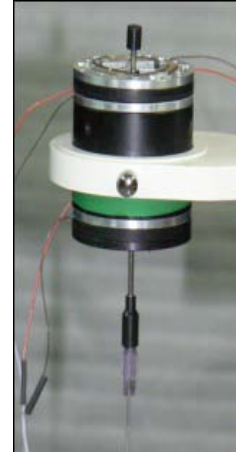
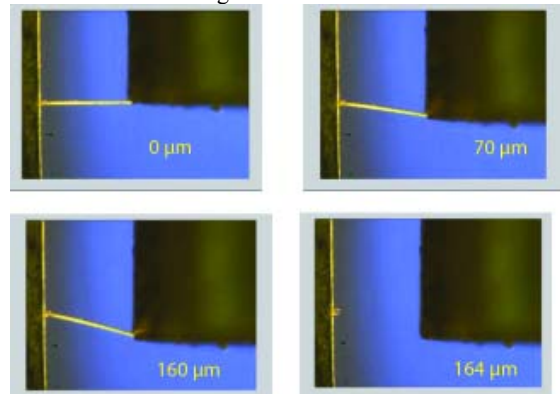


Fig.3 Force sensor



Фиг. 4 The breaking point

The next important step is the calibration of the actuator , which will drive the robot. For this purpose, we assign a capacitance already calibrated power sensor (Femtotools GmbH) to the top of the piezo actuator . In increments of 1  $\mu\text{m}$  tip strain sensor and the power of parallel reporting shift Fig. 5 Find that the difference is about 50  $\mu\text{m}$ , it is distributed linearly. Output voltages  $U_c$  and  $U_m$  of capacity and power MEMS sensors are distributed as shown in the following figure 6:

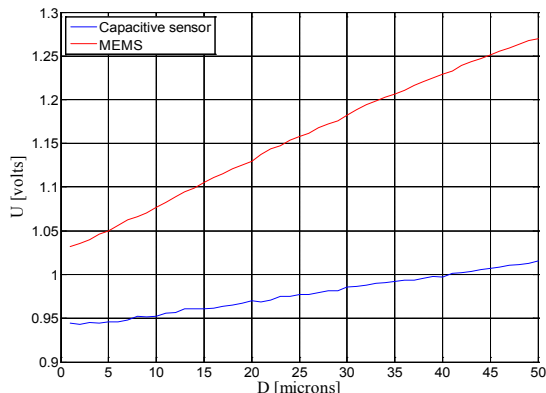


Fig.5. Capacitive sensor and MEMS

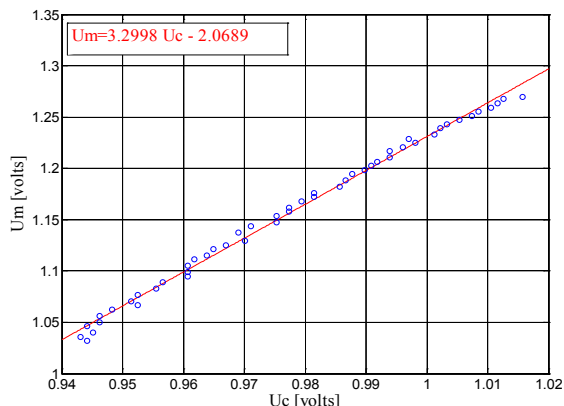


Fig. 6 Output voltages  $U_c$  and  $U_m$

Capacitive sensor has found respect 414.4  $\mu\text{m}/\text{V}$ , which is predetermined in its construction . Therefore , the developed power sensor [4] has been calibrated , e ustanoveno that corresponds to one volt 125.8  $\mu\text{N}$ .

So its established parameters are:

- Sensitivity 2.32 mV /  $\mu\text{m}\cdot\text{V}$ ;
- Offset 10 nm;
- 215.18  $\mu\text{m} / \text{V}$  power factor.

The largest force that can be read with the developed sensor is about 82 mN.

## VI. CONCLUSION

The result of the experimental design is a vector of force that is used to deliver feedback to the device for interaction between man and machine - a joystick. This vector must be able to be a signal that generates the appropriate resistance management joystick, so to recreate the most realistic feel to the operator.

The magnitude of this vector should be sufficiently large to allow the pipette to penetrate through the cell membrane. It must also be sufficiently measured to not break the integrity of the research object.

The proposed approach for force sensing can be used except for the injection of cells, but also to determine turgor of cells for various applications.

## REFERENCES

- [1] Vassil M. Vassilev, Kostadin G. Kostadinov, Ivañlo M. Mladenov, Assen A. Shulev, Georgi I. Stoilov and Peter A. Djondjorov, “Cell Membranes Under Hydrostatic Pressure Subjected to Micro-Injection”, 2011, American Institute of Physics, pp.234-240.
- [2] Fatemeh Karimirad, Bijan Shirinzadeh, Umesh Bhagat, Yongmin Zhong, Sergej Fatikow and Julian Smith, “CellSnake: A Vision-based Methodology to Dynamically Track Cell Deformation during Cell Micromanipulation”
- [3] Tan You Hua, “Cell Mechanical Modeling and Mechanical Properties Characterization”
- [4] T. Miteva., D. Karastoyanov., Full surface tracking by mobile robots., International Conference “Bionics and Prosthetics, Biomechanics, Mechatronics and Robotics” (ICBBM 2012), June 4-8 2012, Varna, Bulgaria, pp 74-77
- [5] Karastoyanov D., Control of Robots and other Mechatronic Systems, Academy Publ. House “Prof. Marin Drinov”, Sofia, 2010, ISBN-10: 987-954-322-415-9
- [6] Karastoyanov D., Energy Efficient Control of Linear Micro Drives for Braille Screen., International Conference on Human and Computer Engineering ICHCE 2013, October 14-15 2013, Osaka, Japan, pISSN 2010-376x, eISSN 2010-3778, pp 860-864
- [7] K. Kostadinov, Robot Technology in Hybrid Assembly Approach for Precise Manufacturing of Microproducts, Proceedings of the 12<sup>th</sup> Mechatronics Forum Biennial International Conference June 28-30, 2010, Swiss Federal Institute of Technology, ETH Zurich, Switzerland, Book 1, pp. 293-300.
- [8] Assen Shulev, Kostadin Kostadinov, Tihomir Tiankov, and Ilia Roussev, Optical Positioning Control of a 3D Micromanipulator, Proc. of 3M-NANO International Conference on Manipulation, Manufacturing and Measurement on the Nanoscale, Changchun, China, 29.08-02.09.2011.

**Kostadin G. Kostadinov** is a member of the Bulgarian Scientists Association. He was born in Kazanlik, Bulgaria in 1957. He has a master degree in Electrical engineering. He graduated Technical University Sofia in 1983. The author received a doctoral degree in 1994, Applied Mechanics from the Institute of mechanics at the Bulgarian Academy of Sciences (BAS). Dr. Kostadinov is a professor in Institute of Mechanics and Head of GIS Transfer Centre. He is conducting research on design, dynamics and intelligent control of robots and mechatronic systems. His professional interests refer to mechanics and biomechanics, industrial engineering and robotics.

**Vladimir K. Kotev** is a member of the Bulgarian Scientists Association. He was born in Sliven, Bulgaria in 1976. He has a master degree in Mechanical engineering. He graduated Technical University Sofia in 2002. The author received a doctoral degree in 2008, Biomechanics from the Institute of mechanics at the Bulgarian Academy of Sciences (BAS). He is an assistant professor in Institute of Mechanics. Dr. Kotev is a postdoctoral fellow under AcomIn project at the IICT – BAS. He is conducting research on design, dynamics and intelligent control of robots and mechatronic systems. His professional interests refer to mechanics and biomechanics, industrial engineering and robotics.

**Daniel M. Penchev** is a doctor student in Institute of Mechanics (BAS). He is conducting research on design, dynamics and intelligent control of robots and mechatronic systems. His professional interests refer to mechanics and biomechanics, software for micro robots.

# Simulation of robot workcell operation by augmented reality technology application

Jozef Novak-Marcincin, Miroslav Janak and Ludmila Novakova-Marcincinova

**Abstract**—The computer aided design, analysis, control, visualization and simulation of robotized workcells is very interesting in this time. Computer Aided Robot Control (CARC) is a subsystem of the system CIM including the computer aided systems of all activities connected with visualization and working of robotized workcells. There are three basic ideas: current CAD/CAM/CAE systems for design and 3D visualization, special PC based control and simulation systems and Augmented Reality Aided Manufacturing (ARAM) systems. This paper describes example of Open Source software application that can be utilized at planning of the robotized workcells, visualization and off-line programming the automated processes realized by authors.

**Keywords**—Augmented Reality, visualization, robot workcell, off-line programming.

## I. INTRODUCTION

Computer Aided Robot Control (CARC) started as an off-line-programming tool for robotized manufacturing workcells. Its prime purpose was to program robots off the shop floor, thereby providing the operators with a safer working environment, an efficient tool to perform trial-and-error routines, a reduction in maintenance and troubleshooting efforts, and better use of the production equipment for real manufacturing purposes rather than preparation work. Last development in area of robot workcell simulation and visualization is application of virtual and augmented reality in this area with out in new scientific branch titled Augmented Reality Aided Manufacturing (ARAM).

Soon the benefits of using CARC tools upstream became clear. Why use Computer Aided only for programming equipment, why not use it up-front, for designing the whole workcell? ARAM tools enabled manufacturing engineers to design the complete workcell in a faster, optimized and error-free fashion. The ability to view the equipment working in a manufacturing environment allowed for much tighter designs

J. Novak-Marcincin is with the Faculty of Manufacturing Technologies, Technical University of Kosice, Bayerova 1, 08001 Presov, Slovakia (phone: 00421-51-7723012; e-mail: jozef.marcincin@tuke.sk).

M. Janak is with the Faculty of Manufacturing Technologies, Technical University of Kosice, Bayerova 1, 08001 Presov, Slovakia (phone: 00421-51-7723012; e-mail: miroslav.janak@gmail.com).

L. Novakova-Marcincinova is with the Faculty of Manufacturing Technologies, Technical University of Kosice, Bayerova 1, 08001 Presov, Slovakia (ph.: 00421-51-7723012; e-mail: ludmila.marcincinova@tuke.sk).

with less error margins, as well as more accurate time and flow calculations.

Thus, ARAM took a significant step forward. Although savings resulting from off-line programming were significant, they were only in the initial phase of production. Computerized process design provided benefits not only in the launch phase, but throughout the product life cycle, as optimized cell layouts and tools paths resulted in reduced capital investment and lower variable manufacturing costs [1].

This paper deals with concrete idea of simple but effective form of augmented reality application in today's very important area of mechanical manufacturing technologies oriented to area of robot and automated devices control. It brings the information on present time of augmented reality technologies development. It describes proposed algorithm of AR application and example of AR utilization in design and control process of robot workcell. In the main part it also deals with utilization of Open Source Application for programs realization, realization of the position sensors device and algorithm of Open Source application realization in laboratory of Faculty of Manufacturing Technologies. It considers further improvements and reserves in area of developing the applicability of programs in preparation phase for robot workcell visualization and control.

## II. DEVELOPMENT OF AUGMENTED REALITY

Augmented Reality (AR) is a growing area in virtual reality research. The world environment around us provides a wealth of information that is difficult to duplicate in a computer. This is evidenced by the worlds used in virtual environments. Either these worlds are very simplistic such as the environments created for immersive entertainment and games, or the system that can create a more realistic environment has a million dollar price tag such as flight simulators. AR system generates a composite view for the user. It is a combination of the real scene viewed by the user and a virtual scene generated by the computer that augments the scene with additional information. The application domains reveal that the augmentation can take on a number of different forms. In all those applications the AR presented to the user enhances that person's performance in and perception of the world. The ultimate goal is to create a system such that the user can not tell the difference between the real world and the virtual augmentation of it. To the user of this ultimate system it would appear that he is looking at a single real scene [2].

The discussion above highlights the similarities and differences between virtual reality and augmented reality systems. A very visible difference between these two types of systems is the immersiveness of the system. Virtual reality strives for a totally immersive environment. The visual, and in some systems aural and proprioceptive, senses are under control of the system. In contrast, an augmented reality system is augmenting the real world scene necessitating that the user maintains a sense of presence in that world. The virtual images are merged with the real view to create the augmented display. There must be a mechanism to combine the real and virtual that is not present in other virtual reality work. Developing the technology for merging the real and virtual image streams is an active research topic.

The computer generated virtual objects must be accurately registered with the real world in all dimensions. Errors in this registration will prevent the user from seeing the real and virtual images as fused. The correct registration must also be maintained while the user moves about within the real environment. Discrepancies or changes in the apparent registration will range from distracting which makes working with the augmented view more difficult, to physically disturbing for the user making the system completely unusable. An immersive virtual reality system must maintain registration so that changes in the rendered scene match with the perceptions of the user. Any errors here are conflicts between the visual system and the kinesthetic or proprioceptive systems. The phenomenon of visual capture gives the vision system a stronger influence in our perception. This will allow a user to accept or adjust to a visual stimulus overriding the discrepancies with input from sensory systems. In contrast, errors of misregistration in an AR system are between two visual stimuli which we are trying to fuse to see as one scene. We are more sensitive to these errors [3].

Milgram describes a taxonomy that identifies how augmented reality and virtual reality work are related. He defines the Reality-Virtuality continuum shown as Fig. 1.

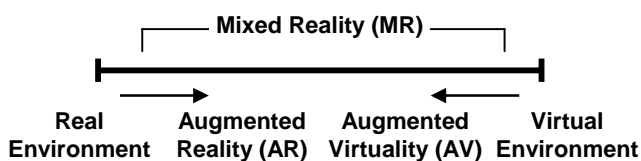


Fig. 1 Milgram's Reality-Virtuality Continuum

The real world and a totally virtual environment are at the two ends of this continuum with the middle region called Mixed Reality. Augmented reality lies near the real world end of the line with the predominate perception being the real world augmented by computer generated data. Augmented virtuality is a term created by Milgram to identify systems which are mostly synthetic with some real world imagery added such as texture mapping video onto virtual objects. This is a distinction that will fade as the technology improves and the virtual elements in the scene become less distinguishable from the real ones.

Milgram further defines a taxonomy for the Mixed Reality displays. The three axes he suggests for categorizing these systems are: Reproduction Fidelity, Extent of Presence Metaphor and Extent of World Knowledge. Reproduction Fidelity relates to the quality of the computer generated imagery ranging from simple wireframe approximations to complete photorealistic renderings. The real-time constraint on augmented reality systems forces them to be toward the low end on the Reproduction Fidelity spectrum. The current graphics hardware capabilities can not produce real-time photorealistic renderings of the virtual scene. Milgram also places augmented reality systems on the low end of the Extent of Presence Metaphor. This axis measures the level of immersion of the user within the displayed scene. This categorization is closely related to the display technology used by the system. Each of these gives a different sense of immersion in the display. In an augmented reality system, this can be misleading because with some display technologies part of the "display" is the user's direct view of the real world. Immersion in that display comes from simply having your eyes open. It is contrasted to systems where the merged view is presented to the user on a separate monitor for what is sometimes called a "Window on the World" view.

The third, and final, dimension that Milgram uses to categorize Mixed Reality displays is Extent of World Knowledge. Augmented reality does not simply mean the superimposition of a graphic object over a real world scene. This is technically an easy task. One difficulty in augmenting reality, as defined here, is the need to maintain accurate registration of the virtual objects with the real world image. This often requires detailed knowledge of the relationship between the frames of reference for the real world, the camera viewing it and the user. In some domains these relationships are well known which makes the task of augmenting reality easier or might lead the system designer to use a completely virtual environment. The contribution of this thesis will be to minimize the calibration and world knowledge necessary to create an augmented view of the real environment [4].

### III. THEORY OF AUGMENTED REALITY

As mentioned in introduction, an AR system generates a complex view where the virtual areas are covered by real environment and offers the basic working place for the user. It is a reciprocal combination of the real scene observed by the camera and a virtual scene generated by the computer logical core that mixtures the both scenes. Based on the previous information it is easy to say that possibilities of AR find the utilization in many industrial spheres like as aeronautics, automobile industry, manufacturing etc. [5].

The entire structure of this part of paper is focused on basic steps and advances which are necessary and need to know for the engineer in the processes of creation of the robot workcell structure. During the realization of this process the engineer can be surprised by many obstacles which are suitable for next examining. Whereupon, it is easy to say that

the correct result has a main impact on final workcell structure. The main task of creating an AR scene is to get an understanding of the position and orientation of the implemented devices.

In the first point of this mentioned process the single 3D objects (entries from workcell plan) need to be created and defined by tools of CAD system. These applications are using special modules which are implemented in the logical core of high CA systems. The 3D model comprises necessary information about its own properties (geometrical value and shape of 3D objects, orientation and position of all 3D objects, mass properties and other characteristics). These data packets are continually sending in the special comparing section of the programming core. By means of it the 3D CAD model will be filled with necessary information about geometry and structural condition [6].

The result of these processes, the data packet is ready to exports on entry area of systems of AR. The single virtual 3D objects needs to obtain information about its own position and orientation value which is used for fixing process on the particular place of the auxiliary model in the real environment. The result of all mentioned steps is logical algorithm which allows seeing a data flow between single blocks. These blocks are collected and presented on the Fig. 2.

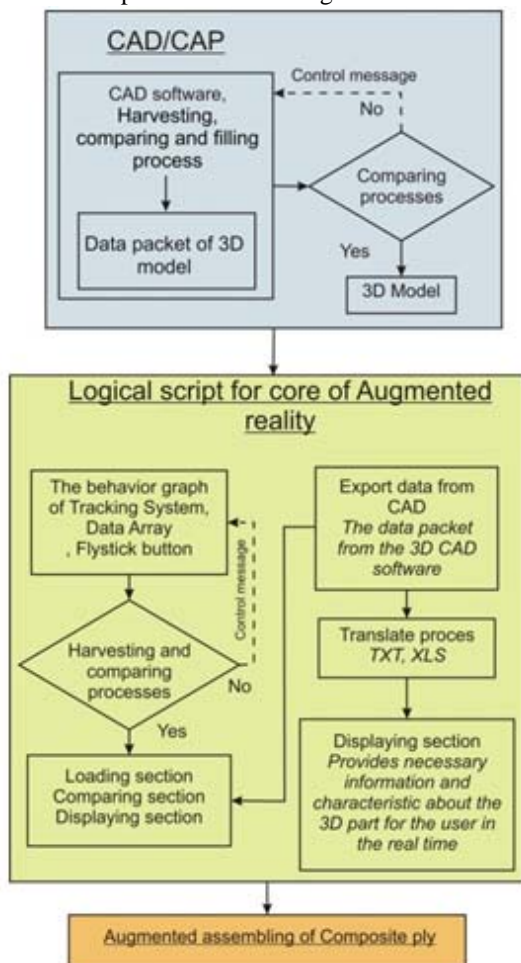


Fig. 2 Logical algorithm of AR application

Nowadays application allows the engineer to use different methods where the characteristic feature lies in a technology of displaying of the collecting positioning point. This group of the displaying process technology includes general methods such as laser visualization method of displaying the final model boundary edge and collection augmented and virtual reality process (Fig. 3).

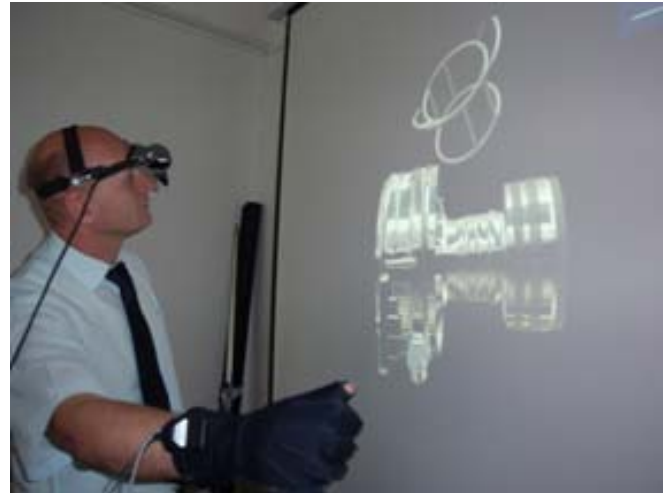


Fig. 3 Visualization by virtual reality technologies

#### IV. AR ROBOT WORKPLACE SIMULATION AND PROGRAMMING SYSTEM

Augmented reality, as a sub-area of the virtual reality, utilizes hardware and software tools for creation of the mixed environment that combines real scene usually present in the form of video sequence with augmented scene consisting of virtual models of additional objects. There are several techniques among those commonly used in augmented reality that are tried to implement into the system of robot programming. The central object of newly created environment was robotic device from Swedish producer ABB - compact robot IRB 140 (Fig. 4).



Fig. 4 Industrial robot ABB IRB 140

When creating the environment of augmented reality that would be suitable for realization of real-time tasks (for example the programming of the robotic device) we have to consider the matter of continual space calibration in order to keep the real and virtual scenes spatially aligned in the final form of one consistent working place. For this purpose we use well known 3D digitization device Kinect in combination with a specialized software tool called Skanect. Kinect firstly allows us to obtain the 3D scan of the real environment and to use this real data while creating the virtual one. Entities from the scan serve as the references for generation of spatial links between computer models and real things, such as machines, tables, robot base. Secondly, the ability of sensing the workplace with depth sensors in real time provides us with direct calibration of the environment and all included devices. This generation of mixed space and co-calibration of its both parts is realized in the software environment of Blender application. This powerful and widely complex graphical solution offers many useful tools, libraries and sub-routines for object programming with excellent level of graphical overview, everything based on the principles of Open Source software philosophy (Fig. 5).

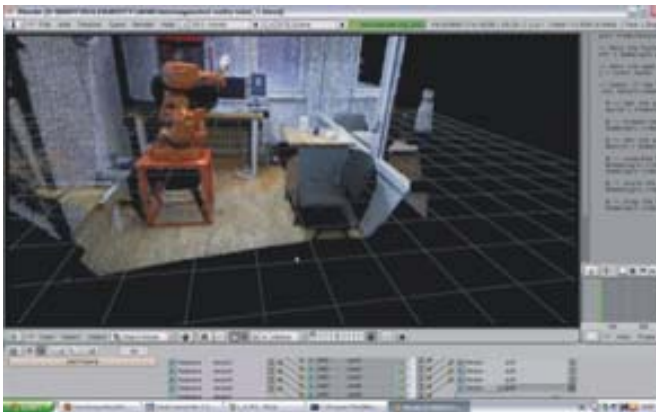


Fig. 5 Real robot workcell in the Blender software

#### A. Application of the color tracking

For real-time detection of position of important objects we use the technique of color markers. Thin paper stripes of different colors are stick on the surfaces of the robot and other devices (table, milling machine). They are either easily locatable by the camera and also suitable from the viewpoint of robot motion description. Color stripes are monitored in pairs, while each pair consists of two stripes which are one to other in upright direction. This way the stripes of equal color create a graphical marker which can be used for monitoring of exact position of each robot axis. Next the relevant command line called in the Blender environment activates the procedure of color tracking checking the position of real robot and recalculating the coordinates of individual motion axis in software environment. Position and orientation of robot model can be then adjusted or proposed (programmed) on the base of the real one. This means that the programmer can create the sequences of a new program also while proceeding from the

positions used in old one or from actual robot position (possible program creation in mixed online/offline mode).

Other possibility to apply the color tracking is to use it for detection of workplace objects and also the task objectives. With a camera suitably located near the end of robot reach zone we can monitor the working area and achieve the location of bodies that are supposed to be handled. Blender integrates the ARToolkit features so it can perform even upgraded level of color tracking - shape detection. With this technique some parts of the programming sequences (basic moves of the robot to desired position) are written automatically, as the virtual model can be led to the objective while avoiding the obstacles detected in its working zone. Accurate finishing of these motions has to be programmed additionally. on the Fig. 6 is presented model of a robot inserted into the live video sequence on the base of the data acquired from combination of Kinect sensing and color tracking [7].

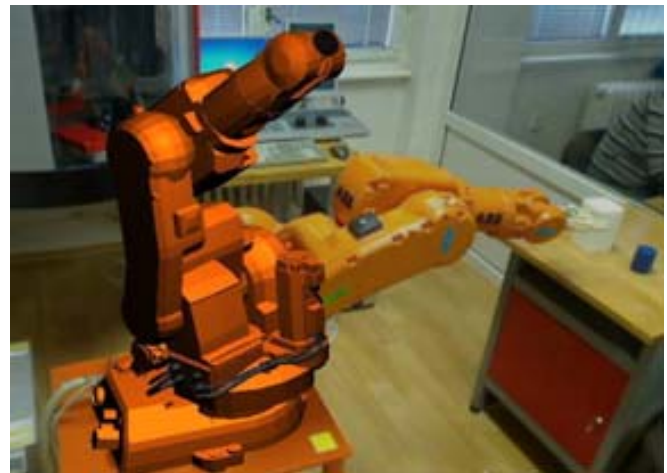


Fig. 6 Virtual model of robot in real environment

#### B. AR displaying of the robotized workcell through the special glass

New perspective possibility of displaying the environment of augmented reality is using of special visualization unit created on the Faculty of Manufacturing Technologies, which utilizes the principle of combined glass-mirror medium [8].

The surface of the glass is either half-silvered or there is a half-leaky foil stick on it that creates a reflection and at the same time allows a view to the working environment with no obstacle or decrease of view quality. This commonly available kind of mirror is often used in gaming, medicine or business presentations. By optical connection of two seemingly different views it creates an ideal platform for the creation of a realistic spatial effect. Displaying is a reversed emission of the view to the reflex surface. It can be provided by computer monitor or classical projector placed over the working area [9].

With a development of the projectors and their displaying technologies we are able to use the advantages of LED projecting. In comparison to the classical light projector the

LED technology does not generate the luminous cone that would reflect in the form of light spot on the displaying glass. The setting up of whole scene becomes easier as you can mount the devices in the necessary displaying angles without the need to prevent the direct light reflection. On the Fig. 7 is presented use of the half-silvered mirror for presentation of virtual model of industrial robot activity in comparison with real robot workcell activity [10].



Fig. 7 Displaying of AR using the half-silvered mirror

### C. Augmented Programming

Programming of the robot with use of above mentioned elements and techniques of AR is possible thanks to the programming character of Blender software. User can control the real robotic device and its virtual model in the same environment using the half-silvered glass (semi-online mode) or the interface of PC monitor or eventually special displaying glasses for VR (offline mode). Either way he controls the virtual robot in the AR environment, while all the key positions and motions desired between them are stored in the graphical form of 3D Blender data. This data are then using the simple scripts of objects programming translated into the syntax code of robot control system.

## V. CONCLUSION

This article describes the solutions on using the environment of virtual/augmented reality in area of industrial robot programming. In the beginning it describes the current state of mentioned problems with respect to the online and offline programming regimes and brings the information of utilization of AR for robot programming realized by other research teams. Main part of this work describes the proposal of new system for augmented programming, which does not utilize commonly used system of the markers. It consists of several techniques widely exploited in many applications of augmented reality, grouping them into one software interface with single purpose - to provide the user with the possibility of easy and comfortable method of program creation in the environment that copies real workcell in best possible way.

This new system for augmented programming is already in operation and still developed and improved at the Faculty of Manufacturing technologies with a seat in Presov, Slovakia. Further research will be focused to the improvements in the area of audio implementation and text information generation. Main difficulty will remain present in interconnection between used software environment and robot control unit.

## ACKNOWLEDGMENT

Ministry of Education, Science, Research and Sport of SR supported this work, contract VEGA No. 1/0032/12, KEGA No. 002TUKE-4/2012 and ITMS project 26220220125.



## REFERENCES

- [1] P. Petruska, J. N. Marcincin, M. Doliak, "ROANS - intelligent simulation and programming system for robots and automated workcell." *Proceedings of the IEEE International Conference on Intelligent Engineering Systems INES*, 1997, p. 451-456.
- [2] S. K. Ong and A. Y. C. Nee, *Virtual and Augmented Reality Applications in Manufacturing*, Springer-Verlag London, 2004, 387 p.
- [3] J. Vallino, *Introduction to Augmented Reality*. Rochester Institute of Technology, Rochester, 2002 (<http://www.se.rit.edu/~jrv/research/ar/>).
- [4] J. Vallino and K. N. Kutulakos, "Augmenting reality using affine object representations." *Fundamentals of Wearable Computers and Augmented Reality*, 2001, p. 157-182.
- [5] S. K. Ong, "A novel AR-based robot programming and path planning methodology," *Robotics and Computer-Integrated Manufacturing*, Vol. 26, No. 3, 2010, p. 227-237.
- [6] J. N. Marcincin, M. Janak, J. Torok, L. N. Marcincinova, V. Fecova, "Verification of a Program for the Control of a Robotic Workcell with the Use of AR." *International Journal of Advanced Robotic Systems*, Vol. 9, 2012, p. 54-54.
- [7] J. N. Marcincin, "Application of the Virtual Reality Modeling Language for Design of Automated Workplaces." *Proceedings of World Academy of Science Engineering and Technology*, Vol. 25, 2007, p. 160-163.
- [8] J. N. Marcincin, M. Doliak, S. Hloch, T. Ergic, "Application of the Virtual Reality Modelling Language to Computer Aided Robot Control System ROANS." *Strojarsvo*, Vol. 52, No. 2, 2010, p. 227-232.
- [9] J. N. Marcincin, P. Brazda, M. Janak, M. Kocisko, "Application of Virtual Reality Technology in Simulation of Automated Workplaces." *Tehnicki Vjesnik*, Vol. 18, No. 4, 2011, p. 577-580.
- [10] J. N. Marcincin, J. Barna, M. Janak, V. Fecova, L. N. Marcincinova, "Composite lay-up process with application of elements of augmented reality." *The Engineering Reality of Virtual Reality*, Proceedings of SPIE, Vol. 8289, Art. No. 82890P, 2012.

**Jozef N. Marcincin** (1964) graduated (MSc) at the Faculty of Mechanical Engineering at TU of Kosice. Since 1997 he is working on Faculty of Manufacturing Technologies. His scientific research is focusing on virtual reality technologies, CAM systems, automation and robotics.

**Miroslav Janak** (1982) graduated (PhD) at the Faculty of Manufacturing Technologies at TU of Kosice. His scientific research is focusing on CAD/CAM systems and programming of robots and NC machines.

**Ludmila Novakova-Marcincinova** (1970) graduated (PhD) at the Faculty of Manufacturing Technologies at TU of Kosice. Her scientific research is focusing on manufacturing technologies, Rapid Prototyping and virtual reality.

# Neural network position-path adaptive regulator for vehicles

V. Pshikhopov, M. Medvedev, and D. Shanin

**Abstract**—In this paper adaptive neural network control system is considered. Structure of discrete neural network proportional-integral-differential (PID) controller is proposed. The intelligent PID controller is 3-layers neural network. Training of the neural network is based on quadratic quality functional and the steepest descent method. Designed intelligent PID controller is tested in control system of electrical motor and control system of small size helicopter. Modeling and experiment results are presented.

**Keywords**—Intelligent control, vehicles, neural networks.

## I. INTRODUCTION

ADAPTIVE control design is the most urgent problem of the modern control theory [1] – [4]. Also this is actual problem for vehicle control systems and robots. The problem of adaptive control for nonlinear systems is complex problem. Therefore intelligent approaches are applied to design control for complex nonlinear systems [5] – [8]. This paper is devoted to control of SISO nonlinear systems by neural network PID-regulator.

There are two conventional control approaches using neural networks [9]. At the first approach the plant is controlled by conventional regulator. Neural network tunes the conventional regulator coefficients. At the second approach neural network and conventional regulator are operating together. But the neural network is the reference model of the adaptive control system.

In these approaches abilities of neural network is limited by abilities of the conventional controller. In addition conventional controller is simple regulator usually. For example conventional controller is PID-regulator.

In this paper we develop PID-controller designed in terms of neural network structure.

## II. NEURAL NETWORK PID-CONTROLLER

Structure of the designed neural network PID-controller is

This work was supported by Russian Scientific Foundation (project 14-19-01533) in Southern Federal University, Rostov-on-Don, Russian Federation.

V. Pshikhopov is with the Southern Federal University, Rostov-on-Don, Russia (e-mail: pshichop@rambler.ru).

M. Medvedev is with the Southern Federal University, Rostov-on-Don, Russia (+7(8634)37-16-94; fax: +7(8634)68-18-94; e-mail: medvmihal@gmail.com).

D. Shanin is with the Southern Federal University, Rostov-on-Don, Russia (e-mail: pshichop@rambler.ru).

presented in fig. 1.

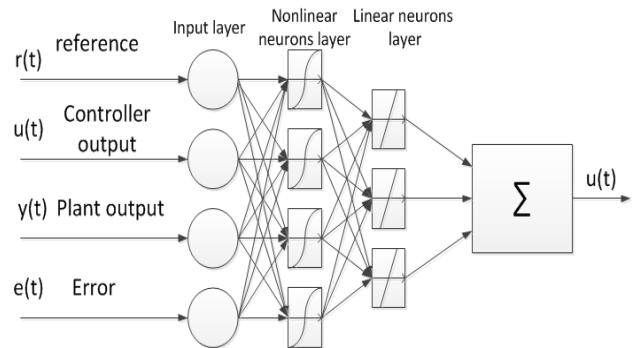


Fig. 1 Structure of the designed neural network PID-controller

The controller has 4 inputs. They are:  $r$  – reference signal;  $u$  – output of controller;  $y$  – output of the controlled plant;  $e$  – control system error.

Every element of the input layer is single input multi output rectifier. There are not activation functions in the input layer. The second layer is based on nonlinear neurons with tangent activation functions. This type of neurons is fit for input data processing and clustering. The third layer calculates components of PID controller on base of training algorithm.

PID-controller in discrete time domain is described by equation

$$u(t) = u(t-1) + k_p e(t) + k_i (e(t) - e(t-1)) + k_d (e(t) - 2e(t-1) + e(t-2)) \quad (1)$$

where  $e(t) = r(t) - y(t)$ ;  $k_p, k_i, k_d$  are gains of PID-controller.

Quality functional is

$$J = 0.5e^2(t+1) \quad (2)$$

Outputs of the linear neurons layer are gains  $k_p, k_i, k_d$ . Let us note these outputs as  $O_1, O_2, O_3$ . Training algorithm of linear neurons layer is based on the steepest descent method [10]. Weight coefficients for the linear neurons layer are

$$\Delta w_{kj}(t+1) = -\eta \frac{\partial J}{\partial w_{kj}} + \alpha \Delta w_{kj}(t) \quad (3)$$

Weight coefficients for the nonlinear neurons layer are

$$\Delta w_{ji}(t+1) = -\eta \frac{\partial J}{\partial w_{ji}} + \alpha \Delta w_{ji}(t) \quad (4)$$

Parameters  $\eta$  and  $\alpha$  determine the speed of training and weight of previous values.

Let us introduce the following notations:

$$\delta_k = \frac{\partial J}{\partial net_k} \quad (5)$$

$$net_k = \sum_k w_{kj} O_j + \theta_k \quad (6)$$

From the chain rule of complex function differentiation we have for the linear neurons layer

$$\frac{\partial J}{\partial w_{kj}} = \frac{\partial J}{\partial net_k} \frac{\partial net_k}{\partial w_{kj}} = \frac{\partial J}{\partial net_k} O_j \quad (7)$$

$$\delta_k = \frac{\partial J}{\partial net_k} = \frac{\partial J}{\partial y(t+1)} \frac{\partial y(t+1)}{\partial u(t)} \quad (8)$$

But we have

$$\begin{aligned} \frac{\partial J}{\partial y(t+1)} &= \frac{\partial J}{\partial e(t+1)} \frac{\partial e(t+1)}{\partial y(t+1)} = \\ &= -(r(t+1) - y(t+1)) \end{aligned} \quad (9)$$

$$\frac{\partial u}{\partial O_k} = \begin{cases} e(t), & k = 1, 2, \dots \\ e(t) - e(t-1), & k = 2, 3, \dots \\ e(t) - 2e(t-1) + e(t-2), & k = 3, 4, \dots \end{cases} \quad (10)$$

From (3) – (9) we have

$$\Delta w_{kj}(t+1) = -\eta \delta_k O_j + \alpha \Delta w_{kj}(t) \quad (11)$$

$$\delta_k = e(t+1) \frac{\partial y(t+1)}{\partial u(t)} O_k (1 - O_k) \quad (12)$$

Similarly for the nonlinear neurons layer we have

$$\begin{aligned} \frac{\partial J}{\partial net_j} &= \sum_k \frac{\partial J}{\partial net_k} \frac{\partial net_k}{\partial O_j} \frac{\partial O_j}{\partial net_j} \frac{\partial net_j}{\partial w_{kj}} = \\ &= - \sum_k \delta_k w_{kj} O_j (1 - O_j) \end{aligned} \quad (13)$$

From (13) and (8) we obtain

$$\Delta w_{ji}(t+1) = -\eta \delta_j O_j + \alpha \Delta w_{ji}(t) \quad (14)$$

$$\delta_j = - \frac{\partial J}{\partial net_j} = \sum_k \delta_k w_{kj} O_j (1 - O_j) \quad (15)$$

On base of (3) – (15) we obtain the neural controller algorithm. This algorithm consists of the following items.

1. Initial tuning of neural emulator.
2. Specification of initial values of coefficients  $w_{kj}$ ,  $w_{ji}$ , limits  $\theta_j$ ,  $\theta_i$ , and coefficients  $\eta$ ,  $\alpha$ .
3. The input to the neural network training sample served. Variables  $u(t)$ ,  $y(t)$ , and  $\delta_k$  are calculated.
4. Weight coefficients of the linear neurons layer are calculated in according with (11).
5. Variable  $\delta_j$  is calculated in according with (15).
6. Weight coefficients of the nonlinear neurons layer are calculated in according with (14).
7. If increments of the weight coefficient (11), (14) are not small then we go to item 3.

### III. MODELING RESULTS

Check the efficiency of the neural network PID-controller is

implemented in Matlab. Model of controlled plant is black box. The controlled plant is an induction motor.

In simulation code the following mathematical model of induction motor is used:

$$\begin{aligned} \dot{x}_1 &= a_1^0 x_3 x_4 - a_7^0 m_s, \\ \dot{x}_2 &= -a_2^0 x_2 + x_1 x_3 + a_3^0 \frac{x_3^2}{x_4} + b^0 u_1, \end{aligned} \quad (16)$$

$$\dot{x}_3 = -a_4^0 x_3 - x_1 x_2 - a_5^0 x_1 x_4 - a_3^0 \frac{x_2 x_3}{x_4} + b^0 u_2,$$

$$\dot{x}_4 = -a_6^0 x_4 + a_3^0 x_2,$$

where  $x_1$  is motor shaft rotation speed,  $x_2$  and  $x_3$  are projection of the stator current for the rotating dq-axis,  $x_4$  is the rotor flux linkage,  $b$  and  $a_i^0$ ,  $i = \overline{1,7}$  are parameters of the motor,  $u_1$  and  $u_2$  are controls, and  $m_s$  is load.

Modeling results of the intelligent control system for induction motor on base of neural network PID-controller are presented in fig. 2 and fig. 3.

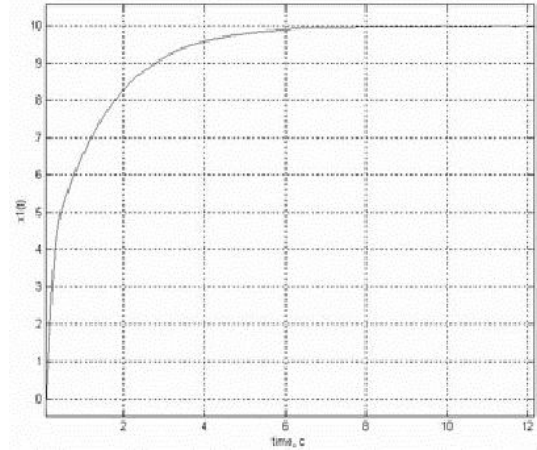


Fig. 2 Transient in the control system without load

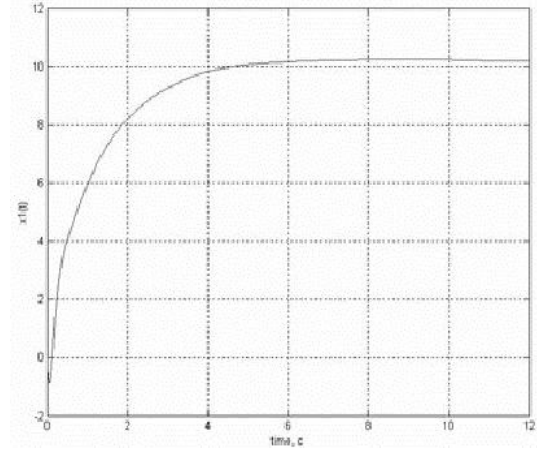


Fig. 3 Transient in the control system with dynamic load

In fig. 2 we can see transient of the control system with nominal load. In fig. 3 we can see transient of the control system with dynamic load. The dynamic load consists of two components. The first component is constant load. The second component is linear function of time. In addition parameters of the motor are interval ones.

If the load is dynamic the dynamic error of control system is

present.

#### IV. EXPERIMENTAL RESULTS

On the base of designed intelligent PID-regulator control system for vehicle is developed. Vehicle is helicopter model Silverlit Picozzz. This model is presented in fig. 4. This model is based on design Sikorsky.



Fig. 4 Helicopter model Silverlit Picozzz

In the design of the rotor missing swashplate and no system of pitch changing. Therefore full control of this model is not able. But it is possible to stabilize the helicopter model in the vertical plane.

Control system is based on information from video camera. Structure of the control system is presented in fig. 5.

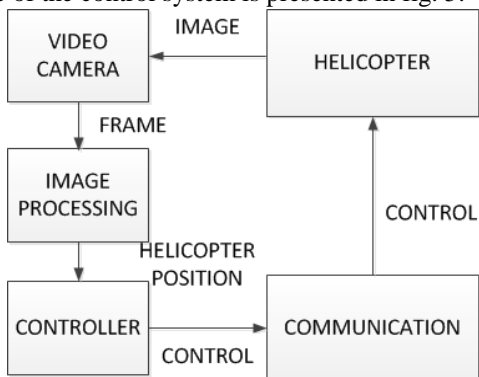


Fig. 5 Structure of the control system

Position of the helicopter is measured by video camera Genius GF112. Camera is operating in continuous video mode. Video from the camera is recorded in format JPG\_24 by code of MatLab. Further color frames is converted into the grayscale format.

Thereafter the grayscale image is converted into the binary format and inverted by the following MatLab code:

```

level = graythresh(I);
bw = im2bw(I,level);
wb = ~ bw;
    
```

Further the image is filtering by MatLab function imclearborder. The result is matrix матрица of dimension [x, y]. This matrix allows to calculate the helicopter position.

Results of computer vision system operating are presented in fig. 6 and fig. 7.

Calculated coordinates of the helicopter are transmitted to the neural network PID-controller implemented by MatLab.



Fig. 6 The image from video camera

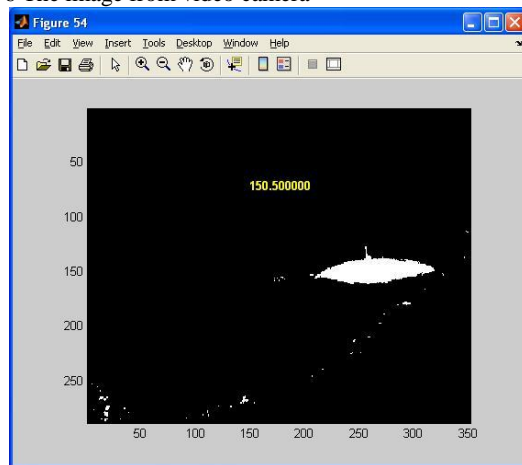


Fig. 7 The processed image

Control is transmitted to the helicopter by wi-fi port. Actuator of the helicopter is DC motor controlled by PWM signal.

The features of the helicopter are:

- non-stationary characteristics of propeller thrusts determined by fast discharge of accumulator;
- PWM control of DC motor has 4 level, therefore the control is discrete one;
- the used model of the helicopter is black box;
- refresh rate of the control is 2 Hz.

Experimental results are presented in fig. 8. The control errors in steady-state mode is decreasing with time because of the neural network controller training. Reference altitude of the helicopter is 15 pixels.

It should be noted that despite the preliminary training the neural network controller the final training is carried out with real helicopter. Therefore it is necessary to ensure the helicopter safety while the neural network controller is training.

#### V. CONCLUSION

In this paper method of intelligent control for SISO plant is proposed. The mathematical model of a plant is black box. Controller is designed on base of neural network. The intelligent controller implements PID regulator. Both integration as well as differentiation is implemented by the

neural networks.

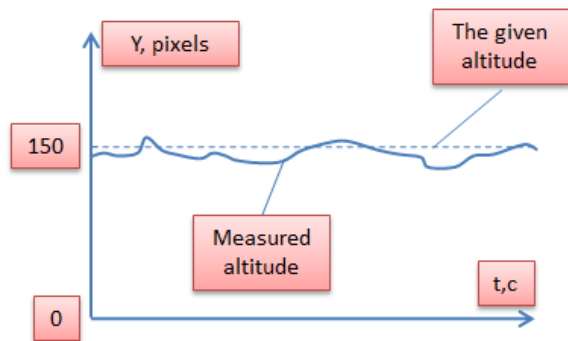


Fig. 8 Experimental results

Applying neural networks to calculate signal time derivatives ensures the following problems solution:

- neural network does not require mathematical model to calculate time derivative of signal;
- neural network differentiator implements signal filtering;
- neural network can be trained on base of harmonic signals of the given frequency range.

In the presented intelligent controller the neural network of 2 layers is used. Training is based on the back propagation method. The first layer consists of 2 neuron with activation function tangent sigmoid. The second layer consists of 5 neurons with linear activation function.

Differentiated signal and its third time derivative are presented in fig. 9 and fig. 10.

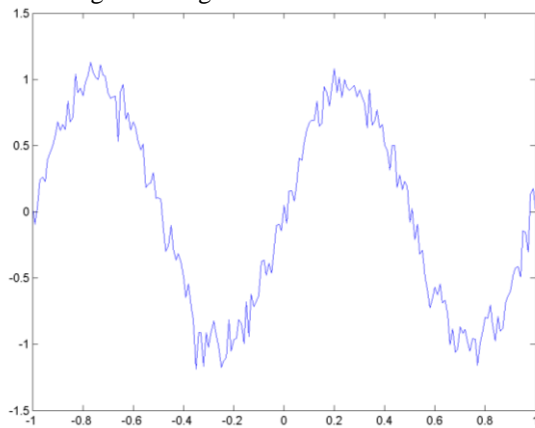


Fig. 9 Differentiated signal with noise

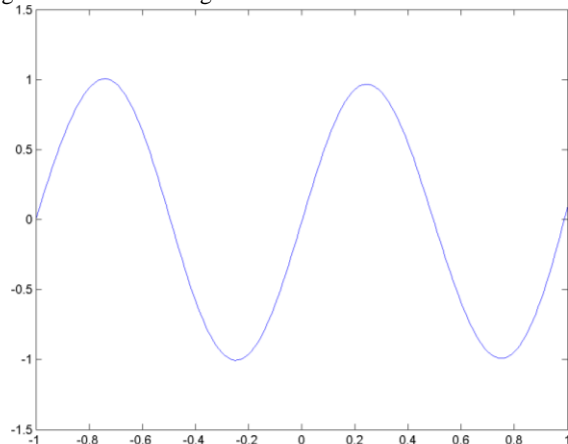


Fig. 10 The third time derivative of differentiated signal

It is clear that neural network differentiator ensures high performance. The most complex problem of the neural network differentiator is problem of conversion network. In addition it is necessary to determine optimal number of the differentiator neurons.

The described approach can be used for control of other vehicles types [10] – [15].

## REFERENCES

- [1] R. Marino, P. Tomei, "Global adaptive output-feedback control of nonlinear systems", *IEEE Transactions on Automatic Control*, 1993, 38 (1), pp. 17-32.
- [2] M. Krstić, I. Kanellakopoulos, P.V. Kokotović, "Adaptive nonlinear control without overparametrization", *Systems and Control Letters*, 1992, 19 (3), pp. 177-185.
- [3] V.Kh. Pshikhopov, V.A. Krukhmalev, M.Yu. Medvedev, R.V. Fedorenko, S.A. Kopylov, A.Yu. Budko, V.M. Chufistov, "Adaptive control system design for robotic aircrafts", *Proceedings - 2013 IEEE Latin American Robotics Symposium, LARS 2013* PP. 67 – 70. doi: 10.1109/LARS.2013.59.
- [4] V.Kh. Pshikhopov, M.Yu. Medvedev, "Block design of robust control systems by direct Lyapunov method", *2011 IFAC Proceedings Volumes (IFAC-PapersOnline)*, 18 (PART 1) Pp. 10875 – 10880.
- [5] T. Zhang, S.S. Ge, C.C. Hang, "Adaptive neural network control for strict-feedback nonlinear systems using backstepping design", *Automatica*, 2000, 36 (12), pp. 1835-1846.
- [6] J.T. Spooner, K.M. Passino, "Stable adaptive control using fuzzy systems and neural networks", *IEEE Transactions on Fuzzy Systems*, Volume 4, Issue 3, 1996, Pages 339-359
- [7] V.Kh. Pshikhopov, A.S. Ali, "Hybrid motion control of a mobile robot in dynamic environments", *In proc. of 2011 IEEE International Conference on Mechatronics, ICM 2011*, pp. 540-545.
- [8] V.Kh. Pshikhopov, M.Y. Medvedev, M.Y. Sirotenko and V.A. Kostjukov "Control System Design for Robotic Airship". *In Proc. of the 9-th IFAC Symposium on Robot Control*. Pp. 123-128. 2009. Gifu, Japan.
- [9] S. Omatu, B. Khalid Marzuki, Y. Rubiyah, "Neuro-Control and its Applications", *Springer Berlin Heidelberg*, 1996, ISBN: 9781447130604.
- [10] V. Pshikhopov, M. Medvedev, V. Kostjukov, R. Fedorenko, B. Gurenko, V. Krukhmalev, "Airship autopilot design", *SAE Technical Papers*. October 18-21, 2011. doi: 10.4271/2011-01-2736.
- [11] V. Pshikhopov, N. Sergeev, M. Medvedev, A. Kulchenko, "The design of helicopter autopilot", *SAE Technical Papers* 5, 2012, doi: 10.4271/2012-01-2098.
- [12] V.K. Pshikhopov, M.Y. Medvedev, B.V. Gurenko, "Homing and docking autopilot design for autonomous underwater vehicle", *Applied Mechanics and Materials*, N 490-491, 2014, PP. 700 – 707. doi: 10.4028/www.scientific.net/AMM.490-491.700.
- [13] V.Kh. Pshikhopov, M.Yu. Medvedev, A.R. Gaiduk, B.V. Gurenko, "Control system design for autonomous underwater vehicle", *Proceedings – 2013 IEEE Latin American Robotics Symposium, LARS 2013*, PP. 77 – 82. doi: 10.1109/LARS.2013.61.
- [14] V. Pshikhopov, M. Medvedev, R. Neydorf, A. Gaiduk, V. Voloshin, "Impact of the feeder aerodynamics characteristics on the power of control actions in steady and transient regimes", *SAE Technical Papers* 5, 2012.
- [15] V. Pshikhopov, V. Krukhmalev, M. Medvedev, R. Neydorf, "Estimation of energy potential for control of feeder of novel cruiser/feeder MAAT system", *SAE Technical Papers* 5, 2012.
- [16] V.Kh. Pshikhopov, M.Yu. Medvedev, "Robust control of nonlinear dynamic systems", *2010 IEEE ANDESCON Conference Proceedings*. doi: 10.1109/ANDESCON.2010.5633481.

# Multiple Bands Antenna with Slots for Wireless Communication System

Evizal Abdulkadir, Eko Supriyanto, T.A. Rahman, S.K.A. Rahim and S.L Rosa

**Abstract**—Rapid growing of user in mobile communication and limited of spectrum created many frequency band used by operator. This letter propose a new antenna design with slots that covered multiple bands common used in mobile communication and long-term evolutions (LTE) system. A single patch antenna operating at 2.6 GHz for LTE band was first designed and then optimization by introducing slots on antenna patch has been done to improve the antenna's bandwidth (BW). As a transmitter antenna requires high gain for effective transmission, air gap and aluminum plate are used as ground element in order to achieve high gain performance. The reflection coefficient of initially designed single patch antenna gives a single band response. However some slots and array elements are introduced into the antenna to obtain multi band response, which covers a few bands. The results obtained from reflection coefficient have shown that the proposed patch antenna is suitable in such telecommunication system applications as GSM, UMTS, LTE, WLAN and WiMAX. The result of simulation reflection coefficient is -34 dB at centre frequency 2.6 GHz and antenna gain is 8.21 dBi..

**Keywords**—Antenna, Wireless, Microstrip, Slot.

## I. INTRODUCTION

SINCE introduced of wireless technology a few decades ago, wireless devices are now commonly used in communication systems, medical and industrial applications, games console, to mention a few. In telecommunication systems, wireless technology is commonly used especially in mobile communication. Nowadays a mobile phone is not only used for voice communication but also often used for transferring data, images and videos. Third generation (3G) technology attempts to use a mobile phone for video call and now LTE; while the fourth generation (4G) technology is expected use mobile phone as broadband media, that support high speed data rate. In order to achieve these requirements, several methods have been proposed; and one of such methods

This work was supported by Cardio Centre Flagship Grant, UniversitiTeknologi Malaysia.

EvizalAbdulkadir is with SekolahTinggiTeknologiPelalawan, Jl.MaharajaIndra No. 379, PangkalanKerinci, 28300 Pelalawan Riau Indonesia.

Prof. Dr. EkoSupriyanto is the director of IJN-UTM Cardiovascular Engineering Centre, UniversitiTeknologi Malaysia, Skudai, Johor, Malaysia (Correspoing author phone: +6075558551-mail: [eko@biomedical.utm.my](mailto:eko@biomedical.utm.my)).

Prof. Dr. T.A. Rahman is the Director of Wireless Communication Centre, Faculty of Electrical Engineering, UniversitiTeknologi Malaysia, 81310 Johor Malaysia

is antenna diversity and spatial multiplexing. A new high-gain antenna design for transmitter, operating at LTE band 2.6 GHz, is proposed in this letter.

In most of the previous researches, it was found that the LTE antenna was mostly used for mobile devices, such as installation in laptop, mobile phone and gadget [1-3]. A design of an antenna with spiral technique mentioned in [4] then in this proposed antenna design introduce some slots to obtain multiple bands antenna. LTE antenna techniques especially for transmitter, have been highlighted in [5]; however, the antenna gains are generally low and their radiation pattern is omni directional [6]. Wide band antenna is one of the objectives in this proposed antenna design, several method and technique to achieve wideband reflection coefficient such as mention in [7]. The proposed antenna in this study operates at LTE band and has directional radiation pattern. Directional radiation pattern and multiple bands have been introduced in order to obtain a high gain antenna.

## II. ANTENNA DESIGN

Typically a transmitter or base station (BS) has multiple antennas for a few sectors of coverage area and high gain antennas are used for efficiency of transceiver. Thus, with the current trends in setting up base transceiver system (BTS), the microstrip antenna technique is usually employed to design a directional antenna[8]. The design of microstrip antenna was started by calculating the basic size of patch. A centre frequency of 2.6 GHz LTE band has been chosen in this design. The material used is FR4 board with following specifications: relative permittivity  $\epsilon_r=4.7$ , height  $h=1.6$  mm and  $\tan \delta=0.019$ . The basic equation of microstrip antenna was used to calculate width (W) and length (L) of patch[8]. Figure 1 shows basic design of microstrip antenna with length and width of patch.

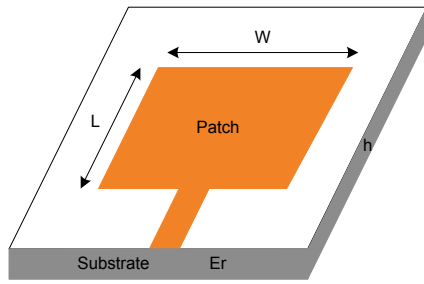


Fig. 1. Basic microstrip antenna.

$$W = \frac{1}{2 f_r \sqrt{\mu_0 \epsilon_0} \epsilon_r} \sqrt{\frac{2}{\epsilon_r + 1}} = \frac{v_0}{2 f_r} \sqrt{\frac{2}{\epsilon_r + 1}} \quad (1)$$

$$L = \frac{1}{2 f_r \sqrt{\epsilon_{eff} \mu_0 \epsilon_0}} - 2 \Delta L \quad (2)$$

where:

$$\epsilon_{eff} = \frac{\epsilon_r + 1}{2} + \frac{\epsilon_r - 1}{2} \left[ 1 + 12 \frac{h}{W} \right]^{-1/2} \quad (3)$$

$$\frac{\Delta L}{h} = 0.412 \frac{(\epsilon_{eff} + 0.3) \left( \frac{W}{h} + 0.264 \right)}{(\epsilon_{eff} - 0.258) \left( \frac{W}{h} + 0.8 \right)} \quad (4)$$

The size of antenna patch has been optimized done to meet reflection coefficient in LTE band 2.6 GHz. Next step is to optimize response in wideband or multiple bands that cover others frequency bands in telecommunication such as GSM, UMTS, WLAN and WiMAX. The single patch antenna design is shown in Figure 2 in which slots have been introduced to achieve wideband and multiple frequency response. Note that all dimensions are in millimetre (mm).

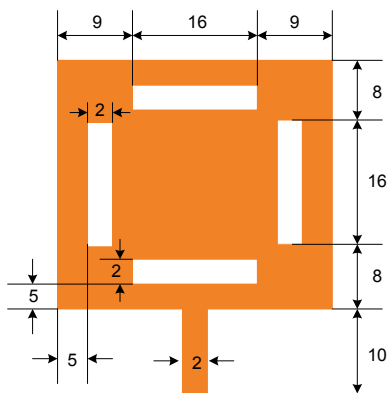


Fig. 2. Single patch antenna design with slots.

As previously mentioned, a BS requires a high gain antenna for efficient transceiver. In this design, an antenna is proposed with array patch to increase gain and which used air gap[9]. The number of patches is 4 x 4; then they are arranged and optimized to achieve optimum reflection coefficient

and multiple bands response. Figure 3 shows the complete diagram of proposed antenna with array 4x4. Some transmission lines are introduced as feeding to the port at the back of antenna.

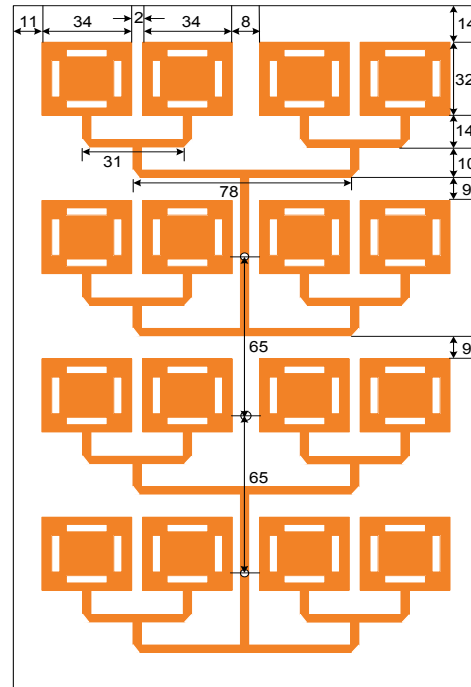


Fig. 3. Proposed high gain array antenna.  
(NB: All dimensions are in mm)

The proposed antenna structure is presented in Figure 4, where Figures 4 (a) and (b) represent the feeding line of the patch's bottom layer and the used air gap between ground and antenna patch, respectively. Aluminum of 1 mm thickness was used for antenna ground, while the air gap is 10 mm to the patch antenna. The SMA bulkhead socket of 50 Ohms impedance was used for the antenna port. The typical connector was drawn and simulated by using 3D CST simulation software.

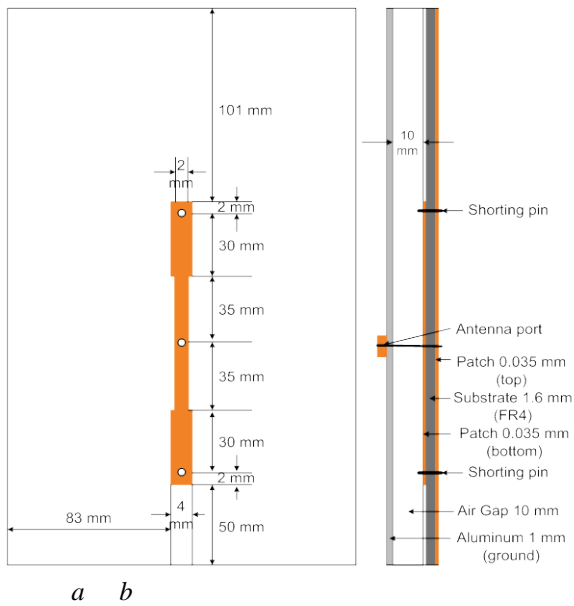


Fig. 4. Proposed antenna structure (a) FR4 back view (b) Side view.

### III. MEASUREMENT SETUP

The measurement setup is aimed at testing the antenna E-field and H-field radiation patterns. Graphs are then plotted to analyze the performances. A centre frequency of 2.6 GHz was used for testing the antenna, which complies with the LTE standards. The test results obtained from the measurement would be compared with the standard requirements to ascertain the acceptability of the proposed antenna. The fabricated array antenna is shown in Figure 5 (a), while a SMA connector bulkhead type is shown in Figure 5 (b). As earlier mentioned, the connector is attached at the ground element of antenna for feeding line connection. The radiation patterns of E-field and H-field, as well as antenna gain will be performed in these measurements.

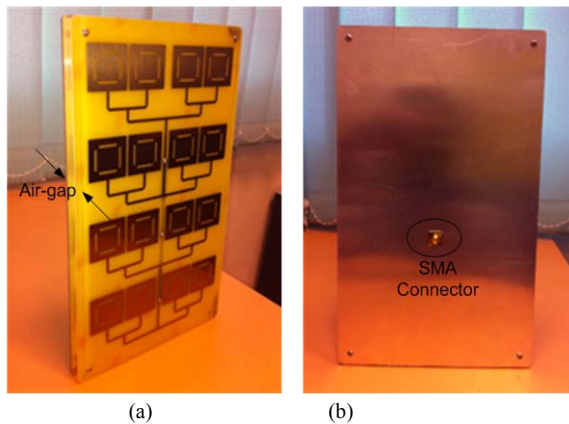


Fig. 5. Fabrications of (a) array antenna (b) ground element.

Figure 6 shows a block diagram of measurement setup of test antenna in anechoic chamber, a transmitter antenna used

to send radio power to be receiving by test antenna and system will record every signal strength values. In this antenna testing, system able to perform automatically to rotate test antenna as represent angle, record and plot a radiation pattern graph in a computer.

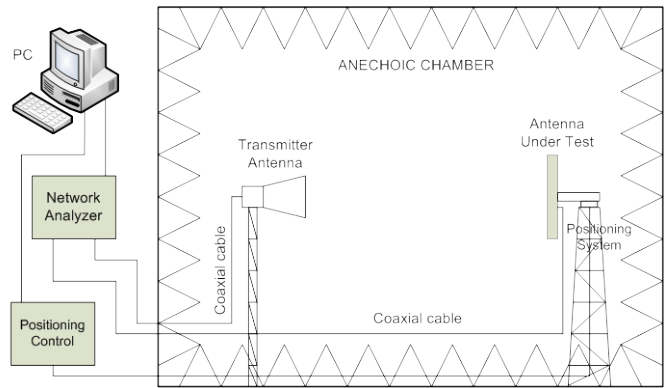


Fig. 6. Block diagram of measurement setup.

Figure 7 shows the test antenna being installed at test gauge in an anechoic chamber room. The test antenna is able to rotate in all directions. Referring to the common measurement setup, a transmitting antenna was used to transmit power to the proposed antenna, and sensitivity of the transmitted signal was recorded by the computer. The antenna performances were measured and tested in terms of both vertical and horizontal radiation patterns. Beside the radiation patterns, other antenna parameters such as gain, efficiency and impedance matching were also measured.

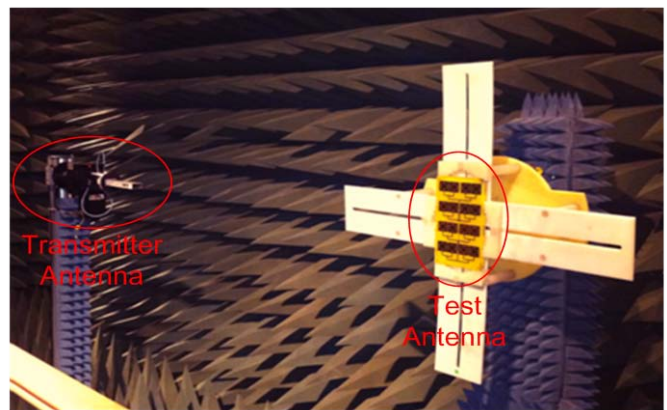


Fig. 7. Test antenna installed at test gauge in anechoic chamber room.

### IV. RESULTS AND DISCUSSION

Figure 8 shows basic simulation of single patch antenna and the results of minimum reflection coefficient. By introducing slots and air gap, a better response was obtained in terms of reflection coefficient and antenna gain. Besides, multiband response was also obtained. Some optimization exercises were performed to achieve acceptable response in

reflection coefficient as required and standardized. The air gap was adjusted from 5 mm to 15 mm. 5 samples were run in the parametric study, and the optimal value of air gap (10 mm) was chosen. The slot dimensions (width and length) were also adjusted, by optimization process, and again the optimal values were obtained (slot size is 2 mm by 16 mm). Arrangement of slots location is crucial, because poor results, as in reflection coefficient and radiation pattern, would be obtained if the slots are misplaced.

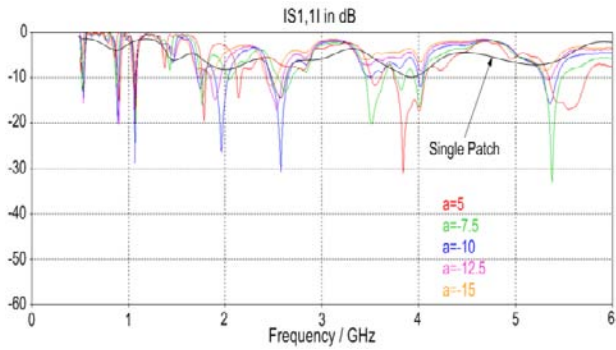


Fig. 8. The antenna array reflection coefficient.

Referring to optimization results presented in Figure 8, slots were introduced in antenna design, and the air gap between patch and ground element was 10 mm. The simulation and measurement results of the final stage of the proposed LTE transmitter antenna are shown in Figure 9. It is observed that both simulated and measured reflection coefficients are in good agreement.

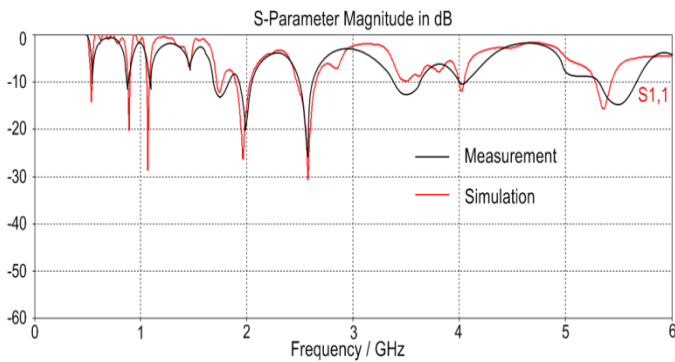


Fig. 9. Proposed array antenna reflection coefficient.

Both the simulation and measurement results have multiple responses, as shown in Figure 9. The most crucial response was observed at 2.6 GHz with maximum reflection coefficient being -34 dB. Other responses are at 900 MHz, 1.7 GHz to 2.7 GHz and 3.5 GHz. The response at 2.0 GHz is wideband, which covers both GSM 1800 and UMTS 2000 bands. The 2.4 GHz band can also be included for Wi-Fi application and the last one, 3.5 GHz covers the WiMAX band and measured results are highlighted in Figure 9. According to the measurement results, the maximum value of reflection coefficient is -26 dB. Note that the main response is also at 2.6

GHz, which is the same as simulation results. Other responses are scattered to some frequencies starting from 900 MHz until 3.5 GHz as shows in Figure 9. Overall, the proposed antenna has a wideband response of reflection coefficient, which makes it suitable for a variety of wireless technology applications.

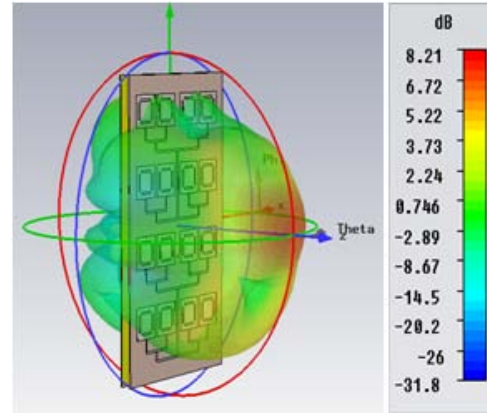
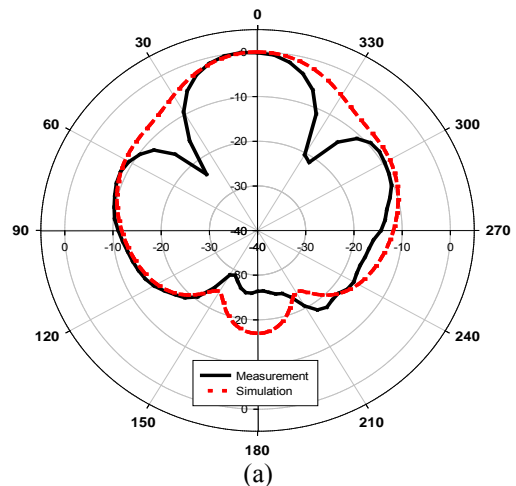
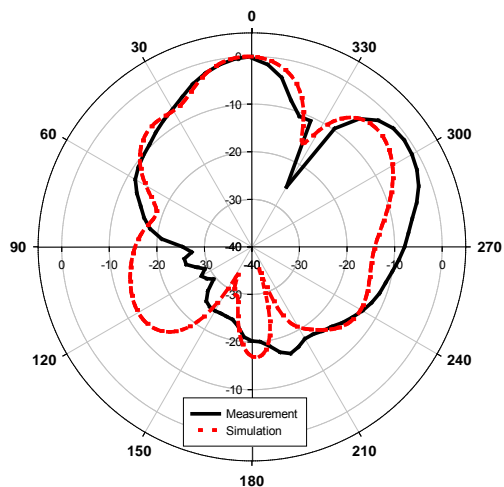


Fig. 10. Array LTE antenna radiation pattern in 3D.

The simulation results of radiation pattern in 3D are shown in Figure 10, where the beamwidth is  $44^\circ$  at -3 dB. The proposed antenna gain, as shown in Figure 10, is 8.21 dBi (maximum); which implies that it is applicable to use in BS due to its narrow beamwidth and high gain.

Measurements of radiation pattern have been done at the center frequency of 2.6 GHz as main response in reflection coefficient. The antenna polar radiation patterns of E-Field and H-Field are shown in Figures 11 (a) and (b) respectively. A directional beam is generated for the E-field at the antenna front, while a minor radiation was generated at the back. Both simulation and measurement results are in good agreement, though with minor shifting in the radiations. The proposed LTE antenna is able to radiate narrow beams forward with narrow beam and minor side lobe on left and right hand sides respectively.





(b)  
Fig. 11. Proposed antenna radiation patterns  
(a) E-field (b) H-field.

## V. CONCLUSION

A high gain antenna has been designed and measured in multiple bands for wireless communication system, especially for telecommunication in LTE band. The proposed antenna was simulated and fabricated using the standard FR4 material. The main response was observed at 2.6 GHz LTE band, with the maximum response being -34 dB. Other responses were also observed at GSM, UMTS, WLAN and WiMAX bands. The antenna also gives a wideband response from 1.7 GHz to 2.7 GHz while the reference of reflection coefficient is -6 dB. The antenna's radiation pattern has been measured in anechoic chamber, and both the simulation and measurement results are in good agreement. Overall, the proposed antenna is suitable for a transmitter due to its narrow beamwidth and high gain antenna.

## REFERENCES

- [1] L. Jaejin, *et al.*, "Miniature Long-Term Evolution (LTE) MIMO Ferrite Antenna," *Antennas and Wireless Propagation Letters, IEEE*, vol. 10, pp. 603-606, 2011.
- [2] R. Yu-Jiun, "Ceramic Based Small LTE MIMO Handset Antenna," *Antennas and Propagation, IEEE Transactions on*, vol. 61, pp. 934-938, 2013.
- [3] C. Yonghun, *et al.*, "Quad-Band Monopole Antenna Including LTE 700 MHz With Magneto-Dielectric Material," *Antennas and Wireless Propagation Letters, IEEE*, vol. 11, pp. 137-140, 2012.
- [4] K.-C. H. a. H.-S. K. Han-Byul Kim, "Cavity-backed Two-arm Spiral Antenna with a Ring-shaped Absorber for Partial Discharge Diagnosis," *Journal of Electrical Engineering & Technology*, vol. Vol.8, pp. 856-862, 2013.
- [5] Y. Jie-Bang and J. T. Bernhard, "Design of a MIMO Dielectric Resonator Antenna for LTE Femtocell Base Stations," *Antennas and Propagation, IEEE Transactions on*, vol. 60, pp. 438-444, 2012.
- [6] M. S. Sharawi, *et al.*, "Four-shaped 2 3 2 multi-standard compact multiple-input-multiple-output antenna system for long-term evolution mobile handsets," *Microwaves, Antennas & Propagation, IET*, vol. 6, pp. 685-696, 2012.
- [7] S. J. a. C.-H. Ahn, "Resistive and Inductive Loading Techniques on Microstrip Antenna for Wideband Application," *Journal of Electrical Engineering & Technology*, vol. Vol.6, pp. 693-696, 2011.
- [8] C. A. Balanis, *Antenna Theory: Analysis and Design*: John Wiley & Sons, 2005.
- [9] M. I. Sabran, *et al.*, "A Dual-Band Diamond-Shaped Antenna for RFID Application," *Antennas and Wireless Propagation Letters, IEEE*, vol. 10, pp. 979-982, 2011.

**Evizal** received his M.Eng. degree from Universiti Teknologi Malaysia, Malaysia in 2008. He is currently a PhD. student at the Wireless Communication Centre, Faculty of Electrical Engineering, Universiti Teknologi Malaysia. He have been worked in several companies that provide system solution in telecommunication and radio frequency identification, currently is continuing his research activity related to the wireless communication, radio frequency identification and wireless sensor network. His research interest is in the field of antenna design, smart system, RFID and sensor network.

**Eko Supriyanto** is a Professor and the Director of IJN-UTM Cardiovascular Engineering Centre, Universiti Teknologi Malaysia. He obtained his PhD in electronics engineering from University of Federal Armed Forces Germany, Hamburg. He worked as an academic staff at this university and a product development manager in a private company in Duesseldorf, Germany, before moved to Malaysia. He is a visiting professor at Ilmenau University of Technology, Germany and guest professor at Department of Radiology, Padjajaran University, Indonesia. His involvement in the computer application in medicine has been started since 1996 for the dialysis machine safety monitoring system. He has 15 patents in the area of biomedical and computer based products. He also obtained more than 24 awards for his achievement from international institutions. He has more than 120 publications in international journals and proceeding and author of few international books. He has been also active in WSEAS conferences since 2009 as an invited speaker, speaker for more than 36 papers and session chairman.

**TharekAbd Rahman** is a Professor at Faculty of Electrical Engineering (FKE), UniversitiTeknologi Malaysia (UTM). He obtained his B.Sc. in Electrical & Electronic Engineering from University of Strathclyde, U.K. in 1979, M.Sc. in Communication Engineering from UMIST Manchester, U.K. and PhD in Mobile Radio Communication Engineering from University of Bristol, U.K. in 1988. He is currently the Director of Wireless Communication Centre (WCC), FKE UTM. His research interests are radio propagation, antenna and RF design and indoor and outdoor wireless communication. HE also conducted various short courses related to mobile and satellite communication to the telecommunication industry and government body since 1990. He has teaching experience in the area of mobile radio, wireless communication system and satellite communication. He has published more than 120 papers related to wireless communication in national/international journal and conference.

**Sharul Kamal Abdul Rahim** obtained his first degree in Electrical Engineering in 1996 from University of Tennessee, U.S.A., M.Sc. in Engineering (Communication Engineering) from UniversitiTeknologi Malaysia (UTM) in 2001 and PhD in Wireless Communication System from University of Birmingham, U.K. in 2007. Currently, Dr. Sharul is an Associate Professor at Faculty of Electrical Engineering, UTM and an academic staff member of Wireless Communication Centre (WCC). His research interest is smart antenna on communication system. He is also a member of IEEE Malaysia section (MIEEE), member Board of Engineer Malaysia (MBEM), member of Institute of Engineer Malaysia (MIEM) and Eta Kappa Nu Chapter (International Electrical Engineering Honour Society, University of Tennessee). He has published a number of technical papers including journals and international conferences on rain attenuation and smart antennas.

# Hybrid FM Stereo Encoder using DDS

## for carrier and pilot signal generation

Manolis G.Tampouratzis <sup>1</sup>

<sup>1</sup>Department of Electronic Engineering  
Faculty of Applied Sciences  
Technological Educational Institute of Crete  
Romanou 3 Chalepa, 73133 Chania, Crete, Greece  
{tampouratzis@chania.teicrete.gr}

George A. Adamidis <sup>2</sup> (MSc in Electronic Physics)

<sup>2</sup> 1 E.K Heraklion – Technical School Laboratories  
Division of Electronics  
Itanou 40 Kipoupoli, 71307 Heraklion, Crete, Greece  
{sv7fid@yahoo.gr}

**Abstract** - An fm-stereo generator device uses a complex modulation system, according to F.C.C standards, to achieve a compatible mono/stereo system of broadcasting. There are several approaches for building an FM-Stereo generator. In the current implementation, we present an hybrid FM-stereo generator which uses both digital and analog techniques. We use Direct Digital Synthesis (DDS) module for carrier and pilot tone generation which gives unlimited control over phase shift and the ability to produce clean (purely sinusoids) signals with great frequency accuracy and stability. Reference clock frequency (or crystal choice) is not very critical in a high resolution DDS and signal generation becomes simple, robust and completely accurate. Finally using DDS also diminishes the necessity of using complex (high order) filtering.

**Keywords** – direct digital synthesis (DDS) , fm stereo generator, pilot signal, carrier, balanced modulator, fm stereo spectrum

### I. INTRODUCTION

FM stereo broadcasting was introduced during the early 1960s. The fm stereo system which approved for use by the F.C.C in the U.S and later was adopted worldwide uses a complex modulation system to achieve a compatible mono/stereo system of broadcasting. Essentially, the system performs the multiplexing of two audio signals and further combines them into a complex baseband signal that modulates the FM carrier.

The system works by broadcasting a sum of the left (L) and right (R) audio channels, a pilot tone of 19 kHz and a double sideband suppressed carrier (DSBSC) sub-channel that contains the difference of the two audio channels (see fig. 1).

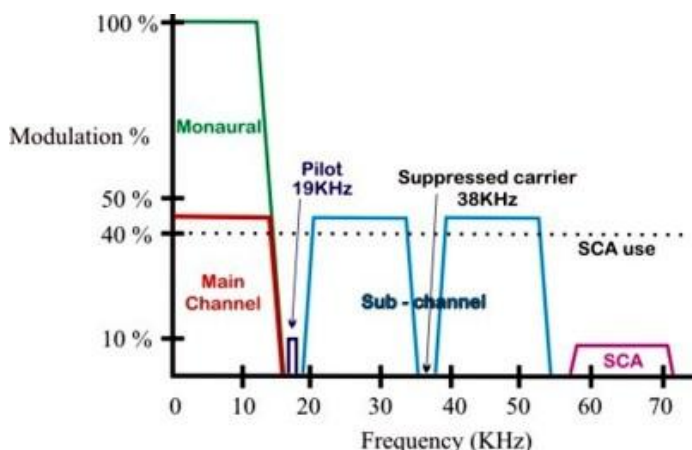


Fig. 1. The Composite FM-Stereo Spectrum

In a simple monaural system, the FM channel is frequency modulated  $\pm 75\text{KHz}$  with the audio information and the monaural audio signal occupies the 0-15KHz spectrum of the transmitted frequency spectrum (see figure 1). When stereo is transmitted, the same monaural signal (left plus right channel combined) remains in the 0-15KHz spectrum of the FM stereo signal and an additional sub – channel, centered at 38 KHz, which is a double sideband suppressed carrier signal (DSBSC) is additionally transmitted (see figure 1). This subcarrier is a left-subtracted-from-right (L-R) signal, which, when fed through a matrix with the monaural main channel on the receiver, forms the individual left and right channels. An additional pilot carrier signal at 19 KHz is also transmitted. The pilot signal is phase-cohered (synchronized), to the suppressed 38 KHz carrier.

In an FM-stereo system, the monaural signal is modulated about 45%, the sub channel and the pilot tone are modulated 45% and 10%, respectively, so that the total modulation for a stereo FM- station is 100%. In modern stations where some SCA or RDS/RBDS subcarriers are also used, the modulation of the main and the sub channel are furthermore reduced in order to the total modulation being kept less than 100% ( $\pm 75\text{KHz}$  deviation).

In an FM-stereo receiver the 19 KHz pilot signal indicates that the transmission is stereo. The receiver regenerates the 38 KHz carrier and then uses coherent detection for the sub-channel. Cohered detection only works when the carrier is present at the receiver. Of course, the receiver can not obtain the 38 KHz carrier from the baseband signal directly (because the carrier is suppressed during transmission). The carrier is actually obtained in the receiver from the 19 KHz pilot signal.

The composite FM-stereo signal that modulates the FM carrier in any FM-station is generated from a device which is often called as an “FM-Stereo Generator” or as an “FM-Stereo encoder”. The typical theoretical diagram of an FM-stereo generator is shown on fig. 2

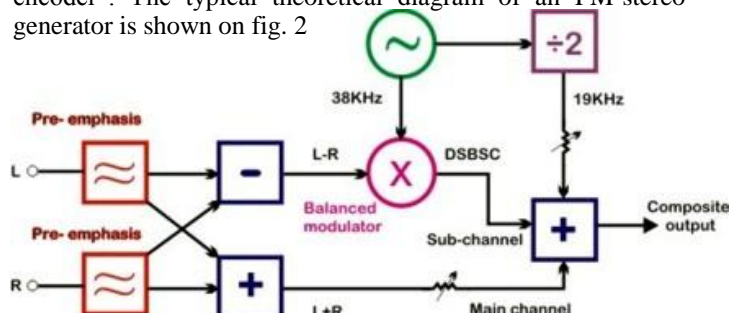


Fig. 2. Typical Theoretical diagram of an FM-Stereo Generator

With respect to figure 2, both the left and the right audio channels are pre-emphasized, just as normal monaural signal would be. Then, the left and the right signals are both added and subtracted on a matrix. The audio signals added (L+R), form the monaural signal which is the main channel. The subtracted signals (L-R) are modulated on a 38 KHz carrier, to form the sub-channel. A balanced modulator is used; because the system requires that the carrier at 38 KHz will be suppressed, leaving only the modulated audio information. The 38 KHz oscillator is divided by 2 to produce the coherent 19 KHz pilot signal. Both the carrier and the pilot signal should be purely harmonics (sinusoidal), otherwise some undesirable (spurious - noise) signals may appear in the composite spectrum.

The three components of the stereo signal, i.e. the main channel, the sub channel and the pilot tone, are combined at the proper ratios (45%, 45%, 10%), forming the composite output.

## II. THE HARDWARE – GENERATION OF CARRIER AND PILOT SIGNALS

Before the DDS era, producing “clean” carrier and pilot signals at 38 and 19 KHz respectively, considered to be a difficult task. An oscillator based on a crystal or a ceramic resonator, was often used. Since there are not many 38 KHz resonators available in the market, carrier and pilot signals often produced after some divisions (usually by 12 and 24) from a 455-456 KHz ceramic resonator. The dividers were digital circuits based on flip-flops and modulo-x counters and they produced pulsed signals rather than “clean” sinusoids. Some filters had to be used for suppressing the harmonics and producing the sinusoids. Unfortunately, the filters could not fully suppress harmonics and they also produced some phase shift (pilot tone was phase sifted in respect to the carrier). Harmonics induced undesirable noise (inmodulation products) and significantly degraded the composite stereo signal. The phase shifts also, made carrier regeneration and coherent detection of the sub-channel problematic at the receiver.

After 90s decade, many designers preferred to use an alternative approach for carrier and pilot generation. That approach based on using a microcontroller for producing the carrier rather using an ordinary oscillator. The pilot tone was still derived by using division by 2. That approach gives some flexibility on choosing the reference crystal, but microcontrollers and dividers produce pulsed (digital) signals and strict filtering was yet essential.

Fortunately, now (in 2014) we have DDS, which gives unlimited control over phase shift and the ability to produce clean (purely sinusoids) signals with great frequency accuracy and stability. Reference clock frequency (or crystal choice) is not very critical in a high resolution DDS and signal generation becomes simple, robust and completely accurate. Using a DDS also diminishes the necessity of using complex (high order) filtering.

Here’s a breakdown of the internal circuitry of a DDS device: its main components are a *phase accumulator*, a means of *phase-to-amplitude conversion* (often a sine look-up table), and a DAC. These blocks are represented in Figure 3.

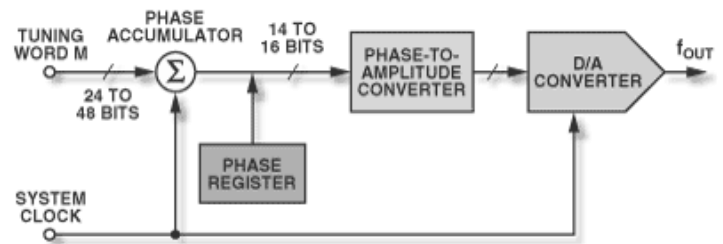


Fig. 3. Components of a direct digital synthesizer.

A DDS produces a sine wave at a given frequency. The frequency depends on two variables, the *reference-clock* frequency and the binary number programmed into the frequency register (*tuning word*).

The binary number in the frequency register provides the main input to the phase accumulator. If a sine look-up table is used, the phase accumulator computes a phase (angle) address for the look-up table, which outputs the digital value of amplitude—corresponding to the sine of that phase angle—to the DAC. The DAC, in turn, converts that number to a corresponding value of analog voltage or current. To generate a fixed-frequency sine wave, a constant value (the phase increment—which is determined by the binary number) is added to the phase accumulator with each clock cycle. If the phase increment is large, the phase accumulator will step quickly through the sine look-up table and thus generate a high frequency sine wave. If the phase increment is small, the phase accumulator will take many more steps, accordingly generating a slower waveform.

A phase-to-amplitude lookup table is used to convert the phase-accumulator’s instantaneous output value with unneeded less-significant bits eliminated by truncation into the sine-wave amplitude information that is presented to the (10-bit) D/A converter. The DDS architecture exploits the symmetrical nature of a sine wave and utilizes mapping logic to synthesize a complete sine wave from one-quarter-cycle of data from the phase accumulator. The phase-to- amplitude lookup table generates the remaining data by reading forward then back through the lookup table. This is shown pictorially in Figure 4.

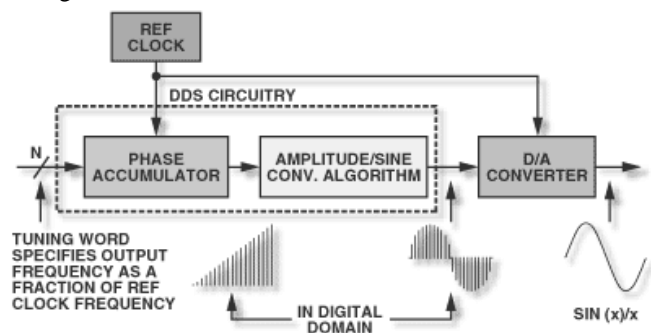


Fig.4 Signal flow through the DDS architecture.

A. The DDS Generator

In this fm-stereo encoder, we use Direct Digital Synthesis (DDS) for carrier and pilot tone generation. Referring to the DDS generator circuit section, the carrier and the pilot signal are generated from two AD9834 DDS ICs. Every AD9834 is used to generate a pure sinusoid signal. Both DDS IC's are kept synchronized by using the same reference clock, and their phase relationship can be digitally controlled. An 18F1220 PIC microcontroller is used to control the DDS generators through I2C signalling interface. The I2C interface is implemented as "bit-banging" on normal I/O.

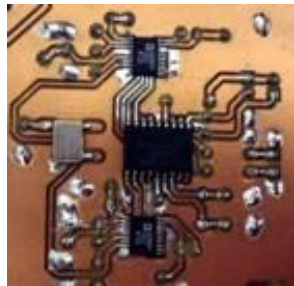
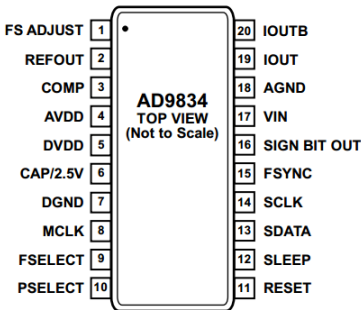
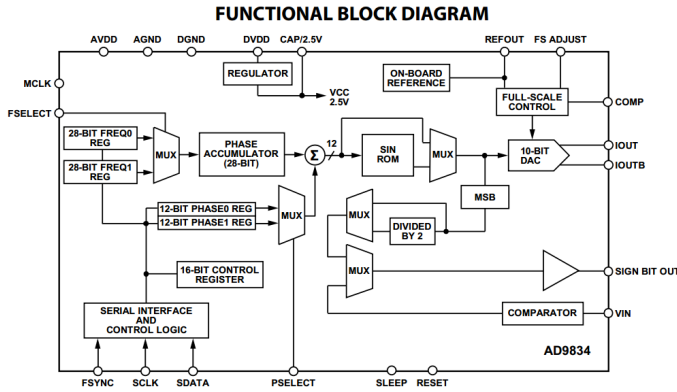


Photo 1. The DDS generator. The carrier and the pilot signal are generated from two AD9834 DDS IC's. An 18F1220 PIC microcontroller (at the center of the photo) is used to control the DDS generators. Both DDS ICs are kept synchronized by the same reference clock (seen at the left side of the photo).

Fig. 6. Functional Block Diagram AD9834 IC – Fig.7 . Pin Configuration AD9834 IC.

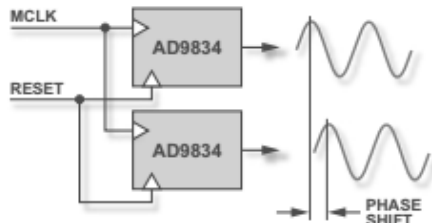


Fig.8 Multiple DDS AD9834s IC's Synchronous Mode Setup of DDS generation with the same reset pin and master reference clock

A reset, after power-up and prior to transferring any data to the DDS, sets the DDS output to a known phase, which serves as the common reference point that allows synchronization of multiple DDS devices. When new data is sent simultaneously to multiple DDS units, a coherent phase relationship can be maintained, and their relative phase offset can be predictably shifted by means of the phase-offset register.

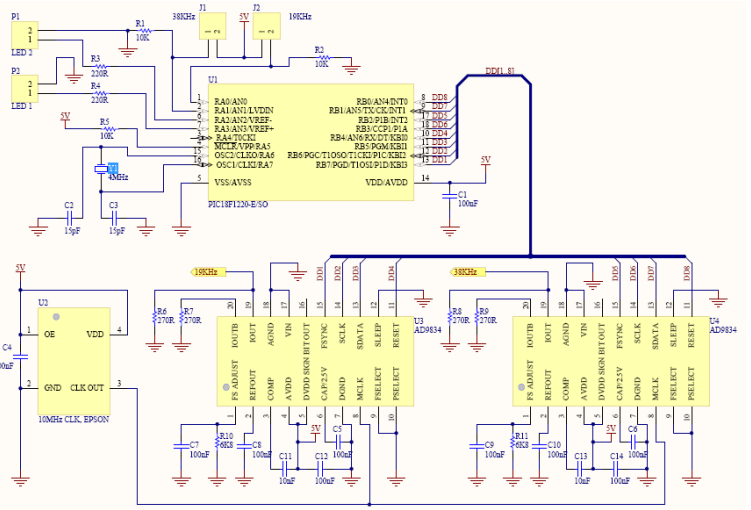


Fig. 5. DDS Section – Carrier and Pilot Tone Generation

The microcontroller is used to initiate the generators with the proper frequency and initial phase during start-up. It is also used to turn off or turn-on any generator at any moment, according to users will. User's commands are triggered from 2 external switches (J1 and J2). The AD9834 offers 28bits resolution over frequency and 12bits over phase control. By using a 10 MHz reference clock, we achieve frequency and phase accuracy of about 0.037 Hz ( $10\text{MHz}/2^{28}$ ) and 0.09 degrees ( $360/2^{12}$ ), respectively. The reference clock frequency is intentionally chosen to be high enough in order to can be easily filtered out from the carrier and the pilot signals, using only some simple R-C filters.

The source code is very simple. The microcontroller is used to initialize the DDS generators and then periodically checks J1 and J2, running on an infinite loop. J1 and J2 are used to turn on or off the carrier and (or) the pilot signal, thus enabling or disabling the stereo broadcasting.

Besides main, there are only very few other routines in the code. These routines are responsible for initializing and turning on or off the carrier and (or) the pilot signal according to user will and also implementing the I2C interface, for the DDS chips, as "bit-banging" on normal I/O. Finally, there is also another essential parameter, regarding the correct phase relationship between the carrier and the pilot signal. The correct phase relationship between those signals is essential for achieving maximum "stereo-separation". The optimum phase relationship has been adjusted once through code, and the stereo encoder was initially calibrated. Initial calibration constants are

kept on some code lines (marked by the “Phase shift value” comment). These code lines are located in the void Pilot\_on (void) routine and are used to set the initial phase parameter on the pilot tone DDS generator (please, refer to the AD9834’s datasheet for more details about the phase parameter).

**B. The Balanced Modulator**

Modern approach on building a low frequency balanced modulator tends to be the use of DSP. However, traditional analogue techniques are still used due to simplicity. After all, the composite fm-stereo signal is a completely analogue signal. We may live in the digital era, but we still using the old and good analogue fm-stereo.

Following the tradition, we use an analogue balanced modulator for the generation of the 38 KHz sub-channel. The modulator is based on the well known MC1496 IC, which is able to suppress the carrier for more than 60dbs.



*Photo 2. The modulator is based on the well known MC1496 IC, which is able to suppress the carrier for more than 60dbs*

Carrier suppression is defined as the ratio of each sideband output to carrier output for the carrier and signal voltage levels specified. The carrier suppression for the MC1496, is very dependent on the carrier input level. A low value of the carrier results in lower signal gain, hence lower carrier suppression. A higher than optimum carrier level results in unnecessary device and circuit carrier feed through, which again degrades the suppression figure. The optimum carrier level for optimum carrier suppression at carrier frequencies in the vicinity of 50 kHz, is about 60mVrms (170 mVp-p). This Optimum value is achieved threw R47 adjustment.

Besides the carrier input, there is also another input for the L-R audio channel. The balanced modulator accepts both signals and performs the multiplication (L-R)\*carrier in the time domain. A multiplication in the time domain is equivalent to frequency shifting in the frequency domain i.e. the L-R audio signal bandwidth is frequency shifted by the carrier frequency. This operation is better known as frequency mixing or shifting and the product of mixing is a DSB (Double Sided Band) signal.

There is a simple R-C filter at the carrier input of the modulator. This filter consists of the R56 and C48 and it is used to suppress the reference clock frequency (10 MHz). The DDS generates the carrier signal by using a 10bit DAC and the reference clock frequency is actually the sampling-frequency of the generated carrier signal. Since the reference clock frequency is much higher than the carrier frequency, it can be easily removed from the carrier signal by using a very simple

low-pass (1st order) filter. The simple low-pass filter produces some phase shift, which is cancelled, threw appropriate phase shifting of the DDS generator. (see Fig. 8)

While the R47 is used to adjust carrier level at the input of the modulator, the R51 potentiometer is used to adjust the carrier suppression level. Carrier suppression better than 60db, can be easily achieved threw the appropriate adjustment of R51. For best performance, the modulator is powered from two independent voltage sources; +12 and -8V, respectively. These are the recommended supply voltages, as described in the MC1496 datasheet.

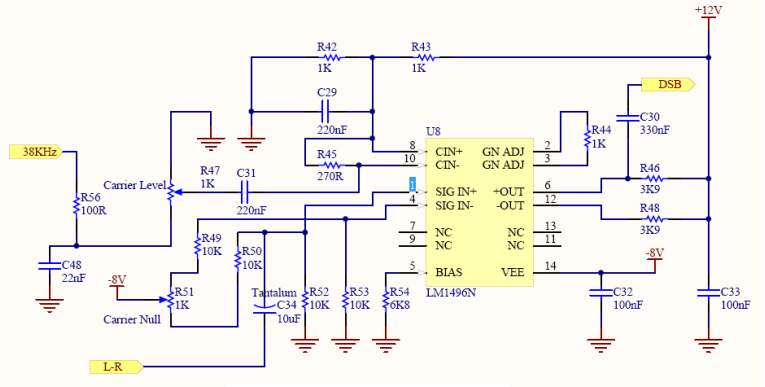


*Fig. 9. Balanced Modulator Section*

**C. The Op-Amp Matrix**

The heart of the fm-stereo generator is the matrix circuit. This circuit accepts the left and the right audio signals, the pilot tone and the DSBSC signal from the modulator, and performs the appropriate additions and subtractions, in order to produce the composite FM–stereo signal. The circuit also pre-emphasizes the left and right audio channel, just as normal monaural signal would be. The matrix circuit is based on operational amplifiers.

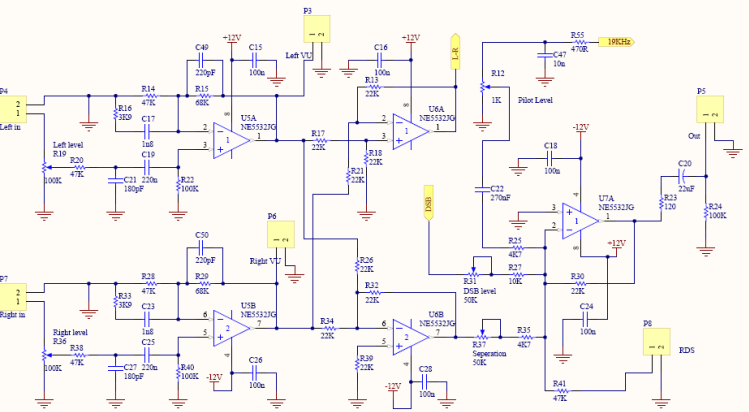


*Fig. 10. The matrix circuit is based on operational amplifiers*

Referring to the matrix electronic schematic, U5A and U5B are used to pre-emphasize the left and right audio channel. U5A, R14-16, R20, R22, C49, C19, C21 and U5B, R28-29, R33, R38, R40, C23, C27, C50 form pre-emphasis networks for the pre-emphasis of the left and the right audio channel, respectively. A pre-emphasis network is actually a high pass filter and pre-emphasis refers to a process designed to increase the magnitude of some higher frequencies with respect to the magnitude of lower frequencies. The pre-emphasis network characteristics are shown on figure 11.

In Europe, fm broadcasters use  $50\mu\text{s}$  pre-emphasis, while it is  $75\mu\text{s}$  in the U.S. Our FM-stereo generator prototype uses  $50\mu\text{s}$  pre-emphasis, because it was built and tested in Europe (Greece). However, it can be easily changed to  $75\mu\text{s}$  by simply changing C17 and C23 to  $2.7\text{nF}$ .

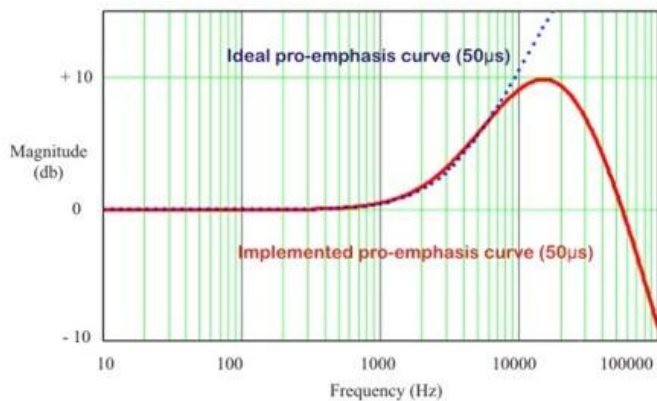


Fig. 11. Pre-emphasis network response curve.

Pre-emphasis on the transmitter and the minor operation (de-emphasis) on the receiver, are used to improve the overall signal-to-noise ratio by minimizing the adverse effects of the noise which is louder at higher frequencies. While the mirror operation is called de-emphasis, the system as a whole is called emphasis.

Fm channel is inherently very noisy and this makes emphasis very essential. Emphasis is also used in monaural broadcasting but it is even more important for FM-stereo. This is due to the fact that the fm-stereo signal carries most of its information in high frequencies located between 22 and 54 KHz and noise tends to be louder on those high frequencies. In the receiver side, decoding the stereo channel into left and right means that the noise is shifted down into the audible range.

Referring to the electronic schematic of the matrix again, U6A is used as a subtractor and produces the L-R signal, and U6B is used as an adder which produces the L+R sum. U7 is the final adder which accepts the pilot tone, the main channel and the sub-channel and produces the composite output. At this final stage, an additional input (P8) is providing for adding any SCA or RDS/RBDS subcarriers.

R12, R31 and R37 are used to adjust the proper ratios for combining the three components of the stereo signal, i.e. the pilot tone level, the sub channel level and the main channel level, respectively. Proper adjustment of these potentiometers is essential for the optimum operation of the stereo-encoder.

R55 and C47 are forming a low-pass filter for the pilot tone. This filter is used to eliminate the reference clock frequency (10 MHz), from the pilot signal. Besides the final output, which is P5, there are two other outputs. Those are the P3 and P6 outputs that are used to provide the left and the right audio signal, respectively, to an external VU-meter.

#### D. The Power Supply Unit

The fm-stereo generator uses a simple linear power supply unit which is based on 78XX and 79XX linear regulators.

Referring to the power supply electronic schematic, U9, U10, U11 and U12 are used to provide +5V, +12V, -12V and -8V respectively. The DDS generator section is powered from +5V only, while the modulator uses both +12V and -8V. The matrix section uses  $\pm 12\text{V}$  of symmetrical power supply.

### III. ASSEMBLY DETAILS

The prototype uses a double-sided printed circuit board with metal-plated holes. Excluding the AD9834 ICs, the PIC microcontroller and the clock generator, all other components are of through-hole type and they are placed on the top-side of the board. The microcontroller, the DDS ICs and the clock generator are placed on the bottom surface of the PCB. All resistors, except for those used on the matrix, are of 1/4W -5% type. In the matrix, I use low-tolerance 1% resistors and low tolerance (5%) capacitors.

The PIC microcontroller was programmed on board, using a MPLAB ICD 3 programmer from Microchip .

#### IV. CALIBRATING THE FM-STEREO ENCODER

The FM-generator, needs to be calibrated before use. The calibration process includes 5 steps as described below:

- **Adjust the carrier level at the input of the modulator.** Connect your oscilloscope on R47's tap. You should measure a 38 KHz sinus waveform, which is the carrier. Adjust R47, in order to get about 160mVp-p on its tap, in respect to ground.
- **Achieve carrier null by means of the bias trim potentiometer R51.** Turn R19 and R36 at zero scale (fully anticlockwise). Connect the oscilloscope on any pin of C30. Normally, you will get a 38 KHz sinus waveform on your oscilloscope. Adjust R51 in order to get 0Vp-p (null the carrier). Well, you will never get the absolute zero, but just some mVp-p (around 5mVp-p or less).
- **Combine main-channel and sub-channel at the proper ratio.** Set R36 at full-scale and R19 at zero-scale. Connect an audio signal generator on R audio input and apply a 1 KHz audio tone of about 0.6Vp-p. Short-circuit J2 to turn off the pilot tone. Measure the output of the generator using an oscilloscope. Adjust R37 and R31 in order to get a 3Vp-p signal, like the one shown on figure 12.

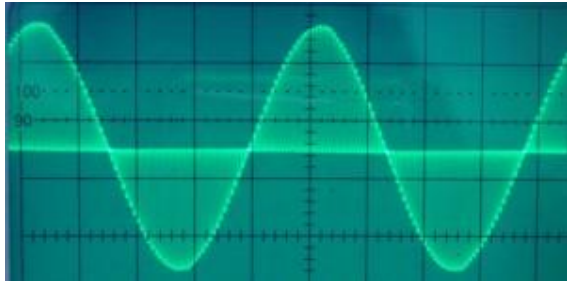


Fig. 12. Right Channel only: Used to Balance Bain and Sub-channel

- **Adjust the pilot level.** Set R19 and R36 at zero scale (full anticlockwise). Open J2 to turn on the pilot tone. Measure the output of the generator using an oscilloscope. You should measure a 19 KHz sine wave. Adjust R12 trimmer, in order to get about a 320mVp-p signal.
- **Adjust the VU-meter.** Set the left and right channel of the VU meter at full scale for 1Vp-p input. Adjust by using the trim potentiometers on VU-meter's board.

## V. CONCLUSION

In this hybrid FM-stereo generator we use mixed digital and analog techniques in order to achieve optimum performance. We use Direct Digital Synthesis (DDS) to produce clean (purely sinusoids) signals with great frequency accuracy and stability for carrier and pilot tone generation. Reference clock frequency (or crystal choice) is not very critical in a high resolution DDS and signal generation becomes simple, robust and completely accurate. Using a DDS also diminishes the necessity of using complex (high order) filtering and we use very simple low-pass, 1st order filtering. The simple low-pass filter produces some phase shift, which is cancelled, threw appropriate phase shifting of the DDS generators. The correct phase relationship between the carrier (38khz) and the pilot (19khz) tone is essential for achieving maximum stereo-separation, and the optimum phase relationship has been adjusted once, threw code, according to trial and error method.

## ACKNOWLEDGMENT

This project is a part of the production line of a new "Start – Up" small Business, "CircuitLib – Electronics". CircuitLib – Electronics was awarded with the First Prize at the "Secondary Student Contest on Business Plans and Innovative Ideas". The Student Contest on Business Plans and Innovative Ideas was organised from TEI of Crete, started on June of 2013 and ended on March of 2014.

## REFERENCES

- [1] Clifford B. Schrock, "FM Broadcast Measurements Using the Spectrum Analyzer" Application Note 26AX-3582-3 ,Techtronix 1981
- [2] Eva Murphy,Colm Slattery "Direct Digital Synthesis (DDS) Controls Waveforms in Test, Measurement, and Communications" Analog Dialogue39-08,August(2005)
- [3] PIC18F1220/1320 Data Sheet 18/20/28-Pin High-Performance, Enhanced Flash Microcontrollers with 10-Bit A/D and nanoWatt Technology 2007 Microchip Technology Inc.
- [4] MC1496,MC1496B Balanced Modulators/Demodulators Datasheet On Semiconductor Components Industries, LLC,October2006 ,- Rev. 10
- [5] Eva Murphy, Colm Slattery "All About Direct Digital Synthesis" Analog Dialogue 38-08, August (2004) <http://www.analog.com/library/analogDialogue/>
- [6] Data Sheet AD9834 - 20 mW Power, 2.3 V to 5.5 V,75 MHz Complete DDS, Analog Devices [www.analog.com](http://www.analog.com)
- [7] CircuitLib – The Electronics Circuit Library [www.circuitlib.com](http://www.circuitlib.com)

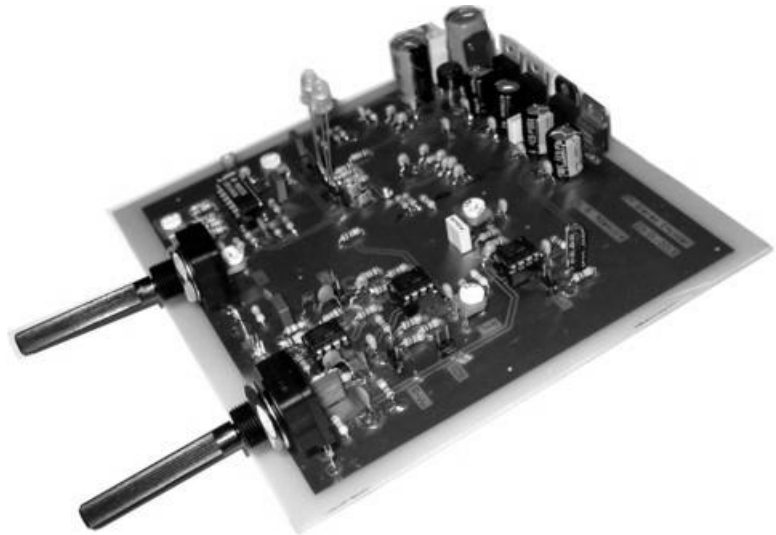


Photo3. The electronic board of the hybrid Fm Stereo Encoder

**Manolis G. Tambouratzis** was born in 1986 at Heraklion ,Crete Greece. In 2011 he graduated from the Department of Electronic Engineering, Faculty of Applied Sciences , TEI of Crete with grade " Very Good" 7.32 / 10 drawing up his internship at the Technical Department of the Hellenic Telecommunications Organisation ( OTE ). He holds a professional License "Radioelectronics Cat B" and a degree in Electronic Communications - Radio-Amateurs ' Cat 1 ' with the distinctive code "SV9RGJ" from 2012. His interests are focus on Electronic Circuits Technology for Telecommunication Applications (RF Systems Design), Wireless Telecommunications Systems Technology and Electromagnetic Fields Measurements from Base Stations Transmitters . He is a member of scientific societies IEEE (Student Branch - TEIoC), FITCE and EETEM and has attended numerous training seminars in the fields of Communications & Information Technology in recent years.

**George A. Adamidis** - Physicist and Electronic Engineer.  
 Studies: Physics (2000), MSc in Electronic Physics (2002), from Aristotle University of Thessaloniki, Greece.  
 Current occupation: High – School teacher in Physics & Electronics, Assistant Researcher in the Centre of Technological Research of Crete.  
 Research interests: Embedded Systems, RF technology, Smart Antennas, Antenna design and Electromagnetic Compatibility.

# Bias driver of the Mach-Zehnder intensity electro-optic modulator, based on harmonic analysis

J. Svarny

**Abstract**—An adjustment of operating point significantly affects performance of the analog intensity modulator of Mach-Zehnder type. Especially, the harmonic distortion figure induced by the modulator itself must be kept at minimum by the set-up. The requirement is vital for a successful optical link design. The paper deals with design and implementation of a specialized circuit - the bias driver for extremely precise and swift retrieval of desired operating point of the modulator. The bias driver works on principle of suppression of second harmonic component detected at the modulator output while the modulator is excited with a low-frequency harmonic signal.

**Keywords**—Electro-optic modulation, bias driver, Mach-Zehnder modulator, modulator drift, harmonic analysis

## I. INTRODUCTION

THE integrated intensity Mach-Zehnder modulator (MZM) represents a powerful mean of external modulation of optical signal. By the MZM an intensity of steady laser beam can be modulated from DC up to GHz range. The device can be described as a two-arm interferometer integrated in LiNbO<sub>3</sub> substrate. It consists of two waveguides linked together with input and output optical Y junctions. The system of electrodes is positioned in tight proximity to the waveguides and arranged in an appropriate configuration to ensure effective generation of electrical field in waveguides region.

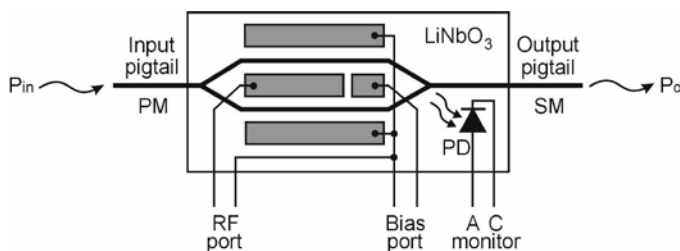


Fig.1 Configuration of integrated intensity MZM

This research has been supported by the European Regional Development Fund and the Ministry of Education, Youth and Sports of the Czech Republic under the Regional Innovation Centre for Electrical Engineering (RICE), project No. CZ.1.05/2.1.00/03.0094.

J. Svarny is with the Department of Technologies and Measurements, Faculty of Electrical Engineering / RICE, University of West Bohemia, Pilsen, Czech Republic (phone: +420-377-634-559; fax: +420-377-634-502; e-mail: svarny@ket.zcu.cz).

Commercially available modulators are usually equipped with separated radiofrequency (RF) port and bias port (Fig.1). The RF port works as balanced "π" input for broadband modulating signal. The bias port serves as an input of driving voltage for the desired operating point set-up.

A voltage applied to the electrical input (either the bias one or the modulating one) modifies the refractive index of the LiNbO<sub>3</sub> substrate. It leads to the phase shift between the light waves moving through the particular waveguides. A zero phase shift between the waves yields constructive recombination and thus maximum intensity at the output pigtail. In case the phase opposition is induced, the recombination is destructive. Minimum of radiation leaves the modulator output pigtail then. Gradual transition between these two extremes allows smooth change of output optical power. Considering excitation of only one electrical port of the MZM at the time (the bias port for instance), the idealized transfer chart can be described by cosine function (1).

$$P_o = \frac{P_{in}\alpha}{2} \left[ 1 + \cos\left(\frac{V_{in}}{V_{\pi}}\pi\right) \right], \quad (1)$$

where  $P_o$  and  $P_{in}$  is output and input optical power respectively,  $V_{in}$  is input voltage of bias port,  $V_{\pi}$  is half-wave voltage of bias port and  $\alpha$  is insertion loss of the modulator. The corresponding transfer chart is depicted by black curve in Fig.2.

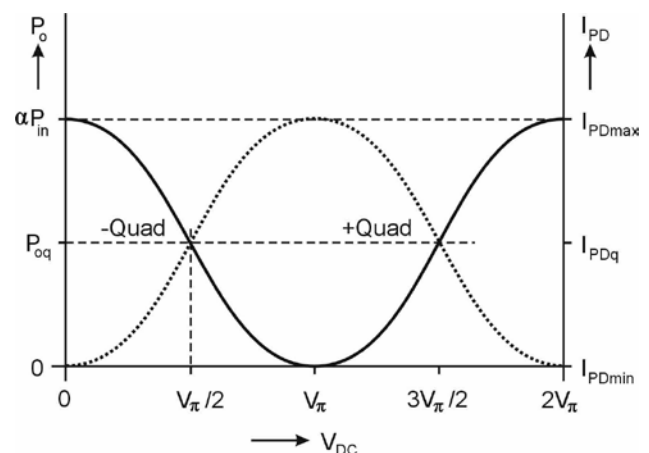


Fig.2 MZM transfer chart and inner PD chart

Some manufacturers equip their modulators with auxiliary - in the substrate buried photodiode (PD). The PD is positioned just behind the output Y junction. Advantageously, the PD signal can be used to monitor the modulator output excluding necessity to use an external tap-coupler. In case of the PowerLog™ FA20 type modulator (Fig.3) by Avanex Inc. [1] that has been used in the presented application the PD works in radiating mode. That means the PD current (dotted curve in Fig.2) is inversely proportional to the output optical power.



Fig.3 PowerLog™ FA20 analog intensity modulator

## II. THE ISSUE SPECIFICATION

One of the major problems linked with practical application of Mach-Zehnder intensity modulators is drift of the operating point. It is caused by pyro-electric, photorefractive and photoconductive phenomena that take action simultaneously in the LiNbO<sub>3</sub> substrate. The movement of the transfer charts due to the drift (gray curves in Fig.4) produces bias error and cause the modulator performance deterioration. That is why the operating point can not be fixed by steady set-up. To achieve desired performance of the device the operating point set-up must be adjustable and well controlled.

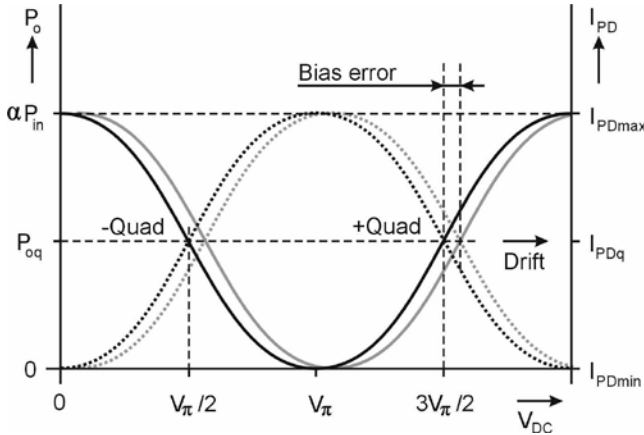


Fig.4 Bias error arise due to the drift

In case of long-period working systems the operating point is preferably stabilized with some kind of automatic feedback controller. There are lots of various techniques to control the operating point [2], [3]. Unfortunately, all the automatic feedback control techniques bring some drawbacks and limitations. Usually, the operating point is stabilized on expense of disturbance of transmitted signal. The stabilization precision and level of disturbance induced by an auxiliary signal or signals have to be well balanced and are subjects of compromise then. On the other hand, in case of short-period

working analog optical links (i.e. when the measurement or transmission process is expected to be finished within several minutes after the set-up), the initial set-up precision seems to be more important. The automatic feedback control is not necessary then. Alternatively, it can be substituted by a from time to time manual adjustment [4]. Nevertheless, the MZM operating point adjustment must be adequately swift, effective and precise.

## III. METHOD

In analog optical links the harmonic distortion figure is the major criterion for the design evaluation. Naturally, the lowest possible harmonic distortion of the link is usually desired. The modulator operating point should be set in accordance with this requirement.

Let us suppose the modulator excited by the bias port only. Simultaneously, the RF port is left open. Provided the input bias voltage is formed by DC component  $V_{DC}$  and superposed AC harmonic component with  $V_{AC}$  amplitude (2), the equation (1) can be rewritten to form (3).

$$V_{in} = V_{DC} + V_{AC} \sin(\omega_{AC}t), \quad (2)$$

$$\begin{aligned} P_o &= \frac{\alpha P_{in}}{2} \left\{ 1 + \cos \left[ \frac{V_{DC}}{V_\pi} \pi + \frac{V_{AC}}{V_\pi} \pi \sin(\omega_{AC}t) \right] \right\} = \\ &= \frac{\alpha P_{in}}{2} + \frac{\alpha P_{in}}{2} \cos \left( \frac{V_{DC}}{V_\pi} \pi \right) \cos \left[ \frac{V_{AC}}{V_\pi} \pi \sin(\omega_{AC}t) \right] - \\ &\quad - \frac{\alpha P_{in}}{2} \sin \left( \frac{V_{DC}}{V_\pi} \pi \right) \sin \left[ \frac{V_{AC}}{V_\pi} \pi \sin(\omega_{AC}t) \right], \quad (3) \end{aligned}$$

The equation (3) can be rearranged by means of formulas (4) and (5).

$$\cos(x \sin y) = J_0(x) + 2 \sum_{k=1}^{\infty} J_{2k}(x) \cos(2ky), \quad (4)$$

$$\sin(x \sin y) = 2 \sum_{k=1}^{\infty} J_{2k-1}(x) \sin[(2k-1)y], \quad (5)$$

where  $J_k(x)$  is a  $k^{\text{th}}$  order Bessel function. Using the Bessel functions the output optical power (3) can be rewritten to reveal particular harmonics (6).

$$\begin{aligned} P_o &= \frac{\alpha P_{in}}{2} + \frac{\alpha P_{in}}{2} \cos \left( \frac{V_{DC}}{V_\pi} \pi \right) J_0 \left( \frac{V_{AC}}{V_\pi} \pi \right) + \\ &+ \alpha P_{in} \cos \left( \frac{V_{DC}}{V_\pi} \pi \right) \sum_{k=1}^{\infty} J_{2k} \left( \frac{V_{AC}}{V_\pi} \pi \right) \cos(2k\omega_{AC}t) - \\ &- \alpha P_{in} \sin \left( \frac{V_{DC}}{V_\pi} \pi \right) \sum_{k=1}^{\infty} J_{2k-1} \left( \frac{V_{AC}}{V_\pi} \pi \right) \sin[(2k-1)\omega_{AC}t] \quad (6) \end{aligned}$$

Similar result can be found in [5] for instance. From the equation (6) formulas for computing the amplitude level of particular  $n^{\text{th}}$  harmonic component (7), (8) can be extracted.

$$P_{o-n-odd} = \left| \alpha P_{in} \sin\left(\frac{V_{DC}}{V_{\pi}} \pi\right) J_n\left(\frac{V_{AC}}{V_{\pi}} \pi\right) \right|, \quad (7)$$

where  
 $n \in \langle 1, 3, 5, \dots \rangle$

$$P_{o-n-even} = \left| \alpha P_{in} \cos\left(\frac{V_{DC}}{V_{\pi}} \pi\right) J_n\left(\frac{V_{AC}}{V_{\pi}} \pi\right) \right|, \quad (8)$$

where  
 $n \in \langle 2, 4, 6, \dots \rangle$ .

Presence of higher harmonic components in the spectrum of the output optical power reveals level of harmonic distortion. Total harmonic distortion is defined as a ratio of sum of higher harmonic components  $P_{on}$  to the fundamental  $P_{o1}$  (9).

$$THD = \frac{\sum_{n=2}^{\infty} P_{on}}{P_{o1}} \cdot 100 = \frac{\sum_{n=1}^{\infty} \left| J_{2n-1}\left(\frac{V_{AC}}{V_{\pi}} \pi\right) \right|}{\left| J_1\left(\frac{V_{AC}}{V_{\pi}} \pi\right) \right|} 100 + \frac{\sum_{n=1}^{\infty} \left| \cos\left(\frac{V_{DC}}{V_{\pi}} \pi\right) J_{2n}\left(\frac{V_{AC}}{V_{\pi}} \pi\right) \right|}{\left| \sin\left(\frac{V_{DC}}{V_{\pi}} \pi\right) J_1\left(\frac{V_{AC}}{V_{\pi}} \pi\right) \right|} 100 \quad (9)$$

Using the equation (9) the figure of harmonic distortion for given operating point set-up ( $V_{DC}$  voltage) and amplitude of modulating voltage ( $V_{AC}$ ) can be calculated.

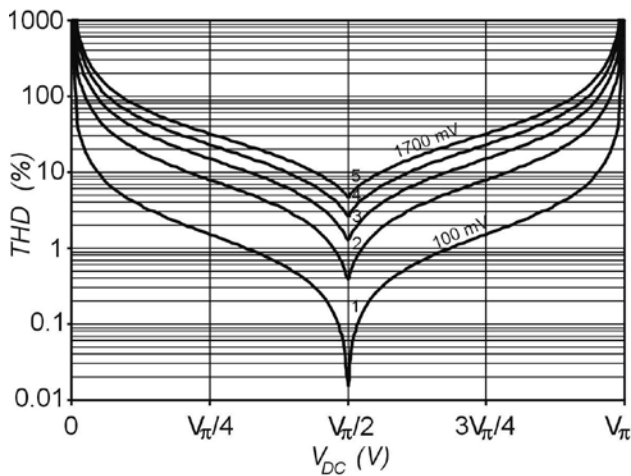


Fig.5 The MZM total harmonic distortion as a function of bias voltage  $V_{DC}$  (amplitude  $V_{AC}$  is a curve parameter)

Particular curves (1..5) in Fig.5 refer to fixed modulating voltages  $V_{AC}$  ranging from 100 mV up to 1700 mV with 400 mV steps. In spite of magnitude of  $V_{AC}$  the lowest harmonic distortion is evidently achieved at quadrature operating point  $V_{DC} = V_{\pi}/2$  (see Fig.5) and integral multiples of  $V_{\pi}/2$  (due to periodicity of transfer function (1)). Using (7) and (8) the dependency of the particular harmonic components as function of DC bias voltage can be depicted as well. The amplitudes of the first and second harmonics were depicted in Fig.6.

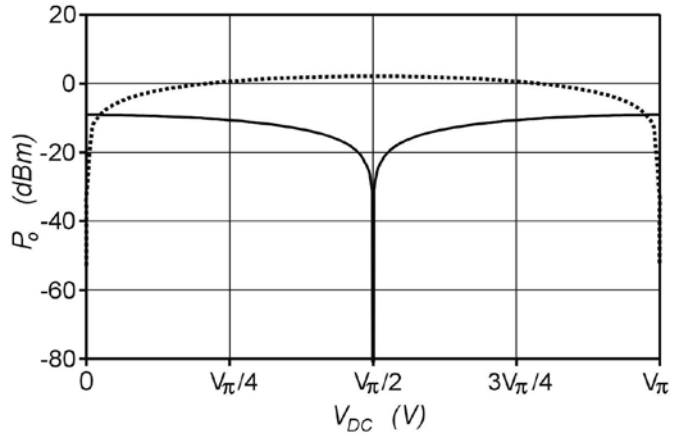


Fig.6 Dependency of 1<sup>st</sup> (dotted curve) and 2<sup>nd</sup> (solid curve) harmonics on DC bias  $V_{DC}$

The dependency of amplitudes of higher odd harmonics would demonstrate the same shape as the fundamental but with higher attenuation. Similarly, all the higher even harmonics would copy the shape of the 2<sup>nd</sup> harmonic component but with diminished amplitude. Fig.6 was depicted for input optical power  $P_{in} = 21.68$  mW, the modulator insertion loss  $\alpha = 0.5$  and modulating voltage  $V_{AC} = 500$  mV.

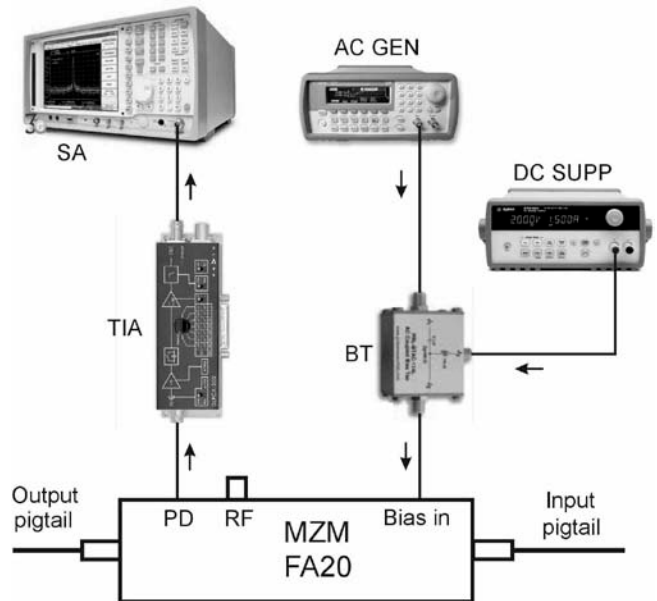


Fig.7 The system for the MZM operating point adjustment built-up of laboratory instrumentation

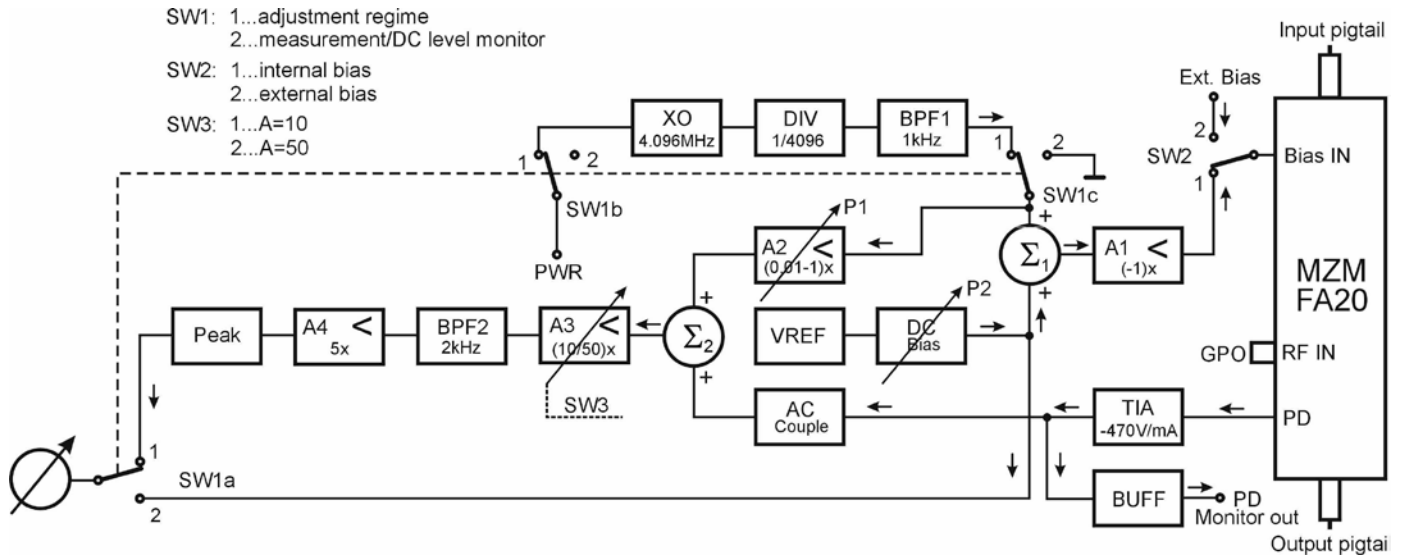


Fig.8 Block diagram of the designed bias driver

Magnitude of 2<sup>nd</sup> harmonic component reaches its minimum just at the desired quadrature point. If the quadrature point is reached the second harmonic virtually fades out. At the same time the total harmonic distortion reaches its minimum as well. Moreover, the second harmonic reflects the position of the operating point around the quadrature region with an extraordinary sensitivity. It brings the possibility to use the minimum of the 2<sup>nd</sup> harmonic component as an indicator of proper set-up. The proposed concept can be implemented using regular laboratory instrumentation (Fig.7).

Unfortunately, whole set of special purpose and fine laboratory instruments have to be used to build the system for operating point set-up. To generate pure enough harmonic signal a low THD function generator (AC GEN) is essential. DC power supply (DC SUPP) generating the bias voltage must be well stabilized and equipped with fine voltage regulation. Low frequency bias-tee (BT) must be used to couple DC and AC signals in front of the modulator bias input port. At the receiving side a trans-impedance amplifier (TIA) have to be used to convert the inner PD current to measurable voltage. Finally a spectrum analyzer (SA) to discover magnitude of 2<sup>nd</sup> harmonic component is necessary.

#### IV. THE BIAS DRIVER DESIGN

The 2<sup>nd</sup> harmonic component is the only part of the output spectrum that has to be tracked in order to achieve desired operating point. That is why, the rather clumsy and over-equipped concept proposed in Fig.7 can be reduced to single circuit based on proper filtration and amplification of input and output signals. The block diagram of proposed bias driver is depicted in Fig.8.

The bias input port of the modulator is excited by manually adjustable DC level and superimposed harmonic signal. The harmonic signal should have steady amplitude and frequency as well. Simultaneously, the inner PD of the MZM detects output signal of the modulator. Following circuitry analyses

presence of 2<sup>nd</sup> harmonic component in the spectrum of detected signal.

The DC level is generated by a voltage reference (VREF) and is manually adjustable by a block equipped with a precise 10-turns potentiometer (DC Bias). The AC part generates 1 kHz sinus signal with amplitude of 500 mV. Purity of the AC signal and especially absence of the 2<sup>nd</sup> harmonic component is important. That is why there was used method based on filtration of square wave signal. The crystal oscillator (XO) generates 4.096 MHz digital signal that is divided and shaped by a binary 12-stage ripple counter 74HC4040 (DIV). By the theory the spectrum of the generated square wave consists of odd harmonics only (Fig.9) and the problem of absence of second harmonic is resolved spontaneously then.

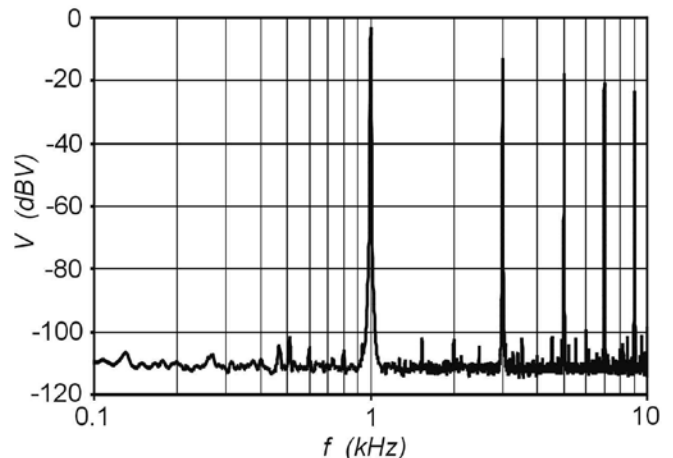


Fig.9 Spectrum of signal at the output of DIV block

The higher odd harmonics cut-off is done by narrow band-pass filter BPF1 with center frequency of 1 kHz. Various types of filters were tested there. Finally, there was chosen two-stage solution of 4<sup>th</sup> order filter using Butterworth approximation, Fig.10. To build-up the filter prototype a low distortion LMC6484 operational amplifiers were used.

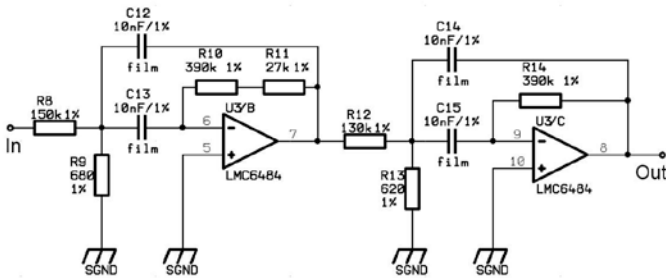


Fig.10 BPF1 filter tuned to 1 kHz

The filter demonstrates sufficient performance on expense of two operational amplifiers only. Suppression of more than 53 dB for 3<sup>rd</sup> harmonic (the nearest higher harmonic) and 65 dB for 5<sup>th</sup> harmonic is guaranteed by the filter (Fig.11).

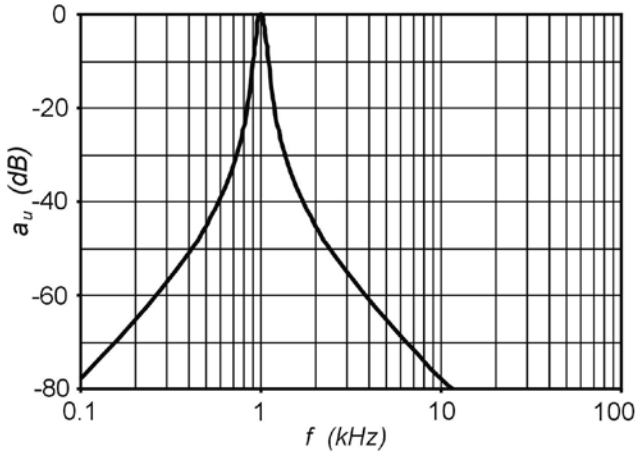


Fig.11 Frequency response of BPF1 filter tuned to 1 kHz

Spectrum of the AC signal at the output of BPF1 proves sufficient purity of the signal. The 3<sup>rd</sup> harmonic is suppressed to 65 dB below the fundamental. The 5<sup>th</sup> harmonic is suppressed to 81 dB below the fundamental. Nevertheless, for the needs of application the suppression of 2<sup>nd</sup> harmonic is most important. The 2<sup>nd</sup> harmonic is 84 dB below the fundamental.

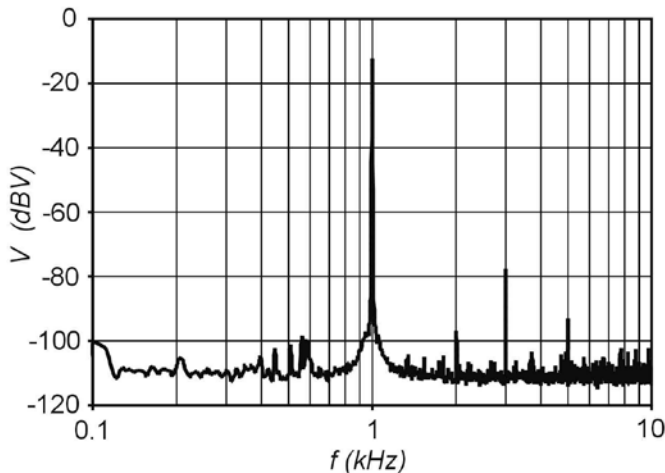


Fig.12 Spectrum of the generated AC signal delivered to the bias port input

The signal from BPF1 block is mixed with DC level from the DC Bias block by means of summing amplifier  $\Sigma_1$ . The following stage gives a 180° phase shift to the signal which is important for analysis of the signal detected by the inner photodiode PD.

The measuring chain starting with PD up to the deflective instrument was designed in order to analyze presence of 2<sup>nd</sup> harmonic in the output spectrum and visualize its magnitude. The inner PD of the MZM generates current that is inversely proportional to the output optical power of the modulator. This signal is converted to the voltage by means of trans-impedance amplifier (TIA). Gain of the TIA was experimentally set to -470 V/mA. The DC level of the TIA output signal is excluded by amplifier with integrating feedback (AC couple stage). To derive 2<sup>nd</sup> harmonic from the spectrum there is necessary to eliminate fundamental in received spectrum at first. This is carried out by summing amplifier  $\Sigma_2$ . Due to overall phase shift of the received signal the summing amplifier  $\Sigma_2$  works as a difference amplifier. At the output of the  $\Sigma_2$  the difference between the received AC signal and by the A2 stage attenuated exciting signal can be found. Actually, there have to be set-up level of attenuation of exciting signal leading to substantial decimation of fundamental at the output of  $\Sigma_2$  block. The point is clearly indicated by noticeable decrease of deflection of the measuring instrument. The signal is amplified by the A3 amplifier and filtered by BPF2 filter then. The BPF2 stage forms a band-pass filter tuned to 2<sup>nd</sup> harmonic regard to the exciting signal. The filter was designed similarly to BPF1 (4<sup>th</sup> order filter using Butterworth approximation implemented by LMC6484 operational amplifiers).

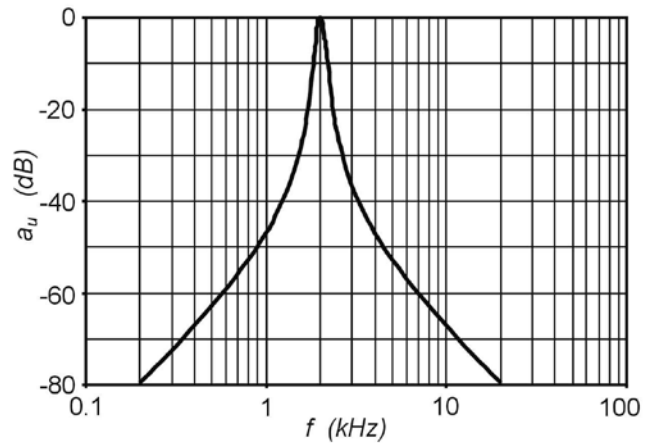


Fig.13 Frequency response of BPF2 filter tuned to 2 kHz

After an additional amplification in A4 block the signal is detected by a peak detector (Peak) and sent to the deflective measuring instrument.

## V. THE DRIVER CONTROL

Operation of the bias driver is controlled by five front-panel elements (two 10-turns potentiometers P1, P2 plus 3 switches SW1, SW2, SW3) and single needle indicator only. For set-up

regime the SW1 and SW2 have to be in position 1. The oscillator generates 1 kHz signal and the indicator measures magnitude of 2<sup>nd</sup> harmonic of PD signal. In case of considerable displacement of operating point (the indicator is saturated) the SW3 has to be switched to position 1 to allow coarse tuning at first. By adjustment of P1 element the fundamental rejection in received signal has to be achieved. The state is indicated by drop of the deflection of the indicator. In the next step the deflection has to be minimized again using P2 element. Subsequently, the gain of the A3 amplifier has to be increased (SW3 to position 2) to allow fine tuning and both of the previous steps should be repeated. Finally, the generator should be switched off (SW1 to position 2) to leave the adjustment regime and let the modulator bias port to be driven by the found DC level only. Simultaneously the indicator is automatically switched over to visualize the DC residuum.

## VI. RESULTS

The designed bias driver was implemented to the FA20 modulator forming a vital part of the specialized electro-optic modulating unit [6]. The operation correctness of the circuit was tested and verified by a spectrum analyzer. The modulator was excited by thermally stabilized laser source [7] and adjusted to the quadrature point by the designed bias driver. Subsequently, the spectrum of the signal at the BUFF stage output (PD Monitor Out) was measured. The measurements revealed -100.4 dBV magnitude of 2<sup>nd</sup> harmonic (i.e. -83.7 dB below the fundamental). By the driver found point is represented by minimum in Fig.14. By deliberate displacement of DC bias using gradual steps of  $\pm 10$  mV (P2) the rest of dependency depicted in Fig.14 was measured.

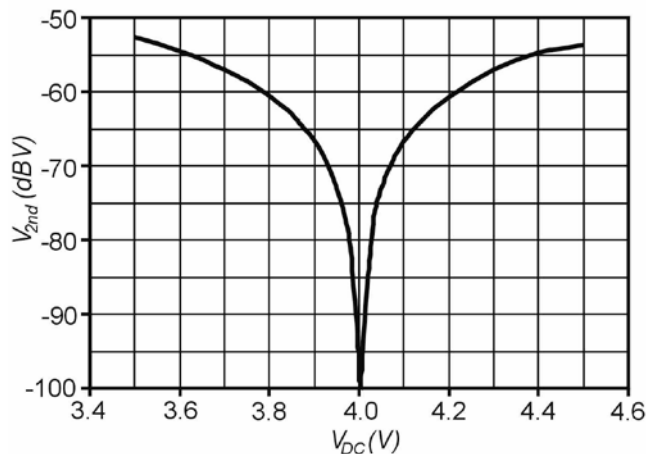


Fig.14 Dependency of 2<sup>nd</sup> harmonic measured at the PD Monitor Out in the proximity of detected operating point

The measured values were extracted from spectrums measured for particular DC voltages. The measurements of spectrums were carried out by means of low-frequency B&K Pulse<sup>TM</sup> analyzer working under the following set-up: DC-25.6 kHz span, 4 Hz step, averaging 200, Hanning window. Fig.14 proves that the bias driver is able to set-up the quadrature point with resolution of several mV.

## VII. CONCLUSION

The design of the bias driver and its verification confirmed the theoretical hypothesis. Harmonics performance of the MZM can be used as useful indicator of proper adjustment of the modulator operating point. The designed circuit represents a compact and effective alternative to rather clumsy and over-equipped concept based on conventional and costly laboratory instrumentation. Moreover, in comparison to the laboratory instrumentation based solution the designed bias voltage driver allows operative, safe and extremely precise adjustment of the operating point at the same time.

## REFERENCES

- [1] Avanex, Inc., "PowerLog<sup>TM</sup> FA-20, 20 GHz Analog Intensity Modulator with Small Form Factor", Data-Sheet, <http://www.avanex.com>
- [2] E. Ackerman, H. Roussel, C. H. Cox, "Bias Controllers for External Modulators in Fiber-Optic Systems", Photonic Systems, Inc. 2001, <http://www.photonicsinc.com>
- [3] A. Chen, E. J. Murphy, "Broadband optical Modulators - Science, Technology and Applications", CRC Press, 2012.
- [4] J. Svarny, "Analysis of quadrature bias point drift of Mach-Zehnder electro-optic modulator", In. Proc. BEC2010, Tallinn, Estonia, 2010, pp. 231-234.
- [5] A. Hilt, "Microwave harmonic generation in fiber-optical links", Journal of Telecommunications and Information Technology, vol.1/2002, pp. 22-28.
- [6] J. Svarny, "Specialized compact external electro-optic modulating unit", In. Proc. TSP2013, Rome, Italy, 2013, pp. 227-230.
- [7] J. Svarny, "Highly stable 20 mW infrared laser source", In. Proc. Applied Electronics 2009, Pilsen, Czech Republic, 2009, pp. 249-252.

# Synthesis and Analysis of a Memristor Frequency Converter for Radio-receiver

Valeri Mladenov, Stoyan Kirilov

**Abstract** — The main purpose of the present investigation is to propose a new memristor application in a frequency converter for a radio-receiving set. A modified memristor model with nonlinear ionic drift is presented and an appropriate PSpice library element is created. Then the present memristor model is used for constructing a frequency mixer. For avoiding nonlinear distortions the memristor element works in a soft-switching mode. A computer simulation of the memristor frequency converter is realized with the use of amplitude-modulated testing signal. For producing a voltage needed for the operation of the intermediate frequency amplifier a heterodyne is also applied in the circuit. The results obtained confirm the efficiency of the memristor frequency-converting circuit.

**Keywords** — memristor, frequency converter, nonlinear ionic drift, frequency mixer.

## I. INTRODUCTION

SINCE 2008 many investigations of the memristor have been realized [1], [2]. The principle of operation and the basic phenomena are investigated. On the main property of the memristor – memorizing the amount of charge passed through it a several applications are presented [3], [4], [5]. A several different models are proposed [2], [3], [5]. The lack of data for the possibility for applying the memristor in frequency converters was a precondition for the present analysis [4].

In Section 2 a simple modified memristor model with Joglekar window function is presented and an appropriate PSpice library element is constructed. The memristor frequency converting circuit is synthesized and described in Section 3 using the PSpice memristor model mentioned above. The analysis of the memristor circuit proposed is presented in Section 4. In Section 5 the concluding remarks are given.

## II. CREATION OF A MODIFIED NONLINEAR MEMRISTOR MODEL AND A SIMPLE PSpICE LIBRARY ELEMENT

The structure of the memristor is given in Fig. 1. The length of the doped region is  $w$  and the length of the element is  $D$  [2].

The researches which results are presented in the paper are financed from Contract № 121PD0072-08 for scientific projects for help of PhD Students of Scientific-Research Sector of Technical University – Sofia for 2013 year.

Valeri Mladenov is a full Professor, Dr. Eng. with the Department of Theoretical Electrical Engineering, Technical University of Sofia, Republic of Bulgaria, (e-mail: valerim@tu-sofia.bg).

Stoyan Kirilov is Dr. Eng. with the Department of Theoretical Electrical Engineering, Technical University of Sofia, Republic of Bulgaria, (phone: +359 2 965 34 45, e-mail: s\_kirilov@tu-sofia.bg).

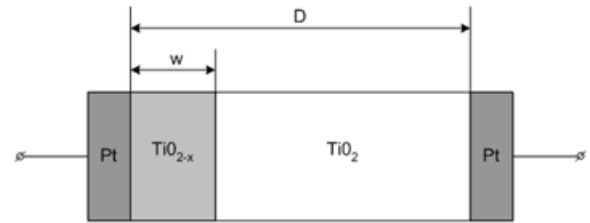


Fig. 1. Structure scheme of the Williams' memristor

The state variable  $x$  is equal to the ratio between the length of the doped region  $w$  and the length of the memristor  $D$  [2]:

$$x = \frac{w}{D} \quad (1)$$

The minimal value of the state variable according to [2] and [3] could be  $x_{min} = 0$ . This announcement is mathematically true when the length of doped region is  $w = 0$ . One of the new ideas in the present paper is based on physical considerations [6], [7]. Really when we apply a voltage in reverse direction for a long time then the doped region will shrink but the oxygen vacancies will remain in this section. The oxygen vacancies are generated in the initial process of electroforming of the memristor and they cannot vanish. Because of that the length of the doped region can have a very small length but this length cannot be zero. So the minimal value of the state variable is very near but not equal to zero. The maximal value of the state variable is equal to unity. It is physically possible because the oxygen vacancies can distribute to the right boundary of the memristor. According to this logic we have:  $x \in [x_{min}, 1]$ . The derivative of the state variable  $x$  with respect to the time  $t$  is [3]:

$$\frac{dx}{dt} = \eta kif(x) \quad (2)$$

The coefficient  $\eta$  shows the polarity of the memristor and is determined as follows:

$$\eta = \text{sign} \left( \int_{t_0}^t u(t') dt' \right) = \text{sign}[x(t) - x_0] \quad (3)$$

The quantity  $x_0 \approx 0.05$  is the initial value of the state variable before applying the voltage across the memristor. It is obvious that the polarity of the memristor is determined in accordance to the difference between the present value of the state variable and its initial value. The coefficient  $k$  is dependent on the memristor parameters and it is [2]:

$$k = \frac{\mu R_{ON}}{D^2} \quad (4)$$

The quantity  $R_{ON} = 100 \Omega$  is the resistance of the memristor in a fully closed state. The quantity  $\mu = 10^{-9} \text{ m}^2/(\text{V}\cdot\text{s})$  is the average value of the ion mobility. The window function used in (2) is [3]:

$$f(x) = 1 - (2x - 1)^{2p} \quad (5)$$

The Joglekar window function in the nonlinear ionic drift memristor model is used for presenting the nonlinear relationship between the velocity of the oxygen vacancies and the memristor current. The exponent in present case is  $p = 1$ . The basic current-voltage relation of the memristor is [2]:

$$u = [R_{ON}x + R_{OFF}(1 - x)]i \quad (6)$$

The number  $R_{OFF} = 16 \text{ k}\Omega$  is the resistance of the element in a fully open state. Follows the approximation used for (6) [2]:

$$R_{ON} - R_{OFF} \approx -R_{OFF} \quad (7)$$

After expressing the current  $i$  from (2) and substituting in (6) we obtain the basic differential equation of the semiconductor memristor element:

$$u dt = \frac{R_{OFF}}{4k\eta} \frac{1}{x} dx \quad (8)$$

The solution of (8) with respect to the state variable  $x$  is:

$$x = x_o \exp\left(\frac{4k}{R_{OFF}} \eta \int_{t_o}^t u(t') dt'\right) \quad (9)$$

It is very important to denote that formula (9) is valid for soft-switching mode. Then the state variable  $x$  does not reach its limit values  $-x \in (x_{min}, 1)$ . A simple PSpice model is created using (6) and (9) [8], [9]. Its circuit is given in Fig. 2.

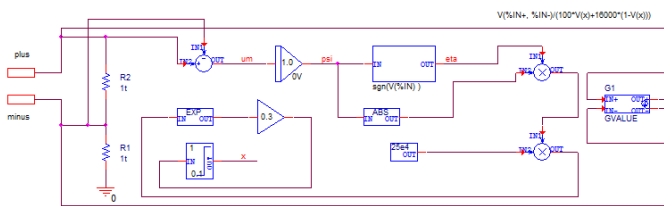


Fig. 2. Modified PSpice memristor model with nonlinear drift

The basic element in the PSpice model is the nonlinear resistor which is obtained by the voltage controlled current source  $G_1$ . Its current-voltage relation is obtained using (6) and (9). The limiting element is used for high level signals.

### III. SYNTHESIS OF A MEMRISTOR FREQUENCY CONVERTER

For creating frequency converter the nonlinearity of the memristor element is used [2], [3]. The frequency converter is presented in Fig. 3. An amplitude-modulated signal source with a frequency of  $768 \text{ kHz}$  is connected in series with a heterodyne with a frequency of  $300 \text{ kHz}$  [10]. In the circuit

presented are connected also a memristor element  $M$  and a parallel resonant circuit containing the elements  $R$ ,  $L$  and  $C$ . The resonant frequency of the parallel resonant circuit is chosen to be equal to the intermediate frequency of the radio receiving set and it has a value of  $468 \text{ kHz}$ .

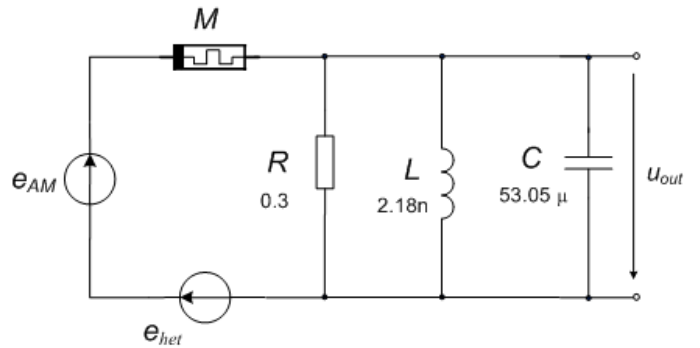


Fig. 3. A memristor frequency converter for intermediate frequency

### IV. ANALYSIS OF THE MEMRISTOR FREQUENCY CONVERTER IN OR CAD PSpice ENVIRONMENT

A PSpice model of the radio frequency converter is given in Fig. 4. It is based on the circuit presented in Fig. 3. The source  $V_1$  is producing an audio signal with a magnitude of  $70 \text{ mV}$  and a frequency of  $10 \text{ kHz}$ . The source  $V_2$  generates a signal with a carrier frequency of  $768 \text{ kHz}$  and a magnitude of  $1 \text{ V}$ . The modulator in the transmitter is realized with the diode  $D_1$  and the parallel resonant circuit consisting of the elements  $C_1$ ,  $L_1$  and  $R_1$ . The time diagram of the amplitude modulated radio signal is given in Fig. 5. Its spectrum is given in Fig. 6. It is obvious that the spectrum contains the signal with a carrying frequency and also side spectral components. The source  $V_3$  represents the heterodyne. Its signal has a frequency of  $300 \text{ kHz}$  and a magnitude of  $50 \text{ mV}$ . This signal is summed with the amplitude-modulated signal described above and after that the signal mixture obtained is applied to the amplifier  $E_1$ . After amplifying the signal mixture is applied to the circuit realized with the memristor element  $M$  and the parallel resonant circuit containing elements  $C_2$ ,  $L_2$  and  $R_2$ . The resonant frequency of the resonant circuit is fixed to be equal to the intermediate radio frequency with a value of  $468 \text{ kHz}$ . The time diagram of the amplitude-modulated signal with intermediate frequency is presented in Fig. 7.

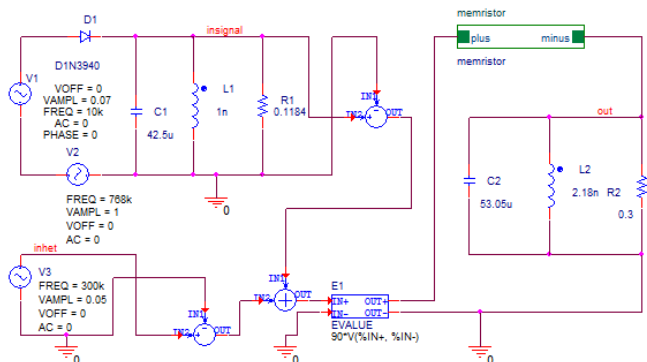


Fig. 4. PSpice model of the memristor frequency converter

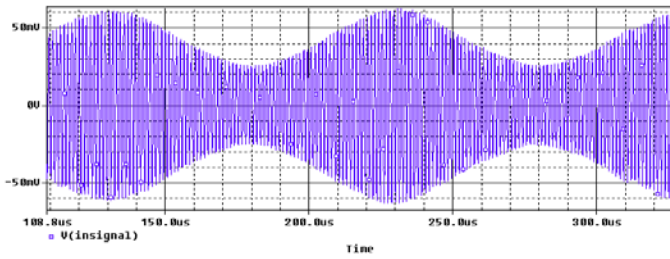


Fig. 5. Time diagram of the input amplitude-modulated radio signal

The spectrum of the signal presented in Fig. 7 is given in Fig. 8. The spectrum consists of a carrier component, lateral components and several additional harmonics with low magnitudes. The existence of these higher harmonics is due to the non-ideal amplitude-frequency characteristic of the respective resonant circuit. The state-flux characteristic of the memristor element is given in Fig. 9. It is interesting to denote that the state variable almost reaches its upper limit. But the state variable does not reach the left limit so the memristor element operates in a soft-switching mode. The current-voltage characteristic of the memristor element for the operating mode is presented in Fig. 10. The operating point of the memristor element depicts a strange trajectory.

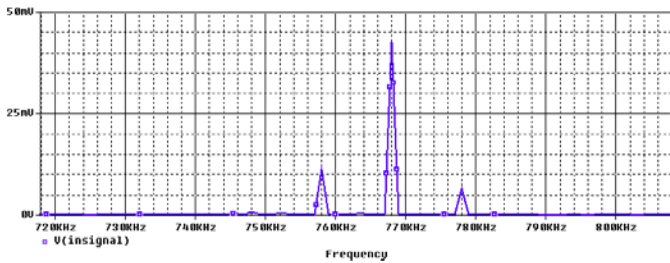


Fig. 6. Spectrum structure of the input amplitude-modulated signal

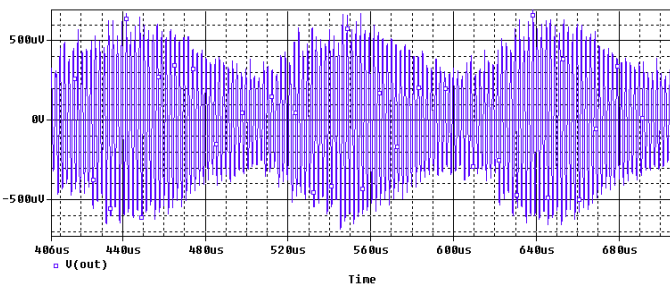


Fig. 7. Diagram of the output AM signal with intermediate frequency

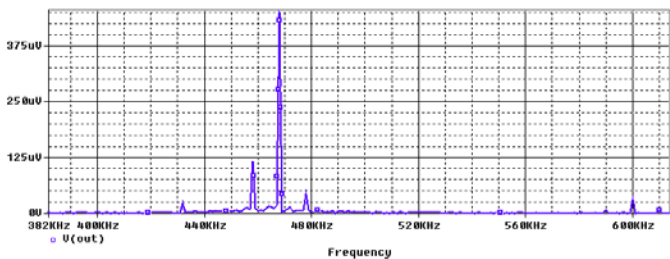


Fig. 8. Spectrum of the output signal with intermediate frequency

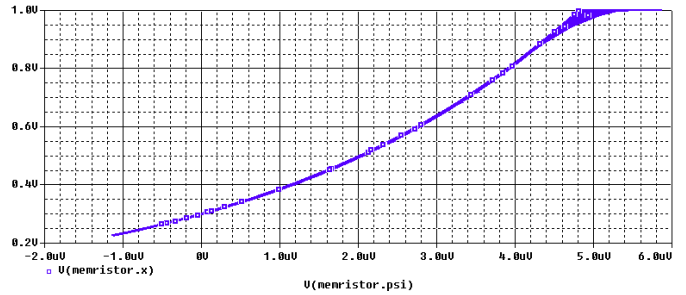


Fig. 9. State-flux characteristic of the memristor element

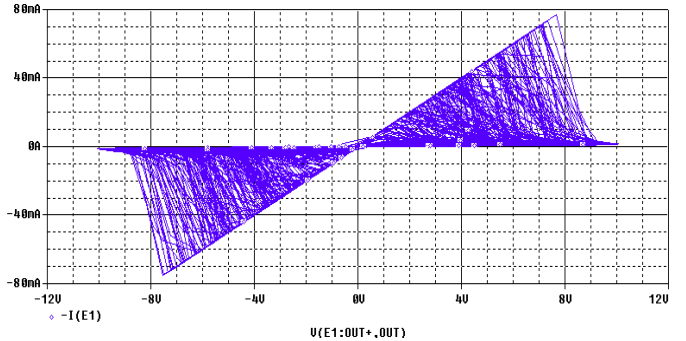


Fig. 10. Current-voltage characteristic of the memristor

One of the reasons for obtaining the bizarre form of the current-voltage characteristic is that the mixture of signals applied to the input of the memristor mixer has variable in time amplitude and frequency.

## V. CONCLUSION

The results from the PSpice simulation confirm the possibility of using the memristor as a nonlinear element in frequency convertor circuits. Practically the capacitances of the capacitors in the resonant circuits in the input circuit of the receiving set and in the heterodyne modify simultaneously, so that the intermediate frequency remains constant.

From the experiments realized it is determined that for producing frequency conversion of an amplitude-modulated radio-signal with retaining the relations between the components in the frequency spectrum the memristor have to operate in the soft-switching region of the state-flux characteristic. Then we can avoid to some extent the nonlinear distortions.

The computer simulations confirm that the memristor element is appropriate for a frequency converting circuits when it operates in a soft-switching mode.

The basic advantages of the memristor frequency convertor with respect to the classical diode convertors are the possibility for miniaturization of the integrated memristor circuits. It is also possible to implement the inductive elements as electronic gyrators with capacitive load using the same technology.

A disadvantage of the new circuit proposed is obtaining nonlinear distortions due to the operation of the memristor element very near to the hard-switching mode.

## REFERENCES

- [1] Chua, L. O. Memristor – The Missing Circuit Element. *IEEE Trans. on Circuit Theory*, Vol. CT-18, pp. 507-519, September (1971)
- [2] Strukov, D. B., G. S. Snider, D. R. Stewart, R. S. Williams. The missing memristor found. *Nature*, 06932, Vol 453, pp. 80 – 83, (2008)
- [3] Joglekar, Y., S. Wolf. The elusive memristor – properties of basic electrical circuits. *European Journal of Physics*, 30, pp. 661 – 675, (2009)
- [4] Göknaar, I., F. Öncül, E. Minayi. New Memristor applications: AM, ASK, FSK, and BPSK Modulators. *IEEE Antennas and Propagation Magazine*, Vol. 55, No. 2, pp. 304 – 313, (2013)
- [5] Ascoli, A., R. Tetzlaff, F. Corinto, M. Gilli. PSpice switch-based versatile memristor model. *ISCAS, IEEE*, ISSN 0271-4302, pp. 205 – 208, (2013)
- [6] Cotton, F. A., G. Wilkinson. *Advanced inorganic chemistry*. A Wiley-interscience publication, New York, (1980)
- [7] Mihaylova, V. *Fundamentals of Physics – part I and II*. Ciela, Sofia, ISBN 978-954-28-0982-1, (2011)
- [8] Gadjeva, E., T. Kouyoumdjiev., S. Farchy, M. Hristov, A. Popov. *Computer modeling and simulation of electronic and electric circuits with Cadence PSpice*. Meridian 22, Sofia, ISBN 978-954-90854-8-8, (2009)
- [9] Brandisky, K., V. Mladenov, S. Petrakieva. *Handbook for solving problems on theoretical electrical engineering with PSpice (OrCAD)– Version 16.3*. King, Sofia, ISBN 978-954-9518-72-6, (2012)
- [10] Dobrev, D., L. Yordanova. *Radiocommunications*. Ciela Soft and Publishing, Sofia, ISBN – 10: 954-649-905-6, (2006)



**Valeri Mladenov** graduated in Electrical Engineering from the Technical University of Sofia, Bulgaria in 1985. He received his Ph.D. from the same institution in 1993. Since 1986 he has been a Lecturer in the Department of Theory of Electrical Engineering at the Technical University of Sofia, Bulgaria, teaching courses on "Theoretical Electrical Engineering I & II", "Circuit Theory", "Electrical Engineering", "Fuzzy Control and Neural Networks", "Discrete Structures". In 1999 he became an Associate Professor. In 2004 he became a Head of the Department of Theory of Electrical Engineering. Since June, 2011 he was a Dean of Faculty of Automation and since Dec. 2011 he is a Vice Rector of the Technical University Sofia. In the same year he became a full-professor. He is also a member of the Senate of the University.

He is a guest lecturer at the Faculty of Electrical Engineering, Eindhoven University of Technology, in the Netherlands, where he teach a course "Nonlinear Systems and Neural Networks". He has been invited lecturer in the Technical University of Ilmenau, Germany, National Technical University of Athens, Greece and many others. Dr. Mladenov's research interests are in the field of nonlinear circuits and systems, neural networks, artificial intelligence, applied mathematics and signal processing. He has received many international research fellowships. He have received many research grants from the Technical University of Sofia, Bulgarian Ministry of Education and Science, DAAD - Germany, NWO - Netherlands, Royal Society - UK, NATO, TEMPUS and others and also with his team he participated in many national and international projects - FP7, DFG, and others. As a member of several editorial boards Dr. Mladenov serves as a reviewer for a number of professional journals and conferences.

Prof. Dr. Mladenov is a Senior Member of the Institute of Electrical and Electronics Engineering, Inc. (IEEE) <http://www.ieee.org/>, member of the IEEE Circuit and Systems Technical Committee on Cellular Neural Networks& Array Computing and Chair of the Bulgarian IEEE CAS/SSCS joint chapter. He has more than 170 scientific papers in professional journals and conferences. He is a co-author of ten books and manuals for students. He is also a member of the Steering Committee of the International Symposium on Theoretical Electrical Engineering (ISTET), member of the Board of Directors of the World Scientific and Engineering Academy and Society (WSEAS) <http://www.wseas.org/> and editor-in-chief of the WSEAS Transactions on Circuits and Systems. He is an organizer and a chair of many International Conferences and Symposiums.



**Stoyan Kirilov** have received Bachelor degree in Chemical Technologies for Semiconductors from the University of Chemical Technologies and Metallurgy, Sofia, Bulgaria in 2002. He receive second Bachelor degree in Telecommunications from the Technical University of Sofia, Bulgaria in 2008. In 2010 he graduated in the same specialty. He received his Ph.D. from the same institution in Theoretical Electrical Engineering in 2014. His main field of study is memristor and memristor circuit analysis, investigation

of nonlinear and linear electronic circuits and devices.

He works as an engineer in the Department of Theoretical Electrical Engineering. He also teaches courses tasks Theoretical Electrical Engineering. His main scientific interests are associated with computer simulations and modeling of memristors and memristor circuits.

Dr. Kirilov has participated in several conferences in Bulgaria and also in Italy and Germany. He has published about 10 articles co-authored with Professor Valeri Mladenov.

# Neural network method of intellectual planning of mobile robotic object movement in the conditions of uncertainty

V. Ph. Guzik, Yu. V. Chernukhin, A. O. Pyavchenko, M. Yu. Polenov, V. A. Pereverzev, and R. V. Saprykin

**Abstract**—The paper is devoted to neural network method of intellectual planning of mobile robotic object movement in the conditions of uncertainty. An option of using an intellectual planner in a trajectory-positional control system in a mobile robotic object is described in the paper. Theoretical basics of building a bionic neural network planner of movements are given. The results of experimental research of the neural network planner of movements in different environments are given.

**Keywords**—Bionic method, neural network planner, intellectual algorithm, uncertainty conditions.

## I. INTRODUCTION

THE task of building control systems for mobile robotic objects (MRO) is currently becoming more and more topical. MROs have become widely spread in organization of rescue and research operations in emergencies, in a military area and in deep underwater researches. The human presence in a hostile environment is completely removed in all the listed scenarios.

Several main methods for building control systems for MRO exist. One of the promising is a method of building a trajectory-positional control system [1] – [3]. Control systems for MROs, which are built according to this principle, support its movement according to the given trajectory in an environment with static and dynamic obstacles [4] – [6]. The trajectory may be approximated by the pieces of lines, circles, ellipses or parabola.

This work was supported by the Russian Scientific Foundation Grant 14-19-01533 and made at the Southern Federal University, Russia.

V. Ph. Guzik is with the Department of Computer Engineering, Southern Federal University, Rostov-on-Don, Russia (e-mail: vfguzik@sfnu.ru).

Yu. V. Chernukhin is with the Department of Computer Engineering, Southern Federal University, Rostov-on-Don, Russia (e-mail: yuchernukhin@sfnu.ru).

A. O. Pyavchenko is with the Department of Computer Engineering, Southern Federal University, Rostov-on-Don, Russia (e-mail: aop61@mail.ru).

M. Yu. Polenov is with the Department of Computer Engineering, Southern Federal University, Rostov-on-Don, Russia (phone: +7(8634)371550; fax: +7(8634)371608; e-mail: mypolenov@sfnu.ru).

V. A. Pereverzev is with the Department of Computer Engineering, Southern Federal University, Rostov-on-Don, Russia (e-mail: pereverzevva@mail.ru).

R. V. Saprykin is with the Department of Computer Engineering, Southern Federal University, Rostov-on-Don, Russia (e-mail: rsaprykin@gmail.com).

This method ensures a high-quality implementation of tactical level of control, which leads to rather precise following the MROs trajectory while solving different types of tasks [7] – [11].

However, in order to successfully apply this method, setting the trajectory of MROs movement by human operator according to data of obstacles positions in object's functioning area is necessary. Unfortunately, such information is often unavailable in real tasks. This leads to a necessity of MRO's functioning in conditions of uncertainty. Thus, the task of building a system of run-time planning of movement, which supports such functioning of an object, is topical. In authors' opinion, exactly applying MRO's movement intellectual planner, which building principles are based on the neural network method of intellectual planning, on tactical level of control system, allows to successfully solve the task of MRO's movement in an a priori non-formalized environment with static and dynamic obstacles.

## II. METHOD

One of the promising trends of building intellectual movement planning systems for MROs is applying bionic approach. It consists in technical imitation of biological systems, providing "intelligent" behavior in a difficult and, a priori, non-formalized environment. This approach is based on exposure and usage of biological analogies, in particular on using results of neurophysiological and neurocybernetic experiments, devoted to studying human and animal neural system. At the same time another point is taken into account – that direct applying of know neurophysiological data for modeling human's psyche does not yet produce useful results due to extreme complexity of simulation object – human brain.

As is well known, human's psyche is a system property of highly evolved matter, manifestations of which on the conscious level can't always be explained by the results of subtle neurophysiological experiments. The problems of creating artificial intelligence in general and intellectual movement planning systems in particular are related to this.

At the same time it should be considered, that different behavioral acts are implemented mostly not on conscious, but rather on subconscious level, and are typical not just for human brain, but also for a brain of simpler organisms, such as

mammals and event insects. It leads to the fact, that the creation of intellectual movement planning systems may be started from the synthesis of devices, which model not all functions of natural highly developed intellect, but only those, which are related to performing of purposeful activities and supporting intellectual behavior in a natural environment. In other words, it is meaningful to start from the modeling of reflex behavior not on a difficult psychological level, but on a simpler neurophysiological one.

Let's analyze a simplified algorithm of functioning of control system of MRO with intellectual movement planner (IMP). Let's assume that MRO functions in some environment and follows a trajectory, previously defined by operator. At this tactical level of control system works. As soon as sensor subsystem of MRO sees unknown and previously undefined obstacle, IMP is invoked. This planner allows safe bypass of an obstacle, until sensor system sees it no more. This planner forms values of angle increments to a current movement course of MRO, which is automatically exploited by the regulator of MRO's control system.

After the bypass of the obstacle planner stops functioning and control is again fully performed by regulator level of control system, returning MRO to the initial trajectory. In general the task of intellectual planning may be represented in the following way (Fig. 1).

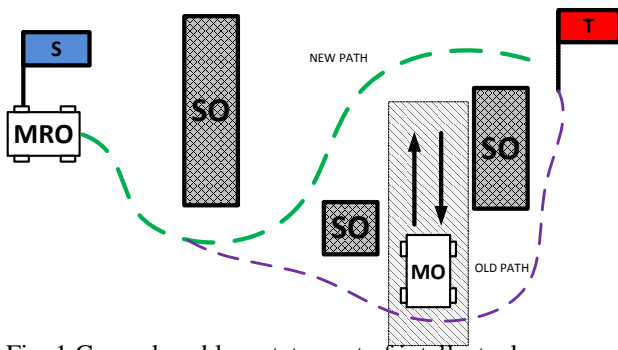


Fig. 1 General problem statement of intellectual movement planning of MRO

MRO from the starting position (S) should reach the target (T), bypassing static obstacles (SO) and moving obstacles (MO) using optimal trajectory (OT). Optimal trajectory may be calculated using the following criteria: minimal distance, minimal time, minimal expenditure of energy and so on.

Currently some understanding about the structure and functions of neural networks, which serve as the basis even for simple behavioral reactions, already exist. In particular, it is known that neural networks consist of separate neural cells – neurons, which function in parallel in time. This allows neural system to compute big amounts of data, which are received from multiple receptors, and to form control actions for actuating mechanisms in real-time. According to bionic approach, neurophysiological data about neural system functioning and, primary, data about functional system of P.K. Anokhin [12] are used as a theoretical processes model in intellectual movement planning systems.

Taking into consideration that afferent synthesis and regulation according to the result are the base of principal

generality of control on different levels of biological organization, it may be assumed that, closing the feedback in the simplest homeostatic through the environment, we will receive theoretical model of the simplest intellectual movement planning system. The implementation of such a functional system by an artificial neural network movement planning system is shown in Fig. 2.

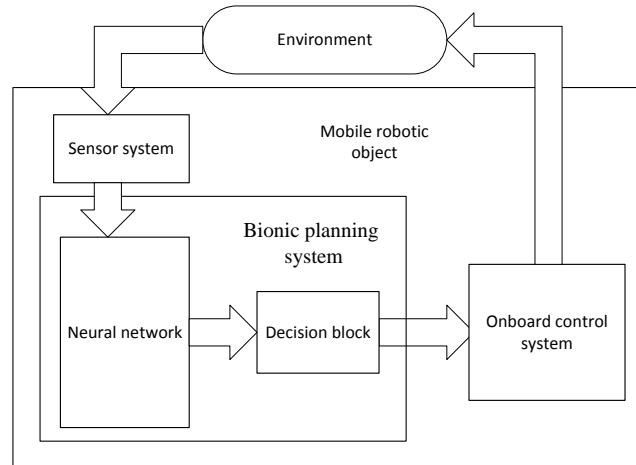


Fig. 2 Implementation of function system by a neural network movement planning system

As we can see on Fig. 2, afferent synthesis is performed by neural network structure of afferent synthesis, decision making is performed by a special decision-making structure (DMS), and actions are implemented by actuate part of on-board MRO's control system. Besides, the structure of MRO includes sensor subsystem (SS), which performs receiving and conversion of information about environment.

If at this point MRO has a limited class of tasks, then according to the principle of perception selectivity in a functional system it is quite enough, that sensors allow to detect only obstacles and target and will be able to treat environment as a set of sectors of three types: free, forbidden and targeted.

Let's further assume that sensor subsystem is able not just to perceive information about environment, not just to classify its' sectors, but also special connections to the subsystem of afferent synthesis, with which a one-to-one mapping between sections of environment and state-driven elements of neural network of afferent synthesis is performed. Since sensor subsystem is stiffly tied to the body of MRO, it is only natural to assume that origin of coordinated environment model, which is displayed in SAS, is also tied to the body of MRO.

Thus, using listed concepts, it is possible to formulate neural network bionic method for intellectual movement planning of MRO [13] – [16].

The idea of the method consists in the following. During the process of active interaction with a priori non-formalized environment, the plan of an environment, which is formed in sensor subsystems and reflects relative positions of target, obstacles and MRO, is reproduced periodically, before each movement step of MRO, in a neural network, consisting of

artificial neurons. Then the gradient of functional is searched in neural network. This gradient determines a set of possible trajectories for reaching the target.

Then the element of the trajectory is formed and exploited. This element is directed along the anti-gradient of the functional, defined in neural network. The difference of the method under inspection is that the trajectory is formed not by sequential deleting of unsuccessful heuristics, but by physical modeling of afferent synthesis process on a neural network.

The information about the position of the target and obstacles relative to MRO and to each other may be interpreted as environmental afferentation, and the fact of catching the target by the sensor subsystem or setting this target on environment's plan by any other means, for example by human operator through communication channel, may serve as a model of launch afferentation. At this it is important that fixing a program step of the future action is directly connected with its implementation and is performed not in the environment's plan, but in the states of MRO itself. In this approach the plan of functioning and the environment, so to speak, merge. At this rather high performance of neural network allows to efficiently consider changes in an environment, which happen at much greater rates.

According to bionic method of intellectual movement planning let's build a system of afferent synthesis (SAS), basing on a neural network, reflecting the space of MRO's functioning. At this we will use the fact, that this work space is a plane  $S$ , which includes free and forbidden for passage sectors, and also a sector, which represents target. Let's use a representation of a model of this space as a planar regular graph  $G(Q, F)$ , where  $Q$  is a set of vertices  $q_j$ , which represent discrete sectors  $\Delta S_j$ ,  $F$  is a set of branches, which connect these vertices. Let each vertex  $q_j$  in  $G(Q, F)$  correspond to a neural-like processor element  $NE_j$ . Let's also connect separate elements with informational bonds as branches of the graph are connected.

This way we get a neural network, which architecture for the case of dividing environment to squares has a form, represented in Fig. 3.

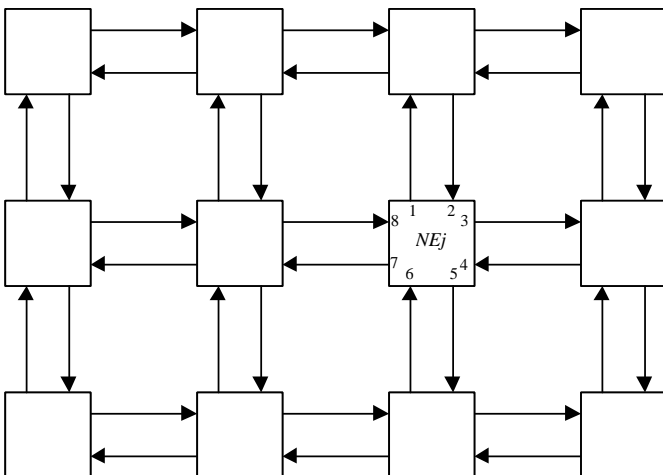


Fig. 3 Neural network for an environment, divided into squares

It may be concluded from bionic method of intellectual movement planning of MRO that in order to reproduce this method in this neural network it is necessary, that each neural element performs the following operations.

1. If element  $NE_j$  represents a free sector in environment, then it should carry the driving signal between its neighboring elements on different size.

2. If element  $NE_j$  represents an occupied sector in the environment, it should block the driving signal transmission from the neighboring elements.

3. If element  $NE_j$  represents the sector in the environment, where the target resides, it should generate driving signals, which can be carried through other, non-blocked elements.

Element  $NE_0$  is selected, because in any given moment of discrete time  $t_i$  it represents the sector of environment, where MRO resides. That is why it should perform the functions of decision-making subsystem, i.e. should be able to determine and fix the directions of the first driving signal.

It is easy to see, that formal neurons may be used as processor elements, implementing functions of the neural network described above. These neurons have unit-driving input and unit-threshold, and also two inhibitory inputs, receiving signals  $P_j$  and  $d$ .

Conventional graphical representation of such formal neuron is in Fig. 4 (a).

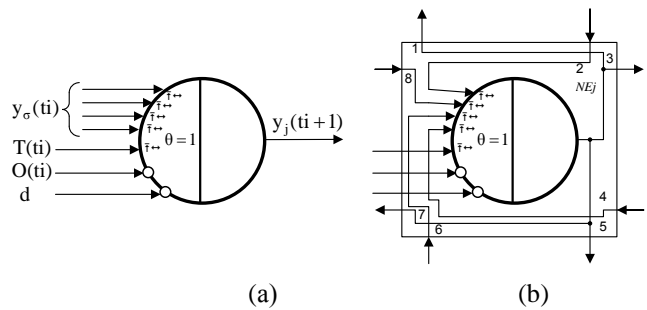


Fig. 4 Conventional graphical representation of formal neuron

Fig. 4 (b) shows the connection between inputs and outputs of formal neuron (FN) when it is used as processor element  $NE_j$ . Connecting  $NE_j$  according to scheme (Fig. 3), we get neural network, which models afferent synthesis (inputs, which represent targets  $T_i$ , obstacles  $O_i$  and signal  $d$ , are not shown in this net).

It is interesting that the functions of special processor element  $NE_0$  may also be implemented by using a group of  $n$  formal neurons, united into an ensemble, which is shown in Fig. 5.

As can be seen in this figure, every  $NE_j$  ( $j = 1, 2, \dots, n$ ) is connected to other neurons of ensemble. These neurons forbid lateral (side) connections. It allows such an ensemble to implement function of decision-making structure, i.e. detect and fix which formal neuron is driven by the signal before others.

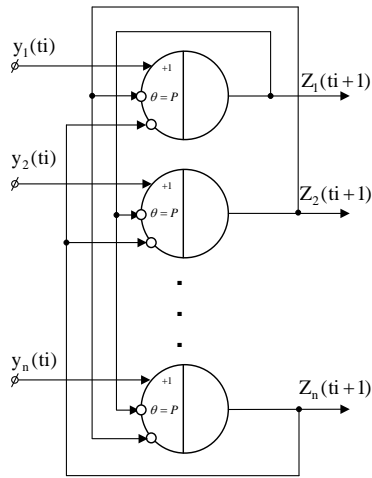


Fig. 5 Neural ensemble, implementing element  $NE_0$

Indeed, in the default state when the signal  $d=1$  is fed to the afferent synthesis net, inputs  $y_j(t_i)$  are fed with zero signals. Since thresholds of all NE in ensemble are defaulted to  $n$ , all outputs  $Z_j(t_i)$  will also have zero value. Zero signals from outputs  $Z_j(t_i)$  in the inversed format are fed to correspondent inputs of NE and drive them. That is why all NE in ensemble hit the state, in which every first  $j$  input unit signal  $y_j(t_i)$  drives output NE and, being received from output to forbidding inputs of other NE in ensemble, will inhibit them. That is why other input signals  $y(t_i)$  from other NE will not drive them.

Thus, SAS and DMS may indeed be implemented on the basis of formal neurons.

By uniting formal neurons of environment model subsystem, systems of afferent synthesis and decision-making systems, we get neural network module, which handles the task of intellectual movement planning of MRO in a priori non-formalized environment. Its structure is shown in Fig. 6.

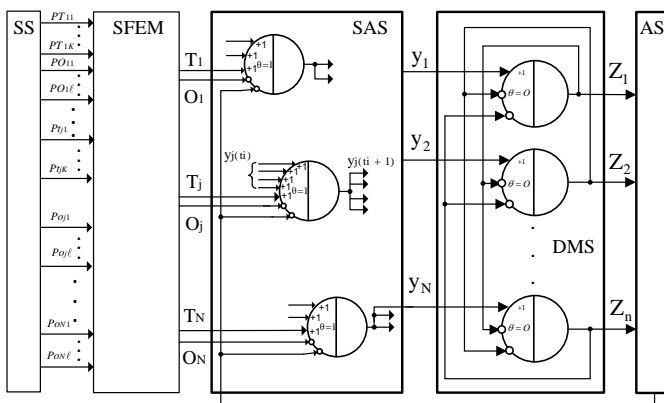


Fig. 6 Neural network implementation of movement planning module

It can be seen in the picture, that information about environment is perceived by receptors of sensor subsystem of MRO and then is sent to the outputs of correspondent FN of the subsystem of forming environment model (SFEM). Information about the target and obstacles in the form of signal sets  $T_j \in \{0,1\}$  and  $O_j \in \{0,1\}$  from outputs of this subsystem is sent to correspondent inputs of processor

elements of system of afferent synthesis SAS.

Elements of SAS implemented by FN are connected as shown in Fig. 3. FN outputs of the rightmost range of SAS are connected not only to other neurons in the structure, but also to driving inputs of DMS's formal neurons. DMS output signals are sent to inputs of actuator subsystem of MRO via on-board control system, which supports MRO's movement in the environment and forms feedback signal  $d$ .

Neural network module functions in the following way. After completing MRO's movement step in the environment, actuator subsystem (AS) of MRO forms short signal  $d=1$ , which inhibits all driving signals of all FNs in SAS.

Information about target's and obstacles' position is sent from SFEM to processor elements of non-driven SAS. Formal neurons, correspondent to busy sectors of  $\Delta S_j$  in environment, are blocked and FN, defining targeting sector, is driven by input signal  $T=1$ . This FN becomes the source for driving SAS. Unit signals from its output are spread in SAS only through open FN and this way reflect all possible trajectories, leading from target to DMS, i.e. ensemble, which models MRO's position in environment.

It is obvious that the signal coming with the shortest path will reach DMS earlier, than the others. DMS fixes on its output the direction of necessary movement, recalculating it to angle increments. Thus the new trajectory element is formed, which is sent then to control system of MRO. Actuator system of MRO performs defined element of trajectory.

After the movement step the position in the environment relatively to obstacles and target will change. But the information from the output of SFEM again will be sent to SAS. It will initiate all listed actions once more. They will be performed in a loop until MRO reaches the target.

At the same time we should take into consideration the fact that reaching the target and optimality of MRO depend a lot on the characteristics of environment and configuration, representing it for SAS. In particular, due to fixed connection of SS with the body of MRO, it is more reasonable to use not rectangular, but polar (radial) coordinate system, and to build SAS accordingly (Fig. 7).

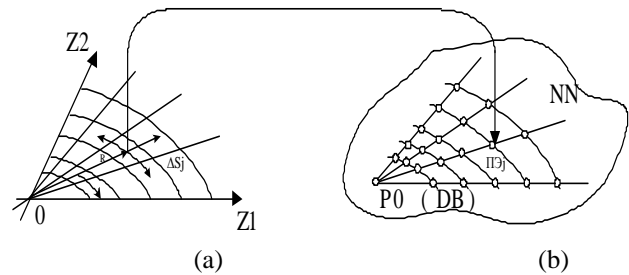


Fig. 7 DMS position

One-to-one correlation between the parts between sectors  $\Delta S_j$  in such model and processor elements of the correspondent neural network (NN) is shown in Fig. 7. It should be noted that radial-concentric architecture of NN has several advantages in comparison to orthogonal option.

First of all, such NN allows to reflect environment with a

variable step of its discretization, i.e. sectors close to MRO's body may be of small size and distant sectors will have considerably bigger sizes and will be modeled with lesser precision. It is well-correlated with the possibilities of known sensor systems, for example ultrasonic sonars, which resolution decreases with the increase of distance. It is important that it allows to considerably reduce the number of NN processor elements without the decrease in the precision of modeling in the direct closeness to MRO. In turn, reducing the number of processors leads to reducing the size of radial-concentric neural network in comparison to equivalent orthogonal structure, increasing its reliability and reducing required power, which is very important for on-board systems.

Radial-concentric configuration of NN has one more advantage: its usage leads to lesser movement planning error of MRO in comparison to orthogonal configuration.

The targeted object is not physical in many tasks and can't be detected by sensor system, but rather is just a direction or some check point with the given coordinates. In this case extra layer of neural elements is added to neural network. Imaginary targeted object is then projected to this layer (Fig. 8 a). At this the process of decision-making and forming an angle of deviation from current trajectory during sending command to on-board control system of MRO is shown in Fig. 8 b.

The structure of neural network with the decision-making net for 3D case is shown in Fig. 9.

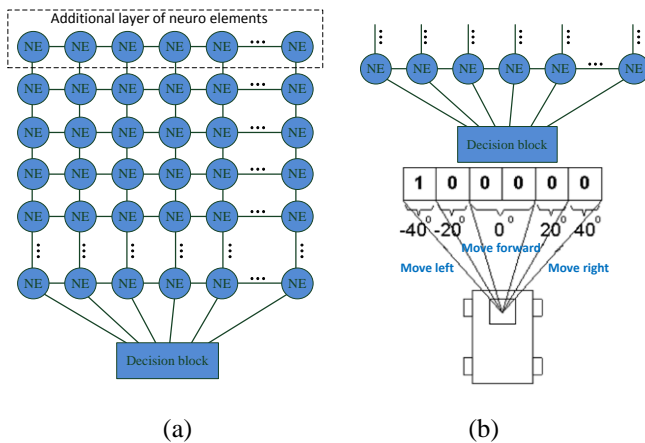


Fig. 8 Neural network with extra layer and decision-making block

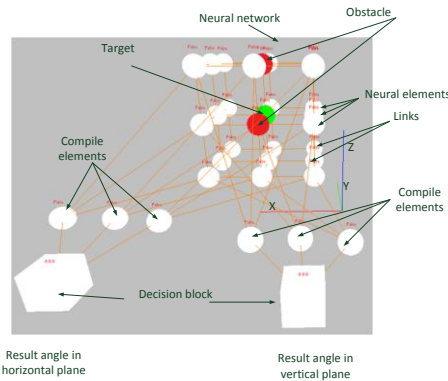


Fig. 9 Complete architecture of neural network of afferent synthesis and decision-making for the case of 3D environment

### III. EXPERIMENTS AND RESULTS

Described neural network bionic method for building intellectual movement planner of MRO was researched on the basis of several robotic platforms [18] – [20] and showed high results in performance and precision (Fig. 10, Fig. 11).



Fig. 10 Researching the neural network movement planner of MRO on the basis of Hemisson robotic platform



Fig. 11 Researching the neural network movement planner of MRO on the basis of independently self-developed robotic platform

During the experiments the main task for MRO was reaching target sector with autonomus movement of the object from the starting point, bypassing detected obstacles. The targeted sector (object) was visible for sensor subsystem of MRO and was represented by color or light marker. Obstacles were represented by planar rectangles of dark color.

In order to test neural network bionic method of planning on a wider range of tasks, special complex of virtual modelling NAME was developed [17]. This complex allows to model neural network planner both in artificially created simplified environments (Fig. 12, Fig. 13) and environments, which are relatively closer to real ones (Fig. 14 - Fig. 17), where 1 is a model of MRO; 2 is a model of sensor subsystem (camera); 3 – model of environment; 4 – targeted object; 5 – obstacles; 6 – picture from a virtual camera; 7 – model of environment, adapted for neural network.

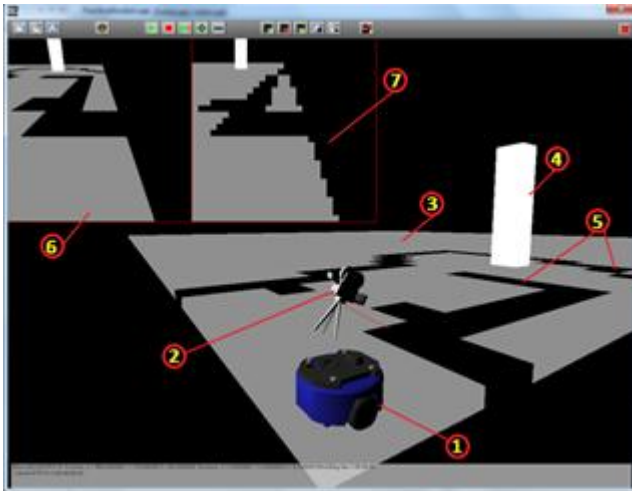


Fig. 12 Simplified environment in a form of a labyrinth



Fig. 14 Model of MRO in overwater environment

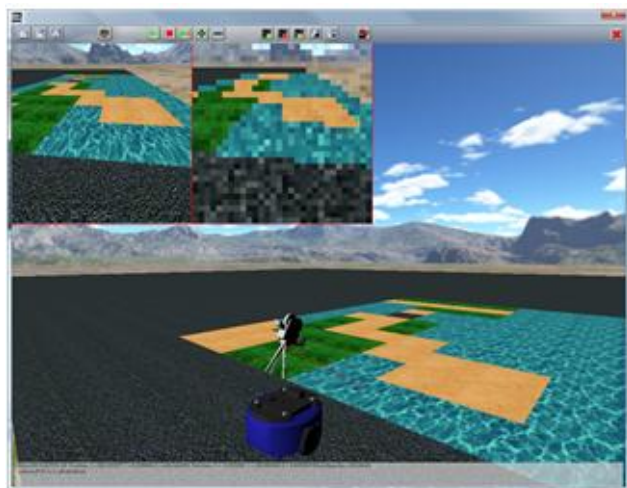


Fig. 13 Simplified environment with partially passable sectors

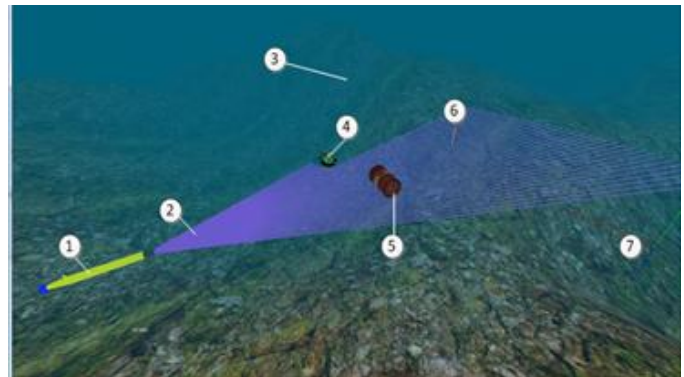


Fig. 15 MRO model in underwater environment

The main advantage of the offered neural network movement planner of MRO is its invariance relative to environment of functioning. The researches were held for overwater environment (Fig. 14), underwater environment (Fig. 15), land environment (Fig. 16) and aerial environment (Fig. 17).

During these researches appropriate sensor subsystems were selected. According to the selected subsystem different methods of modeling environment were adopted.

In Fig. 14 model of MRO in the form of autonomous boat is shown. It is functioning in the conditions of complex relief with artificial obstacles [21][20] – [23].

In Fig. 15 model of MRO in the form of autonomous unmanned underwater apparatus (AUUA) [24] is shown. It is functioning in the conditions of complex bottom relief with artificial obstacles,

where 1 – model of MRO in the form of AUUA; 2 – model of sensor subsystem of MRO (sonar); 3 – landscape; 4 – mine-obstacle; 5 – barrel-obstacle; 6 – current targeted object; 7 – zero point of scene coordinates.

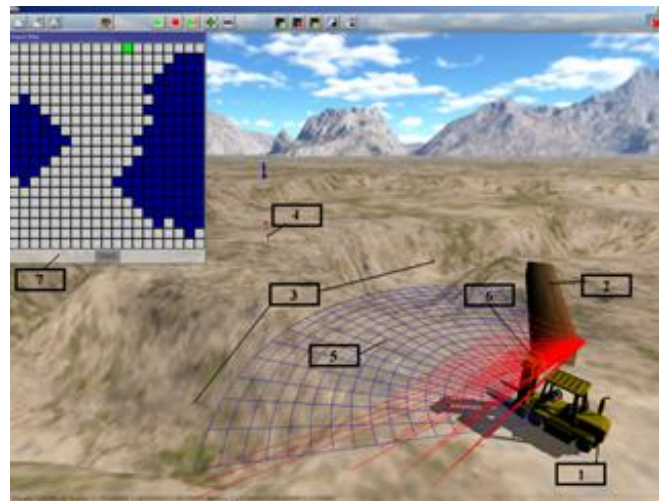


Fig. 16 MRO model in land environment

In Fig. 16 model of MRO in the form of autonomous wheeled robot is shown. It is functioning in the conditions of complex relief with artificial obstacles, where 1 – model of MRO; 2 – artificial obstacle; 3 – natural obstacle (ravine); 4 – targeted object; 5 – sensor model of the type “facet eye”; 6 – sensor model of the type “laser range finder”; 7 – model of environment adopted for neural network.

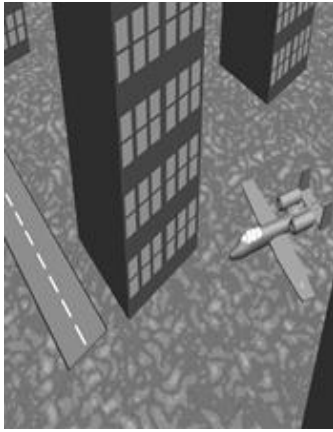


Fig. 17 MRO model in aerial environment

In Fig. 17 model of MRO in the form of autonomous aircraft is shown. It functions in the city conditions with artificial obstacles in the form of buildings.

#### IV. CONCLUSION

Applying bionic approach for building intellectual system of movement planning of MRO, based on neural network of formal-logical type, allows to provide MRO's functioning in a difficult, a priori non-formalized environment, without the necessity of preliminary detailed checking of a region and robot's functioning environment. Also applying neural network planner provides safe functioning of MRO in an environment with both static and moving obstacles. The results of experimental researches of neural network movement planner allow to use it as a subsystem on tactical level of planning for trajectory-position control system of MRO.

#### REFERENCES

- [1] V. Kh. Pshikhopov, A. S. Ali, "Hybrid motion control of a mobile robot in dynamic environments," in *Proc. Int. Conf. on Mechatronics, ICM 2011*, pp. 540–545.
- [2] V. Kh. Pshikhopov, M. Yu. Medvedev, "Robust control of nonlinear dynamic systems," in *IEEE ANDESCON Conf. Proc.*, ANDESCON, Bogota, Sep. 2010.
- [3] V. Kh. Pshikhopov, M. Yu. Medvedev, "Document Block design of robust control systems by direct Lyapunov method," in *Proc. of the 18th IFAC World Congress*, 2011, pp. 10875–10880.
- [4] V. Pshikhopov, M. Medvedev, R. Neydorf, V. Krukhmalev et al., "Impact of the feeder aerodynamics characteristics on the power of control actions in steady and transient regimes," *SAE Technical Papers*, no. 01, 2012.
- [5] R. Neydorf, V. Krukhmalev, N. Kudinov, V. Pshikhopov, "Methods of statistical processing of meteorological data for the tasks of trajectory planning of MAAT feeders," 2013, *SAE Technical Papers*.
- [6] V. Pshikhopov, V. Krukhmalev, M. Medvedev, R. Neydorf, "Estimation of energy potential for control of feeder of novel cruise/feeder MAAT system," *SAE Technical Papers*, no. 01, 2012.
- [7] V. K. Pshikhopov, M. Yu. Medvedev, B. V. Gurenko, "Homing and Docking Autopilot Design for Autonomous Underwater Vehicle," *Applied Mechanics and Materials*, 2014, pp. 490–491.
- [8] V. Pshikhopov, N. Sergeev, M. Medvedev, A. Kulchenko, "The design of helicopter autopilot," *SAE Technical Papers*, no. 01, 2012.
- [9] V. Kh. Pshikhopov, M. Yu. Medvedev, A. R. Gaiduk, B. V. Gurenko, "Control system design for autonomous underwater vehicle," in *Latin American Robotics Symposium*, 2013, pp. 77–82.

- [10] V. Pshikhopov, M. Medvedev, V. Kostjukov, R. Fedorenko et al., "Airship Autopilot Design," *SAE Technical Paper*, no. 01, 2011.
- [11] V. Kh. Pshikhopov, V. A. Krukhmalev, M. Yu. Medvedev, R. V. Fedorenko, S. A. Kopylov, A. Yu. Budko, V. M. Chufistov, "Adaptive control system design for robotic aircrafts," in *IEEE Latin American Robotics Symposium*, 2013, pp. 67–70.
- [12] P. K. Anokhin, "General theory of body functional system," *Progress of biologic and medical cybernetics*. Moscow: Medicina, 1974, pp. 52–110.
- [13] A. V. Kalyaev, Yu. V. Chernukhin, V. P. Noskov, I. A. Kalyaev, *Homogeneous control structures of adaptive robots*. Moscow: Nauka, 1990.
- [14] Yu. V. Chernukhin, *Microprocessor and neurocomputer control of adaptive mobile robots*. Taganrog: TREI publ., 1993.
- [15] Yu. V. Chernukhin, *Artificial intelligence and neurocomputers*. Taganrog: TSURE publ., 1997.
- [16] Yu. V. Chernukhin, *Neuroprocessor networks*. Taganrog: TSURE publ., 1999.
- [17] Yu. V. Chernukhin, R. V. Saprykin, "Virtual modeling system of intellectual agents' behavior when exploring natural functioning environment," *Izvestiya SFedU. Engineering sciences*, no. 11, pp. 19–24, Nov. 2008.
- [18] Yu. V. Chernukhin, R. V. Saprykin, E. I. Romanchak, Yu. S. Dolenko, "Software-hardware simulation of external environment for mobile robots with neuronetwork control on the basis of Hemisson robotkit," *Proc. XV Int. Neurocybernetics Conf.*, Rostov-on-Don, 2009. pp. 212–215.
- [19] Yu. V. Chernukhin, Yu. S. Dolenko, P. A. Butov, "The bionic approach of sensory data processing in neural network control systems of intelligent mobile robots," *Izvestiya SFedU. Engineering sciences*, no. 5, pp. 194–199, May 2012.
- [20] V. Ph. Guzik, V. V. Kureichik, M. Yu. Polenov, Yu. V. Chernukhin et al., *Intellectual systems*, Rostov-on-Don: SFedU Publ., 2013.
- [21] V. Kh. Pshikhopov, Yu. V. Chernukhin, A. A. Fedotov, V. Ph. Guzik, M. Yu. Medvedev, et al., "Development of intelligent control system for autonomous underwater vehicle," *Izvestiya SFedU. Engineering sciences*, no. 3, pp. 87–101, Mar. 2014.
- [22] V. Ph. Guzik, A. A. Priemko, "Parallel algorithm of intellectual underwater vehicle movement direction detection according to environment map," in *Proc. of IX Conf. of Perspective systems and control tasks*, Taganrog, 2014. pp. 433–441.
- [23] V. Ph. Guzik, A. A. Priemko, "Microprocessor implementation of the neuronetwork trajectory planner for the adaptive mobile robot using the environment map," *Izvestiya SFedU. Engineering sciences*, no. 4, pp. 178–183, Apr. 2014.
- [24] V. Ph. Guzik, Yu. V. Chernukhin, A. O. Pyavchenko, V. A. Pereverzev, R. V. Saprykin, "Structural organization of hierarchical distributed system for unmanned underwater vehicle motion planning," in *Proc. of 6-th Conf. of control problems*, Rostov-on-Don, 2013, vol.4. pp. 198–202.

# Automatic rehabilitation device based on robot and machine vision

Miloslav Feriančík, Ondrej Líška

**Abstract**— Article deals with the description of an automatic rehabilitation devices, which one part is focuses on the field of machine vision and second one on motion control of an industrial robot utilizing for the patient rehabilitation activities. And their subsequent implementation into the control software. For the control of autonomous movement and navigate an industrial robot we need to solve a number of significant tasks (load change, direction, speed and trajectory of movement, object detection, exact position, safety circuit, etc.). Another part is Hardware and Software Support of navigation an industrial robot for rehabilitation activities and other systems to detect the object, determining the correct position and robot control, without it wouldn't be possible to create control applications using machine vision.

**Keywords**—robot, machine vision, rehabilitation, control, effector

## I. INTRODUCTION

Automated rehabilitation devices as a whole has the task make easier, more efficient and in some cases may even completely replace the work of rehabilitation workers. With the increase in human population at retirement age is continuously increasing the number of patients. One solution to this situation is the automated rehabilitation devices, to facilitate the work of rehabilitation therapist, or eventually replace them altogether. Automated rehabilitation devices has the task to use the latest knowledge in the field of the automation, robotics and actual rehabilitation activities.

## II. THE BASIC STRUCTURE OF THE REHABILITATION SYSTEM

The basic structure of the rehabilitation system consists of a pointing device, which is a robot. Rehabilitation of a patient is provided by robot by executing the movement of the upper limb according to the desired task exercises. Rehabilitation is done either passively or actively. Passive rehabilitation is done in the case that the patient has impaired motor function so that it is not able to spontaneously move with the upper limb. In this case, the robot moves with the hand of a patient who does not expend almost no energy to carry out a training exercise. Active Rehabilitation is the case if the patient is already at a stage that can move an arm, at least to some extent. Then his robot, depending on the patient's ability to perform certain

movements helps guidance, or delivering the necessary power to achieve target point movement ie before moving from one (starting) position to the second (final) position. For this type of active rehabilitation is specially designed device called. active mechanical effector. It is a device through which the patient has the fixed arm to the end point of robot. This effector is equipped with a scanning device that records the movement of the patient hand. Robot moves along the limb of the patient and, if deviation from the specified direction of movement the robot hits and corrected the movement. Robot helps the patient even if they do not own "power" to achieve a defined objective. The system is also equipped with a camera system that consists of a web camera and cognitive application. The role of cognitive application is monitoring the course of rehabilitation and its partial control and evaluation. Rehabilitation exercise consists in collecting objects in space. Grasping each subject by the patient is monitored by a camera and guided the help of robot. Current position will be determined on the basis of cognitive applications according to the position of the object.

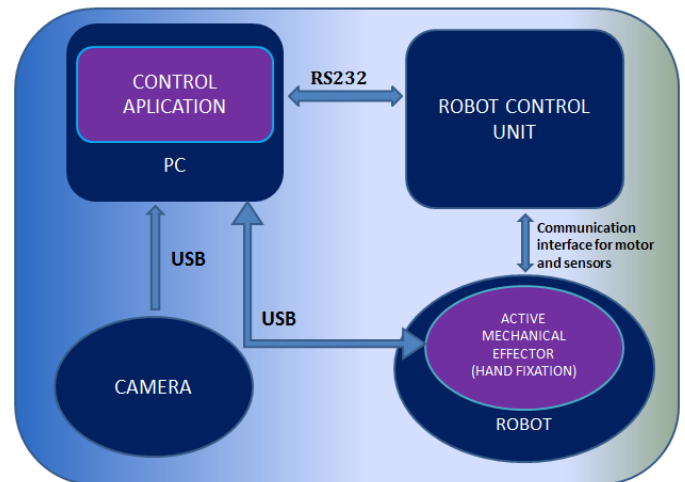


Fig. 3 Scheme of connection

## III. CONTROL APPLICATION

The control system application for an automated rehabilitation device based on industrial robot using machine vision. It is a way to control the robot using machine vision, which is to control the robot using an external application.

Control software will consist of two basic parts:

a) of processes of image processing such as recognition,

detection of object and the following processes associated with  
 b) the processes connected with the control of pointing device and his movement.

The control application is developed in C # programming language. To recognition is used graphics library Aforge.net. Using it is possible to recognize individual objects by color. In real time you can change the color palette, and track objects under them. For the image sensing is used commercially available webcam LifeCam HD-6000 (fig.2). It is capable of working in high definition 720p (HD). For simple tasks of recognizing and determining the position may suit their functional parameters (Sensor: CMOS Video: 1280 x 720 pixels, frequency: 30 frames / second, auto focus). Another advantage is that it has a USB (Universal Serial Bus) interface, which is readily available and driver installation is simple. Using a camera we obtain information about the location of objects, which patient should to grab and also we can track the movement of the patient. To verify the accuracy of the position in which the robot is we can get this information directly from the control unit.



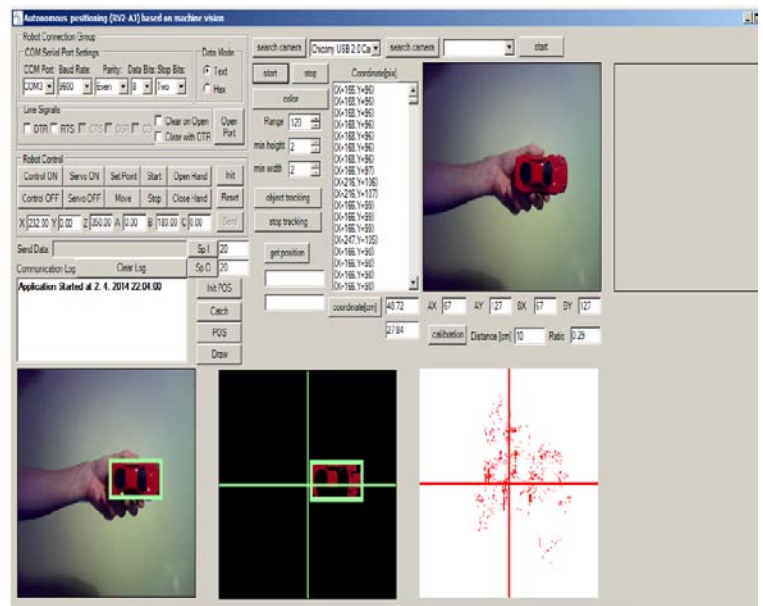
Fig. 2 webcam LifeCam HD-6000[8]

The second part of the control applications, was created to control the movement of the robot. For software testing was used industrial manipulator Mitsubishi RV-2AJ (Fig. 3). The robot weighs 17 kg, has 5 degrees of freedom and is capable of working radius of 410 mm effectively manipulate weights up to 2 kg. Top speed handling is 2153 mm / s and a positioning accuracy of + / - 0.02 mm. Programming of the robot control unit is based on a 64-bit processor. For communication PC with the robot controller is used standard interface RS-232C. Controlling the robot is based on sending the internal commands for managing and checking the control unit of robot and commands to control the robot for a particular programming language. Software solution used for communication MELFA BASIC language and therefore it is possible to use the same control program for other types of robots and other applications where it is necessary to externally regulate industrial robots. Robot motion is ensured by sending individual commands. To obtain information about the current state of the robot is sent the request in repeated intervals. In figure 3 is a sample of application to control the robot with external recognition, by which we can control its movement.



Fig. 3 Mitsubishi RV-2AJ Robot [9]

Fig. 4 Application to control industrial robot using image recognition



#### IV. ACTIVE MECHANICAL EFFECTOR

The robot is only move when the commands are sending to the control unit. Otherwise, it is static and it is impossible to move with it. Hand of the patient is fixed to the end point of the robot. Therefore, to achieve an active rehabilitation needs, but also to any other manipulation, control the movement of the robot in dependence on the movement of the patient. Otherwise it was not possible to make any movement. In some special cases, it may merely be an indication of movement. It is necessary to monitor the speed and direction of movement, in which the patient is moved so that it can be copied.

Active mechanical effector whose scheme is shown in Figure 5, is formed by mechanical transmission and scanner electronics, which the robot is able to replicate patient motion.

It works on the principle of joystick control. If the patient moves the hand, the joystick moves in the same direction. Then the effector control unit detects moving the joystick, evaluates the direction and range of motion and sends this information to control applications on a PC. The control application then sends a command to the robot controller for robot motion in specific axes, in which the movement was recorded. The command to move is sent repeatedly until it reaches the zero position of the joystick. This enables copying of patient motion.

If the patient is unable to achieve the desired goal, the robot can reach the guidance movement. Then the control application does not take into consideration the location information of the joystick, but is governed by the co-ordinates in the planned trajectory. It sends the command to move the robot until it returns to the tolerance interval field coordinates of the nearest point of the trajectory. This cycle is repeated until the patient reaches the specified target. In figure 6 is the control unit of the active mechanical effector which communicates with a PC.

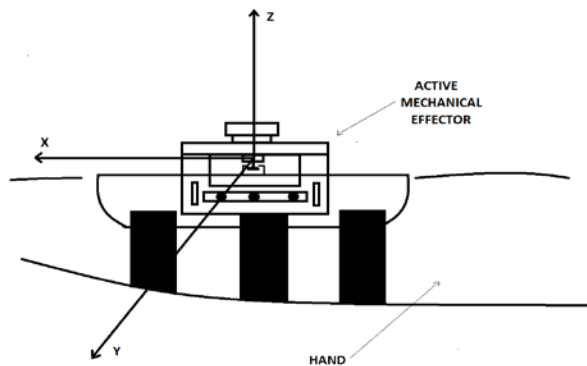


Fig.5 Scheme of active mechanical effector

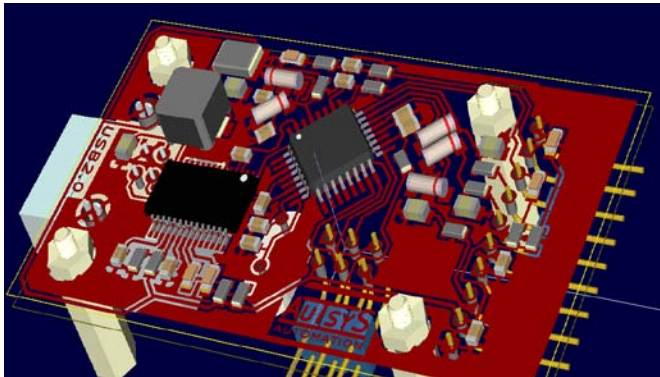


Fig. 6 controller for active mechanical effector

## V. CONCLUSION

Article deals with the use of a robot and machine vision rehabilitation. Describes the system structure for automated rehabilitation device and its basic parts such as image processing and motion control of the robot. The first part is a camera system, which consists of a web camera and recognition application that image processing using graphics library Aforge.net. The second part is intended for external

control of the robot, which provides the movement of a pointing device.

The next step in solution this task which strongly emphasizes is the draft security warning circuit, design of the algorithm for generating motion trajectories and other tasks with which we can achieve an autonomous rehabilitation device.

## ACKNOWLEDGMENT

The research leading to these results has received funding from the European Community's Structural Funds, project „Research and development of intelligent nonconventional actuators on basis of artificial muscles“, ITMS 26220220103.

## REFERENCES

- [1] Virius M.:C# - Hotové řešení, Brno, Computer Press, 2006, ISBN: 80-251-1084-2
- [2] Mitsubishi Industrial Robot, RV-1A/2AJ Series, Robot Arm Setup & Maintenance, 2007, Tokyo, Japan, p462.
- [3] Kragic, D. - Christensen, H. I.: Survey on Visual Servoing for Manipulation. Centre for Autonomous Systems, Numerical Analysis and Computer Science, Sweden
- [4] Sashi S Kommu: Rehabilitation Robotics, I-Tech Education and Publishing, 2007, Vienna, Austria, ISBN 978-3-902613-01-1
- [5] Exoskeletons and robotic prosthetics: A review of recent developments.(2009). Industrial Robot; the Industrial Robot, 36(5), 421.
- [6] Lünenburger, L., Colombo, G., Riener, R., & Dietz, V. Clinical assessments performed during robotic rehabilitation by the gait training robot lokomat. Paper presented at the International Conference on Rehabilitation Robotics (ICORR), 345–348.
- [7] Feriančík, M. - Líška, O. - More, M.: Navigation of industrial manipulator based on computer vision, 2013. In: Transfer inovácií. Č. 28 (2013), s. 140-142. - ISSN 1337-7094
- [8] Microsoft LifeCam HD-6000, [cit. 2011-02-24]. < <http://www.cnet.com.au/microsoft-lifecam-hd-6000-339306262.htm>>
- [9] Mitsubishi RV-2AJ Robot, [cit. 2011-02-12]. < <http://www.robots.com/mitsubishi.php?robot=rv-2aj>>
- [10] Židek, K. - Hošovský, A. - Maxim, V.: Real-time safety circuit based on combined MEMS sensor data for rehabilitation device, 2012, In: ICCS 2012, IEEE, P. 786-790. - ISBN 978-1-4577-1866-3
- [11] Židek, K. - Piteř, J. - Galajdová, A. - Fodor, M.: Rehabilitation device construction based on artificial muscle actuators, 2012, In: BioMed 2012, IEEE, P. 855-861. - ISBN 978-0-88986-909-7

# High-Q Current-Mode CMOS Companding Bandpass Tunable Filter

A. Kircay

**Abstract**— In this study, a new design technique for high-Q current-mode bandpass filter using non-inverting lossy integrator is presented. The proposed new CMOS bandpass filter is designed by this new method. The most important advantage of the method uses only non-inverting lossy integrator structure for designing bandpass filters. MOSFETs square-law based non-inverting lossy integrator structure is used for realizing CMOS bandpass filter. At the same time, the proposed CMOS bandpass filter is a companding filter, since companding CMOS non-inverting lossy integrators are employed for realizing the filter circuit. The designed filter has a very simple structure, since it uses only MOSFETs and two grounded capacitors. All transistor aspect ratios (W/L)s are of the same value except for three transistors. The center frequency, the quality factor, and gain of the filter can be adjusted electronically. High-order bandpass filters can be designed using this method due to ability to tune all parameters. The bandpass is tunable in the center frequency range from 1Hz to 150MHz, with a Q quality factor that can be tuned from 1 to 100, ( $DR > 60dB$ ) dynamic range with THD (%) < 2 total harmonic distortion, and operated with a single supply voltage of 2.5V. The proposed filter can be applied for low voltage/power applications because of companding circuit. The designed circuit has been simulated in PSPICE using TSMC 0.35  $\mu$ m CMOS process parameters.

**Keywords**—current-mode circuits, CMOS, bandpass filter, companding circuit, non-inverting lossy integrator, electronically tunable.

## I. INTRODUCTION

THE current-mode filters have been receiving considerable attention due to their potential advantages such as inherently wide bandwidth, higher slew rate, wider dynamic range, simple configuration, high frequency operation, low voltage operation, and low power consumption [1-4]. An important number of elementary mathematical functions can be obtained easier from current signals rather than from voltage. Mathematical operations of adding, subtracting or multiplying signals represented by currents are simpler to perform than when they are represented by voltages. For this reason, integrated current-mode system realizations are closer to the transistor level than the conventional voltage-mode realizations and therefore simpler circuits and systems should

A. Kircay is associated prof. of Electrical-Electronics Engineering at Harran University, Sanliurfa, TURKEY (corresponding author to provide phone: +90-414 318 30 00-1089; e-mail: kircay@harran.edu.tr).

result [1-6]. On the other hand the high order filters can be implemented by using two or more filter blocks in cascade. Many techniques have been proposed in the literature to design the bandpass filter.

The block diagram consisting of lossless and lossy integrators and feedback is commonly used to realize filter circuits by designers [7-13]. The novelty of this study is an application of block diagram based on first-order lowpass or only non-inverting lossy integrator block method to realize high-Q, second-order current-mode bandpass responses. The proposed filter has advantages with respect to other filter structures that minimum components are used to realize a filter function. Then, the feedback is applied to the filter through the filter structure, in order to obtain high quality factor values than 1/2. The quality factor of second-order bandpass filter can be increased by using a feedback circuit that provides a current gain. The input and output signals are currents, and proposed filter can be described completely in terms of current-mode. It has very simple structure, and can give bandpass responses for a single input. For high-Q filter design, the new approach design method can be widely used due to its simple structure and tunable capability. Also, the filter circuit is very simple, can readily be integrated, are suitable for high-frequency applications, and can operate with a power supply as low as 2.5 V.

Up to now, several second-order bandpass filters have been presented in the literature [14-20]. In this study, the proposed filter has advantages with respect to other bandpass filters that only transistors and grounded capacitors are required to realize the filter circuit. It provides large dynamic range and lower total harmonic distortion. It has a high-Q and the center frequency of the filter can be electronically tuned by changing external current. The quality factor, and gain can be adjusted. It is suitable for low voltage/power applications.

In Section II, the new design method is presented. The proposed of the bandpass filter is discussed in Section III. Simulation results are presented in Section IV.

## II. THE PROPOSED HIGH-Q CMOS BANDPASS TUNABLE FILTER

The proposed second-order CMOS bandpass filter is realized by a block diagram. The block-diagram realization can be obtained by combining the non-inverting lossy integrator blocks,  $k$  gain block with the three arithmetic blocks as shown in Fig. 1 [12], [13]. The arithmetic block represents a node where the currents are being summed or

subtracted depending on the direction of current flow at that node [12], [13]. Then, the feedback is applied to the filter through the current amplifier circuit, in order to obtain high quality factor values than 1/2. The quality factor of second order bandpass filter can be increased by using a feedback circuit that provides a current gain [12], [20].

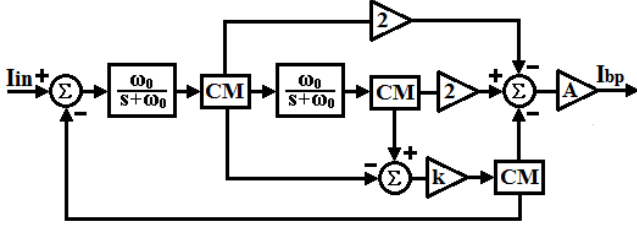


Fig.1. Block diagram of current-mode bandpass filter.

The second-order bandpass filter transfer function can be written from Fig. 1 as follows,

$$T(s) = \frac{I_{out}(s)}{I_{in}(s)} = -A \frac{(2-k)\omega_0 s}{s^2 + (2-k)\omega_0 s + \omega_0^2} \quad (1)$$

where  $A$  is gain,  $\omega_0$  is the center frequency and  $Q = 1/(2-k)$  is quality factor of the filter.

The realization of the proposed filter in Fig. 1 will be achieved by employing the topology of non-inverting lossy integrator, which is given in Fig. 2. The non-inverting lossy integrator was proposed by Mulder [21-23]:

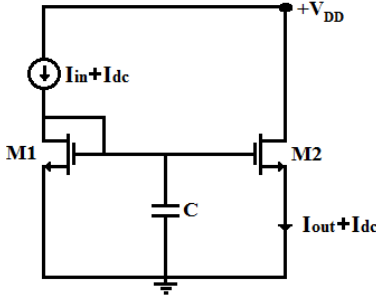


Fig.2. The non-inverting lossy integrator.

The square-law characteristic of an MOS transistor is

$$I_{DS} = \frac{\mu_0 C_{ox} W}{2L} (V_{GS} - V_{th})^2 \quad (2)$$

where  $\beta = \mu_0 C_{ox} W / L$ ,  $I_{DS}$ ,  $V_{GS}$ , and  $V_{th}$  are the device transconductance parameter, the drain source current, the gate-to-source voltage and the threshold voltage, respectively. Small-signal transconductance  $g_m$  of the MOS transistor in the strong inversion region, given by [21]:

$$g_m = \frac{\partial I_{DS}}{\partial V_{GS}} = \beta(V_{GS} - V_{th}) \quad (3)$$

From Fig.2, the KCL, and KVL equations can be written [21], [23]:

$$I_{DS1} = I_{in} + I_{dc} - I_{CAP} \quad (4)$$

$$I_{DS2} = I_{out} + I_{dc} \quad (5)$$

$$V_{CAP} = V_{GS1} = V_{GS2} \quad (6)$$

The capacitor current can be given by

$$I_{CAP} = C \dot{V}_{CAP} = C \dot{V}_{GS2} \quad (7)$$

The output current is the drain current of a M2 transistor and derivative of the output current is

$$\dot{I}_{DS2} = \dot{I}_{out} = \beta(V_{GS2} - V_{th}) \dot{V}_{GS2} \quad (8)$$

combining (4) with (8) and we obtain

$$I_{in} + I_{dc} - I_{DS1} = C \frac{\dot{I}_{out}}{\beta(V_{GS} - V_{th})} \quad (9)$$

$$I_{in} - I_{out} = C \frac{\dot{I}_{out}}{\beta(V_{GS} - V_{th})} \quad (10)$$

$$\dot{I}_{out} + \frac{\beta(V_{GS} - V_{th})}{C} I_{out} = \frac{\beta(V_{GS} - V_{th})}{C} I_{in} \quad (11)$$

When the amplitude of  $I_{in}$  is small with respect to  $I_{dc}$ , the transconductance  $g_m$  of the output transistor is approximately constant [21]. Therefore, the relation between the capacitor voltage and the output current  $I_{out}$  is almost linear. The transfer function of the filter core can be described by a linear differential equation [21]:

$$\dot{I}_{out} + \frac{\sqrt{2\beta I_{dc}}}{C} I_{out} = \frac{\sqrt{2\beta I_{dc}}}{C} I_{in} \quad (12)$$

Using the Laplace transform, the topology in Fig. 2 is a non-inverting lossy integrator with the following transfer function:

$$\frac{I_{out}(s)}{I_{in}(s)} = \frac{\omega_0}{s + \omega_0} \quad (13)$$

which represents the transfer function of lowpass filter or non-inverting lossy integrator.

The cut-off frequency of the integrator:  $\omega_0 = \frac{\sqrt{2\beta I_{dc}}}{C}$

The realization of the CMOS bandpass filter circuit using Fig.1 and Fig.2 is shown in Fig. 3.

The proposed filter parameters,  $\omega_0$ ,  $A$ ,  $Q$  were obtained from Fig.1, Fig. 2, and Fig.3 as follows,

The center frequency of filter:  $\omega_0 = \frac{\sqrt{2\beta I_{dc}}}{C}$ ,

The gain of filter:  $A$ ,

The quality factor of filter:  $Q = 1/(2 - k)$

### III. SIMULATION RESULTS

If you are using *Word*, use either the Microsoft Equation Editor or the *MathType* add-on (<http://www.mathtype.com>) for equations in your paper (Insert | Object | Create New | Microsoft Equation or MathType Equation). “Float over text” should *not* be selected.

The proposed filter was simulated by using *TSMC 0.35 μm Level 3 CMOS* process parameters. The transistors *M1-M22*, *M25* aspect ratios are:  $(W/L)_n=(W/L)_p=6\mu/1\mu$ , and the transistors *M23*, *M24* and *M26* aspect ratios depend on quality factor and gain. The circuit parameters are chosen as;  $V_{DD}=2.5V$ ,  $I_{dc}=80\mu A$ ,  $C=5pF$ . The natural frequency of the filter is  $f_0 \approx 10MHz$ , Quality Factor of filter is  $Q = 1$ , and gain is  $A = 1$ . The gain response of the bandpass filter is shown in Fig. 4. The phase response of the bandpass is shown in Fig. 5.

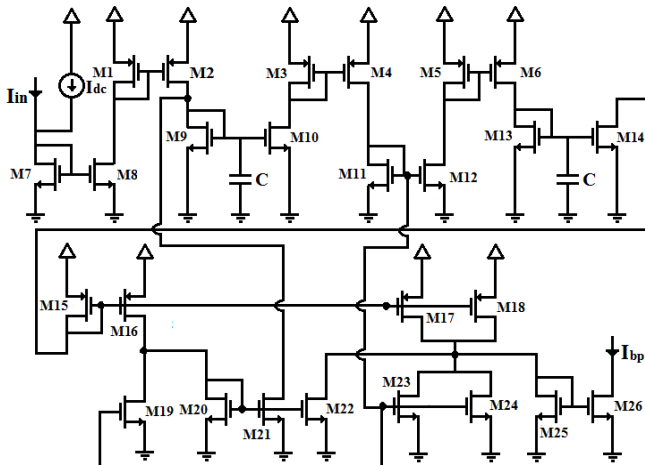


Fig.3. High-Q CMOS Bandpass Tunable Filter

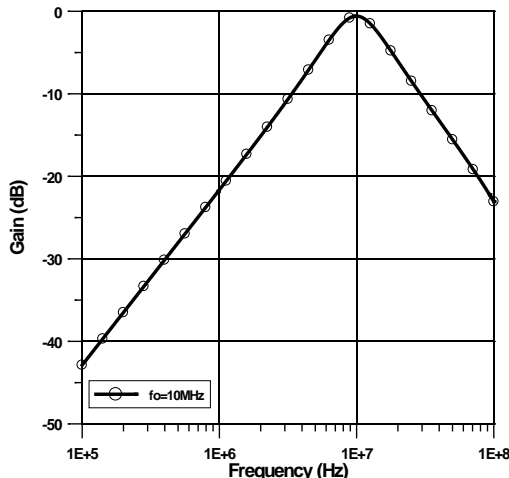


Fig.4. The gain response of the proposed filter.

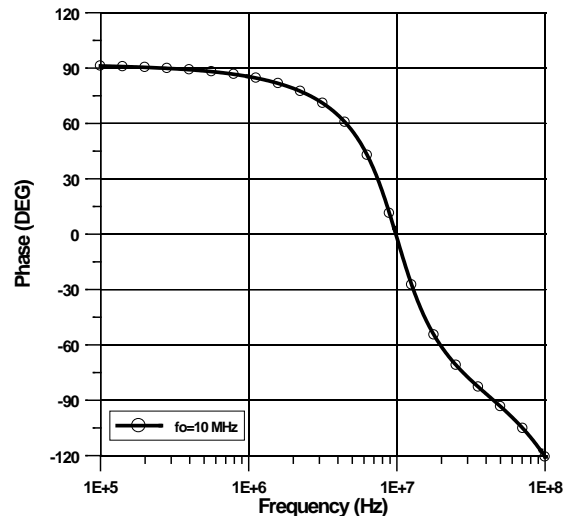


Fig.5. The phase response of the proposed filter.

The center frequency was observed by changing the external current  $I_{dc}$  as shown in Fig. 6. For this property, the external currents were changed from  $1\mu A$  to  $80\mu A$  and the filter center frequency was tuned from  $1.2MHz$  to  $10MHz$ .  $Q$ -tuning characteristics were observed by changing the external current as shown in Fig. 7. For this purpose,  $k$  was changed with varying the values and the  $Q$  was tuned from 1 to 100. The gain  $A$  tuning values can be controlled by changing *M26* aspect ratios.

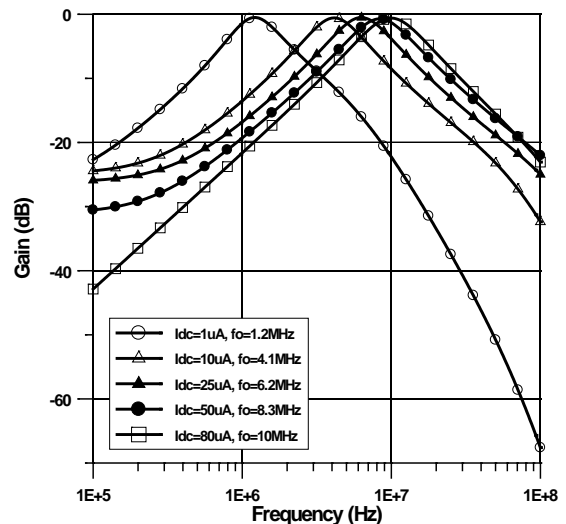


Fig.6. The tuning center frequency of the filter by changing the external current  $I_{dc}$

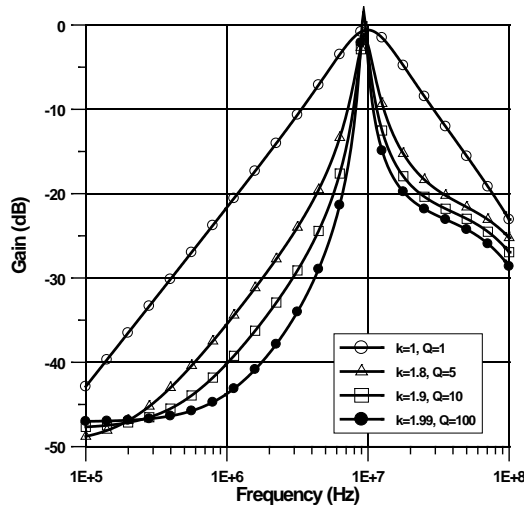


Fig.7. Q-tuning characteristics of the filter by changing k.

Fig.8 depicts center frequency of the filter as function of control  $I_{dc}$  for six different integrable capacitor values  $0.1pF$ ,  $1pF$ ,  $10pF$ ,  $100pF$ ,  $1nF$  and  $10nF$ . The filter can be controlled over a very wide frequency range of  $1Hz$  to  $150MHz$ .

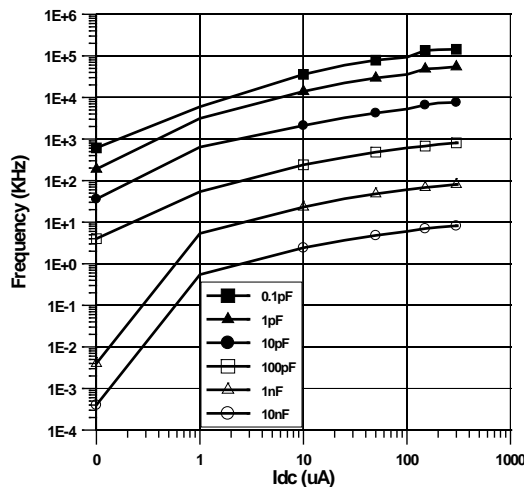


Fig.8. Simulated center frequency as a function of control  $I_{dc}$  for six different capacitor values.

The output signal's THD (Total harmonic distortion (%)) was measured with different input current value. The filter was set to  $10MHz$  center frequency with  $I_{dc} = 80uA$  and the input frequency was also set to the same value. Then, a sinusoidal signal was applied to the filter with different input currents,  $0.1uA$ ,  $1uA$ ,  $5uA$ ,  $10uA$ ,  $20uA$ ,  $40uA$  and  $100uA$ . The results of total harmonic distortion  $THD (%) < 2$ . At the same time, the proposed filter provides large dynamic range ( $DR > 60dB$ ). The performances and properties of the proposed filter are summarized in Table I. The design is based on block diagram and non-inverting lossy integrator. Tolerable differences are observed that realization of this filter in simulation has provided.

TABLE I. PERFORMANCES AND PROPERTIES OF THE PROPOSED FILTER

Proposed Filter	
Synthesis method	Non-inverting lossy integrator
Responses	Bandpass
Center frequency	Tunable
Gain	Tunable
Quality factor	Tunable
Supply voltage	2.5 V
Configuration	CMOS
THD (%)	<2
Dynamic range	>60 dB
Total power dissipation	<1 mW

#### IV. CONCLUSIONS

In this work, a new current-mode CMOS bandpass filter structure is presented. A systematic synthesis procedure to derive the filter circuit is also given. PSPICE simulations are provided to confirm the theoretical analysis. The proposed filter has the following advantages: i) based CMOS and current-mode, ii) has a very simple structure, and employs only MOSFETs and capacitors, iii) provides high-Q bandpass responses simultaneously for a single input signal, iv) suitable for low voltage/power applications, v) can be electronically tuned, vi) has a wide bandwidth, vii) suitable for VLSI (very large-scale integration) technologies.

#### REFERENCES

- [1] Sedra, A. and Roberts, G. W., "All current-mode frequency selective circuits", *Electronics Letters*, 25, 759-761, 1989.
- [1] Chang, M.C. and Toumazou, C., "3V MOS current conveyor for VLSI technology", *Electronics Letters*, 29, 317-318, 1993.
- [2] Cam, U. and Kuntman, H., "A new CCII based sinusoidal oscillator providing fully independent control of oscillation condition and frequency", *Microelectronics Journal*, 11, 913-919, 1998.
- [3] Abuelma'atti, M. T., Bentrchia, A., "A Novel current-mode OTA-C universal filter" *J. of Active and Passive Electronic Devices*, 2: 279-284, 2007.
- [4] Kilinc, S., "Analog circuit design using current and transresistance amplifier" Dokuz Eylul University, *Graduate School of Natural and Applied Sciences*, Izmir, Turkey, 2006.
- [5] Kircay, A. and Cam, U. "Differential Type Class-AB Second-Order Log-Domain Notch Filter", *IEEE Transactions on Circuits and Systems-I: Regular Papers*, Vol:55, Iss:5, pp.1203-1212, 2008.
- [6] Sinencio E. S., Geiger, R. L., "Generation of continuous-time two integrator loop OTA filter sstructure" *IEEE Trans. on Circuits and Syst.*, 35: 936-946, no.8, 1988.
- [7] Angulo, J.R., Robinson, M., Sinencio, E. S. "Current-mode continuous-time filters: Two design approaches" *IEEE Trans. on Circuits Syst.-II: Anaog and Digital Signal Processing*, 39: 337-341, no.6, 1992.
- [8] Sun, Y., Hill, C. "Low-Power Fully Differential CMOS Filter for Video Frequencies". *IEEE Trans. on Circuits Syst.-II: Analog and Digital Signal Proc.*, 48: 1144-1148, no. 12, 2001.
- [9] Tsukutani, T., Sumi, Y., Kinugasa, Y., Higashimura, M., Fukui, Y. "Versatile active-only biquad circuits with loss-less and lossy integrators" *Int. J. of Electronics*, vol. 91, no. 9, 525-536, 2004.
- [10] Mulder, J., Serdijn, W. A., Van der Woerd, A. C., Van Roermund, A. H. M. "An Instantaneous and Syllabic Companding Translinear Filter" *IEEE Tran. on Circuits and Systems-I: Fundamental Theory and Applications*, vol. 45, no. 2, 150-154, 1998.

- [11] Keserlioğlu M.S., Kırçay A., ‘Kare-Kök Ortamlı Akım-Modlu Elektronik Olarak Ayarlanabilir Evrensel Süzgeç’, *ELECO’2010, Elektrik-Elektronik-Bilgisayar Mühendisliği Sempozyumu ve Fuarı*, Aralık, 2010, Bursa, Türkiye
- [12] Kırçay, A. and Cam, U., "A Novel Log-Domain First-Order Multifunction Filter", *ETRI Journal*, vol.28, no.3, pp.405-408, Jun. , 2006
- [13] Zele, R. H., Allstot, D. J. "Low-Power CMOS Continuous-Time Filters" *IEEE Journal on Solid-State Circuits*, Vol.31, No:2, 1996.
- [14] Chang, Z. Y., Haspeslagh, D. and Verfaillie, J. "A Highly Linear CMOS – Bandpass Filter with On-Chip Frequency Tuning" *IEEE Journal on Solid-State Circuits*, Vol.32, No:3, 1997.
- [15] Chen, S. W., Wu, J.W., Wu, J. D., and Li, J. S., "Tunable active bandpass filter design" *Electronics Letters*, Vol. 47 No. 18, 2011
- [16] Oualkadi, A., Paillot, J. M., Alam, R., "New high-Q discrete-time LC bandpass filter design with center frequency broadband tuning" *Analog Integr Circ Sig Process*, 48:151–157, 2006
- [17] Manetakos, K., Toumazou, C., "A 50 MHz High-Q Bandpass CMOS Filter" 1997 *IEEE International Symposium on Circuits and Systems*, Hong Kong, June 9-12,1997,
- [18] Ngiamvibool, W. S., Srisuchinwong, B., "A 10.7-MHz fully balanced, high-Q, 87-dB-dynamic-range current-tunable Gm-C bandpass filter" *Analog Integr Circ Sig Process*, 58:143–151, 2009.
- [19] Fabre, A., Armani H. ve Saaid, O., "Current-Mode Band-Pass Filters with Q-Magnification", *IEEE Transactions on Circuits and Systems-II: Analog and Digital Signal Processing*, 43: 839-842, no. 12, 1996.
- [20] Mulder, J. "Static and dynamic translinear circuits", *Delft University Press*, Netherlands, 1998.
- [21] Mulder, J., Serdijn, W. A., Van der Woerd, A. C., Van Roermund, A. H. "Dynamic Translinear Circuits-An Overview" *Analog Integrated Circuits and Signal Processing*, Vol.22, Issue 2, pp.111-126, 2000.
- [22] Ozoguz, S., Abdelrahman, T., Elwakil, A. S., "Novel approximate square-root domain allpass filter with application to multiphase oscillators" *Analog Integrated Circuits and Signal Processing*, Vol. 46, pp.297-301, 2006.

**A. Kırçay** received B.Sc. degree in electrical and electronics engineering from Firat University in 1996, M.Sc. degree from Pamukkale University in 2001, and Ph.D. degree from Dokuz Eylül University in 2007. From 1998-2001 he served as research and teaching assistant at Pamukkale University, Department of Electrical and Electronics Engineering. From 2001-2007 he served as research and teaching assistant at Dokuz Eylül University, Department of Electrical and Electronics Engineering. From 2008-2010, he worked as assist. professor at Pamukkale University Department of Electrical and Electronics Engineering. He is currently working as assoc. professor at Harran University Department of Electrical and Electronics Engineering. His current research interests include analog signal processing, current-mode circuits, microelectronics, log-domain circuits, square-root-domain filters. He is author or co-author of many journal papers. He has also served as a reviewer for many scientific journals in electronics engineering.

# Motorized remote control of Transesophageal Echocardiography (TEE) probe tip: Preliminary testing

Dolwin C. C. Kho, Christina Pahl, Eko Supriyanto, Yin M. Myint, Ahmad A. M. Faudzi, Maheza I. M. Salim

**Abstract**—The existence and implementation of wireless technology within the medical area and its clinical application do not only improve the quality of the patients life, but also the efficiency of medical staff. This paper proposes a state-of-the-art and low cost remote positioning control unit. A new concept of the remote control was designed and after implementation in its medical target equipment tested. With this proposed idea, the Transesophageal Echocardiography (TEE) is able to be controlled remotely. The TEE movements and position were adjusted using wireless technology, Radio Frequency (RF). It is possible to monitor Patients' condition from a room, which is separated from the surgical theater. Furthermore, it is shown that the developed system enables archieving data collected during real-time remote monitoring.

**Keywords**—Transesophageal Echogardiography, remote control, radio frequency, clinical application.

## I. INTRODUCTION

**T**RANSESOPHAGEAL echocardiography or TEE, is an alternative procedure for further cardiac examination like transthoracic echocardiogram. It is used to evaluate, diagnose the cardiac condition and to monitor patients during the peri-operative period of cardiac surgeries as well as

This work was supported in part by the National Heart Institute of Malaysia (IJN).

D. C. C. Kho is under the University of Technoplogy Malaysia (UTM). Faculty of Biosciences and Medical Engineering. IJN-UTM Cardiovascular Engineering Centre, Skudai, Johor, Malaysia.

C. Pahl is under Ilmenau University of Technology (TUIL), Faculty of Mechanical Engineering, Department for Biomechatronics, 100 565, Ilmenau, Germany as well as University of Technoplogy Malaysia (UTM). Faculty of Biosciences and Medical Engineering. IJN-UTM Cardiovascular Engineering Centre, Level 2, Block B, Building V01, 81310, Skudai, Johor, Malaysia. (corresponding author to provide phone: +60 (0)102348580; e-mail: christina.pahl@tu-ilmenau.de).

E. Supriyanto is Head of Department for Clinical Science and Engineering and Head of Diagnostics Research Group at the University of Technology Malaysia, Faculty of Biomedical Engineering and Health Science, Skudai, Johor, Malaysia.

Y. M. Myint is under the University of Technoplogy Malaysia (UTM). Faculty of Biosciences and Medical Engineering. IJN-UTM Cardiovascular Engineering Centre, Skudai, Johor, Malaysia.

A. A. M Faudzi is under the University of Technoplogy Malaysia (UTM). Faculty of Biosciences and Medical Engineering. IJN-UTM Cardiovascular Engineering Centre, Skudai, Johor, Malaysia.

M. I. M. Salim is under the University of Technoplogy Malaysia (UTM). Faculty of Biosciences and Medical Engineering. IJN-UTM Cardiovascular Engineering Centre, Skudai, Johor, Malaysia.

hemodynamically unstable patients [1]. The cardiac data provided by the TEE provide clearer images compared to Transthoracic Echocardiography (TTE) data and are also less affected by interference originating from ribs, lungs and

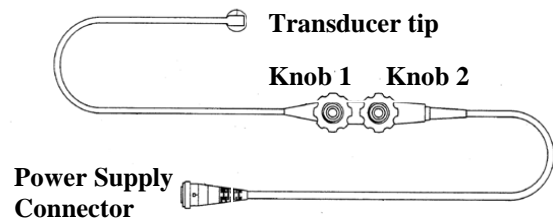


Fig.1 conventional TEE probe used for surgical procedures

subcutaneous tissue. The low degree of invasiveness of TEE and its capability to visualize and assimilate the dynamic information are helpful in changing the course of patient management [2]. As for TEE, there is a specialized probe, of an approximately one meter long flexible instrument, containing an ultrasound transducer at the tip which is passed into the esophagus of patients. Fig. 1 shows the physical of the TEE probe. The cardiac images are obtained by manually adjusting the transducer tip. The transducer at the tip of the probe is usually positioned within the esophagus right before the stomach and directly behind the heart.

The tip is rotated and moved towards some specific angles and directions in order to acquire images of the heart at several different coordinates. The position and orientation of the TEE probe can be altered by several standard manipulations, for example, advancement into or withdrawal from the esophagus, turning rightward or leftward, rotating forward or backward, and anteflex or retroflex [3]-[5]. These maneuvers have to be adjusted manually by turning the probe shaft and adjusting the knobs as well as electronic switch of the probe control unit using both hands simultaneously. The need of this manual probe adjustment to any specific position will therefore create an uncomfortable condition during diagnosis and surgery monitoring. Furthermore it is important to acquire precise coordinates of the probe position [6]. It is often inconvenient

for the sonographer to operate the control unit of the ultrasound machine while performing the TEE procedure [7].

The aim of developing this remote positioning control unit is to remote control and adjust position as well as orientation of the TEE probe tip towards specific angles and directions via RF wireless technology. This is used in order to acquire cardiac images. This system will eventually help doctors or surgeons to remotely monitor the condition of cardiac patients. RF was used here due to its low cost attitude. The application of TEE within clinical procedures can be traced back for more than a decade. It was first applied in 1976, where the instrument was a rigid, mechanical sector, a scanning device that may cause discomfort during intubation [8]–[10].

TEE was then improved with the application of phased array technology [11]. Later, TEE has been improved by using an electrically powered motor that was coupled to the flexible endoscope shaft as well as to the articulation section including the probe [12], [13]. The application of the motor to the shaft was used in order to minimize overtorque situations, whereas the articulation section was used for the locking mechanism in a given bent position of the probe.

In this study, a state-of-the-art remote positioning control unit foreseen to adjust the position of the TEE probe tip via RF wireless technology is presented. In section II, the proposed hardware is explained. Section III presents the software architecture, and the last section presents the discussion and conclusion.

## II. PROPOSED HARDWARE SYSTEM

### A. Proposed System

The proposed system acquires a position command or any position signal data from a particular source. Then it can transfer command data to the TEE probe by the use of RF. Subsequently the TEE probe tip will move and can be adjusted according to the received signals. With the developed system,



Fig. 2 basic diagram of the proposed system

real-time remote monitoring data or diagnosis information of

the patients' heart are achieved. In this way, doctors will be supported in monitoring more patients out of different surgical theatres with increased efficiency. The general diagram of the proposed approach is given in Fig. 2.

### B. Remote Positioning Control Setup

For the setup of the wireless communication system, a pair of RF wireless transmitter and receiver module were used. Signals were generated in order to be transferred by the transmitter. These include position signal data which is received by the corresponding receiver. A parallax joystick is used to provide position signals at the transmitter part. A prototyped TEE probe can be connected to the receiver side and so that it can move simultaneous to the movement of the joystick. The prototyped probe consisted of two units of servo motors. The servo motor will be remotely controlled by the joystick and was interfaced with Arduino Uno. The block diagram of the setup is given in Fig. 3.

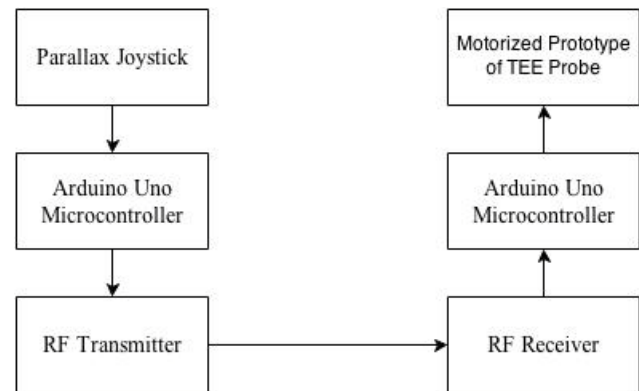


Fig. 3 block diagram of the remote positioning control unit

### C. Sequence of Signal Detection Algorithm

In the following the steps of the proposed position signal detection algorithm are given:

- 1) From the transmitter side, microcontroller reads any value from the analog pin if available. The value is range within and include 0 and 1023.
- 2) If there is a value, map the value to degree, which will be from 0 to 180.
- 3) Write the mapped value to serial data.
- 4) Display the value onto serial monitor.
- 5) Send the corresponding value to the receiver.
- 6) Any data from receiver will then be sent to the microcontroller and write to the servo motors.
- 7) Servo motors will be triggered to move in accordance to the degree received.
- 8) The degree of movement of the motor will be displayed on a new serial monitor.

Fig. 4 shows the flowchart in developing the algorithm of the remote positioning control system.

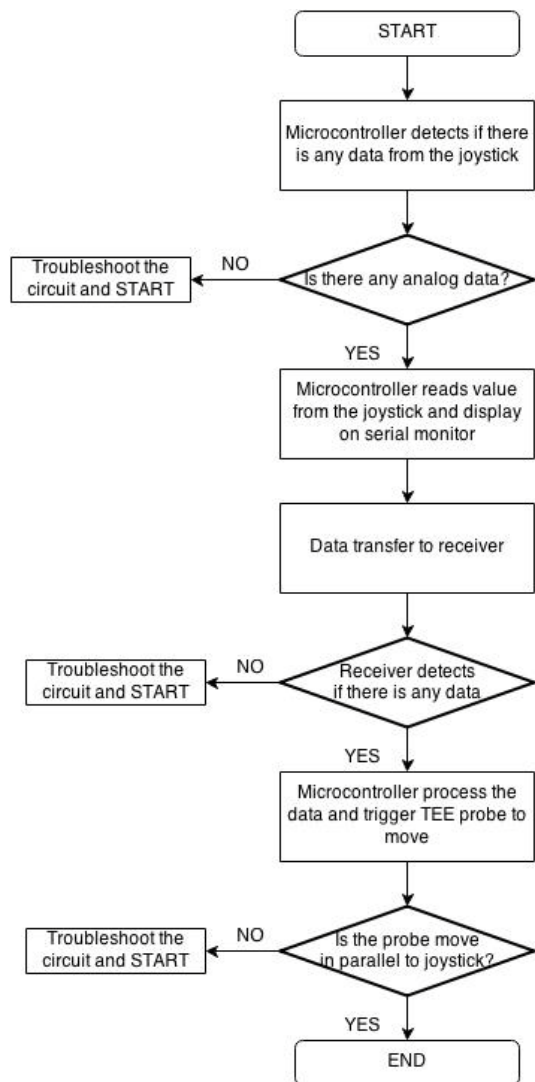


Fig. 4 flowchart of the algorithm

### III. SOFTWARE ARCHITECTURE

The whole operation of the proposed remote positioning control system is software controllable, thus the software can be reprogrammed several times without any major changes on the hardware designed. RF 433 MHz transmitter-receiver module was used in this study. Basically, this module is a one-way communication that sends signals or data without feedback from the receiver.

During the remote positioning control runtime, a connection between the transmitter and receiver is established when the baud rate and bit rate of the signal transmission was configured at the same value. After connection is established, transmitter will keep updating the receiver with the latest position signal data. Fig.5 shown the design framework of the proposed system.

The software architecture design includes programming Arduino Uno to read data from its analog input pin and move the motors as an end results. Arduino Uno is programmed using Arduino IDE ver.1.0.5-r2.

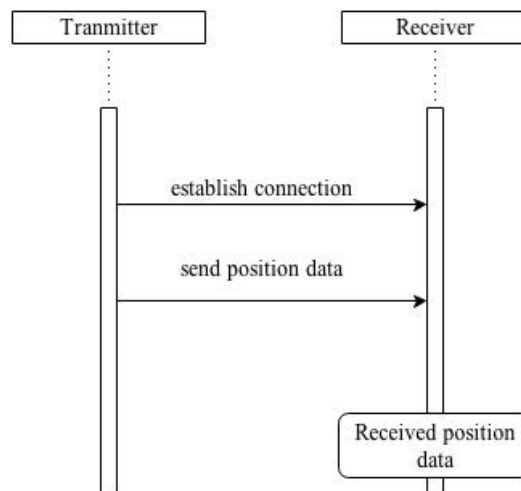


Fig. 5 design framework of the proposed system

### IV. RESULTS AND DISCUSSION

For the preliminary testing, five LEDs were used to indicate the position of the joystick. The preliminary test is done in order to validate if the RF wireless technology is able to send signals within a range of distance and also to test its resistance to obstacles indoor. The LEDs are arranged in a circle on the breadboard. The LED in the middle represents the joystick in rest. This test was done in a range of distance of 48 meters, separated by a transparent wall in between. The LEDs test results are given in Fig. 5(a) until Fig. 5(i).

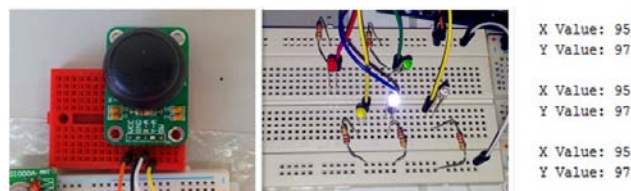


Fig. 5(a) joystick in still position, no movement

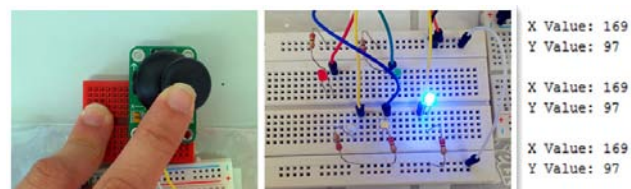


Fig. 5(b) joystick on positive x-axis

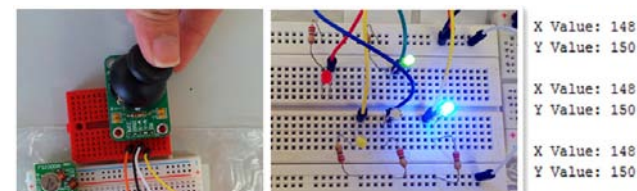


Fig. 5(c) joystick in first quadrant position

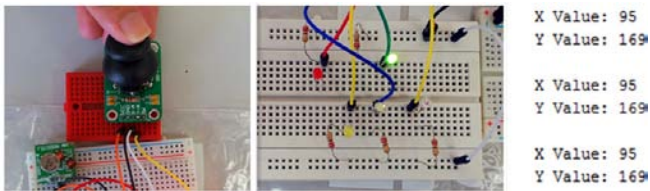


Fig. 5(d) joystick on positive y-axis

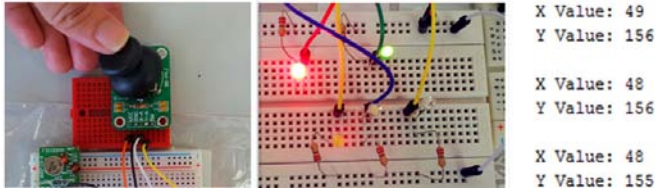


Fig. 5(e) joystick in second quadrant position

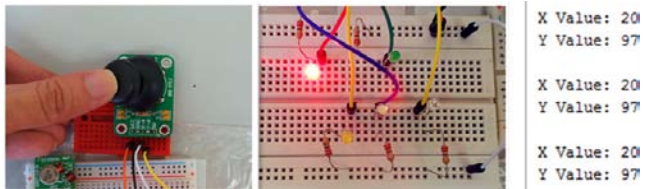


Fig. 5(f) joystick on negative x-axis

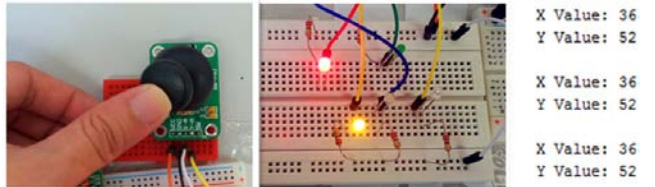


Fig. 5(g) joystick in third quadrant position

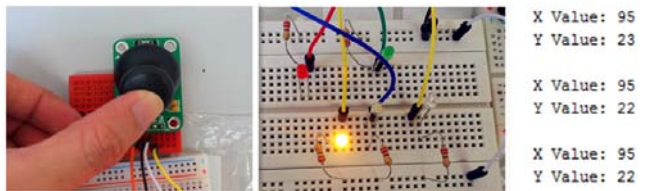


Fig. 5(h) joystick on negative y-axis

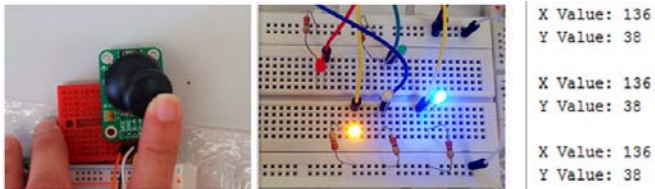


Fig. 5(i) joystick in fourth quadrant position



Fig. 6(a) joystick in still position, no movement



Fig. 6(b) joystick on positive x-axis



Fig. 6(c) joystick in first quadrant position



Fig. 6(d) joystick on positive y-axis



Fig. 6(e) joystick in second quadrant position



Fig. 6(f) joystick on negative x-axis



Fig. 6(g) joystick in third quadrant position



Fig. 6(h) joystick on negative y-axis



Fig. 5(i) joystick in fourth quadrant position

From the preliminary results, it can be seen that the LEDs are blinked in accordance to which quadrant the joystick is in at that particular moment. RF wireless technology can be used to transmit signals through obstacles such as walls.

Testing was proceeded with controlling of the servo motors. In the results given in Fig. 6(a) until Fig. 6(i) shown that servo motors were able to be controlled by the parallax joystick. This test was also done within distance of 48 meters, separated by a transparent wall in between. Therefore, RF wireless technology has validate its ability to transmit position signals from joystick to control servo motors.

## V. CONCLUSION

This study has presented preliminary testing on wireless remote control of the TEE probe tip position and orientation using RF wireless technology. The position signals are acquired from a parallax joystick and sent to LEDs and servo motors via RF wireless technology. The preliminary results has proven that signals transmission using RF are able to transmit through obstacles, which proven can be used between two separate rooms. The whole concept constitutes a distributed architecture and helps to increase patients' cardiac monitoring. With this system, it can be used to monitor patients remotely from different surgical theaters.

## ACKNOWLEDGEMENTS

The work contained in this paper was supported by Flagship grant (2013-2014) of University of Technology Malaysia; "Development of Remote Controlled Transesophageal Echocardiography Probe Positioning System" (Vote No.: Q.J130000.2445.00G92), and Flagship grant (2014-2015) of University of Technology Malaysia; "Development of Transesophageal Echocardiography Probe Remote Positioning Control Unit" (Vote No.: Q.J130000.2409.01G69).

## CONFLICT OF INTEREST

The authors declare that they have no conflict of interest.

## REFERENCES

- [1] I. G. Burwash and K. L. Chan, "Transesophageal Echocardiography," in *Otto C. M. The Practize of Clinical Echocardiography*, Philadelphia: Elsevier Saunders, 2007, pp. 3-25.
- [2] R. M. Savage, S. Aronson, J. S. Shanewize, E. B. Mossad and M. G. Licina, "Intraoperative Echocardiography; Cardiac Anesthesia-Principle and Clinical Practize," in F. G. Estafanous, G. P. Barash and J. G Reeves, Philadelphia, 2001, pp. 237-294.
- [3] A. F. Edward, A. S. Jeffrey, H. B. Jaqueline and E. G. Martin, "Transesophageal Echocardiography: Procedures and Clinical Application," in American College of Cardiology, New York, 1991, pp. 1333-1348.
- [4] J. P. Miller, "Two-Dimensional Examination," in *Essentials of Two-Dimensional Imaging*, pp. 24-52.
- [5] F. Robert, K. John and R. Marco, "Core Topics in Transesophageal Echocardiography," Cambridge University Press, 2013.
- [6] C. Pahl, E. Supriyanto, N. H. B. Mahmood, J. Yunus, " Cervix Detection Using Squared Error Subtraction," *Modelling Symposium (AMS)*, 2012, pp. 29-31.
- [7] B. Frank, W. K. Perry and A. L. Eugene, " Transesophageal Ultrasonic Scanhead," U.S. Patent 5,050,610, 1991.
- [8] L. Frazin, J.V. Talano, L. Stephanides, H. S. Loeb, L. Kopel and R. M. Gunnar, " Esophageal Echocardiography," in *Circulation*, 1976, pp. 102-108.
- [9] K. Hisanaga, A. Hisanaga, N. Hibi, K. Nishimura and T. Kambe, " High speed rotating scanner for transesophageal cross-sectional echocardiography," in *American Journal of Cardiology*, 1980, pp. 837-842.
- [10] E. J. Gussenhoven, M. A. Taams and J. Roelandt, " Transesophageal two-dimensional echocardiography: its role in solving clinical problems," in *J Am Coll Cardiol.*, 1986, pp.975-979.
- [11] M. Schluter, B. A. Langenstein and J. Polster, " Transesophageal cross-sectional echocardiographywith a phased array transducer system: technique and initial clinical results," 1982, pp. 67-72.
- [12] J. S. Rodney, K. M. Martin, G. Goerge and T.F. James, "Transducer Positioning System," U.S. Patent 5,181,514, 1993.

- [13] P. G. George, " Ultrasonic Transesophageal Probe with Detachable Transducer Tip," U.S Patent 5,634,466, 1997.

# Manipulator development for telediagnosics

Adam Kurnicki, Bartłomiej Stanczyk, and Bartosz Kania

**Abstract**— This paper presents development of the light-weight manipulator with series elastic actuation for medical telediagnosics (USG examination). General structure of realized impedance control algorithm was shown. It was described how to perform force measurements based mainly on elasticity of manipulator links

**Keywords**— telediagnosics, elastic manipulator, impedance control, force measurement.

## I. INTRODUCTION

Modern society increasingly requires specialized medical care. Unfortunately, in most countries there is a lack of physicians. This situation is steadily deteriorating and this is particularly evident in a limited number of specialists who are not always available to the medical unit due to geographical (e.g. provincial hospitals), time (after regular working hours) or other logistic constraints. This circumstance provides an incentive for the development of many types of medicine-related services performed remotely ranging from Telepsychiatry, Telerehabilitation, Teledentistry, etc. to Telesurgery.

Usually a successful medical treatment depends on a timely and correct diagnosis which is crucial in typical emergency situations. Specialist (a doctor) needs some time to get to patient from home or from another hospital. If doctor could perform the diagnostics remotely, and e.g. make a decision about a surgical intervention, the hospital staff could use the time during which the doctor is travelling and prepare the patient. Currently there exist no devices enabling complete remote medical examination and diagnostics based on contemporary medical standards [1].

Presented work is a part of the project which addresses telediagnosics in clinical environments. Multifunctional robotic system, which will allow performing a real remote physical and ultrasonographic (USG) examination was designed. The system, see Fig. 1, consists of a mobile robot operating in a hospital, and a remote interface placed at the doctor's location. The role of the mobile robot is twofold: firstly- it acts as a full

embodiment of the doctor; secondly it is an intelligent robot system equipped with advanced perception, reasoning, and learning abilities.

One of the most important elements of the system (i.e. mobile robot part) is manipulator with palpation and USG effector. Cable-driven 6DoF manipulator to form wrist, elbow and shoulder was developed. The drives are based on series elastic actuation principles and form a lightweight and safe solution. To achieve semi-autonomous functionality of the manipulator, a special control system PC-based real-time operating system and hardware security controller were designed.

## II. DESIGN OF ELASTIC MANIPULATOR

### A. Manipulator Requirements

In industrial or laboratory settings the safety of the human operators/users can be guaranteed through barriers. The safety requirements increase drastically when robots physically interact with humans, as in our case, since a single malfunction can endanger the life or health of the patient. Therefore it is extremely important to take safety into account during each phase of the design and development. Unfortunately, there exist no industry-standard approach to designing safety-critical robots for physical human-robot interaction. De Santis et al. formulated an atlas of physical human robot interaction with special focus on safety and dependability [2].

Based on the above information, the following guidance should be taken into account during the design of a robot arm:

- 1) the inertia of the moving parts should be kept as low as possible by means of lightweight design by locating the drives in the robot base and transmitting the mechanical power to the joints using cable actuation - reduction of the potentially catastrophic consequences of the robot hitting a human,
- 2) robot surface should be covered with soft material; no sharp elements should be on the robot surface [3],
- 3) safe limits for the maximum moving weight and velocities of the arm have to be found by simulation and ensured on the robotic system [4],
- 4) the drives should be torque limited and backdrivable so that the user may change the robot position just by touching and moving it with bare hands,
- 5) human body parts (ie. fingers, hands) and clothing parts should be protected against clamp in between joints, cables or any other protruding elements,

The research leading to these results has received funding from the European Community's Seventh Framework Program (FP7/2007-2013, ICT 2013-10) under grant agreement no. 610902.

A. Kurnicki is with the Automation and Metrology Department, Lublin University of Technology, ul. Nadbystrzycka 38a, 20-618 Lublin, Poland, e-mail: a.kurnicki@pollub.pl.

B. Stanczyk, is with Accrea Engineering, ul. Hiacyntowa 20, 20-143 Lublin, Poland (e-mail: b.stanczyk@accrea.com).

B. Kania is with the Automation and Metrology Department, Lublin University of Technology, ul. Nadbystrzycka 38a, 20-618 Lublin, Poland (e-mail: b.kania@pollub.pl).

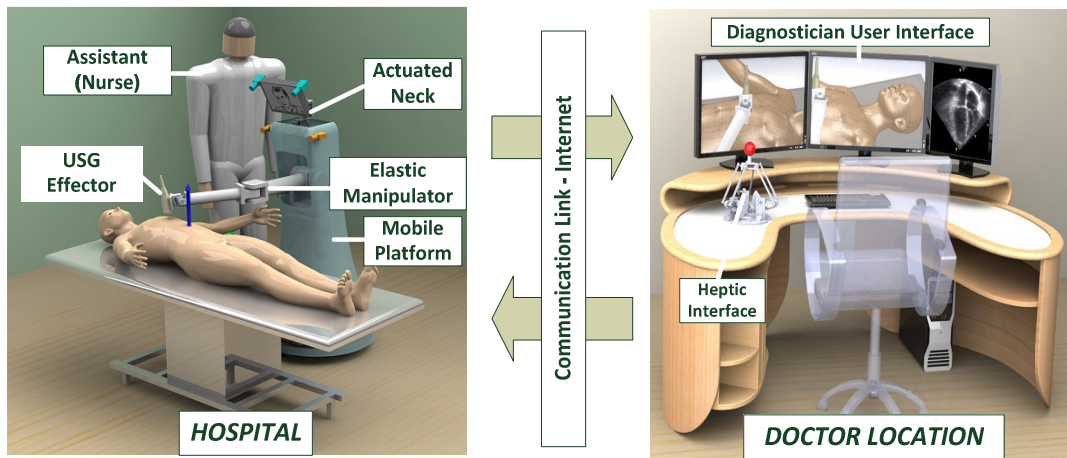


Fig. 1 Diagnostic system overview

- 6) user should be protected against electric shock -ideally, no voltage higher than 48 V DC should be present in the robot,
- 7) robot should recognize the interaction forces exerted by the surrounding humans or objects not only at the end effector or at the joints - adequate force sensors and manipulator workspace should be comparable to that of a human arm,
- 8) overall weight should be maximum 5kg and payload of 3 kg.

The above requirements are not acceptable in the industrial robotic design, where the accuracy, speed and durability in long term operation are the predominant, so the industrial manipulators couldn't be used. Accordingly to [5] our robot has to sacrifice high accuracy and performance in favor of safety so the search area of possible existing and suitable manipulator was rehabilitation and care robotics. The following robot arms were investigated: DLR-III Lightweight Robot [6], Barrett WAM-Arm [7], Kinova JACO [8], Assistive Robotic Manipulator iARM [9], BioRob-Arm [10], Meka A2 Compliant Arm [11], Robotnik modular arm and ACCREA arms [12]. Their parameters are summarized in Table I. However, all these arms do not meet the requirements as mentioned above, e.g. due to too high weight or size, too small workspace, or they are not available.

*B. Mechanical Design*

Given the above design requirements, 6DOF cable-driven manipulator was designed. The links of the manipulator are actuated using actuators with serial elasticity. Overview of this manipulator presents Fig. 2. All heavy motors are placed in the manipulator base. Compliant transmission mechanically decouples the lower link inertia from the heavy motors, which leads to even less apparent inertia during impacts. The joints are multi-actuated using differential kinematic structures, so that an uncontrolled behavior of one motor will not be able to produce dangerous motion of the link. Second joint (shoulder) of manipulator is passively gravity compensated. Gear reduction ratios were reduced as much as possible to ensure backdrivability of the actuators. In order to realize force control algorithms, there are linear springs (two per each joint) mounted in series with cables, in similar way presented in work [10]. It requires use of two encoders at each joint, one mounted on the motor shaft and the second (more precise) directly on the joint. This solution makes it possible to eliminate expensive force sensor JR3 mounted at the end of the manipulator or to support results of his measurements in the control algorithm.

The Denavit-Hartenberg parameters for the manipulator are listed in Table II, the corresponding set of frames is shown in joints  $q$  (vector of angular positions or velocities in joint space

TABLE I. MANIPULATORS AND THEIR PARAMETERS

Parameter	Unit	DLR III	Barrett WAM	KINOVA	iARM	AMOR	Biorob	Meka A2	Robotnik	ACCREA
Degrees of Freedom	-	7	7	6	6	7	4	7	7	7
Total weight	[kg]	14	27	5	9	9	4,4	11,4	19	10
Mass of moving parts	[kg]	no data	no data	5	no data	no data	1	11,4	19	5
Maximum Load	[kg]	7	3	1,5	1,5	2,5	2	2	no data	2,5
Reach	[cm]	93,6	100	90	90	95	70	no data	130	80
Backdrivability	-	YES	YES	YES	YES	no data	YES	YES	YES	YES
Absolute position tolerance	[mm]	no data	2	8	no data	2,5	no data	no data	no data	4
Relative position tolerance	[mm]	no data	0,2	1,6	no data	1,3	no data	0,2	0,5	1
Prices	EURC	90 000	50 000	40 000	n/a	35 000	30 000	60 000	50 000	n/a

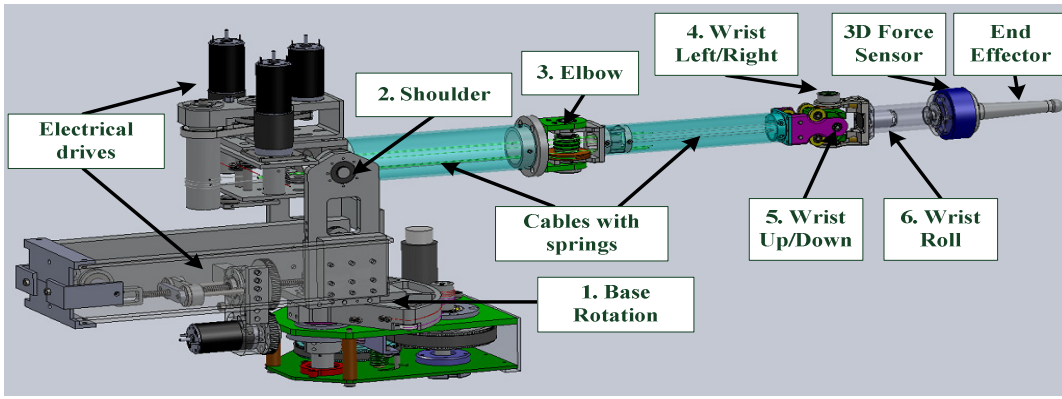


Fig. 2 Design of the 6 DoF elastic manipulator

TABLE II. MANIPULATOR DENAVIT-HARTENBERG PARAMETERS

Joint no	Link offset $a_i$ (mm)	Link twist $\alpha_i$ (rad)	Link length $l_i$ (mm)
1	195.0	$\pi/2$	0
2	0	$-\pi/2$	293.3
3	0	0	312.0
4	0	$\pi/2$	0
5	0	$\pi/2$	0
6	194.0	0	0

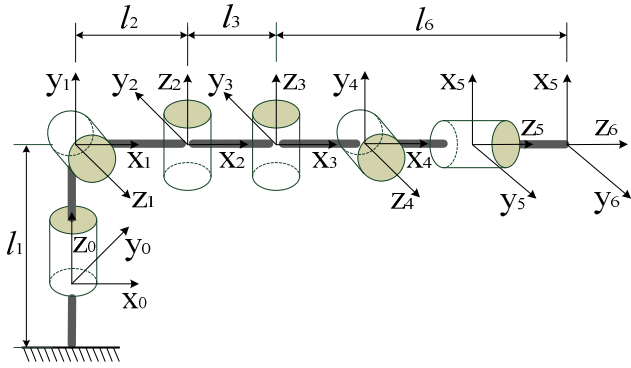


Fig. 3 Design of the 6 DoF elastic manipulator

and the motors shafts  $\theta$  (vector of angular positions or velocities in motor space) was described in (1)

$$q = G * \theta \quad (1)$$

where  $G$  is a gear ratio and coupling matrix as in (2)

$$G = \begin{bmatrix} G_1 & 0 & 0 & 0 & 0 & 0 \\ 0 & G_2 & 0 & 0 & 0 & 0 \\ 0 & 0 & G_3 & 0 & 0 & 0 \\ 0 & 0 & -G_3 & \frac{G_4}{2} & \frac{G_5}{2} & 0 \\ 0 & 0 & 0 & \frac{G_4}{2} & \frac{G_5}{2} & 0 \\ 0 & 0 & 0 & -\frac{G_4}{2} & -\frac{G_5}{2} & G_6 \end{bmatrix} \quad (2)$$

where  $G_i$  is gear ratio of  $i$ -th joint.

### III. MANIPULATOR CONTROL SYSTEM

The main task of the control system is the implementation of tediagnosics task (USG), i.e., movement of the end-effector through the patient body, according to the position, orientation and force desired by the operator (doctor). In that case the most suitable is use of impedance control algorithm [12]. In order to realize above task, real time control with sampling period 1ms (or less) and accurate manipulator dynamic model should be implemented [12].

#### A. Control System Structure

General structure of designed control system presents Fig. 4. This structure consists of three main elements:

- 1) controlled object - elastic manipulator,
- 2) controller - PC computer with real time operation system (RT Preempt or Xenomai), two multifunctional analog/digital I/O cards, force sensor JR3 card and implemented control algorithm,
- 3) hardware safety system and motor current controllers (servoamplifiers).

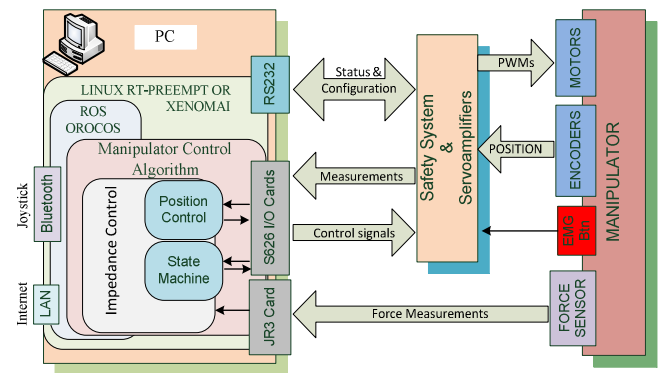


Fig. 4 Structure of manipulator control system

The main task of the safety system is to protect the user in case of emergency, mainly caused by different types of device malfunctions in the control system, as failure of: encoders (eg open or short circuit), servoamplifiers (overload or

overvoltage), PC controller (hang or crash) and the detection and response to other irregularities as such as joint overspeed.

The basic components of control algorithm, which was developed using Matlab-Simulink software, are impedance control algorithm and state machine. The state machine defines all kinds of situations in which the manipulator can be found starting from initialization of the security system and joints homing, through mode and task selection adequately to the demands of the operator or assistant and ending at the appropriate reaction in failure situation. The impedance control algorithm strategy presents Fig. 5. As mentioned in [12] the goal of the impedance control is to make the end-effector behave as an linear and decoupled mechanical impedance characterized by a virtual mass  $M_p$ , damping  $D_p$  and stiffness  $K_p$  matrices with regard to measured contact Cartesian force  $F$ . This can be written as follows:

$$M_p * p'' + D_p * p' + K_p * p = F \quad (3)$$

where  $p$  denotes the difference between desired  $p_d$  and compliance  $p_c$  frames (position and orientation). The compliant frame describes the end-effector position and orientation when it is in contact with the environment (patient) and then impedance controller modifies desired frame according to measured forces. When there is no contact  $p_c$  is identical with  $p_d$ . This algorithm requires a valid measurement of the force exerted on the end-effector. To achieve this without force sensor JR3 (based on elasticity of each joint drive cables with springs) accurate manipulator dynamic model is required.

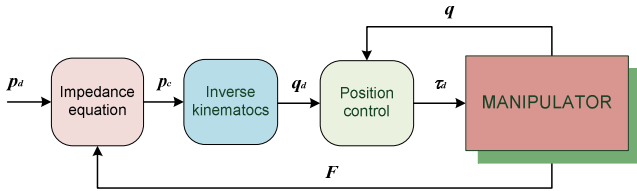


Fig. 4 Impedance control strategy

### B. Manipulator Dynamic Model and Force Measurement

The general dynamical model of rigid manipulator can be written in the form:

$$M(q) * q'' + C(q, q') * q' + D * q' + g(q) = \tau - J^T * F \quad (4)$$

where  $q$  is the vector of joint positions (angles),  $M$  is the inertia matrix,  $C(q, q') * q'$  is the vector of Coriolis and centrifugal torques,  $D$  is diagonal friction matrix,  $g$  is a vector of gravitational torques,  $\tau$  is the vector of driving torques,  $J$  is the Jacobian matrix relating joint velocities  $q'$  to the vector of end-effector Cartesian velocities  $x'$ . Because of relatively slow motion of manipulator parts vector  $C(q, q') * q'$  can be assumed as negligible and then (4) will be in form:

$$M(q) * q'' + D * q' + g(q) = \tau - J^T * F \quad (5)$$

According to [10], in case of elastic actuator, driving torques  $\tau$  can be calculated as:

$$\tau = k_e * (q_m - q) \quad (6)$$

where  $k_e$  is the vector of elasticity factors,  $q_m$  is the vector of drive shaft positions.

Every driving-cable in our elastic manipulator has one spring mounted in series (two identical springs per joint) as it was shown on Fig. 6.

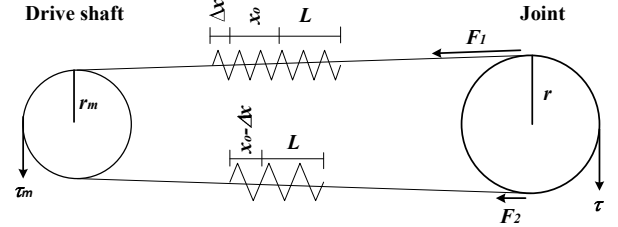


Fig. 6 Force measurement principle on the base on manipulator elasticity

Every spring is pretensioned which causes spring elongation  $x_0$ . According to situation presented on Fig 6 torque  $\tau$  is calculated as:

$$\tau = r * (F_1 - F_2) \quad (7)$$

where  $r$  is the radius of joint pulley,  $F_1$ ,  $F_2$  are upper side and lower side forces. The difference between the values of both forces  $F_1 - F_2$  depends on spring elongation  $\Delta x$  and it is calculated in two cases: first when  $|\Delta x| \leq x_0$

$$(F_1 - F_2) = 2 * k * \Delta x \quad (8)$$

and second when  $|\Delta x| > x_0$

$$(F_1 - F_2) = k * (\Delta x \pm x_0) \quad (9)$$

where  $k$  is the spring constant and sign before  $x_0$  depends on the spring which is stretched the more. Spring elongation  $\Delta x$  is obtained as:

$$\Delta x = r_m * q_m - r * q \quad (10)$$

where  $r_m$  is the radius of motor shaft pulley.

Cartesian force  $F$ , at the end-effector, can be calculated through equation obtained from (5):

$$F = (J^T)^{-1} * (\tau - M_e(q) * q'' - D_e * q' - g_e(q)) \quad (11)$$

where  $M_e$ ,  $D_e$  and  $g_e$  are the same matrices and vectors as in (5) but with the exclusion of the impact of this part which relates to the drive (i.e. the engines and gearboxes).

Series of experiments were carried out in which were compared the measured forces obtained using described above

method and the measurements obtained from force sensor. These experiments were made in different conditions i.e. different position and orientation of end-effector and different force direction. These experiments were performed under different conditions, i.e. different positions and orientations of the end-effector and for different directions of impacts. Fig. 7 presents force measurements in case of force acting parallel to the direction  $x_0$  (Fig 7a) and in case of force acting parallel to the direction  $y_0$  (Fig 7b).

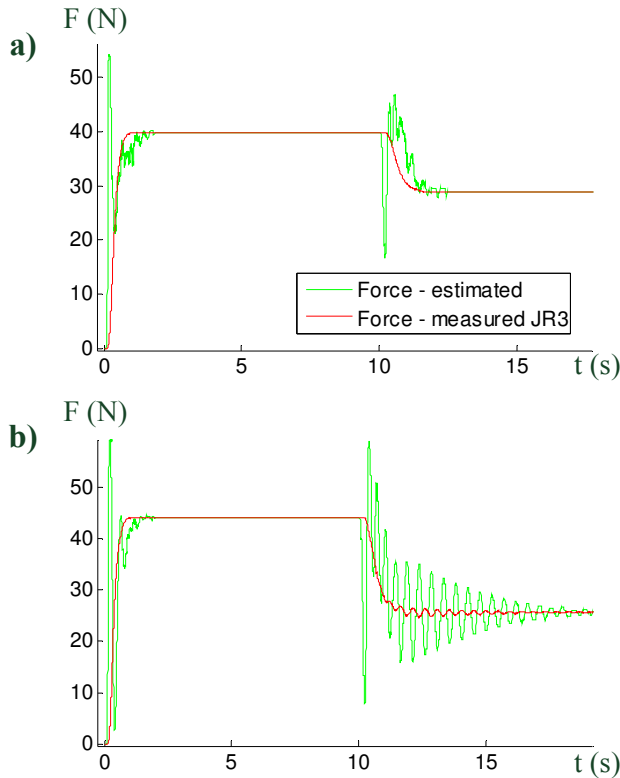


Fig. 7 Experimental results: a) force waveforms in case of force acting parallel to the direction  $x_0$ , b) force waveforms in case of force acting parallel to the direction  $y_0$

#### IV. CONCLUSION

This paper presented the development of elastic manipulator for medical telediagnosics. We pointed out how desired is to design new type of manipulator in case of lack commercially available manipulator. The control system with impedance control algorithm was designed for this manipulator. In order to perform force measurements, method which utilizes the flexibility of links was developed. Experiments confirmed the correct operation of the system, especially in steady state. The differences in the waveforms of forces under dynamic conditions is mainly caused due to inaccuracies of the model parameters. In order to use this type of measurement in the control algorithm, the model accuracy should be improved.

#### REFERENCES

- [1] G. Herold, "Herold's Internal Medicine", Vol 1 and 2, Lulu Enterprises Incorporated, 2011.
- [2] A. De Santis, B. Siciliano, A. De Luca and A. Bicchi, "An atlas of physical human-robot interaction", Mechanism and Machine Theory 43, 2008.
- [3] J.-J. Park, S. Haddadin, J.-B. Song and A. Albu-Schäffer, "Designing optimally safe robot surface properties for minimizing the stress characteristics of human-robot collisions", IEEE International Conference on Robotics and Automation, 2011, pp. 5413-5420.
- [4] S. Haddadin, A. Albu-Schäffer and G. Hirzinger, "Safe physical human-robot interaction: measurements, analysis and new insights", Robotics Research, Springer, 2011, pp. 395-407.
- [5] G. Pratt and M. Williamson, "Series Elastic Actuators", Proceedings of the IEEE International Conference on Intelligent Robots and Systems, 1995 pp., 399-406.
- [6] G. Hirzinger, N. Sporer, M. Schedl, J. Butterfaß, M. Grebenstein, "Torque-Controlled Lightweight Arms and ArticulatedHands: Do We Reach Technological Limits Now?" The International Journal of Robotics Research, Vol. 23, No. 4-5, 2004, pp. 331-340.
- [7] [http://www.barrett.com/robot/DS\\_WAM.pdf](http://www.barrett.com/robot/DS_WAM.pdf).
- [8] V. Maheu, J. Frappier, P. S. Archambault, F. A. Routhier, "Evaluation of the JACO robotic arm: clinico-economic study for powered wheelchair users with upper-extremity disabilities", Proc. 2011 IEEE Intl. Conf. on Rehabilitation Robotics (ICORR), 2011, pp. 1-5.
- [9] G. Romer, H. J. A. Stuyt and A. Peters, "Cost- savings and economic benefits due to the assistive robotic manipulator (ARM)", Proceedings of the 2005 IEEE 9th International Conference on Rehabilitation Robotics, Chicago, IL, USA, 2005, pp 201-204.
- [10] T. Lens, J. Kunz and O. Stryk, "Dynamic Modeling of the 4 DoF BioRob Series Elastic Robot Arm for Simulation and Control", Proceedings of the Intl. Conf. on Simulation, Modeling, and Programming for Autonomous Robots (SIMPAR 2010), Springer, 2010, pp. 497-508.
- [11] [http://mekabot.com/wiki/doku.php?id=user\\_guides:arm\\_a2r4](http://mekabot.com/wiki/doku.php?id=user_guides:arm_a2r4).
- [12] Stanczyk, B., "Development and Control of an Anthropomorphic Telerobotic System", Dissertation, Technische Universität München, 2006.

**Adam Kurnicki** Ph.D (2004) and M. Sc. (1999) in Electrical Engineering and Computer Science from Lublin University of Technology, Poland. My interests include realime control, process diagnosis using artificial intelligence methods, neuro-fuzzy control systems.

**Bartłomiej Stanczyk** Ph.D (2006) in Technical Science from TU Muenchen, Germany and M. Sc. (1998) in Electrical and Control Engineering from TU Lublin, Poland. Between 1998 and 2006 worked as research assistant at the TU Lublin (Poland), Berlin and Munich (Germany), involved in various research projects on robust and digital control. During my PhD time he focused on teleoperation, redundant kinematics and impedance control of robotic manipulators. Currently, his main interests are robot design and system engineering. He is also active as a consulting engineer for various companies in Germany. I have several years of experience in system engineer for safety critical mechatronic systems gained at aerospace (MTU, AES, Airbus) and automobile industry (Audi).

**Bartosz Kania** M. Sc. (2013) in Electrical Engineering and Computer Science from Lublin University of Technology, Poland. Actually research assistant at the TU Lublin.

# A 5-tap Half-rate DFE Receiver for Data-Edge Simultaneous Equalization

Sung-Won Choi, Hyun-Wook Lim, and Bai-Sun Kong

**Abstract**—The paper presents a 5-tap half-rate DFE receiver for data-edge simultaneous equalization. The proposed DFE receiver can cancel ISIs at data transition edges as well as at data sampling points by employing a novel equalization method based on received waveform shaping. The proposed DFE receiver is designed in a 45-nm LP CMOS process. The evaluation results indicate that edge ISI is reduced by 30% with no degradation on data ISI cancellation. It also indicates that the output jitter of a CDR designed with the proposed DFE is reduced by 19% compared to the conventional data-based DFE.

**Keywords**—Decision feedback equalizer, data-based DFE, edge-based DFE

## I. INTRODUCTION

AS the data rate of an electric channel increases, inter-symbol interference (ISI) is getting larger due to limited bandwidth of the channel. The decision feedback equalization (DFE) is commonly used to solve this problem [1]. A traditional DFE approach that is called the data-based DFE (D-DFE) [2], [3] cancels post-cursor ISIs without amplifying noise. Fig. 1(a) shows the eye diagram of a D-DFE, in which we can recognize that the voltage margin at the center of a data eye is extended. But, unfortunately, the timing margin at data transition edges is still not enough due to a large amount of edge ISI.

CDR used for clock and data recovery usually takes advantage of timing information derived from zero-crossing points or transition edges of received signals. To get the timing information, CDR often uses an edge sampler that samples signal values at transition edges. Thus, if the equalized signal has a large amount of ISI at transition edges, the recovered clock may not have transitions at required timing points, resulting in an unreliable sampling of the channel data. Hence, minimizing

This work was supported by Samsung Electronics, and by the Basic Research Program through the National Research Foundation of Korea funded by the Ministry of Education under Grant 2013R1A1A2A10009535. Design tools were supported by IDEC KAIST.

S.-W. Choi is with the College of Information and Communication Engineering, Sungkyunkwan University, Suwon, Korea. He is also with Device Solution, Samsung Electronics, Yongin, Korea (phone: +82-31-299-4616; fax: +82-31-299-4938; e-mail: margarine8@skku.edu).

H.-W. Lim is with the College of Information and Communication Engineering, Sungkyunkwan University, Suwon, Korea. He is also with System LSI, Samsung Electronics, Korea (e-mail: hyunwook.lim@samsung.com).

B.-S. Kong is with the College of Information and Communication Engineering, Sungkyunkwan University, Suwon, Korea (e-mail: bskong@skku.edu).

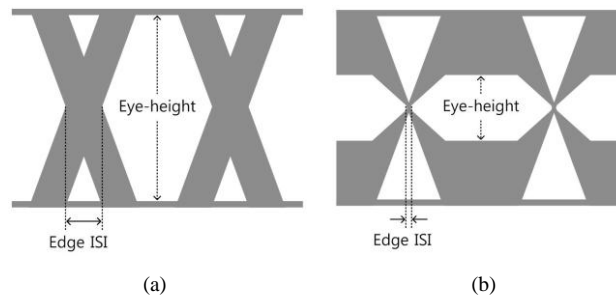


Fig. 1. Eye diagram of (a) data-based DFE and (b) edge-based DFE

the edge ISI at CDR input is very important for reducing the deterministic jitter at CDR output [4] and for improving the jitter tolerance of a CDR. Recently, edge-based DFEs (E-DFEs) [5], [6] are proposed to minimize the amount of ISI at data edges. The eye diagram of an E-DFE is depicted in Fig. 1(b), which indicates that the E-DFE have reduced the edge ISI substantially. But, as can be seen by the figure, there is an incomplete mitigation of ISI at data centers, resulting in an eye height reduction. A recent DFE receiver [7], [8] tries to reduce timing jitter without the degradation of eye height. The receiver uses a D-DFE for input data equalization and an E-DFE for edge data equalization. But, in this implementation, separate D-DFE and E-DFE with the same architecture have been employed. So, the approach is considered to be a bulky and power-hungry solution due to doubled area and power dissipation.

This paper introduces a novel DFE architecture to eliminate ISIs at data edges and centers simultaneously using a single equalizer. The proposed DFE equalizes the entire shape of the response to eliminate both the edge and data ISIs simultaneously. The remaining sections are as follows. Section II describes the proposed DFE concept and implementation details of a 5-tap half-rate DFE receiver embedding the proposed scheme. The performance comparison is presented in Section III. Section IV concludes the paper.

## II. PROPOSED 5-TAP HALF-RATE DFE

### A. Equalization Concept

The conceptual comparison between the conventional D-DFE and the proposed waveform-shaping DFE (WS-DFE) to equalize received signal are represented in Fig. 2. Limited bandwidth of the channel attenuates received signal for a single-bit pulse (Fig. 2(a) and (d)). The shaded region in these figures represents the area eliminated by each DFE. As for the

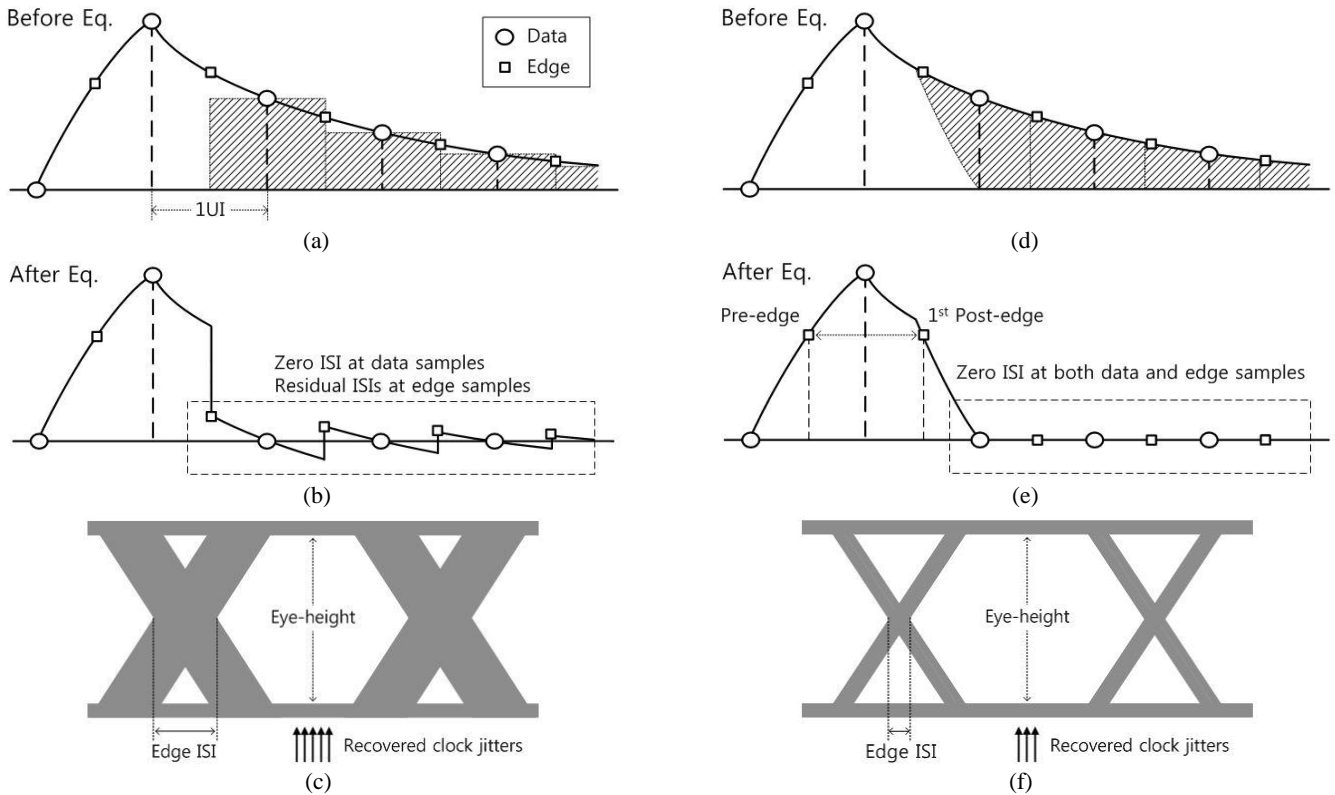


Fig. 2. Single-bit pulse response (a) before equalization, (b) after equalization, and (c) eye diagram for conventional data-only DFE. Single-bit pulse response (d) before equalization, (e) after equalization, and (f) eye diagram for proposed waveform-shaping DFE.

conventional approach, tap coefficients for equalization are basically constant, and set only to eliminate ISIs at data centers. So, they are not able to thoroughly eliminate ISIs at transition edges (Fig. 2(b)). The resulting residual ISIs at edge samples reduce the horizontal eye opening of received data (Fig. 2(c)), and make more jitter of recovered clock as explained previously. Reduced horizontal eye opening and larger clock jitter cannot ensure a reliable operation of the receiver.

Meanwhile, as for the proposed approach, tap coefficient values do not remain constant, but are made to be variable and adjusted to properly tailor or cancel the whole shape of ISIs in a single-bit pulse response. More specifically, for providing accurate timing information to CDR and stable data information to slicers, the magnitude of ISI at the first post-edge point is set equal to that at the pre-edge point [6], and the remaining ISIs at following data and edge sampling points are all eliminated (Fig. 2(e)). The resulting substantial reduction of edge ISIs extends the horizontal eye opening (Fig. 2(f)), and allows jitter reduction of recovered clock. Wider horizontal eye opening and reduced jitter will foster a reliable operation of the receiver.

Detailed diagrams to show how the proposed WS-DFE can reshape the single-bit pulse response in Fig. 2(d) into the desired form in Fig. 2(e) are illustrated in Fig. 3. Fig. 3(a) highlights by slash lines the area to be cancelled by the first tap. To eliminate this area, the proposed DFE tailors three ISI sub-areas (area A, B, and C), as shown in Fig. 3(b)-(e). Areas A and B are first subtracted from the received waveform (Fig. 3(b)), resulting in a tailored waveform (Fig. 3(c)) where zero ISI at the first post-edge and post-data cursors. A DFE tap with a constant

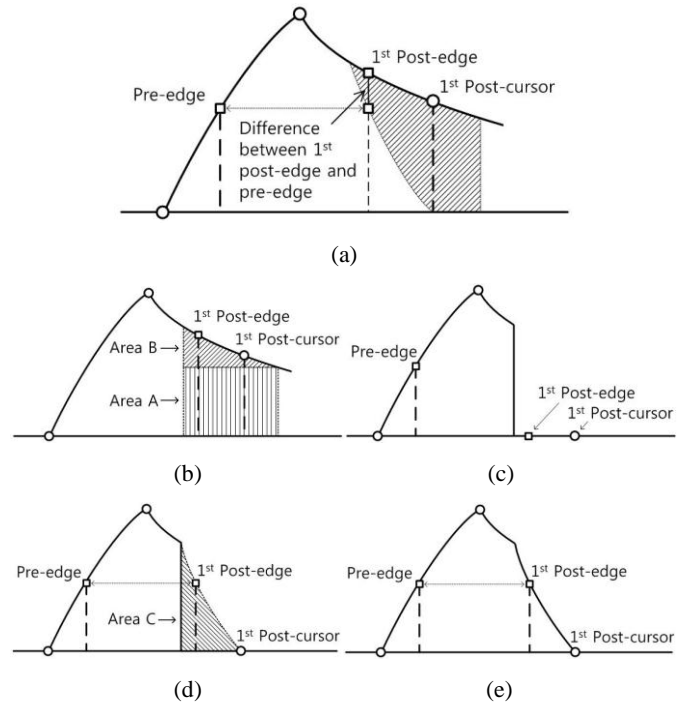


Fig. 3. Waveform reshaping for eliminating edge and data ISIs.

current can be used to cover area A, and another DFE tap with a variable current can cover area B. At the same time, area C is added to match the magnitude of the first post-edge with that of the pre-edge, resulting in the waveform shown in Fig. 3(d). A DFE tap with another variable current can cover area C. Then,

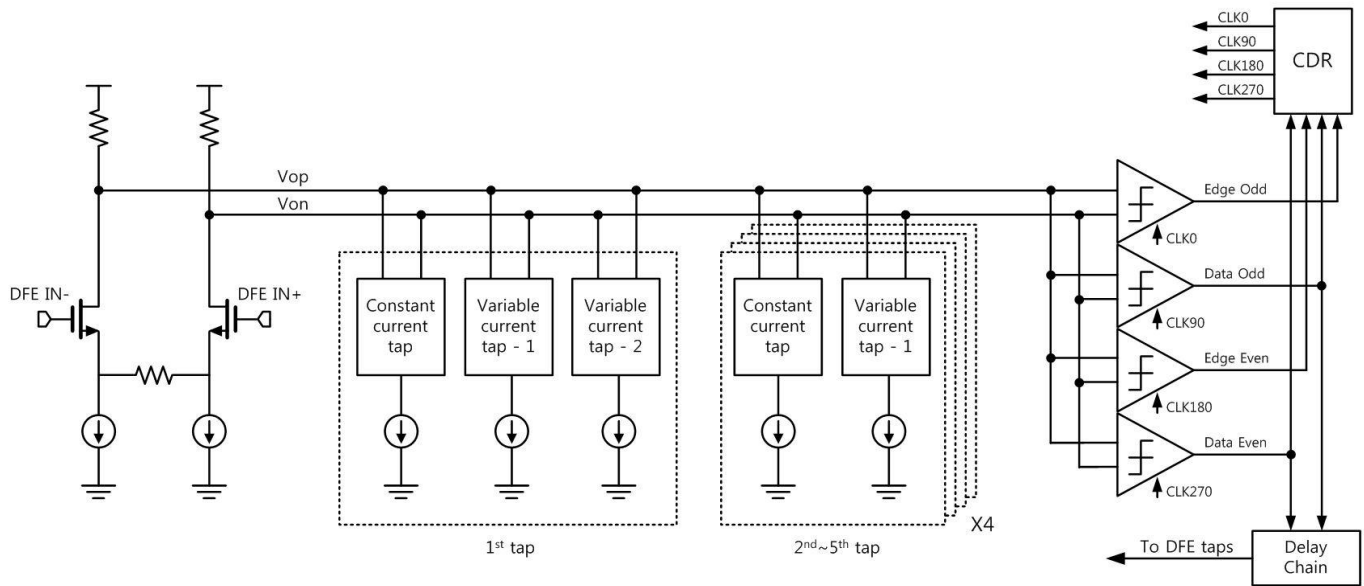


Fig. 4. Overall architecture of proposed WS-DFE

as shown in Fig. 3(e), the first post-edge and the pre-edge will have the same magnitude, and ISI at the first post-cursor point will be zero. For the other taps, a tap with a constant current and another tap with a variable current are used to eliminate ISIs at edge and data sampling points like Fig. 3(b) and (c).

**B. Equalizer Implementation**

The overall architecture of the proposed 5-tap half-rate WS-DFE is depicted in Fig. 4. It adopts the current-summing amplifier with resistive load, and is operated by half-rate differential clock. The summing nodes of the DFE are driven to slicers for data sampling, and the sampled data are fed into CDR for clock and data recovery. In the proposed DFE, as mentioned earlier, one constant-current tap and two variable-current taps are used for the first tap, whereas one constant-current tap and one variable-current tap are used for all the other taps in the receiver.

The structure of the constant-current tap in the proposed WS-DFE is the same as that of the tap in the conventional D-DFE. The structure of the variable current generator for the variable-current tap is shown in Fig. 5(a). The opposite side of the generator is complementary to the circuit shown here. A high-pass filter is used for generating the required variable current. After the clock passes through the RC high-pass filter, the pulse described in Fig. 5(a) is generated at the high-pass filter output, which turns the switch transistor on and turns it off gradually. To adjust the shape and magnitude of the tap coefficient, the value of R and the current of I-DAC are tuned. The shape of the current is controlled by changing the value of R. The peak value of the current is determined by the amount of the I-DAC current. Adjustment of the variable current according to the change of R is shown in Fig. 5(b). As the resistor value increases, the slope of the current becomes gradual. A proper value of R can be used to adjust tap coefficient values to cancel the overall shape of the ISI for a single-bit pulse response.

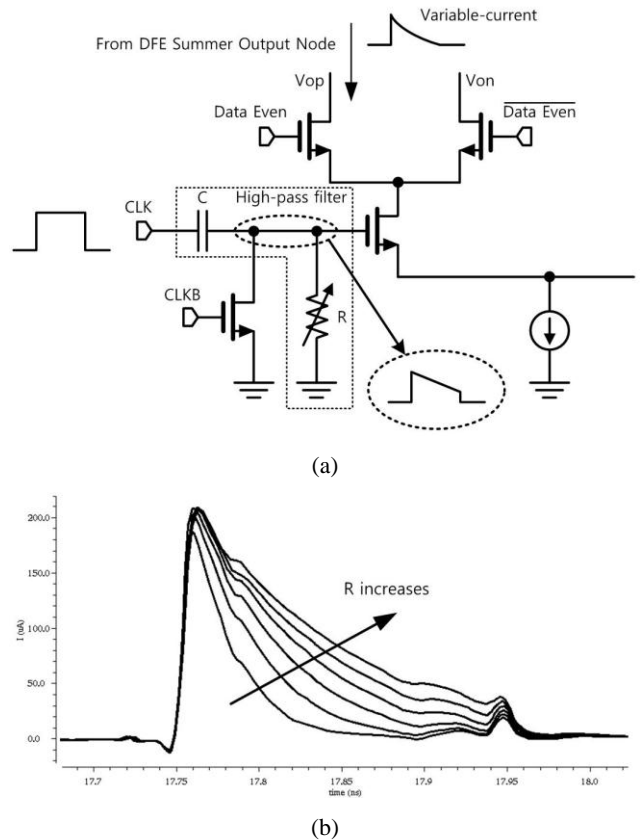


Fig. 5. Variable current generation: (a) circuit diagram, (b) current vs. resistance

**III. SIMULATION RESULTS**

The proposed 5-tap half-rate DFE receiver was designed in a 45-nm LP CMOS process. A 40” FR4 trace with 16dB loss at 2.5GHz including receiver package loss was used as the channel. Transmit swing is set to 200mVpp. The proposed DFE receiver

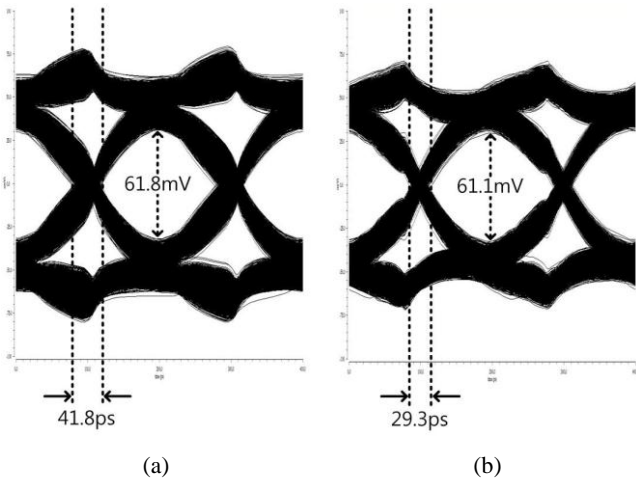


Fig. 6. Simulated eye diagram; (a) conventional D-DFE, (b) proposed WS-DFE

is clocked by 2.5GHz differential clock to operate at 5Gb/s or 200ps UI at 1.1 V. Fig. 6 shows simulated eye-diagram for the conventional D-DFE and proposed WS-DFE receivers. As shown by the figure, the proposed DFE has a reduced ISI at edges without degrading the eye height. The amount of edge ISI of the conventional DFE is 41.8ps, whereas that of the proposed DFE is 29.3ps, indicating 30% improvement.

The reduction of edge ISI of the proposed WS-DFE will lead to an improvement on jitter performance of CDR. To verify this aspect, a CDR with bang-bang phase detector (BBPD) [9] is implemented. The CDR uses a half-rate phase-locked loop (PLL) for clock recovery, consisting of BBPD, loop filter, VCO and clock buffers. The comparison between the jitter performance of CDRs with the conventional D-DFE and with proposed WS-DFE is shown in Fig. 7. It indicates that the jitter of the CDR with the proposed DFE is reduced from 20.5ps to 16.6ps, resulting in 19% improvement. Table I summarizes the performance of DFEs, such as the number of taps, vertical and horizontal eye-opening, edge ISI, and CDR jitter. The conventional D-DFE and proposed WS-DFE use the same number of taps to allow the same capacity to cancel ISIs at data sampling points. The proposed WS-DFE reduces edge ISI by 30% resulting in 8% improvement on the horizontal eye-opening while providing almost the same eye height. It also improves CDR jitter performance by 19%.

IV. CONCLUSION

In this paper, a novel 5-tap half-rate DFE is proposed. The proposed DFE cancels ISIs at both data center and edge simultaneously without using multiple equalizers. Due to efficient reduction of edge ISI, the proposed DFE can help improve the jitter performance of a CDR.

REFERENCES

[1] B. S. Song, and David C. Soo, "NRZ Timing Recovery Technique for Band-Limited Channels," IEEE J. Solid-State Circuits, vol. 32, pp. 514 - 520, April 1997.

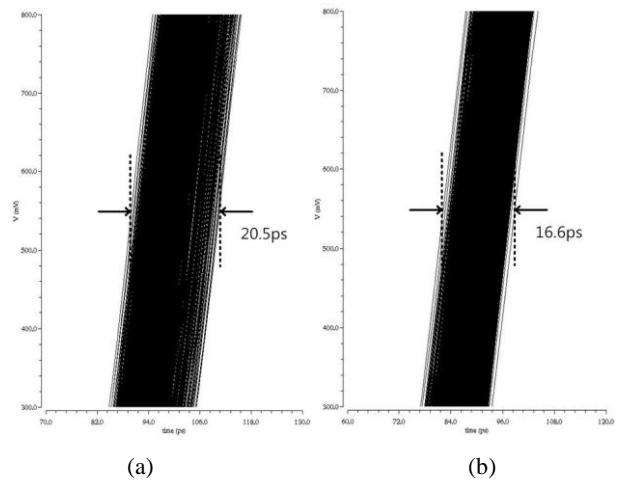


Fig. 7. CDR output jitter with (a) conventional D-DFE and (b) proposed WS-DFE

TABLE I  
COMPARISON BETWEEN CONVENTIONAL AND PROPOSED DFE

	Conventional	Proposed	Improvement
Number of Taps	5	5	-
Vertical Eye Opening (mV)	61.8	61.1	-1%
Horizontal Eye Opening (ps)	158.2 (0.78UI)	170.7 (0.85UI)	8%
Edge ISI (ps)	41.8 (0.22UI)	29.3 (0.15UI)	30%
CDR Jitter (ps)	20.5 (0.1UI)	16.6 (0.08UI)	19%

[2] T. Beukema et al., "A 6.4-Gb/s CMOS SerDes core with Feed-Forward and Decision-Feedback Equalization," IEEE J. Solid-State Circuits, vol. 40, no. 12, pp. 2633-2645, Dec. 2005.

[3] J. F. Bulzacchelli et al., "A 10-Gb/s 5-Tap DFE/4-Tap FFE Transceiver in 90-nm CMOS Technology," IEEE J. Solid-State Circuits, vol. 41, no. 12, pp. 2885-2900, Dec. 2006.

[4] J. Buckwalter and A. Hajimiri, "A 10 Gb/s data-dependent jitter equalizer," in Proc. IEEE Custom Integrated Circuits Conf., Oct. 2004, pp. 39-42.

[5] S. Wu et al., "Design of a 6.25Gbps Backplane SerDes with TOP-down Design Methodology," DesignCon East, 2004.

[6] J. Ren et al., "Performance Analysis of Edge-based DFE," Electrical Performance of Electronic Packaging, 2006.

[7] K.-L. J. Wong, and Chih-Kong Ken Yang, "A Serial-Link Transceiver with Transition Equalization," ISSCC Dig. Tech. Papers, 2006, pp. 223-232.

[8] K.-L. J. Wong et al., "Edge and data adaptive equalization of serial-link transceivers," IEEE J. Solid-State Circuits, vol. 43, no. 9, pp. 2157-2169, Sep. 2008.

[9] M. Ramezani, C. Andre, and T. Salama, "Analysis of a half-rate bang-bang phase-locked-loop," IEEE Trans. Circuits Syst. II, Analog Digit. Signal Process., vol. 49, no. 7, pp. 505-509, Jul. 2002.

# Principles of structural organization of the intellectual movement planning system for mobile robotic object

V. Ph. Guzik, Yu. V. Chernukhin, A. O. Pyavchenko, V. A. Pereverzev, and R. V. Saprykin

**Abstract**—The paper is devoted to the principles of structural organization of the intellectual movement planning system (IMPS) for mobile robotic object (MRO). This system is intended for use as a part of a position-trajectory control system (PTCS). The functional tasks of such system at different levels of PTCS's hierarchy are shown here. IMPS defines the presence of multisensor lookout subsystem, supports correlated space-time processing of data flow, uses of a high-speed method of environment modeling space formation, supports the method of probabilistic finding of obstacles using adaptive thresholds of detection, defines the safe route of object movement within the active zone of the locator. Also IMPS supports tools of the test-monitor control with the capability of remote visual monitoring of the experiments. The paper also presents the results of practical implementation and the prospects for further research.

**Keywords**—Intellectual movement planning system, robotic mobile object, position-trajectory control system.

## I. INTRODUCTION

MODERN position-trajectory control systems of platform type's MRO, as a rule, based on the hierarchical principle and include three logical levels of control: strategic, tactical and executive [1] – [3]. It should be noted that the strategic level of PTCS includes base and local components [2]. If the base component of PTCS is allocated out of the MRO then the local one is always embedded within the object.

The intellectual movement planning system for MRO is integrated into a position-trajectory control system at all three levels. This system has a distributed nature of the components placement. The topicality of such subject matter is dictated by presence of exigency for creation of a new type MRO, solving

This work was supported by the Russian Scientific Foundation Grant 14-19-01533 and made at the Southern Federal University, Russia.

V. Ph. Guzik is with the Department of Computer Engineering, Southern Federal University, Rostov-on-Don, Russia (e-mail: vfguzik@sfnu.ru).

Yu. V. Chernukhin is with the Department of Computer Engineering, Southern Federal University, Rostov-on-Don, Russia (e-mail: yvchernukhin@sfnu.ru).

A. O. Pyavchenko is with the Department of Computer Engineering, Southern Federal University, Rostov-on-Don, Russia (phone: +7(8634)371656; fax: +7(8634)371428; e-mail: aop61@mail.ru).

V. A. Pereverzev is with the Department of Computer Engineering, Southern Federal University, Rostov-on-Don, Russia (e-mail: pereverzevva@mail.ru).

R. V. Saprykin is with the Department of Computer Engineering, Southern Federal University, Rostov-on-Don, Russia (e-mail: rsaprykin@gmail.com).

tasks of inspection and monitoring of emergency technological objects in hard-to-rich places, as a rule, dangerous to the person, and possessing a high degree of autonomy in decision-making in conditions of non-stationary, in advance uncertain surrounding conditions.

## II. FUNCTIONAL PROBLEMS SOLVED BY THE IMPS

Further in this paper, functional tasks performed at each level of IMPS will be discussed separately. Thus, at the strategic level, IMPS should solve the following problems:

- interactive mission preparation for MRO with setting time and cost requirements, taking into account the need for safe movements using the map of given area;
- strategic planning of the object mission with consideration of limitations on decision making. That is knowing the constraints of the autonomous power supply, time limits (arrival times to checkpoints), and a map of the required area of earth surface, the system operator can create the MRO route, using classic navigation algorithms;
- load of mission data into onboard movement planning system of MRO;
- carrying out of prestarting and procedural checks, the functional background control over a status of subsystems of the subordinated control level;
- IMPS operating modes controls, including regular, test-monitor and functional diagnostics modes;
- mission execution monitoring;
- conflicts resolution, which cannot be solved at subordinated levels of system, for example, decision making on other direction of movement in connection with that the tactical level on a course of moving finds out an impassable site;
- automatic adjustment of the parameters values in case of unattainable mission checkpoints in accordance with predetermined criteria (replanning of their allocation, recalculation of targeted times of MRO arrival to the relevant checkpoints, taking into consideration the energy reserves and based on previously obtained statistical information).

Moreover, the strategic level of IMPS should be integrated as appropriate instrumental and resident software in the general software environment of mobile robotic object PTCS,

providing analysis of an emergency situation and a decision-making on how to get out of it; formation of coordinating control actions on subsystems of subordinate levels depending on the state of the current situation, support for high level protocols of command and information interaction.

IMPS should function at the tactical and executive levels with a binding to the time of data acquisition from the combined sensor subsystem (CSS). This subsystem, as usual, represents a set of sensors for measuring environment parameters [9] – [12]. Its structure includes multibeam forward looking locator (MFL), which provides scanning of the environment with the purpose of detection and localization of obstacles.

Let MRO moves along some path specified in mission by the strategic level of planning system.

According to [1] – [11] the motion path consists of line segments, parabola or arcs of different radius where the object velocity is permanent.

Junction points of such adjacent segments will be considered as control points (checkpoints). Then for the correct decision about the movement direction with reference to the current trajectory, in the general case, IMPS should have information about:

- coordinates of the current and the next checkpoint in the coordinate system the same with the IMPS;
- current position of the object as it moves along the

- trajectory between the control points with a binding to uniform onboard time;
- current course of the object in two-, and, if necessary, in three-dimensional space;
- angular beamwidth of MFL and the values of the measured parameters of a current environment;
- type of movement (moving to horizon on a straight line, on an arch, moving on a vertical, on an inclined plane);
- current values of linear velocities and accelerations of MRO in all three coordinate axes, and the restrictions on the maximum allowable value;
- probable directions of applied external influences and about expected values of their sizes in the nearest checkpoints of an operating trajectory.

All these data should be received from the on-board computer (OBC) of PTCS and used by IMPS to calculate bearing on the next checkpoints of operating trajectory. In the case of a detection and localization of obstacles by the system in the active zone of locator the values of current azimuthally angles of the trajectory deviation should be calculated also.

Fig. 1 shows a functional modular structure of IMPS, reflecting data processing and conversion from MFL to calculate and issue course angles to OBC.

This processing includes:

- reception from OBC and execution of commands, including information about current and strategic

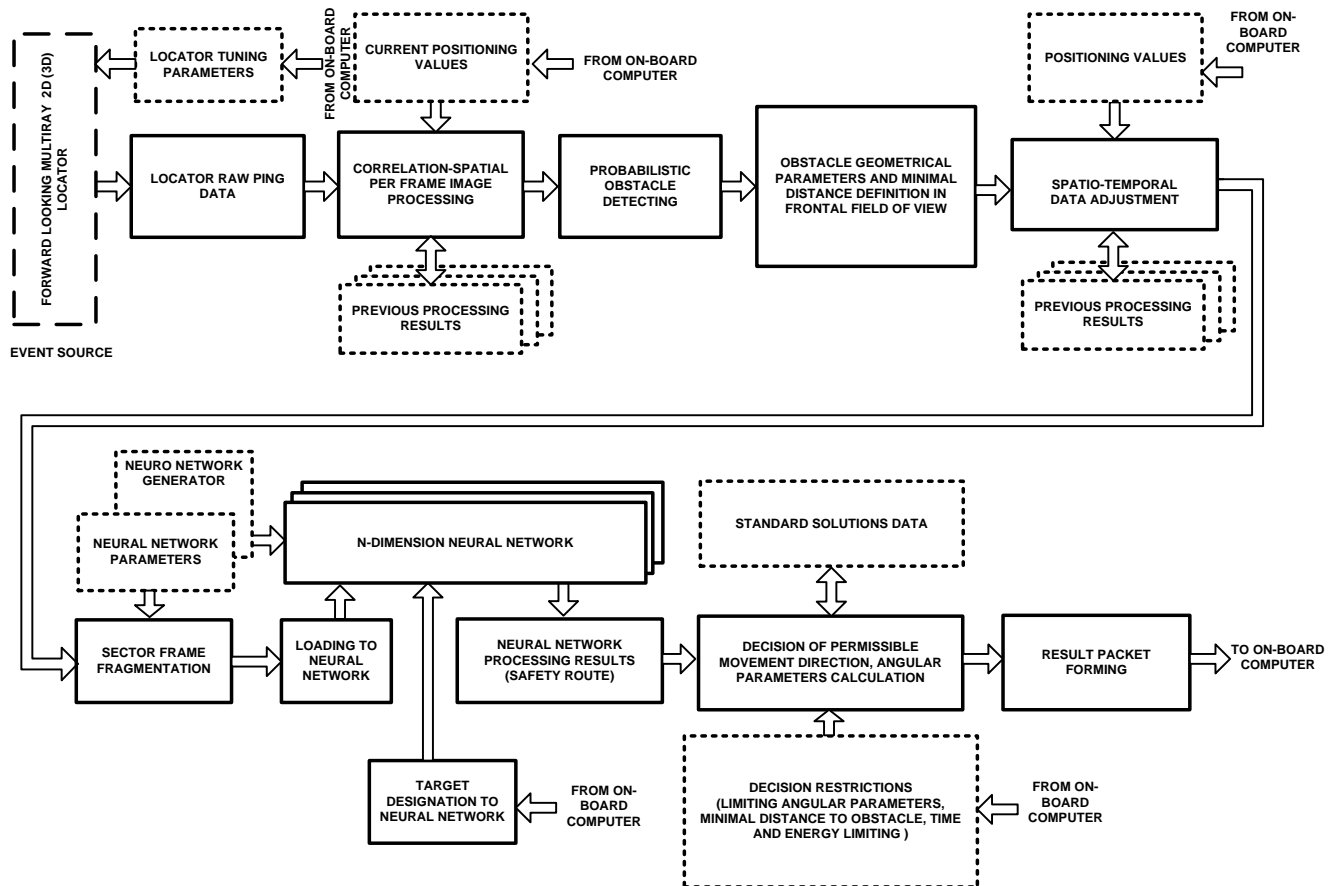


Fig.1 – Functional-modular streaming structure of IMPS

- objectives;
- reception and execution of control commands on working modes;
- reception from MFL and performing spatio-temporal correlation processing of "raw" images to suppress noise and determination the current threshold detection of obstacles;
- obstacle detection probability in the current environment;
- definition the sizes of obstacles within the area of MFL detection;
- determination of the distance to the nearest obstacle, detected in the trajectory of the MRO;
- determination of the movement direction to a target within the area of MFL detection in accordance with commands received from the OBC;
- calculation of the possible safe movement trajectory for the MRO with regards to its weight, size and kinematic features using of neural network algorithms;
- calculation of values of angular parameters of demanded change of a direction of safe movement to in advance set purpose in case of detection of obstacles in a current route of moving MRO;
- timely sending to OBC of values of settlement parameters according to the agreed protocols of command and information interaction;
- self-control of hardware and software condition of IMPS, when it's switched on, and timely notification to PTCS if fault is detected;
- support of test-monitor control mode based on the principles of the client-server architecture with possibility of remote visual control over the course of experiments using wireless channel.

So, it should be noted that in response to the commands from PTCS in case of detected obstacles, IMPS determines new trajectory for safe moving and calculates the parameters of detected obstacles, the new angular parameters for the desired direction of future movement (Fig. 2).

Zero values of angular parameters indicate that there is no need to change the direction of movement: "Obstacle free path" (see Fig. 2 d).

Values exceeding certain maximum value and limited by the

capacity of the locator considered in-correct and indicate that tactical level of IMPS is incapable of making an appropriate decision at the moment, due to lack of reliable data on the safe passing of an obstacle.

In this case, the decision about the further direction of movement is made by the upper strategic planning level of IMPS on the basis of a priori data about the current area of navigation, on motion and obstacle parameters of the object, including its possible spatial coordinate.

### III. PRINCIPLES OF STRUCTURAL ORGANIZATION OF THE IMPS

As have shown researches carried out by authors [13]–[19], the IMPS, focused on solving the above sequence of functional tasks, should be based on the principles of multimode, intellectualization of strategic and tactical levels of planning on the basis of the bionic approach, parallel-pipeline data processing in real time, polymodular client-server architecture, standardization and unification of intermodular interfaces, reconfigurability, supporting of mechanisms of background debugging with application of the management removed the test-monitor.

The structure of the tactical and executive levels of the onboard IMPS developed according to the listed above principles is shown in Fig. 3.

Moreover, multi-layered neural network (N-dimensional neural network) is included in the structure for the general case.

The number of the neural network layers is directly dependent on the capacity of the MFL, used as part of the executive level of the IMPS [20].

Truncated multidimensional view of a neural network is assumed to apply when the MFL with two mutually perpendicular located antennas of sector reception is used, for example, 2D forward looking platform such, as Blueview FLS450-X. This neural network contains two mutually perpendicular intersecting neural network planes.

In case if flat-directional diagram locator will be used as MFL, for example, Blueview P900-X, then a neural network will consist of a single neural network plane.

The proposed structure has several advantages such as:

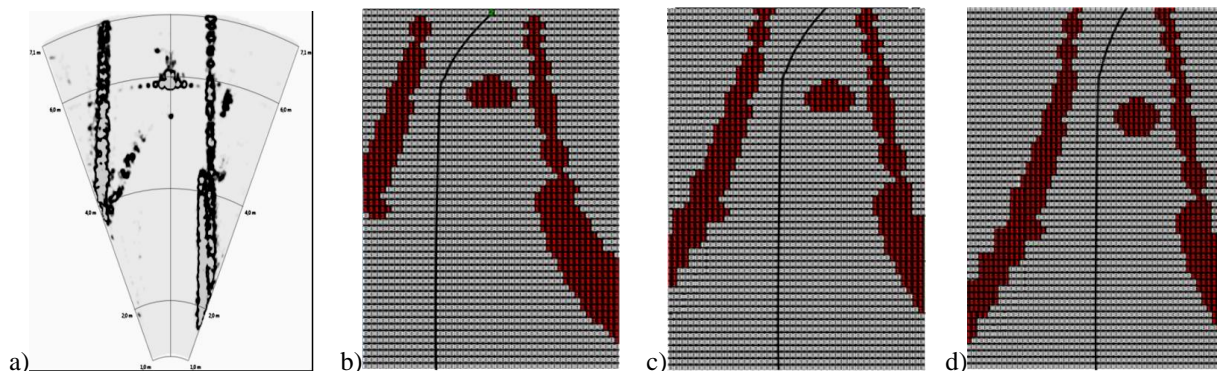


Fig. 2 – The frame of contrast image from MLL in gray shades (a). Model representation of the frame and trajectory of MRO (b, c, d)

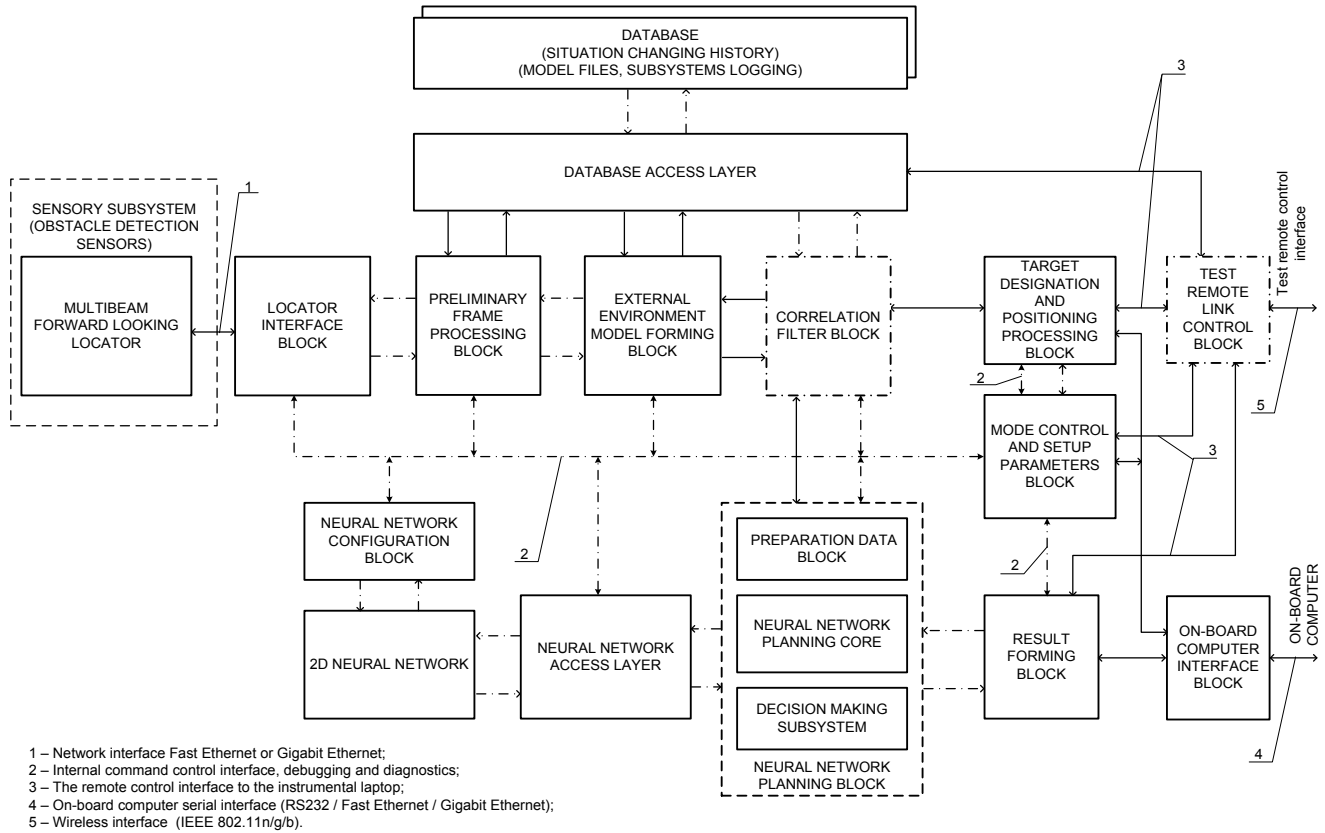


Fig.3 – The structure of the intellectual movement planning system for MRO

- sensing the surrounding space at the rate of MRO movement;
- operative search and probabilistic obstacle detection of static and dynamic types. On the minimum size of detectable obstacles affect the parameters of the established type of MFL, used digital filtering algorithms, the current level of noise pollution useful signal;
- determination of the direction of further movement taking into account the current state of the environment and pre-known location of the target;
- support of remote configuration of IMPS's internal architecture to the required level of processing complexity;
- the resilience to system failures and malfunctions;
- expandability of functionality and modernization of the individual modules of the system without altering the rest and without disrupting already-established command and information flows both within the IMPS and PTCS.

- effective detection range is 0.6 to 60.0 m;
- typical angular horizontal resolution – 1°;
- error of determining the distance is not more than 1% of the established working range;
- angle of horizontal review relative to the longitudinal axis of the MRO -22.5° to +22.5°;
- vertically width of the beam – 20° (+-10° up/down to the horizon);

IV. THE OBTAINED RESULTS AND FURTHER RESEARCH

The principles considered above have been successfully tested within prototype of IMPS, which has been created special for use in MFL of hydroacoustic type (Fig. 4).

This system prototype uses BlueView P900-45 sonar and provides:

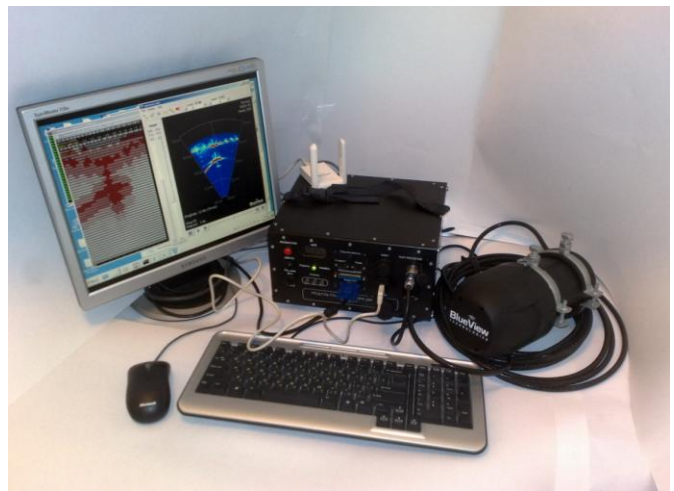


Fig. 4 – The general view of demonstration prototype of IMPS with application of hydroacoustic type MLL

- speed of delivery of the decision results to OBC, PTCS – depending on the distance, but at least 90 measurements per minute. The sample rate of issuance of treated data equal approximately 180 measurements per minute, if the sonar is working on the effective distance.
- sonar interface – Fast-Ethernet;
- OBC's interface – Fast-/Gigabit Ethernet;
- supply voltage to the sonar is supplied through PoE-connector. The range is 12-32V.

Some successful results of the prototype working are shown on the Fig.5. This results have been obtained from neural network in the process of MRO performing the automatic safe passing of an obstacle with signal filtration (orange line) and without it's (blue line). The method of adaptive

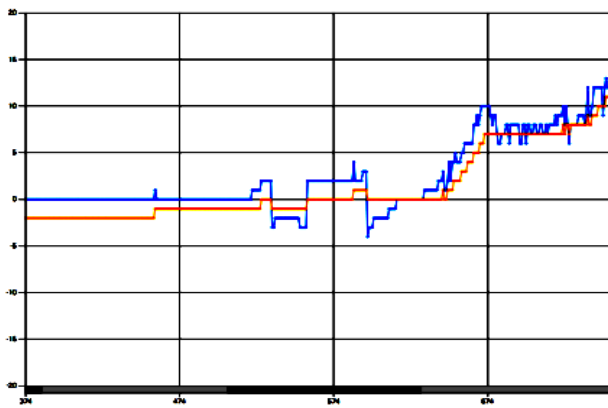


Fig. 5 – Results of the neural network working

exponential moving average has been used in this filter.

Further research, on the basis of the developed IMPS integrated into PTCS, assumes creation of the onboard real time intelligent management system with high level of independence and self-sufficiency, which will be able [21]:

- to achieve targets in a highly dynamic environment with high levels of heterogeneous uncertainties;
- to adjust targets, as well as create new targets and complexes of the targets, on the basis of evaluative and normative installations, downloaded into the system;
- to extract new knowledge, gain experience in solving variety of problems;
- to support self-learning using this experience, to modify own behavior (reaction to change of a situations) based on obtained knowledge and experience.

#### REFERENCES

- [1] V. Kh. Pshikhopov, A. S. Ali, "Hybrid motion control of a mobile robot in dynamic environments," in *Proc. Int. Conf. on Mechatronics, ICM 2011*, pp. 540–545.
- [2] V. Kh. Pshikhopov, M. Yu. Medvedev, "Robust control of nonlinear dynamic systems," in *IEEE ANDESCON Conf. Proc.*, ANDESCON, Bogota, Sep. 2010.
- [3] V. Kh. Pshikhopov, M. Yu. Medvedev, "Document Block design of robust control systems by direct Lyapunov method," in *Proc. of the 18th IFAC World Congress*, 2011, pp. 10875–10880.
- [4] V. Pshikhopov, M. Medvedev, R. Neydorf, V. Krukhmalev et al., "Impact of the feeder aerodynamics characteristics on the power of control actions in steady and transient regimes," *SAE Technical Papers*, no. 01, 2012.
- [5] R. Neydorf, V. Krukhmalev, N. Kudinov, V. Pshikhopov, "Methods of statistical processing of meteorological data for the tasks of trajectory planning of MAAT feeders," 2013, *SAE Technical Papers*.
- [6] V. Pshikhopov, V. Krukhmalev, M. Medvedev, R. Neydorf, "Estimation of energy potential for control of feeder of novel cruise/feeder MAAT system," *SAE Technical Papers*, no. 01, 2012.
- [7] V. K. Pshikhopov, M. Yu. Medvedev, B. V. Gurenko, "Homing and Docking Autopilot Design for Autonomous Underwater Vehicle," *Applied Mechanics and Materials*, 2014, pp. 490–491.
- [8] V. Pshikhopov, N. Sergeev, M. Medvedev, A. Kulchenko, "The design of helicopter autopilot," *SAE Technical Papers*, no. 01, 2012.
- [9] V. Kh. Pshikhopov, M. Yu. Medvedev, A. R. Gaiduk, B. V. Gurenko, "Control system design for autonomous underwater vehicle," in *Latin American Robotics Symposium*, 2013, pp. 77–82.
- [10] V. Pshikhopov, M. Medvedev, V. Kostjukov, R. Fedorenko et al., "Airship Autopilot Design," *SAE Technical Paper*, no. 01, 2011.
- [11] V. Kh. Pshikhopov, V. A. Krukhmalev, M. Yu. Medvedev, R. V. Fedorenko, S. A. Kopylov, A. Yu. Budko, V. M. Chufistov, "Adaptive control system design for robotic aircrafts," in *IEEE Latin American Robotics Symposium*, 2013, pp. 67–70.
- [12] A. V. Kalyaev, Yu. V. Chernukhin, V. P. Noskov, I. A. Kalyaev, *Homogeneous control structures of adaptive robots*. Moscow: Nauka, 1990.
- [13] Yu. V. Chernukhin, *Microprocessor and neurocomputer control of adaptive mobile robots*. Taganrog: TREI publ., 1993.
- [14] Yu. V. Chernukhin, *Artificial intelligence and neurocomputers*. Taganrog: TSURE publ., 1997.
- [15] Yu. V. Chernukhin, *Neuroprocessor networks*. Taganrog: TSURE publ., 1999.
- [16] Yu. V. Chernukhin, R. V. Saprykin, "Virtual modeling system of intellectual agents' behavior when exploring natural functioning environment," *Izvestiya SFedU. Engineering sciences*, no. 11, pp. 19–24, Nov. 2008.
- [17] Yu. V. Chernukhin, Yu. S. Dolenko, P. A. Butov, "The bionic approach of sensory data processing in neural network control systems of intelligent mobile robots," *Izvestiya SFedU. Engineering sciences*, no. 5, pp. 194–199, May 2012.
- [18] V. Ph. Guzik, V. V. Kureichik, M. Yu. Polenov, Yu. V. Chernukhin et al., *Intellectual systems*, Rostov-on-Don: SFedU Publ., 2013.
- [19] V. Ph. Guzik, A. A. Priemko, "Microprocessor implementation of the neuronetwork trajectory planner for the adaptive mobile robot using the environment map," *Izvestiya SFedU. Engineering sciences*, no. 4, pp. 178–183, Apr. 2014.
- [20] V. Kh. Pshikhopov, Yu. V. Chernukhin, A. A. Fedotov, V. Ph. Guzik, M. Yu. Medvedev, et al., "Development of intelligent control system for autonomous underwater vehicle," *Izvestiya SFedU. Engineering sciences*, no. 3, pp. 87–101, Mar. 2014.
- [21] V. Ph. Guzik, Yu. V. Chernukhin, A. O. Pyavchenko, V. A. Pereverzev, R. V. Saprykin, "Structural organization of hierarchical distributed system for unmanned underwater vehicle motion planning," in *Proc. of 6-th Conf. of control problems*, Rostov-on-Don, 2013, vol.4. pp. 198–202.

# CMOS 60 GHz Power Amplifier Using Simple Open Drain and Source Architecture

Ki-Jin Kim, Sanghoon Park, Suk-hui LEE, and K.H. Ahn

**Abstract**—This paper presents a new 60 GHz amplifier design method using TSMC 90 nm CMOS technology. The proposed design scheme is based on the way of the distributed amplifier design with open gate & open drain. The proposed architecture is analyzed and we define the upper limit to adopt proposed method in designing 60 GHz amplifier. To verify the effectiveness of the proposed scheme, the 60 GHz power amplifier with three cascade structure is designed and measured. Thanks to the proposed design structure, the fabricated power amplifier shows 29 dB peak gain, 25 dB gain over the 56–65 GHz, 11.5 dBm OP1dB, 13 dBm saturation power and peak 18.8 % PAE(Power Added Efficiency) under 2V supply voltage. Judging from the measurement results, the suggested architecture is a promising way for the future millimeter wave CMOS amplifier.

**Keywords**— power amplifier, 60 GHz communication, 802.11ad, millimeter wave.

## I. INTRODUCTION

THE unlicensed bandwidth between 57 ~ 66 GHz is licensed for high speed short range wireless communication such as WPAN (Wireless Personal Area Network). Current standards governing 60 GHz communication require almost 10m communication range for robust communications. For a 60 GHz SoC solution, a low cost CMOS PA(Power Amplifier) which enables to produce 10 dBm OP1dB(Output P1dB) is inevitable. Like the ISM communication device, the PA is the most power hungry device in 60 GHz system therefore the gain and efficiency of the PA are designed as high as possible. These requirements in designing millimeter PA are very challenging especially when a silicon process is adopted. Recently designed CMOS PAs [1,2] showed more than 10 dBm output power. However the reported gain was not sufficient to boost signal from mixer because OP1dB of the millimeter wave up mixer was around -10 dBm[3]. Therefore additional buffer is needed before PA which requires additional power. As the operating frequency goes up, the trans-conductance of the CMOS device decreases quickly which results in low efficiency.

This research was funded by the MSIP (Ministry of Science, ICT & Future Planning), Korea in the ICT R&D Program 2014.

Ki-Jin Kim is with the Convergence Communication Components Research Center of Korea Electronics and Technology Institute, Korea (corresponding author to provide phone: 82-31-789-7226; fax: 82-31-789-7259; e-mail: sergeant@keti.re.kr).

Sanghoon park, Suk-hui Lee and K. H. Ahn are with the Convergence Communication Components Research Center of Korea Electronics and Technology Institute, Korea (corresponding author to provide phone: 82-31-789-7225; fax: 82-31-789-7259; e-mail: khajoh@keti.re.kr).

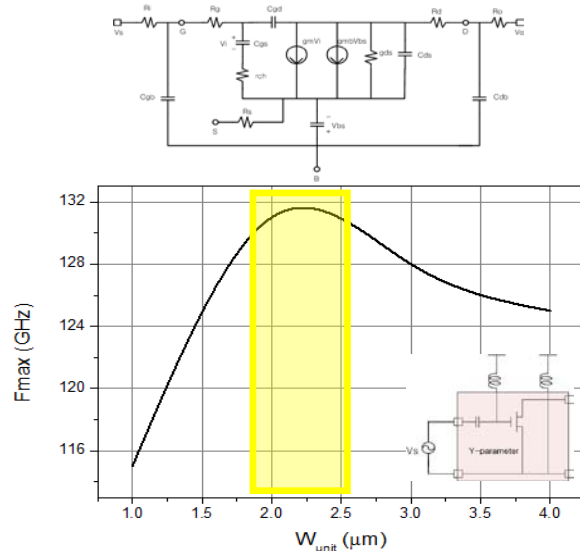


Fig 1. Small signal model of the transistor and the calculated  $F_{max}$  result with respect to the unit width of the transistor( $W_{unit}$ ).

That's why the PAEs(Power Added Efficiency) of the previous studies are considerably low (<10%). Thus the high efficiency PA is the key enabler in designing low power millimeter wave communication systems. The recent study demonstrated 25 % PAE by using SOI technology(Silicon on Insulator)[4].

In this paper, we present a new power amplifier design method using OGDPA(Open Gate & Drain Power Amplifier) structure. To verify the effectiveness of the OGDPA, a CMOS PA with high gain, high efficiency, and high output power simultaneously using 90 nm CMOS technology is designed and fabricated. This paper is organized as follows: In section 2, the structure of the OGDPA is introduced and analyzed. As a result of section II, the upper limit to apply proposed architecture is illustrated. The following section describes the proposed PA circuit implementation in detail. In section IV, the simulated and measured results are explained. Finally, conclusion is summarized in section V.

## II. PROPOSED POWER AMPLIFIER ARCHITECTURE

In designing CMOS millimeter-wave PA, RFIC designers inevitably confront trade-off relation among output power, gain and efficiency. In this section, we briefly comment the transistor geometry and research the reason of the above-mentioned trade-off relationship and finally suggest a new concept to break the trade-off.

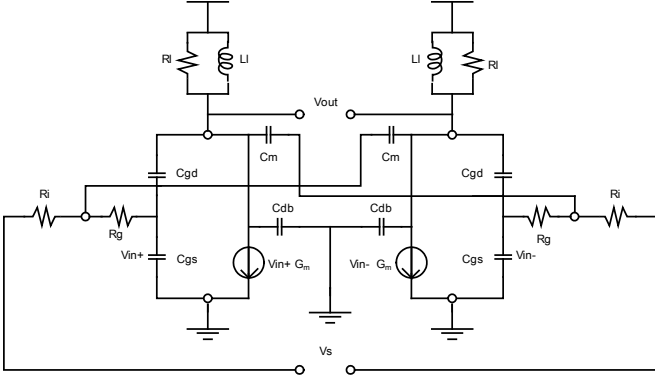


Fig 2. Small signal model of the differential amplifier with  $C_m$  capacitor

### A. Physical Geometry Optimization

The  $F_{max}$  (maximum oscillation frequency) is an indicator of the device operating frequency as an amplifier. Fig 1 shows small signal model of the millimeter wave transistor and these parameters are calculated from Y-parameter extraction. Then the geometry related  $F_{max}$  equation is

$$F_{max} = \frac{f_t}{2\sqrt{\frac{R_s W_{unit}^2}{12(3)l} (g'_{ds} + 2f_t C'_{gd}) + g'_{ds} (R'_i + R'_s)}} \quad (1)$$

where  $f_t$  is unit current gain frequency,  $W_{unit}$  is unit width of the transistor, an  $g'_{ds}$  is drain source conductance at a unit width. In equation (1), the relation between  $F_{max}$  and the physical transistor geometry  $W_{unit}$  is revealed and the relation is depicted in Fig 1. As a conclusion, this paper chooses  $2\mu\text{m}$  unit width geometry thought design process to maximize device operating frequency.

### B. Trade-offs in Designing Millimeter Wave Amplifier

Fig 2 illustrates small signal model of differential amplifier with capacitor  $C_m$ . A voltage gain, the optimum value of  $C_m$  and large signal  $G_m$  are

$$\frac{R_L G_m + j\omega_0 R_L (C_m - C_{gd})}{1 + R_L (R_i + R_g) (\omega_0 C_{gd})^2 + j\omega_0 (R_i + R_g) [C_{gs} + C_{gd} (1 + G_m R_L)] + R_i C_m (1 - G_m R_L)} \quad (2)$$

$$C_m = \left(1 + \frac{R_g}{R_i}\right) \left(C_{gd} + \frac{C_{gs}}{g_m R_L + 1}\right) \quad (3)$$

$$G_m \cong \frac{C_{ox} (V_{gs} - V_t)}{j\omega \frac{R_s W_{tot}}{36} (C_{ox} l + C_{GDO})} \quad (4)$$

The equations (2-4) explains that the gain is inversely proportional to the transistor size ( $C_{gs} + C_{gd}$ ) and operating frequency and inserting  $C_m$  compensates a size dependent Fig 3. Gain and phase distortion enhancement by manipulating  $C_m$  value

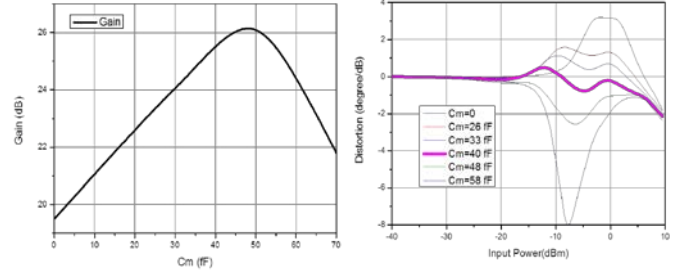


Fig 3. Gain and phase distortion enhancement by manipulating  $C_m$  value

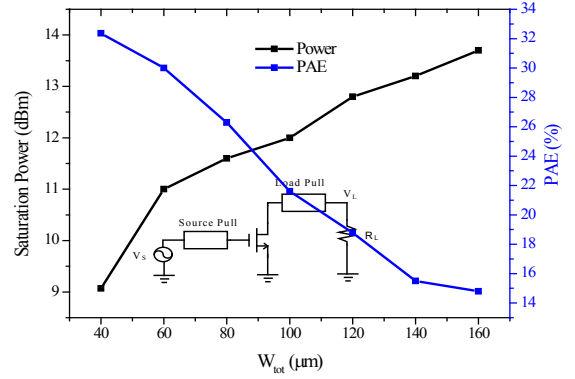


Fig 4. Amplifier's saturation power and PAE vs. transistor total size ( $W_{tot}$ )

gain reduction effect. Also, a size dependent phase distortion which is severe at 60 GHz is equated below:

$$Phase\ Distortion \cong \frac{(R_g + R_i) C_{gs} \omega (1 - \alpha C_m) V_s^2}{2} \quad (5)$$

According to the equation the phase distortion is proportional to signal dependent value of  $C_{gs}$  and operating frequency. The distortion is also mitigated by inserting  $C_m$ . In the 60 GHz where the operating frequency is almost 30 times comparing to the normal ISM communication systems, the gain reduction and phase distortion become serious and cause gain, efficiency and linearity problems even though those effects are almost ignored in ISM applications. A 6 dB gain improvement and 2 degree phase distortion reduction produce contrary evidence to the seriousness of abovementioned problems (Fig 3). Therefore inserting  $C_m$  is very effective way of designing millimeter wave amplifier. However, it requires differential structure and in-output baluns.

To produce high output power, a size of a transistor's total width ( $W_{tot}$ ) increases accordingly. However the large  $W_{tot}$  causes more gain reduction and more phase distortion which resulting in low PAE. Fig 4. explains this phenomenon well. To generate 13 dBm output power, the  $W_{tot}$  of 120  $\mu\text{m}$  is needed. In this transistor size, the PAE drops from 32 % to 18%. On the other hand, the  $W_{tot}$  of below 40  $\mu\text{m}$  shows almost the same PAE as the PAE of ISM band PAs. Therefore the problems can be ignored when below the critical transistor size is adopted.

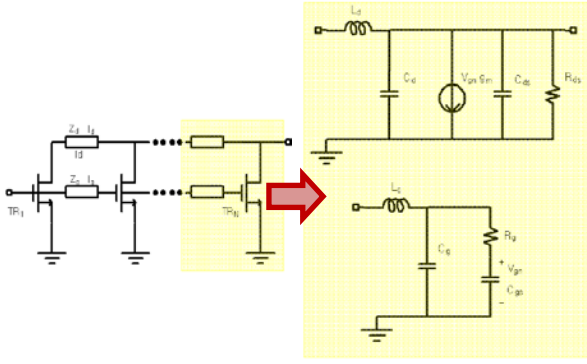


Fig 5. The structure of the common source amplifier's open gate termination

Baluns which are needed in differential circuits, consume large area and produce insertion loss. So it is desirable to parallelize small sized transistors without baluns.

### B. Analysis of the OGDPA structure

Recent study showed that 13.5 dBm OP1dB and 6.6% PAE PA with combining 8 small sized transistors by complex transformer networks[5]. By using small sized transistor, it demonstrated excellent gain while producing high power however the reported efficiency is quite low due to the complex power combining scheme.

Propagation wave power combination is generally used in DA(Distributed Amplifier). The delay elements used in DA combine forward output waves and absorbed reflected waves at the termination load. This is a good candidate for a power combining method; however it isn't used for PA structure because the half of the total output power is delivered to the termination load.

Fig 5 shows proposed wave domain power combining scheme. Instead of using termination at gate and drain, the proposed structure leaves the gate and the drain open. So this paper calls this structure OGDPA(Open Gate & Drain Power Amplifier). The propagation wave constants of gates and drains are:

$$\gamma_g = \alpha_g + j\beta_g \cong \sqrt{-\omega^2 l_g [C_g + C_{gs} (1 - j\omega R_g C_{gs})] / l_g} \quad (6)$$

$$\cong \frac{\omega^2 R_g C_{gs}^2 Z_g}{2l_g} + j\omega \sqrt{l_g (C_g + C_{gs} / l_g)}$$

$$\gamma_d = \alpha_d + j\beta_d \cong \frac{Z_d}{2R_{ds} l_d} + j\omega \sqrt{L_d (C_d + C_{ds} / l_d)} \quad (7)$$

and the propagated gate and drain voltages are

$$V_{g1}(\omega) \cong V_s \left( \frac{1}{1 + j\omega R_g C_{gs}} \right) \left( 1 + \Gamma_g e^{(2N-1)\gamma_g l_g} \right) \quad (8)$$

$$V_{gN}(\omega) \cong V_s \left( \frac{1}{1 + j\omega R_g C_{gs}} \right) \left( e^{-(N-1)\gamma_g l_g} \right) \quad (9)$$

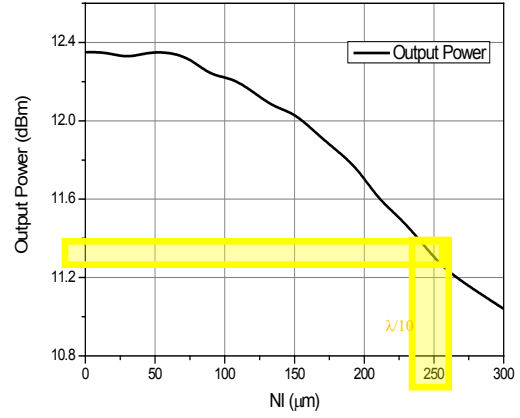


Fig 6. 1dB output power drop point vs. total length( $N \cdot l$ ;  $N$ :number of delay elements,  $l$ : length of the delay element)

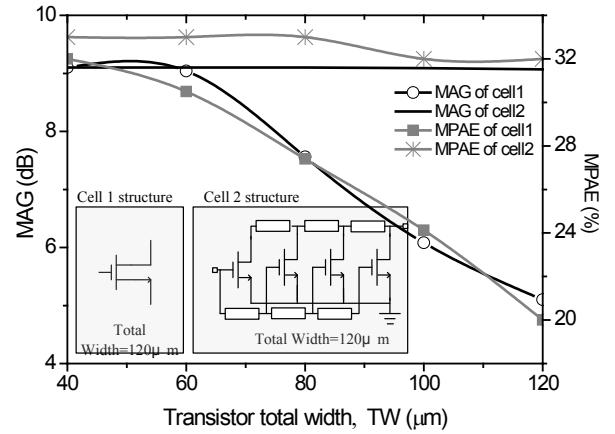


Fig 7. Gain(MAG) and efficiency(PAE) characteristics of the OGDPA structure at the total 60  $\mu\text{m}$  total delay length.

$$V_{o1}(\omega) \cong Z_l \frac{g_m V_{g1}}{C_{gs} + C_{gd}} \left( e^{-(N-1)\gamma_d l_d} \right) \quad (10)$$

$$V_{oN}(\omega) \cong Z_l \frac{g_m V_{gN}}{C_{gs} + C_{gd}} \left( 1 + \Gamma_d e^{(2N-2)\gamma_d l_d} \right) \quad (11)$$

Then the output power is

$$P_l = \frac{1}{2Z_l} \sum |V_{oN}|^2 \quad (12)$$

For simplicity this paper applies below condition

$$\beta_g l_g = \beta_d l_d = \beta l \quad (13)$$

The output characteristic versus length of the total delay is plotted in Fig 6. Like the definition of P1dB point, this paper defines OP1dB(Output Power 1dB Drop Point) and calculates corresponding total delay length. As depicted in Fig 6, OP1dB occurs when the total length reaches  $\lambda/10$ . On the contrary,

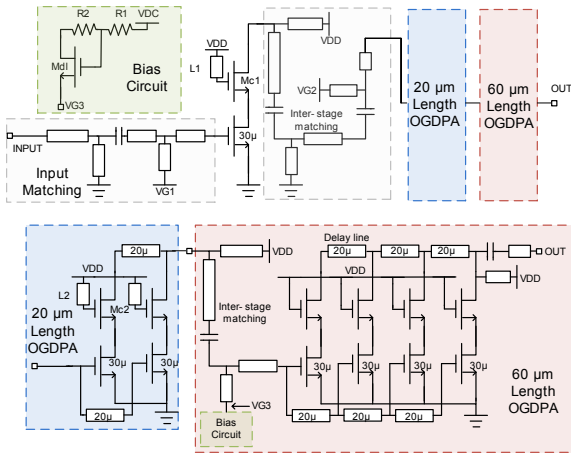


Fig 8. Proposed CMOS PA structure with cascode OGDPA

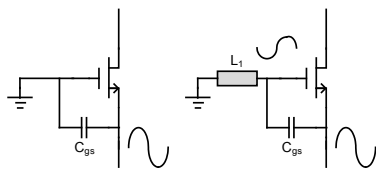


Fig 9. The positive effect of the gate inductors(L1, L2) to boost effective  $V_{gs}$

small transistor’s voltage waves connected by under  $\lambda/10$  transmission lines produce high output power without combining losses. Thus this paper defines total delay length  $\lambda/10$  as an upper limit to adopt proposed OGDPA.

Fig 7 shows the simulation comparison between cell 1: single  $120 \mu\text{m}$  transistor and cell 2: OGDPA transistor with  $60 \mu\text{m}$  total delay length( $60\mu\text{m}$  is enough length to connect 4 small transistors in layout perspective). In cell 1, the gain and PAE of  $40 \mu\text{m}$   $W_{tot}$  drop from 9 dB and 32 % to 5dB and 20 % at  $120 \mu\text{m}$   $W_{tot}$ . The reason is already explained before. On the other hand in cell 2, the gain and PAE remain constant even the  $W_{tot}$  reaches  $120 \mu\text{m}$ . Therefore, it is possible to design to have high gain, high output power and high efficiency at the same time in designing millimeter wave amplifier by using OGDPA architecture.

### III. IMPLEMENTED CIRCUITS

Fig 8. is a proposed CMOS PA architecture which is fabricated to verify the OGDPA concept. The PA consists of three parts, input matching amplifier, driver amplifier and power amplifier. Input amplifier provide  $50\Omega$  impedance and ESD(Electrostatic Shock Discharge) protection by using transmission lines[7]. The transmission lines are also used as inter-stage matching components for maximizing power transfer. The gate inductors L1 and L2 are inserted to boost gain called

GB(Gain Boosting). An inductor at the gate of the Common Gate structure provides positive feedback which increases the effective  $V_{gs}$  voltage. Fig 9 explains this phenomenon. This paper adopts two GB inductors in matching and driver amplifier to enhance gain.

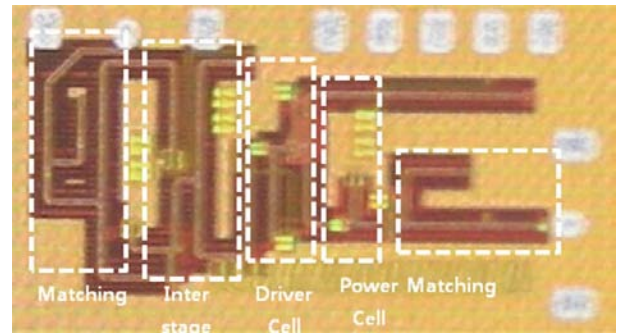


Fig 10. The chip photo of the proposed PA with die size of 0.14 mm x 0.5 mm

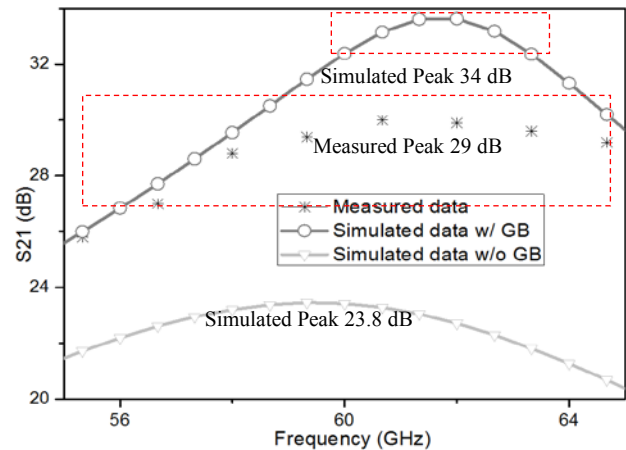


Fig 11. The simulated and measured small signal S-parameter data for 2-V supply

The  $20 \mu\text{m}$  and the  $60 \mu\text{m}$  cascode OGDPA are used as driver amplifier and power amplifier. To apply 2-V supply voltage, a cascode structure is chosen in this paper. According to the Fig 4, all of the transistor core sizes are fixed to  $30 \mu\text{m}$  in which degradation of gain and efficiency is negligible.

In addition, a novel bias circuit called DL(Diode Linearizer) is used in this paper. As shown in Fig 8, the DL consists the resistor divider and diode connected transistor which is applied at the power amplifier stage. As explained in section 2, signal dependent  $C_{gs}$  generates phase distortion which reduces OP1dB and efficiency[8]. By properly sizing the R1, R2, and transistor the DL circuit generates harmonics that compensate the effect of the non-linear  $C_{gs}$ . So the output characteristics of OP1dB and efficiency can be improved.

### IV. SIMULATED AND MEASURED RESULTS

The whole circuit of the PA is simulated with Cadence Spectre. The die photo is shown in Fig 10. The chip size with all test pad is  $0.14 \text{ mm} \times 0.5 \text{ mm}$ . The PA was measured using on wafer probing. Fig 11 plots the small signal S-parameters from  $55 \sim 65 \text{ GHz}$  and shows good fit between simulated and measured data for 2-V supply. The simulation result of inserting two GB circuits shows 10.2 dB gain boosting in millimeter

suggested architecture is an attractive design solution for next generation high speed communications.

REFERENCES

- [1] Darwn, D., Sarkar, S., Sen, P., Leung, M., Mallavarpu, N., Pinel, S. and Laskar, J., "60 GHz CMOS amplifier with 20-dB gain and 12 dBm Psat," *Microwave symposium Digest 2009*, pp. 537-540
- [2] Chowdhury, D., Reyanaert, P. and Niknejad, A., "A 60 GHz 1V +12.3 dBm transformer-coupled wideband PA in 90 nm CMOS" *IEEE ISSCC 2009*, pp. 560-562.
- [3] M. Tanomura, Y. Hanada, S. Kishimoto, M. Ito, N. Orihashi, K. Maruhashi, and H. Shimawake, "TX and RX front-ends for 60 GHz band in 90 nm standard bulk CMOS," *IEEE Int. Solid-State Circuits Conf. Tech. Dig.*, pp. 558-559, Feb 2008.
- [4] Siligaris, A. Hamada, Y., Mounet, C, Raynaud, C. and Vincent, P., "A 60 GHz Power Amplifier with 14.5dBm Saturation Power and 25 % Peak PAE in CMOS 65nm SOI," *IEEE Journal of Solid-State Circuits vol.45, no. 7*, pp. 1286-1294, July 2010.
- [5] Sofiane, A., Yohann, L., Nejdad, D., Bernardo, L., Robert, P., Didier, B., Eric, K., "Optimized Power Combining Technique to Design a 20 dB Gain, 13.5 dBm OCP1 60GHz Power Amplifier Using 65nm CMOS Technology," *IEEE Int. Solid-State Circuits Conf. Tech. Dig.*, pp. 562-563, Feb 2008.
- [6] J. N. Chang and Y.S. Lin, "60 GHz CMOS power amplifier with Psat of 11.4 dBm and PAE 15.8%," *Electronic Letters*, vol. 48, no. 17, Aug 2012
- [7] Ki-Jin Kim, K. H. Ahn, and J. W. Yu, "A Design Methodology for the 60 GHz CMOS Power Amplifier using on chip Transformers," *Microwave Optical Technology Letters*, vol. 53, no. 3, pp 506-509, Mar, 2010
- [8] Ki-Jin Kim, Tae Ho Lim, S. H. Park and K. H. Ahn, "A High Efficiency CMOS Power Amplifier with a Diode Linearizer and Voltage Combining Transformers," *Applied Mechanics and Materials*, vol. 110-116, pp 5500-5504, 2012

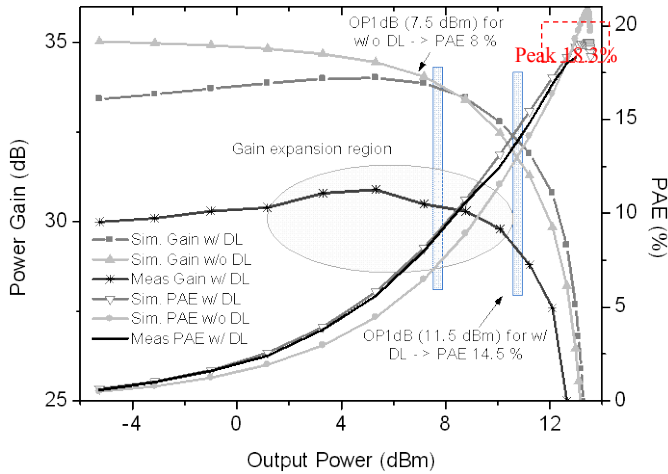


Fig 12. The simulated and measured power gain and PAE vs  $P_{out}$

wave frequency. The 5 dB gain drop is caused by layout resistive loss of GB circuit which is good for stability and bandwidth. The 3-dB bandwidth range is 56 ~ 65 GHz. The measured power gain and PAE versus  $P_{out}$  characteristics at 60 GHz are plotted in Fig 12. Due to the DL circuit OP1dB is enhanced from 7.5 dBm to 11.5 dBm. As shown in Fig 12, the gain positive harmonics generated by the DL circuit causes gain expansion which compensates gain compression caused by non-linear  $C_{gs}$ . At 13 dBm output power, the measured PAE is 18.3 % also the measured PAE at OP1dB is 14.5 %. These numbers are quite well matched with simulation results. Table I summarized the reported state-of-art performances of the CMOS PA. As can be seen, the PA with OGDPA achieves excellent power gain, best PAE and output power considering 90nm technology. These results indicate that the proposed design method is very promising for 60 GHz CMOS amplifier topology.

**Table I. Performance Comparison**

ref	Technology	Data rate	Power Consumption	Sensit-ivity
2	CMOS 90nm	3 Gbps	103 mW	-16 dBm
5	CMOS 90nm	3.5 Gbps	108 mW	-40 dBm
10	SiGe 0.25 $\mu$ m	4 Gbps	27.5 mW	-22 dBm
11	CMOS 90nm	1.2 Gbps	51 mW	-47 dBm
12	CMOS 90nm	3 Gbps	36 mW	-44 dBm
This Work	CMOS 65 nm	3 Gbps	21.5mW	-50 dBm

V. CONCLUSIONS

In this paper, we report a new structure of the millimeter wave amplifier for the future 60 GHz communication systems using 90 nm CMOS process. By introducing PGDPA structure, propagation wave can be combined easily without complex transformer networks. The small signal peak gain of 29 dB, the peak PAE of 18.3 %, and the saturated output power of 13 dBm are measured at 60 GHz. These results demonstrate the

# Cascade wave-based control applied to the servomotor

Ondřej Marek

**Abstract**—The wave-based control of flexible mechanical systems is based on the idea of sending waves into the mechanical system, measuring the incoming waves and avoiding the resending these waves back into the system. Many simulations were formerly performed. The stability was proven too. This paper describes the possible implementation of wave-based control to the real motor which moves the lumped-mass flexible mechanical chain. The paper deals with the impact of the external disturbance forces which can be either harmonic forces or forces caused by the passive resistances. The organization of the paper is following. After introduction in I, the wave-based control is briefly described in II. The cascade wave-based control is established. The chapter III deals with the simulation results and IV and V deal with the experiment.

**Keywords**— Wave-based control, WBC, Wave-based control implementation, cascade wave-based control, residual vibrations, vibration suppression

## I. INTRODUCTION

THE wave-based control of flexible mechanical systems is based on the idea of sending waves into the mechanical system, measuring the incoming waves and avoiding the resending of these waves into the continuum again. It is described in many already existing papers. Many simulations were formerly performed [1][3][4][5]. The stability of wave-based method applied to the lumped-mass chain was proven too [6]. This paper describes the implementation of enhanced wave-based control to the real motor which moves the flexible mechanical system. In the section II the wave-based control is briefly described. The cascade wave-based control is introduced and explained. The simulation experiment in which the cascade wave-based control was applied is described in the section III. The simulation deals mostly with the vibration suppression caused by the external forces. The advantages of the cascade wave-based control are shown. The section IV briefly repeats how to implement the wave-based control to real servomotor control. In the section V the experimental results are shown when the position command was set and passive resistances were apparently occurring. The comparison between classical wave-based control and cascade wave-based control is presented.

O. Marek works at VUTS Liberec, Czech Republic (e-mail: ondrej.marek@vuts.cz).

## II. WAVE-BASED CONTROL

### A. Wave-based Control – classical approach

Wave-based control (WBC) is the relatively new and breakthrough control method [1]. It allows controlling the mechanical system without the full knowledge of the system mathematical model. It requires only the partial knowledge of the system instead of input shaping method [9][10]. The system description for the wave-based control is the same as for the simple systems so for the complex systems if the number of actuators is equal. The number of required measured signals for feedback is the same too. The basic idea of WBC is shown in Fig. 1.

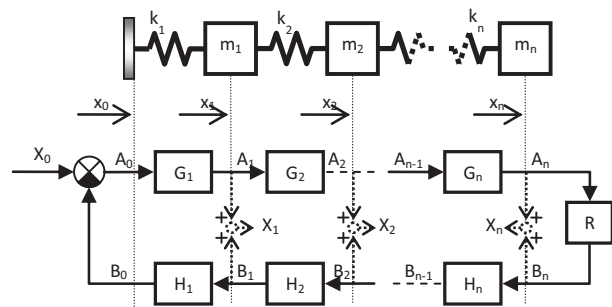


Fig. 1 Wave model of lumped mass system

The dynamics of the system from Fig. 1 can be modeled by classical approach, i.e. by  $n$  differential equations of motion, or alternatively by the wave model. The mechanical system in Fig. 1 is artificially considered as a block diagram shown below (in Fig. 1). The positions of particular masses  $x_i$  consist of two components  $a_i$  and  $b_i$ . The equation (1) shows the basic formula of the wave model where  $A_i$  respectively  $B_i$  are the variables between the blocks  $G_i$  respectively  $H_i$ .

$$X_i(s) = A_i(s) + B_i(s) \quad (1)$$

$$A_i(s) = G_i(s)A_{i-1} \quad (2)$$

$$B_i(s) = H_{i+1}(s)B_{i+1} \quad (3)$$

The values  $a_i(t)$  and  $b_i(t)$  physically do not exist. Only the sum  $a_i(t) + b_i(t)$  that equals the certain position  $x_i(t)$  of the certain mass  $m_i$  exists. The transfer functions  $F_{ij}$  between the positions particular masses  $m_i$  and  $m_j$  are given by the nature of the mechanical system.

If  $G_i(s) = H_i(s) = G(s)$  is considered then the formulas (4)-(6) are valid.

$$A_1(s) = G(s)A_0(s) \quad (4)$$

$$B_0(s) = G(s)B_1(s) = G(s)(X_1(s) - A_1(s)) = G(s)(X_1(s) - G(s)A_0(s)) \quad (5)$$

$$X_0(s) = A_0(s) + B_0(s) = A_0(s) + G(s)(X_1(s) - G(s)A_0(s)) \quad (6)$$

The wave-based algorithm and the number of measured signals do not depend on the number of masses in the chain [1][2].

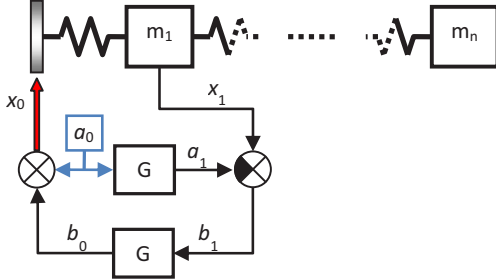


Fig. 2 Wave-based Control

In the control algorithm only  $a_0(t)$  and  $b_0(t)$  waves are used. The launch wave  $a_0(t)$  is the input variable in the control algorithm. The reflected wave  $b_0(t)$  is computed from the signals  $a_0$  and measured  $x_1$ . The most important value is  $x_0$  which is the controlled position of the actuator. The speed limits of the actuator have to be taken into account too and therefore the required displacement value goes through the shaper first. The shaper builds the shape of  $a_0$  in time. The control algorithm shows the Fig. 2. The final value of  $a_0$  equals the half of the desired displacement and remains constant. The reflected wave  $b_0$  reaches the same value as  $a_0$  after some time and using formula (1) it becomes obvious. This comes from the theory in [1], [2] and [3]. Fig. 3 shows the scheme of the control algorithm which needs the block representing  $G(s)$  only. The transfer function  $G(s)$  can be arbitrary chosen using proposed formula (7).

$$G(s) = \frac{\kappa}{s^2 + \zeta s + \kappa} \quad (7)$$

The parameters  $\kappa$ ,  $\zeta$  are positive.

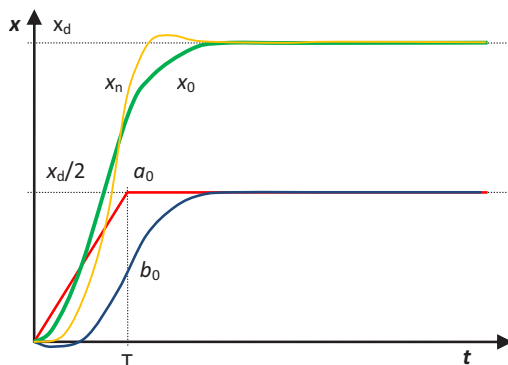


Fig. 3 Wave propagation during the repositioning the n-mass chain

The wave-based control is stable when applied to the lumped-mass system, this was proven. The disadvantage is the inability to suppress the disturbance forces. The external

forces cause the position error of the final position after the repositioning. This is quite limiting property because the friction or the other passive resistances behave like the external forces. When the wave-based control is used in the real device, the passive resistances occur everywhere.

### B. Cascade Wave-based Control

The ‘‘Cascade Wave-based Control’’ means in fact the PID regulator in front of the classic wave-based control (Fig. 4). These two regulators are in cascade therefore this combination is called cascade wave-based control (CWBC). The PID regulation controls mainly the final value of  $a_0$  in order to reach the desired position  $x_{final}$ . This helps to perform the exact positioning to the desired position. The cascade wave-based control can suppress the vibration caused by harmonic excitation too.

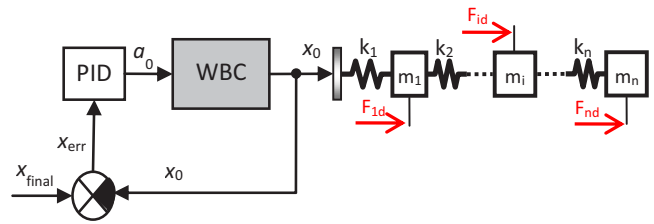


Fig. 4 Cascade Wave-based Control

## III. SIMULATION RESULTS

For the simulation purpose the three-mass mechanical system is considered as the simulation model. The stiffness  $k_1 = k_2 = k_3 = 100$  N/m and masses  $m_1 = m_2 = m_3 = 1$  kg. The natural frequencies of this system are  $f_1 = 0.71$ Hz;  $f_2 = 1.98$ Hz;  $f_3 = 2.87$ Hz. The disturbance force acts on the mass  $m_2$ . The transfer function  $G(s)$  was set as in (8).

$$G(s) = \frac{2}{p^2 + \sqrt{2}p + 2}, \quad p = \frac{s}{\omega}, \quad \omega = \sqrt{\frac{k_1}{m_1}} \quad (8)$$

### A. Disturbance response – the force pulses

The disturbance force  $F_{2d}$  shape is defined as in Fig. 5. It consists of periodic rectangular pulses which are 5N high and 0.25s long. The response of the system without any control is displayed in Fig. 6.

If the wave-based control (no cascade) is applied to the system the oscillation of the system is suppressed and system occurs in a static position periodically. Because no repositioning is required, the signal  $a_0$  equals zero throughout. The wave-based control is stable but the system obviously moves step by step. The external forces cause that effect which was mentioned before. The wave-based control suppresses the wave  $b_0$  which appeared because of the force  $F_{2d}$ .

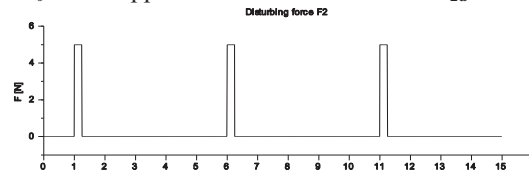


Fig. 5 The disturbing force  $F_{2d}(t)$

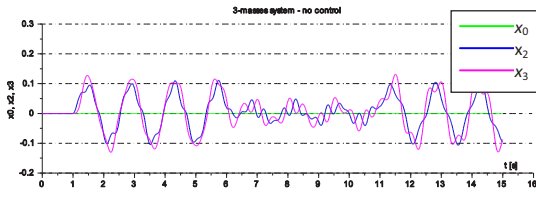


Fig. 6 The response of the system with no control

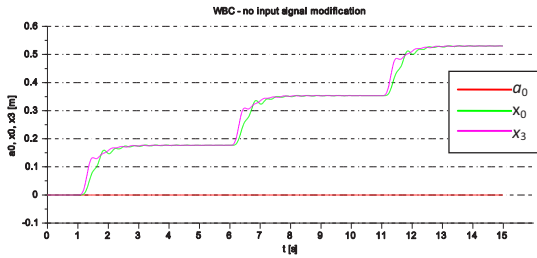


Fig. 7 The response of the system with wave-based control

To ensure the constant position of the system the cascade wave-based control is needed. It uses the simple PID regulator in front of WBC. The PID regulation affect the  $a_0$  value in order the  $x_0$  remains the desired value (in this case  $x_0=0$ ). The Fig. 8 shows the behaving of the system with the cascade wave-based control. The wave  $a_0$  is not constant and it is varying using formula (9). The tendency of  $x_0$  and  $x_3$  to remain zero is obvious. The constants  $K_P=1$   $K_I=1$  are used.

$$a_0(t) = K_P x_{err}(t) + K_I \int_0^t x_{err}(t) dt + x_{err}(0) \quad (9)$$

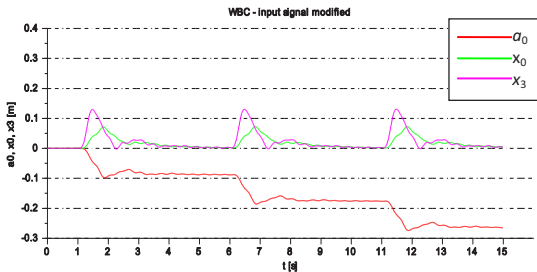


Fig. 8 The response of the system with cascade wave-based control

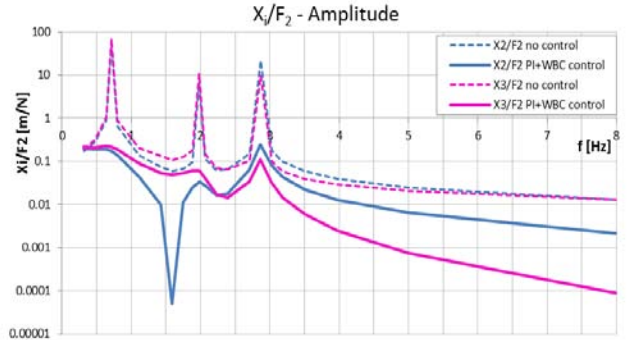
### B. Disturbance response – the harmonic force

If the force  $F_{2d}$  is harmonic with the particular frequency the response of the three-mass system can be derived or measured. The amplitude characteristics can be obtained too (Fig. 9).

Let us consider the force  $F_{2d}$  is prescribed using formula (10).

$$F_{2d}(t) = A_{F_2} \sin(2\pi f t) \quad (10)$$

The cascade wave-based method suppresses the amplitudes in the whole frequency range 0.5Hz-10Hz. The high damping effect is observable when the disturbing force has the resonance frequency ( $f_1=0.71\text{Hz}$ ;  $f_2=1.98\text{Hz}$ ;  $f_3=2.87\text{Hz}$ ).


 Fig. 9 The amplitude characteristics  $X_j/F_{2d}$ 

## IV. WAVE-BASED CONTROL IMPLEMENTATION

In general the servomotors use encoders which measure the position of the rotor. The encoders are already very exact devices in this time. The necessary feedback used by wave-based control is supposed to use the signal from this device in order to avoid installing extra sensors. The control strategy is following. Firstly the regulation in the torque mode is set. In the section II the wave-based control is described for the mass-spring chain case. The analogy of this chain has been used (Fig. 10). Apparently the simple P regulation is analogical to the repositioning through the spring. The gain of P regulation  $K_1$  represents the first stiffness in the mass-spring chain actually. The torque  $T(t)$  applied on the rotor is then computed using formula (11) [7][8].

$$T(t) = K_1(x_1(t) - x_0(t)) \quad (11)$$

The strategy is the same when cascade wave-based control or simple wave-based control is used. The required position  $x_0(t)$  is always transferred to the torque  $T(t)$  using (11).

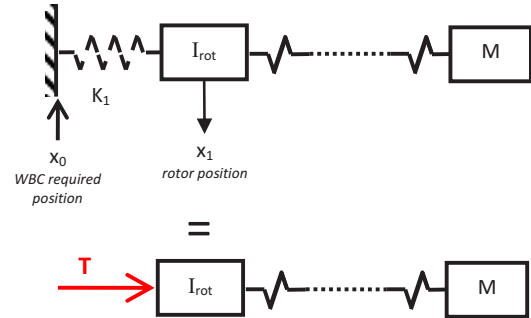


Fig. 10 The lumped-mass chain analogy

## V. EXPERIMENT

### A. The experiment description

The two degrees of freedom system was chosen. The servomotor drives two flywheels coupled with relatively thin shafts in the series. This system has the first natural frequency below 10Hz. Both flywheels have the momentum of inertia  $0.1 \text{ kgm}^2$ . The values of the shafts stiffness were not particularly measured, but they were approximately calculated. It is not needed to know the exact values when using wave-based control.

Tab. 1 Devices in the chain

Motor	Yaskawa SGMG-V $n_{rated} = 3000$ rpm, $T_{rated} = 15.8$ Nm, rotor inertia $I_{rot} = 0.00123$ kgm <sup>2</sup>
Gearbox	Neugard, gear ratio $i=5$
Shaft 1	$\varnothing d = 10$ mm, length $l = 260$ mm
Flywheel 1	$I_1 = 0.1$ kgm <sup>2</sup>
Position sensor	Renishaw Signum - RSM20
Shaft 2	$\varnothing d = 12$ mm, length $l = 270$ mm
Flywheel 2	$I_2 = 0.1$ kgm <sup>2</sup>
Sensor 2	Larm 305/6000 PB



Fig. 11 The experiment – motor drives two flywheels in series

B. Wave-based control implementation

The implementation was performed in the same way like it is described in the session IV. The servomotor works in the torque mode and the whole regulation is performed in the controller. The calculation time is 0.001s which is sufficient time to control systems with the natural frequencies around 10Hz. The Fig. 12 recapitulates the wave-based control implementation and Fig. 13 shows the implementation of the cascade wave-based control. The difference  $(x_1 - x_0)$  is multiplied by arbitrary chosen constant  $K_1$  and the torque  $T$  is computed.

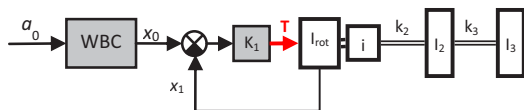


Fig. 12 The experiment – two flywheels in series and WBC

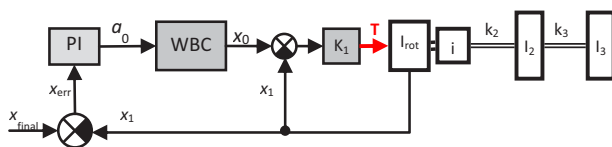


Fig. 13 The experiment – two flywheels in series and CWBC

C. Results

Firstly it is good to show how the system behaves when wave-based control is not used. The classical cascade control (position – velocity – torque – current) is performed. The system can be even unstable which shows the Fig. 14. It describes the response of the system when servo works in the position mode and the position command of 0.6 rad was performed. The system is oscillating after the repositioning and the amplitudes are even growing.

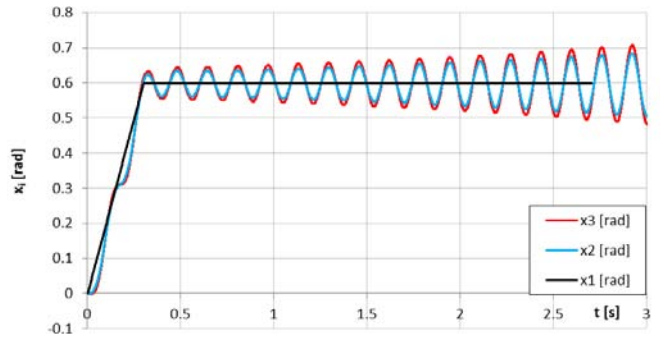


Fig. 14 The response of the system (servo in the position mode)

Secondly the basic wave-based control was performed. The request is to rotate the rotor of 36 rad. The flywheels have five times lower angular displacement because of the gearbox. The Fig. 15 shows the results. All positions and torques are recomputed to the motor side, also the positions of the flywheels. The mechanical system is stable but the rotor turned of 28 rad approximately. The request to turn of 36 rad is not satisfied. This is caused by the presence of the passive resistances.

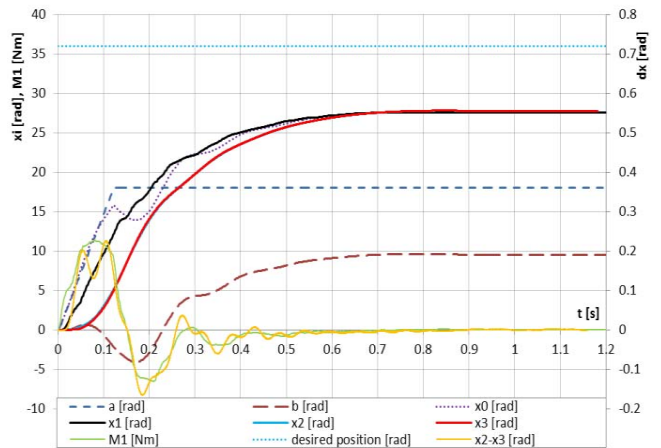


Fig. 15 The experiment – wave-based control

Thirdly the cascade wave-based control was implemented in the experiment. The request is to rotate the rotor of  $10\pi$  rad.

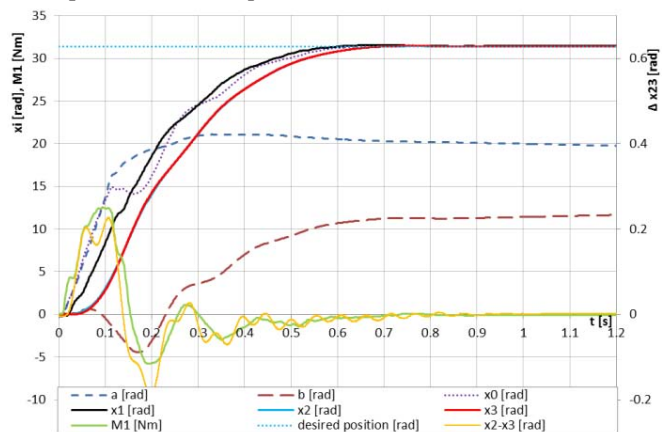


Fig. 16 The experiment – cascade wave-based control

The Fig. 16 shows the perfect result. The desired position was obtained using cascade wave-based control. The passive resistances caused that  $a_0(t>1s)$  is not the half of the desired position, the PID regulator has increased this value, but it does not have any negative effect.

## VI. CONCLUSIONS

The paper describes the cascade wave-based control that is in fact PID and WBC in series. It shows the advantages and the benefits. One of the benefits is the ability to suppress the external vibrations and the influence of external forces. The paper describes also the possibility of wave-based control implementation in the real servomotor. The only needed sensor is the encoder which measures the position of the rotor. No other expensive additional sensor is needed. The paper shows also the effect of the passive resistances. The resistances can negatively affect the strength of the wave-based control because the resistances cause the system does not reach the required position. The cascade wave-based control can solve that problem. The particular experimental results are shown in the section V.

## ACKNOWLEDGMENT

This work was supported by the grant GAP101/11/2110 “Advanced control of precise positioning mechanisms by forming the input” of the Czech Science Foundation.

## REFERENCES

- [1] W. J. O'Connor “Wave-echo Position Control of Flexible Systems: Towards an Explanation and Theory”. In: Boston: American Control Conference, 2004, p. 4837-4842
- [2] W. J. O'Connor, “Wave-based Modeling and Control of Lumped Multibody Flexible Systems”, In: [CD]. Madrid: Proc. of Multibody Dynamics 2005, ECCOMAS Thematic Conference, 2005, p. 1-6
- [3] W. J. O'Connor, “Slewing Control of Space Structures with Flexible Joints: A Wave-based Approach”, In: [CD]. Milano: Proc. of Multibody Dynamics 2007, ECCOMAS Thematic Conference, 2007, p. 1-9
- [4] O. Marek, M. Valášek, “Wave-Based Control of Motion of Flexible Bodies” In: *Multibody Dynamics 2009*. Warszawa: Oficyna wydawnicza Politechniki Warszawskiej, 2009, p. 102-103. ISBN 978-83-7207-813-1.
- [5] O. Marek, M. Valášek, “Control of Translational Motion of Flexible Bodies by Wave Method”. 2008. 104-108. ISSN 1801-1217.
- [6] M. Valášek, O. Marek, “Stability analysis of wave-based control of flexible systems.” In: *The 1st Joint International Conference on Multibody System Dynamics IMSD* [CD]. Lappeenranta (Finland): Lappeenranta University of Technology, 2010, p. 1-8. ISBN 978-952-214-778-3.
- [7] O. Marek, “Servo Control Using Wave-Based Method.” In: J. Beran, et al. *Advances in Mechanisms Design*. Springer, 2012, p. 531-536. ISBN 978-94-007-5124-8.
- [8] O. Marek, M. Valášek, “Servo Control Using WBC Method.” In: *Bulletin of Applied Mechanics*. 2010. Praha. s. 71-76. ISBN 978-83-7207-813-1.
- [9] P. Beneš, “Input Shaping Control with Generalized Conditions”, Praha 2012. Ph.D. thesis.
- [10] W. Singhose and W. Seering, “Generating Vibration-Reducing Inputs with Vector Diagrams”. In: Prague: 8th World Congress on the Theory of Mechanics and Mechanisms, 1991, p. 315-318

# Effect of Deposition Volume on PVC-based Mn(TPP)Cl Membrane for FET Sensitive to Histamine

S.F. Mohammed Esa, Khuan Y Lee and R Jarmin

**Abstract**—Histidine is a type of amino acid contained in fish muscle tissue that is capable to produce histamine, a toxin, in the presence of decarboxylated enzyme. Consumption of histamine exceeding the safety limit of 100ppm legislated by FDA leads to allergic reaction that incurs symptoms such as diarrhea, vomiting, headache, low blood pressure and facial swelling, known as Scombroid poisoning. Current methods for histamine detection such as HPLC and TLC are more expensive, more skill dependent, more laborious and more time consuming, relative to ISFET, which gives ISFET the advantage of miniaturization enabling and in-situ monitoring enabling. Majority of literature on ISFET has been reporting on its application for pH detection, the H<sup>+</sup> ions. However, ISFET can be adapted to detect other ion type, such as histamine in our research. This has been the first attempt in adapting ISFET to be sensitive to histamine. We have developed a PVC based membrane plasticized with dioctyl phthalate, dissolved in tetrahydrofuran, enhanced with ionophore Mn(TPP)Cl and polyHEMA layer on the insulator gate of ISFET, for this purpose. Our work here is to examine the effect of deposition volume on the performance of adapted ISFET at a conditioning time of 3hours, for concentration of histamine ranging from 10<sup>-6</sup> molar to 10<sup>-1</sup> molar. The histamine sensitivity tests on five functionally tested blank ISFET, S4B, S4C, S4H, S4I and S4J, show that volume of membrane deposited has an effect on the Nerstian response to histamine. Even though the Nerstian slope differs for concentration range between 10<sup>-2</sup> to 10<sup>-1</sup> and 10<sup>-4</sup> to 10<sup>-2</sup> molar of histamine solution, the adapted ISFET S4H and S4I yields the highest slope consistently, indicating deposition volume of 15-20  $\mu$ L of membrane solution is optimal for sensitivity to histamine.

**Keywords**—ISFET; histamine; PVC-membrane; deposition volume; conditioning time

This work was supported in part by the Ministry of Education (MOE), Malaysia, under Grant RMI/ERGS 5/3 (20/2013); the Research Management Institute, Universiti Teknologi MARA, Malaysia under Grant Research Intensive Fund 600-RMI/DANA 5/3/RIF (40/2012), 600-RMI/DANA 5/3/RIF (79/2012), 600-RMI/DANA 5/3/RIF (373/2012), 600-RMI/DANA 5/3/PSI (158/2013) and 600-RMI/DANA 5/3/CIFI (42/2013).

S.F. Mohammed Esa is with the Faculty of Electrical Engineering, Universiti Teknologi MARA, 40450 Shah Alam, Selangor DE, Malaysia. (e-mail: fatimah\_redang@yahoo.com)

Khuan Y Lee is with the Faculty of Electrical Engineering, Computational Physiologic Detection Group, Brain & Neuroscience Communities of Research, Universiti Teknologi MARA, 40450 Shah Alam, Selangor DE, Malaysia and NAPL, Mimos Berhad, Malaysia. (phone: 603-5543-6088; fax: 603-5543-5077; e-mail: leeyoorkhuan@salam.uitm.edu.my).

R Jarmin is with the Faculty of Electrical Engineering, Universiti Teknologi MARA, 40450 Shah Alam, Selangor DE, Malaysia and NAPL, Mimos Berhad, Malaysia. (e-mail: roziah353@salam.uitm.edu.my).

## I. INTRODUCTION

HISTAMINE is a toxin produced by the reaction of amino acid, histidine, in the presence of decarboxylated enzyme. It reproduces rapidly over a wide temperature range, any above 40°C, but not below freezing condition, less than -20°C. Histamine that is starting to reproduce right after thawing does not change the appearance, color and odour of the fish. Freezing after only slows down the production of histamine with no change to the histamine content already contained in the fish muscle tissue. Once produced, histamine cannot be destroyed with canning, heating or cooking, making it a looming danger.

Scombroid poisoning occurs if consumption of histamine exceeds 100ppm, the safety level designated by the Food and Drug Administration (FDA) of USA[1-2]. Scombroid poisoning is a reaction to being allergic to histamine. This allergic reaction distinct itself from other allergic reactions as follows: the inflicted subject has no previous allergy to the food in question, the outbreak and the presence of histamine in the implicated food [3]. Symptoms of scombroid poisoning include headache, vomiting, diarrhea, facial swelling, thirst, skin rash and low blood pressure [4]. Severity of this symptom depends on the immunoglobulin, which varies from person to person. Normally, the symptoms become apparent one hour after digesting seafood containing high level of histamine. In the extreme case, this allergic reaction could cause death.

A variety of methods have been developed for histamine detection such as high performance liquid chromatography (HPLC), thin layer chromatography (TLC), gas chromatography, amperometric, chronopotentiometry and capillary zone electrophoresis [5-7]. However, the detection limit of capillary analysis is high. The colorimetric method compares the difference in color intensity visually. Only TLC and HPLC employs direct measurement of the primary variable, histamine. However, these chromatography methods employ expensive equipment [9].

Sensor technology brings about the ion-selective electrodes (ISE). It is simple, durable, inexpensive and capable of reliable response over a wide range of concentration. Their fast response time, low detection limit and good selectivity make potentiometric detection suitable for direct and rapid detection of chemically and biologically compounds [10-11]. An

offshoot of this development is the Ion-Sensitive Field Effect Transistor (ISFET), a chemical field effect transistor introduced by Bergveld in the 1970's [12].

ISFET is a potentiometric sensor that accommodates a wide range of chemical and biochemical measurements. Unlike the ISE, the manufacturing of ISFETs is based on semiconductor IC technology. Sensing, pre-processing and computation can be encapsulated on the same chip with interface for information processing and data storage. This makes development of new ISFET based devices and sensors small, simple and cost effective, an advantage over the ISE. In comparison to current techniques such as TLC, HPLC, ISFET also has advantage over size, sensitivity, cost and power consumption. In addition, ISFET is dispensable of wet chemistry laboratory analysis. All the above attributes favors ISFET for miniaturization and portability.

The purpose of our work is to research into designing ISFET for detection of histamine, for quality control over fish freshness and minimizing occurrences of Scombroid poisoning. For FET to be sensitive to histamine, it needs to be adapted with a membrane, of which deposition volume of membrane solution is an important factor. Here, we aim to study the effect of deposition volume of membrane solution on the Nernstian slope of sensitivity for ISFET, in tandem with concentration of histamine. Fundamental theory on adapted ISFET is introduced in Section II. Methods to select functional blank ISFET, prepare and deposit membrane are explained in Section III. Findings from pH and histamine sensitivity test to determine the optimal deposition volume of membrane is discussed in Section IV.

## II. THEORY ON ISFET

Being a potentiometric type sensor, ISFET is used to measure electrical potential difference at the interface of ionic solution. The ISFET have the basic structure of an electronic analogue MOSFET, except that its metal gate is replaced with reference electrode of ISFET and an open contact for ion detection. The reference electrode produces a charge when the ionic solution makes contact with the bare gate insulator.

With reference to the site binding theory, the presence of hydroxyl (Si-OH) group at the surface of metal oxide accepts or donates a proton ( $H^+$  -ion), giving a negative or positive charge in the solution, until equilibrium is achieved. A current flows through ISFET as the number of Si-OH and the  $H^+$  -ions is being balanced.

For ISFET of our design as shown in Figure 1, the gate For ISFET of our design as shown in Figure 1, the gate insulator layer (silicon nitrate,  $Si_3N_4$ ) generates an interface potential on the gate once it detects  $H^+$  -ions. The potential developed across the insulator layer depends on the number of  $H^+$  -ions in contact with it, which can be related to the pH value of the electrolyte. The gate potential modulates the current flow from source to drain, as ISFET is switched on.

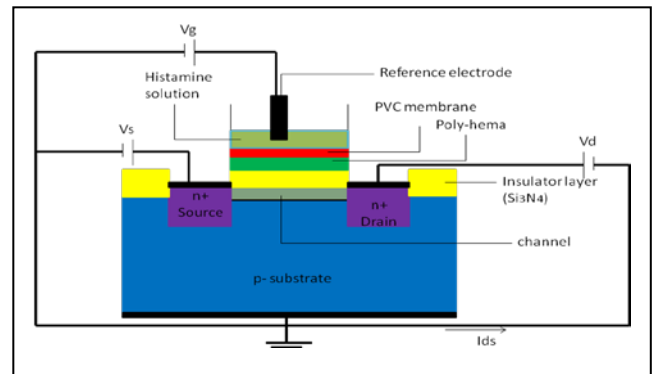


Figure 1. Structure of ISFET with PolyHEMA and PVC Membrane

ISFET can be adapted to detect ions besides  $H^+$  -ions. In our research, histamine is the target ion. An ion selective plasticized PVC membrane concocted with a membrane cocktail recipe, uniquely for histamine, makes the adaptation [13]. The membrane cocktail recipe that enables selectivity of the histamine ion is constituted of the following.

Membrane Support made of synthetic PolyVinyl Chloride (PVC ( $C_2H_3Cl$ ) $_n$ ) is the holding material. PVC is the third most widely produced plastic, after polyethylene and polypropylene. Pure PVC is a white, brittle solid. Mixed with plasticizer such as DiOctyl Phthalate (DOP,  $C_6H_4(C_8H_17COO)_2$ ), the flexibility and durability of PVC membrane is improved as it softens the membrane. DOP is an organic compound. It is the most common in the class of phthalate plasticizers. It is colorless, viscous and soluble in oil but insoluble in water. Its lipophilic and hydrophobic nature restricts diffusion of membrane components to the external solution and improves membrane adhesion to the gate area. Solvent, TetraHydroFuran (THF, ( $CH_2$ ) $_4O$ )), dissolves the solid membrane. THF is a moderately polar, aprotic solvent for PVC with dielectric constant of 7.6 and is water miscible. Ionophore, 5-,10-,15-,20-TetraPhenyl Porphyrinato Manganese (III) Chloride ( $Mn( TPP) Cl$ ), exhibits high affinity for histamine ions and acts as an ion carrier that recognizes and transports histamine ions across the membrane. Its efficiency determines the sensitivity of ISFET sensor.

## III. METHODOLOGY

A blank p-type ISFET with n-channel and  $Si_3N_4$  as an insulator layer is selected for detection of histamine. As shown in Figure 2, the ISFET chip was electrically bonded onto a printed circuit board and encapsulated meanwhile the sensitive gate area is left opened for contact with the electrolyte. It is here that membrane enabling ISFET for histamine detection is deposited.

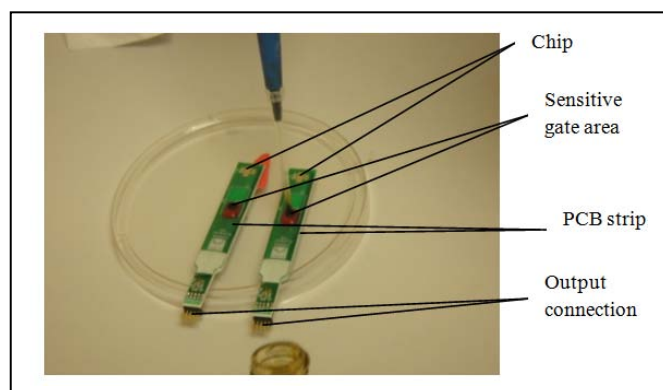


Figure 2. Blank P-Type ISFET with n-Channel and Si<sub>3</sub>N<sub>4</sub> as Insulator Layer

### A. ISFET Selection

Functional ISFET is selected using pH sensitivity test. The purpose of this process is to separate the functional ISFETs from defective ones, from the fabrication process. The sensitivity test ensures insulator of ISFET will be sensitive to H<sup>+</sup> ion. The threshold for acceptable sensitivity is 45mV/dec, recognized by MIMOS, the Malaysia National Research & Development Centre in Information & Communication Technology under purview of the Malaysian Ministry of Science, Technology and Innovation.

Figure 3 shows the experimental setup for the pH sensitivity test. The blank ISFET is dipped into three sets of pH buffer solution, differing in their level of pH: pH4 for acidic, pH7 for neutral and pH10 for alkaline. At temperature 25°C, the gate voltage ( $V_G$ ) are recorded at constant drain current ( $I_D$ ) of 100 $\mu$ A for every sweep.

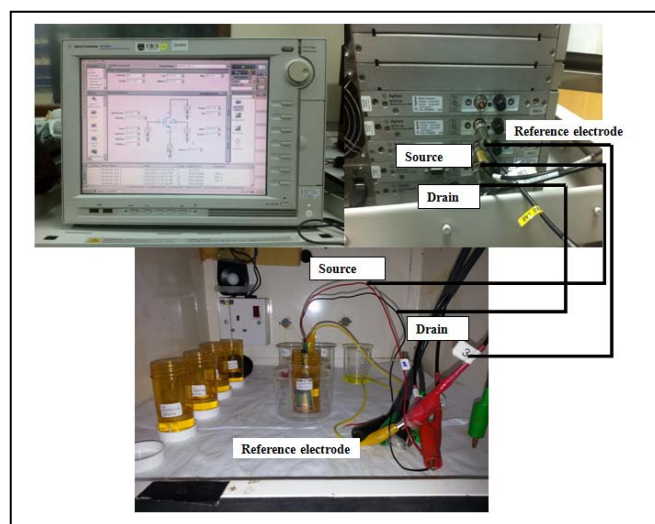


Figure 3. Experimental Setup for ISFET pH Sensitivity Test

### B. Membrane preparation

Here, a PVC membrane technology based n-channel Si<sub>3</sub>N<sub>4</sub> ISFET is prepared. Recipe for the membrane solution is concocted by dissolving Mn(TPP)Cl, DOP and PVC synthetic membrane, in proportion as tabulated in Table 1, to give a total mass of 50mg in 500 $\mu$ l of THF. All the chemicals were

used as received from Sigma. It is important to ensure that all the solid particles must be thoroughly dissolved.

TABLE 1: RECIPE OF MEMBRANE COCKTAIL

	Chemicals	Amount
Membrane Support	PolyVinyl Chloride (PVC)	15mg (30%)
Plasticizer	DiOctyl Phthalate (DOP)	30mg (60%)
Solvent	TetraHydroFuran (THF)	500 $\mu$ L
Ionophore	5-, 10-, 15-, 20-TetraPhenyl Porphyrinato Manganese (III) Chloride (Mn(TPP)Cl)	5mg (10%)

### C. Membrane deposition

After the selection for functional ISFETs and preparation of membrane solution, the membrane was then deposited on the gate insulator layer, in accordance to steps depicted in Figure 4.

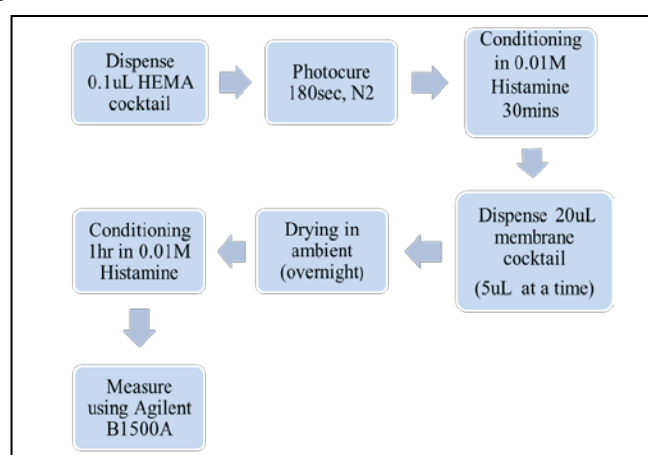


Figure 4. Procedural Flow of Membrane Deposition

Firstly, 0.1 $\mu$ l of our HEMA cocktail is dispensed on the ISFET. PolyHEMA layer (see Figure 1) is introduced before the membrane to absorb the aqueous buffer solution of salts at the membrane/gate oxide interface. This helps to overcome the ill-defined phase boundary between the membrane and gate oxide and reduces the influence of CO<sub>2</sub> as acidic agent, thus stabilizes potential developed in the membrane [14-15]. Then it is photo-cured in a N<sub>2</sub> room for 180 seconds. After that, it is conditioned in 10<sup>-1</sup> mol/L of histamine for 30 minutes before a total of 20 $\mu$ l of our membrane cocktail as prescribed in Table 1 is dispensed on the ISFET with a micro-pipette, 5 $\mu$ l at a time. Then, the ISFET is left dried overnight at ambient room condition. Finally, the membrane deposition process is completed with conditioning of the ISFET in 10<sup>-1</sup> mol/L of histamine for 60 minutes.

### D. Sensitivity test for histamine

Five ISFETs which pass the pH sensitivity test from Section IIIA are deposited with PVC-based membrane as in Section IIIC before they are used for sensitivity test for histamine.

The experiment is performed in the dark box to avoid interference from other sources such as temperature, light. All the leads from drain, source and reference junction in the dark box are then connected to Agilent Technology Semiconductor

Device Analyzer (B1 500A), as in Figure 3. Each ISFET was deposited with different volumes of membrane solution and the gate voltage ( $V_G$ ) are recorded at constant drain current ( $I_D$ ) of  $100\mu A$  for every sweep, at temperature  $25^\circ C$ . Measurement at each volume of the membrane solution is repeated six time, as the volume is varied from  $5\mu L$  to  $25\mu L$ , at an increment of  $5\mu L$ , while the range of histamine concentration from  $10^{-6}$  molar to  $10^{-1}$  molar. The pH value of solution is kept controlled at pH7.

#### IV. RESULTS & DISCUSSION

Result from the pH sensitivity test is shown first in Section A for selection of functional ISFET. Result from histamine sensitivity test is shown in Section B to observe the effect from deposition volume of membrane.

##### A. pH Sensitivity Test

Figure 5 displays the pH sensitivity of the five blank ISFETs, S4B, S4C, S4H, S4I and S4J. All the blank ISFETs show linear range from pH4 – pH10, with regression coefficient of 0.9999. They also exhibit good Nerstian slope between 47-48mV per unit change in pH, excelling the sensitivity threshold set by MIMOS, 45mV/pH. Hence, all the ISFETs can then be deposited with membrane for histamine detection.

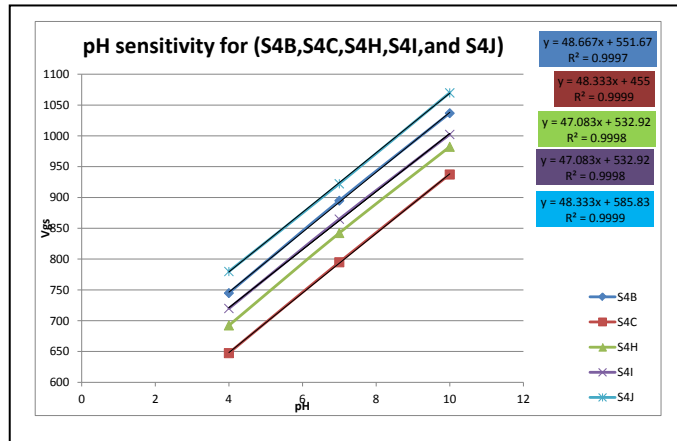


Figure 5. pH Sensitivity Test of ISFET

##### B. Histamine sensitivity test

Figure 6 shows the sensitivity graph of adapted ISFET in response to different volumes of membrane solution, as histamine concentration is varied from  $10^{-6}$  to  $10^{-1}$  molar, at conditioning time of 3 hours.

It can be observed that volume of membrane solution has an effect on the Nerstian response of the adapted ISFETs. For concentration range between  $10^{-2}$  to  $10^{-1}$  molar of histamine solution, adapted ISFET S4H (green) and S4I (purple) with  $15\mu L$  and  $20\mu L$  of membrane solution yields highest Nerstian slope  $97.5mV/dec$  and  $85mV/dec$  respectively. Meanwhile, for concentration range between  $10^{-4}$  to  $10^{-2}$  molar of histamine solution, adapted ISFET S4H (green) and S4I (purple) again gives the highest Nerstian slope of  $16.25mV/dec$  and  $13.75mV/dec$  respectively. Adapted ISFET S4B depicts

moderate sensitivity of  $52.5mV/dec$  and  $11.25mV/dec$  for histamine concentration of  $10^{-2}$  to  $10^{-1}$  molar and  $10^{-4}$  to  $10^{-2}$  molar. Adapted ISFET S4C and S4J with  $10\mu L$  and  $25\mu L$  of membrane solution are not responsive to histamine solution over the entire concentration range.

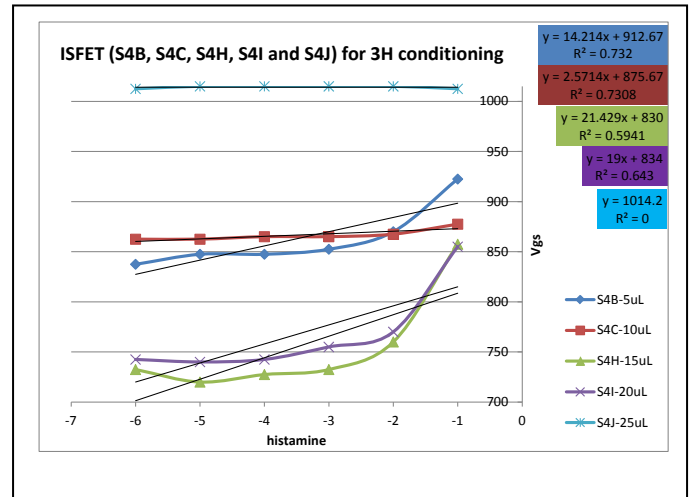


Figure 6. Sensitivity of Histamine in Response to Different Volumes of Membrane Solution with 3 hour of conditioning

#### V. CONCLUSION

This study intends to examine the effect of deposition volume of membrane solution on the Nerstian slope of sensitivity of ISFET with PVC-based membrane, Polyhema and Manganese tetraphenylporphyrin as ionophores. From the pH sensitivity test, all the five blank ISFETs, S4B, S4C, S4H, S4I and S4J produces good linear Nerstian slope between 47-48mV per unit change in pH, from pH4 – pH10. They meet the sensitivity threshold of 45mV/pH by MIMOS and hence verified functional. The histamine sensitivity test shows that volume of membrane solution has an effect on the Nerstian response of the adapted ISFETs. For concentration range between  $10^{-2}$  to  $10^{-1}$  molar of histamine solution, adapted ISFET S4H and S4I with  $15-20\mu L$  of membrane solution yields the highest Nerstian slope  $97.5mV/dec$  and  $85mV/dec$  respectively. Meanwhile, for concentration range between  $10^{-4}$  to  $10^{-2}$  molar of histamine solution, adapted ISFET S4H and S4I again gives the highest Nerstian slope of  $16.25mV/dec$  and  $13.75mV/dec$  respectively. Thus, it can be concluded that  $15-20\mu L$  of membrane solution is optimal for sensitivity to histamine.

#### ACKNOWLEDGMENT

The author would like to thank the Faculty of Electrical Engineering, Universiti Teknologi MARA, Malaysia, for the support and assistance given to the authors in carrying out this research; MIMOS Berhad, Malaysia for the technical support and permission given to use the facilities in the NAPL laboratory.

## REFERENCES

- [1] Yue Hu, Zhiong Huang, Jian Li, Hong Yang, "Concentrations of biogenic amines in fish squid and octopus and their changes during storage," *Food Chemistry*, vol. 135, no. 4, pp. 2604-2611.
- [2] Yuko Torido, Hajime Takahashi, Takashi Kuda, Bon Kimura, "Analysis of the growth of histamine-producing bacteria and histamine accumulation in fish during storage at low temperature," *Food Control*, vol. 26, no. 1, pp. 174-177.
- [3] J. Dennis Grey Allen, "Regulatory control of histamine production in North Carolina harvested Mahi-mahi (*Coryphaena hippurus*) and yellowfin tuna (*Thunnus Albacares*): A HACCP-BASED industry survey," Department of Food Science, North Carolina State University, Raleigh, NC, 2004.
- [4] 4. James M. Hungerford, "Scombroid poisoning: A review," *Toxicol*, vol. 56, no. 2, pp. 231-243, 2010.
- [5] R. Jeya Shakila, T. S. Vasundhara, and K. V. Kumudavally, "A comparison of the TLC-densitometry and HPLC method for the determination of biogenic amines in fish and fishery products," *Food Chemistry*, vol. 75, no. 2, pp. 255-259, 2001.
- [6] W. Liao, H. Paek, C. Mabuni et al., "Use of capillary electrophoresis with UV detection as a screening method to determine histamine in fish samples," *Journal of Chromatography A*, vol. 853, no. 1, pp. 541-544, 1999.
- [7] S. Páez, J. Bartolá, and E. Fábregas, "Amperometric biosensor for the determination of histamine in fish samples," *Food Chemistry*, vol. 141, no. 4, pp. 4066-4072.
- [8] J. Lapa-Guimaraes and J. Pickova, "New solvent systems for thin-layer chromatographic determination of nine biogenic amines in fish and squid," *Journal of Chromatography A*, vol. 1045, pp. 223-232, 07/03/2006 2004.
- [9] R. Jeya Shakila, T. S. Vasundhara, and K. V. Kumudavally, "A comparison of the TLC-densitometry and HPLC method for the determination of biogenic amines in fish and fishery products," *Food Chemistry*, vol. 75, no. 2, pp. 255-259, 2001.
- [10] M. K. Amini, S. Shahrokhian and S. Tangestaninejad, "Porphyrins as carriers in poly(vinyl chloride)-based membrane potentiometric sensors for histamine," *The Analyst*, 1999, 124, pp 1319-1322. M. Young, *The Technical Writer's Handbook*. Mill Valley, CA: University Science, 1989.
- [11] M. Javanbakht, A. Mohammadi, M. R. Ganjali, P. Norouzi, F. Faridbod and H. Pirelahi, "PVC-Based on Thiopyrilium Membrane Electrodes for Determination of Histamine," *Journal of the Chinese Chemical Society*, 2007, 54, pp 1495-1504.
- [12] P. Bergveld, "Thirty years of ISFETOLOGY: What happened in the past 30 years and what may happen in the next 30 years," *Sensors and Actuators B: Chemical*, vol. 88, pp. 1-20, 2003.
- [13] E. Bakker, P. Buhlmann and E. Pretsch, "Carrier-Based Ion-Selective Electrodes and Bulk Optodes. 1. General Characteristics," *Chemical Reviews*, Vol 97, No. 8, pp 3083-3132, 1997.
- [14] M. Dawgul, D. G. Pijanowska, A. Krzyskow, J. Kruk and W. Torbicz, "An influence of polyHEMA gate layer on properties of ChemFETS," *Sensors*, 3, pp 146-159, 2003.
- [15] R. Jarmin, Khuan Y Lee, H. Hashim, N. Abd Rashid, M. A. Mohd Noor, "A Novel Mn(TPP)Cl-Ionophore DOP-Plasticizer PVC Membrane for n-Channel Silicon Nitrate ISFET Sensitive to Histamine".

# Linearity Error of Force Transducers arising from Nonlinear Elasticity

Jang H. Yi

**Abstract**—The linearity error of strain gage-based force transducers due to the nonlinear stress-strain behavior of an aluminum alloy is numerically calculated and analyzed using three regression models. It is found that a typical linearity error of 0.03% full scale can be obtained when the maximum deviation from the linear stress-strain behavior is in the range of 1%–2% of tensile strength depending on the regression model used. The difference between the average stress in a tension gage and the average stress in a compression gage does not appear to significantly affect the linearity error.

**Keywords**— linearity, load cells, strain gages, tensile modulus.

## I. INTRODUCTION

A strain gage-based force transducer such as a load cell consists of an elastic element and strain gages installed on the surface of the elastic element and converts a load-induced deformation into an electrical signal proportional to the load. Force transducers have been used in robots for measuring forces exerted on joints or forces generated by actuators [1]. In general, the electrical output of the transducer is a nonlinear function of the input deformation, typically expressed in microstrain units [2]. The maximum deviation of the transducer output from the straight line between the transducer output with no load applied (zero output) and the output at rated capacity (full scale output) is referred to as the linearity error.

Commercial load cells are ranked into differing accuracy classes. A specific accuracy class specifies a combined error including temperature effects, linearity error and hysteresis, typically less than 0.1% of full scale output [3]. Various methods for compensating for these errors have been proposed and analyzed [4]–[7].

It was experimentally determined that microstructural changes induced from heat treatments can affect the hysteresis performance of force transducers [8]. It was also found that the linearity and hysteresis performance parameters of a overloaded load cell can be essentially restored by subjecting the load cell to conditioning similar to that which it received in initial manufacture [9]. These findings suggest that deviations from the previous state of crystalline structure resulting from a particular type of conditioning may affect the elastic response of

the material, making the degree of nonlinearity more or less severe depending on the conditioning.

In this paper, the contributions of the nonlinear elastic response of an aluminum alloy to the transducer linear error will be numerically calculated and analyzed. The nonlinear stress-strain behavior will be modeled using three regression methods, and it will be shown that the nonlinear elasticity may cause the transducer linearity error.

## II. LINEARITY ERROR

A bending beam load cell shown in Fig. 1 is designed to produce an output signal  $V_o/V_s$  (mV/V) given by

$$\frac{V_o}{V_s} = \frac{R_4}{R_3 + R_4} - \frac{R_2}{R_1 + R_2}. \quad (1)$$

where the gage resistors,  $R_1$  and  $R_3$  (nominal resistance 350  $\Omega$ ), are subjected to an average tensile stress of about 40 MPa and  $R_2$  and  $R_4$  are subjected to an average compressive stress of 40 MPa when a 1 kgf load is applied as shown in the Wheatstone bridge circuit in Fig. 2. For the load cell shown in Fig. 1, Wheatstone bridge nonlinearity does not contribute to the transducer linearity error [10]. Let  $E$  be the linearity error given by

$$E = \frac{V_o}{V_s} \Big|_{\text{half load}} - \frac{V_o/V_s \Big|_{\text{full load}}}{2}. \quad (2)$$

The full scale output  $V_o/V_s \Big|_{\text{full load}}$  is the output signal under full load (1kgf). A tensile modulus of 73 GPa results in an average strain of 550  $\mu\epsilon$  (microstrain) under full load, which in turn yields a change in resistance of  $K \times 0.00055 \times 350 \Omega = 0.38 \Omega$ , where  $K = 2$  is the gage factor. Then from Eq. (1)

$$\frac{V_o}{V_s} \Big|_{\text{full load}} = \frac{350.38}{700} - \frac{349.62}{700} \approx 1.08 \text{ mV/V}. \quad (3)$$

Ideally the half scale output should be exactly one half (0.54 mV/V) of the full scale output. However, commercial load cells show deviations from this ideal linear behavior. It has been observed in our lab that the linearity error of the load cell shown in Fig. 1 is typically 0.03% full scale (0.0003 mV/V), or less.

This work was supported in part by the Korean Evaluation Institute of Industrial Technology under the World Class 300 Project.

J. H. Yi is with CAS Corporation, Yangju-si, Gyeonggi-do, Republic of Korea (phone: +82-10-3169-2010; fax: +82-31-836-0730; e-mail: yijangho.cas@gmail.com).

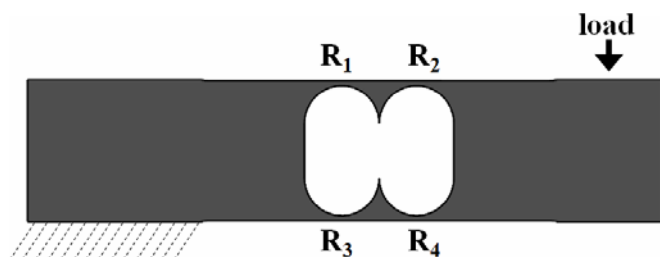


Fig. 1 Aluminum alloy load cell.

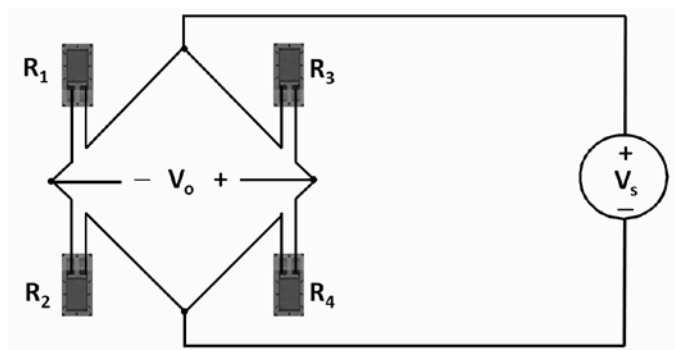


Fig. 2 Wheatstone bridge circuit.

### III. NONLINEAR ELASTICITY

Most metals are known to exhibit linear elasticity in the elastic region as illustrated in Fig. 3. In this work, it is assumed that the aluminum alloy machined to make the load cell in Fig. 1 has a nonlinear stress-strain property as illustrated in Fig. 3 (dashed curve), and only the contributions of this material nonlinearity to the transducer linear error will be examined although other factors such as hyperelastic properties of strain gage backing materials used in the industry may also contribute to the linearity error.

To characterize the nonlinear stress-strain behavior of the aluminum alloy, three regression models are considered as shown in Fig. 4. A third degree polynomial model is shown as solid curve; a third order Ogden model conventionally used to describe the nonlinear stress-strain behavior of rubbers is shown as dotted curve [11]; and an inverted sinusoidal curve is shown as dashed curve. The maximum deviation from the linear stress-strain behavior is set to approximately 1% of the tensile strength (320 MPa) of the aluminum alloy for the three models.

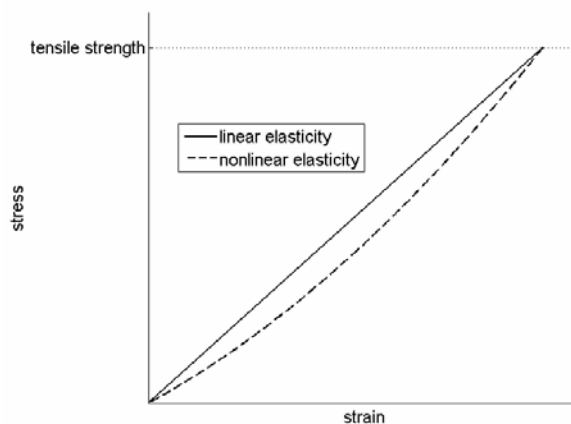


Fig. 3 Stress as a linear (solid) and nonlinear (dashed) function of strain.

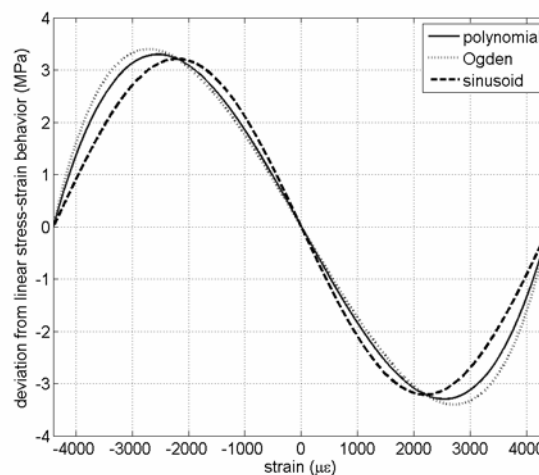


Fig. 4 Nonlinear stress-strain models: polynomial (solid), Ogden (dotted), and sinusoid (dashed).

### IV. FINITE ELEMENT ANALYSIS

Commercially available finite element analysis software was used to compute the stress distribution over the gage areas. The 3D load cell model consists of nine parts: the body, the four gage areas (the dimension of each gage area is 3 mm × 1.5 mm), and the four transitional “wells” that surround the gage areas (except the surfaces) and properly connect the elements in two adjacent meshes as shown in Fig. 5. The element size of the body mesh was set to 1 mm. The gage areas are composed of much finer elements of 0.1 mm to provide smoother stress distributions.

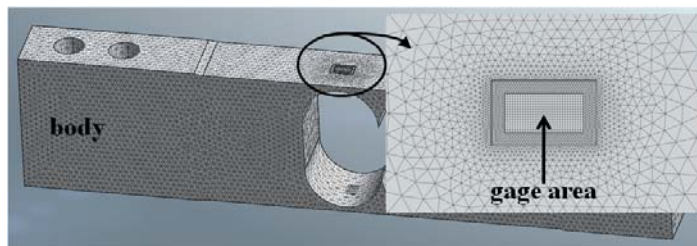


Fig. 5 Meshes generated with different element sizes.

## V. SIMULATION RESULTS

The distribution of stress in the horizontal direction (positive going from  $R_1$  to  $R_2$  in Fig. 1) under full load (1 kgf) is shown in Fig. 6. Salient stress concentrations are shown over the gage areas. The maximum stress (46.9 MPa) was produced in  $R_1$  and another tension gage  $R_4$  exhibited 4% less peak stress (45.01 MPa); the minimum stress (-46.9 MPa) was produced in  $R_3$  and the peak stress over  $R_2$  was -45.01 MPa.

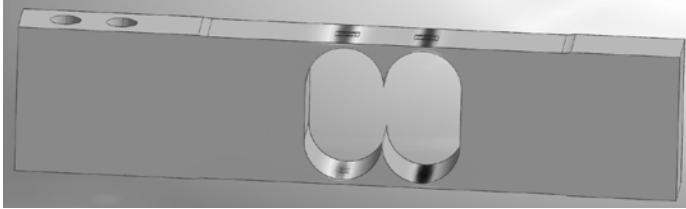


Fig. 6 Stress distribution.

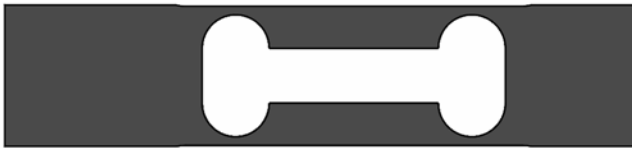
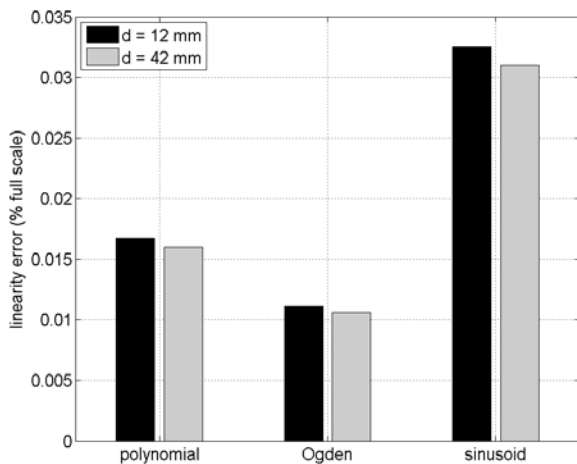

 Fig. 7 Load cell with  $R_1$  and  $R_2$  separated by 42 mm.

 Fig. 8 Linearity error when  $d = 12$  mm and  $d = 42$  mm.

 Table I. Effects of the distance between  $R_1$  and  $R_2$  (sinusoidal stress-strain model).

	avg. stress in $R_1$ (MPa)	avg. stress in $R_2$ (MPa)	avg. stress ratio $ R_2/R_1 $	$V_o/V_s$ (half load) (mV/V)	$V_o/V_s$ (full load) (mV/V)	Linearity error (% full scale)
$d=12$	39.336	-36.465	0.927	0.5359	1.0711	0.0325
$d=42$	39.334	-38.021	0.967	0.5469	1.0932	0.0310

 A. Distance between  $R_1$  and  $R_2$ 

Let  $d$  be the distance between  $R_1$  and  $R_2$  ( $d = 12$  mm in Fig. 1). Consider another load cell with  $d = 42$  mm shown in Fig. 7. This load cell is designed to produce comparable stresses over the gage areas. The linearity error obtained from the aforementioned regression models is shown in Fig. 8. The

sinusoidal model results in the largest error due to its steepest initial slope (see Fig. 4), whereas the Ogden model results in the smallest error due to its least severe degree of nonlinearity up to 2,000 microstrain (see Fig. 4).

Table I shows how the ratio of the average stress in  $R_2$  to the average stress in  $R_1$  gets closer to unity as  $d$  gets larger when the sinusoidal model is employed (fourth column). The linearity error in the last column, however, is not significantly affected by the change in  $d$ . Thus, the difference between the average stress in the tension gage and the average stress in the compression gage does not appear to play a significant role in determining the linearity error as far as the contributions of the nonlinear elasticity are concerned.

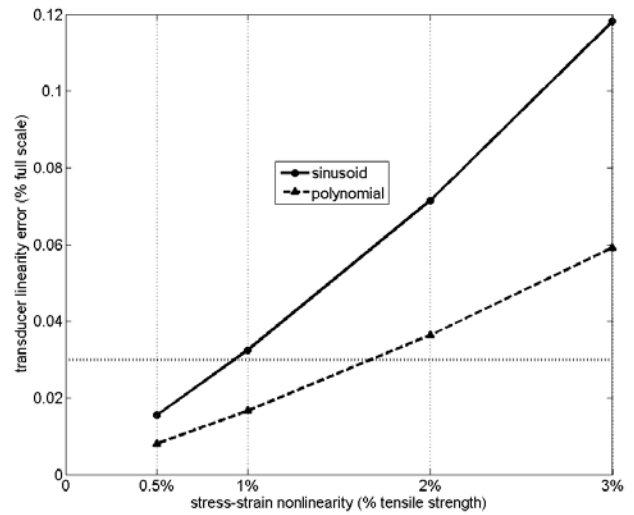


Fig. 9 Linearity error with varying stress-strain nonlinearity.

## B. Degree of Stress-Strain Nonlinearity

As mentioned above, the maximum deviation from the linear stress-strain behavior was set to about 3.2 MPa (1% of tensile strength) for the results presented thus far. Fig. 9 shows how the linearity error of the load cell in Fig. 1 changes as the degree of stress-strain nonlinearity varies. Assuming that the linearity error should not exceed 0.03% full scale, the degree of stress-strain nonlinearity should be less than 1% of tensile strength if the actual stress-strain behavior of the aluminum alloy follows the sinusoidal model, or less than 2% of tensile strength if it follows the polynomial model.

## ACKNOWLEDGMENT

The author would like to thank J. W. Choi and J. H. Park for their invaluable support.

## REFERENCES

- [1] M. Laffranchi, N. G. Tsagarakis, and D. G. Caldwell, "A variable physical damping actuator (VPDA) for compliant robotic joints," *2010 IEEE International Conference on Robotics and Automation (ICRA)*, Anchorage, AK, May 2010, pp. 1668-1674.
- [2] L. C. Shull, "Basic Circuit," in *Strain Gage User's Handbook*, R. L. Hannah, and S. E. Reed, Ed. London: Elsevier Science Publishers Ltd., Bethel, CT: Society for Measurement Mechanics, 1992, pp. 91-92.

- [3] K. E. Norden, *Handbook of Electronic Weighing*, Weinheim, Germany: Wiley-VCH Verlag GmbH, 1998, pp. 27-29.
- [4] J. H. Yi, "Temperature dependence of zero point in force transducers: material properties of strain gages causing such dependence," *Experimental Techniques*, to be published.
- [5] J. H. Yi, "Temperature dependence of zero point in force transducers II: how to account for the effects of a zero balancing resistor," *Experimental Techniques*, to be published.
- [6] J. E. Starr, "Compensation of strain gauge transducer non-linearity," U.S. Patent 3 034 346, May 15, 1962.
- [7] N. C. Griffen, "Hysteresis-compensated weighing apparatus and method," U.S. Patent 5 308 931, May 3, 1994.
- [8] S. Fank, and M. Demirkol, "Effect of microstructure on the hysteresis performance of force transducers using AISI 4340 steel spring material," *Sensors and Actuators A: Physical*, vol. 126, no. 1, pp. 25-32, Jan. 2006.
- [9] F. M. Tovey, "Effects of Overload on Load Cell Performance," *Experimental Techniques*, vol. 5, no. 3, pp. 8-9, 1981.
- [10] *Errors Due To Wheatstone Bridge Nonlinearity*, Vishay Precision Group Tech Note TN-507-1, Vishay Precision Group, Malvern, PA, 2010, pp. 77-81.
- [11] R. W. Ogden, "Large Deformation Isotropic Elasticity - On the Correlation of Theory and Experiment for Incompressible Rubberlike Solids," *Proceedings of the Royal Society of London. Series A, Mathematical and Physical Sciences*, vol. 326, no. 1567, pp. 565-584, Feb. 1972.

# Effect of Field Plate Length on Power Performance of GaN Based HEMTs

Gokhan Kurt<sup>1</sup>, Ahmet Toprak<sup>1</sup>, Ozlem A. Sen<sup>1</sup>, Ekmel Ozbay<sup>1,2,3</sup>

<sup>1</sup> Nanotechnology Research Center-NANOTAM, Bilkent University, 06800 Ankara, TURKEY

<sup>2</sup> Department of Electrical and Electronics Engineering, Bilkent University, 06800 Ankara, TURKEY

<sup>3</sup> Department of Physics, Bilkent University, 06800 Ankara, TURKEY

**Abstract** — In this work, we report GaN high-electron-mobility-transistors (HEMTs) on SiC with field plates of various dimensions for optimum performance. 0.6  $\mu\text{m}$  gate length, 3  $\mu\text{m}$  drain source space AlGaN/GaN HEMTs with field-plate lengths of 0.2, 0.3, 0.5, and 0.7  $\mu\text{m}$  have been fabricated. Great enhancement in radio frequency (RF) output power density was achieved with acceptable compromise in small signal gain. When biased at 35V, at 3dB gain compression, for a HEMT of 0.5  $\mu\text{m}$  field plate length and 800  $\mu\text{m}$  gate width a continuous wave output power of 36,2dBm (5.2 W/mm), power-added efficiency (PAE) of 33% and small signal gain of 11.4 dB, for a HEMT 0.5  $\mu\text{m}$  field plate length and 1000  $\mu\text{m}$  gate width a continuous wave output power of 37,2dBm (5.2 W/mm), power-added efficiency (PAE) of 33,7% and small gain of 10.7 dB were obtained at 8 GHz using device without using via hole technology.

**Index Terms** — Field Plate, GaN HEMT, RF power applications, coplanar waveguide, power amplifiers.

## I. INTRODUCTION

Gallium Nitride (GaN) based high-electron-mobility-transistor (HEMT) devices are of great interest for high radio frequency (RF) power applications due to highly demanded physical and electrical properties of AlGaN/GaN HEMTs offer far superior features such as high current density, high breakdown voltage, high thermal conductivity and high saturation velocity compared to gallium arsenide (GaAs) based HEMTs. Although, there is significant work on GaN HEMTs using field plates with very high output power densities for microstrip line (MSL) passive technology [1]-[4], yet to date, there have been only few reports on the effect of field plate length on HEMTs without via hole technology, i.e. HEMTs suitable for coplanar waveguide (CPW) passive technology [5].

In this work, a systematic study of the effect of field plate dimensions on small signal gain, power, efficiency and cut off frequency is presented. GaN-HEMTs are fabricated with different field plate lengths. All the field plate structures are deployed in the vicinity of the gate contacts on the  $\text{Si}_3\text{N}_4$  dielectric passivation layer. The electric field modification that is because of the field plates helps to smooth the peak value of the electric field on the channel caused by gate contact at the drain side of the gate edge. Thus it improves the breakdown voltage and the power performance of the HEMT. The benefit is also a reduced high-field trapping effect. As the field plate

functions by reducing the electric field at the edge of the gate on the drain side, it prevents electron emission and electron trapping. As a result it helps the reduction of the current collapse effect of the transistors. In addition to power performance, field plate structures have also impact on the noise performance of HEMTs.

The performance of HEMTs with six and eight gate fingers are measured. The gate dimensions of the measured HEMTs are 0.6  $\mu\text{m} \times 6 \times 125 \mu\text{m}$  and 0.6  $\mu\text{m} \times 8 \times 125 \mu\text{m}$  and average gate-to-gate distance is 60  $\mu\text{m}$  (Fig. 1). The schematic of the designed HEMT (0.6  $\mu\text{m} \times 6 \times 125 \mu\text{m}$ ) is given in Fig. 2. In this schematic,  $L_{gs}$  is 0.7  $\mu\text{m}$ ,  $L_g$  is 0.6  $\mu\text{m}$ ,  $L_{gd}$  is 1.7  $\mu\text{m}$  and four different field plate lengths are designed as 0.2  $\mu\text{m}$ , 0.3  $\mu\text{m}$ , 0.5  $\mu\text{m}$  and 0.7  $\mu\text{m}$ . The thickness of the  $\text{Si}_3\text{N}_4$  dielectric passivation layer is 300 nm.

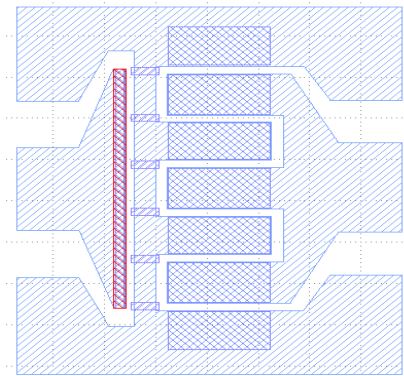


Fig. 1 Layout of the field-plated AlGaN/GaN HEMT structure.

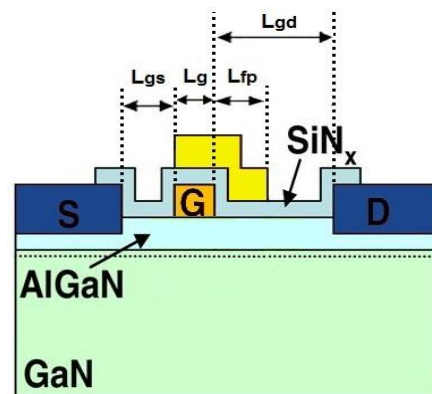


Fig. 2 Schematic of field-plated AlGaN/GaN HEMT structure

## II. DEVICE REALIZATION

AlGaIn/GaN HEMT epitaxial structure was grown on a semi-insulating SiC substrate by metal organic chemical vapor deposition. The structure consists of, 15 nm-thick AlN nucleation layer, a 2  $\mu\text{m}$ -thick undoped GaN buffer layer, an approximately 1.5 nm-thick AlN interlayer, a 20 nm-thick undoped Al<sub>0.22</sub>GaN<sub>0.78</sub> layer and a 2 nm-thick GaN cap layer on the top of the structure. The Hall mobility was 1384  $\text{cm}^2\text{V}^{-1}\text{s}^{-1}$  whereas the sheet carrier concentration was  $1.51 \times 10^{13} \text{ cm}^{-2}$ .

Fabrication process flow diagram of the HEMTs is given in Fig. 3.

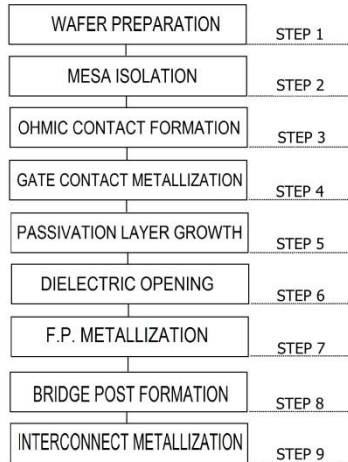


Fig. 3 Flow chart of GaN HEMT fabrication process with field plate step.

Mesa etching was performed with ICP-RIE with a  $\text{Cl}_2/\text{BCl}_3/\text{Ar}$  gas mixture. Ohmic contacts formation was done by Ti/Al/Ni/Au metal stack with the thicknesses of 12 nm, 120 nm, 35 nm and 65 nm, respectively. Ohmic contact metals were deposited by e-beam evaporation method. They were annealed in an nitrogen ambient at 850  $^\circ\text{C}$  for 30 s. After ohmic contacts had been formed, the TLM measurements were done. Ohmic contact resistance was 0.6  $\Omega\text{-mm}$  and the measured sheet resistance was 460  $\Omega\text{-}\square^{-1}$ . Ni/Au was deposited for gate contacts and subsequently an intermediate DC test measurement was done in order to check on whether the fabrication is proceeding as it is planned beforehand. This on-wafer DC operation test measurement of the devices was done prior to  $\text{Si}_3\text{N}_4$  dielectric passivation using an Agilent B1500A semiconductor device parameter analyzer. In this measurement, the peak extrinsic transconductance ( $g_m$ ) value was 215 mS/mm and the maximum current density value was 875 mA/mm. As the next step in fabrication, the device was passivated with a 300 nm-thick  $\text{Si}_3\text{N}_4$  layer grown by plasma-enhanced chemical vapor deposition. After the passivation, the openings, where the interconnect metal will be deposited on, were formed by means of dry etching of ICP-RIE with  $\text{CHF}_3$  gas. Thereafter, the test transistors were used to have DC test measurements again. Hence, we could observe the development impact of dielectric passivation on the transistors with this second DC test measurement.

After the passivation maximum current density was 1100 mA/mm and maximum extrinsic transconductance,  $g_m$  was 260 mS/mm. After this step, electron beam lithography is used to define the field plate regions and these regions were deposited with Ti/Au metals. The field plate structures were connected to the gate electrode with a gate bus. The air bridge post structures were constituted for preventing any case of being short circuit of the metals by functioning as a jumper. Finally, a relatively thick Ti/Au metal stack with e-beam evaporation had been deposited as an interconnection on the sample, and then the fabrication process was completed with this last step. Fig. 4 shows a  $0.6 \times 6 \times 125 \mu\text{m}$  HEMT's optical microscope image.

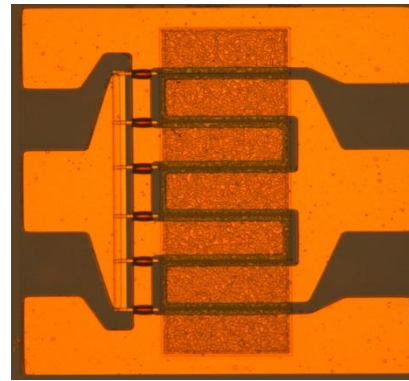


Fig. 4 Optical microscope image of fabricated  $6 \times 125 \mu\text{m}$  HEMT.

## III. RESULTS AND DISCUSSIONS

DC on wafer measurements were performed using an Agilent B1500A semiconductor device parameter analyzer. For DC I-V characterization  $0.6 \mu\text{m} \times 2 \times 100 \mu\text{m}$  the test transistor was used. The gates were biased from -4 to 1 V in a step of 1 V and drain current-voltage ( $I_{\text{DS}}-V_{\text{DS}}$ ) characteristics is measured. The maximum current densities  $I_{\text{ds, max}}$  for all devices are nearly identical and around 1100 mA/mm except for the field plate length of 0.6  $\mu\text{m}$ . For the device with  $L_{\text{fp}}$  0.7  $\mu\text{m}$ , the current density drops since the distance between the field plate and the drain is smaller. The devices are completely pinched off at  $V_{\text{gs}} = -4\text{V}$  and knee voltage is below 4 V which shows the excellence of ohmic contacts (Fig. 5).

In DC measurements, the extrinsic transconductance ( $g_m$ ) is also measured. The peak transconductance value for all field plate lengths are above 250 mS/mm except for  $L_{\text{fp}} = 0.7 \mu\text{m}$  and measured at  $V_{\text{gs}} = -3.2\text{V}$ . These results show that DC I-V transfer characteristics are independent of field plate length, the change in DC I-V transfer characteristics are due to the distance between field plate and drain contact, and in order not to decrease the current density and transconductance, this distance should be higher than 1.1  $\mu\text{m}$ . Fig. 6 shows the transconductance ( $g_m-V_{\text{ds}}$ ) characteristics of a  $0.6 \mu\text{m} \times 2 \times 100 \mu\text{m}$  AlGaIn/GaN HEMT with  $L_{\text{fp}} = 0.2, 0.3, 0.5,$  and 0.7  $\mu\text{m}$ .

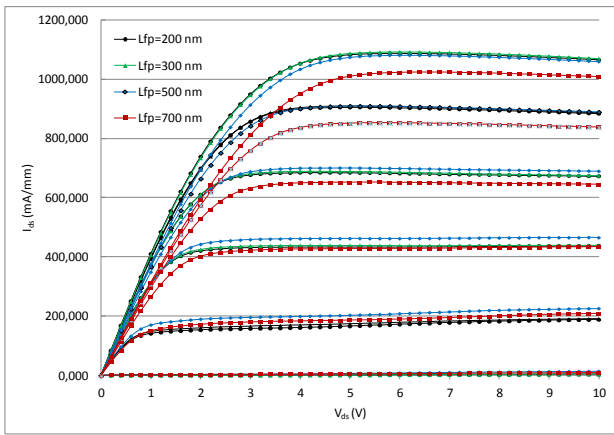


Fig. 5 Drain current-voltage ( $I_{DS}$ - $V_{DS}$ ) characteristics of a  $0.6 \mu\text{m} \times 2 \times 100 \mu\text{m}$  AlGaIn/GaN HEMT with  $L_{fp} = 0.2, 0.3, 0.5,$  and  $0.7 \mu\text{m}$ . The gate bias was swept from  $-4$  to  $1$  V in a step of  $1$  V.

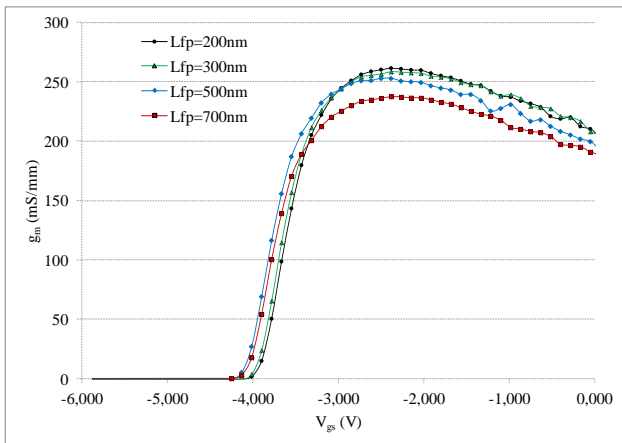


Fig. 6 Transconductance ( $g_m$ - $V_{gs}$ ) characteristics of a  $0.6 \mu\text{m} \times 2 \times 100 \mu\text{m}$  AlGaIn/GaN HEMT with  $L_{fp} = 0.2, 0.3, 0.5,$  and  $0.7 \mu\text{m}$ .

On-wafer radio frequency (RF) measurements were carried out using a Cascade Microtech Probe and an Agilent E8361A PNA in the 1–20 GHz range. In small signal RF measurements the HEMTs with six fingers and with gate width of  $6 \times 125 \mu\text{m}$  ( $0.6 \mu\text{m} \times 6 \times 125 \mu\text{m}$ ) are used. Short-circuit current gain  $|H_{21}|$  and Mason's unilateral power gain  $G_u$  derived from on-wafer S-parameter measurements as a function of frequency for the devices with field-plate length of 0.2, 0.3, 0.5 and  $0.7 \mu\text{m}$  (Fig. 7). With these measurements, it was seen that, for all the field plate lengths, the unity current gain cut off frequency,  $f_t$  was above 20 GHz, and maximum oscillation frequency  $f_{max}$  was above 30 GHz. This is reasonable since the gate lengths of all the HEMTs are same. As the field plate length increases, the gate resistance decreases. But due to the 300-nm-thick Si<sub>3</sub>N<sub>4</sub> passivation layer, the gate capacitances especially  $C_{gd}$  also increase. As a result, the change in  $f_{max}$  is negligible.

Large signal load pull measurement is carried on using Maury Microwave automated load pull system at 8 GHz. The data were taken on-wafer at room temperature without any thermal management.

First of all,  $0.6 \mu\text{m} \times 6 \times 125 \mu\text{m}$  HEMTs are measured at a drain bias of 35 V, and the output power, gain and power added efficiency (PAE) values are obtained (Fig. 8). The output power of the device with  $L_{fp}$  of  $0.5 \mu\text{m}$  at

3dB gain compression is 5.2 W/mm with an PAE of 33% and a small signal gain of 11.4dB at 8 GHz. Fig. 8 shows the large-signal performance of the  $0.6 \mu\text{m} \times 6 \times 125 \mu\text{m}$  with  $L_{fp} = 0.2, 0.3, 0.5,$  and  $0.7 \mu\text{m}$  at 8 GHz.

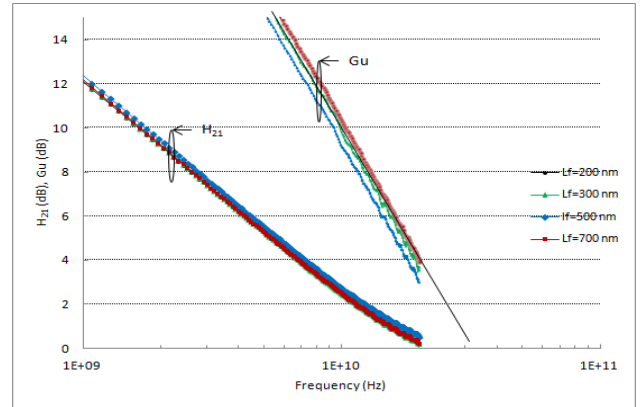


Fig. 7 Short-circuit current gain  $|H_{21}|$  and unilateral power gain of a  $0.6 \mu\text{m} \times 6 \times 125 \mu\text{m}$  AlGaIn/GaN HEMT with  $L_{fp} = 0.2, 0.3, 0.5,$  and  $0.7 \mu\text{m}$ . Device was biased at  $V_{DS} = 25$  V and  $V_{gs} = -3.0$  V

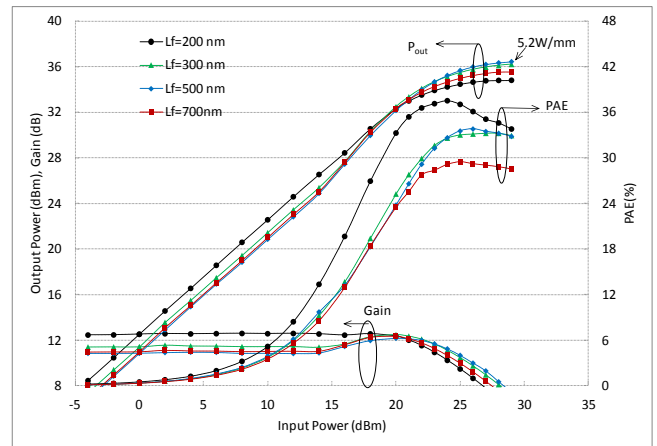


Fig. 8 Large-signal performance of the  $0.6 \mu\text{m} \times 6 \times 125 \mu\text{m}$  with  $L_{fp} = 0.2, 0.3, 0.5,$  and  $0.7 \mu\text{m}$  at 8 GHz. The device was biased with  $V_{ds} = 35$  V and  $V_{gs} = -2.4$  V

At a drain bias of 35 V, power densities of 3.3, 4.7, 5.2 and  $4.2 \text{ W/mm}$  ( $@3\text{dB}$  gain comp.) and small signal gain of 12.2, 11.6, 11.4, 11.2 dB were measured for devices with  $L_{fp}$  of 0.2, 0.3, 0.5 and  $0.7 \mu\text{m}$ , respectively (Fig. 9).

The DC, small signal and large signal results are summarized in TABLE 1.

From these results, it can be observed that, with the increase in field plate length, the output power density increases notably, with a negligible decrease in small signal gain unless the drain gate distance is above  $1.1 \mu\text{m}$ . When drain gate distance is above  $1.1 \mu\text{m}$ , the parasitic capacitance  $C_{gd}$  increases and this capacitance limits the output power.

As a second power measurement, the HEMTs with highest power performance are measured under different drain bias voltages.  $0.6 \mu\text{m} \times 8 \times 125 \mu\text{m}$  HEMTs with  $L_{fp}$  of  $500 \text{ nm}$  are measured at 25V, 30V, 32V and 35V drain bias. Out power values of 35.3dBm, 36.4dBm, 36.9dBm and, 36.6dBm ( $@2\text{dB}$  gain compression) and PAE of 43.7%, 37.8%, 36.9% and 33.6% were measured for devices with  $V_{DS}$  of 25, 30, 32 and 35V (Fig. 10). Results are summarized in TABLE II.

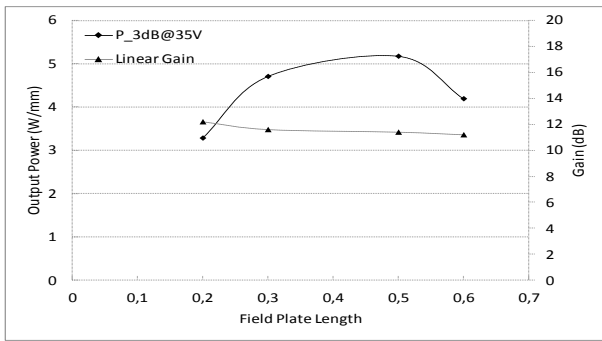


Fig. 9 Power performance versus length of field plate  $L_{fp}$  for devices of  $0.6 \mu\text{m} \times 6 \times 125 \mu\text{m}$  when measured at 8 GHz with drain biases of 35 V.

TABLE 1

Summary Of The Results Of The Field-Plated AlGaIn/GaN  $0.6 \mu\text{m} \times 6 \times 125 \mu\text{m}$  HEMTs with Varying Field-Plate Length

$L_{fp}$ ( $\mu\text{m}$ )	$g_{m,max}$ (mS/mm)	$I_{ds,max}$ (mA/mm)	$f_t$ (GHz)	$f_{t,max}$ (GHz)	Gain (dB)	Power (W/mm)
0.2	261	1080	20.2	32	12.2	3.3
0.3	259	1100	20.1	31	11.6	4.7
0.5	253	1080	20.3	30	11.4	5.2
0.7	237	975	20.2	31	11.2	4.2

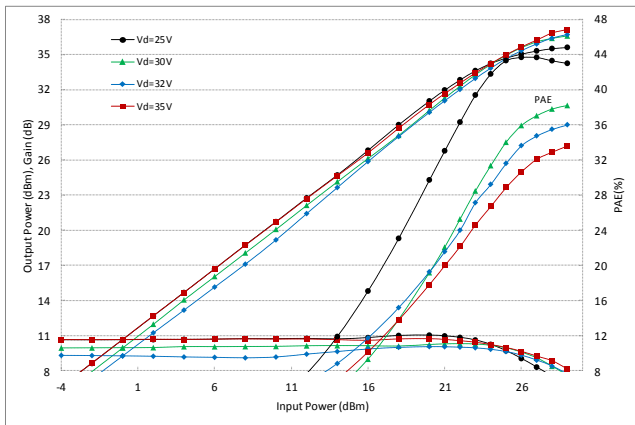


Fig. 10 Power performance versus drain bias  $V_{DS}$  for  $0.6 \mu\text{m} \times 8 \times 125 \mu\text{m}$  with  $L_{fp} 0.5 \mu\text{m}$  when measured at 8 GHz.

TABLE 1

Summary Of The Results Of The Field-Plated AlGaIn/GaN  $0.8 \mu\text{m} \times 6 \times 125 \mu\text{m}$  HEMTs with  $L_{fp} 0.5 \mu\text{m}$  Varying  $V_{ds}$

$V_{ds}$	Gain (dB)	Power (dBm) @2dB comp	Power (W/mm) @3dB comp	PAE (%)
25	10.6	35.3	3.4	43.7
30	9.9	36.4	4.35	37.8
32	9.3	36.9	4.9	36.9
35	10.6	36.6	4.6	33.6

IV. CONCLUSION

A systematic study has been performed to investigate the effect of a field plate on DC characteristics, small signal gain and large signal performance of GaN-channel HEMTs without via-hole technology. With  $0.6 \mu\text{m}$  gate length,  $300 \text{ nm}$ -thick  $\text{Si}_3\text{N}_4$  as a dielectric layer and  $3 \mu\text{m}$  drain-source spacing, optimum field plate length was found to be  $0.5 \mu\text{m}$ . These devices with field plate length of  $0.2 \mu\text{m}$ ,  $0.3 \mu\text{m}$  and  $0.5 \mu\text{m}$  exhibited high current densities of more than  $1.0 \text{ A/mm}$  and peak extrinsic

transconductances of more than  $250 \text{ mS/mm}$ . The DC I-V as well as transfer characteristics were essentially independent of the length of the field plate length. It was observed that when the space between the drain contact and the field plate decreases below  $1.1 \mu\text{m}$ , the positive effect of the field plate on power densities are not observed.

With the increase of the field-plate length, degradation in the values small signal gain was observed, but there was significant improvement in power densities. Also, at 8 GHz, a CW output power density of  $5.2 \text{ W/mm}$  with PAE of 33% and a large signal gain of 8.2dB at 3dB gain compression at 8 GHz was obtained for device with a field plate length of  $0.5 \mu\text{m}$  without via-hole technology. In addition, at 8 GHz, a CW output power of 36.9dBm with PAE of 37% and a large signal gain of 8.4dB at 2dB gain compression at 8 GHz was obtained for  $0.6 \mu\text{m} \times 8 \times 125 \mu\text{m}$  HEMTs at 32V drainbias with a field plate length of  $0.5 \mu\text{m}$  without via-hole technology.

In order to improve the power density performance the drain-source spacing should be improved as a future work and then it would be possible to obtain larger field plate lengths without any degradation in power density values.

ACKNOWLEDGEMENT

The authors would like to acknowledge Yildirim Durmus, Ogulcan Ariyurek, Huseyin Cakmak, Pakize Demirel, Omer Cengiz, Orkun Arican, Sinan Osmanoglu, Dogan Yilmaz, Burak Turhan and Ayca Emen for valuable support.

This work is supported by the projects DPT-HAMIT, DPT-FOTON, NATO-SET-193 and TUBITAK under Project Nos., 113E331, 109A015, 109E301. One of the authors (E.O.) also acknowledges partial support from the Turkish Academy of Sciences.

REFERENCES

- [1] U. K. Mishra, P. Parikh, Y. F. Wu, "AlGaIn/GaN HEMTs-an overview of device operation and applications," *Proceedings of the IEEE*, vol. 90, pp. 1022-1031, 2002.
- [2] Y.-F. Wu, A. Saxler, M. Moore, R. P. Smith, S. Sheppard, P. M. Chavarkar, T. Wisleder, U. K. Mishra, P. Parikh, "30-W/mm GaN HEMTs by Field Plate Optimization," *IEEE Electron Device Lett.*, vol. 25, pp. 117-119, March 2004.
- [3] V. Kumar, G. Chen, S. Guo, and I. Adesida, "Field-Plated  $0.25\text{-}\mu\text{m}$  Gate-Length AlGaIn/GaN HEMTs With Varying Field-Plate Length," *IEEE Transactions on Electron Device.*, vol. 53, pp. 1477-1480, June 2006.
- [4] Y. Ando, Y. Okamoto, H. Miamoto, T. Nakayama, T. Inoue, and M. Kuzuhara, "10 W/mm AlGaIn-GaN HFETs with a field modulating plate," *IEEE Electron Device Lett.*, vol. 24, no. 5, pp. 289-291, May 2003
- [5] F. Van Raay, R. Quay, R. Kiefer, F. Benkhelifa, B. Raynor, W. Pletschen, M. Kuri, H. Massler, S. Müller, M. Dammann, M. Mikulla, M. Schlechtweg, G. Weimann, "A Coplanar X-Band AlGaIn/GaN Power Amplifier MMIC on s.i. SiC Substrate" *IEEE Microwave And Wireless Components Letters*, vol. 15, pp.460-462, July 2005
- [6] F. Van Raay, R. Quay, R. Kiefer, F. Benkhelifa, B. Raynor, W. Pletschen, M. Kuri, H. Massler, S. Müller, M. Dammann, M. Mikulla, M. Schlechtweg, G. Weimann, "A Coplanar X-Band AlGaIn/GaN Power Amplifier MMIC on s.i. SiC Substrate" *IEEE Microwave And Wireless Components Letters*, vol. 15, pp.460-462, July 2005.

# An Efficient Hybrid Voltage/Current mode Signaling Scheme for On-Chip Interconnects

M. Kavicharan, N.S. Murthy, and N. Bheema Rao

**Abstract**— Conventional voltage and current mode signaling schemes are unable to meet the speed requirements and power specifications in deep submicron technologies. The challenges posed by aggressive interconnect scaling forces VLSI circuit designers to look for alternative signaling techniques at nanometre technology nodes. Voltage mode signaling is very slow while current mode signaling suffers from serious static power dissipation problem. This paper presents a novel hybrid voltage/current mode VLSI interconnect signaling scheme which addresses the above problems. In which, both the proposed interconnect driver and receiver circuits are controlled by an efficient Schmitt trigger based control circuit which generates control signals based on input data transitions. These circuits switch from voltage mode to current mode for high data rates thus reducing the delay and dynamic power dissipation significantly. Performance comparison shows that the proposed hybrid scheme is 2 to 2.5 times faster than existing voltage mode schemes for the data rates more than 400 Mbps. It is also observed from the simulation results that the power dissipation and the power delay product (minimum energy) of the proposed scheme are much better than those of voltage and current mode schemes for data rates of >20 Mbps.

**Keywords**—Current mode, Delay, Hybrid mode, Power, Power delay product, Schmitt trigger, Voltage mode, VLSI Interconnect.

## I. INTRODUCTION

AS the technologies are scaling down, the performance of On-chip global interconnects has become a bottleneck in modern VLSI chips. The conventional signaling schemes [1]-[4] such as voltage-mode are not able to meet the speed requirements and power specifications of future technology generations. Hence, these specifications force designers to look for alternative signaling techniques for addressing interconnects scaling problems. Voltage mode with repeaters insertion scheme for driving long interconnects was a popular scheme to reduce delay, but increases significant power

This work was sponsored by the MHRD, Govt. of India as a Research Project on Modeling and Noise Reduction in VLSI Interconnect Structures in the DSM Regime.

M. Kavicharan is pursuing his Ph.D in the Dept. of ECE at the National Institute of Technology, Warangal, India. (phone: 91-9010614822; e-mail: kavicharan@nitw.ac.in).

N. S. Murthy is a senior Professor at the National Institute of Technology, Warangal, India. (e-mail: nsm@nitw.ac.in).

N. Bheema Rao is a Assoc. Professor in the Dept. of ECE at the National Institute of Technology, Warangal, India. (e-mail: nbr.rao@gmail.com).

dissipation in VLSI circuits. The delay dependence on the line length changes from quadratic to linear [1], but power dissipated by repeater circuits increases linearly with line length [5]. With aggressive interconnect down scaling, line length increases leading to more number of repeaters which further increases the power dissipation. As an alternative to voltage mode signaling with repeaters, current-mode signaling was developed and validated for SRAM circuits [6]-[8]. Later current mode scheme was improved by [9]-[13] for better performance.

The conventional current mode scheme signal propagation can be up to three times faster than voltage mode scheme [14]. The significant reduction of delay in current mode signaling is due to loading of the line with low impedance receiver which shifts the system dominant pole [15]. In general, an important advantage of current mode signaling over voltage mode signaling is that, its dynamic power dissipation component can be significantly reduced as a result of smaller voltage swings in the interconnect [3]. However, the major drawback with conventional current mode scheme is the static power consumption at low data rates. Hence, current mode scheme is generally suitable only for long buses carrying high activity data.

In ideal voltage mode signaling, driver drives an open circuited interconnect, which causes the output to follow input. In the case of current mode signaling, load is a short circuited interconnect (ideally zero) and hence there exists a continuous current path. This leads to static power dissipation, which limits its use in short interconnects or low data rates, hence voltage mode is better at lower data rates [16]. In addition, it has also been observed that [17], current mode signaling consumes even more power than voltage mode with repeaters. This is the motivation to develop a novel hybrid voltage/current mode circuit which offers the advantages of both voltage mode and current mode for low and high data rates respectively. Repeater less signaling over 10mm line using the proposed hybrid scheme is presented in this paper, which is the major difference from another hybrid scheme [18].

This paper presents an adaptive bandwidth approach using a hybrid voltage/current mode circuit which operates in current mode for high input data rates otherwise in voltage mode with much reduction in static power dissipation. The performance of the proposed hybrid scheme is compared with voltage mode

and current mode circuits in terms of 50% delay and power consumption. Another important metric for design of all electronic circuits is power delay product, which indicates the degree of energy dissipation in a circuit. Hence, power delay product as a figure of merit should have minimum value for good design. It has been found that, out of existing voltage and current mode schemes, the proposed hybrid scheme has better power delay product for input data rates of above 20 Mbps.

The rest of the paper is organised as follows. Section 2 presents a brief discussion on voltage and current mode interconnects in an attempt to clear the basic idea of various modes. In section 3, the proposed hybrid voltage/current-mode scheme is discussed along with Schmitt trigger based control circuit. Section 4 compares the performance of proposed scheme with current mode scheme and voltage mode schemes. Conclusions are drawn in section 5.

### II. VOLTAGE MODE VS CURRENT MODE

The generalised distributed RLC model of voltage/current mode interconnect is shown in Fig.1. The unit length Resistance, Capacitance and Inductance are represented as  $R$ ,  $C$  and  $L$  respectively, and  $dl$  is denoted as length of each lumped section. The driver is modelled as an inverter with an output capacitance of  $C_s$  and receiver is approximated as a parallel combination of  $R_L$  and  $C_L$  respectively. Input signal  $V_{in}$  employs random input data of Non-return-to-zero (NRZ) format.

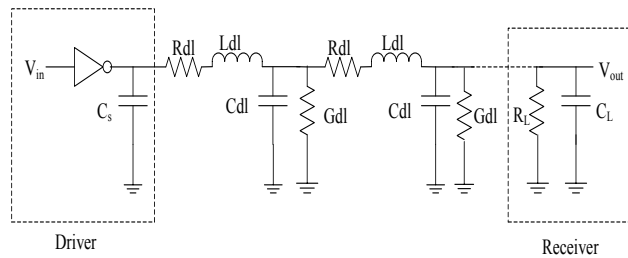


Fig. 1 Generalised distributed RLC model of voltage/current mode interconnect.

According to signaling point of view, both voltage and current-mode driver circuits are similar and drive distributed model of RLC interconnect. On the other hand, current mode receiver offers low impedance load while voltage mode receiver provides a high impedance capacitive termination [15]. Fig.1 shows that, for a voltage mode receiver of load capacitance  $C_L$ , addition of a parallel low impedance resistance  $R_L$  will change its operation to current mode.

### III. HYBRID VOLTAGE/CURRENT MODE SCHEME

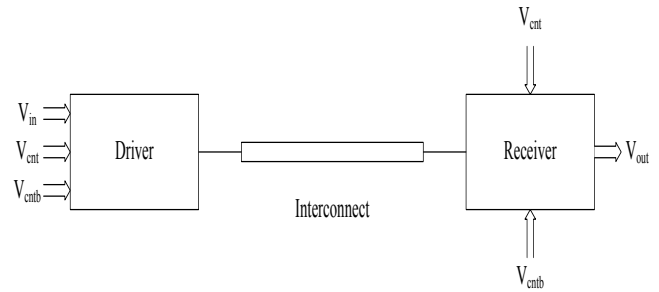


Fig. 2 Block diagram of proposed hybrid voltage/current-mode Scheme

The block diagram of the proposed hybrid voltage/current-mode scheme for global interconnects is shown in Fig.2. It consists of driver and receiver circuits with input and control signals. The necessary control signals are generated by Schmitt trigger based control circuit. The same control signals should be given to both the driver and receiver circuits with proper timing synchronization. The driver and receiver circuits operate in two modes (voltage-mode and current-mode) based on control signals ( $V_{cnt}$ ,  $V_{cntb}$ ). If the control signals are  $V_{cnt}=1$  and  $V_{cntb}=0$  the circuit operates in current-mode for high data rates otherwise in voltage-mode for low data rates.

#### A. Control signal generation circuit

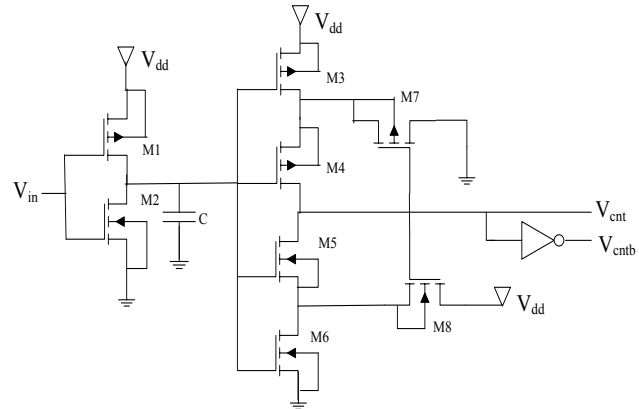


Fig. 3 control signal generation circuit

Fig.3 shows schematic of control signal generation circuit, which generates control signals ( $V_{cnt}$  and  $V_{cntb}$ ) based on input data transitions. The circuit consists of an inverter based charge pump and a Schmitt trigger [19]. The conventional Schmitt Trigger complete design is presented by Filanovsky and Baltes [20]. The circuit is designed such that for higher input data rates the control signal  $V_{cnt}$  is high and for slowly varying signals control signal  $V_{cnt}$  is low, depending on the duration of the input pulse width.

If the voltage across capacitor is zero, transistors  $M5$  and  $M6$  are OFF and  $M3$  and  $M7$  are in linear mode of operation hence, the control voltage  $V_{cnt} = V_{dd}$ . When the capacitor voltage rises above  $V_m$ ,  $M6$  becomes ON and  $M8$  source node voltage starts decreasing, it causes  $M5$  to be ON and control

voltage starts decreasing. For fast data activity, the capacitor does not have enough time to charge/discharge hence, the capacitor voltage remains below threshold voltage  $V_{th}$ , leading to  $V_{cnt} = V_{dd}$ . Similarly for slow variation of input data activity, the capacitor voltage and feedback transistors ensure  $V_{cnt}$  to be below  $V_{th}$ . Thus, for small variation in input data activity the control voltage  $V_{cnt}$  signal is low otherwise high.

Control voltage must be high before the high frequency input signals are applied such that current mode operation (low impedance load) can be invoked at the driver and receiver circuits without delay. In the absence of input data transitions or low data rate signals control voltage  $V_{cnt}$  can be automatically discharged to low such that power dissipation is minimized in voltage mode operation. The charging time of control signal defines the setup time which ensures the input data signal transitions must be stable before the stable state of control voltage.

**B. Hybrid voltage/current-Mode Driver Circuit**

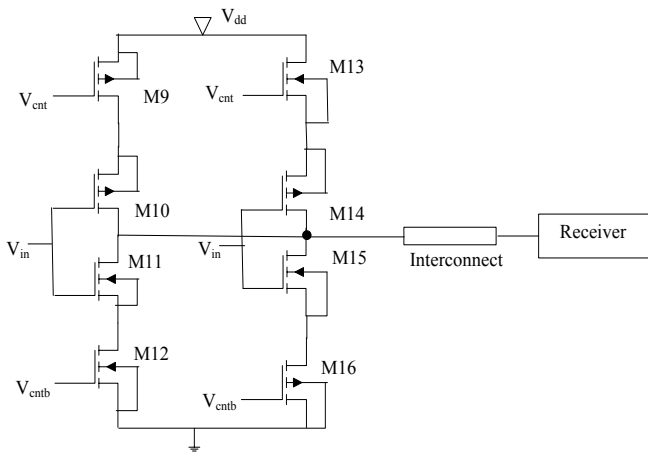


Fig. 4 Hybrid voltage/current-mode Driver circuit

Fig. 4 shows the schematic of hybrid voltage/current mode driver circuit. Transmitter section has two drivers: voltage mode driver and current mode driver. Left half of the hybrid voltage/current mode driver circuit consists of M9 PMOS switch, an inverter and M12 NMOS switch connected in series. When  $V_{cnt}$  is low M9 is ON and the inverter (M10-M11) operates in voltage-mode, forcing the line to operate in full-swing voltage mode due to the high input impedance of the inverter.

For higher data rates when  $V_{cnt}$  is high, activates the right half of the driver circuit and operates in current-mode with low swing (Fig. 7). This causes the dynamic power dissipation of current mode operation to be lower than voltage mode full swing operation. When  $V_{cnt}$  is high, M13 NMOS gives weak high and M16 PMOS gives weak low. Hence, the voltage swing on the wire can be reduced. Depending on the control signals, input data can be transmitted either through left half voltage mode driver or right half current mode driver.

**C. Hybrid voltage/current-Mode Receiver Circuit**

The hybrid voltage/current-Mode receiver circuit is shown in Fig. 5, consists of a voltage mode receiver, diode connected M22 and M23 transistors followed by a low gain amplifier (an inverter with gain  $A \sim 25$ ). The receiver operates in voltage mode and current mode depending on  $V_{cnt}=0$  and 1 respectively. In voltage mode the receiver operates in full swing mode whereas in current mode the receiver input voltage swings around the switching threshold of the diode connected inverter. The inverter acts as a low gain amplifier and will generate full swing voltage levels at the output.

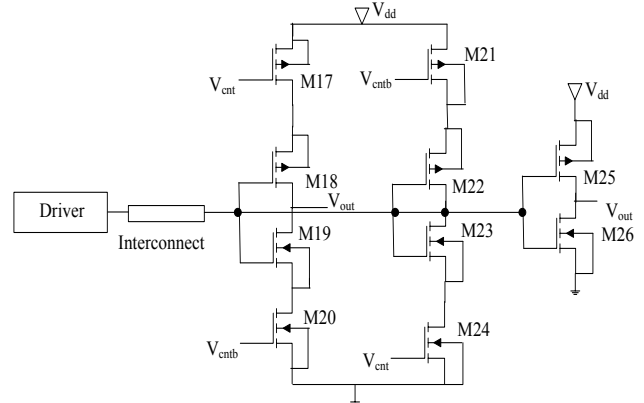


Fig. 5 Hybrid voltage/current-Mode Receiver circuit

The diode connected inverter and inverter as an amplifier are designed such that switching threshold is constant. In current mode the driver voltage swings around switching threshold of diode connected inverter, which is shown in Fig. 7. The output data  $V_{out}$  follows the input data  $V_{in}$  with a delay of 0.5 ns for current mode operation of hybrid scheme, whereas in voltage mode the obtained delay is 1.31 ns.

**IV. SIMULATION RESULTS**

The operation of the proposed hybrid voltage/current mode scheme was simulated in 180nm CMOS technology for  $V_{dd}$  of 1.8V. The presented schemes were designed for the line length of 10mm with typical line dimensions using predictive technology model (PTM) [21] of 180nm technology. The per unit length interconnect parameters were extracted using the field solver TCAD Raphael and are presented as follows:  $R=42.5\Omega/cm$ ,  $L=2.311\text{ nH/cm}$ ,  $C=17.43\text{ pF/cm}$ ,  $G=0.443S/cm$  and  $R_s=0.00135\ \Omega/cm$ . The simulation results of voltage mode, current mode [23] and proposed hybrid voltage/current mode are obtained using HSPICE W-element method. As per 1999.4 release of HSPICE, at high frequency operation the imaginary term of the skin effect has been added for accurate frequency response.

The frequency dependent resistance including skin effect is given by

$$R(f) = R + R_s(1 + j)\sqrt{f}$$

where  $R$  is the DC resistance and  $R_s$  is the skin effect resistance.

Table1. Performance comparison @20 Mbps (wire length=10 mm) of various schemes

Scheme	Delay (ns)	Power ( $\mu$ W)	Power Delay product(ns- $\mu$ W)
Voltage-Mode	1.283	7.13	9.14
Voltage-Mode with Repeaters [22]	1.069	16.45	17.58
Current-Mode [23]	0.296	140.35	41.54
Proposed hybrid scheme	1.317	7.259	9.56

Table1 shows the performance comparison between the various schemes for 10 mm line at low data rate of 20 Mbps. In this case hybrid voltage/current mode scheme switches to voltage mode scheme at low data rates and hence the advantage of zero static power is utilised. As compared to other schemes the delay and power dissipation of proposed scheme are approaching voltage mode scheme. The power delay product of the proposed hybrid voltage/current scheme is much less than the voltage mode scheme with repeaters [22], current mode scheme [23] and almost equal to simple voltage mode scheme.

Table2. Performance comparison @400 Mbps (wire length=10 mm) of various schemes

Scheme	Delay (ns)	Power ( $\mu$ W)	Power Delay product(ns- $\mu$ W)
Voltage mode	1.283	144.4	185.26
Voltage mode with repeaters[22]	1.069	181.2	193.7
Current mode[23]	0.296	190.2	56.29
Proposed hybrid scheme	0.502	80.29	40.3

Table2 shows the performance comparison between the various schemes for 10mm line at high input data rate of 400 Mbps. In this case hybrid voltage/current mode scheme switches to current mode and hence the advantage of high speed operation is utilized at high data rate. Increasing the data rate to 400 Mbps yields better improvements in relative performance for the proposed scheme approximately 2.5 times decrease in delay over the voltage mode scheme [1] and approximately half of the power is saved when compared with the above schemes. Furthermore, the power delay product as a figure of merit is much better when compared with other schemes.

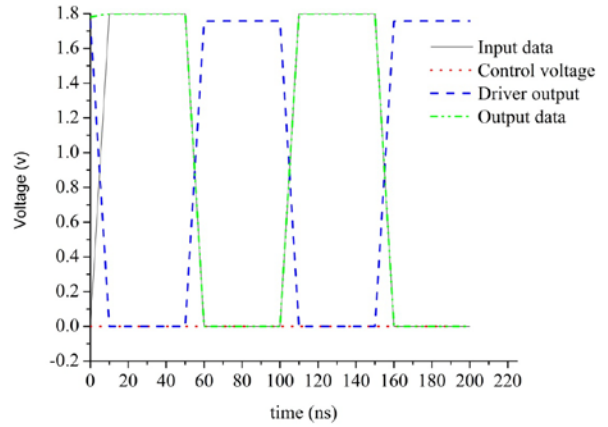


Fig. 6 Simulated waveforms of input signal, control signal, Receiver input signal and Output signal of voltage mode interconnect operation when control voltage=0.

Fig. 6 shows an input data stream ( $V_{in}$ ), control voltage ( $V_{cnt}$ ), voltage mode driver output and the output data of proposed scheme. As stated earlier, for slow input data activities the control voltage  $V_{cnt}$  is set as low and operates in voltage mode. The proposed scheme operates in voltage mode and the driver output is having large swing which is in contrast with the current mode driver output small swing, as shown in Fig. 7.

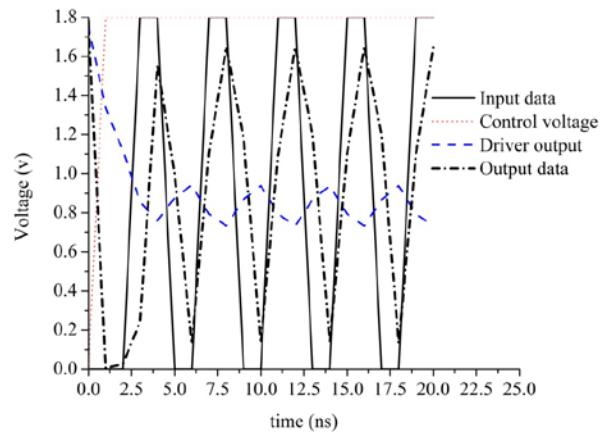


Fig. 7 Simulated waveforms of input signal, Control voltage, Driver output and Output signal of current mode interconnect operation when control voltage=1.

Fig. 7 shows an input data stream ( $V_{in}$ ), control voltage ( $V_{cnt}$ ), current mode driver output and the output data of proposed scheme. For high data rates of input, the output of control signal  $V_{cnt}$  is set as high and operates in current mode. From the Fig. 7 it is clear that, the driver output voltage of current mode scheme has low swing of 0.2 V when compared with voltage mode driver output full swing of 1.8 V results in lower delay.

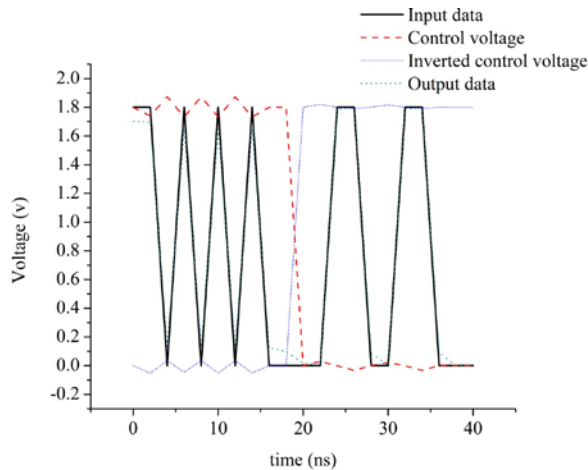


Fig. 8 Simulated waveforms of input data, control voltage, its inversion and output data of hybrid voltage/current mode circuit.

Fig.8 shows an arbitrary input data stream ( $V_{in}$ ), control voltage ( $V_{cnt}$ ), inverted control voltage ( $V_{cntb}$ ) and the resultant output data of proposed scheme. These control signals  $V_{cnt}$  and  $V_{cntb}$  are generated using Schmitt trigger based control circuit (Fig. 3). It is apparent that for low data rates (20 Mbps) the generated control signal is low and for higher data rates (500 Mbps) the inverted control signal is low, thus ensuring the voltage and current mode operations respectively. The obtained output of proposed hybrid circuit follows the input with negligible attenuation.

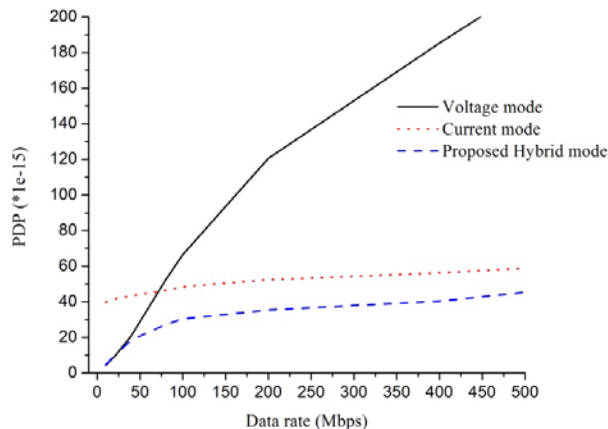


Fig. 9 Comparison between the voltage mode, current mode and proposed hybrid voltage/current mode interconnect schemes for Power delay product vs Data rate.

Fig.9 shows the power delay product of various schemes for multiple input data rates. It is noticed that the proposed scheme is much better for high data rate applications (>20 Mbps). Power delay product of proposed hybrid voltage/current mode outperforms the existing voltage and current mode schemes. At higher data rates, the power delay product of full-swing voltage mode and low swing current mode signaling are likely to become more dominant as seen from Fig. 9. The minimum power delay product is achieved for

the proposed hybrid voltage/current mode scheme as compared to others, which is the prime requirement in high performance VLSI systems.

## V. CONCLUSIONS

The proposed hybrid voltage/current-mode scheme combines the benefits of voltage-mode and current-mode techniques. The circuit switches to voltage mode or current mode based on the control signal which is input data dependent. At lower data rates the circuit operates in voltage-mode scheme whereas it switches to current-mode scheme for higher data rates, thus it includes the advantages of both voltage mode (zero static power consumption) and current mode (for high speed operation). At data rate of 400 Mbps, the proposed scheme has approximately 2.5 times decrease in delay over the voltage mode scheme and approximately half of the power is saved when compared with the presented schemes. For the data rates of >20 Mbps, the proposed hybrid voltage/current mode circuit power delay product is better than the existing schemes. The proposed scheme also provides an alternative solution for the placement-constrained repeater inserted wires.

## REFERENCES

- [1] H. B. Bakoglu, *Circuits, Interconnections, and Packaging for VLSI*, Addison-Wesley Company, Reading, MA 1990.
- [2] Y.I. Ismail, E.G. Friedman, "Optimum repeater insertion based on a CMOS delay model for on-chip RLC interconnect," in *1998 Proc. IEEE ASIC*, pp. 369-373.
- [3] Adler and E. G. Friedman, "Repeater design to reduce delay and power in resistive interconnect," *IEEE Trans. Circuits Syst. I*, vol. 45, pp. 607-616, May 1998.
- [4] K. Banerjee, A. Mehrotra, "A power-optimal repeater insertion methodology for global interconnects in nanometer designs," *IEEE Trans. Electron. Devices*, 49 (11) 2002.
- [5] Atul Maheshwari and Wayne Burleson, "Current sensing techniques for global interconnects in very deep submicron (VDSM) CMOS," *IEEE Computer Society Workshop on VLSI*, 2001.
- [6] E. Seevinck, P. van Beers, and H. Ontrop, "Current-mode techniques for high-speed VLSI circuits with application to current sense amplifier for CMOS SRAM's," *IEEE J. Solid-State Circuits*, vol. 26, pp. 525-536, Apr. 1991.
- [7] M. Izumikawa and M. Yamashina, "A current direction sense technique for multiport SRAM's," *IEEE J. Solid-State Circuits*, vol. 31, pp.546-551, Apr. 1996.
- [8] T. Blalock and R. Jaeger, "A high-speed sensing scheme for 1T dynamic RAM's utilizing the clamped bit-line sense amplifier," *IEEE J. Solid-State Circuits*, vol. 27, pp. 618-625, Apr. 1992.
- [9] A. Katoch, H. Veendrick, and E. Seevinck, "High speed current-mode signaling circuits for on-chip interconnects," in *IEEE International Symposium on Circuits and Systems, (ISCAS)*, May 2005, Kobe Japan, vol. 4, pp. 4138-4141.
- [10] A. Maheshwari and W. Burleson, "Differential current-sensing for on-chip interconnects," *IEEE Transactions on Very Large Scale Integration Systems*, vol. 12, no. 12, pp. 1321-1329, Dec 2004.
- [11] R. Bashirullah, L. Wentai, and R. K. Cavin, "Current-mode signaling in deep submicrometer global interconnects," *IEEE Transactions on Very Large Scale Integration (VLSI) Systems*, vol. 11, no. 3 , pp. 406-417, June 2003.
- [12] Tuuna S, Nigussie E, Isoaho J, Tenhunen, H., "Modeling of Energy Dissipation in RLC Current-Mode Signaling," *IEEE Transactions on Very Large Scale Integration (VLSI) Systems*, vol.20, no.6, pp.1146,1151, June 2012.

- [13] Dave M, Jain M, Shojaei Baghini M, Sharma D, "A Variation Tolerant Current-Mode Signaling Scheme for On-Chip Interconnects," *IEEE Transactions on Very Large Scale Integration (VLSI) Systems*, vol.21, no.2, pp.342,353, Feb. 2013.
- [14] Katoch A, Seevinck E, Veendrick H, "Fast signal propagation for point to point on-chip long interconnects using current sensing," *Proceedings of the 28th European Solid-State Circuits Conference, 2002. ESSCIRC 2002*, pp.195,198, 24-26 Sept. 2002.
- [15] Bashirullah R, Wentai Liu, Cavin R, "Accurate delay model and experimental verification for current/voltage mode on-chip interconnects," *International Symposium on Circuits and Systems, 2003. ISCAS '03*, vol.5, pp.169-172, 25-28 May 2003.
- [16] Dave M, Baghini M.S, Sharma D, "Low power current mode receiver with inductive input impedance," *International Symposium on Low Power Electronics and Design (ISLPED)*, pp.225-228,11-13 Aug. 2008.
- [17] V. Venkatraman and W. Burleson, "Robust multi-level current-mode on-chip interconnect signaling in the presence of process variations", *Proceedings of Sixth International Symposium on Quality Electronic Design*, pp. 522–527, March 2005.
- [18] R. Bashirullah, W. Liu, R. Cavin III, and D. Edwards, "A hybrid current/voltage mode signaling scheme with adaptive bandwidth capability," *IEEE Trans. Very Large Scale Integr. (VLSI) Syst.*, vol. 12, no.8, pp. 876–880, Aug. 2004.
- [19] Jan M. Rabaey, Anantha Chandrakasan, and Borivoje Nikolic *Digital integrated circuits-A design perspective*. Prentice Hall, 2ed edition, 2004.
- [20] Filanovsky I.M, Baltes H, "CMOS Schmitt trigger design", *IEEE Transactions on Circuits and Systems I: Fundamental Theory and Applications*, vol. 41, no.1, pp.46-49, Jan 1994.
- [21] "Berkely Predictive Technology Model", Available: <http://www-device.eecs.berkeley.edu/ptm>.
- [22] R. Chandel, S. Sarkar, R.P. Agarwal, "Delay analysis of a single voltage-scaled-repeater driven long interconnect," *Microelectronics International Journal* 22 (3) (2005) 28–33.
- [23] M. M. Tabrizi, N. Masoumi, and M. M. Deilami, "High speed current-mode signaling for interconnects considering transmission line and crosstalk effects," in *Proc. MWCAS*, 2007, pp.17-20.

# Effect of High Temperature On The Transconductance Of AlGa<sub>N</sub>/AlN/GaN High Electron Mobility Transistors (HEMT)

Rajab Yahyazadeh, Zahra Hashempour, Gasem Abdollahi, Belal Baghdarghi  
[yahyazadehs@gmail.com](mailto:yahyazadehs@gmail.com)

*Department of Physics, Islamic Azad University of Khoy Branch, Khoy, Iran 58135/175*

**Abstract**-An analytical-numerical model for the electronic current of two dimensional quantum well AlGa<sub>N</sub>/AlN/GaN in high electron mobility transistors has been developed in this paper that is capable of accurately predicting the effect of temperature on the electronic current of two dimensional quantum well and transconductance. Salient features of the model are incorporated of fully and partially occupied sub-bands in the interface quantum well. In addition temperature dependent of band gap, quantum well electron density, threshold voltage, mobility of electron, dielectric constant, polarization induce charge density in the device are also taken into account. The calculated model results are in very good agreement with existing experimental data for high electron mobility transistors device.

## 1- Introduction

Over the past few years, AlGa<sub>N</sub>/AlN/GaN high electron mobility transistors have emerged strongly as attractive candidates for high-power, high temperature, high speed applications at frequencies well into the microwave region. The presence of strong spontaneous and strain-induced polarization fields due to lattice mismatch between AlGa<sub>N</sub>/AlN/GaN is the important characteristic of the AlGa<sub>N</sub>/AlN/GaN material system. These polarization fields have been attributed to the reduced symmetry of the wurtzite crystal structure and the polar bonding nature of GaN and its alloy [1]. The AlGa<sub>N</sub>/AlN/GaN material system is unique in that extremely high two-dimensional electron gas concentrations ( $>10^{13}\text{cm}^{-2}$ ) are readily generated without modulation doping. The high breakdown fields ( $3\times 10^6\text{ V/cm}$ ) resulting from the wide band gaps of GaN and AlGa<sub>N</sub> enable the use

of much higher drain biases than can typically be used in the AlGaAs/GaAs system [2, 3, and 4]. Together with these high field properties, the high saturated electron drift velocity ( $\sim 10^7\text{cm/s}$ ) in GaN can be exploited for superior high frequency performance. More recently, high performance GaN-based transistors such as electron mobility transistors have been fabricated and reported by several groups [5, 6]. The effect of temperature on the electronic current of two dimensional quantum well was

previously observed and was related to electron threshold voltage without including optical phonon scattering [7, 8]. In the present work, a new model for electronic current of two dimensional quantum well is presented. This is achieved by (i) using a self-consistent solution to the Schrödinger and Poisson equations in order to obtain the Fermi level ( $E_{\text{F}}$ ) specified relative to the bottom of triangular well, and band bending of GaN ( $E_{\text{B}}$ ), (ii) take into account the temperature dependent quantum well width, (iii) take into account analytical relation for electronic current and charge density in two dimensional quantum well, (iv) using a more accurate model for mobility, (v) using the electron traps effects in the surface, interface and buffer layers, and (vi) incorporating a simple, realistic model for the ungated area in the AlGa<sub>N</sub>/Ga<sub>N</sub> electron mobility transistors device.

## 2- Model description

In order to obtain accurate values for the Fermi energy, the energies of quantized levels within the two dimensional electron gas (2DEG), the occupancy of the various sub-bands, the intrasub-band and intersub-band coupling coefficients ( $H_{mn}$ ) for the two dimensional electron gas in AlGa<sub>N</sub>/AlN/GaN heterostructures; both the Schrödinger and Poisson equations must be solved self-consistently. This has been achieved by solving Schrödinger's equation and simultaneously taking into account the electrostatic potential obtained from Poisson's equation, as well as the image and exchange-correlation potentials using Numerov's numerical method.

In the self-consistent calculation, the nonlinear formalism of the polarization-induced field as a function of Al mole fraction in Al<sub>m</sub>Ga<sub>1-m</sub>N/AlN/GaN heterostructures has been assumed, as well as taking into account all fully and partially-occupied sub-bands within the interface two dimensional electron gas potential well [9, 10]. Using such an approach, it is possible to calculate the two dimensional electron mobility taking into account the combined contributions from each of the individual electron scattering

mechanisms. At high temperature ( $T \geq 300\text{K}$ ), inelastic polar optical phonon scattering dominates over all other scattering mechanisms. In the linearized Boltzmann equation, the different scattering rates can be separated in to two type: (i) elastic scattering due to acoustic and piezoelectric phonons, ionized impurities and interface roughness, etc, and (ii) inelastic scattering due to polar optical phonons in order to take in to consideration all scattering mechanism in the mobility calculation, it is solve numerically using an iterative technique [11].

The field effect transistors model used in calculations is shown schematically in Figure1, where the x –direction is along the two dimensional electron gas channel, the z –direction is along the growth direction, and the region I and III represent the ungated channel portions of the field effect transis

tors, and region II represents the gated area of the device.

To calculate the total drain current, the both 2DEG channel and AlGaN barrier currents have been calculated.

The expression of device current can be obtained as [12, 13]

$$I_{ds} = I_{2DEG} + I_{AlGaN}$$

$$= \frac{-\alpha_2 + \sqrt{\alpha_2^2 - 4\alpha_1\alpha_3}}{2\alpha_1} + \frac{Z\mu_N q^2 N_D^2}{\epsilon_{AlGaN}} \left[ \frac{d_{AlGaN}}{2} (d_2^2 - d_1^2) - \frac{1}{3} (d_2^3 - d_1^3) \right] \quad (1)$$

for  $d_1, d_2 < d_{AlGaN}$

$$I_{ds} = \frac{-\alpha_2 + \sqrt{\alpha_2^2 - 4\alpha_1\alpha_2}}{2\alpha_1}$$

for  $d_1, d_2 > d_{AlGaN}$

With

$$\alpha_1 = \left( \frac{q^2 D Z \mu(x, T) C_t}{\epsilon_{AlGaN}(m) + 2q^2 D} \right) (R_d^2 + 2R_s R_d) - \left( \frac{2R_s + R_d}{E_1} \right)$$

$$\alpha_2 = L_g + \frac{V_{ds}}{E_1} + 2q^2 D Z \mu(x, T) C_t (2R_s + R_d) \times \frac{\left( V_{gs} + V_{vg} - V_{th}(m, T) - \frac{KT}{q} - V_{ds}(R_s + R_d) \right)}{\epsilon_{AlGaN}(m) + 2q^2 D}$$

$$\alpha_3 = \frac{2q^2 D Z \mu(x, T) C_t \left( \frac{V_{ds}^2}{2} - V_{ds} \left( V_{gs} + V_{vg} - V_{th}(m) - \frac{KT}{q} \right) \right)}{\epsilon_{AlGaN}(m, T) + 2q^2 D}$$

$$E_1 = \frac{E_c V_{sat}}{\mu_0 E_c - V_{sat}}$$

$$C_t(m, T) = \left( \frac{\epsilon_{AlGaN}(m, T)}{d_{AlGaN} + \Delta d + d_i} \right) + \frac{C_B \times C_S}{C_B + C_S}$$

Where  $E_c$ ,  $V_{sat}$ ,  $\epsilon_{AlGaN}(m)$ ,  $d_{AlGaN}$  and  $D = 4\pi m^* / h^2$ , are the critical field, saturation velocity, dielectric constant, barrier thickness and conduction band density of state respectively.  $R_s$ , and  $R_D$  are the source and drain resistance respectively,  $Z$  is the channel width,  $L_G$  is the channel length,  $\mu_N = \mu_{AlGaN}$  is the 3D electron mobility as function of temperature,  $\mu_0$  is low field mobility,  $V_{ds}$  is applied drain to source voltage,  $V_{VG}$  is the virtual gate which formed between gate-drain and near the gate because of the reduction in the amount of net positive charge on surface.  $C_t$  is total capacitance. The capacitance,  $C_t$ , is equivalent capacitance for the capacitances of AlGaN barrier ( $C_{AlGaN}$ ), spacer layer ( $C_i = \epsilon_{AlGaN}(m) / d_i$ ) [12], band bending in GaN ( $C_{GaN}$ ) [13], interface traps ( $C_S$ ) [14] and two dimensional electron gas ( $C_{2DEG} = \epsilon_{AlGaN} / \Delta d$ ).  $d_1$  and  $d_2$  are the depletion layer thickness in two gate ends (region II) and are given by: [13,14]

$$d_1 = \alpha + (\alpha^2 + \beta_1^2)^{1/2}$$

$$d_2 = \alpha + (\alpha^2 + \beta_2^2)^{1/2}$$

where

$$\alpha = \left( \frac{2\varepsilon_{AlGaN}}{qN_D} \right) [qN_S + \varepsilon_{GaN}E_B - \sigma(m) + qN_D d_i / \varepsilon_{GaN}]$$

$$\beta_1 = \left( \frac{2\varepsilon_{AlGaN}}{qN_D} \right) [V_{BI} - V_{GS} - V_{VG} - E_{Fi}/q - \Delta E_C/q + I_{AlGaN}R_S] - d_i^2 \quad (2)$$

$$\beta_2 = \left( \frac{2\varepsilon_{AlGaN}}{qN_D} \right) [V_{BI} - V_{GS} - V_{VG} - E_{Fi}/q - \Delta E_C/q + V_{DS} - I_{AlGaN}(R_D + R_S)] - d_i^2,$$

where  $d_i$  is the spacer layer thickness in AlGaN barrier,  $V_{BI}$  is the Schottky barrier at metal/AlGaN in interface,  $\Delta E_C$  is the conduction band discontinuity between AlGaN and GaN,  $N_D$  is the donor density in AlGaN, where  $R_S$  and  $R_D$  are the source and drain contact resistance respectively,  $V_{VG}$  is the virtual gate which formed between gate-drain and near the gate because of the reduction in the amount of net positive charge on surface,  $E_C(T)$  is the electric field in the saturation regime,  $k_B$  is Boltzmann constant.  $N_S$  is the total sheet carrier concentration within the well so that can be obtained as:[15]

$$N_S(T, m) = \frac{\varepsilon_{AlGaN}(T, m)}{(d_{AlGaN} + d_i + \Delta d(T, m))} \times (V_{GS} - V_T(T, m) + E_F(T, m)) \quad (3)$$

The threshold voltage ( $V_T$ ) is given by the following relation [16,17]:

$$V_T(T, m) = V_{BI} - \Delta E_C(T, m) - \frac{\sigma_{pz}(T, m)d_{AlGaN}}{\varepsilon_{AlGaN}(T, m)} - \frac{qN_d d_{AlGaN}^2}{2\varepsilon_{AlGaN}(T, m)} \quad (4)$$

$$\Delta E_C(T, m) = 0.75(E_g^{AlGaN}(T, m) - E_g^{GaN}(T, m)) \quad (5)$$

Where  $\sigma(m)/q$  is the polarization induced charge density at heterostructure interface,  $N_D$  is the donor density in AlGaN [18]. This discontinuity ( $\Delta E_C$ ) dependent on the band gaps of GaN ( $E_g^{GaN}(T, m)$ ) and AlGaN ( $E_g^{AlGaN}(T, m)$ ). In this model, taking into account temperature dependent of band gaps analytical relations [19]. Where  $E_F(T, m)$ ,  $q$ ,  $m$ ,  $V_{GS}$ , the Fermi level (specified relative to the bottom of triangular well), electron charge, Al mole fraction in AlGaN barrier and the applied gate to source voltage respectively [7,20] also  $d_{AlGaN} = d_2$  is the depletion layer thickness in the gate

edge near the drain side and  $\Delta d$  is the effective thickness of 2DEG. In the analytical calculation, it has been assumed that the mobility and the saturation velocity have been dependent on Al mole fraction.[6,20]

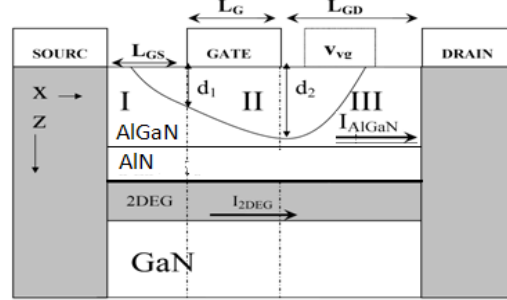


Fig. 1. Schematic HEMT structure used for model calculation

Where  $\mu(T)$  is the total mobility of 2DEG channel, so that in this model total mobility can be obtained as [21]:

$$\mu_{total} = \begin{cases} \frac{\mu_{2DEG}N_S + \mu_{AlGaN}N_{AlGaN}}{N_S + N_{AlGaN}} & \text{for } d_2(\text{barrier thickness}) \\ \mu_{2DEG} & \text{for } d_2 \geq \text{barrier thickness} \end{cases} \quad (6)$$

So that  $N_{AlGaN}$  is the density of electron real space transfer from the 2D (2DEG channel) to 3D state (in AlGaN barrier). It should be mentioned that even at room temperature, the mobility of 3D-electron gas is around 50% smaller the mobility of 2D-electrons [21].

In order to obtain accurate values for mobility of 2DEG channel, the occupancy of the various sub-bands, the intrasub-band and intersub-band coupling coefficients ( $H_{mn}$ ), and the sheet carrier concentration for the 2DEG in AlGaN/AlN/GaN heterostructures; both the Schrödinger and Poisson equations must be solved self-consistently. This has been achieved by solving Schrödinger's equation and simultaneously taking into account the electrostatic potential obtained from Poisson's equation, as well as the image and exchange-correlation potentials using Numerov's numerical method. In the self-consistent calculation, the nonlinear formulism of the polarization-induced field as a function of Al mole fraction in  $Al_mGa_{1-m}N/AlN/GaN$  heterostructures has been assumed, as well as taking into account all fully and partially-occupied sub-bands within the interface 2DEG potential well [23]. Using such an approach, it is possible to calculate the 2D-electron mobility taking into account the combined contributions from each of the individual electron scattering mechanisms.

The small signal parameter such as the transconductance,  $g_m$ , can be define by differentiating of  $I_{DS}$  with respect to  $V_{gs}$  keeping respectively  $V_{ds}$  constant.[24,25]

$$g_m = \left. \frac{\partial(I_{2DEG} + I_{AlGaN})}{\partial V_{GS}} \right|_{V_{DS} = \text{const}} \quad (7)$$

$$= g_{m(2DEG)} + g_{m(AlGaN)}$$

In this model, the channel temperature varies at each operating point depending on the device power [18, 26]:

$$T_{ch} = T_0 + I_{DS} V_{DS} R_{th} \quad (8)$$

Where  $R_{th}$  is the thermal resistance which is dependent on temperature .The thermal resistance for AlGa<sub>N</sub>/AlN/GaN HEMTs has been calculated using a Mont Carlo simulation, so that the thermal resistance increases approximately linearly with increasing 2DEG channel temperature, Such as increase in  $T_{ch}$  will also reduce the 2DEG mobility leading to a lower  $I_{DS}$  for a given  $V_{DS}$  and  $V_{GS}$ , the self-heating effect is clearly most severe at high  $V_{DS}$  and  $V_{GS}$  [20].

The capacitance, C, is equivalent capacitance for the capacitances of AlGa<sub>N</sub> barrier ( $C_{AlGaN}$ ) [21], band bending in Ga<sub>N</sub> ( $C_{GaN}$ ) [22], interface traps ( $C_S$ ) [23], spacer layer [24,] and two dimensional electron gas ( $C_{2DEG} = \epsilon_{AlGaN}(m,T)/(\Delta d_{2DEG}(z,T))$ ) m is the Al mole fraction of Al<sub>m</sub>Ga<sub>1-m</sub>N/GaN and  $\epsilon_{AlGaN}(m,T)$  is the dielectric constant so that given by analytical relation [27]. In the model effective width of 2DEG ( $\Delta d_{2DEG}(z,T)$ ) at each point in the channel in the x direction depends on the density of electron at that point and temperature. This has been achieved by solving Schrödinger's and Poisson's equations.

For the energy levels corresponding to the two dimensional electron gas, we assumed the presence of five sub-bands within the interface single-well.

To calculate the exact electrical properties in high electron mobility transistors, one need to include the electron traps effects such as interface and surface traps, and Ga<sub>N</sub> barrier trap in calculation. As a result of lattice mismatch between AlGa<sub>N</sub> and Ga<sub>N</sub>, and possibly compositional non-uniformity caused by alloy clustering, there could be considerable amount of trap states at the AlGa<sub>N</sub>/Ga<sub>N</sub> interface. The

electrical behavior of the interface trap states can be modeled as a capacitive ( $C_S$ ) and a conductive ( $G_S$ ), where  $G_S$  is negligible at the model biases.

It should be mentioned that the solution obtained holds for  $V_{DS}$  in the range  $2\phi_{F0} \leq V_0$ ,  $V_{DS} = V_0$  the channel concentration  $N_S$  is zero at the drain side and drain current is pinch off.

### 3- Results and discussion

To assess the validity of this combined analytical–numerical model for the effect of temperature on the electronic current of two dimensional quantum well, a comparative study has been undertaken comparing theoretically obtained  $I-V$ ,  $N_S$ ,  $\mu$  and  $V_T$  curves with experimental results from Refs. 16,18, 19and27 for AlGa<sub>N</sub>/AlN/GaN based HEMT. The material and device details are presented in Table 1 and all other material parameters have been taken from Refs. 13,22,23 and 28. The results presented in Fig.2 shows the mobility at sheet carrier concentrations as a function of temperature. As shown in Fig. 2, the mobility decrease monotonically with increasing temperature for ranging 200 to 500K; this behavior suggests that phonon scattering is the dominant scattering mechanism at high temperature, in agreement with number of previous studies [21, 22] .The reduce dependence of mobility on temperature for lower carrier concentration suggests that scattering by dislocations and defect is more significant for lower carrier concentration. Fig.3 shows the sheet carrier concentrations and threshold voltage of two dimensional electron gases as a function of temperature. As shown in Fig. 3, the absolute of threshold voltage  $|V_T|$  (voltage that to require for formation of two dimensional quantum well in interface AlGa<sub>N</sub>/AlN/GaN) decrease with the increase of temperature as a results decrease of depth and Fermi level in quantum well. With decreasing in depth of quantum well, decrease the discontinuity in band gaps and occupancy of the various sub-bands (sheet carrier concentrations). The result shows that change in threshold voltage  $|-0.2|$  and sheet carrier concentrations  $0.3 \times 10^{12} \text{ cm}^{-2}$  of device with increase in temperature from 200K to 600K.

As a result , to calculate an exact current –voltage (I-V) curve to see temperature effects in AlGa<sub>N</sub>/AlN/GaN based HEMTs for applied gate bias and high drain voltage, one needs to include the temperature effects of band gaps , quantum well electron density , threshold voltage, mobility of electron , dielectric constant , polarization induce charge density in the device thus Fig.4 shows the variation of drain current versus drain-source voltage with including theses effects in comparison with existence experimental data in

literature. As evident from this figure there is a good agreement between the model calculations and experimental data.

Another possible reason for the mismatch between present model and experimental results is the increase in device leakage current at elevated temperatures. Fig. 5 shows the of drain source current versus Gate-source voltage in comparison with existence experimental data of the AlGaIn/GaN HEMT device at three different temperatures. At high temperature (500 K), leakage current superimposes on the drain current, which has not yet been incorporated in this model. Fig. 6, show the DC transconductance as a function of the gate to-source biasing at different temperatures for 0.3 and 0.5 Al doping density respectively. This proposed model quite accurately predicts the overall trend of the transconductance. There are small mismatches between the experimental and the model results which increase with the rise of temperature due to the increased leakage current as shown in Fig. 5 and bulk resistances.

#### 4- Conclusions

An accurate analytical-numerical model for the effect of temperature on the electronic current of two dimensional quantum well has been developed the AlGaIn/GaN high electron mobility transistors. This model is able to accurately predict the drain-source electronic current of two dimensional quantum well and transconductance in high drain voltage. The model incorporates by including temperature effects on the quantum well electron density; threshold voltage, mobility of electron; dielectric constant and polarization induce charge density in the device. Evidence for the applicability of the developed model is provided by the fact that the current – voltage characteristics calculated for dependent of temperature, shows good agreement with published experimental data

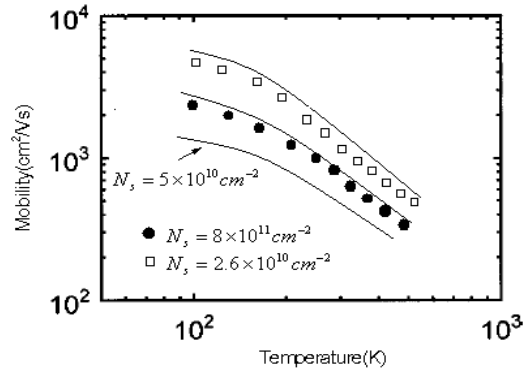


Fig. 2 shows the mobility at sheet carrier concentrations of  $5 \times 10^{10}, 8 \times 10^{11}, 2.6 \times 10^{12} \text{ cm}^{-2}$  as a function of temperature in comparison with existence experimental data from Ref. [12].

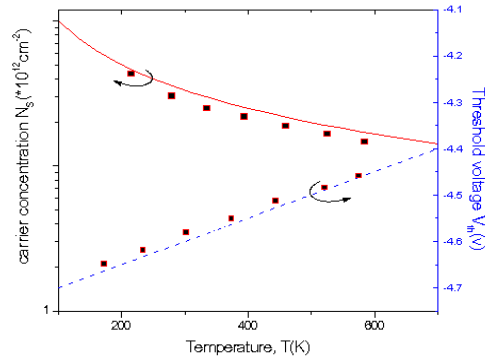


Fig.3 shows the sheet carrier concentrations and threshold voltage of two dimensional electron gas as a function of temperature in comparison with existence experimental data from Ref. [6, 8]

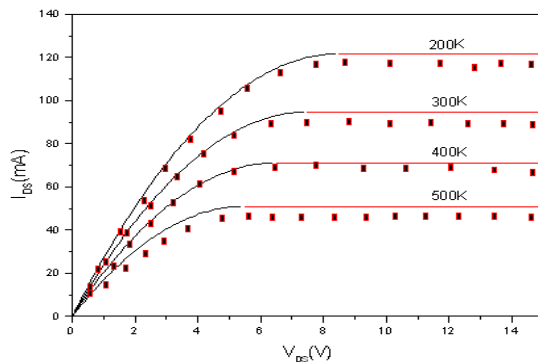


Fig.4 shows the variation of drain current versus drain-source voltage in comparison with existence experimental data from Ref. [16, 17]. Temperature is stepped in 100 K from 200 K to 500K.

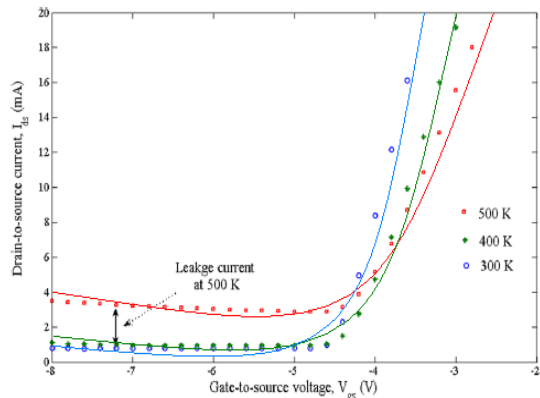


Fig.5 shows the variation of drain source current versus Gate-source voltage in comparison with existence experimental data from Ref. [16, 17]. (for  $V_{ds} = 10V$ )

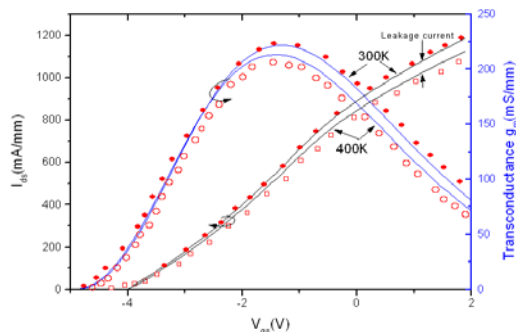


Fig.6 shows the variation of transconductance and total drain source current as function of gate source voltage for the in 300K and 400k. The dots represents Exp. Data from Ref. [27].

**References:**

[1]. W. Lu, V. Kumar, E. L. Pinter, and I. Adesida, " DC, RF, and microwave noise performance of AlGaIn-GaN field effect transistors dependence of aluminum concentration " IEEE Trans. Electron Devices, 50, 1069 (2003).  
 [2]Endoh A., Yamashita Y., Ikeda K., et al. High performance AlGaIn/GaN metal-insulator-semiconductor high electron mobility transistors fabricated using SiN/SiO<sub>2</sub>/SiN triple-layer insulators. *Jpn. J. Appl. Phys.*, 2006, 45: 3364-3367.  
 [3].J.Kuzmik, S.Bychikhin, M.Neuburger, A.Dadgar, A.Krost, E.Kohn, and D.Pogany, " Transient thermal characterization of AlGaIn/GaN HEMTs grown on silicon" IEEE Trans.Electron Devices, 52, 1698(2005)

[4].X.Z.Dang, P.M.Asbeck, E.T.Yu, G.J.Sullivan, M.Y.Chan, B.T.Mcdermott, K.S.Boutrons and J.M.Redwing," Measurement of drift mobility in AlGaIn/GaN heterostructure field effect transistor" Appl. Phys.Lett. 74, 3890(1999).  
 [5]. M.K.Chattopadhyay, S.Tokekar" Analytical model for the transconductance of microwave AlGaIn-mN/GaN HEMTs including nonlinear macroscopic polarization and parasitic MESFET conduction " *Solid – State Electronic* 50 (2007)220  
 [6]. P. Gangwani, S.Pandey, S Halder, M Gupta, R.S.Gupta" Analytical approach for high temperature analysis of AlGaIn/GaN HEMT" *Microelectronic Journal* 38 (2007) 848  
 [7].A. Asgari, M. Kalafi," The control of two-dimensional-electron-gas density and mobility in AlGaIn/GaN heterostructures with Schottky gate" *Material Science and Engineering C* 26 (2006)898.  
 [8].H. Rohdin, N. Moll, A. M. Bratkovsky, and C. Y. Su, *Phys. Rev. B*, 59, 13102 (1999).  
 [9].P. Roblin, H. Rahdin, "High-speed heterostructure devices from device concepts to circuit modeling", Cambridge university press, 277 (2002)  
 [10].E. J. Miller, X. Z. Dang, H. H. Wieder, P. M. Asbeck, and E. T. Yu, *J. Appl. Phys.* 87, 8070 (2000).  
 [11].G. Koley, V. Tilak, Ho-Young Cha, L. F. Eastman, and M. G. Spencer, *IEEE Electron Device Letters*, 8, 473 (2002).  
 [12].P. Gangwani, S.Pandey, S Halder, M Gupta, R.S.Gupta" Analytical approach for high temperature analysis of AlGaIn/GaN HEMT" *Solied-State Electronics* 51 (2007).  
 [13]. R.Yahyazadeh, A.Asgari, and M.Kalafi, "Effect of depletion layer on negative differential conductivity in AlGaIn/GaN high electron mobility transistor. *Physica E*, 2006, 33: 77 -82.  
 [14].C. Anghel, A. M. Lonescu, N. Hefyene, R. Gillon, *European Solid-State Device Research, 33r Conference on ESSDERC*, 03, pages: 449-452, Sept. 16-18 (2003).  
 [15]Rashmi,A.Kranti,S.Halder,R.S.Gupta, "An accurate charge control model for spontaneous and piezoelectric polarization dependent two dimensional electron gas sheet charge density of lattice mismatched AlGaIn/GaN" *Solid state electronics* vol.46,(2002)621-630  
 [16]L.Bouguen,L.Konczewicz,S.Contreras.B.Jouault,J.Camassel,Y.Cordier,High emperature behavior of AlGaIn/AlN/GaN Hall FET sensors, *Material Science and Engineering B* 165 (2009) 1-4  
 [17]. Rashmi, A. Kranti, S. Haldar, M.Gupta, and R. S. Gupta," Comprehensive analysis of small-signal parameters of fully strained and partially relaxed high Al-content lattice mismatched AlGaIn-mN/GaN HEMTs " *IEEE Trans. On Microwave Theory Tech.* 51, 607 (2003).  
 [18].S.P. Kumar, A.Agrawal, Sakkara, M. Gupta" An analysis for AlGaIn/GaN modulation doped field effect transistor using accurate velocity-field dependence for high power microwave frequency applications" *Microelectronic Journal* 37 (2006) 1339  
 [19]. L.Hsu, and W.Walukiewicz, "Effect of polarization fields on transport properties in AlGaIn/GaN heterostructure. *J. Appl. Phys.*, 2001, 89: 1783.  
 [20]. J. Deng, R. Gaska, M. S. Shur, M. A. Khan, J. W. Yang, *Materials Research Society Symposium-Proceedings* , V595, p w4.5.1 (2000).  
 [21].J. Deng, R. Gaska, M. S. Shur, M. A. Khan, J. W. Yang, *Materials Research Society Symposium-Proceedings* , V595, p w4.5.1 (2000).  
 [22]. A.Asgari, L.Faraone, M.Kalafi" A quasi-two-dimensional charge transport model of AlGaIn/ GaN high electron mobility transistor" *Physica E* 28 (2005) 491  
 [23].W.Jin, W.Liu, S.K.H.Fung, P.C.H.Chan, C.Hu, *IEEE Trans.Electron Device* 481(2001)730  
 [24].S.Kabra, H.Kaur, S.Halder, M. Gupta, R.S.Gupta" Temperature dependent analytical model of sub-micron GaN MESFETs for microwave frequency applications" *Solid – Stat Electronics* 20 (2007) 41  
 [25].R.Yahyazadeh, Z.hashempour, M.Kalafi, M.R.Aboulhasani "Analytical model for the cut off frequency and minimum noise of AlGaIn/GaN high electron mobility transistor" *Journal of Material Science and engineering* (2009) vol 3, No.12, pp.22-25

- [26]. Y.F.We,B.P.Keller,P.Fini,S.Keller,T.J.Jenkins,L.T.Kehias,S,P.Denbaares,and U.K.Mishra,IEEE Electron Device Lett.,vol.19,no.2,pp.50-53,Feb.1998.
- [27].M.Li,Y.Wang, " 2--D analytical Model for Current-Voltage Characteristics and Transconductance Of AlGa<sub>N</sub>/Ga<sub>N</sub>",IEEE Trans,on Electron Devices Vol.55,No.1,Jun (2008) 261-2

**Corresponding author:** Rajab Yahyazadeh (1969), male, Ph.D., research fields: experimental and theoretical study of crystal growth, theoretical study of optical and electrical properties of bulk and low-dimensional semiconductor (nitride material), modeling of semiconductor devices and modeling of nanoelectronic devices. E-mail: [yahyazadehs@gmail.com](mailto:yahyazadehs@gmail.com).

# Analog Non-Linear Function Synthesizer: HSPICE Design and Simulation

Madina Hamiane

**Abstract**—An analog non-linear function synthesizer is presented based on a polynomial expansion model. The proposed function synthesizer model is based on a 10th order polynomial approximation of any of the required non-linear functions. The polynomial approximations of these functions can then be implemented using basic CMOS circuit blocks. In this paper, a circuit model is proposed that can simultaneously synthesize and generate many different mathematical functions. The circuit model is designed and simulated with HSPICE and its performance is demonstrated through the simulation of a number of non-linear functions.

**Keywords**—HSPICE Simulation, Non-linear function synthesizer, polynomial approximation model, CMOS Transistors.

## I. INTRODUCTION

ANALOG nonlinear circuits have many applications, especially in signal processing, communication, instrumentation, neural networks, and medical equipment. As a result, a large number of analog signal processors have been discussed in the literature. Initially, analog signal processors were designed with the use of passive electronic components such resistors and simple semiconductor devices such as diodes and BJT transistors. With the advent of JFET and MOSFET transistors, the non-linear characteristics of these devices have then been exploited in the design of such processors. Many approaches involving the use of piecewise-linear function approximations of non-linear functions have been reported in the literature [1],[2]. In this respect, BJT and BiCMOS transistors have been used to simulate non-linear functions.

More recently, CMOS analog circuits based on the exponential-law and the square-law characteristics of a MOS transistor operating in weak and strong inversion respectively have been reported [3],[4]. These circuit realizations present some disadvantages the two most important being the realization of only one function at a time and their operation in voltage-mode or mixed current and voltage mode. However in current-mode circuits wider signal bandwidths and larger dynamic ranges of operation can be obtained as opposed to voltage-mode circuits.

A CMOS current-mode analog signal synthesizer has recently been proposed [7]. The circuit was based on a third order Taylor's series expansions of nonlinear functions which restricted the number of functions that can be realized and the accuracy of their realizations.

Madina Hamiane is with the Department of Telecommunication Engineering, Ahlia University, Manama, Kingdom of Bahrain (email: [mhamiane@ahlia.edu.bh](mailto:mhamiane@ahlia.edu.bh))

## II. MODEL FORMULATION

In this paper, a CMOS-based circuit model of a current-mode analog function synthesizer that can realize a large number of non-linear functions is presented. The circuit model is based on a 10<sup>th</sup>-order polynomial approximation of any non-linear function and is compatible with the CMOS technology currently used in digital signal processing.

Another advantage of the proposed model is the operation of the CMOS transistors in the strong inversion region, leading to the possible circuit operation at high frequencies. Other advantages of the proposed circuit model are the simultaneous realization of many nonlinear functions at a time that do not need the use of piece-wise linear approximation. In the proposed circuit model, a 10<sup>th</sup> order polynomial of the form:

$$f(x) = a_0 + a_1x + a_2x^2 + a_3x^3 + a_4x^4 + a_5x^5 + a_6x^6 + a_7x^7 + a_8x^8 + a_9x^9 + a_{10}x^{10} \quad (1)$$

$$|x| < 1$$

is used to approximate non-linear functions with a high degree of accuracy.

## III. PROPOSED CIRCUIT MODEL

In current mode, with the variable  $x$  representing the normalized input current, (1) can be realized by taking the sum of the eighted output currents of a number of building blocks that consist of the traditional class-AB current mirror circuit to provide both power-raising and amplification of the current input, and adding it to a constant current. One such building block is the squaring unit shown in Fig.1.

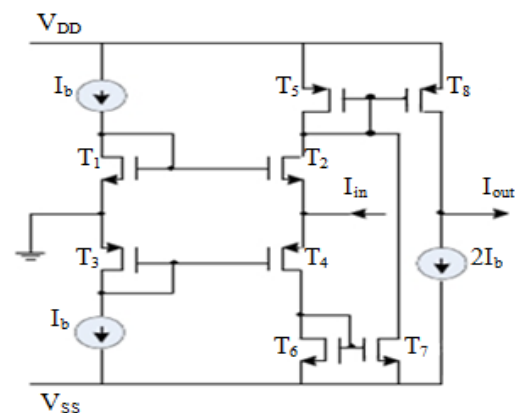


Fig.1: Modified current mirror to provide output currents proportional to the square of the input current

where  $I_{in}$  is the input current,  $I_b$  the bias current, and  $I_{out}$  is the output current. The aspect ratios ( $W/L$ ) of transistors  $T_1 - T_8$  of Fig.1 are shown in TABLE I.

TABLE I  
ASPECT RATIOS ( $W/L$ ) FOR THE TRANSISTORS OF FIG. 1

Transistor	$T_1$	$T_2$	$T_3$	$T_4$	$T_5$	$T_6$	$T_7$	$T_8$
$W/L$	1/1	1/1	1/1	1/1	1/1	1/1	1/1	1/1

The Transistors  $T_1$  and  $T_2$  as well as  $T_3$  and  $T_4$  are assumed to be well matched and transistors  $T_1$  through  $T_8$  are assumed to have the same value of the transconductance parameter i.e.,  $\beta_n = \beta_p$  and are operating in their saturation region. With these assumptions, the translinear principle is applied to produce the output current  $I_{out}$  which can be then expressed as [7]

$$I_{out} = \frac{I_{in}^2}{8I_b} \quad (2)$$

In order to obtain another output current proportional to the input current, two additional transistors  $T_9$  and  $T_{10}$  are added with aspect ratios 1/2 and 1/1 respectively as shown in Fig. 2. From this circuit, output currents of value  $a_1 x$  or  $a_2 x^2$ , can be obtained by using additional current mirrors of different aspect ratio values ( $W/L$ )

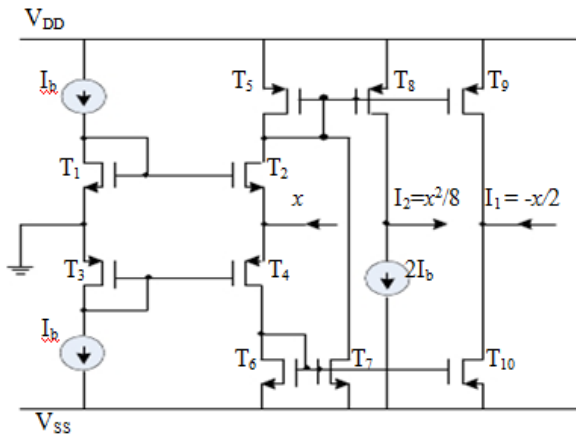


Fig. 2 Modified squaring circuit of Fig. 1 to provide output currents proportional to the input current and its square.

Again, by applying the translinear principle, the output current  $I_1$  is given by:

$$I_1 = -\frac{I_{in}}{2} \text{ or } \frac{I_1}{I_b} = -\frac{x}{2} \quad (3)$$

where  $x = I_{in}/I_b$  represents the normalized input current. Equation (2) can also be re-written using the normalized input current as:

$$I_2 = \frac{I_{in}^2}{8I_b} \text{ or } \frac{I_2}{I_b} = \frac{x^2}{8} \quad (4)$$

In order to obtain a current proportional to  $x^3$ , the following relation is used:

$$\frac{(x + x^2)^2}{8} - \frac{(x - x^2)^2}{8} = \frac{x^3}{2} \quad (5)$$

The corresponding circuit will therefore require two modified squaring circuits with inputs proportional to the difference and the sum of the input current and its square. The required third order term in (1) can then be obtained by selecting appropriate values of the aspect ratios ( $W/L$ ). Therefore and in order to obtain output currents proportional to even and odd powers of the input current, the modified squaring circuit of Fig. 2 along with (4) and (5) are repeatedly used. TABLE II-(a) and II-(b) give the details of the inputs that are used to produce output currents proportional to  $x^3$  through  $x^{10}$ .

TABLE II-(a)

OUTPUT CURRENTS PROPORTIONAL TO ODD POWERS OF INPUT CURRENTS				
$I_{in}$	$x + x^2$ and $x - x^2$	$x + x^4$ and $x - x^4$	$x + x^6$ and $x - x^6$	$x + x^8$ and $x - x^8$
$I_1$	$x^3/2$	$x^5/2$	$x^7/2$	$x^9/2$

TABLE II-(b)

OUTPUT CURRENTS PROPORTIONAL TO EVEN POWERS OF INPUT CURRENTS					
$I_{in}$	$x$	$x^2$	$x^3$	$x^4$	$x^5$
$I_2$	$x^2/8$	$x^4/8$	$x^6/8$	$x^8/8$	$x^{10}/8$

It can therefore be seen that higher-order terms of (1) can be obtained by repetitive use of the circuit model of Fig. 2 without the need for dedicated current multipliers. With this design and the addition of a normalized DC current, any nonlinear function can be realized using MOSFET current-mirrors with the appropriate aspect ratios ( $W/L$ ). Fig.3 shows the basic circuit model of the function synthesizer where B refers to the squaring circuit model of Fig. 2. The circuit shows only outputs proportional to  $x$  through  $x^6$ .

#### IV. SIMULATION RESULTS

The basic circuit model of Fig. 3 was used in the simulation of a number of nonlinear functions. The corresponding polynomial expansion coefficients  $a_i, i = 1, \dots, 10$  for selected functions are given in TABLES III-a and III-b, and the transistors' aspect ratios were selected accordingly. HSPICE circuit simulation environment was used and the simulation was carried out using the BSIM2 level 39 MOSFET transistor models with  $L=0.1\mu m$ , bias current  $I_b=1\mu A$  and supply voltages  $V_{DD} = -V_{SS} = 2V$ .

For each function simulation, the input current was changed from  $0 \mu A$  to  $1\mu A$ , and the output currents through load resistances of  $1=M\Omega$  was obtained. A DC current source =  $1\mu A$  was added to the output node to represent the constant term in equation (1) which equals, according to TABLES III-(a) and III-(b), either to 1 or zero.

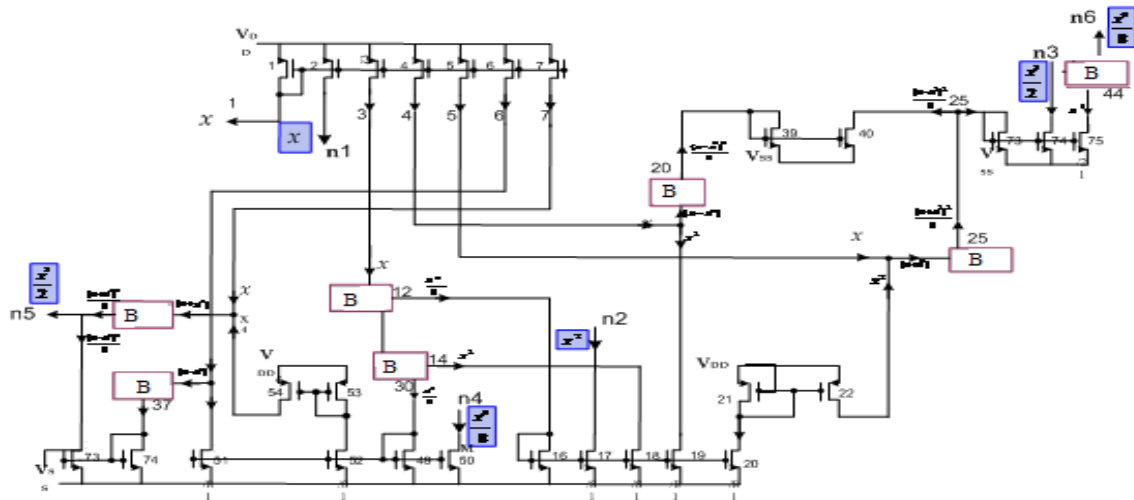


Fig. 3 Basic circuit model for the function synthesizer showing outputs proportional to the first 6 terms of the polynomial expansion

TABLE III-(a)

POLYNOMIAL EXPANSION COEFFICIENTS FOR SELECTED FUNCTIONS						
Function	$a_0$	$a_1$	$a_2$	$a_3$	$a_4$	$a_5$
$\sin(x)$	0	1	0	-1/6	0	1/120
$\frac{1}{\sqrt{1+x}}$	1	-1/2	3/8	-5/16	35/128	-0.2461
$\tanh(x)$	0	1	0	-1/3	0	2/15
$\ln(1-x)$	0	-1	-1/2	-1/3	-1/4	-1/5
$e^x$	1	1	1/2	1/6	1/24	1/120
$J_1(x)$	0	1/2	0	-1/16	0	1/384
$I_0(x)$	1	0	1/4	0	1/64	0
$\sqrt{1-x^2}$	1	0	-1/2	0	-1/8	0

TABLE III-(b)

POLYNOMIAL EXPANSION COEFFICIENTS FOR SELECTED FUNCTIONS					
Function	$a_6$	$a_7$	$a_8$	$a_9$	$a_{10}$
$\sin(x)$	0	-1/5040	0	1/362880	0
$\frac{1}{\sqrt{1+x}}$	0.2256	-0.2095	0.1964	-0.1855	0.1762
$\tanh(x)$	0	-17/315	0	0.0219	0
$\ln(1-x)$	-1/6	-1/7	-1/8	-1/9	-1/10
$e^x$	1/720	1/5040	1/40320	1/362880	1/3628800
$J_1(x)$	0	-1/18432	0	1/1474560	0
$I_0(x)$	1/2304	0	1/147456	0	1/14745600
$\sqrt{1-x^2}$	-1/16	0	-5/128	0	-7/256

The exact nonlinear functions were calculated and their graphs compared with those of the simulated functions as illustrated in Fig. 4 and Fig. 5. Inspection of these figures clearly shows that the simulated results are in excellent agreement with the calculated ones. TABLE IV shows the

range of input current values for which the error between corresponding functions is less than 1% which further reflects the accuracy of the proposed function synthesizer circuit model.

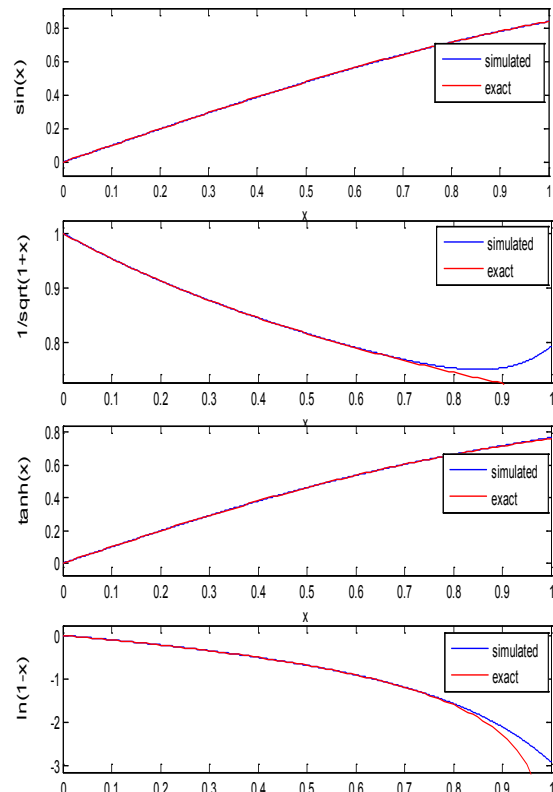


Fig. 4 Simulated and calculated functions from TABLES III-(a) and III-(b)

REFERENCES

- [1] M.Benammar, "Precise, wide-range approximation to a sine function suitable for analog implementation in sensors and instrumentation applications", *IEEE Transactions on Circuits and Systems-I: Regular Papers*, Vol. 52, 2005, pp. 262-270
- [2] B.Maudy and S.Gift, "Novel pseudo-exponential circuits", *IEEE Transactions on Circuits and Systems-II: Express Briefs*, Vol. 52, 2005, pp. 675-679.
- [3] M.Tavakoli and R.Sarpehkar, "A sinh resistor and its application to tanh linearization", *IEEE Journal of Solid-State Circuits*, Vol. 40, 2005, pp. 536-543
- [4] C.A.De La Cruz-Blas, A.J.Lopez-Martin and J.Ramirez-Angulo, "Compact power-efficient class-AB CMOS exponential voltage converter", *Electronics Letters*, Vol. 42, 2006, pp. 127-128.
- [5] T.Arthansiri and V.Kasensuwan, "current-mode pseudo-exponential-control variable-gain amplifier using 4<sup>th</sup>-order Taylor's series approximation", *Electronics Letters*, Vol. 42, 2006, pp. 379-380.
- [6] M.A.Hashiesh, S.A.Mahmoud and A.M. Soliman, "New 4<sup>th</sup>-quadrant CMOS current-mode and voltage-mode multipliers", *Analog Integrated Circuits and Signal Processing*, Vol. 45, 2005, pp. 295-307
- [7] M.T.Abuelma'atti, "Universal CMOS current-mode analog function synthesizer", *IEEE Transactions on Circuits and Systems-I: Fundamental Theory and Applications*, Vol. 49, 2002, pp. 1468-1474

**Madina Hamiane** received her BSc in Electronics from Universite des Sciences et de la Technologie Houari Boumediene (USTHB), Algeria; and her Master's and PhD degrees in Cybernetics and Control Engineering from the University of Reading, UK, and the University of Sheffield, UK, respectively. She is now with the College of Engineering at Ahlia University in the Kingdom of Bahrain. Dr. Hamiane's current research interests span signal processing, pattern recognition, biomedical signal and image analysis, computer simulation of electronic and control systems.

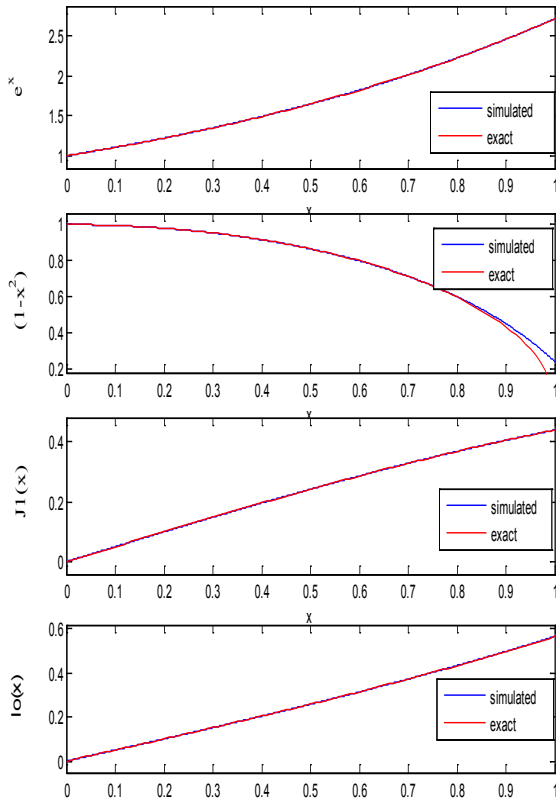


Fig. 5 Simulated and calculated functions from TABLES III-(a) and III-(b)

TABLE IV  
RANGE OF INPUT CURRENT VALUES

Function	$\sin(x)$	$\frac{1}{\sqrt{1+x}}$	$\tanh(x)$	$\ln(1-x)$
Range of $x$	$< 1 \mu\text{A}$	$< 0.8 \mu\text{A}$	$< 1 \mu\text{A}$	$< 0.8 \mu\text{A}$
Function	$e^x$	$J_1(x)$	$I_0(x)$	$\sqrt{1-x^2}$
Range of $x$	$< 1 \mu\text{A}$	$< 1 \mu\text{A}$	$< 1 \mu\text{A}$	$< 0.9 \mu\text{A}$

V. CONCLUSION

Simulation of a simple non-linear function synthesizer using MOSFET transistor models available in HSPICE simulation environment has been presented. The circuit model was based on approximating any nonlinear function with the first 10 terms in its polynomial expansion. The circuit model that realizes any of these functions consists of power-factor raising circuits built around a basic current squarer circuit, a weighted current amplifier and a dc current source. The proposed simulation model can be easily modified to implement many functions by proper selection of the transistors' aspect ratios. Simulation of a number of nonlinear functions verified the validity of the proposed function synthesizer circuit model.

# Wireless Remote Control of Transesophageal Echocardiography (TEE) Probe

Dolwin C. C. Kho, Christina Pahl, Eko Supriyanto, Yin M. Myint, Ahmad A. M. Faudzi, Maheza I. M. Salim

**Abstract**—Transesophageal Echocardiography (TEE) is intensively used in operating theaters as a surgical monitoring device as well as in cardiovascular diagnostics rooms. The usage of TEE requires a few hours and is sometimes also performed under X-Ray exposure. This may result in a radiation contamination of the operator. In order to decrease this health burden, this setup proposes a wireless TEE probe remote control. We used a microcontroller based system in order to control movement and position of the probe. The input for the microcontroller is sent wirelessly using radio frequency. In this research we used a combination of LED setups to simulate all possible movements and positions of the probe. Results show that the system is capable of remote controlling the TEE probe from a distance of more than 2 meters.

**Keywords**—Transesophageal Echocardiography, remote control, radio frequency, clinical application.

## I. INTRODUCTION

TRANSESOPHAGEAL echocardiography or TEE, is an alternative procedure for further cardiac examination like transthoracic echocardiogram. It is used to evaluate, diagnose the cardiac condition and to monitor patients during the peri-operative period of cardiac surgeries as well as hemodynamically unstable patients [1]. The cardiac data provided by the TEE provide clearer images compared to Transthoracic Echocardiography (TTE) data and are also less affected by interference originating from ribs and lungs. Fig. 1 shows conventional TEE probe used for surgical procedures. The low degree of invasiveness of TEE and its capability to visualize and assimilate the dynamic information are helpful in changing the course of patient management [2]. As for TEE, there is a specialized probe, of an approximately one meter long flexible instrument, containing an ultrasound transducer at the tip which is passed into the esophagus of

This work was supported in part by the National Heart Institute of Malaysia (IJN) and Cardio Centre Flagship Project.

D. C. C. Kho, E. Supriyanto, Y.M.Myint, A.A.M Faudzi, and M.I.M are under the IJN-UTM Cardiovascular Engineering Centre, Faculty of Biosciences and Medical Engineering, University of Technology Malaysia (UTM), Skudai, Johor, Malaysia.

C. Pahl is under Ilmenau University of Technology (TUIL), Faculty of Mechanical Engineering, Department for Biomechatronics, 100 565, Ilmenau, Germany as well as University of Technology Malaysia (UTM), Faculty of Biosciences and Medical Engineering, IJN-UTM Cardiovascular Engineering Centre, Level 2, Block B, Building V01, 81310, Skudai, Johor, Malaysia.

patients. The following Fig. 1 shows the TEE probe. The cardiac images are obtained by manually adjusting the transducer tip. The transducer at the tip of the probe is usually positioned within the esophagus right before the stomach and directly behind the heart.

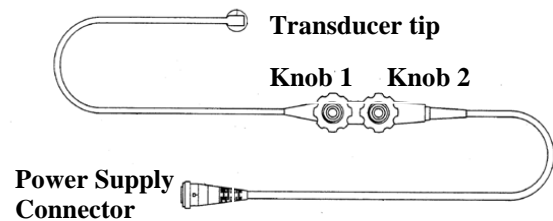


Figure 1. Existing TEE probe that currently being used in most surgical procedures.

The tip is rotated and moved towards some specific angles and directions in order to acquire images of the heart at several different coordinates. The position and orientation of the TEE probe can be altered by several standard manipulations, for example, advancement into or withdrawal from the esophagus, turning rightward or leftward, rotating forward or backward, and anteflex or retroflex [3-5]. These maneuvers have to be adjusted manually by turning the probe shaft and adjusting the knobs as well as electronic switch of the probe control unit using both hands simultaneously. The need of this manual probe adjustment to any specific position will therefore create an uncomfortable condition during diagnosis and surgery monitoring. Furthermore it is important to acquire precise coordinates of the probe position [6]. It is often inconvenient for the sonographer to operate the control unit of the ultrasound machine while performing the TEE procedure [7].

The aim of developing this remote positioning control unit is to remote control and adjust position as well as orientation of the TEE probe tip towards specific angles and directions via RF wireless technology. This is used in order to acquire cardiac images. This system will eventually help doctors or surgeons to remotely monitor the condition of cardiac patients. RF was used here due to its low cost attitude. The application of TEE within clinical procedures can be traced back for more than a decade. It was first applied in 1976, where the instrument was a rigid, mechanical sector, a scanning device

that caused discomfort during intubation [8]–[10].

Then TEE was improved with the application of phased array technology [11]. Later, TEE has been improved by using an electrically powered motor that was coupled to the flexible endoscope shaft as well as to the articulation section including the probe [12], [13]. The attachment of the motor to the shaft was used in order to minimize overtorque situations, whereas the articulation section was used for the locking mechanism in a given bent position of the probe.

In this study, a state-of-the-art remote positioning control unit forseen to adjust the position of the TEE probe tip via RF wireless technology is presented. In section II, the proposed hardware is explained. Section III presents the software architecture, and the last section presents the discussion and conclusion.

## II. PROPOSED HARDWARE SYSTEM

### A. Proposed System

The proposed system acquires a position command or any position signal data from a particular source. Then it can transfer command data to the TEE probe using RF. Subsequently the TEE probe tip will move and can be adjusted according to the received signals. A GUI is used to display the status of the TEE probe tip and also to monitor the cardiac images. If an emergency situation occurs, such as error, the GUI will display “ERROR”. With the developed system, real-



Fig. 2 Basic diagram of the proposed system

time remote monitoring data or diagnosis information of any patients' heart are achieved. In this way, doctors will be supported in monitoring more patients out of different surgical theatres with increased efficiency. The general diagram of the proposed approach is given in Fig. 2.

### B. Remote Positioning Control Setup

For the setup of the wireless communication system, a pair of RF wireless transmitter and receiver modules were used. Signals were generated in order to be transferred by the transmitter. These include position signal data which are received by the corresponding receiver. A parallax joystick is used to provide position signals at the transmitter part. A

prototyped TEE probe can be connected to the receiver side and so that it can move simultaneous to the movement of the joystick. The prototyped probe consists of two units. A servo motor that will be remotely controlled by the joystick and an Arduino Uno microcontroller. Lastly is used as in order to encode and decode signal data to serial data. The block diagram of the complete setup is given in Fig. 3.

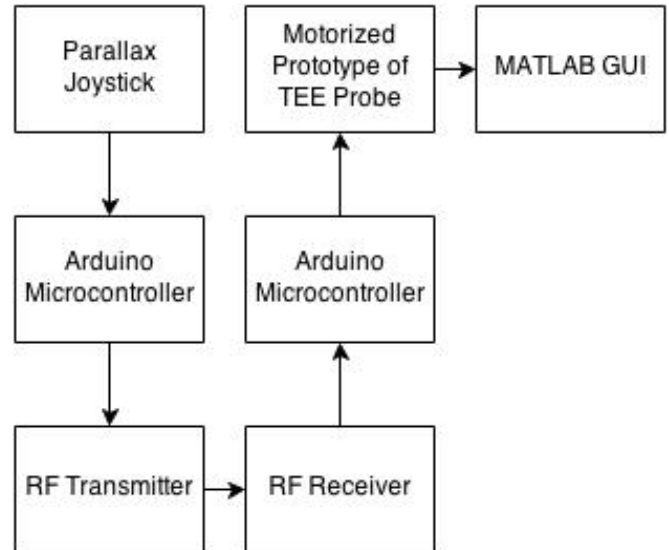


Fig. 3 Block diagram of the remote positioning control unit

### C. Sequence of Signal Detection Algorithm

In the following steps of the proposed position signal detection algorithm are given:

- 1) Read any value from the analog pin if available. The value would be between 0 and 1023.
- 2) If there is a value, map the value to degree, which will be from 0 to 180.
- 3) Write the mapped value to serial data.
- 4) Display the value onto serial monitor.
- 5) Send the corresponding value to the receiver.
- 6) Any data from receiver will then be sent to the microcontroller and then to the servo motor.
- 7) Servo motor will be triggered to move in accordance to the degree received.
- 8) The degree of movement of the motor will be displayed on a new serial monitor.

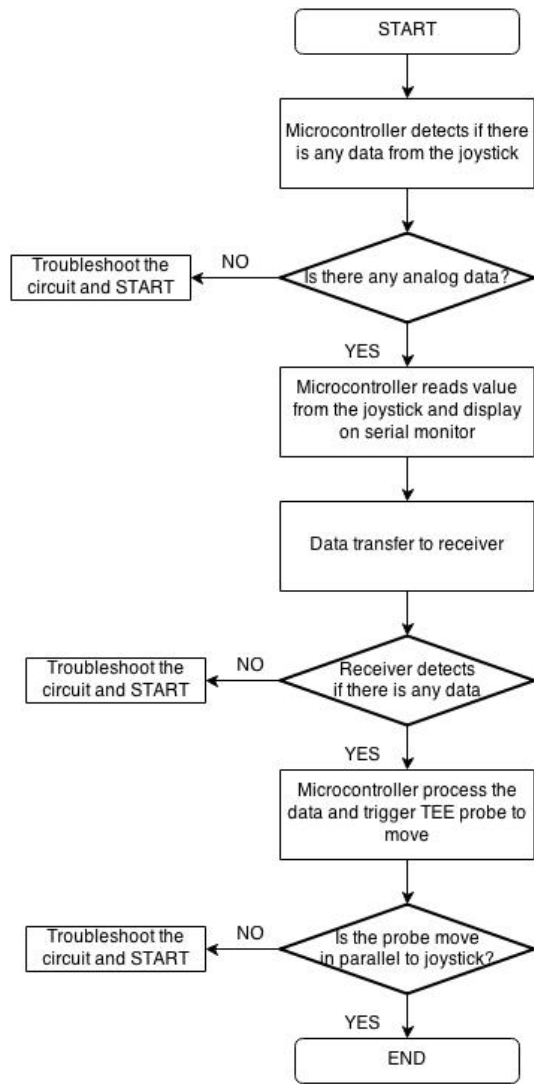


Fig. 4 Flowchart of remote control system

Fig. 4 shows the flowchart in developing the algorithm of the remote positioning control system.

### III. SOFTWARE ARCHITECTURE

The software system consists of GUI monitoring that enables monitoring of the movements and adjustment of the probe. Furthermore, it allows to view the cardiac images. Every movement made by the probe tip will be displayed on the screen of the GUI. The main menu of the GUI displays the cardiac images. The software architecture is designed using MATLAB GUI.

### IV. RESULTS AND DISCUSSION

For the need of preliminary testing, five LEDs were used to indicate the position of the joystick. The preliminary test is done in order to see if the RF wireless technology is functioning. It is also used to find out if it is able to transfer signal data from the transmitter to the receiver. The LEDs are arranged in a circle on the breadboard. The LED in the middle represents the joystick in rest. This test is done in a range of

distance of 48 meters, separated by a transparent wall in between. Preliminary test results are given in Fig. 5(a) until Fig. 5(i).

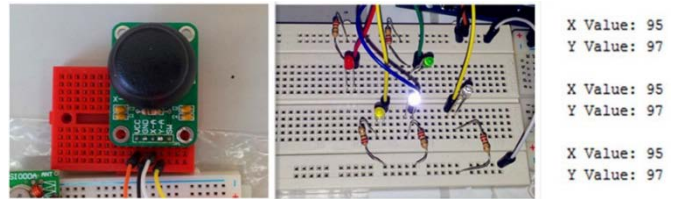


Fig. 5(a) joystick in still position, no movement

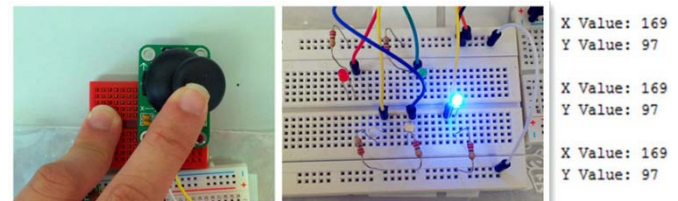


Fig. 5(b) joystick on positive x-axis

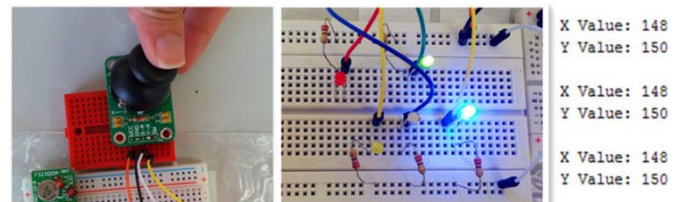


Fig. 5(c) joystick in first quadrant position

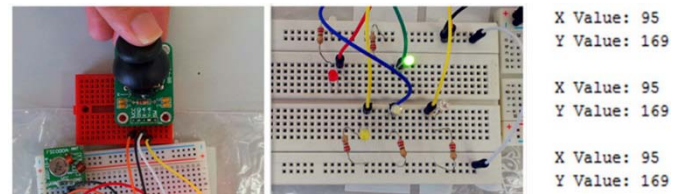


Fig. 5(d) joystick on positive y-axis

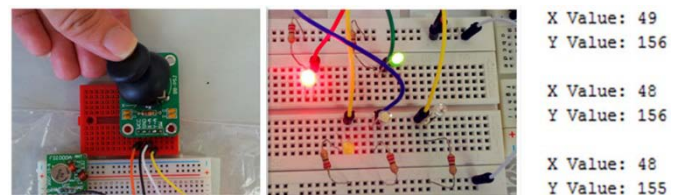


Fig. 5(e) joystick in second quadrant position

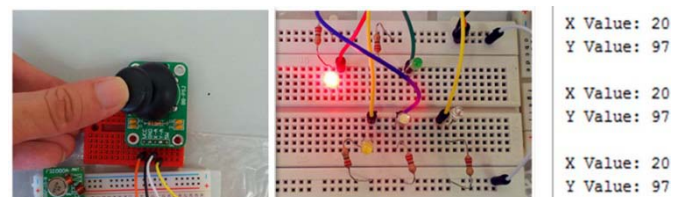


Fig. 5(f) joystick on negative x-axis

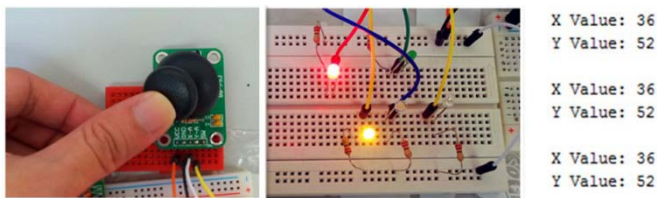


Fig. 5(g) joystick in third quadrant position

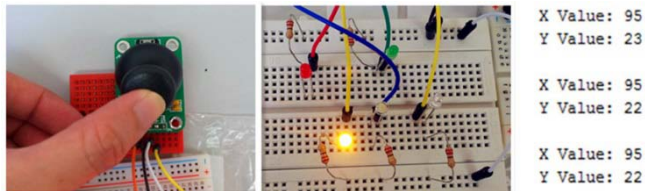


Fig. 5(h) joystick on negative x-axis

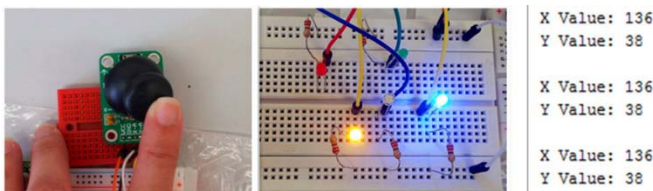


Fig. 5(i) joystick in fourth quadrant position

From the preliminary results, it can be seen that the LEDs are blinked in accordance to which quadrant the joystick is in at that particular moment. This was documented during the performance of the setup from a distance of more than 2 meters. The signals did not show any malfunctioning when sent through a concrete wall of a thickness of 20 cm.

## V. CONCLUSION

In this study an adequate method for medical environment diagnosis using wireless TEE probe tip position control is presented. The position signal data are acquired and subsequently sent to the TEE probe via Radio Frequency waves. The status or current position of the tip is displayed on a GUI. The whole concept is based on distributed architecture and supports the operator to perform long-distance monitoring during cardiac surgery and diagnosis. This method results in the exclusion of negative effects for the TEE user. Our system is able to be integrated into any conventional mechatronic TEE probe control system.

## ACKNOWLEDGMENT

This research is supported by research university grant Q.J130000.2409.01G69 from Ministry of Education Malaysia.

## REFERENCES

[1] I. G. Burwash and K. L. Chan, "Transesophageal Echocardiography," in *Otto C. M. The Practize of Clinical Echocardiography*, Philadelphia: Elsevier Saunders, 2007, pp. 3-25.  
 [2] R. M. Savage, S. Aronson, J. S. Shanewize, E. B. Mossad and M. G. Licina, "Intraoperative Echocardiography; Cardiac Anesthesia-Principle and Clinical Practize," in F. G. Estafanous, G. P. Barash and J. G Reeves, Philadelphia, 2001, pp. 237-294.

[3] A. F. Edward, A. S. Jeffrey, H. B. Jaqueline and E. G. Martin, "Transesophageal Echocardiography: Procedures and Clinical Application," in American College of Cardiology, New York, 1991, pp. 1333-1348.  
 [4] J. P. Miller, "Two-Dimensional Examination," in *Essentials of Two-Dimensional Imaging*, pp. 24-52.  
 [5] F. Robert, K. John and R. Marco, "Core Topics in Transesophageal Echocardiography," Cambridge University Press, 2013.  
 [6] C. Pahl, E. Supriyanto, N. H. B. Mahmood, J. Yunus, "Cervix Detection Using Squared Error Subtraction," *Modelling Symposium (AMS)*, 2012, pp. 29-31.  
 [7] B. Frank, W. K. Perry and A. L. Eugene, " Transesophageal Ultrasonic Scanhead," U.S. Patent 5,050,610, 1991.  
 [8] L. Frazin, J.V. Talano, L. Stephanides, H. S. Loeb, L. Kopel and R. M. Gunnar, " Esophageal Echocardiography," in *Circulation*, 1976, pp. 102-108.  
 [9] K. Hisanaga, A. Hisanaga, N. Hibi, K. Nishimura and T. Kambe, " High speed rotating scanner for transesophageal cross-sectional echocardiography," in *American Journal of Cardiology*, 1980, pp. 837-842.  
 [10] E. J. Gussenhoven, M. A. Taams and J. Roelandt, " Transesophageal two-dimensional echocardiography: its role in solving clinical problems," in *J Am Coll Cardiol.*, 1986, pp.975-979.  
 [11] M. Schluter, B. A. Langenstein and J. Polster, " Transesophageal cross-sectional echocardiographywith a phased array transducer system: technique and initial clinical results," 1982, pp. 67-72.  
 [12] J. S. Rodney, K. M. Martin, G. Goerge and T.F. James, "Transducer Positioning System," U.S. Patent 5,181,514, 1993.  
 [13] P. G. George, " Ultrasonic Transesophageal Probe with Detachable Transducer Tip," U.S Patent 5,634,466, 1997.

# A Novel Delay and Overshoot Estimation model for VLSI Global Interconnects

M.Kavicharan, N.S.Murthy, and N. Bheema Rao

**Abstract** — In this paper, we propose a novel, simple and accurate delay and overshoot estimation model for VLSI Global Interconnects, based on new matrix Pade-type approximant (MPTA). This model reduces the computational complexity by considering rational function denominator as scalar polynomial and avoiding matrix inversion. The proposed model provides a simpler rational function approximation for estimating delay and overshoot in lossy VLSI interconnects. With the reduced order lossy interconnect transfer function, finite ramp responses are obtained and line delay and signal overshoot are estimated. The estimated delay and overshoot values are compared with the Pade model and HSPICE W-element model. The 50% delay results are in good agreement with those of HSPICE within 0.5% error while the overshoot error is within 1% for a 1 mm long interconnect. For global lines of length more than 1 mm in SOC (system on chip) applications, the proposed model is found to be nearly two times more accurate than existing model. Further more the proposed model is computationally more efficient than HSPICE and pade model.

**Keywords** – Delay, matrix rational model, ramp input, RLC interconnects, transient analysis, transfer function, new MPTA approximant.

## I. INTRODUCTION

Accurate estimation of delay and overshoot is crucial for the design of high speed systems at VLSI technology. As the physical dimensions in VLSI technologies scale down, interconnect delay dominates the gate delay in determining circuit performance [1]. Hence, for the design of complex circuits, simple, fast and more accurate analytic models are useful for IC designers to predict the interconnect effects.

Originally VLSI interconnects were modeled as RC lines and single pole Elmore-based models [2], [3] because of long channel device delay dominance over negligible interconnect delay. However the Elmore model fails at high frequencies since it does not consider the inductance effects [4]. It is necessary to use a second-order model, which includes the effect of inductance. Kahng et al. considered equivalent Elmore delay model based on the Resistance Inductance and Capacitance (RLC) of the interconnects [4] and [5]. Ismail et al. [6] proposed two pole model to capture far end time domain solution for single line interconnect.

A simplified voltage transfer function obtained using Taylor series approximation for transient analysis [7], [8] has less accuracy in delay calculation. Nakhla et al. [9] use modified nodal analysis (MNA) for obtaining far end and near end responses of interconnects. Roy [10] extended [9] for obtaining more accurate far end responses of coupled RLC interconnects using delay algebraic equations.

A matrix rational-approximation model for SPICE analysis of high-speed interconnects is presented by Dounavis et al. [11], [12]. However, the approximations made to derive these models contributed to more inaccuracy. This has been improved using Pade approximation model [13] to estimate the delay of interconnects. All the above models still suffer from accuracy and computational efficiency and need better models to efficiently estimate delay and overshoot of interconnects.

In this paper, we present an improved analytic delay model by extending the concepts developed by Dounavis et al. [11]-[13] for on-chip RLC interconnects. The estimated delay and overshoot values of the proposed model are compared with Pade model [13] and HSPICE. The proposed model is based on new matrix Pade' type approximant (MPTA) [14] and [15], which is simple in structure and easier to implement. For the same order (2/2), the proposed model offers better accuracy than Pade model for global interconnects of length 1-5 mm. The proposed model is used to solve the Telegrapher's equations for the first time.

The new MPTA model [15] has matrix Pade-type approximation, whose denominator is a scalar polynomial in terms of a matrix-valued linear functional on the polynomial space. The Pade model with rational matrix approximation has numerator and denominator matrices which need inverse matrix operations leading to severe computational complexity. The proposed model reduces the computational complexity by considering rational function denominator as scalar polynomial and avoiding matrix inversion.

The remainder of the paper is organized as follows. Section II briefly describes the mathematical analysis to determine the linear transfer function of RLC interconnects and to find the transient analysis. Section III presents the proposed new MPTA model for single RLC line, while section IV deals with the comparison of the proposed model with Pade and standard HSPICE models. Conclusions appear at the section V.

## II. ANALYSIS OF RLC INTERCONNECT

The analysis of on-chip RLC interconnects begins with Telegrapher's equations in frequency domain. All the closed-form RLC interconnects models assume quasi-TEM (transverse electromagnetic) mode of signal propagation. The Telegrapher's equations are a pair of linear partial differential equations, which illustrate the voltage and current on a transmission line with distance and time as transmission line variables.

The solution of interconnects are described by telegrapher's equations as

$$\frac{\partial}{\partial x} V(z,s) = -(R + sL)I(z,s) \quad (1)$$

$$\frac{\partial}{\partial x} I(z,s) = -sCV(z,s) \quad (2)$$

where 's' is a Laplace-transform variable, z is a variable which represents position; V(z,s) and I(z,s) stand for the voltage and current vectors of the transmission line, respectively, in the frequency domain; and R, L and C are the per unit length (p.u.l.) resistance, inductance, and capacitance matrices, respectively.

The solution of (1) and (2) can be written as an exponential matrix function as

$$\begin{bmatrix} V(d,s) \\ -I(d,s) \end{bmatrix} = e^{\phi d} \begin{bmatrix} V(0,s) \\ I(0,s) \end{bmatrix} \quad (3a)$$

where

$$\phi = \begin{bmatrix} 0 & -Z \\ -Y & 0 \end{bmatrix}$$

In (2) 'd' is the length of the transmission line, with Z=R+sL and Y=sC. The exponential matrix of (3a) can be written in terms of cosh and sinh functions as

$$e^{\phi d} = \begin{bmatrix} \cosh(d\sqrt{ZY}) & -Y_0^{-1} \sinh(d\sqrt{YZ}) \\ -Y_0 \sinh(d\sqrt{YZ}) & \cosh(d\sqrt{YZ}) \end{bmatrix} \quad (3b)$$

where

$$Y_0 = Y(\sqrt{YZ})^{-1}$$

Equation (3a) does not have a direct representation in the time domain, so it is difficult to analytically predict the delay and overshoot of transmission lines. Hence, there exists demand for approximate models. The basic idea of the matrix rational-approximation model is to use predetermined coefficients to analytically obtain rational functions for (3a). To obtain a passive model, the exponential function is approximated and the resultant model is used for obtaining time response.

A single RLC line is shown in Fig. 1. The line is driven by a 1-V finite ramp with rise times of 0.1 ns and 0.05ns. This represents a point-to-point interconnection driven by a transistor (modeled as a resistance R<sub>s</sub>) and connected to the next gate (modeled as a capacitance C<sub>l</sub>).

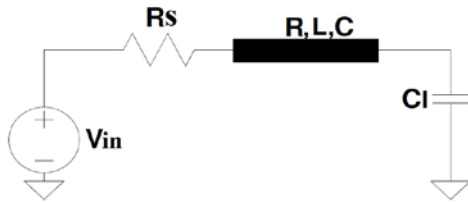


Fig.1. Circuit model of the single-line distributed RLC interconnect.

The frequency-domain solution at the far end can be expressed as

$$V_f = \frac{V_{in}}{(1 + sR_s C_l) \cosh(\Gamma d) + (R_s Y_0 + s C_l Y_0^{-1}) \sinh(\Gamma d)} \quad (4)$$

where

$$\Gamma = \sqrt{YZ}$$

In (4), R<sub>s</sub> is the source resistance at the near end, C<sub>l</sub> is the load capacitance at the far end, and V<sub>in</sub> is the input voltage. It is extremely difficult to find the time domain response of this complex transfer function, hence an approximate transfer function has been derived using new MPTA model. The time response of this function is used for estimation of delay and overshoot in single RLC interconnect.

### III. PROPOSED NEW MPTA MODEL

This model is based on new MPTA approximation [14], [15]. For the power series expansion of a function f(x), where 'x' is a complex variable

$$f(x) = C_0 + C_1 x + C_2 x^2 + \dots + C_n x^n + \dots, C_i = (C_i^{(uv)}) \in C^{sxt}; x \in C \quad (5)$$

The exponential matrix (4) can be written as above series and the closed form rational function approximation for an exponential matrix in (4) is written as

$$R_{mn}(x) = P_{mn}(x) / \tilde{v}(x) \quad (6)$$

is called as new MPTA approximant and is denoted by (m/n) f(x)

where

$$P_{mn}(x) = \tilde{v}(x) \sum_{i=0}^{m-n} c_i x^i + x^{m-n+1} \tilde{W}_1(x), \quad (7)$$

$$\tilde{v}(x) = x^n v(x^{-1}), \quad (8)$$

Let 'v' be a scalar polynomial of degree n

$$v(x) = b_0 + b_1 x + \dots + b_n x^n \quad (9)$$

These coefficients b<sub>0</sub> to b<sub>n</sub> can be calculated using [15].

Further more

$$\tilde{W}_1(x) = x^{n-1} W_1(x^{-1}), l = m - n + 1 \quad (10)$$

$$\tilde{W}_1(x) = \sum_{l=0}^{n-1} \left( \sum_{i=0}^l b_{n-1+i} c_{i+m-n+1} \right) x^l \quad (11)$$

For the 2/2 approximation order, the rational approximation is

$$R_{22}(x) = P_{22}(x) / \tilde{v}(x) \quad (12)$$

where

$$P_{22}(x) = \tilde{v}(x) c_0 + z \tilde{W}_1(x)$$

and

$$v(x) = b_0 + b_1 x + b_2 x^2$$

Thus, R<sub>22</sub> represents a table of rational functions, each element of which is an approximant of original series (5) and obtained from the series of below steps.

Calculation procedure for estimating delay and overshoot using new MPTA approximants are as follows.

- (i) Telegrapher’s equations are solved and the solution is written as exponential matrix and the derived transfer function (4) is approximated using the new MPTA model.
- (ii) The coefficients  $W_1$  of the resultant exponential function are calculated using (11).
- (iii)  $P_{mn}(x)$  can be calculated for any order of  $m/n$  from the relation (7). However, for validation with Pade model (2/2), the proposed model (12) is calculated with  $m=n=2$
- (iv) Total sums of the numerator  $P_{22}(x)$  and the denominator are calculated and the approximated transfer function is obtained.
- (v) Ramp response of the transfer function is obtained to estimate delay and overshoot of interconnect.

IV. SIMULATION RESULTS

A single RLC line is presented in this section to demonstrate the validity and efficacy of the proposed model. The results obtained using MATLAB R2010a operating on HP 64-bit Intel i5 processor with clock speed of 2.53 GHz, are compared with HSPICE W element model.

The typical interconnect parameters [13] considered for simulation of single RLC interconnect are given in Table-I. The Pade approximation [13], and proposed new MPTA model are implemented in MATLAB for the same set of input parameters.

Table I: The values of Interconnects parameters [13]

$V_{dd}$	1V
Length	0.1mm to 0.5cm
Resistance	88.29 $\Omega/cm$
Capacitance	1.8pF/cm
Inductance	15.38nH/cm
Input ramp rise/fall time	0.1ns
Source resistance	20 $\Omega$ to 100 $\Omega$
Load capacitance	0.05fF to 0.1fF

The far-end response to a finite ramp input of single interconnect is plotted in Fig. 2. The plots compare the responses of proposed and Pade model [13]. It is evident from Fig. 2 that, the proposed new

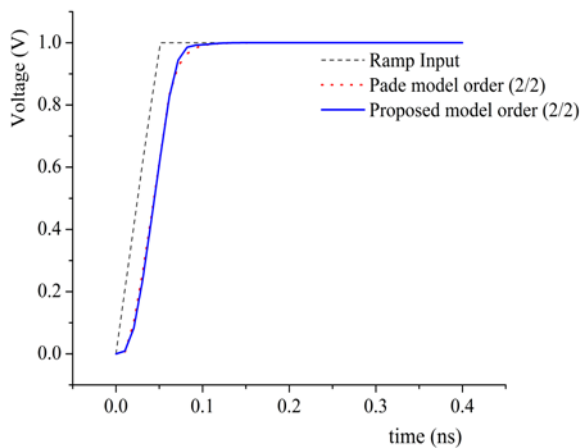


Fig.2. Transient response of single interconnect line, with length = 0.5mm,  $R_s=50\Omega$ ,  $C_l=50fF$  and Rise time=0.05ns.

MPTA model and Pade model [13] match very closely for the same order of 2/2. However, computational complexity of the proposed model is less than that of the Pade model, because for the same accuracy the former needs less number of poles than the latter.

Fig. 3 shows the results of finite ramp response for the rise time of 0.1ns, line with length of 0.5mm, source resistance of 100 $\Omega$  and load capacitance of 100fF. The obtained overshoot of proposed model matches with existing Pade model [13] for the same approximation order of 2/2.

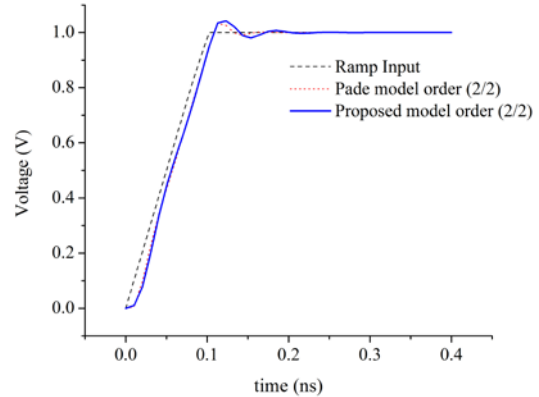


Fig.3. Ramp response of single line when length =0.5mm,  $R_s=50\Omega$  and  $C_l=50fF$  and Rise time=0.1ns.

Tables II and III give the comparisons of 50% delay and overshoot values obtained using HSPICE W element model, Pade model [13] and proposed model for various lengths, source Resistances, load Capacitances and rise times. These tables include the average and maximum error percentages values of Pade model and proposed model with respect to HSPICE. From Table II, the Pade model of order 2/2 has average and maximum error of 0.73% and 3.9%, whereas proposed model has 0.41% and 1.53% respectively.

For global interconnects (1-5 mm) the proposed model works much better than Pade model for delay and overshoot estimation. Both Pade and proposed models perform similarly for smaller length (<1mm) interconnects but for longer lengths of 5mm, proposed model has less error percentage.

From Table III, it is observed that the Pade model [13] has maximum overshoot error of 1.05%, while the proposed model has an error of 0.96%. In the case of overshoot estimation the proposed model is best for all cases. Overall, the average error percentages of delay and overshoot estimations are within 1% for the proposed model.

Table II: Comparisons of 50% delay of HSPICE W Element, Pade model and proposed model for various lengths, source Resistances, load Capacitances and input Ramp rise times.

L (mm)	R <sub>s</sub> (Ω)	C <sub>L</sub> (fF)	t <sub>r</sub> (ns)	HSPICE	Pade model [13] order 2/2	Proposed Model order (2/2)
				50% delay (ps)	50% delay (ps)	50% delay (ps)
0.1	50	50	0.1	53.45	53.5	53.5
	100	100	0.05	36.45	36.5	36.5
0.5	50	50	0.1	57.33	57.5	57.6
	100	100	0.05	43.79	43.9	43.95
1	50	50	0.1	61.92	61.95	61.94
	100	100	0.05	52.94	53.1	53.05
5	50	50	0.1	135.6	136.7	136.5
	100	100	0.05	125.11	120.2	123.2
Average error % w.r.t. HSPICE					0.73	0.41
Maximum error % w.r.t. HSPICE					3.9	1.53

Table III: Comparisons of Overshoot of HSPICE W Element, Pade model and proposed model for various lengths, source Resistances, load Capacitances and input Ramp rise times.

L (mm)	R <sub>s</sub> (Ω)	C <sub>L</sub> (fF)	t <sub>r</sub> (ns)	HSPICE	Pade model [13] order (2/2)	Proposed Model order (2/2)
				Overshoot (V)	Overshoot (V)	Overshoot (V)
0.1	50	50	0.1	1.004	1.005	1.005
	100	100	0.05	1	1	1
0.5	50	50	0.1	1.035	1.045	1.045
	100	100	0.05	1	1	1
1	50	50	0.1	1.071	1.081	1.075
	100	100	0.05	1	1	1
5	50	50	0.1	1.143	1.155	1.147
	100	100	0.05	1	1	1
Average error % w.r.t. HSPICE					0.378	0.209
Maximum error % w.r.t. HSPICE					1.05	0.96

The computational complexity of the proposed model is less as compared to Pade model, because inverse matrix operation is not needed, which reduced the number of poles required from 5 to 3 at the same approximation order (2/2). As a result the CPU computation time is less as compared to Pade model.

Table IV: CPU time comparison of various models with HSPICE models

Pade model [13] (ms)	Proposed model (ms)	HSPICE W element model (ms)
40	28	15

The CPU computation time to calculate the transfer functions of various models into poles and residues is provided in Table IV. The CPU time of proposed model is a onetime expense to find poles and residues for any input switching pattern, whereas HSPICE analysis is based on numerical integration that has to be performed for each input switching pattern, thus proving that the proposed model is computationally more efficient.

### V. CONCLUSION

This paper presents a novel MPTA based closed form model for delay and overshoot estimation of high speed VLSI interconnects in DSM regime. A single line interconnect has been used for validating

the proposed model by comparing with the Pade model and HSPICE. The delay and overshoot estimations average error percentages are within 1% for the proposed model. In SOC (system on chip) applications, for global lines of lengths 1-5 mm the proposed model is found to be more accurate than existing model. The proposed model is computationally more efficient than HSPICE and Pade model.

### REFERENCES

- [1] Semiconductor Industry Association, The International Technology Roadmap for Semiconductors, 1999.
- [2] W. C. Elmore, "The transient response of damped linear networks with particular regard to wideband amplifiers," J. Appl. Phys., vol. 19, no.1, pp. 55-63, Jan. 1948.
- [3] T.Sakurai, "Closed-form expressions for interconnection delay, coupling, and crosstalk in VLSI's," IEEE Trans. Electron Devices, vol. 40, no. 1, pp. 118-124, Jan. 1993.
- [4] Kahng A B, Muddu S, "An analytical delay model for RLC interconnects", IEEE Trans. Computer-Aided Design of Integrated Circuits and Systems, pp. 1507-1514, 1997.
- [5] Kahng A B, Muddu S, "Two-pole analysis of interconnection trees", Proc. of IEEE MCMC Conf.(MCMC-95), Santa Cruz, California, USA, pp. 105-110, 1995.
- [6] Xiaopeng Ji, Long Ge, Zhiquan Wang, "Analysis of on-chip distributed interconnects based on Pade expansion," Journal of Control Theory and Applications, 7 (1) pp. 92-96, 2009.

- [7] Ren Yinglei, Mao Junfa and Li Xiaochun, "Analytical delay models for RLC interconnects under ramp input", *Frontiers of Electrical and Electronic Engineering in China*, vol. 2, pp. 88-91, March 2006.
- [8] Y. I. Ismail, E. G. Friedman, and J. L. Neves, "Equivalent Elmore delay for RLC trees," *IEEE Trans. Comput.-Aided Design Integr. Circuits Syst.*, vol. 19, no. 1, pp. 83–97, Jan. 2000.
- [9] N.Nakhla, A.Dounavis, R.Achar, M.Nakhla, "DEPACT: Delay extraction based Passive Compact Transmission-Line Macromodeling algorithm," *IEEE Transactions on Advanced Packaging*, vol. 28, issue 1, pp. 13-23, Feb 2005.
- [10] S.Roy, A. Dounavis, "Efficient Delay and Crosstalk Modeling of RLC Interconnects using Delay Algebraic Equations," *IEEE Transactions on Very Large Scale Integration Systems*, vol. 2, issue 2, pp. 342-345, Feb. 2011.
- [11] A. Dounavis, R. Achar, and L. Xin, "Passive closed-form transmission-line model for general-purpose circuit simulators," *IEEE Trans. Microw. Theory Tech.*, vol. 47, no. 12, pp. 2450–2459, Dec. 1999.
- [12] A. Dounavis, R. Achar, and M. Nakhla, "A general class of passive macromodels for lossy multiconductor transmission lines," *IEEE Trans. Microwave Theory Tech.*, vol. 49, no. 10, pp. 1686–1696, Oct. 2001.
- [13] S. Roy and A. Dounavis, "Closed-Form Delay and Crosstalk Models for RLC On-Chip Interconnects using a Matrix Rational Approximation," *IEEE Transactions on Computer-Aided Design of Integrated Circuits and Systems*, vol. 28, issue 10, pp. 1481 - 1492, Oct. 2009.
- [14] C. Brezinski. *Pade-Type Approximation and General Orthogonal Polynomials*. Birkhäuser, Basel, 1980.
- [15] C. Q. Gu. Matrix Pade-type approximant and directional matrix Pade approximant in the inner product space. *J Comput. Appl. Math.* 2004, 164-165: 365-385.

# A Fuzzy Based Controller for Wind Energy Conversion System Using PWM CSI with Diode Rectifier and Buck Converter

Shahram Javadi, Mehrnaz FardAmiri

**Abstract**—In this paper, a fuzzy based controller is proposed for wind energy conversion systems (WECSs) that operate in the range of several mega-Watts and are based on permanent magnet synchronous generator (PMSG). A diode rectifier, a buck converter, and a pulse-width-modulated (PWM) current source inverter (CSI) comprise this converter. The system has two DC current requirements that are analyzed and compared. These requirements are i) maximum power point tracking (MPPT) that must be achieved by the generator and diode rectifier and ii) the desired grid power factor that must be obtained by the grid and PWM CSI. It is shown through theoretical analysis that, in order to achieve all the control objectives in the full wind turbine operating range, a buck converter is necessary. Furthermore, a fuzzy based control scheme is presented in this paper for compensating the reactive power of the grid. To decrease the system loss, the DC current is controlled at the lowest required level. The proper performance of the proposed system over a wide range of operating conditions is demonstrated through simulation results on a 1.5 MW.

**Keywords**—Current source inverter, Diode rectifier, DC current minimization, PMSG, WECS.

## I. INTRODUCTION

IN recent years, there has been a rapid growth in wind energy conversion system (WECS) that triggers technology advancements in industry. Due to its high efficiency and elimination of the gear box, the direct-drive permanent magnet synchronous generator (PMSG) has attracted the attention of many researchers. In spite of the fact that most of the commercial WECSs use voltage source converters, configurations that are based on current source converter (CSC) seem to be promising solutions as the power ratings of individual turbines increase. The current source converters have been widely used in high-power drive applications. This kind of converter has some outstanding features such as grid friendly waveform, compact technology, and simple control scheme [1].

The CSC configurations used in WECS are classified into three main groups. The first group employs PWM current

This work was supported in part by the Islamic Azad University, Central Tehran Branch.

Sh. Javadi is assistant professor in Islamic Azad University, Central Tehran Branch in Electrical Engineering Department (corresponding author, e-mail: sh.javadi@iauctb.ac.ir).

M. Fardamiri is M.Sc. graduate of Electrical Engineering Department, Islamic Azad University, Central Tehran Branch (e-mail: m.fardamiri@yahoo.com).

source rectifier (CSR) and PWM current source inverter (CSI) [2] therefore, high levels of freedom are provided for the control objectives. However, the control scheme design is complicated and the switching devices are relatively expensive. The second group of configurations uses a diode rectifier and thyristor inverter. This group is reliable, benefits from a well-established technology, and has low costs [3]. However, disadvantages such as lack of reactive power control, extra costs of the compensation system, and poor grid waveforms make it a less proper choice for modern WECS. The third type of configuration is composed of diode rectifier and PWM CSI inverter. In this configuration, within a limited range, both the active and reactive powers that are transferred to the network could be controlled.

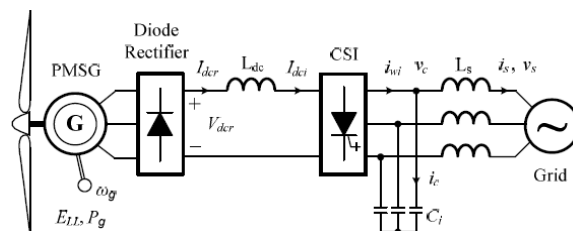


Fig 1. A PMSG-based WECS using PWM CSI and diode rectifier

Using the results of DC current analysis carried out on the third configuration, this paper presents a full scale PWM CSI with a diode rectifier and a buck converter. Also, a control scheme is developed to optimize the system operation. Simulation results on a two mega-watt system are also included

## II. DC CURRENT ANALYSIS

Generally, in WECS, the flow of power is unidirectional. This means that the power always flows from the wind turbine to the grid. Diode rectifiers are reliable and inexpensive devices that could be used as generator side converters in order to transfer the AC power to DC power. Figure 1 shows the configuration a PWM CSI and a diode rectifier that are employed in a PMSG-based WECS. Next, in this paper, it will be shown through DC current analysis that this system has a fairly limited range of operation.

### 2.1. Generator side DC current analysis

In order to achieve proper operation of generator, the DC current requirements must be analyzed. To carry out this analysis, a simplification can be made by considering the output of the diode rectifier as a constant DC current,  $I_{dcr}$ .



The DC current  $I_{dci}$  and the reactive power of the grid are regulated by the PWM SCI so that the power could be properly delivered to the grid. The voltage oriented synchronous frame is the basis of the control scheme developed in this paper. This control scheme uses the space vector modulation (SVM) scheme with flexible modulation index and delay angle controls.

In the grid voltage oriented synchronous frame, the q-axis component of the grid voltage,  $v_{sq}$ , becomes equal to zero; therefore, the magnitude of the grid voltage becomes equal to its d-axis component,  $v_{sd}$ . Following equations can be used to calculate the active and reactive powers of the grid:

$$P = 1.5(v_{sd} i_{sd} + v_{sq} i_{sq}) = 1.5v_{sd} i_{sd} \quad (11)$$

$$P = 1.5(v_{sq} i_{sd} - v_{sd} i_{sq}) = -1.5v_{sd} i_{sq} \quad (12)$$

The power requirements of the grid determine the DC current reference. Using equations (11) and (12), the active and reactive power references can be converted into grid d- and q-axis current references. The current references of the converter are provided by the sum of the calculated capacitor current and grid reference currents. Assuming that modulation index,  $m_i$ , is kept at its maximum value which is equal to unity, then the reference current can be derived using (9).

However, it should be noted that at low levels of power where only 0.3  $I_{dci}$  pu is enough for satisfying the system operation, this high value is not efficient. Both device switching loss and conduction loss are could be decreased if the DC current reference is set to the minimum value.

The active power output control is responsible for regulating the DC current therefore. The fuzzy controller provides the reference for adjusting the active current of the grid,  $i_{sd}$ . The fuzzy rules are given in Table 1. The membership function for inputs and outputs of fuzzy controller is shown in Figure 4.

The given reactive power reference is used to calculate the reactive current reference of the grid. Finally, using the reference converter currents which are the total of reference grid currents and capacitor currents, the converter modulation index,  $m_i$ , and delay angle for SVM gating generation are calculated.

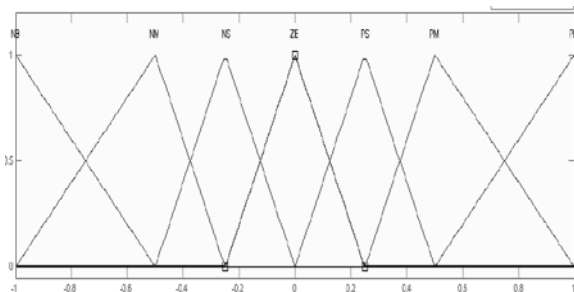


Fig 4. Membership function for inputs and outputs of fuzzy controller

Table 1. Fuzzy rules for fuzzy controller.

Ce e	NB	NM	NS	ZZ	PS	PM	PB
NB	NB	NB	NB	NB	NM	NS	ZZ
NM	NB	NB	NB	NM	NS	ZZ	PS
NS	NB	NB	NM	NS	ZZ	PS	PM
ZZ	NB	NM	NS	ZZ	PS	PM	PB
PS	NM	NS	ZZ	PS	PM	PB	PB
PM	NS	ZZ	PS	PM	PB	PB	PB
PB	ZZ	PS	PM	PB	PB	PB	PB

### 3.2. Control for the buck converter

The MPPT from the generator of the wind turbine is achieved by regulating the speed of the generator to the optimum point. The wind speed information is fed to the MPPT block and then the optimum turbine speed reference is generated for the generator speed regulator. Since the diode rectifier is not a controllable device, the generator speed or power output can only be adjusted by DC voltage or current or regulation of the diode rectifier output. This regulation is carried out by controlling the duty cycle of the buck converter. The input and out power of the buck converter is expressed by the following equation:

$$I_{dci} = \frac{I_{der}}{D} \quad (13)$$

In the equation above, D represents the duty cycle of the buck converter.

Since the grid voltage has stiff characteristic, the DC current loop of the PWM CSI is designed in such a way that it is much faster than the generator speed control loop. Therefore, in the design of the control loop for the buck converter, it could be assumed that  $I_{dci}$  is constant. Therefore, DC current level at the diode rectifier side is directly adjusted by tuning the duty cycle. This causes the operating torque and speed of the generator to change.

## 4. Simulation Results

The Matlab/Simulink environment has been used to simulate the proposed system and control scheme. Table 2 shows the system parameters. Both transient responses and steady state operations of the entire system under different wind speeds are considered in the simulation. The proper reactive power control is also verified under different power factor reference, 0.95 lagging and 0.95 leading, and unity.

Detailed profiles of PF reference, reactive power reference, and wind speed that is used in simulation are provided in Table 3. When inductive reactive power is injected into the grid by the PWM CSI, a positive value is assumed for the reactive power.

Figure 5 and Figure 6 show the waveform of simulation. When a step change from half (6 m/s) to the nominal value (12 m/s) occurs in wind speeds at  $t=1$  seconds, as it is shown in Figure 6 (a) and (c), the duty cycle of the buck converter accordingly adjusts the rotational speed of the PMSG. The rotor speed properly follows the reference in steady state. This means that the maximum power is achieved at the corresponding wind speed. Figure 6 (b) displays the generated active power which is related to the wind speed change i.e. 0.25 MW at 6m/s and 1.5 MW at the nominal wind speed. Also, the DC link current displayed in Figure 6 (e) change accordingly to accommodate the variations in active/reactive powers. The modulation index of the PWM CSI being kept close to unity (Figure 6 (d)) indicates that under all operating conditions, the current of the DC link is kept fixed at its minimum level in steady state.

The simulation results of another test are given in Figure 6. The reactive power reference and wind speed change according to Table 3. Figure 7 (a) shows the active and reactive power of CSI. As can be seen from this figure the active power output increases with the wind speed step change and the reactive power properly follows the references given in Table 2. Figures. 6 (b) and 6 (c) show the Dc link current and the duty cycle of the buck converter, respectively. These two values change depend on the wind speed and the reactive power reference. Figure 6 (d) shows the grid voltage and current in the duration 2.4 to 2.6 (secs) in which the reactive power reference changes from +0.5 MW to -0.5 MW. At first the current is leading to the voltage (positive reactive power reference) and at second the current is lagging to the voltage (negative reactive power reference).

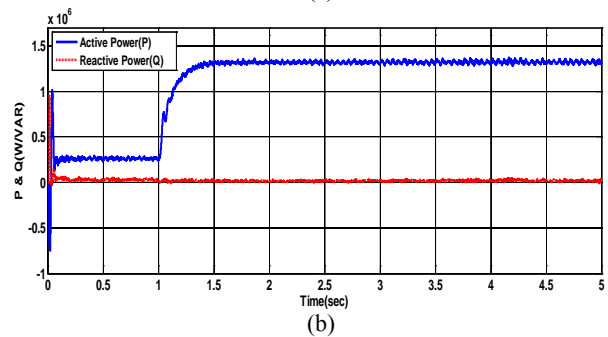
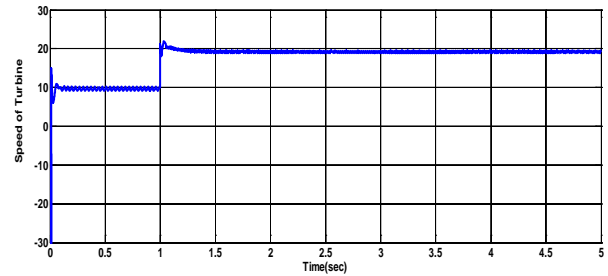
Table. 2. System parameters used in the simulation

<b>Generator parameters</b>		
(Rated, pu based on generator side)		
Apparent Power	2 MVA	1 pu
Stator phase voltage	1732 V (rms)	1 pu
Stator current	513 A (rms)	1 pu
Frequency	11 Hz	1 pu
Power factor	0.75	1 pu
Pole pairs	30	1 pu
Magnetic flux linkage	37.7 Wb (rms)	1 pu
$L_{d1}, L_{q1}$	19.4 mH	0.398 pu
<b>DC link parameters</b>		

(pu based on generator side)		
$C_{d1}$	2100 $\mu$ F	1 pu
$L_{d1}$	48.8 mH	1 pu
<b>Grid side parameters</b>		
(Rated, pu based on grid side)		
Apparent Power	1.5 MVA	
Phase voltage	1732 V (rms)	1 pu
Line current	405 A (rms)	1 pu
Power factor	0.95	
Frequency	60 Hz	1 pu
$L_g$	1.08 mH	0.12 pu
$C_g$	471 $\mu$ F	0.6 pu

Table. 3. Wind speed, PF and reactive power references

Time Duration (s)	0-0.5	0.5-1	1-1.5	1.5-2	2-2.5	2.5-3
Wind Speed (m/s)	6			12		
Q <sub>ref</sub> (MW)	0.5	-0.5	0	0	0.5	-0.5



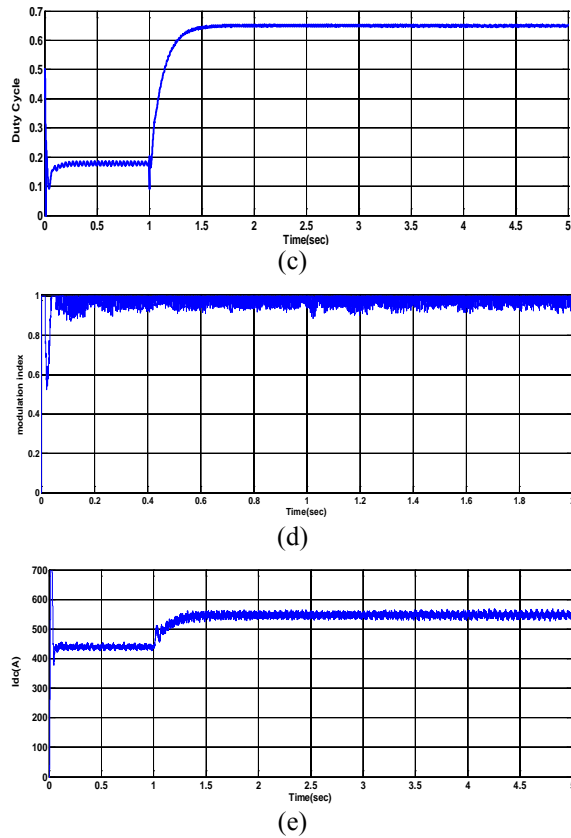


Fig 5. Simulation waveforms under various wind speeds and power factor requirements. a) Wind turbine and rotor speed b) Grid active and reactive powers. c) Duty cycle of the buck converter. d) Modulation index of the PWM CSI. e) the DC link current.

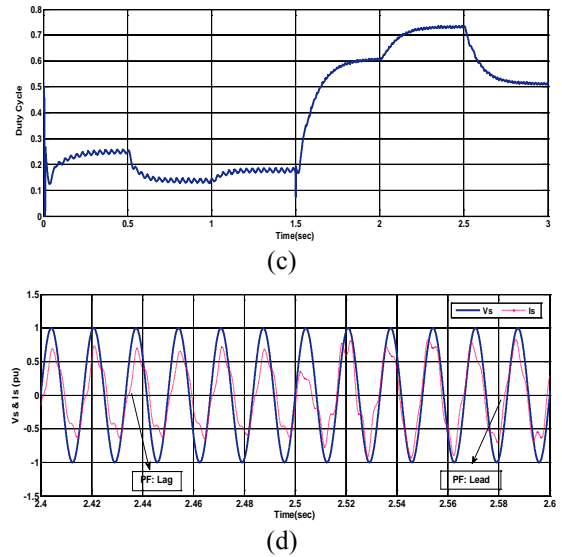
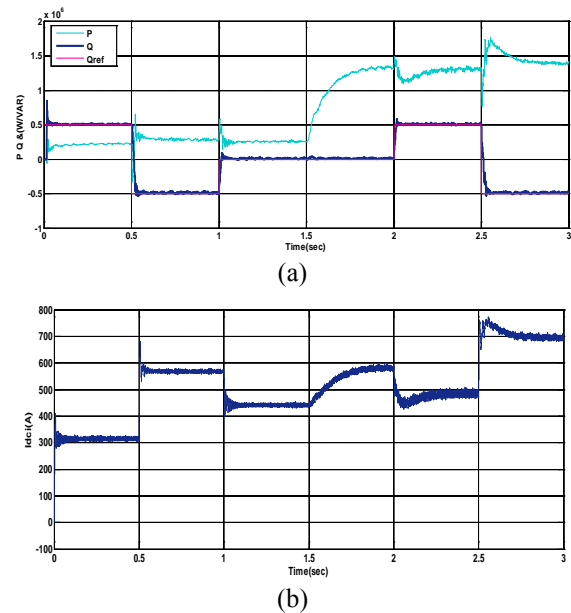


Figure 6. Simulation waveforms of grid voltage and current under various wind speeds and power factor requirements. (a) Grid voltage and current waveforms at 6m/s (Unity PF). (b) at 12m/s (Unity PF). (c) at 12m/s (PF=0.95 leading). (d) at 12m/s (PF=0.95 lagging).

### I. CONCLUSION

In this paper, a state-of-the-art configuration is proposed for PMGS-based WECS. This configuration is composed of a diode rectifier, a PWM CSI, and a buck converter. Through a comprehensive steady-state DC current analysis of the configuration of diode rectifier connected with PWM CSI, it is shown that the existence of a buck converter is necessary for full range active/reactive power control. A fuzzy control scheme is also developed for the proposed configuration so that it can achieve maximum power tracking from the fluctuating wind and grid power factor control requirements (unity, leading or lagging). Moreover, in order to decrease the total power loss, the operating DC current in the PWM CSI is minimized. Simulation results revealed that the proposed configuration and control scheme has an appropriate performance

### II. ACKNOWLEDGMENT

The authors thanks Islamic Azad University, central Tehran branch for all helps and supports.

### REFERENCES

- [1] Bin Wu, "High-Power Converters and AC Drives," Wiley IEEE Press, March 2006.
- [2] Jingya Dai, Dewei Xu, Bin Wu, "A Novel Control System for Current Source Converter Based Variable Speed PM Wind Power Generators", Power Electronics Specialists Conference, PESC 2007, pp. 1852-1857, 2007.
- [3] Z. Chen, E. Spooner, "Current source thyristor inverter and its active compensation system," IEE Proc.-Gener. Transm. Distrib., vol. 150, No. 4, July 2003.
- [4] Ned Mohan, Tore M. Undeland, William P. Robbins, "Power Electronics:

Converters, Applications, and Design,” 3rd edition, Wiley, October 2002.

- [5] Wei Li, Chad Abbey, Géza Joós, “Control and Performance of Wind Turbine Generators based on Permanent Magnet Synchronous Machines Feeding a Diode Rectifier,” Power Electronics Specialists Conference, 2006. PESC '06. 37th IEEE 18-22, pp. 1-6, June 2006.
- [6] Yun Wei Li, Pande, M., Zargari, N.R., Bin Wu, “DC-Link current minimization for high-power current-source motor drives,” IEEE Trans. Power Electron., vol. 24 , pp. 232 – 240, 2009.

**Dr. Shahram Javadi** received his B.Sc. from Amirkabir University, M.Sc. from K.N.T. University of Technology and Ph.D. from I.A.U., Science and Research Branch in Electrical Engineering. He has been in charge of faculty member at Technical and Engineering Faculty in I.A.U., Central Tehran Branch (1996-Now) and has taught courses in the Electrical Engineering Department. He has also served as Visiting Professor at the ISEL, Institute /Superior of Engineering of Lisbon since 2008 while he is currently Professor and Director Research of I.A.U., Central Tehran Branch, IRAN.

He is an active researcher in Artificial Intelligence, Smart Grids, Power Electronic and Control Systems. He is author of 2 books and has published over than 30 papers in international books, journals and conferences.

He is director general of international journal of electrical engineering smart systems (IJSEE) and editorial board of international conference on mechanical engineering (IASEM) and one of the active members of WSEAS, World Scientific and Engineering Academy and Society.

Dr. Javadi is the member of International & Technical Committee of WSEAS, IEEE, Cigre, Academic board for International Power System conference PSC, Academic board for Power System Protection & Control conference PSPC, Member of Scientific Committee of Power Systems Protection & Control conference PSPC, Member of IAEEE (Iranian Association of Electrical & Electronics Engineers), Member of Scientific Committee of Iranian Wind Energy Society and Member of Iranian Fuzzy Systems Society.

# Analysis of AM-to-PM Distortion Effect on ACPR Performances

<sup>1</sup>Eun-Hee Kim, <sup>1</sup>Hoyong Kang, and <sup>2</sup>Kwyo Lee

<sup>1</sup>ETRI, Daejeon, Korea, <sup>2</sup>KAIST, Daejeon, Korea

**Abstract**— This paper presents nonlinearity analysis of general AM transmitters, especially the AM-to-PM deterioration. In addition, linear approximation is applied to represent phase deviation depending on output amplitude of power amplifier. We adopt saturated class-A and class-E power amplifiers to compare their AM-to-PM characteristics. Then, we expect the resulted transmitter output spectrum of AM modulated signals, including unwanted side tones. It is helpful to derive ACPR performance degradation for AM modulated signals and to design overall RF systems.

**Index Terms**— AM-to-PM distortion analysis, ACPR degradation from AM-to-PM effect, nonlinearity of switching power amplifier, polar modulator

## I. INTRODUCTION

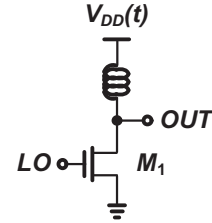
In recent years, many research groups focus on TX linearization technique, and it is steadily continued to invent new linearization methods. Except for the linearization methods based on multiple power amplifiers, such as outphasing or Doherty technique, they can be categorized into two types. Corresponding to the directivity of correction signal in auxiliary path, the one is feed-forward linearization, and the other is based on feedback linearization. Considering the trade-off between system complexity and phase correction capability, it is necessary to comprehend the AM-PM distortion effect on ACPR performance of TX.

In this paper, to estimate the ACPR performance degradation, analytical approaches on AM-to-PM distortion is presented. Section II deals with the simplified AM-to-PM mechanism of general switching power amplifiers, classified as class-E type ones. To expect its effect on system performances, detailed analysis is given in section III, and conclusions are discussed in section IV.

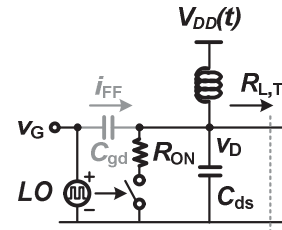
## II. MECHANISMS OF AM-TO-PM DISTORTION

Fig. 1 (a) shows the topology of a general class-E switching power amplifier based on modulated supply voltage of  $V_{DD}(t)$ , and its behavioral model is given in Fig. 1 (b) [1]. For constructing the behavioral model, a switching transistor is replaced with series network of an ideal switch and its on-resistance  $R_{ON}$ , and the switch is activated in accordance with the polarity of input LO signal. It is desirable that the output RF signal maintains constant phase regardless of output amplitude, exactly opposite to the LO; however, a side effect occurs due to

This work was supported by internal R&D fund projects (14RC1310) of Electronics and Telecommunications Research Institute (ETRI), Republic of Korea, “Sensor network platform technology development for hazardous materials monitoring”.



(a) topology of class-E PA (except output matching)



(b) simplified behavioral model of class-E PA  
Fig. 1. Topology and behavioral model of class-E PAs

parasitic capacitance of  $C_{gd}$ , between gate and drain terminal of the switching transistor  $M_1$ . Then, additional current path through the capacitor is created, and it results that the feed-forward current of  $i_{FF}$  flows from the gate to drain terminal. The feed-forward current of  $i_{FF}$ , represented with grey-color, can be expressed as

$$i_{FF}(t) = (v_D(t) - v_G(t)) \cdot j\omega C_{gd} \quad (1)$$

where  $v_D(t)$  and  $v_G(t)$  is the time-varying drain and gate voltage of switching transistor. Then, the output drain voltage can be derived as

$$v_D(t) = -V_{DD}(t) + v_{FF}(t) = -\beta(t) \cdot V_{DD} + R_{L,T} \cdot i_{FF}(t) \quad (2)$$

where  $\beta(t)$  is the ratio of the supply voltage to output voltage, and  $R_{L,T}$  is the load impedance at drain terminal.

In the equation, the former product term equals to an ideal drain voltage with non-linearly amplitude-modulated envelope, which maintains constant phase of  $180^\circ$ . On the other hand, the latter term with  $90^\circ$  phase, caused by the feed-forward current, brings additional phase rotation on the output. It results in the phase output of drain voltage as

$$\theta(t) = \tan^{-1} \left( \frac{V_{FF}(t)}{V_{DD}(t)} \right) \quad (3)$$

$$= \tan^{-1} \left\{ \frac{(R_{L,T} \cdot i_{FF}(t))}{(\beta(t) \cdot V_{DD})} \right\}$$

, and it means that the output signal undergoes phase rotation affected by the envelope of amplitude-modulated

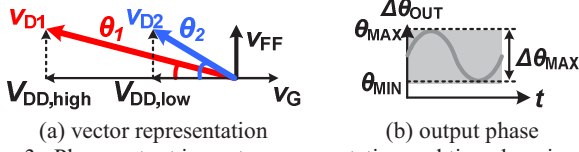


Fig. 3. Phase output in vector representation and time domain

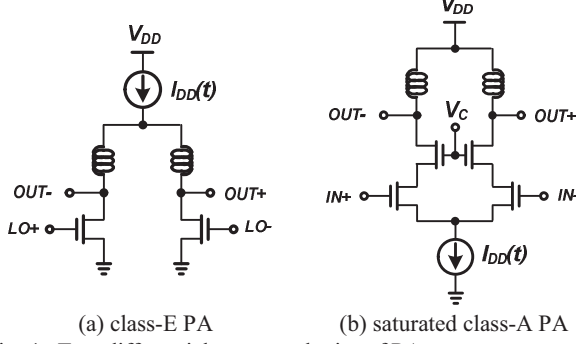


Fig. 4. Two differential-type topologies of PA

output. Fig. 3 (a) depicts representation with vector diagram depending upon magnitude of output drain voltage. As the magnitude of supply voltage changes, output phase differs between  $\theta_1$  and  $\theta_2$ , and it results the maximum phase variation, given as

$$\Delta\theta_{MAX} = \tan^{-1}(V_{FF}/V_{DD,low}) - \tan^{-1}(V_{FF}/V_{DD,high}) \quad (4)$$

where the output phase of  $\Delta\theta_{OUT}$  forms the shaded-region as shown in Fig. 3 (b).

### III. ANALYSIS OF AM-TO-PM DISTORTION

To estimate the relation between output amplitude and phase practically, two topologies of differential power amplifiers are applied as follows.

1) *for class-E power amplifiers*: Fig. 4 (a) shows the differential topology of class-E power amplifier as the first example, which adopts supply modulation for delivering AM modulated signals [2]. Under varying output amplitude, its simulated phase response is shown in Fig. 5. When applying linear approximation between output amplitude and modulated phase deviation roughly, at maximum modulation index of 100%, the maximum phase difference reaches up to  $(\pi/8)$ .

2) *for saturated class-A power amplifiers*: The differential topology of saturated class-A power amplifier is depicted in Fig. 4 (b) [3]. It has almost similar topology to that of class-E power amplifier except that cascode transistor is additionally inserted between switching transistors and differential output terminals; however, the cascode stage performs a crucial role in alleviating the amount of phase deviation. As shown in the Fig. 5, under the linear approximation, the

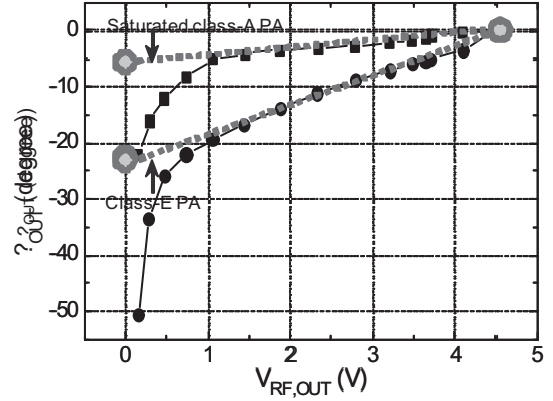


Fig. 5. Simulated phase response of class E PAs and saturated class A PAs

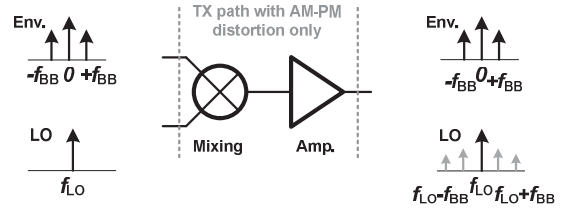


Fig. 6. Side tone generated by AM-to-PM distortion

maximum phase deviation shrinks to  $(\pi/30)$ , even at modulation depth of 100%.

Especially, in the both cases, it is remarkable that the output phase response has approximately linear relation proportional to their output amplitude. It means that the equations of output envelope and phase can be expressed as below.

$$V_{OUT}(t) = V_{CM} + (mi/2) \cdot \Delta V_{OUT,MAX} \cdot \cos \omega_{BB}t \quad (5)$$

$$\theta_{OUT}(t) = \theta_{CM} + (mi/2) \cdot \Delta\theta_{OUT,MAX} \cdot \cos \omega_{BB}t \quad (6)$$

Based on the output phase equation of (6), numerical analysis of AM-to-PM effect on TX output spectrum is performed. Fig. 6 provides conceptual diagram for the relation between the AM-to-PM distortion and RF output spectrum in the TX path. Assumed that virtual envelope output has perfectly linear relation with input signal, the non-linear mechanism from AM-to-PM distortion is supposed to be reflected on their output LO as a whole.

Assuming that an ideal LO signal is  $\cos(\omega_{LO}t + \phi_N(t))$ , after passing through the TX, the effective LO signal at TX output can be extracted as

$$\begin{aligned} V_{LO,eff}(t) &= A \cdot \cos(\omega_{LO}t + \phi_N'(t) + \theta_{OUT}(t)) \\ &= A \cdot \left\{ \begin{array}{l} \cos(\omega_{LO}t + \phi_N'(t)) \cdot \cos(\Delta\theta \cdot \cos \omega_{BB}t) \\ -\sin(\omega_{LO}t + \phi_N'(t)) \cdot \sin(\Delta\theta \cdot \cos \omega_{BB}t) \end{array} \right\} \quad (7) \end{aligned}$$

TABLE I QUADRATURE COEFFICIENTS OF AMPLITUDE-MODULATED PA OUTPUT

	Coefficient of $A_n$ (in-phase)	Coefficient of $B_n$ (quadrature)
	$\cos(\omega_{LO} \pm n\omega_{BB})t$	$\sin(\omega_{LO} \pm n\omega_{BB})t$
$n=0$	$(1 - mi^2 \cdot \Delta\theta_{OUT,MAX}^2 / 4) \cdot (2 - mi) / 2$	$mi^2 \cdot \Delta\theta_{OUT,MAX} / 4$
$n=1$	$(1 - 3/8 \cdot mi^2 \cdot \Delta\theta_{OUT,MAX}^2) \cdot mi / 4$	$mi \cdot (2 - mi) \cdot \Delta\theta_{OUT,MAX} / 4$
$n=2$	$-mi^2 \cdot (2 - mi) \cdot \Delta\theta_{OUT,MAX}^2 / 16$	$mi^2 \cdot \Delta\theta_{OUT,MAX} / 8$
$n=3$	$-mi^3 \cdot \Delta\theta_{OUT,MAX}^2 / 32$	0

where  $A$  is voltage gain of TX path and  $\phi_N'(t)$  is phase noise property of LO signal after TX. The  $\Delta\theta$  is output phase deviation at specific modulation index, equal to  $(mi/2) \cdot \Delta\theta_{MAX}$ . Using Taylor series expansion, it can be developed as following, represented with the terms of phase deviation and modulation index.

$$V_{LO,eff}(t) = A_V \cdot \left\{ \begin{array}{l} (1 - \Delta\theta^2/4) \cdot \cos(\omega_{LO}t + \phi_N'(t)) \\ + (\Delta\theta/2) \cdot \sin((\omega_{LO} \pm \omega_{BB})t + \phi_N'(t)) \\ - (\Delta\theta^2/8) \cdot \cos((\omega_{LO} \pm 2\omega_{BB})t + \phi_N'(t)) \end{array} \right\} \quad (8)$$

It reveals that the AM-to-PM distortion of PA induces unwanted side tones around LO frequency. Applying an ideal AM envelope with modulation index of  $mi$ ,

$$V_{BB}(t) = \left( \frac{2 - mi}{2} \right) + \left( \frac{mi}{2} \right) \cdot \cos \omega_{BB}t \quad (9)$$

, the PA output signal of  $V_{PA}(t)$  is derived as

$$V_{PA}(t) = A_V \cdot \left\{ \begin{array}{l} \frac{K_1 \cdot (2 - mi)}{2} \cdot \cos \omega_{LO}t \\ + \frac{K_2 \cdot mi}{2} \cdot \sin \omega_{LO}t \\ + \frac{(K_1 + K_3) \cdot mi}{4} \cdot \cos(\omega_{LO} \pm \omega_{BB})t \\ + \frac{K_2 \cdot (2 - mi)}{2} \cdot \sin(\omega_{LO} \pm \omega_{BB})t \\ + \frac{K_3 \cdot (2 - mi)}{2} \cdot \cos(\omega_{LO} \pm 2\omega_{BB})t \\ + \frac{K_2 \cdot mi}{4} \cdot \sin(\omega_{LO} \pm 2\omega_{BB})t \\ + \frac{K_3 \cdot mi}{4} \cdot \cos(\omega_{LO} \pm 3\omega_{BB})t \end{array} \right\} \quad (10)$$

where the coefficients of  $K_1$ ,  $K_2$ , and  $K_3$  are given as  $(1 - \Delta\theta^2/4)$ ,  $(\Delta\theta/2)$ , and  $-(\Delta\theta^2/8)$ , respectively. The coefficients are summarized in Table I. To investigate ACPR affected by AM-to-PM, we can utilize the above quadrature coefficient for each frequency component.

$$ACPR_{@ \pm 1CH} = 20 \cdot \log_{10} \left( \frac{\sum V_{adjacent}}{\sum V_{reference}} \right) \quad (11)$$

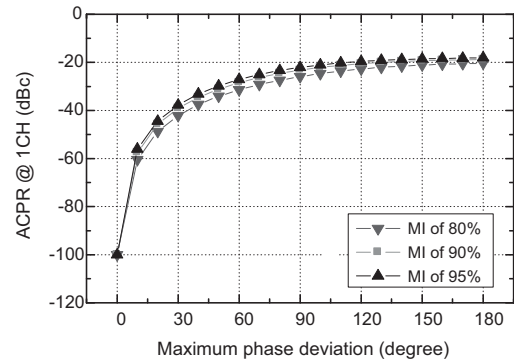


Fig. 7. ACPR results with varying maximum phase deviation

where  $ACPR_{@ \pm 1CH}$  is the channel power ratio between reference channel and its first adjacent channel. In this paper, mobile RFID regulation is applied as an example in which the channel bandwidth is five times as data rate of transmitted signal. Then, the ACPR performance can be derived as shown in Fig. 7 under varying phase deviation and modulation index.

#### IV. CONCLUSIONS

A novel analysis to estimate the AM-to-PM distortion effect on TX output spectrum is presented in detail. Under various modulation depth and maximum phase deviation, we investigate the ACPR performances according to mobile RFID regulations. We expect that this analysis method will provide valuable guidance in TX system design procedures and performance evaluation.

#### REFERENCES

- [1] Reynaert and M. Steyaert, "A 1.75-GHz polar modulated CMOS RF power amplifier for GSM-EDGE," *IEEE J. Solid-State Circuits*, vol. 40, no. 12, Dec. 2005.
- [2] S. C. Cripps, *RF Power Amplifiers for Wireless Communications*, Norwood, MA: Artech House, 1999.
- [3] E. Kim, K. Lee, and J. Ko, "An isolator-less CMOS RF front-end for UHF mobile RFID reader," *IEEE Int. Solid-State Circuits Conf. Dig. Tech. Papers (ISSCC)*, 2011.

# Self-Localization in RFID-Tag Information Networks Using Extended UFIR Filtering

JUAN POMARICO-FRANQUIZ, YURIY S. SHMALIY

Universidad de Guanajuato

Department of Electronics Engineering Key Lab. Adv. Proc. Contr. for Light Industry

Palo Blanco, 36885, Salamanca

MEXICO

juanjose2003@hotmail.com, shmaliy@ugto.mx

SHUNYI ZHAO

Jiangnan University

Wuxi, Jiangsu

P. R. CHINA

shunyi@alberta.ca

*Abstract:* The radio frequency identification (RFID) tags have proved their usefulness for vehicle self-localization in grid navigation spaces. Each tag can deliver information about the 2D or 3D local surrounding. To use this information, high accuracy in vehicle localization is required. We show that the recently designed extended finite impulse response (EFIR) filter meets this need. The EFIR filter produces an unbiased estimate while ignoring the noise statistics which are often unknown to the engineer. The EFIR filter is tested and compared to the extended Kalman filter (EKF). Better performance of the EFIR filter is demonstrated.

*Key-Words:* Extended FIR filter, extended Kalman filter, RFID tag, indoor localization.

## 1 Introduction

The methods which utilize facilities of the radio frequency identification (RFID) tags [1] have gained currency for indoor vehicle (robot) localization in the last decade. Each tag has its own identification (ID) number corresponding to unique coordinates of location and may be either active [2] or passive [3, 4]. Information describing the surrounding can also be programmed in the tag [5] that makes the RFID tag-nested grids highly attractive for industrial and other needs. This information, however, may be useful only if vehicle localization is provided with high accuracy. The multilateration algorithms based on observation and averaging over some time interval are most widely used here [6, 7]. Other algorithms [8, 9] can also be employed, including the directional ones [10, 11] and hybrid structures [1, 9, 12–15].

A common drawback of the multilateration and other “algebraic” algorithms is that noise reduction often cannot be provided efficiently or otherwise the bias error can be large. The probabilistic particle or Monte Carlo filters were constructed in [16, 17] to show much better performance. An application of the extended Kalman filter (EKF) [18] was shown in [19, 20] and a comparison of the extended, quadrature, and particle Kalman filters was recently given in [21]. A disadvantage of the Kalman filter-based estimators is that noise is required to be white and its statistics and the initial error statistics are known in order for the EKF to be suboptimal. Otherwise, the

performance of EKF may be poor [22–25].

The FIR alternative to the Kalman filter has been under the development for decades [26–28]. It is known to be more robust than the Kalman filter under the unbounded disturbances [29]. It is also less sensitive to noise and distributions and produces smaller round-off errors owing to averaging. Furthermore, complex optimal FIR (OFIR) structures [26, 27] do not demonstrate essential advantages against simple unbiased FIR (UFIR) ones [30] which ignore the noise statistics and initial error statistics [23, 27]. The difference between the OFIR and UFIR estimates vanishes by large averaging intervals that makes the iterative UFIR filter [31] highly attractive for applications.

## 2 RFID Tag-Based Vehicle Localization

We consider a schematic diagram given in Fig. 1 assuming that a vehicle travels in direction  $d$  and its trajectory is controlled by the left and right wheels. The incremental distances vehicle travels by these wheels are  $d_L$  and  $d_R$ , respectively. The distance between the left and right wheels is  $b$  and the stabilized wheel is not shown. The vehicle moves in its own planar Cartesian coordinates  $(x_r, y_r)$  with a center at  $M(x, y)$ .

It is supposed that the vehicle is equipped with a fiber optic gyroscope (FOG) [32] which provides measurements of the pose angle  $\Phi$ . On a grid RFID tag-nested floorspace, a vehicle always passes by a

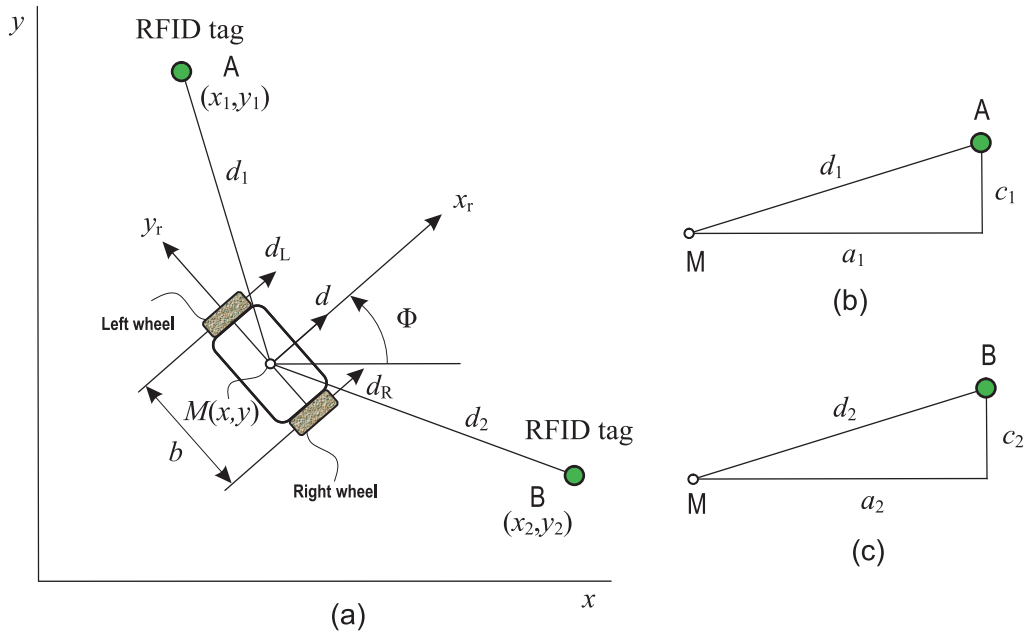


Figure 1: Two-dimensional schematic geometry of a vehicle travelling between two RFID tags with an angle  $\Phi$  measured using a FOG.

pair of tags  $A(x_1, y_1)$  and  $B(x_2, y_2)$  and the reader installed on a vehicle is able to measure the distances  $d_1$  and  $d_2$ . Because altitudes are generally different of the points of installation of the reader and tags, the projections  $a_1$  and  $a_2$  to the vehicle plane are calculated following Fig. 1b and Fig. 1c, where  $c_1$  and  $c_2$  are known. From the vehicle odometry, the incremental distance  $d_n$  and change in heading  $\phi_n$  are provided at discrete time index  $n$  by

$$d_n = \frac{1}{2}(d_{Rn} + d_{Ln}), \quad (1)$$

$$\phi_n = \arctan \frac{d_{Rn} - d_{Ln}}{b} \cong \frac{1}{b}(d_{Rn} - d_{Ln}). \quad (2)$$

The unknown vehicle coordinates  $x_n$  and  $y_n$  and heading  $\Phi_n$  are obtained by the vehicle kinematics with equations

$$f_{1n} = x_n = x_{n-1} + d_n \cos \left( \Phi_{n-1} + \frac{1}{2} \phi_n \right) \quad (3)$$

$$f_{2n} = y_n = y_{n-1} + d_n \sin \left( \Phi_{n-1} + \frac{1}{2} \phi_n \right) \quad (4)$$

$$f_{3n} = \Phi_n = \Phi_{n-1} + \phi_n, \quad (5)$$

in which the values  $x_{n-1}$ ,  $y_{n-1}$ , and  $\Phi_{n-1}$  at time  $n-1$  are projected to time  $n$  by the time-variant incremental distances  $d_{Ln}$  and  $d_{Rn}$  via (1) and (2).

## 2.1 Vehicle State-Space Model

We now introduce a state vector  $\mathbf{x}_n = [x_n \ y_n \ \Phi_n]^T$  of unknown variables and an input vector  $\mathbf{u}_n =$

$[d_{Ln} \ d_{Rn}]^T$  of incremental distances. The random components in these values are supposed to be additive, zero mean, white Gaussian, and uncorrelated. Accordingly, we introduce the state noise vector  $\mathbf{w}_n = [w_{xn} \ w_{yn} \ w_{\Phi n}]^T$  and the input noise vector  $\mathbf{e}_n = [e_{Ln} \ e_{Rn}]^T$ . Then equations (3)-(5) suggest that the vehicle nonlinear state equation is

$$\mathbf{x}_n = \mathbf{f}_n(\mathbf{x}_{n-1}, \mathbf{u}_n, \mathbf{w}_n, \mathbf{e}_n), \quad (6)$$

where  $\mathbf{f}_n = [f_{1n} \ f_{2n} \ f_{3n}]^T$  has components given by (3)-(5). The noise sources  $\mathbf{w}_n$  and  $\mathbf{e}_n$  are zero mean,  $E\{\mathbf{w}_n\} = \mathbf{0}$  and  $E\{\mathbf{e}_n\} = \mathbf{0}$ , have the covariances  $\mathbf{Q} = E\{\mathbf{w}_n \mathbf{w}_n^T\}$  and  $\mathbf{L} = E\{\mathbf{e}_n \mathbf{e}_n^T\}$  and a property  $E\{\mathbf{w}_i \mathbf{e}_j^T\} = \mathbf{0}$  for all  $i$  and  $j$ .

Following Fig. 1, the measured distances  $d_{1n}$  and  $d_{2n}$  as well as angle  $\Phi_n$  are coupled with unknown state variables  $x_n$ ,  $y_n$ , and  $\Phi_n$  as

$$\alpha_{1n} = d_{1n} = \sqrt{(y_1 - y_n)^2 + (x_1 - x_n)^2 + c_1^2}, \quad (7)$$

$$\alpha_{2n} = d_{2n} = \sqrt{(y_2 - y_n)^2 + (x_2 - x_n)^2 + c_2^2}, \quad (8)$$

$$\alpha_{3n} = \Phi_n = \Phi_n. \quad (9)$$

For the observation vector  $\mathbf{z}_n = [z_{1n} \ z_{2n} \ z_{3n}]^T$ , nonlinear function vector  $\mathbf{h}_n(\mathbf{x}_n) = [\alpha_{1n} \ \alpha_{2n} \ \alpha_{3n}]^T$ , and measurement additive noise vector  $\mathbf{v}_n = [v_{1n} \ v_{2n} \ v_{3n}]$ , the state observation equation can be written as

$$\mathbf{z}_n = \mathbf{h}_n(\mathbf{x}_n) + \mathbf{v}_n, \quad (10)$$

where noise  $\mathbf{v}_n$  is white Gaussian with zero mean,  $E\{\mathbf{v}_n\} = \mathbf{0}$ , the covariance  $\mathbf{R} = E\{\mathbf{v}_n\mathbf{v}_n^T\}$ , and the properties  $E\{\mathbf{v}_i\mathbf{w}_j^T\} = \mathbf{0}$  and  $E\{\mathbf{v}_i\mathbf{e}_j^T\} = \mathbf{0}$  for all  $i$  and  $j$ .

## 2.2 Expanded State-Space Model

To use EFIR filtering, we expand  $\mathbf{f}_n \triangleq \mathbf{f}_n(\mathbf{x}_{n-1}, \mathbf{u}_n, \mathbf{w}_n, \mathbf{e}_n)$  as follows:

$$\mathbf{f}_n = \mathbf{F}_n\mathbf{x}_{n-1} + \bar{\mathbf{u}}_n + \mathbf{W}_n\mathbf{w}_n + \mathbf{E}_n\mathbf{e}_n, \quad (11)$$

where  $\hat{\mathbf{x}}_n = [\hat{x}_n \ \hat{y}_n \ \hat{\phi}_n]$  is the estimate of  $\mathbf{x}_n$ ,  $\bar{\mathbf{u}}_n = \mathbf{f}_n(\hat{\mathbf{x}}_{n-1}, \mathbf{u}_n, \mathbf{0}, \mathbf{0}) - \mathbf{F}_n\hat{\mathbf{x}}_{n-1}$  is known and  $\mathbf{F}_n$ ,  $\mathbf{W}_n$ , and  $\mathbf{E}_n$  are Jacobian. Matrix  $\mathbf{F}_n = \left. \frac{\partial \mathbf{f}_n}{\partial \mathbf{x}} \right|_{\hat{\mathbf{x}}_{n-1}}$  can be found to be

$$\mathbf{F}_n = \begin{bmatrix} 1 & 0 & -d_n \sin(\hat{\phi}_{n-1} + \frac{1}{2}\phi_n) \\ 0 & 1 & d_n \cos(\hat{\phi}_{n-1} + \frac{1}{2}\phi_n) \\ 0 & 0 & 1 \end{bmatrix}. \quad (12)$$

and it is equal to  $\mathbf{W}_n$  for the model considered. Matrix  $\mathbf{E}_n = \left. \frac{\partial \mathbf{f}_n}{\partial \mathbf{u}} \right|_{\hat{\mathbf{x}}_n^-}$  can be written as

$$\mathbf{E}_n = \frac{1}{2b} \begin{bmatrix} be_{cn} + d_n e_{sn} & be_{cn} - d_n e_{sn} \\ be_{sn} - d_n e_{cn} & be_{sn} + d_n e_{cn} \\ -2 & 2 \end{bmatrix}, \quad (13)$$

where  $e_{cn} = \cos\left(\hat{\phi}_n^- + \frac{\phi_n}{2}\right)$  and  $e_{sn} = \sin\left(\hat{\phi}_n^- + \frac{\phi_n}{2}\right)$ .

Similarly to (6),  $\mathbf{h}_n(\mathbf{x}_n)$  can be expanded at  $n$  as

$$\mathbf{h}_n(\mathbf{x}_n) = \mathbf{H}_n\mathbf{x}_n + \bar{\mathbf{z}}_n, \quad (14)$$

where  $\bar{\mathbf{z}}_n = \mathbf{h}_n(\hat{\mathbf{x}}_n^-) - \mathbf{H}_n\hat{\mathbf{x}}_n^-$  is known and

$$\mathbf{H}_n = \begin{bmatrix} \frac{\hat{x}_n^- - x_1}{u_{1n}} & \frac{\hat{y}_n^- - y_1}{u_{1n}} & 0 \\ \frac{\hat{x}_n^- - x_2}{u_{2n}} & \frac{\hat{y}_n^- - y_2}{u_{2n}} & 0 \\ 0 & 0 & 1 \end{bmatrix}, \quad (15)$$

where  $u_{1n} = \sqrt{(y_1 - \hat{y}_n^-)^2 + (x_1 - \hat{x}_n^-)^2 + c_1^2}$  and  $u_{2n} = \sqrt{(y_2 - \hat{y}_n^-)^2 + (x_2 - \hat{x}_n^-)^2 + c_2^2}$ .

The estimation error is computed as

$$\mathbf{P}_n = E\{(\mathbf{x}_n - \hat{\mathbf{x}}_n)(\mathbf{x}_n - \hat{\mathbf{x}}_n)^T\}. \quad (16)$$

The extended Kalman filtering (EKF) algorithm developed for this model is listed in Table 1 and EFIR filtering algorithm is listed in Table 2. The latter requires only  $N$  and  $K$  to start computing and updating iteratively all the matrices via  $\mathbf{z}_n$  and  $\mathbf{y}_n$  [33, 34]. Since linear measurement  $\mathbf{y}_n$  is unavailable, we employ the output of the EKF on an interval of first  $N_{\text{opt}}$  points. To run the EKF, we set approximately the noise covariances and initial errors. To run the EFIR filter,  $N = N_{\text{opt}}$  is found via test measurements assuming known  $\mathbf{x}_n$  by minimizing (16).

Table 1: Extended Kalman Filtering Algorithm

---

<b>Input:</b> $\mathbf{z}_n, \hat{\mathbf{x}}_0, \mathbf{P}_0, \mathbf{R}, \mathbf{Q}, \mathbf{L}$	
1:	<b>for</b> $n = 1 : M$ <b>do</b>
2:	$\hat{\mathbf{x}}_n^- = \mathbf{f}_n(\hat{\mathbf{x}}_{n-1}, \mathbf{u}_n, \mathbf{0}, \mathbf{0})$
3:	$\mathbf{P}_n^- = \mathbf{F}_n(\mathbf{P}_{n-1} + \mathbf{Q})\mathbf{F}_n^T + \mathbf{E}_n\mathbf{L}\mathbf{E}_n^T$
4:	$\mathbf{K}_n = \mathbf{P}_n^- \mathbf{H}_n^T (\mathbf{H}_n \mathbf{P}_n^- \mathbf{H}_n^T + \mathbf{R}_n)^{-1}$
5:	$\hat{\mathbf{x}}_n = \hat{\mathbf{x}}_n^- + \mathbf{K}_n[\mathbf{z}_n - \mathbf{h}_n(\hat{\mathbf{x}}_n^-)]$
6:	$\mathbf{P}_n = (\mathbf{I} - \mathbf{K}_n \mathbf{H}_n) \mathbf{P}_n^-$
7:	<b>and for</b>
<b>Output:</b> $\hat{\mathbf{x}}_n$	

---

Table 2: Extended UFIR Filtering Algorithm

---

<b>Input:</b> $\mathbf{z}_n, \mathbf{y}_n, K, N$	
1:	<b>for</b> $n = N - 1 : M$ <b>do</b>
2:	$m = n - N + 1, \quad s = m + K - 1$
3:	$\tilde{\mathbf{x}}_s = \begin{cases} \mathbf{y}_s, & \text{if } s < N - 1 \\ \hat{\mathbf{x}}_s, & \text{if } s \geq N - 1 \end{cases}$
4:	$\mathbf{G}_s = \mathbf{I}$
5:	<b>for</b> $l = m + K : n$ <b>do</b>
6:	$\tilde{\mathbf{x}}_l^- = \mathbf{f}_l(\tilde{\mathbf{x}}_{l-1}, \mathbf{u}_l, \mathbf{0}, \mathbf{0})$
7:	$\mathbf{G}_l = [\mathbf{H}_l^T \mathbf{H}_l + (\mathbf{F}_l \mathbf{G}_{l-1} \mathbf{F}_l^T)^{-1}]^{-1}$
8:	$\mathbf{K}_l = \mathbf{G}_l \mathbf{H}_l^T$
9:	$\tilde{\mathbf{x}}_l = \tilde{\mathbf{x}}_l^- + \mathbf{K}_l[\mathbf{z}_l - \mathbf{h}_l(\tilde{\mathbf{x}}_l^-)]$
10:	<b>and for</b>
11:	$\hat{\mathbf{x}}_n = \tilde{\mathbf{x}}_n$
12:	<b>and for</b>
<b>Output:</b> $\hat{\mathbf{x}}_n$	

---

### 3 Mobil robot Localization

In this section, we consider a robot travelling on an indoor grid floorspace. The floorspace is nested with RFID tags which coordinates of locations are saved in robot memory. Each tag has a circular detection areas with the detection range  $r$ . We suppose that a robot has a reader that is able to measure distances to at least two RFID tags at once. We also assume that the robot is equipped with a FOG to measure the pose angle  $\Phi_n$ . The reading region is such that two or more tags are observed at the same time. An example is a reader with an elliptical antenna diagram used to detect tags on a floor or ceiling [21].

To test the EFIR and EKF algorithms, all noise sources are supposed to be additive, stationary, zero mean, white Gaussian, and uncorrelated. Accordingly, we introduce the estimation error variances  $\sigma_x^2$ ,  $\sigma_y^2$ , and  $\sigma_\Phi^2$  and specify the noise covariance matrix (7) with the main diagonal  $\text{diag } \mathbf{Q} = [\sigma_x^2 \ \sigma_y^2 \ \sigma_\Phi^2]$  and all other components zeros. For the noise variances  $\sigma_L^2$  and  $\sigma_R^2$  in the input distances  $d_{Ln}$  and  $d_{Rn}$ , we specify (8) with the main diagonal  $\text{diag } \mathbf{L} = [\sigma_L^2 \ \sigma_R^2]$  and all other components zeros. Finally, for the measurement noise variances  $\sigma_{v1}^2$ ,  $\sigma_{v2}^2$ , and  $\sigma_{v3}^2$ , we specify (13) with the main diagonal  $\text{diag } \mathbf{R} = [\sigma_{v1}^2 \ \sigma_{v2}^2 \ \sigma_{v3}^2]$  and all other components zeros.

A robot travels free on a grid floorspace nested with 35 tags (Fig. 2) without the corrections of its deviation from the planned path. In order to learn the effect of noise upon the estimates, we set realistic variances for the noise sources,  $\sigma_L = \sigma_R = 1$  sm,  $\sigma_{v1} = \sigma_{v2} = 15$  sm, and  $\sigma_{v3} = 2^\circ$ , and require the variances in the state noise to be  $\sigma_x = \sigma_y = 1$  sm and  $\sigma_\Phi = 0.5^\circ$ . To run the EKF, we roughly set the noise covariances with  $p \neq 1$  as  $p\mathbf{Q}$ ,  $\mathbf{R}/p$ , and  $\mathbf{L}/p$ , the initial state with an error of 10%, and allow  $\mathbf{P}_0 = 0$ . We then employ the EKF output as linear measurement  $\mathbf{y}_n$  for the EFIR filter at the beginning interval of  $N$  points.

Employing test reference measurements, we find  $N_{\text{opt}} = 20$  by minimizing the MSE (16) by  $N$  as

$$N_{\text{opt}} = \arg \min_N \{ \text{tr } \mathbf{P}(N) \}. \quad (17)$$

The robot path was planned to be stepwise as dashed in Fig. 2. In free travelling, noise corrects the trajectory and we notice that in the ideal case of  $p = 1$  and exactly known  $\mathbf{x}_0$  the estimates provided by the EFIR filter and EKF are consistent and fit well the actual robot path (not shown).

An analysis of errors sketched in Fig. 3 reveals the following. Under the ideal conditions of fully known model and noise statistics, the EKF slightly

outperforms the EFIR filter. However, it loses an ability of accurate filtering under the more realistic conditions implying  $p \neq 1$  and unknown initial state. Figure illustrates this case for  $p = 5$  and error of 10% in the initial state. Table 3 gives average errors computed for the EFIR filter with  $N_{\text{opt}} = 20$  and EKF for  $p$  set around unity. As can be observed, even relatively small errors associated by  $p = 3$  and  $p = 0.3$  make the EKF more noisy. Moreover, the EKF demonstrates divergence with  $p < 0.4$  that is exhibited in Fig. 4 for  $p = 0.2$ . Note that divergence can be watched at some intervals and it may disappear after the tags are switched out. Namely this effect causes large errors in the EKF for the coordinate  $x_n$  with  $p = 0.3$  in Table 3. Overall, the EKF produced unacceptable and rapidly increased errors with  $p > 3$  and  $p < 0.4$ .

### 4 Concluding Remarks

One of the powerful tools for industrial and other applications is the recently developed technique called the grid RFID tag-nested navigation space. Using information about the surrounding delivered by the tag, a vehicle can fulfil its duties most completely. To reach and use this information efficiently, each tag must be identified reliably and vehicle localization provided with high accuracy. We have shown that recently derived the EFIR filter is more accurate than the EKF in vehicular localization in RFID tag-nested navigation space under the conditions of not fully known noise covariances and initial state. The EFIR filter that produces unbiased estimates by iterative averaging completely ignores the noise statistics which are typically unknown to the engineer. Its algorithm has the Kalman form and noise reduction in its output becomes more efficient when  $N \gg 1$ . Although higher accuracy and stability of the EFIR filter were demonstrated in a comparison with the EKF, some concern about the environmental effects and real operation conditions still remains. We work on it now and plan to report the results un near future.

#### References:

- [1] T. Sanpechuda and L. Kovavisaruch, "A review of RFID localization: Applications and techniques," in *Proc. 5th Int. Conf. Elect. Eng./Electron., Comput., Telecommun. Inf. Technol.*, May 2008, pp. 769772.
- [2] M. N. Lionel, Y. Liu, Y. C. Lau, and A. P. Patil, "LANDMARC: Indoor location sensing using active RFID," *Wirel. Netw.*, vol. 10, pp. 701-710, Nov. 2004.
- [3] S. Park and S. Hashimoto, "Autonomous Mobile Robot Navigation Using Passive RFID in Indoor En-

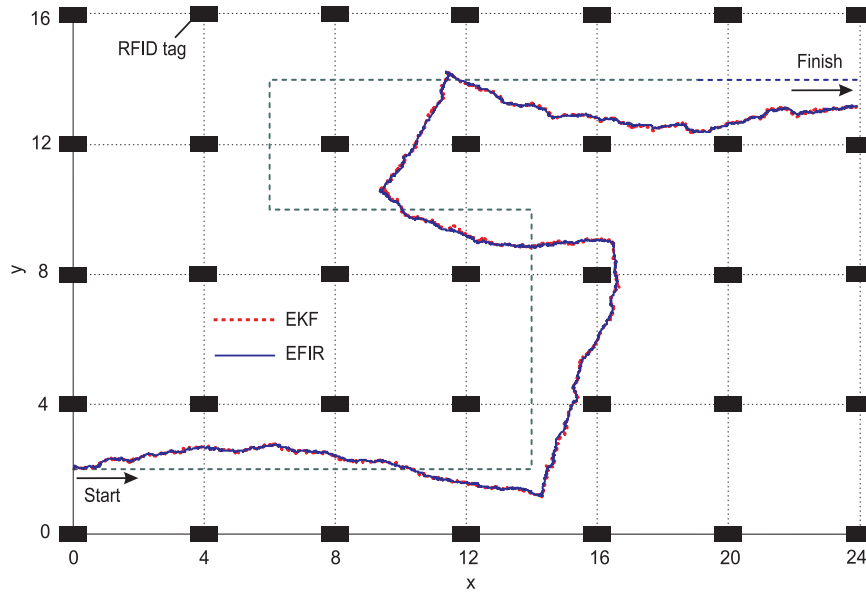


Figure 2: EKF and EFIR filtering estimates of robot localization over 5260 points on a grid navigation floorspace nested with RFID tags for  $p = 3$ , initial state error of 10%, and  $N_{opt} = 20$ . The planned path is dashed and the estimates fit the actual path (not shown).

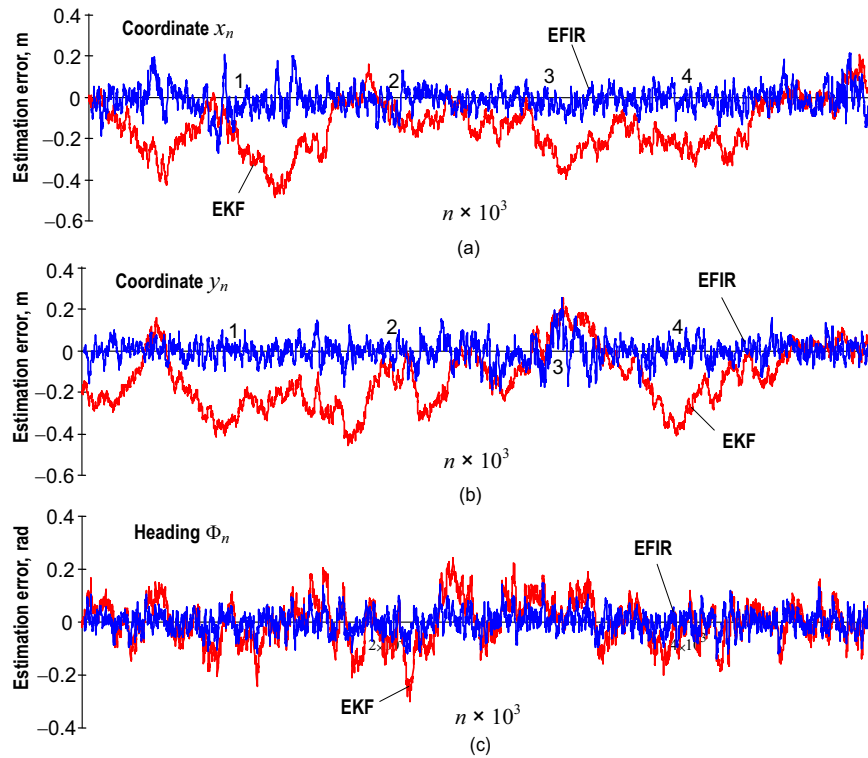
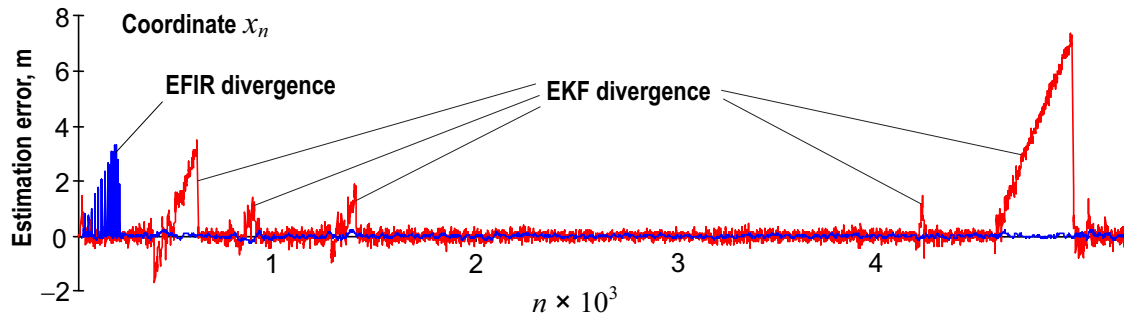


Figure 3: Typical estimation errors provided by EKF and EFIR filter for the location of a robot travelling free on a grid navigation floorspace (Fig. 2): (a) coordinate  $x$ , (b) coordinate  $y$ , and (c) heading angle  $\Phi$ .

Table 3: Average Errors (Excluded  $N_{\text{opt}} = 20$  points of Transients) Corresponding to Fig. 2 by EFIR Filter and EKF.

	$x$ , sm		$y$ , sm		$\Phi$ , $10^{-4}$ rad	
	bias	$\sigma$	bias	$\sigma$	bias	$\sigma$
EFIR	-1.470	5.710	-0.465	5.280	-2.166	400.0
EKF ( $p = 3$ )	-5.820	8.520	-5.160	9.960	7.756	493.0
EKF ( $p = 1$ )	-1.440	4.810	-0.477	5.010	4.730	231.0
EKF ( $p = 0.3$ )	27.48	113.46	-0.281	12.10	6.579	349.0

Figure 4: Divergence of the EKF with  $p = 0.2$ . Divergence in the EFIR/Kalman filter during the first  $N_{\text{opt}} = 20$  points is caused by the EKF divergence. With  $n > N_{\text{opt}}$ , the EFIR filter is stable.

- vironment”, *IEEE Transactions on Industrial Electronics*, vol. 56, pp. 2366–2373 Jul. 2009.
- [4] S. S. Saab and Z. S. Nakad, “IEEEA standalone RFID indoor positioning system using passive tags,” *IEEE Trans. on Industr. Electron.*, vol. 58, May 2011.
- [5] S. Willis and S. Helal, “RFID information grid for blind navigation and wayfinding,” in *Proc. IEEE Int. Symp. on Wearable Computers*, 2005, pp. 3437.
- [6] A. Smaliagic, and D. Kogan, “Location sensing and privacy in a context-aware computing environment,” *IEEE Wireless Communications*, vol. 9, pp. 1017, Oct. 2002.
- [7] D.G. Seo and J.M. Lee, “Localization algorithm for a mobile robot using iGS,” in *Proc. 17th World Congress The Int. Fed. of Autom. Control*, Seoul, Korea, July 6–11, 2008, pp. 742–747.
- [8] S. Han, H. Lim, and J. Lee, “An efficient localization scheme for a differential-driving mobile robot based on RFID system,” *IEEE Trans. Ind. Electron.*, vol. 54, pp. 3362–3369, Dec. 2007.
- [9] J. Zhou and J. Shi, “RFID localization algorithms and applications a review,” *J. Intell. Manuf.*, vol. 20, pp. 695–707, Dec. 2009.
- [10] Y. Zhang, M. G. Amin, and S. Kaushik, “Localization and Tracking of Passive RFID Tags Based on Direction Estimation,” *Int. Journal of Antennas and Propagation*, vol. 2007, art. 17426, pp. 1–9, 2007.
- [11] A. Papapostolou and H. Chaouchi, “RFID-assisted indoor localization and the impact of interference on its performance,” *Journal of Network and Computer Applications*, vol. 34, pp. 902913, May 2011.
- [12] H. Chae and K. Han, “Combination of RFID and vision for mobile robot localization,” in *Proc. IEEE Int. Conf. Intell. Sensors, Sensor Netw. Inf. Process.*, 2005, pp. 7580.
- [13] B.-S. Choi, J.-W. Lee, J.-J. Lee, and K.-T. Park, “A Hierarchical Algorithm for Indoor Mobile Robot Localization Using RFID Sensor Fusion,” *IEEE Trans. on Industr. Electron.*, vol. 58, Jun. 2011.
- [14] W. Gueaieb and M. S. Miah, “An intelligent mobile robot navigation technique using RFID technology,” *IEEE Trans. Instrum. Meas.*, vol. 57, pp. 19081917, Sep. 2008.
- [15] T. Deyle, H. Nguyen, M. S. Reynolds, and C. C. Kemp, “RFID-guided robots for pervasive automation, Pervasive Comput.,” vol. 9, pp. 3745, Apr./Jun. 2010.
- [16] D. Hahnel, W. Burgard, D. Fox, K. Fishkin, and M. Philipose, “Mapping and localization with RFID technology,” in *Proc. IEEE Int. Conf. on Robotics and Automation*, vol. 1, pp. 1015–1020, 2004.
- [17] A. Howard, “Multi-robot simultaneous localization and mapping using particle filters,” *The Int. Journ. of Robotics Research*, vol. 25, pp. 1243–1256, Dec. 2006.
- [18] H. Cox, “On the estimation of state variables and parameters for noisy dynamic systems,” *IEEE Trans. Automat. Contr.*, vol. AC-9, pp. 5–12, Jan. 1964.

- [19] U. Klee, T. Gehrig and J. McDonough, "Kalman filters for time delay of arrival-based source localization," *EURASIP Journal on Applied Signal Process.*, vol. 2006, pp. 1–15, Jan. 2006.
- [20] E. DiGiampaolo and F. Martinelli, "A passive UHF-RFID system for the localization of an indoor autonomous vehicle," *IEEE Trans. on Industr. Electron.*, vol. 59, pp. 3961–3970, Oct. 2012.
- [21] E. DiGiampaolo and F. Martinelli, "Mobile robot localization using the phase of passive UHF-RFID signals," *IEEE Trans. on Industr. Electron.*, vol. 61, pp. 365–376, Jan. 2014.
- [22] B. Gibbs, *Advanced Kalman Filtering, Least-Squares and Modeling*, New York: Wiley, 2011.
- [23] Y. S. Shmaliy, "An iterative Kalman-like algorithm ignoring noise and initial conditions," *IEEE Trans. Signal Process.*, vol. 59, pp. 2465–2473, Jun. 2011.
- [24] R. J. Fitzgerald, "Divergence of the Kalman filter," *IEEE Trans. Autom. Control*, vol. AC-16, pp. 736–747, Dec. 1971.
- [25] F. Daum, "Nonlinear filters: beyond the Kalman filter," *IEEE A&E Systems Magazine*, vol. 20, pp. 57–69, Aug. 2005.
- [26] W. H. Kwon and S. Han, *Receding Horizon Control: Model Predictive Control for State Models*. London: Springer, 2005.
- [27] Y. S. Shmaliy, "Linear optimal FIR estimation of discrete time-invariant state-space models," *IEEE Trans. Signal Process.*, vol. 58, pp. 3086–3096, Jun. 2010.
- [28] A. M. Bruckstein and T. Kailath, "Recursive limited memory filtering and scattering theory," *IEEE Trans. Inf. Theory*, vol. IT-31, pp. 440–443, May 1985.
- [29] A. H. Jazwinski, *Stochastic Processes and Filtering Theory*, New York: Academic, 1970.
- [30] Y. S. Shmaliy, "Unbiased FIR filtering of discrete time polynomial state space models," *IEEE Trans. on Signal Process.*, vol. 57, pp. 1241–1249, Apr. 2009.
- [31] Y. S. Shmaliy, "Suboptimal FIR filtering of nonlinear models in additive white Gaussian noise," *IEEE Trans. Signal Process.*, vol. 60, pp. 5519–5527, Oct. 2012.
- [32] K. Komoriya and E. Oyama, "Position estimation of a mobile robot using optical fiber gyroscope," in *Proc. IEEE/RSJ/GI Int. Conf. Intell. Robots Syst.*, vol. 1, pp. 143–149, 1994.
- [33] J. Pomárico-Franquiz, S. H. Khan, and Y. S. Shmaliy, "Combined extended FIR/Kalman filtering for indoor robot localization via triangulation", *Measurement*, vol. 50, pp. 236–243, Apr. 2014.
- [34] J. Pomárico-Franquiz, Y. S. Shmaliy, "Accurate self-localization in RFID tag information grids using FIR filtering," *IEEE Trans. Industrial Informatics*, vol. 10, no. 2, pp. 1317–1326, May 2014.
- [35] F. Ramirez-Echeverria, A. Sarr, and Y. S. Shmaliy, "Optimal memory for discrete-time FIR filters in state space," *IEEE Trans. Signal Process.*, vol. 62, pp. 557–561, Feb. 2014.

# Strength Analysis of the Complex Planetary Gears

Sung Gil Han, Yoo-In shin, Chan Heon Yoon, and Chul Ki Song

**Abstract**—Although planetary gear systems are operating in small volumes, it possesses huge efficiency because of the compact combination of gears in the planetary gear system. It also has an outstanding efficiency of just 3% for power transmission tantamount to the power loss that occurs on each of the shift stages.

Structure equipment requires to obtain higher efficiency and larger torque, recently. According to these needs, we have designed the complex planetary gear system to make larger torque.

In this paper, a strength design evaluation for the complex planetary gear system was performed to ensure the gears' stability and durability during operation time.

**Keywords**—Complex planetary gear system, Strength verification, Durability, Reduction gear

## I. INTRODUCTION

**P**LANETARY gear systems normally consist of a centrally pivoted sun gear, a ring gear, and several planet gears found between the sun gear and ring gear. Compared to traditional gear boxes, the planetary gear systems have some advantages.

Planetary gear systems possess larger efficiency in small volumes because of the compact combination of gears in the planetary gear system. They also have an outstanding efficiency of just 3% for power transmission tantamount to the power loss that occurs on each of the shift stages. Through this aspect, we can figure out that the rate of transmissible input energy in the planetary gear system is smaller than the mechanical loss which comes from a gear box. Based on the advantages mentioned above, the planetary gear system has been designed. [1]-[6]

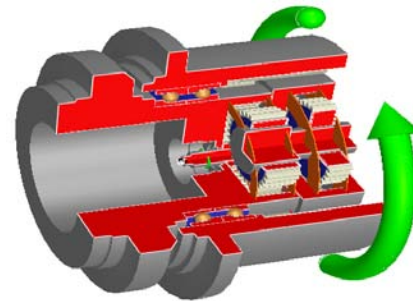
Optimum modeling for analysis is needed to carry out a more precise analysis result. Therefore, the modeling for strength and durability analysis is focused on gear train part.[7]

This research was financially supported by the Ministry of Education and Korea Institute for Advancement of Technology (KIAT) through the Human Resource Training Project for Regional Innovation and "the export-strategic FGCV R&D project" conducted by the ministry of knowledge and economy and the Korea Institute of Industrial Technology.

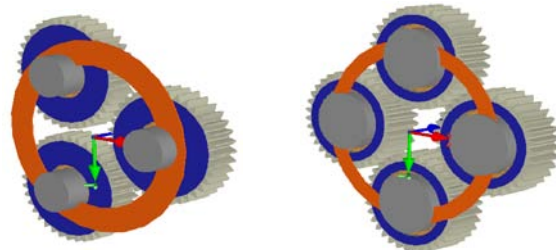
Sung Gil Han, Yoo-In Shin, Department of Mechanical and Aerospace engineering, Graduate School, Gyeongsang National University, 501, Jinju-daero, Jinju, Gyeongnam, 660-701, Korea (boheman\_gil@nate.com)

Chan Heon Yoon, Youngdong Tech Co., Changwon, Gyeongnam, 641-847, Korea (yd1938@yahoo.co.kr)

Chul Ki Song, Department of Mechanical Engineering, ERI Gyeongsang National University, 501, Jinju-daero, Jinju, Gyeongnam, 660-701, Korea (cksong@gnu.ac.kr)



a. Reduction gear



b. 1st planetary gear system      c. 2nd planetary gear system

**Fig. 1 3D modeling of the reduction gear (Romax DESIGNER)**

## II. STRENGTH ANALYSIS OF PLANETARY GEAR SYSTEM

### A. Boundary Conditions and Load conditions

In this research, SCM420H is applied to the planetary gear system as its materials.

SCM420H is widely used as a component material of industrial reduction gear. The material properties are shown in Table 1.

Power to drive the planetary gear system is generated from the hydraulic motor of the driving system. The maximum output of hydraulic motor is 210.5 Nm and 1,294.5 rpm. Analysis for stability and durability of the planetary gear system design should be performed under extreme load conditions. Thus, outputs in maximum torque are applied as input conditions for analysis. The average temperature in the planetary gear system is established at 60°C, and the lubricant is established SAE 80W grade which is generally used for planetary gear systems as well.[8]-[9]

Table 1 Material properties

Material	Tensile strength (MPa)	Yield strength (MPa)	Heat treatment	Surface hardness (Hv)
SCM420H	932	792	annealing, carburizing	800

Table 2 Input conditions

Precondition	Test load case
Temperature ( ° C)	60
Speed (rpm)	1,294.5
Torque (Nm)	210.5
Lubricant	SAE 80W

In addition, according to evaluation standards for the lifetime of RS B 0095, the standard of track drive units for small excavators [10], input conditions are established to verify durability for driving over 1,000 hours. The input conditions are arranged in Table 2 and applied to the three researches.

*B. The Results of Strength Analysis for Gears*

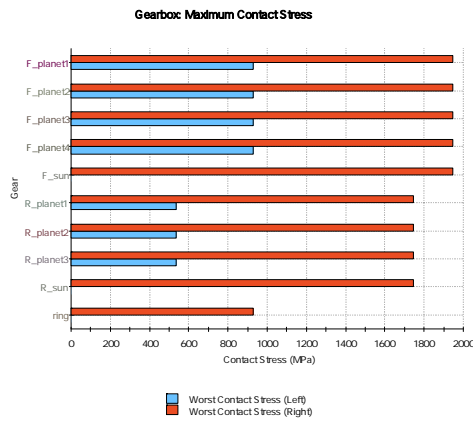
Strength analysis is performed to evaluate the stability of gears in the planetary gear system. The result of the strength analysis is shown in Figure 2 and Table 3.

III. DURABILITY ANALYSIS OF PLANETARY GEAR SYSTEM

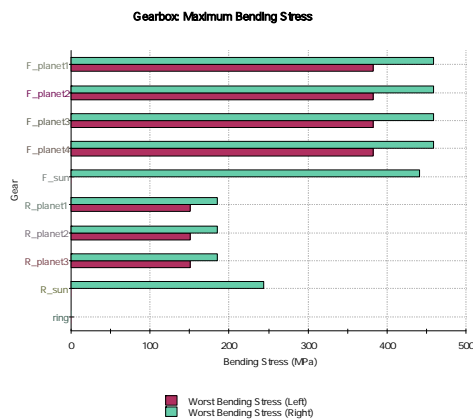
Durability analysis for driving over 1,000 hours is performed by the standard of RS B 0095. The results are arranged in Figure 3 and Table 4.

Table 3 Strength analysis result

Gear		Contact stress (MPa)		Safety factor
		left	right	
Ring		-	930.0	2.289
1st	Sun	-	1,745.0	0.981
	Planetary	534.2	1,745.0	1.054
2nd	Sun	-	1,947.0	1.000
	Planetary	930.0	1,947.0	1.038



a. contact stress



b. bending stress

Fig. 2 Stress of the planetary gear system

Gear		Bending stress (MPa)		Safety factor
		left	right	
Ring		-	-	+Infinity
1st	Sun	-	243.8	2.002
	Planetary	150.6	185.1	1.925
2nd	Sun	-	440.7	1.193
	Planetary	382.9	458.6	0.820

REFERENCES

- [1] I. H. An, M. J. An, Z. Xu, S. K. Lyu, "A Study on the Effect of the Honing in SCM420H Planetary Gear", Journal of the KSMPE, Vol.10, No. 3, pp. 13-18, 2011
- [2] F. Chaari, T. Fakhfakh, and Haddar, "Dynamic Analysis of a Planetary Gear Failure Caused by Tooth Pitting and Cracking", Journal of Failure Analysis and Prevention, Vol. 6 No. 2, pp. 73~78, 2006
- [3] Milosav Ognjanovic', Miloš Ristic', Predrag Živkovic, "Reliability for design of planetary gear drive units", An International Journal of Theoretical and Applied Mechanics, 2013
- [4] Nicholas, P.C., Gear Design and Application, Mcgraw Hill, New York, pp.94~121.
- [5] Brownlee, K. A, Hodges, J. L, Rosenblatt, M, "Evaluation of fatigue strength", Journal of America stat. Assn, Vol. 48, pp. 29~35, 1953
- [6] J. H. Yang, H. O. Kim, H. D. Lee, "An Experimental Study on Improvement of Contact Stress of Bevel Gear, Conference of the KSPE, pp. 873, 2011
- [7] S. G. Han, Y. I. Shin, H. C. Kim, H. C. Kim, H. C. An and C. K. Song, "Strength Design Evaluation of the Double Planetary Gears", Conference of the Eighth International Symposium on Mechanics, Aerospace and Informatics Engineering 2013, pp. 62-63, 2013
- [8] A. Kahraman, "Load Sharing Characteristics of Planetary Transmissions," Mech. Mach. Theory, 29, pp. 1151-65, 1994.
- [9] S, G, Lyu, and K. M. Kim, "A Study on the Bending Fatigue Strength of Sintering Spur Gear:", the Korea Institute of Industrial Safety, Vol. 9, No. 3, pp. 28-33
- [10] Korea Agency for Technology and Standard, "RS B 0095", 2005

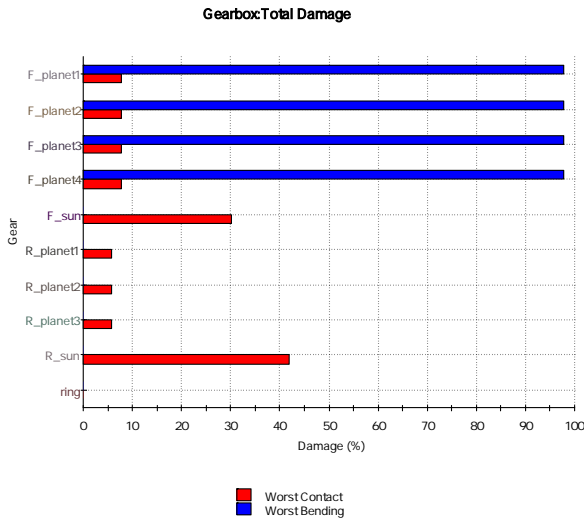


Fig. 3 Bending-Contact damage

Table 4 Durability analysis result

Gear	Pass /Fail	Combined life (hr)	Contact life (hr)		Bending life (hr)	
			Left	Right	Left	Right
Ring	Pass	N/A	N/A	N/A	N/A	N/A
1st	S	Pass	2,385	N/A	2,385	N/A
	P	Pass	1.7e4	N/A	1.7e4	N/A
2nd	S	Pass	3328.0	N/A	3328.0	N/A
	P	Pass	1,023	N/A	1.3e4	6.6e4

IV. CONCLUSION

In this research, complex planetary gear system which is used in the driving system of excavator has been performed to analyze the durability and stability. At the result of the strength analysis, the sun gear in 1st planetary gear set and the planetary gear in 2nd planetary gear set are not achieved to safety factor 1.0. Those gears are not satisfy the safety factor, but nevertheless those gears has a enough durability over 1,00 hours.

ACKNOWLEDGMENT

This research was financially supported by the Ministry of Education and Korea Institute for Advancement of Technology (KIAT) through the Human Resource Training Project for Regional Innovation and "the export-strategic FGCV R&D project" conducted by the ministry of knowledge and economy and the Korea Institute of Industrial Technology.

## Haptics based Robotic Prosthetic Leg

Y.Kalyan Chakravarthy<sup>1</sup>, R.Harish Kumar<sup>2\*</sup>, B.Deepika<sup>2</sup>, Dr.A.Srinath<sup>3</sup>

<sup>1</sup>Research Scholar in Mechanical Engineering, KL University, Guntur.Dist A.P, India 522 502

<sup>2</sup>Undergraduate Student in Electronics and Computer Engineering, KL University, Guntur.Dist A.P, India\*  
Corresponding Author

<sup>3</sup>Department of Mechanical Engineering, K L University, Guntur Dist, A.P, India 522 502

**Abstract--** Robotic prosthetic leg is active prosthetic leg that supports the required with above or below knee amputations. It mimics the action of normal human leg, reflecting typical movements involved during stance and swing phases of human walking cycle. Information about how to measure angle, speed of swing during walking and running at different speeds was presented. Precise movements of this robotic prosthetic leg are achieved using haptic technology. Sensors are placed on the sound leg that traces its continuous motion and the same is replicated for the movement of robotic prosthetic leg. These sensors capture the movements of sound leg and foot to the microprocessors. Using this data, corresponding actuators are actuated with required angle and speed to reciprocate the sound leg movements. This movement makes the person comfortable while walking, taking stairs.

**Keywords:** Robotic-Prosthetic, amputations, Haptics, mimics, Articulation, Gait cycle

### I. INTRODUCTION

In orthopedic medicine, prosthesis, prosthetic or prosthetic limb is an artificial device extension that replaces a missing body limb. It is part of the field of bio-mechatronics, the science of using mechanical devices with human muscle, skeleton, and nervous systems to assist or enhance motor control lost by trauma, disease, or defect. Prostheses are typically used to replace parts lost by injury (traumatic) or missing from birth (congenital) or to supplement defective body parts. Inside the body, artificial heart valves are in common use but lungs are less common and under active technology development. Other medical devices and aids that can be considered prosthetics include artificial eyes.

This paper provides solution that helps the people with above or below knee amputation to walk normally providing an active leg rather than a passive one. This is

developed on the phenomenon that, during locomotion both legs perform similar action but at different point of time. So in brief, reproducing the movements of the un-amputated leg in the robotic leg can make the person walk. Trans-femoral amputees with passive prostheses have been shown to expend 60% more metabolic energy [1] and exert three times the affected-side hip power and torque [2] when compared to healthy subjects during leveled walking.

#### 1.1 Analysis of gait cycle

The gait cycle has two basic components, the *swing phase* and the *stance phase*.

- Stance: phase in which the limb is in contact with the surface
- Swing: phase in which the foot is in the air for limb advancement.

Considering this gait cycle, both legs undergo same phases at certain interval of time. When the movement is even then both the legs undergo these phases one after other at equal intervals of time.

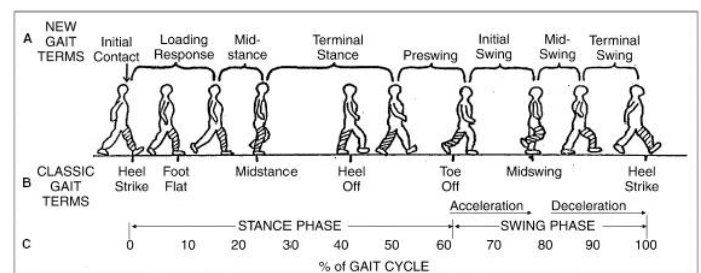


**Figure 1:** Gait analysis [3]

#### 1.2 Knee anatomy

The knee joint is an important aspect to the human anatomy, particularly regarding movement, including walking and running. There are two main bones that are present within the knee joint, the femur and the tibia. The femur rests on the top of the tibia and when these two bones come together, the hinge joint of the knee is

formed. It is covered by the patella, also known as the kneecap. The patella fits into the groove that is formed when these two bones come together. The ends of the tibia and the femur are covered by articular cartilage, which acts as cushioning between these bones. The lateral meniscus, which is located on the outer side of the knee, and medial meniscus, which is located on the inner side of the knee, is also present in the knee joint and they are the shock absorbers between the bones [12].

### 1.3 Active Knees

Although lower limb prostheses have traditionally been passive, there have been attempts at providing active versions. Most of the developed hydraulic and pneumatic powered knees are tethered to an external power supply because associated prostheses suffer from high energy consumption. Flowers and Mann [14] and Stein and Flowers [15] suggested a powered electro-hydraulic knee joint tethered to a power source. They used a hydraulic cylinder controlled by a 4/3 servo valve to actuate the knee. Recently, Sup [16] developed a pneumatically actuated powered-tethered lower limb which is controlled by a computer to alter the impedance of the actuators. Aeyels et. al [13] developed the first micro-controller based knee joint which comprised of an electromagnetic brake. The embedded systems control of the active knee is being proposed in this paper.

### 1.4 Mathematical Analysis

Since the parameters of prosthetic knee have an essential Effect on its function, they should be studied to make a Prosthetic gate as close as possible to an intact leg. Some Studies have engaged in mathematical simulation of this parameters [6]. [7] Describes a control mechanism for an Above knee leg through a mathematical model. Radcliffe presented a mathematical model of a Four bar polycentric knee [8]. [9] appraised the influence of Prosthetic knee inertial characteristics through a Mathematical model. Technically, this principle of one leg repeating the same movement of the other can be incorporated in to this robotic leg. But, to design this leg one should need the forces acting at the joints and thereby torque required to move the leg. Mathematical analysis provides the values of torque required to move the leg.

To obtain the equations of motion for a system with serial kinematic chain, two methods can be used

- Newton-Euler
  - Multi-body robot seen as a whole.
  - Constraint (internal) reaction forces between the links are automatically eliminated: in fact, they do not perform work.
  - Closed-form (symbolic) equations are directly obtained.
  - Best suited for study of dynamic properties and analysis of control schemes.
  
- Lagrangian formulation
  - Dynamic equations written separately for each link/body.
  - Inverse dynamic equations in real time are evaluated in a numeric and recursive way. It is best for synthesis (implementation) of model based control schemes.
  - By elimination of reaction forces and back substitution of equations, we still get closed-form dynamic equations (identical to those of Euler-Lagrange!)

Both Newton-Euler and Lagrangian formulation are equivalent and give similar equations of motion. The Newton-Euler is based on Newton's Second Law of Motion, and on analysis of forces and moments of constraints acting between adjacent links. The resultant equations include the coupling forces and moments, and thus extra mathematical procedures are demanded to eliminate these extra terms. Conversely, the straight forward Lagrangian formulation is an energy-based approach to dynamics and automatically all workless forces such as internal forces are ignored in this approach. Hence, Lagrangian dynamics is simpler than Newton-Euler.

Therefore, Lagrangian formulation is utilized in this work to drive the equation of motion and solve the inverse dynamics of the system which is essential for torque control of actuators.

$$\tau_1 = m_1 r_1 (r_1 \ddot{\theta}_1 + x_a'' \cos \theta_1 + y_a'' \sin \theta_1 + g \sin \theta_1) + m_2 L_1 (L_1 \ddot{\theta}_1 + x_a'' \cos \theta_1 + y_a'' \sin \theta_1 + g \sin \theta_1) + m_2 r_2 \left( r_2 \ddot{\theta}_2 + g \sin \theta_2 + x_a'' \cos \theta_2 + y_a'' \sin \theta_2 + L_1 (\ddot{\theta}_1 + \ddot{\theta}_2) \right) \cos(\theta_1 - \theta_2) + L_1 (\dot{\theta}_1^2 + \dot{\theta}_2^2) \sin(\theta_1 - \theta_2) + I_2 \ddot{\theta}_2 + I_1 \ddot{\theta}_1 - L_2 F_1 \cos \theta_2 - L_2 F_2 \sin \theta_2 - L_1 F_1 \cos \theta_1 - L_1 F_2 \sin \theta_1$$

$$\tau_2 = m_2 r_2 \left( r_2 \ddot{\theta}_2 + g \sin \theta_2 + x_a'' \cos \theta_2 + y_a'' \sin \theta_2 + L_1 \ddot{\theta}_1 \cos(\theta_1 - \theta_2) - L_1 \dot{\theta}_1^2 \sin(\theta_1 - \theta_2) \right) - L_2 F_1 \cos \theta_2 - L_2 F_2 \sin \theta_2 + I_2 \ddot{\theta}_2$$

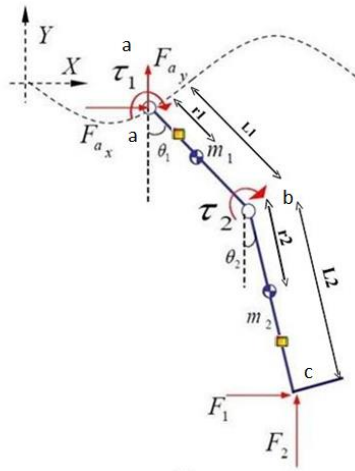


**Figure 2:** Stick diagram showing the accelerometer locations on the leg

1.4 Methodology

Many ankle-foot prostheses use a multitude of sensors to feed information into the controller [11]. These sensors include: accelerometers, rotary potentiometers, and force transducers [10]. In order to create human like movements in the lower limb, one should know the angle of rotation and speed of the swing. Either accelerometer or potentiometer can be employed to measure the angle and speed of the swing. But each of

these sensors is accurate at a certain parameter and approximates the other parameter.

Three combinations are possible, one with potentiometer alone, one with accelerometer alone and one with the combination of accelerometer and potentiometer. In these combinations there are certain constraints to be considered, they are hardware complexity, software complexity, accuracy.

1.5 Accelerometer approach

Accelerometer alone is good at measuring proper acceleration, so the speed of the swing can be calculated accurately but multiple accelerometers and some math is required to approximate the angular position. Three accelerometers are required to approximate the angle [4] made by the leg at knee. Increase in sensors results in hardware complexity and difficulty in wearing these sensors.

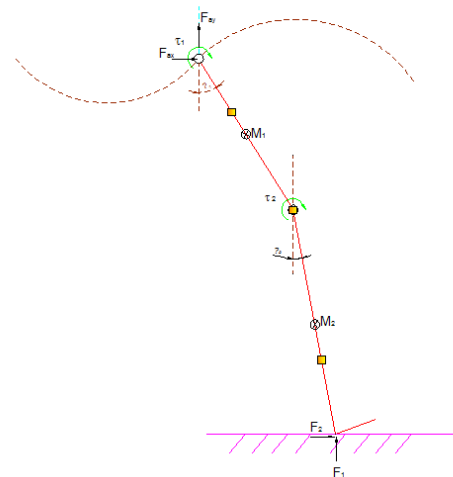


**Figure 3:** Stick diagram showing the accelerometer locations on the leg

1.6 Potentiometer approach

Potentiometer can be calibrated to return accurate angular positions but it requires a clever algorithm to estimate the speed of the swing. Software considers certain number of frames and estimates the speed, this certainly increases software complexity and speed measurement may not be accurate. Potentiometers are placed on the sides of the knee for angle measurement.

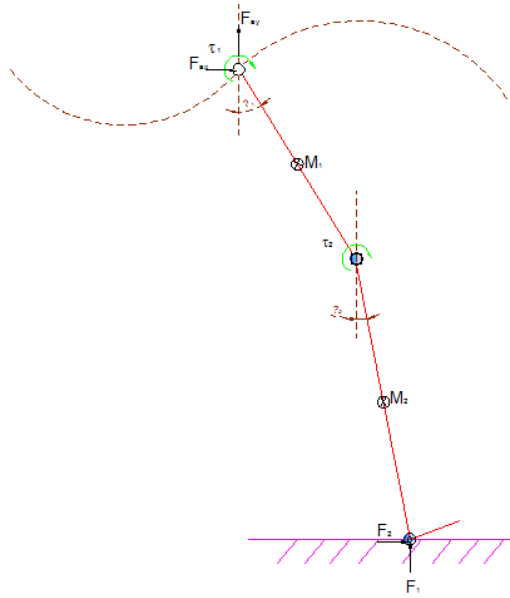


**Figure 4:** Stick diagram showing the potentiometer locations on the leg

*1.7 Accelerometer and potentiometer combination*

When both accelerometer and potentiometer combination is used, accuracy is maintained but there is a hardware complexity. Here hardware complexity means more sensors to be placed on the sound leg.

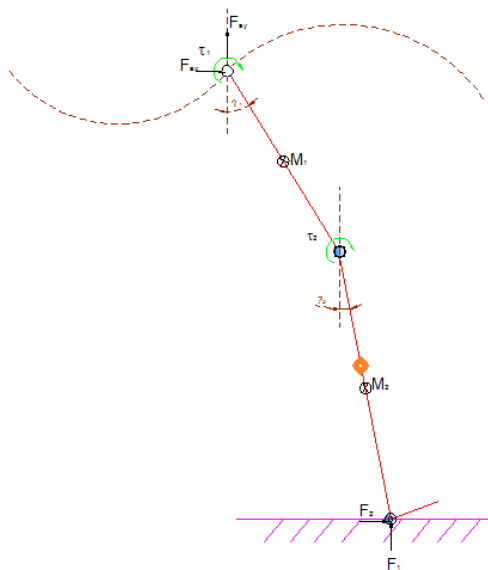


**Figure 5:** Stick diagram showing the accelerometer and potentiometer locations on the leg

*1.8 Embedded System*

ATMEGA\* 8 microcontroller is used in this embedded system; with system clock of 16MHZ. Arduino bootloader is burned into this controller so that firmware developed in arduino environment can be directly used. It has built in analog to digital converter pins which are used to interface the analog sensors like potentiometer and accelerometer. It supports several communication protocols, interrupts which aids in forming a distributed system.

*1.9 Distributed Computing*

Distributed system is a software system in which components located on networked computers communicate and coordinate their actions by passing messages. The components interact with each other in order to achieve a common goal. Three significant characteristics of distributed systems are: concurrency of components, lack of a global clock, and independent failure of components. Examples of distributed systems vary from SOA-based systems to massively multiplayer online games to peer-to-peer applications.

A computer program that runs in a distributed system is called a distributed program, and distributed programming is the process of writing such programs. There are many alternatives for the message passing mechanism, including RPC-like connectors and message queues. An important goal and challenge of distributed systems is location transparency.

Distributed computing also refers to the use of distributed systems to solve computational problems. In distributed computing, a problem is divided into many tasks, each of which is solved by one or more computers, which communicate with each other by message passing.

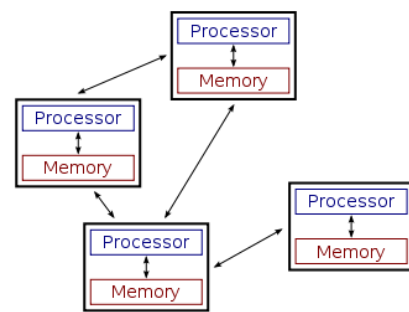


**Figure 6:** Distributed System

Single Microcontroller cannot handle data acquisition and movement replication with required efficiency. To achieve greater functionality and overcome processor latency, Multiprocessor environment is best suitable. By using distributed computing, one Microcontroller is dedicated for reading knee angle and time intervals. Other microcontroller is dedicated entirely for fetching the data from sound leg and replicating it on the robotic limb. Entire motor driving circuitry is connected to this controller.

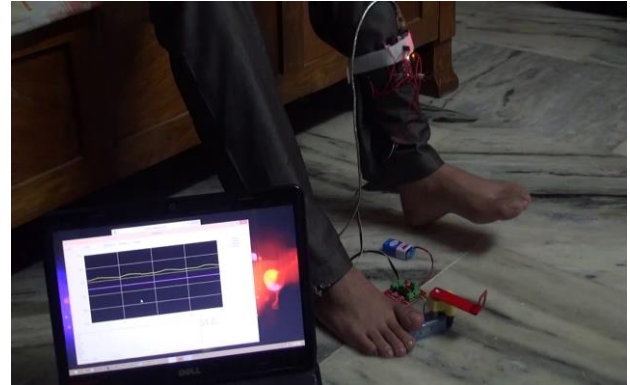


**Figure 7:** Author's prototype- Accelerometer arrangement

## II. Experimental Analysis

To make such a robust and adaptable system, thorough analysis is required. To estimate the threshold of forward and backward swing and angle of the leg, general walking and running states should be analyzed. Different subjects (human volunteers) of distinct age, weight and gender were chosen for the analysis as these parameters are dependent on the gait cycle [5]. Parameters observed are the position variables, time and speed at which subject is walking or running.

Theoretically these position sensors return dynamic position data in real time. To program the embedded system for tracking the user movements, these sensors were tested to analyse their suitability. These position sensors are not actually position sensors; but are modified so as to measure the position. They were made wearable to verify them in lab. Both accelerometer and potentiometer readings were individually plotted and analysed as follows.

### 2.1 Accelerometer

In this analysis, 3-Dimensional accelerometer is used. It is interfaced with an arduino\* board, which is programmed to return the data of accelerometer as serial data to the computer. MATLAB running on the computer plots the graph using serial data. Position sensor is hooked up with the arduino board and it is strapped to the subject's leg. Subjects were made to walk/run on the treadmill at varying speeds. *The swing of the sound leg is tracked by the accelerometer, which can be reproduced on the robotic-prosthetic leg.*

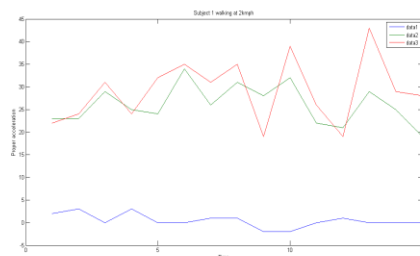


**Figure 8:** Accelerometer Values of a typical subject walking at 2 Kmph

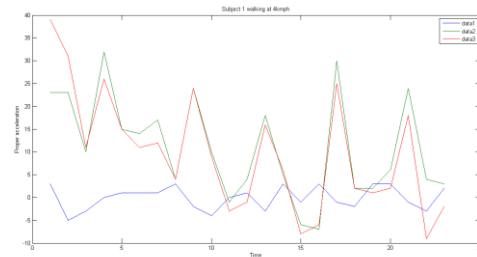


**Figure 9:** Accelerometer Values of a typical subject walking at 4 Kmph

### 2.2 Potentiometer

In this analysis, 10K Potentiometer is used. It is interfaced with an arduino board, which is programmed to return the data of potentiometer as serial data to the computer. MATLAB running on the computer plots the graph using serial data. A special framework is made on the potentiometer to use it as a position sensor. *This framework is glued on the leg so that potentiometer imitates*

the movement of the joint. Subjects were made to walk/run on the treadmill at varying speeds.



**Figure 10:** Author’s feedback sensor – potentiometer arrangement

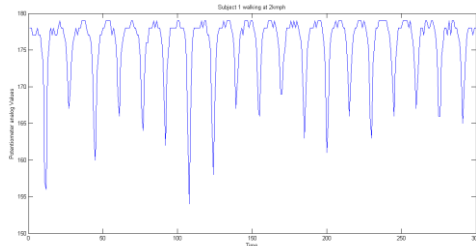


**Figure 11:** Potentiometer Values of a typical subject walking at 2 Kmph

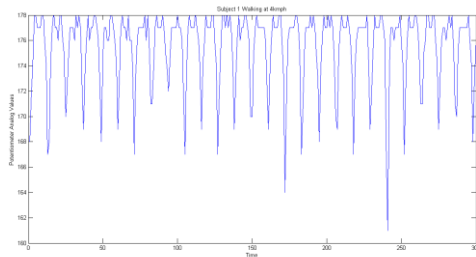


**Figure 12:** Potentiometer Values of a typical subject walking at 4 Kmph

### 2.3 Software Algorithm

Following algorithm records the sound leg movements. This can be used for both potentiometer and accelerometer also.

1. Processor reads the data from position sensors.
2. Forward swing or backward swing is detected when the threshold of respective movements are crossed.

3. Present movement is stored.
4. Program checks if the present movement is different from past movement.
5. If yes, step 6 executes, if no, program re-executes from step 1.
6. Movement is stored and program checks if timer is running or not.
7. If yes, timer value is stored and timer reset occurs and program continues from step 1
8. If no, timer is initiated and program continues from the first step.

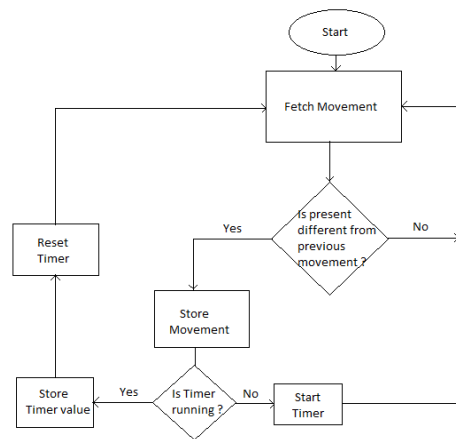


**Figure 13:** Movement recorder program flowchart

### 2.4 Movement replication

Meager recording of the movements and time intervals between every movement is not sufficient, but it is meant to be replicated by the robotic limb to achieve the natural movement. A triggering sensor placed on the thigh of amputated leg notifies the processor to reproduce the stored movements in the robotic leg by activating corresponding actuators for certain time.

## III. Conclusion

The developed robotic prosthetic leg can be attached to the thigh part of the above knee amputee in such a way that it is firm. Sensors are placed on the sound leg. Entire system is embedded inside the robotic-prosthetic leg. This model has certain limitations while walking on rocky terrains and climbing slope (however these aspects are being undertaken in the authors’ future

work). But it makes the person comfortable while walking, while taking the stairs.

#### IV. Future Scope

This model can be further developed through neural network interface or using Electromyography Sensors (EMG) on the thigh muscles. It further increases the precision and timing of the robotic leg. As of now person should wear the sensors on the sound leg so that movements of sound leg were synchronized with robotic leg but micro accelerometers can be embedded into the body and data can be transmitted using wireless protocols.

#### V. Acknowledgements

The authors are grateful to the support of Dr. B. Nageswara rao Professor, KL University, India, for providing his suggestions and guidelines to mathematically model the systems presented in this paper.

#### VI. References

1. R. L. Waters, J. Perry, D. Antonelli, and H. Hislop, Energy cost of walking of amputees – Influence of level of amputation, *Bone and Joint Surgery-American* Vol. 58, no. 1, pp. 42-46, 1976.
2. D. Winter, *The Biomechanics and Motor Control of Human Gait: Normal, Elderly and Pathological*, 2nd ed.: University of Waterloo Press, 1991.
3. Source National Center for Biotechnology Information
4. Roozbeh Borjani, *Design Modeling, and Control of an Active Prosthetic Knee*, Mechanical , Waterloo, Ontario, Canada, 2008.
5. Gait analysis /Factors and parameters – Wikipedia
6. Dabiri Y, Najarian. S, Honarvar M.H , *Passive Controller Design for Swing Phase of a Single Axis Above-Knee Prosthesis*.
7. John Wallach, Edward Saibel , *Control Mechanism Performance Criteria for an above knee leg prosthesis, , Biomechanics*, Vol. 3, pp. 87-97, 1970.
8. Simulation of Swing phase dynamics in above knee prostheses, M. Y. Zarugghi and C. W. Radcliffe, J. *Biomechanics*, Vol. 9, pp. 283-292, 1976
9. A Method for Optimization of Above-Knee Prosthetic Shank-Foot Inertial Characteristics, J. C. Beck, J. Czerniecki, *Gait & Posture* 1994; 2: No 2.
10. Jimenez-Fabian R., et al. "Review of control algorithms for robotic ankle systems in lower-limb orthoses, prostheses, and 2012 Florida Conference on Recent Advances in Robotics 6 Boca Raton, Florida, May 10-11, 2012 exoskeletons". *Medical Engineering & Physics*. 34 (2012): pp. 397-408
11. Arvind Parsan, Sabri Tosunoglu. *A Novel Control Algorithm for Ankle-Foot Prosthesis*, Miami, Florida, USA.
12. Thesis on Analysis of a Lower Limb Prosthesis by Victoria S. Richardson.
13. Aeyels, B.; Peeraer, L.; Vander Sloten, P.; Van der Perre, G.; "Development of an above-knee prosthesis equipped with a microcomputer controlled knee joint: First test results," *Journal of Biomedical Engineering*, vol. 14, pp. 199–202, May 1992.
14. Carlson, J.D.; Matthis, W.; Toscan, J.R.; "Smart prosthetics based on magnetorheological fluids," *Proceedings of SPIE*"01: The International Society for Optical Engineering, vol. 4332, pp. 308-316, 2001.
15. Stein. J. L, Flowers. W. C, *Stance phase control of above-knee prostheses: knee control versus SACH foot design*, *Journal of Biomechanics*, vol. 20, no.1, pp. 19–28, 1988.
16. Bohara. A, Goldfarb. M, *Designed and Control of a Powered Transfemoral Prosthesis*, *The International Journal of Robotics Research*, vol. 27, no. 2, pp. 263-273, Feb. 2008.

# Turning Control for Quadruped Robots in Trotting on Irregular Terrain

Jeong Hoon Lee<sup>1</sup> and Jong Hyeon Park<sup>2</sup>

**Abstract**—This paper proposes that a quadruped robot turns with an accurate turning radius through natural motion even if irregular terrain exists at the turning location. For an accurate and stable turning motion, two distinctive methods are proposed. First, the robot imitates a turning motion of animals such as a horse and a dog with their spine. To implement this, a scheme that is similar to a steering system of four-wheel-driven vehicle (4WS) at a low speed. Second, variable impedance control is used in passing an irregular terrain during the turning and maintaining a stable posture control. At the posture control, geometrical compensation scheme is additionally used for more accurate and sensitive control. Despite using these control methods, errors occur between desired turning radius and actual turning radius. In this paper, the errors are appropriately compensated in two steps. First of all, the errors are compensated by changing the stride and the directions of the axes of rotation of the feet motion when the errors are small. But, if the errors grow larger than a threshold, they are compensated by moving the feet in the lateral direction. The effectiveness of the proposed control schemes was verified in computer simulations.

## I. INTRODUCTION

Animals such as a horse and a dog turn everywhere and every time, and it consists of complicated movement of bones and muscles. Animal's turning is not calculative but instinctive, and very natural. Quadruped robots are difficult to turn naturally like an animal because the robot's legs consist of simple combinations of actuators and links [1]. Therefore, a comprehension of animal locomotion is preferentially required for the robot turning accurately and naturally.

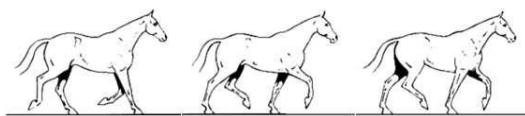


Fig. 1. Trotting of a horse

A horse and a dog have locomotion such as walk, trot, canter, gallop, and these locomotion are performed by natural transition of motion depending on various situations and environments [2]. Especially, the trot used in this study is locomotion which moves simultaneously diagonal to legs such as a left fore leg and a right hind leg. Due to this foot step type, the trot has the best energy efficiency in comparison with the other locomotion [3]–[5].

Also, an appropriate foot trajectory needs for the robot to trot stably, so an ellipsoidal trajectory is used [6], [7].

<sup>1</sup>J. Choo is with Dept. of Mechanical Engineering, Hanyang University, Seoul, 133-791, Korea. ljhdragon@naver.com

<sup>2</sup>J. H. Park is with School of Mechanical Engineering, Hanyang University, Seoul, Korea. jongpark@hanyang.ac.kr

The ellipsoidal trajectory was made through observation of animal locomotion. Therefore, it comes naturally to not only a transformation of the trajectory but generation of a periodic motion. By the transformation and the periodic motion, the robot can turn. They are represented dynamic equations matching a operation type of differential system and a steering system of vehicle.

But, because it is impossible to express perfectly the robot locomotion by kinetics and kinematics, many assumptions and linearization need. Therefore, it is important to compensate appropriately large and small errors occurred in this process. To compensate the errors, basically PID control is used, and also impedance control is used to cope with impact generated during the locomotion and unstable environment such as uneven and slippery surfaces [7]–[9].

But, impedance control is difficult to compensate large disturbance because it exists a range of parameters coping with size of disturbances. Therefore, another control method needs to control roll and pitch angle generated excessively by disturbances. To control the roll and the pitch angle, the robot uses geometrically computed values resulting from slanting of the robot body, and it is implemented by changing height of contacted legs on the surface [10], [11].

In this paper, an elaborate control scheme for a quadruped robot to turn with an accurate turning radius even on an irregular terrain is proposed. In this scheme, the robot imitates turning of animals with their spine, and variable impedance control is used. Also, a geometrical method is used for posture control additionally. Errors occurred between desired turning radius and actual turning radius during the turning are compensated through a stepwise approach. When errors are small, they are compensated by changing the stride and the direction of the axis of rotation for the elliptical motion of each feet. But, if the errors grow larger than a threshold, the foot trajectory is compensated by moving the feet in the lateral direction. The stability of the turning and the performance of the control scheme were verified in computer simulations.

## II. GENERATION OF FOOT TRAJECTORY FOR TURNING

Animal's turning consists of diverse and complicated mechanisms. To turn, quadrupeds such as a horse and a dog lean their body by taking down shoulder in the turning direction, and they control a velocity by changing the stride between outside legs and inside legs. Also, while animals draw the outside legs, they stretch the inside legs. These behaviors are observed more clearly at high speed locomotion such as dog race. A noteworthy part of this animal's turning mechanism is similar to operational principle of a differential

system and a steering system of four-wheel drive (4WS). Therefore, a basic control methods for the turning is methods for changing the stride between outside legs and inside legs as the differential system and rotating the trajectory on z-axis as the steering system.

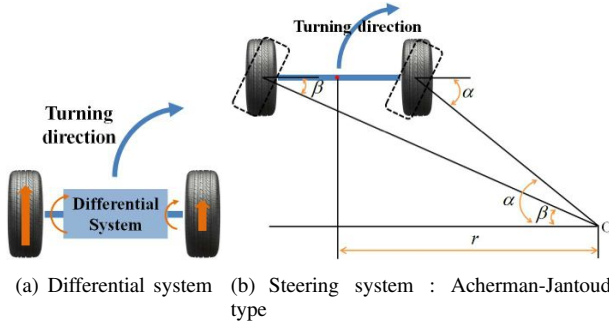
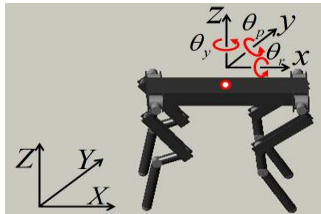


Fig. 2. Differential system and steering system in a car

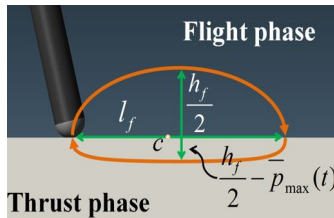
### A. Half-Ellipsoidal Foot Trajectory

In this paper, a desired foot trajectory of the robot take a form of half-ellipsoid. The half-ellipsoidal trajectory is very similar to animal's one, and the advantages is as follows.

1. It is rhythmical and continuous.
2. Transformation of the trajectory is easy.
3. The robot can move forward without changing the body height in comparison with a whole ellipsoidal trajectory.



(a) Robot model : RPY angles of yaw  $\phi_y$ , pitch  $\phi_p$ , roll  $\phi_r$



(b) Half-ellipsoidal trajectory

Fig. 3. Coordinate systems, body angles and ellipsoidal trajectory

The foot trajectory is generated with respect to the robot body, and each direction of axis(x-y-z) and RPY angles is same as shown in Fig. 3(a). The equations of the half-ellipsoid are

$$\bar{x}(t) = \frac{l_f}{2} \sin\left(\frac{2\pi}{T}t + \theta_i\right) + c_1, \quad \text{for } 0 \leq t \leq T \quad (1)$$

$$\bar{y}(t) = c_2, \quad \text{for } 0 \leq t \leq T \quad (2)$$

$$\bar{z}(t) = \frac{h_f}{2} \cos\left(\frac{2\pi}{T}t + \theta_i\right) + \bar{p}(t) + c_3, \quad \text{for } 0 \leq t \leq T \quad (3)$$

where  $l_f$  is the stride,  $h_f$  is the maximum foot height,  $T$  is the one step period,  $\theta_i$  is the initial phase,  $c_1$ ,  $c_2$  and  $c_3$  are center points of the ellipsoid, and  $\bar{p}(t)$  is a 3rd order polynomial equation. Especially,  $\bar{p}(t)$  is used to generate the half-ellipsoid and prevent non-differentiable point. This can avoid a occurring problem when impedance control module is composed.

### B. Rotation of Foot Trajectory

A car steering system is rotated wheels, and it is similar to being rotated the foot trajectory of the robot on z-axis. The trot is locomotion moving the four legs simultaneously. Therefore, the trot is associated with movement of 4WS. Especially, 4WS has a feature called a opposite direction at low speed which has a opposite phase of fore wheels and rear wheels. Also, the opposite direction is very similar to turning of animal with the spine, so it is suitable for applying to turning of the robot without the spine as shown in Fig. 4. The painted rectangles of Fig. 4(c) are a range of the stride.

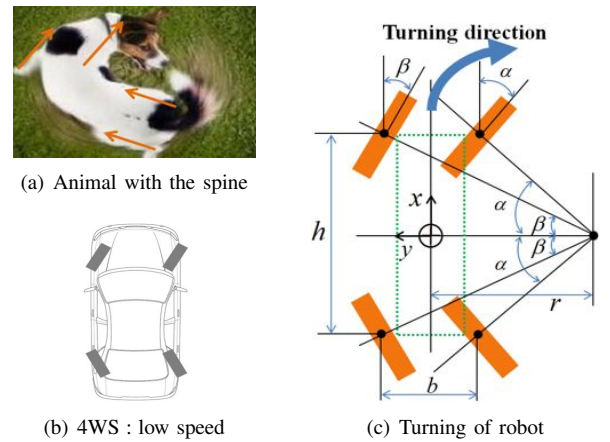


Fig. 4. Turning of robot : Differential system of 4WS

The circle drawn by tracing the foot trajectory is that the inner circle is smaller than the outer circle. It is associated with the fundamental steering system, Ackerman-Jantoud type, and the equations are

$$\alpha = \tan^{-1}\left(\frac{h}{2r - b}\right) \quad \text{and} \quad \beta = \tan^{-1}\left(\frac{h}{2r + b}\right),$$

where  $h$  and  $b$  are the length and the width of the robot body, respectively,  $r$  is the turning radius, and  $\alpha$  and  $\beta$  are the inner and outer steering angles, respectively. Eventually, the trajectory rotates  $\alpha$  and  $\beta$  on z-axis as shown in Fig. 4(c), and rotation matrix is used for the rotation.

$$\begin{bmatrix} \bar{x}_r(t) \\ \bar{y}_r(t) \\ \bar{z}_r(t) \end{bmatrix} = \begin{bmatrix} \cos \phi_{\alpha\beta} & -\sin \phi_{\alpha\beta} & 0 \\ \sin \phi_{\alpha\beta} & \cos \phi_{\alpha\beta} & 0 \\ 0 & 0 & 0 \end{bmatrix} \begin{bmatrix} \bar{x}(t) \\ \bar{y}(t) \\ \bar{z}(t) \end{bmatrix}, \quad (4)$$

where  $\phi_{\alpha\beta}$  means  $\alpha$  or  $\beta$  according to location of legs. Therefore,  $\bar{x}_r(t)$ ,  $\bar{y}_r(t)$  and  $\bar{z}_r(t)$  are the foot trajectory during the turning.

### C. Transformation of Foot Trajectory

As shown in Fig. 4(c), the angular velocity of the robot body rotating at given turning radius is the same as the outer and inner legs'. But, the outer and inner legs differ in the linear velocity. Therefore, difference between the linear velocity of inner legs and the linear velocity of outer legs is calculated using this correlation.

$$w = \frac{v + v_o}{r + \frac{b}{2}} = \frac{v + v_i}{r - \frac{b}{2}} = \frac{v}{r}, \quad (5)$$

$$v_o = -v_i = \frac{vb}{2r}, \quad (6)$$

where  $w$  is an angular velocity of the robot body,  $v$  is a linear velocity of the robot body, and  $v_o$  and  $v_i$  are variation of the linear velocity of inner and outer legs, respectively. Therefore,  $v + v_o$  and  $v + v_i$  are linear velocities of outer and inner legs, respectively.

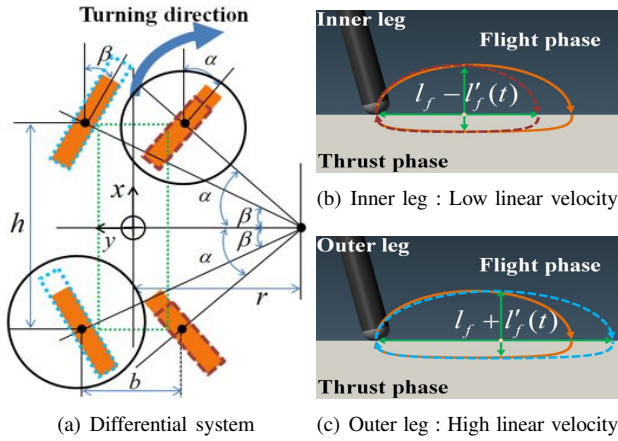


Fig. 5. Turning of robot : Differential system of 4WS

Changing the rotating velocity of inner and outer wheels by the differential gear is similar to changing the stride as shown dotted lines in Fig. 5. To perform this, a transformation of the trajectory needs. The half-ellipsoidal trajectory can transform easily, but the length of the trajectory, the stride dose not. If the transformation of the stride is attempted forcedly, continuity of the trajectory is difficult to be guaranteed. Therefore, a method for natural transformation of the trajectory needs, so this paper proposes to make the stride into a function over time.

$$\bar{x}(t) = \frac{l_f \pm \bar{l}_f(t)}{2} \sin\left(\frac{2\pi}{T}t + \theta_i\right) + c_1, \quad \text{for } 0 \leq t \leq T \quad (7)$$

which is a form that  $\bar{l}_f(t)$  is added to (1).  $\bar{l}_f(t)$  is 3rd polynomial equation ranging in size from 0 to  $v_o$ , and a plus sign and a minus sign mean the outer foot trajectory and the inner foot trajectory, respectively. Of course, (7) is also rotated by (4).

### D. Banked Roll Angle of Robot Body

When a car turning a circular track at given speed is no slip in any direction, equations that no friction between the road and wheels exists are

$$N_c \sin \theta_b = m \frac{v^2}{r}, \quad (8)$$

$$N_c \cos \theta_b - mg = 0, \quad (9)$$

where  $N_c$  is reaction force,  $\theta_b$  is a banked angle,  $r$  is a turning radius and  $v$  is a linear velocity of the car.  $\theta_b$  is found by solving simultaneous equations (8) and (9).

$$\theta_b = \tan^{-1}\left(\frac{v^2}{gr}\right). \quad (10)$$

Angle  $\theta_b$  can be also applied to the banked roll angle of the robot body in turning as shown in Fig. 7.

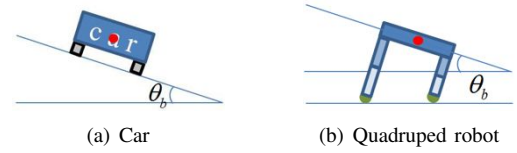


Fig. 7. Banked roll : Car and Quadruped robot

When angle  $\theta_b$  is applied to the robot,  $r$  and  $v$  are the given turning radius and the stride per second, respectively. Eventually, the robot leans the body at  $\theta_b$  during the turning.

### III. IMPEDANCE CONTROL

Impedance control is effective, especially for reducing the disturbance. The irregular terrain is a kind of disturbance. Therefore, impedance control plays important roles in turning on irregular terrain.

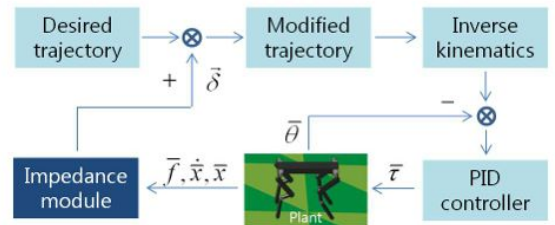


Fig. 8. Impedance control block diagram

As shown in Fig. 8, input of the impedance module is force  $\bar{f}$ , then output is position offset  $\bar{\delta}$ . Therefore, this impedance control can be defined admittance control.

$$\ddot{\delta} = \frac{1}{M}[\bar{f} - B\dot{\delta} - K\delta], \quad (11)$$

where  $M$ ,  $B$  and  $K$  are parameters of impedance module.  $M$  is the mass,  $B$  is the critical damping ratio  $B = 2\sqrt{MK}$  and

$K$  is the stiffness. The critical damping ratio can decrease most rapidly effects of impact (i.e., overshoot) changing the desired trajectory. After integrating  $\ddot{\delta}$  of (11) twice,  $\delta$  is added to the desired trajectory.

#### IV. CONTROL FOR THE ROBOT POSTURE

Although impedance control is used to locomotion of the robot, the robot is difficult to trot stably in all environment. Because there is a limit to the parameter of impedance control which can cope with the disturbance. Therefore, if the robot encounters disturbance such as irregular terrain during the turning, the roll angle  $\phi_r$  and the pitch angle  $\phi_p$  of the robot body increase rapidly. So, the body angles must be controlled for the robot turning stably. In trotting,  $\phi_r$  and  $\phi_p$  affect each other. But, if correlation of the angles is not figure out, simultaneously compensating the angles rather make the posture unstably. Therefore, method for compensating the excessive  $\phi_r$  that generally has larger range of variation than  $\phi_p$  is selected. For example, if the sizes of rolling and pitching of the robot body are almost identical (i.e., in stable trotting),  $\phi_p$  is always smaller than  $\phi_r$ . Because the robot body is rectangle that the length  $h$  is taller than the width  $b$  as shown in Fig. 4(c).

##### A. Geometrical Compensation of Roll Angle

The most common method for compensating the excessive  $\phi_r$  is a geometrical method as shown in Fig. 9.

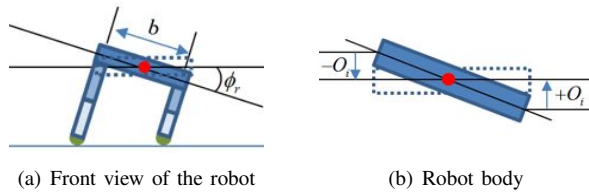
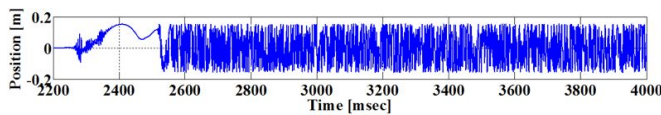


Fig. 9. Geometrical compensation :  $O_i$

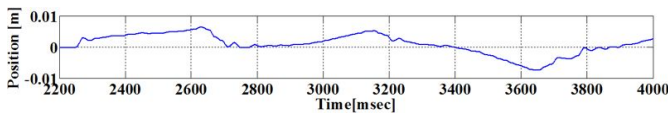
The equation of the size (i.e.,  $O_i$ ) is

$$O_i = \frac{b}{2} \sin(\phi_r - \theta_b), \quad (12)$$

where  $O_i$  is  $O$  of  $i_{th}$  state.  $i_{th}$  state means order of sampled roll angles with sample time.  $\theta_b$  is a banked roll angle. Therefore, unstability of the posture can be modified by adding  $O_i$  to (3).



(a)  $O_i$  in sample time, 0.001sec



(b)  $O_i$  in sample time, 0.02sec

Fig. 10. Comparison of  $O_i$  with sample time

But,  $O_i$  is generated very unstable values as shown in Fig. 10(a) because the robot works in very short sample time, 0.001 sec during the simulation.

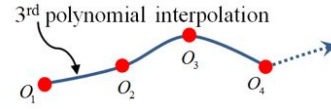


Fig. 11. 3rd polynomial interpolation of  $O_i$

Therefore, the robot is required appropriate sample time which can reflect the accurate body angles not having a short oscillation cycle. In this paper, the determined sample time of  $\phi_r$  is 0.02 sec, and because of altered sample time, interpolation is required as shown in Fig. 11.

##### B. Variable Impedance Control And Geometrical Compensation

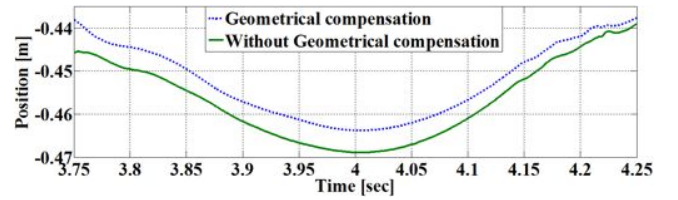


Fig. 12. Foot trajectory compensated by impedance control on z-axis

But, method for compensating the excessive  $\phi_r$  by moving the center of the foot trajectory is not suitable for the locomotion using impedance control. Because, by impedance control,  $O_i$  is also compensated. The dotted line of Fig. 12 is made by  $O_i$ , 0.01 m, but generally the trajectory on z-axis is compensated by about 0.005 m. In other words, the error is compensated only half. To solve this problem, variable impedance control that can control the excessive  $\phi_r$  changing impedance parameter in real time is used in form of servo control as shown in Fig. 13.

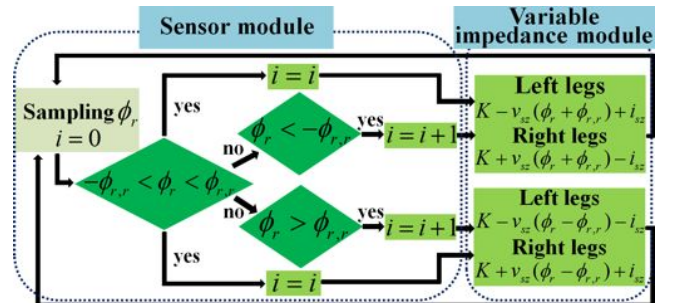


Fig. 13. Variable impedance control:  $\phi_{r,r}$  is reference roll angle.

$$\ddot{\delta} = \frac{1}{M_i} [f - B_i \dot{\delta} - K_i \delta], \quad (13)$$

where  $M_i$ ,  $K_i$  and  $B_i$  are the impedance parameters of  $i_{th}$  state. Especially,  $K_i$  of (13) means  $K \pm v_{sz}(\phi_r + \phi_{r,r}) \mp i_{sz}$  and  $K \pm v_{sz}(\phi_r - \phi_{r,r}) \pm i_{sz}$  of Fig. 13, and it is a linear

function of stiffness that variable is  $\phi_r$ .  $i_{sz}$  and  $v_{sz}$  of the linear function are a y-intercept and a slope, respectively.  $B_i$  is the critical damping ratio. Also, After integrating  $\dot{\delta}$  of (13) twice, position offset  $\delta$  is added to the desired trajectory as shown in Fig. 8. But, such servo control is difficult to control the excessive  $\phi_r$  sensitively and accurately. Therefore, additionally the geometrical method is used to make up for this fault. In other words, the size of  $O_i$  decreases by multiplying the gain, and The decreased  $O_i$  can control  $\phi_r$  sensitively and accurately.

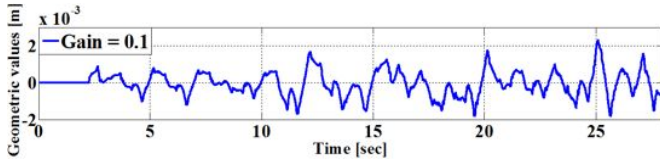


Fig. 14.  $O_i$  multiplied by gain

This is similar to method compensating error using PID controller. Variable impedance control is used to main control method for compensating the excessive  $\phi_r$  like using proportional control of PID controller, and the occurred steady state error and slowed speed of response is compensated by the geometrical method like using integral control and differential control of PID controller.

### C. Compensation of Turning Error

Although introduced methods such as transformation and rotation of the trajectory, posture control, etc. is used appropriately, still the turning error exists between desired turning radius and actual turning radius.

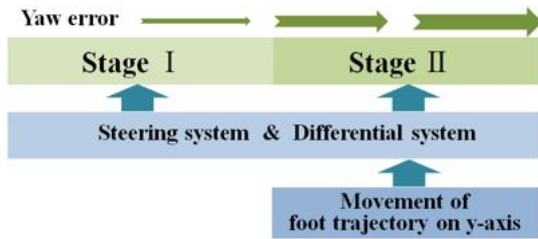


Fig. 15. Stepwise compensation method

Therefore, the error needs to be compensated appropriately, so a stepwise approach is used as shown in Fig. 15.

At first stage that the error is smaller than the threshold, the error is compensated by differential system and steering system. In other words, the variation of the stride and the rotation of the foot trajectory are added to (7) and (4), respectively during one step period. At the second stage that the error grows larger than the threshold, the foot trajectory on y-axis is moved as shown in Fig. 16(b). The equation of the second stage is

$$\bar{y}(t) = c_2 + \bar{m}(t), \quad \text{for } 0 \leq t \leq T \quad (14)$$

which is a form that  $\bar{m}(t)_f$  is added to (2).  $\bar{m}(t)_f$  is 3rd polynomial equation, and the size (i.e.,  $r_a - r_d$  as shown in

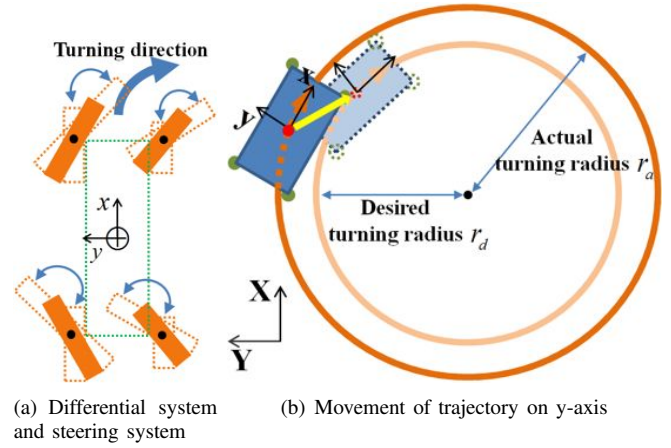


Fig. 16. Compensation of turning error

Fig. 16(b)) is determined by considering workspace of the robot.

## V. SIMULATION

As shown in Fig. 3(a), the robot model simplifies a hardware model HUNTER (Hanyang UNIVERSITY TETRAPOD Robot) developed by Hanyang University. HUNTER is 0.5 m tall and 0.35 m wide. Its head-to-tail length is 0.6 m. It weights about 24 kg.

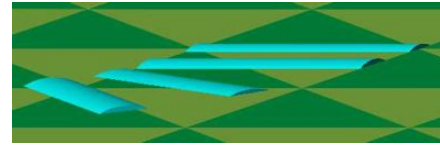


Fig. 17. Irregular terrain model

The simulation is processed by using Mathworks's Matlab and Functionbay's RecurDyn. Spring coefficient and damping coefficient between ground and robot foot are each 2000 kN/m and 1.0 kN·s/m. Dynamic friction coefficient and static friction coefficient are 0.6 and 0.9, respectively.  $l_f$  and  $h_f$  are 0.100 m and 0.080 m, respectively, the one step period is 1 sec and the turning radius is 1.5 m. As shown in Fig. 17, irregularities of the terrain are 0.017 m, 0.02 m, 0.015 m and 0.017 m in a clockwise direction, respectively.

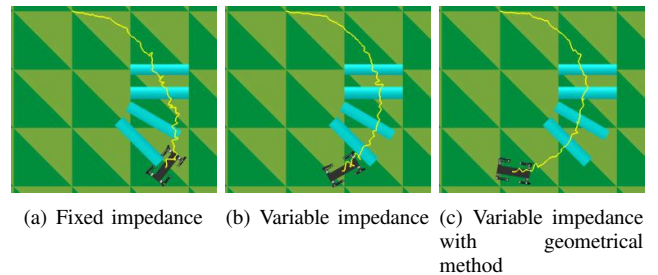


Fig. 18. Top view of the robot during the turning

Fig. 18 shows results depending on each condition. When fixed impedance control is used, the robot escapes the route.

In the case of Fig. 18(b) using variable impedance control, the distance traveled is shorter than in the case of Fig. 18(c) because the robot body excessively sways by the rolling. Also, Fig. 19 shows that the robustness and the stability of the proposed posture control is verified. And, as shown in Fig. 20, variable impedance control is performed appropriately.

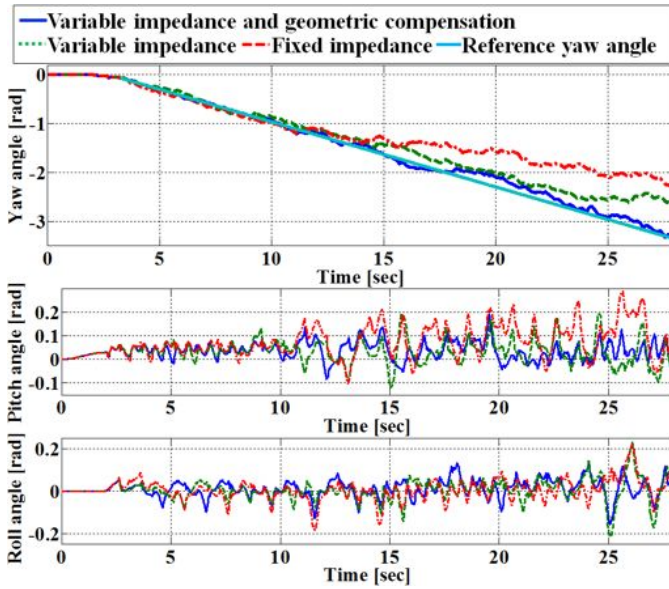


Fig. 19. Body angles ( $\phi_r$ ,  $\phi_p$ ,  $\phi_y$ ) on each condition

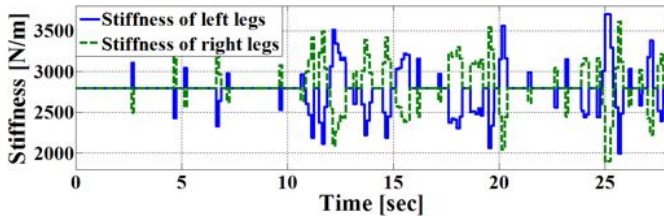


Fig. 20. Variable impedance control for robot posture control

Figs. 21 and 22 show that the generation of the foot trajectory during the turning and the stepwise compensation of the turning error is operated appropriately. In other words, Fig. 21 is the foot trajectory generated by the differential system, the steering system and the posture control, and Fig. 22 is the application result of (14).

### VI. CONCLUSION

In this paper, various methods for the quadruped robot turning accurately on irregular terrain is proposed. Basically the robot imitates the operation type of differential system and steering system of 4WS at low speed. Especially, the steering system of 4WS at low speed, an opposite direction is represented as animal's turning with the spine. Also, variable impedance control and geometrical compensation is simultaneously used to eliminate unstability of the posture generated during the robot turning. The turning error existing between desired turning radius and actual turning radius is

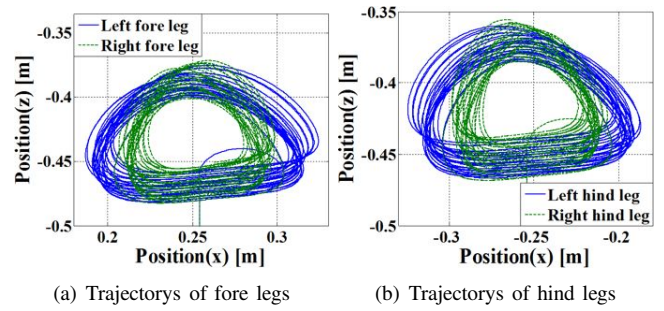


Fig. 21. Trace of foot trajectory

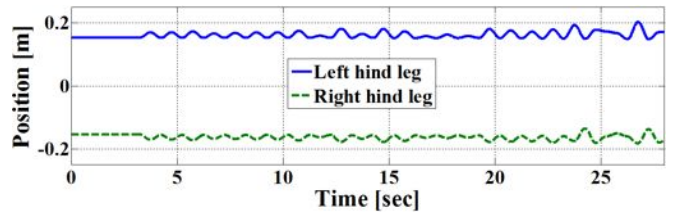


Fig. 22. Movement of foot trajectory on y-axis

compensated by stepwise approach. The variation of the stride and the rotation of the foot trajectory is used at the first stage and the method moving the center of the foot trajectory on the y-axis is used at the second stage. The proposed control methods have shown even better stability and performance than the control groups.

### REFERENCES

- [1] L. R. Palmer III and D. E. Orin, "Intelligent control of high-speed turning in a quadruped," *Journal of Intelligent and Robotic Systems*, vol. 58, no. 1, pp. 47–68, 2010.
- [2] R. M. Alexander, *Principles of animal locomotion*. Princeton University Press, 2003.
- [3] J. Glower and U. Ozguner, "Control of a quadruped trot," in *Proceedings of IEEE International Conference on Robotics and Automation*, 1986, pp. 1496–1501.
- [4] R. Kurazume, S. Hirose, and K. Yoneda, "Feedforward and feedback dynamic trot gait control for a quadruped walking vehicle," in *Proceedings of IEEE International Conference on Robotics and Automation*, 2001, pp. 3172–3180.
- [5] M. H. Raibert, "Trotting, pacing and bounding by a quadruped robot," *Journal of biomechanics*, vol. 23, pp. 79–98, 1990.
- [6] K. Y. Kim, O. Kwon, J. S. Yeon, and J. H. Park, "Elliptic trajectory generation for galloping quadruped robots," in *Proceedings of IEEE International Conference on Robotics and Biomimetics*, 2006, pp. 103–108.
- [7] J. H. Lee and J. H. Park, "Control for quadruped robots in trotting on horizontal and slanted surfaces," in *Control Conference (ASCC), 2013 9th Asian*. IEEE, 2013, pp. 1–6.
- [8] J. H. Park, "Impedance control for biped robot locomotion," *IEEE Transactions on Automatic Control*, vol. 17, no. 6, pp. 870–882, 2001.
- [9] R. Ikeura and H. Inooka, "Variable impedance control of a robot for cooperation with a human," in *Robotics and Automation, 1995. Proceedings., 1995 IEEE International Conference on*, vol. 3. IEEE, 1995, pp. 3097–3102.
- [10] M. Raibert, K. Blankespoor, G. Nelson, R. Playter et al., "Bigdog, the rough-terrain quadruped robot," in *Proceedings of the 17th World Congress*, 2008, pp. 10 823–10 825.
- [11] H. Kimura, Y. Fukuoka, and A. H. Cohen, "Adaptive dynamic walking of a quadruped robot on natural ground based on biological concepts," *International Journal of Robotics Research*, vol. 26, no. 5, pp. 475–490, May 2007.

# An enhancement text method for image acquired via digital cameras by PDE's stable model

Hassan El Bahi, Zouhir Mahani and Abdelkarim Zatni

Université Ibn Zohr, ESTA, Laboratoire Matériaux, Systèmes et Technologies de l'information  
B.P: 33/S, 8000 Agadir - Maroc  
elbahihassan@gmail.com; z.mahani@uiz.ac.ma; a.zatni@uiz.ac.ma,  
<http://www.esta.ac.ma/>

**Abstract**— This paper presents a new stable approach to enhance text in document image acquired by camera phones. It aims at investigating the stability analysis of this approach through the examination of a model giving the relationship between reflection and luminance of the image, through the consideration of the luminance estimated by partial differential equation (PDE) method. Then we deduce the reflection from the luminance already calculated and the acquired image. In this paper we relied on the stability analysis of von Neumann to study stability of partial differential equation (PDE). This approach offers excellent results in terms of legibility and the preservation of textual information in real-world situation especially in images acquired from camera phones in low luminosity and other distortions problems. The efficiency of this method is illustrated by its capacity to ameliorate the process of Optical Character Recognition (OCR) in text documents recognition.

**Keywords**—Document-image, stability analysis, PDE, Von Neumann.

## I. INTRODUCTION

One of the most confronting problems in digital image processing is the restoration of degraded images, especially in images taken by digital devices (mobile phone and digital cameras). The resulting image is different from the expected picture due to some disturbing factors which appear when taking images [1]. Like noise (for example in a bad reception data), blur (due to bad development), or loss of quality (due to bad brightness).

The problems arising from the improvement and restoration of images were widely discussed in different scientific papers, and since the invention of the discipline of digital image processing, in the '60s and the development of promising computing resources. The improvement and restoration of images has been the main problem and it still receives an increasing attention by specialists.

The image enhancement aims at making the image more meaningful to the human eye who's the only final judge of the effectiveness of any treatment. Restoration intend to correct the distortions introduced during the previous steps of the acquisition or transmission.

Many methods based on partial differential equations (PDE) have emerged in recent years in the areas of image processing and computer vision that solve problems generally related to the improvement and restoration of images, Edge detection , Segmentation, Morphology ... (see [2.3.4.11]).

The image is supposed to be obtained from a digital device - more exactly a camera phone, or a digital camera, in the rest of our work we are going to focus on the camera phone images in which the problems is mostly apparent.

This paper is an attempt to further the work displayed in [5, 11] by a further examination and study of the stability.

A basic camera phone produce usually images of bad quality documents – which means it must be really tedious, if not impossible, to be read by someone or an optical character recognition system (OCR). Due to conception constraints, camera-phone has some limitations that we have to take into account if we want to produce readable documents.

This paper is divided into the following sections: Section 1 provides a description of our method of improving noisy or blurry pictures taken by a mobile device. Section 2 we present the use of partial differential equations (PDE) in image enhancement. Section 3 we study the stability of our PDE method in two cases: one-dimensional (1D) and two dimensional case (2D). Finally, some numerical results illustrate this work in Section 4.

## II. THE MODEL

We consider two kinds of problems due to the acquisition of a document picture via a camera phone: image distortion and noise.

In the following, we address a distortion also called a non-

uniform illumination or variations of brightness [6], which is the main cause behind the major image processing difficulties. One of the main effects of distorting the image is shadows. A shadow in image processing is conceived as a region of low brightness and high gradients contours. Shadows are separated into two types, the first type is the own shadow and the second type is the one due to the acquisition. Own shadow occurs when light hits a surface with deviation. This causes the diminution of the brightness of the pixels corresponding to the area as the incidence angle deviates from the surface normal. The brightness attains its minimum level when the incident light and the surface normal are orthogonal. We also notice another kind of shadow, which occurs when the light source is veiled by an object before the reflection of light on the surface. Other distortions problems such as blurring or warping are not evoked in this paper.

We consider an image  $u \in \mathbb{R}^{N_1 \times N_2}$  where  $N_1$  and  $N_2$  are two integers. The non uniform illumination can be modeled as a multiplicative effect. This modeling combining the reflectance and the luminance of the image was proposed by Barrow and Tenenbaum in 1978 [5]. That said, due to various factors that may be involved in the construction of the image (the illumination of the object, the geometry of the scene acquired, the camera settings ...), such modeling is very difficult to tackle.

In 1999 a generative model of the image, based on a combination of Fredholm integral equation and modeling of settings of the camera was proposed by Laszlo [9]. This model remains quite complicated to implement. Thus; the global illumination method [9] remains the most widely used:

$$u(x, y) = I(x, y) \cdot v(x, y) \cos_{\theta}(x, y) + b(x, y) \quad (1)$$

$u(x, y)$  is the grayscale of the pixel  $(x, y)$ ,  $I$  is the luminance or the non uniform illumination,  $v(x, y)$  the reflectance and  $\cos_{\theta}(x, y)$  the cosine of the angle between the incident light ray and the surface normal at the point of the object. In image processing, this modeling is even more simplified by integrating  $\cos_{\theta}(x, y)$  on the component  $I(x, y)$ . Thus, the final model becomes:

$$u(x, y) = I(x, y) \cdot v(x, y) + b(x, y) \quad (2)$$

This modeling of the image is far from perfect, because it does not take into account neither the problems of geometry of the object (the presence of surfaces which can create shadows on the object ...), or external factors in the formation of the image. The advantage of this simple model is to estimate the reflectance of an object from an approximation of its luminance.

### III. THE PDE METHOD

From the module already defined in section 2 the noise can be neglected for the moment. Thus, the result becomes as the following:

$$u(x, y) = I(x, y) \cdot v(x, y) \quad (3)$$

Then we apply the log to the equation (3):

$$\begin{aligned} \log(u(x, y)) &= \log(I(x, y)v(x, y)), \\ \log(u(x, y)) &= \log(I(x, y)) + \log(v(x, y)), \\ &\Rightarrow \tilde{u} = \tilde{I} + \tilde{v} \end{aligned} \quad (4)$$

A new approach was proposed by [11] to estimate  $\tilde{I}$  which is in fact the solution of the partial differential equation (PDE) (4) then he concludes  $\tilde{v}$  by the subtraction of  $\tilde{I}$  from  $\tilde{u}$ .

$$\begin{cases} w_t = d \max(0, d \Delta^A w), \\ \frac{\partial w}{\partial t} = 0 \\ w(t=0) = u, \end{cases} \quad (5)$$

The grayscale of the text equals 1 if it is smaller than the background or equals -1 in the case that the grayscale of the text is larger than the image background.

As it is defined by:

$$\Delta^A := \operatorname{div}(\varphi'(|\nabla u|) \frac{\nabla u}{|\nabla u|}) \quad (6)$$

We decompose the divergence operator:

$$\operatorname{div}(\varphi'(|\nabla u|) \frac{\nabla u}{|\nabla u|}) = \frac{\varphi'(|\nabla u|)}{|\nabla u|} u_{tt} + \varphi''(|\nabla u|) \cdot u_{nn} \quad (7)$$

With:

$$\begin{aligned} u_{tt} &= \tau^t \nabla^2 u \tau = \frac{1}{|\nabla u|^2} (u_{x1}^2 \cdot u_{x2x2} - 2u_{x1} \cdot u_{x2} \cdot u_{x1x2} + u_{x2}^2 \cdot u_{x1x1}) \text{ and} \\ u_{nn} &= \tau^t \nabla^2 u n = \frac{1}{|\nabla u|^2} (u_{x1}^2 \cdot u_{x1x1} + 2u_{x1} \cdot u_{x2} \cdot u_{x1x2} + u_{x2}^2 \cdot u_{x2x2}) \end{aligned}$$

An example of function that can be used:

$$\varphi(x) = \sqrt{1+t^2} \quad (8)$$

So  $\frac{\varphi'(|\nabla u|)}{|\nabla u|} = \frac{1}{2(1+|\nabla u|^2)^{3/2}}$  and

$$\varphi''(|\nabla u|) = \frac{1}{2(1+|\nabla u|^2)^{1/2}}$$

By following the approach [11] he estimates that  $\tilde{v}$  can be calculated as follow:

$$\tilde{v} = \frac{(1+s)}{2} \max(\tilde{u}) - s |\tilde{I} - \tilde{u}| \quad (9)$$

In practice, we identify only certain points (because of the scan of the image). This is why we need to define an approximation of equation (5) (for more details see [11]).

#### IV. STABILITY ANALYSIS

The aim of this part is to study Stability Analysis of the partial differential equation (PDE) (5). Generally speaking the stability of particular solution of a PDE implies that if the system starts with an initial condition that approximates the particular solution of a PDE, the system will stay near it for all time.

BA Jacobs [10] assumed that the PDE method of [11] is complicated since it implies numerous steps which may make its implementation difficult especially after a number of iterations. Thus our objective in this part is to demonstrate the stability of the PDE method of [11]. We relied on the stability analysis of von Neumann which is a method for testing the stability of numerical schemes using the method of finite difference of partial differential equation (PDE).

The expression Von Neumann:

$$u_i^n = U^n e^{iwi\Delta x}$$

##### A. One-dimensional Case (1D):

We can use two approaches to discrete this equation. The first is an explicit scheme; we use a forward scheme of order 1 to evaluate the time derivative and a central scheme of second-order for the second derivative in space of equation (5), and by putting:

$$r = \frac{d \times \Delta t}{\Delta x^2} \text{ and } u(x, t_n) = e^{ik\Delta x}$$

The scheme description becomes:

$$u_j^{n+1} = G(k) e^{ik\Delta x j} \quad (10)$$

With:

$$G(k) = 1 - 2r(1 - \cos(k\Delta x)). \quad (11)$$

Where  $G(k)$  is the growth factor. The scheme is stable [13] if  $|G(k)| < 1 \forall k$ , in the worst case we have  $G(k) = 1 - 4r$ . So the scheme is stable conditionally if  $r \leq 1/2$ .

The second is an implicit scheme; we use a backward scheme of order 1 to evaluate the time derivative and a central scheme of second-order for the second derivative in space. In this case with same transformation, the Growth factor becomes:

$$G(k) = \frac{1}{1 + 4r \sin^2\left(\frac{k\Delta x}{2}\right)} \quad (11)$$

So Von Neumann's condition is proven thus the scheme is unconditional stable.

##### B. Two-dimensional Case (2D):

We consider the following equation of two dimensions:

$$\frac{\partial u}{\partial t} = \frac{\partial^2 u}{\partial x^2} + \frac{\partial^2 u}{\partial y^2} \quad (12)$$

And we use a scheme of order 1 to evaluate the time derivative and a scheme centered of order 2 to approximate the second derivative in space. We put  $r_1 = \frac{\Delta t}{\Delta x^2}$  and  $r_2 = \frac{\Delta t}{\Delta y^2}$

we find:

$$G(k) = 1 + 2r_1(\cos(k\Delta x) - 1) + 2r_2(\cos(k\Delta y) - 1) \quad (13)$$

In the worst cases we have:

$$G(k) = 1 - 4\left(\frac{\Delta t}{\Delta x^2} + \frac{\Delta t}{\Delta y^2}\right) \quad (14)$$

If  $\Delta x = \Delta y = h$  the stability condition is:  $\Delta t \leq \frac{h^2}{4}$

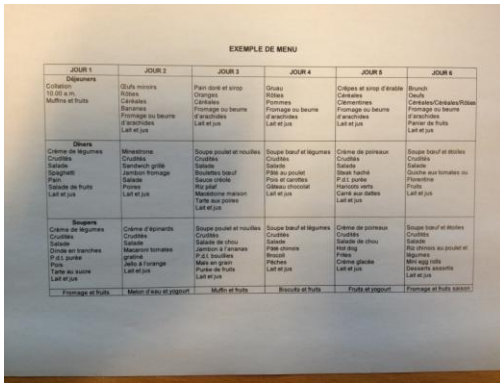
#### V. NUMERICAL RESULTS

In this section, we present some simulation results showing the effectiveness and the robustness of our method. We show the ability and the stability of the suggested approach in terms of enhancement and preservation of textual information in images acquired from camera phone in low luminosity and other distortions factors.

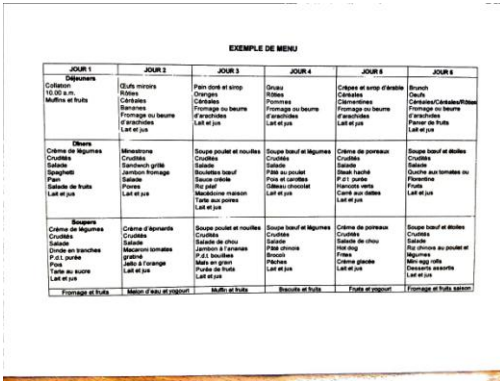
In all examples the original images are obtained from a camera phone (Iphone 4GS).

Figure 1 shows an example of text enhancement by the suggested method by estimating the reflectance. The image is affected by its own shadow. The resulting image is distortions-free (absence of shadow) and resulting estimations are correct and completely similar.

Figures 2 and 3 show the performance of the proposed approach to provide an excellent result in cases of further distortion factors. In figure 2 the acquired image is taken in low lightning conditions whereas the original image in figure 3 is affected by its own shadow and the drop shadow. This approach provides better results in terms of readability and printability of the resulting document-image.

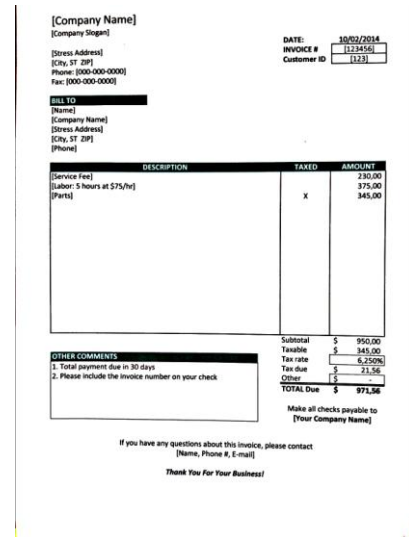


(a) Original image



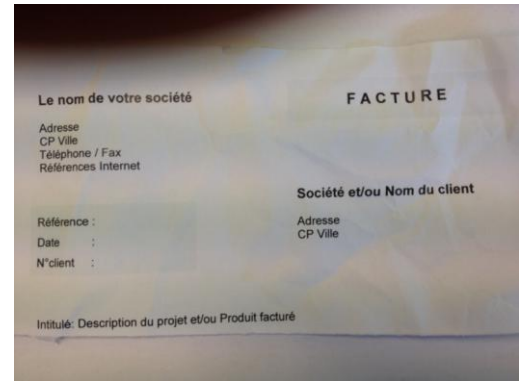
(b) Text enhancement

Fig. 1 Original image obtained from an Iphone 4GS

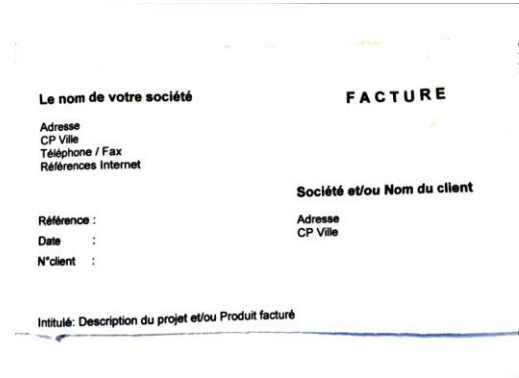


(b) Text enhancement

Fig. 2 Original image obtained from an Iphone 4GS

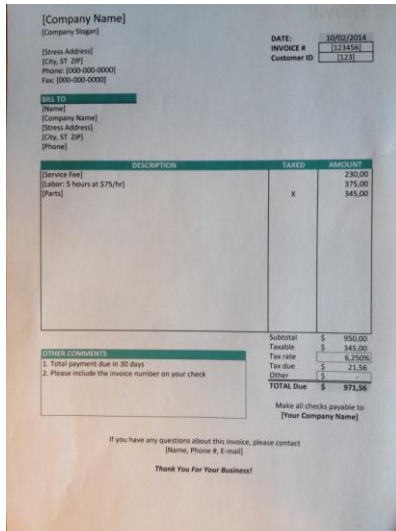


(a) Original image



(b) Text enhancement

Fig. 3 Original image obtained from an Iphone 4GS



(a) Original image

## VI. CONCLUSION

This paper proposes a stable method to enhance text in the documents image obtained from a camera phone. It suggests a method which is based on anisotropic PDE's model. This work relied on Von Neumann stability analysis to prove the stability

of PDE method in two cases the first one is one-dimensional case (1D) in which we used explicit and implicit schemes. The second one is the two dimensions case (2D). This method provides the best result in terms of robustness and effectiveness in the examined cases, especially in low lightning conditions and the presence of shadows, moreover this method has shown that it is simple and unsophisticated to implement.

In brief, this method has shown excellent result when applied to ameliorate the process of Optical Character Recognition (OCR) in text documents recognition from images obtained via camera phones even with presence of distorting factors.

#### REFERENCES

- [1] Henry S. Baird, "The State of the Art of Document Image Degradation Modeling," In *Proc. of 4th IAPR International Workshop on Document Analysis Systems*. Rio de Janeiro, 2000, pp. 1–16.
- [2] F. Drira, F. Le Bourgeois and H. Emptoz, "Document images restoration by a new tensor based diffusion process: Application to the recognition of old printed documents," *10th International Conference on Document Analysis and Recognition (ICDAR09)*. Barcelone, 2009, pp. 321–325.
- [3] B. Smith, "RSLDI: Restoration of single-sided low-quality document images," *Pattern Recognition, Special Issue on Handwriting Recognition*. no. 42, pp. 3355-3364 (2009).
- [4] I. Nwogu, Z. Shi, and V. Govindaraju, "Pde-based enhancement of low quality documents," In *The (ICDAR07)*, page 541-545, Vol.01, 2007.
- [5] S. Saoud, Z. Mahani, M. El-Rhabi and A. Hakim, "Document scanning in a tough environment: application to camera phone," *International Journal of Imaging and Robotics (IJIR), Special issue on Practical Perspective of Digital Imaging for Computational Applications*, 9(1):1-16, 2013.
- [6] J. Kim and H. Lee, "Joint nonuniform illumination estimation and deblurring for bar code signals," *Optic Express.*, vol. 15, issue 22, pp. 14817–14837, 2007.
- [7] H.G. Barrow and J.M. Tenenbaum," Recovering intrinsic scene characteristics from images," In *CVS78*, pages 326, 1978.
- [8] Szirmay-Kalos Laszlo, "Monte-Carlo Global Illumination Methods - State of the Art and New Developments," *SCCG'99*, Invited talk, 1999.
- [9] A. Jacobs and E. Momoniat, "A novel approach to text binarization via a diffusion-based model," *Applied Mathematics and Computation*, vol. 225: 446–460, 2013.
- [10] Z. Mahani, J. Zahid, S. Saoud, M. El Rhabi and A. Hakim, "Text enhancement by pde's based methods," *Lecture Notes in Computer Science, Image and signal Processing*, 7340:65-76, 2012.
- [11] M. El Rhabi and G. Rochefort, Realeyes3D SA, patent. Available : <http://patentscope.wipo.int/search/en/WO2009112710>
- [12] Numerical Methods for Partial Differential Equations, Spring 2009. Available: <http://ocw.mit.edu/courses/mathematics/18-336-numerical-methods-for-partial-differential-equations-spring-2009/lecture-notes/>

# Prosthesis Design for Bilateral Hip Disarticulation Management

Ing. Mauricio Plaza Torres PhD, Ing. William Aperador. PhD  
UNIVERSIDAD MILITAR NUEVA GRANADA

**Abstract**—Hip disarticulation is an amputation through the hip joint capsule, removing the entire lower extremity, with closure of the remaining musculature over the exposed acetabulum. Tumors of the distal and proximal femur were treated by total femur resection; a hip disarticulation sometimes is performed for massive trauma with crush injuries to the lower extremity. This article discusses the design of a system for rehabilitation of a patient with bilateral hip disarticulations. The prosthetics designed allowed the patient to do natural gait suspended between parallel articulate crutches with the body weight support between the crutches. The care of this patient was a challenge due to bilateral amputations at such a high level and the special needs of a patient's mobility.

**Keywords**— Amputation, prosthesis, mobility, hemipelvectomy

## I. INTRODUCTION

Hip disarticulation is the removal of the entire lower extremity through the hip joint. Hip disarticulation amputations are relatively rare [1],[2],[3]. For this reason there is not much research on this area to give a solution specific to self-mobility. They are usually performed when a malignant disease of the pelvis, hip joint or upper thigh cannot be treated by more conservative means. Sometimes they are performed if osteomyelitis of the pelvis or proximal femur or certain massive benign tumors in the pelvic region has not responded to less radical procedures [4],[5].

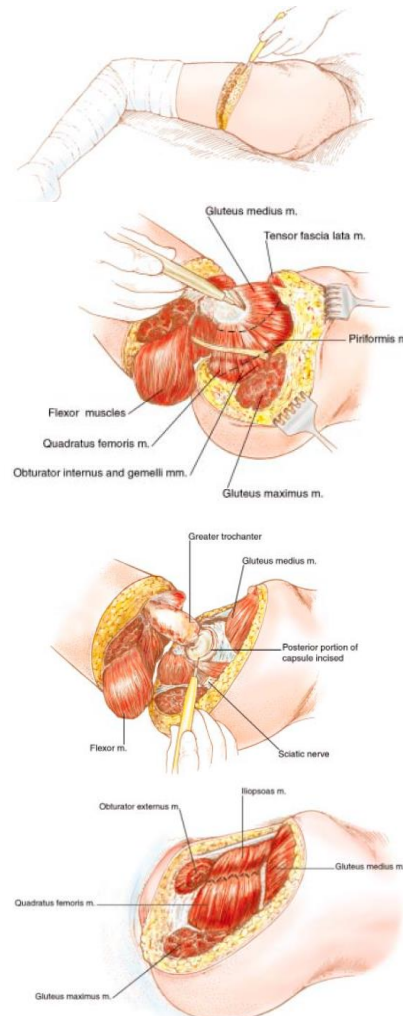


Fig 1. Surgical Procedure

The surgical procedure includes

- ✓ Completion of the skin incision
- ✓ Division of tensor fascia lata, gluteus maximus, and rectus femoris muscles
- ✓ Transection of the muscles inserting into the greater trochanter
- ✓ Release of specimen
- ✓ Approximation of obturator externus and gluteus medius over the joint capsule

- ✓ Approximation of gluteal fascia to the inguinal ligament and pubic ramus
- ✓ Skin closure

Who had bilateral hip disarticulation amputations, including transection of ischia to the level of the horizontal ramus of the pubis was treated prosthetically and rehabilitated. Prosthetic fitting failed because of chronic tissue breakdown over the remaining bony prominences [6],[7],[8]. The prosthesis had to provide mobility by gait training and the design of the mat avoid tissue breakdown. Paraplegics face a number of medical, psychological and emotional issues, which can usually be managed in resource-rich centers with adequate social support. [9],[10],[11].

However, in developing countries, with some resources, living with paraplegia and its associated complications is considerably more difficult especially to self-mobility actions. [12],[13],[14] Hip disarticulation orthosis has some advantages for the paraplegic patient, such as increased independence, a lighter body weight and minimization of local infection. Disadvantages, however, include impaired cosmetic appearance; need some training to acquire stability and good balance and loss of body image (Fig 2).

## II. EVALUATION

The prosthetics designed allowed the patient to do natural gait suspended between parallel articulate crutches with the body weight support between the crutches.(Fig 3.) The majority of the weight was distributed to the support system over the bony prominences release a portion of the weight from the forearms.

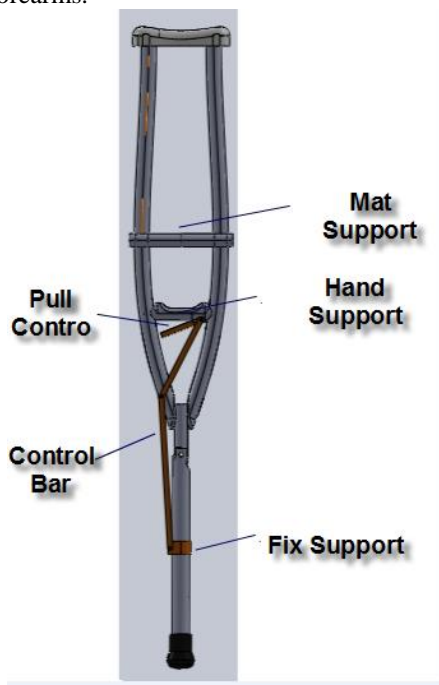


Fig 2. Crutches design

## III. DESIGN CONSIDERATION

The support mold was design to distribute weight primarily to the shelf created by the spinal and posterior thorax region. Reliefs were provided over bony prominences via plaster build-ups on the mold.

The mold was to provide a surface which would allow the patient to sit erect without external support. The socket was laminated with polyester resin at 80% rigid, 20% flexible. This system satisfied the walk action by parallel bars or addition of artificial limbs made the entire design functional for transfer and mobility.

The patient was able to ambulate in the parallel bars with a swing through gait.[15],[16] A lay up of four layers of nylon stockinette was made over the socket and again laminated with polyester resin. This patient could not tolerate any distal pressure due to a large ulcer over the sacrum. His amputations were secondary to circulatory problems and diabetes. A minimal amount of extension of the socket was needed as his pelvis was intact and only needed suspension to protect the unhealed area. This patient desires lower limbs for gait provided by parallel bars or artificial limbs for mobility. The socket only provided him with protection for his wounds, sitting balance, and ease in transfer.

## IV. FABRICATION AND FITTING

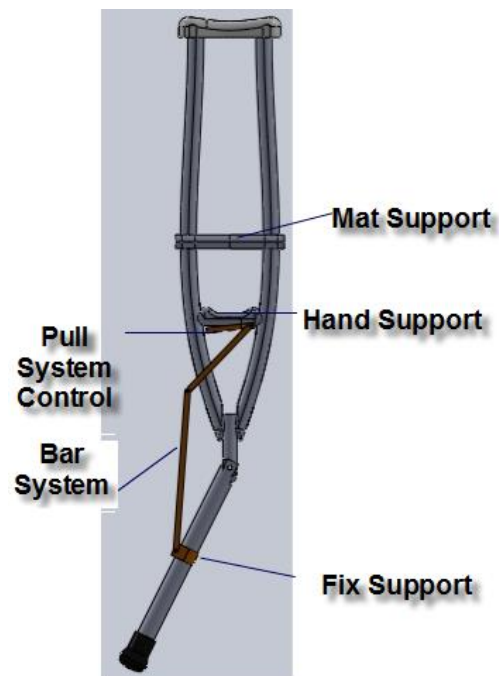


Fig 3. Articulate Crutches System

A plastic pad was formed over the mold for fit in sitting, standing and prone positions. Reliefs were provided to the bony prominences, and two crutches were provided to allow

gait in normal way. Cushions system was located at the axilla level sufficiently to prevent impingement during upper-extremity motion such as flexion and extension of the glen humeral joint and lateral trunk bending. A spring system was placed at the level of the arm to allow adjustments the level of the crutch as the same way of the knees. The spring could adjust the amount of weight both side during the gait. Lower manual system were attached to the metallic bar using for manual locking knees are implemented, While this modular spring system would have provided weight switch, the components and covering would withstand the stress and forces encountered when the patient gait.[17],[18]

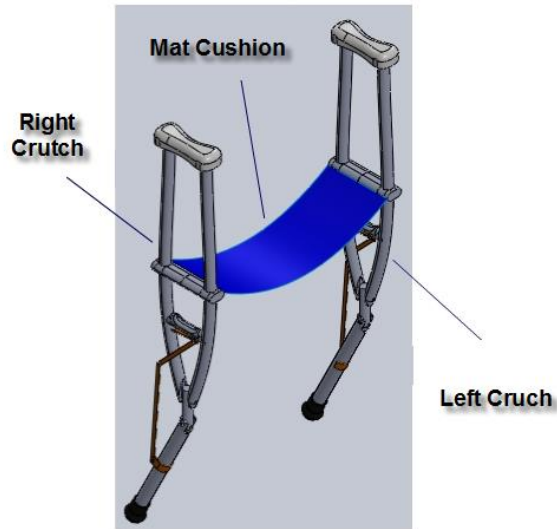


Fig 4. Complete system

Static alignment of the prosthesis was performed on stand position. The hip joints were spaced with a 40 cm dimension between outside edges and positioned to provide full support. The joint on the crutch allow flexion-extension, free degree of movement for adduction and two thigh segments to achieve a support the arm and axilla. The prosthesis is 80 cm from hip joints to floor on extended position and knee center system is located at 50 cm.

The prosthesis was laminated with carbon fibers and acrylic resin. The pad affixed of the cushion provided an air chamber to release pressures to the distal residual limb.

The finished prosthesis is seen in Figure 4. Before regular use, training is necessary, is possible gaitting in natural way.

The socket was further modified to provide relief to the right and left movement and the transverse process of stand-up process.

## V. REHABILITATION

The patient's rehabilitation goals included training for short distances for specific activities of daily living such as stand up

and gait without the use of a wheelchair. In addition, the design helped maintain the extension posture moment at the hips necessary to maintain balance when standing.[19],[20]

The designed system was dynamically assessed in sitting and standing to provide maximum balance and stance stability. The articulate crouch provided additional trunk stability on gait process and sitting balance. Training Exercises may include planar and diagonal sit-ups in supine and upper trunk extension in prone and supine positions. [21],[22],[23],[24]

All activities incorporate compensatory movement patterns to enhance functional gait abilities. [21],[22],[23]

Trunk support through a mat is provided. The system also enhanced lateral trunk motion. The flex sections were design to achieve a level base while long-sitting on the floor.[24],[25] Upright balance activities must be performed while wearing the prosthesis in natural way. Rehabilitation for standing is initiated in parallel bars for musculoskeletal system improve, progressing from bilateral upper-extremity support with the design system to independent standing and gait. [26],[27]

Balance is challenged by movement of arms, and the trunk. Training begins in the parallel bars and progresses to forearm crutches system. He progressed with forearm crutches for distances of up indoors and short distances outside. Pressure points are monitored during the training. [28],[29],[30],[31],[32]

## VI. CONCLUSION

Functional goals of the system design were met through the careful fitting and dynamic design of the prosthesis in response to self-mobility for paraplegics patients with Bilateral Hip Disarticulation

The initial effort in this case was to get the patient erect at a normal sitting height and provide gait opportunity. Patient could be supported under his ribs with our hands while another prosthetics balanced his upper trunk.

With the prosthesis the patient is able to live independently for mobility actions. A solid support system is important to recovery from any hip disarticulation problem. The support comes from a design system for mobility to release friends and family from this responsibility.

The decision to proceed with a design of prosthesis for bilateral hip replacement can be a very practical one. Recovery from a bilateral hip replacement can be difficult. From practical point of view at the beginning is very difficult to maneuver, for this reason it is necessary a specific training to control the designed system. The final design system allows patients with bilateral hip replacement to perform mobility in natural way.

## REFERENCES

- [1] Coley BL, Higinbotham NL, Romieu C: Hemipelvectomy for tumors of bone: Report of fourteen cases. *Am J Surg* 1951; 82:27-43.
- [2] Dankmeyer CH Jr: Prosthetic management of adult hemicorporectomy and bilateral hip disarticulation amputees. *Orthot Prosthet* 1981; 35:11-18.
- [3] Davis BP, Warner R, Daniel R, et al: The problem of fitting a satisfactory prosthesis following hemipelvectomy. *Inter-Clin Info Bull* 1964; 3:5-9.
- [4] Desio MA, Leonard JA: Above-knee prosthesis for hip disarticulation (abstract). *Arch Phys Med Rehabil* 1986; 67:667-668. Foort J: Construction and fitting of the Canadian-type hip-disarticulation prosthesis. *Artif Limbs* 1957; 4:39-51.
- [5] Foort J. Some experience with the Canadian-type hip-disarticulation prosthesis. *Artif Limbs* 1957; 4:52-70.
- [6] Friedmann L. Comments and observations regarding hemipelvectomy and hemipelvectomy prosthetics. *Orthot Prosthet*; 21:271-273.
- [7] Giaccone V, Stack D. Temporary prosthesis for the hip-disarticulation amputee. *Phys Ther*; 57:1394-1396.
- [8] Gillis L: A new prosthesis for disarticulation at the hip. *J Bone Joint Surg*; 50:389-391.
- [9] Glatly HW: A preliminary report on the amputee census. *Artif Limbs* 1963; 7:5-10. Greene M: Four bar knee linkage analysis. *Orthot Prosthet*; 37:15-24.
- [10] Hampton F: A hemipelvectomy prosthesis. *Artif Limbs*; 8:3-27.
- [11] Hampton F: A Hemipelvectomy Prosthesis. Chicago, Northwestern University Prosthetic Research Center, p 32.
- [12] Huang CT: Energy cost of ambulation with Canadian hip disarticulation prosthesis. *J Med Assoc State Ala*; 52:47-48.
- [13] Hutter CG: Improved type of hip-disarticulation on prosthesis. *J Bone Joint Surg [Am]*; 35:745-748.
- [14] Imler C, Quigley M: A technique for thermoforming hip disarticulation prosthetic sockets. *J Prosthet Orthot*; 3:34-37.
- [15] Iwakura H, Abe M, Fujinaga H, et al: Locomotion of the hemipelvectomy amputee. *Prosthet Orthot Int*; 3:111-114.
- [16] Jay GR, Sabolich L: A bilateral above-knee/hip disarticulation fitting. *Inter-Clin Info Bull*; 11:9-12.
- [17] Jensen JS, Mandrup-Poulsen T: Success rate of prosthetic fitting after major amputations of the lower limb. *Prosthet Orthot Int*; 7:119-122.
- [18] Lehneis HR, et al: Prosthetics Management for High Level Lower Limb Amputees. New York, Institute of Rehabilitation Medicine.
- [19] Leppanen RE: A temporary prosthesis for hip disarticulation. *Phys Ther*; 49:987-990.
- [20] Littig DH, Lundt JE: The UCLA anatomical hip disarticulation prosthesis. *Clin Prosthet Orthot*; 12:114-118.
- [21] Lyquist E: Canadian-type socket for a hemipelvectomy. *Artif Limbs*; 5:130-132.
- [22] The flexible socket system as applied to the hip disarticulation amputee. *Orthot Prosthet* ; 39:44-47.
- [23] Marx HW: Some experience in hemipelvectomy prosthetics. *Orthot Prosthet*; 00:259-270.
- [24] McLaurin CA: Hip Disarticulation Prosthesis, Report No. 15. Toronto, Canada, Prosthetic Services Centre, Department of Veterans Affairs
- [25] Pinzur MS, et al: An easy-to-fabricate modified hip disarticulation temporary prosthesis (technical note). *Orthot Prosthet*; 40:58-60.
- [26] Radcliffe CW: The biomechanics of the Canadian-type hip-disarticulation prosthesis. *Artif Limbs*; 4:29-38.
- [27] Sabolich J, Guth T: The CAT-CAM-HD. A new design for hip disarticulation patients. *Clin Prosthet Orthot*; 12:119-122.
- [28] Shurr DG, Cook TM, Buckwalter JA, et al: Hip disarticulation: A prosthetic follow-up. *Orthot Prosthet*; 37:50-57.
- [29] Simons BC, Lehman JF, Taylor H, et al: Prosthetic management of hemicorporectomy. *Orthot Prosthet*; 22:63-68.
- [30] Solomonidis SE, Loughran AJ, Taylor J, et al: Biomechanics of the hip disarticulation prosthesis. *Prosthet Orthot Int*; 1:13-18.
- [31] Van der Waarde T: Ottawa experience with hip disarticulation prostheses. *Orthot Prosthet*; 38:29-33.
- [32] Waters RL, et al: Energy costs of walking of amputees: The influence of level of amputation. *J Bone Joint Surg [Am]*; 58:46.

# Authors Index

Abdollahi, G.	257	Jarmin, R.	238	Pavlovsky, V. E.	46
Abdulkadir, E.	173	Jatsun, S. F.	34, 46	Penchev, D. M.	160
Acar, N. C.	150	Javadi, S.	277	Pereverzev, V. A.	194, 223
Adamidis, G. A.	178	Júnior, R. S.	133	Pogosov, D. B.	60
Agrawal, G.	40	Kalyaev, I. A.	146	Polenov, M. Y.	194
Ahn, K. H.	78, 228	Kang, H.	283	Pomarico-Franquiz, J.	286
Amamra, A.	88, 111	Kania, B.	214	Pshikhopov, V. K.	60, 94, 169
Aouf, N.	88, 111	Kavicharan, M.	251, 272	Pyavchenko, A. O.	194, 223
Aperador, W.	314	Kho, D. C. C.	209, 268	Rahim, S. K. A.	173
Archambault, P. S.	27, 51	Kim, E.-H.	283	Rahman, M. H.	27, 51
Ayob, M. A.	139	Kim, K.-J.	78, 228	Rahman, T. A.	173
Baghdarghi, B.	257	Kircay, A.	204	Rao, N. B.	251, 272
Bagherzadhalimi, A.	98	Kirilov, S.	190	Rosa, S. L.	173
Biolek, D.	65	Kolka, Z.	65	Saad, M.	27, 51
Biolkova, V.	65	Kong, B.-S.	219	Salim, M. I. M.	209, 268
Bobál, V.	105, 121	Kostadinov, K. G.	160	Saprykin, R. V.	194, 223
Borekci, S.	150	Kotev, V. K.	160	Savitsky, A. V.	46
Chakravarthy, Y. K.	296	Kubalčík, M.	105	Sen, O. A.	247
Chalupa, P.	105	Kumar, R. H.	296	Shaikh-Husin, N.	115
Chernukhin, Y. V.	194, 223	Kurnicki, A.	214	Shanin, D.	169
Choi, S.-W.	219	Kurt, G.	247	Shin, Y.-I.	293
Chufistov, V.	94	Lee, J. H.	303	Shmaliy, Y. S.	286
Cruciani, S.	56	Lee, Kw.	283	Silva, J. R.	133
Deepika, B.	296	Lee, Kh. Y.	238	Slasten, L. M.	146
Derbel, N.	71	Lee, S.-H.	78, 228	Song, C. K.	293
Di Maria, E.	98	Levin, I. I.	146	Souza, J. A. L.	133
Dordopulo, A. I.	146	Lim, H.-W.	219	Srinath, A.	296
Dostal, P.	82, 105, 121	Líška, O.	201	Stanczyk, B.	214
Dostrašil, P.	155	Mahani, Z.	309	Supriyanto, E.	115, 139, 173
Edelmoser, K. H.	127	Mahjoub, S.	71	Supriyanto, E.	209, 268
El Bahi, H.	309	Marek, O.	233	Surakusumah, R. F.	139
Emelyanova, O. V.	46	Marsono, M. N.	115	Svarny, J.	184
Esa, S. F. M.	238	Medvedev, M.	94, 169	Talarico, C.	40
FardAmiri, M.	277	Miyagi, P. E.	133	Tampouratzis, M. G.	178
Faudzi, A. A. M.	209, 268	Mladenov, V.	190	Tei, Y. Z.	115
Feliziani, M.	56	Mnif, F.	71	Toprak, A.	247
Feriančík, M.	201	Moscato, L. A.	133	Torres, M. P.	314
Ferrarezi, R. C.	133	Mouats, T.	88	Vojtěšek, J.	82, 121
Filho, D. J. D. S.	133	Murthy, N. S.	251, 272	Vorochayev, A. V.	34
Gudkov, S. V.	146	Myint, Y. M.	209, 268	Vorochayeva, L. Y.	34
Guzik, V. P.	194, 223	Novak-Marcincin, J.	164	Wang-Roveda, J.	40
Hamiane, M.	264	Novakova-Marcincinova, L.	164	Yahyazadeh, R.	257
Han, S. G.	293	Ochoa-Luna, C.	27, 51	Yi, J. H.	243
Hashempour, Z.	257	Ozbay, E.	247	Yoon, C. H.	293
Hau, Y. W.	115	Pahl, C.	139, 209, 268	Zatni, A.	309
Himmelstoss, F. A.	127	Park, J. H.	303	Zhao, S.	286
Janak, M.	164	Park, S.	78, 228		